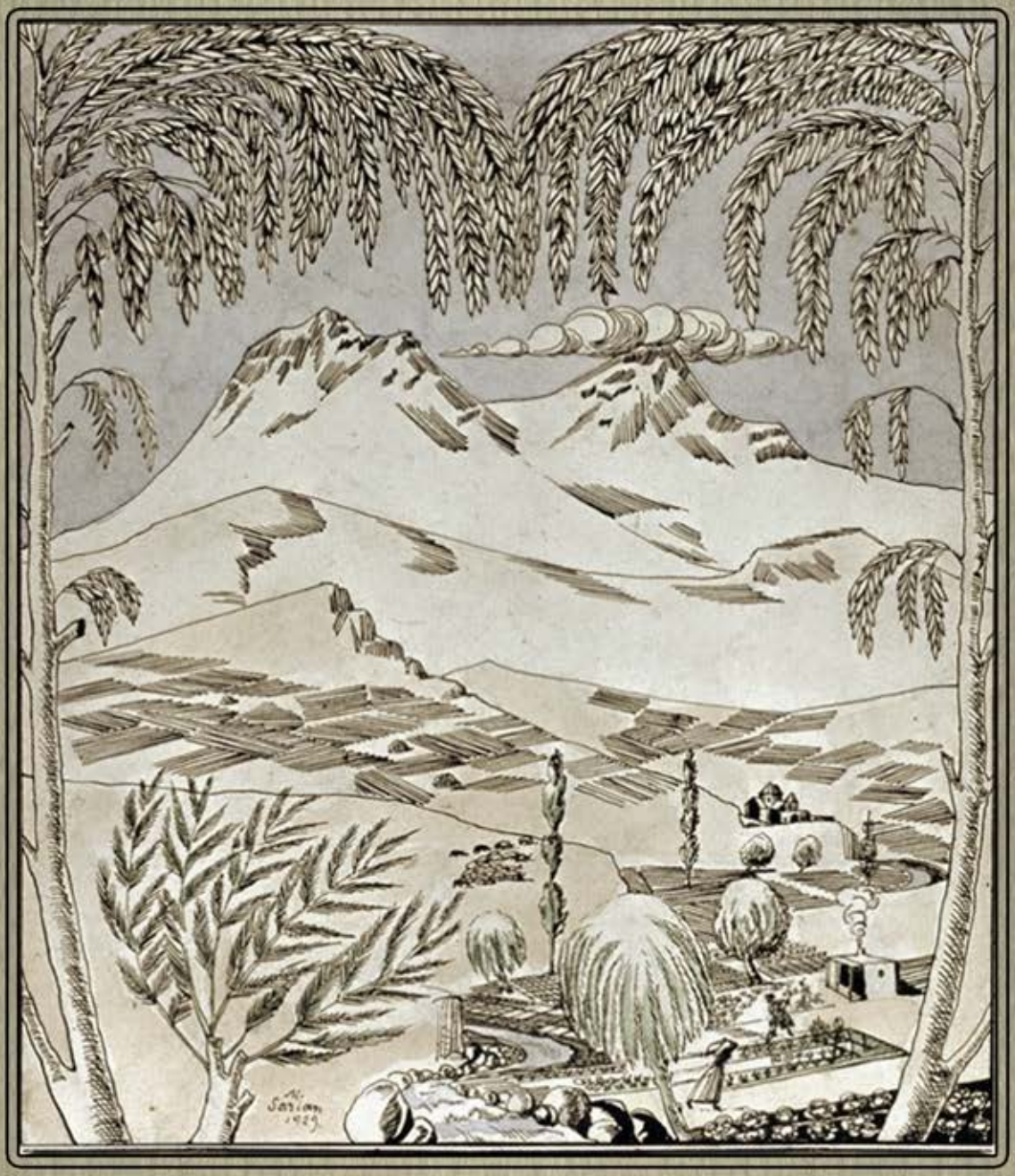
Sarian
1929

# *Prof. Ashot Chilingarian*

## *SELECTED PUBLICATIONS*

### *PART 2 (1989-2018)*

*Cosmic Ray Division, Yerevan Physics Institute*

*YEREVAN - 2018*

**C O N T E N T**

*I counted my years and realized that I have less time to live by, than I have lived so far. I feel like a child who won a pack of candies: at first, he ate them with pleasure but when he realized that there was little left, he began to taste them intensely. I have no time for endless meetings where the statutes, rules, procedures and internal regulations are discussed, knowing that nothing will be done.*

*I no longer have the patience to stand absurd people who, despite their chronological age, have not grown up. My time is too short: I want the essence; my spirit is in a hurry. I do not have much candy in the package anymore.*

*I want to live next to humans, very realistic people who know how to laugh at their mistakes and who are not inflated by their own triumphs and who take responsibility for their actions. In this way, human dignity is defended and we live in truth and honesty. It is the essentials that make life useful.*

*I want to surround myself with people who know how to touch the hearts of those whom hard strokes of life have learned to grow with sweet touches of the soul. Yes, I'm in a hurry. I'm in a hurry to live with the intensity that only maturity can give. I do not intend to waste any of the remaining desserts. I am sure they will be exquisite, much more than those eaten so far.*

*My goal is to reach the end satisfied and at peace with my loved ones and my conscience. We have two lives and the second begins when you realize you only have one.*

*Mario de Andrade*

*Я подсчитал свои годы и понял, что у меня меньше времени на жизнь, чем уже прожито. Я чувствую себя ребенком, которому подарили коробку конфет: сначала он ел их быстро одну за другой, но, когда он понял, что осталось немного, он начал их смаковать.*

*У меня нет времени для бесконечных встреч, где обсуждаются законы, процедуры и внутренние правила, зная, что ничего не будет сделано. У меня больше нет терпения противостоять абсурдным людям, которые, несмотря на свой физический возраст, остались неразвитыми духовно.*

*Мое время уходит: я хочу понять сущность вещей; мой дух торопится. У меня больше нет конфет в коробке. Я хочу жить рядом с людьми, простыми людьми, которые умеют смеяться над своими ошибками и не кичатся своими успехами, которые несут ответственность за свои действия. Которые понимают, что такое человеческое достоинство и живут в истине и честности. Это основное, что делает жизнь хоть немного осмысленной.*

*Я хочу окружить себя людьми, которые знают, как прикасаться к сердцам тех, кого тяжелые удары жизни научили чувствовать чуткие движения души. Да, я спешу. Я спешу жить с интенсивностью, которую может дать только зрелость. Я не собираюсь растрачивать последние десерты. Я уверен, что они будут изысканными, гораздо содержательнее, чем те, что поглощал до сих пор. Моя цель - довести до конца удовлетворение и мир с моими близкими и моей совестью.*

*У нас две жизни, а вторая начинается, когда вы понимаете, что у вас есть только одна.*

*Марио де Андраде*

# SCIENTIFIC BIOGRAPHY OF ASHOT CHILINGARIAN

Professor Ashot Chilingarian is the Head of Cosmic Ray Division (CRD) of A.Alikhanyan National laboratory (Yerevan Physics Institute, YerPhI).

Dr. Chilingarian earned his Ph.D. in 1984 and Doctorate of Science in Physics and Mathematics in 1991 from YerPhI. From 1971 to 1993 he was a scientist, senior scientist and data analysis group leader at the Yerevan Physics Institute. In 1993 Ashot Chilingarian became the deputy director of Yerevan Physics Institute, as well as head of the Cosmic Ray Division, in 2008 – 2017 was director of the Yerevan Physics Institute.

Prof. A. Chilingarian has a vast experience in high-energy astrophysics, cosmic ray physics, machine learning, data acquisition, multivariate statistical data analysis, space weather, atmospheric electricity and lightning physics. He has made substantial contribution to the measurement of cosmic ray composition and energy spectrum using facilities on Mt.Aragats, Armenia and in Karlsruhe, Germany. He developed advanced analysis methods for the photon shower identification for Cherenkov telescopes in gamma ray astronomy, which substantially enhanced the sensitivity of the gamma ray imaging telescopes.

In 80-ths, Prof. A. Chilingarian developed methodology of machine learning for high-energy physics and astrophysics experiments. He is the author of the ANI (Analysis and Nonparametric Inference) computer code library, which has been extensively used during the last few decades for multidimensional analysis of data from modern cosmic ray detectors. He introduced the "multidimensional nonlinear cuts" method for analyzing data

from the Atmospheric Cherenkov Telescopes (ACT); these techniques help to reliably proof existence of the flux of very high-energy gamma rays from the Crab nebula measured by the Whipple Cherenkov telescope thus establishing the new window to the Universe. The methodology of the event-by-event analysis of the Extensive Air Shower experiments, introduced by him allows the estimation of the energy spectra of the separate groups of primary nucleolus; the partial spectra of primary cosmic rays measured by MAKET-ANI and KASCADE detectors prove the mass-dependent position of the knee and helps to develop particle acceleration models in Supernovae explosions now confirmed by gamma ray observatories on board of AGILE and FERMI satellites. A.Chilingarian introduced a new probability distribution for calculation of chance probability for the "peak" detection in searches of "new physics", which will help to avoid fake inference usually occurred when dealing with small statistics and applying multiple cuts.

New statistical models developed by A.Chilingarian, i.e. new multivariate methods of probability density local estimation, Bayesian and neural network models of particle classification and background rejections plays key role in data analysis from most important high-energy astrophysics experiments on the particle acceleration in Universe and on gamma ray sources of very high energy. In a new topic of high-energy physics in atmosphere, Aragats group first time detects correlated large fluxes of electrons, gamma rays and neutrons from thunderclouds.

Outside his field, Prof. Chilingarian has been interested in applying his data analysis methods to pattern recognition and genome analysis. In 2000-2001 he collaborated with the Huntsman cancer institute in Utah, USA to develop multivariate methods of DNA micro-array data treating based on quantification of different types of gene expression in normal and tumor-affected tissues. This work culminated in a patent application by Utah University.

The main scientific results of Ashot Chilingarian are as follows:

- Discovery of the features of Galactic Cosmic Ray spectra such as: the very sharp change of the power spectral index (~1) for the light nucleus group at 2-4 PeV and no pronounced change in the heavy nucleus group (at least for energies 20-30 PeV). Discovery of the charge depended "knee" in the energy spectra pointing to the shock acceleration initiated by the supernova blasts as a most probable mechanism of particle acceleration.
- Discovery of energetic protons (with energies greater than 20 GeV) accelerated in the vicinity of the Sun on 20 January 2005 during Ground Level Enhancement (GLE) event N 69.
- Discovery of simultaneous fluxes of electrons, gamma rays and neutrons measured at mountain altitudes, proving the existence of the new high-energy phenomenon (so called Thunderstorm Ground Enhancements - TGEs) in the thunderstorm atmospheres.
- Discovery of the "Cloud extensive showers - CESs" – extended showers initiated in thunderclouds by the electrons accelerated in cloud electrical fields – first direct evidence of the Relativistic Runaway Electron Avalanches (RREA) in the terrestrial atmosphere.
- Discovery of long lasting radiation from the thunderclouds (up to several hours) that radically changed fundamental perception of the atmospheric natural radioactivity.
- Development of the Aragats Space Environmental center (ASEC) and Armenian geophysics measurements network. Both are equipped with various particle detectors, field meters and meteorological stations for monitoring of ionization radiation, disturbances of geomagnetic and electric field and lightnings.

- Founding of the worldwide network of new particle detectors for researches in space weather and solar physics, named SEVAN (Space Environment Viewing and Analysis Network). Nodes of the SEVAN network are now operating in Armenia, India, Bulgaria, Croatia and Slovakia.
- Introducing of new model of lightning initiation;
- Founding of Armenian Geophysics Network in 6 location of Armenia and Arcakh.

Connected to these discoveries are many international publications in peer-reviewed journals as Physical Review (Phys.Rev), Astroparticle physics, Atmospheric Research, Nuclear Instruments and Methods in Physics, Advances in Space Research, and many others. The value of the presented work is excellent and is absolutely honoured by the scientific community, which is evidenced by more than 5000 citations.

Currently he is Armenia's representative to the International Space Weather Initiative. He is the founder and spokesperson for the ANI and ASEC collaborations, and fellow of the American Physical Society, associate editor of the Space Weather and Space Climate (SWSC) journal and serves as reviewer for many international periodicals.

Prof. Chilingarian has authored ~350 scientific publications (with about 50 in the last 5 years) and served on many international scientific and editorial boards. His scientific activities are outstanding in Armenia and especially the atmospheric and lighting research work is world leading. His group is by far the most prolific science group in Armenia. Prof. Chilingarian has been chairperson of several international conferences, such as "Solar Extremely Events" (SEE-2005), "Forecasting Of the Radiation and Geomagnetic Storms" (FORGES 2008), "Thunderstorm and Elementary Particle Acceleration" (TEPA-2010-2018) and given numerous presentations in the fields of high energy and cosmic ray physics and high-energy phenomena in the atmosphere.

Award: "Data Visualisation Interactive Network for the Aragats Space-environmental Center" – *DVIN for ASEC* received the World Summit on Information Society award, in Geneva, in December 2003, as the world's best project in the category of e-science.

Armenia president award in Physics: High Energy Phenomena in the Thunderstorm Atmosphere (2013).

Nomination as best reviewer of Astroparticle physics and Advances in Space Research, Elsevier Journals, 2014;

Armenian Engineers and Scientists of Americas (AESA's) Scientist of the Year Award – 2017;

First prize of the competition of best scientific publications, Institute of Space Research, Russian Academy of science, 2017.

His current interests include the galactic and solar cosmic ray origin and acceleration, atmospheric electricity and lightning phenomena, detection of secondary cosmic ray fluxes at the Earth's surface, space weather and space climate. Solar particles interact with the magnetosphere, ionosphere and the atmosphere, thus influencing the near-Earth environment and abruptly changing the "space weather", seriously impacting space-born and Earth-based technologies, including telecommunication, navigation, disaster warning, weather forecasting, military systems, etc. Therefore, it is of big importance to study space weather to be able to create reliable forewarning services.

Currently, Prof. Chilingarian is continuing his research projects on Aragats Space Environmental Center and dealing with the following research topics:

1. Research of the high-energy physics in Earth's atmosphere (Aragats research station of YerPhI); High-energy physics in the atmosphere is a new science branch investigated fluxes of elementary particles originated from the relativistic electrons accelerated in strong electric fields of the thunderstorms. Fluxes of particles are directed both to open space where they are detected by orbiting gamma ray

observatories and to the Earth's surface. The largest facilities on the earth's surface detecting electrons, gamma rays and neutrons (TGEs) as well as radio bursts, electric fields, lightning flashes are located on Aragats in Armenia.

2. Lightning initiation and relation of particle fluxes and atmospheric discharges. The problem of the thundercloud electrification and how lightning is initiated inside thunderclouds is one of the biggest unsolved problems in atmospheric sciences. The relationship between thundercloud electrification, lightning activity, wideband radio emission and particle fluxes have not been yet unambiguously established

Modern science is impossible without a large-scale scientific cooperation; therefore the involving of the young researchers in the international projects from the very beginning is a very important aspect of the education process, which is taken by Prof. Chilingarian accordingly very serious: his new master courses for the new generation of students in Space Education center of YerPhI (courses) has a special emphasis on participation in current international research projects of the institute. Prof. Chilingarian is professor and co-director of Armenian - Russion laboratory of atmospheric research at National Research Nuclear University MEPhI (Moscow Engineering Physics Institute). Recently he joins the Scientific Advisory Committee of the EU project "Research Center of Cosmic Rays and Radiation Events in the Atmosphere, CRREAT".

Collaborative work with DESY on preparation of CTA experiment and with MAGIC on atmospheric research as well as with the Institute for Data Processing and Electronics in Karlsruhe (IPE, KIT) on development of the platform for multivariate data analysis are such joint projects, where lively international knowledge exchange and long-time experience gained through the practical work on Aragats provide a fruitful ground for better understanding of cosmic rays impact on Earth's atmosphere.

Under supervision of Prof Chilingarian, operations of the research at the Aragats research facilities could be secured and further national funds could be triggered and activated to support the research, which is an asset to Armenia, and a shining example of clever use of limited means to do internationally competitive science. The research on Aragats is an important signal to the young generation in Armenia, that research is a viable and worthwhile endeavour at their home country. Prof Chilingarian has always managed to attract a sizeable group of young scientists working on cosmic rays and atmospheric electricity. New students generation educated in frame of the master program lead by Prof Chilingarian and strongly involved in joint projects with International community will for sure contribute for further discovering in the research field concerning the galactic, solar and atmospheric cosmic ray.

Available online at www.sciencedirect.com
ScienceDirect
Advances in Space Research 44 (2009) 1183–1193
ADVANCES IN SPACE RESEARCH (a COSPAR publication)
www.elsevier.com/locate/asr

# Cosmic Ray research in Armenia

A. Chilingarian [a,*], R. Mirzoyan [b], M. Zazyan [a]

[a] Cosmic Ray Division, Yerevan Physics Institute, Alikhanyan Brothers St. 2, Yerevan 36, Armenia
[b] Max-Planck-Institute for Physics, Foehringer Ring 6, 80805 Munich, Germany

Received 4 March 2008; received in revised form 12 November 2008; accepted 14 November 2008

Dedicated to 100th anniversary of Artem Alikhanyan, born in 1908.

**Abstract**

Cosmic Ray research on Mt. Aragats began in 1934 with the measurements of East–West anisotropy by the group from Leningrad Physics-Technical Institute and Norair Kocharian from Yerevan State University. Stimulated by the results of their experiments in 1942 Artem and Abraham Alikhanyan brothers organized a scientific expedition to Aragats. Since that time physicists were studying Cosmic Ray fluxes on Mt. Aragats with various particle detectors: mass spectrometers, calorimeters, transition radiation detectors, and huge particle detector arrays detecting protons and nuclei accelerated in most violent explosions in Galaxy. Latest activities at Mt. Aragats include Space Weather research with networks of particle detectors located in Armenia and abroad, and detectors of Space Education center in Yerevan.


*Keywords:* Cosmic Rays; Particle detectors; Space weather; History of physics

## 1. Introduction

Particles of highest energies bombarding Earth's atmosphere provide vast information on the most violent processes in the Universe. One of the "main players" reflecting physical processes in stellar systems are particles and stripped nuclei arriving at Earth from interstellar space and from Sun. These are known under the name of Galactic and Solar Cosmic Rays (GCR and SCR). Cosmic Rays (CR) were discovered almost 100 years ago by the ionization effects of the secondary fluxes (particle showers), produced by the interactions of primary particles in the terrestrial atmosphere. Exploiting different physical processes of shower interactions with atmosphere (particle multiplication, fluorescence, Cherenkov light emission in atmosphere and in water, acoustic waves, and radio waves emissions) different experimental techniques were developed to detect cosmic rays above and on the Earth's surface, underground and underwater. Fifty years ago with the launch of the first satellite on 4 October 1957 experiments in space directly detected primary cosmic rays and confirmed that our nearest star, the Sun, is a particle accelerator.

Direct measurements of particle fluxes by facilities onboard satellites and balloons provide excellent charge and energy resolutions but, due to the severe limitation of payload and the progressively weaker flux of higher energy CR, can perform measurements mostly in KeV–GeV energy region. In TeV–PeV region only surface based techniques of detecting secondary particle showers can provide data on energy and types of primary particles, although with an uncertainty inherent to indirect methods, based on the extensive use of numerical models and simulation techniques.

One of the first permanent high-mountain research stations was established in Armenia 65 years ago. The *Aragats* and *Nor-Amberd* research stations of the Cosmic Ray Division (CRD) of the Yerevan Physics Institute (YerPhI) named after Alikhanyan are located on slopes of Aragats, the highest mountain of modern Armenia (see Figs. 1 and

* Corresponding author.
*E-mail address:* chili@aragats.am (A. Chilingarian).

0273-1177/$36.00 © 2009 COSPAR. Published by Elsevier Ltd. All rights reserved.
doi:10.1016/j.asr.2008.11.029

Fig. 1. Aragats research station (altitude 3200 m).

Fig. 2. Abraham Alikhanov (left) and Artem Alikhanyan.

4), at 3200 and 2000 m elevation, respectively. The scientific history of Cosmic Ray research at Aragats can be traced back to 1934 when a group from Leningrad Physics-Technical Institute and Norair Kocharian from Yerevan State University (YSU),[1] measured the East–West cosmic ray anisotropy (Kocharian, 1940). These measurements stimulated the interest of famous physicists, the brothers Artem and Abraham Alikhanyan (see Fig. 2), who organized a scientific expedition to Aragats in 1942. Since then, expeditions on Aragats continued uninterruptedly, in spite of the World War II, insufficient funding, and electricity and fuel shortages during the recent history of Armenia.

In the 40s and the 50's the cosmic rays were the main source of information about the properties of elementary particles. Later CR research has lead to new, modern branches of physics named "Astroparticle Physics", "High Energy Astrophysics" and "Space Weather". The most important dates and achievements of Cosmic Ray research at Aragats can be itemized as follows:

- 1942 – First expedition to Aragats;
- 1943 – Foundation of the Physical–Mathematical Institute of Yerevan State University; now Yerevan Physics Institute after Artem Alikhanyan;
- 1945–1955 – Foundation of Aragats high-mountain research station. Experiments at Aragats with mass spectrometer of Alikhanyan–Alikhanov: investigations of the composition of secondary CR (energies <100 GeV); exploration of the "third" component in CR; observation of particles with masses between μ-meson and proton;
- 1957 – Installation of the ionization calorimeter, detection of particles with energies up to 50 TeV;
- 1960 – Foundation of the Nor-Amberd high-mountain research station;
- 1970 – Modernization of the Wide-gap Spark Chambers;
- 1975 –Experiment MUON: measurements of the energy spectrum and charge ratio of the horizontal muon flux;
- 1975 – Installation of the Neutron supermonitors 18NM64 at Aragats and Nor-Amberd research stations;
- 1977 – Experiment PION: measuring pion and proton energy spectra and phenomenological parameters of CR hadron interactions;
- 1981–1989 – ANI Experiment: Commence of MAKET-ANI and GAMMA surface detector arrays for measuring cosmic ray spectra in the "knee" region ($10^{14}$–$10^{16}$ eV);
- 1985–1992 – Design and tests of the system of atmospheric Cherenkov telescopes, introduction of multivariate methods for signal detection from γ-ray point sources;
- 1993–1996 – Development of new methodology of multivariate, correlation analysis of data from Extensive Air Shower detectors, event-by-event analysis of shower data from KASCADE experiment; classification of primary nucleus;
- 1996–1997 – Renewal of cosmic ray variation studies at Aragats: installation of the solar neutron telescope and resumption of Nor-Amberd neutron monitor;
- 2000 – Foundation of Aragats Space Environmental Center (ASEC) – for Solar Physics and Space Weather research; measurements of the various secondary fluxes of cosmic rays; inclusion of the large surface arrays in monitoring of the changing fluxes of secondary cosmic rays;
- 2003 – Detection of intensive solar modulation effects in September–November in the low energy charged particle, neutron and high energy muon fluxes;
- 2004 – Measurement of the spectra of heavy and light components of GCR, observation of very sharp "knee" in light nuclei spectra and absence of "knee" in heavy" nuclei spectra;
- 2005 – Measurements of highest energy protons in Solar Cosmic Rays (GLE 70 at 20 January; detection of Solar protons with $E > 20$ GeV);

[1] Later the first dean of the Physical Department of YSU.

- 2007 – Start of SEVAN (Space Environmental Viewing and Analysis Network) – a new type of world-wide network of particle detectors for monitoring of geophysical parameters.

## 2. The mass-spectrometric period of scientific research on Mt. Aragats

The history of scientific research on Mt. Aragats can be divided into several periods. The first – mass-spectrometric period – lasted about 15 years. Experiments with magnetic spectrometer designed by the Alikhanyan brothers lead to the discovery of protons in CR (Alikhanyan et al., 1945) and narrow air showers (Alikhanyan and Asatiani, 1945).[2] According to the viewpoint of that time, CRs were believed to have a pure electromagnetic origin (Anderson and Neddermeyer, 1937), therefore the presence of protons in CR strongly contradicted the established concepts. The origin of narrow showers could not be electromagnetic because of their great penetrability. Later narrow showers were thoroughly studied with the Aragats ionization calorimeter (Grigorov et al., 1958).

Using the Alikhanyan–Alikhanov magnetic spectrometer Kocharian obtained the energy spectra of muons and protons with energies up to several GeV (Kocharian et al., 1957). Till now this data remain one of the best measurements of the secondary cosmic ray fluxes at mountain altitudes.

The mass spectrometer method (see the picture of memorial magnet on Mt. Aragats in Fig. 3), performing the simultaneous measurement of the momentum and absorption length of charged particles, provided the effective particle mass analysis. This method presents the first evidence of the existence of particles with masses ranging from μ-meson to proton; however, only some of the many peaks in mass distributions measured at Aragats were later verified to be "real" particles and became known as π- and K-mesons. Other "particles" with masses heavier than μ-meson, including so called varitrons (Alikhanyan and Alikhanov, 1951), "discovered" using the Aragats mass spectrometer, turned to be artifacts due to fluctuations in the mass distributions. Nonetheless, the discussion on varitrons led to several excellent experimental and theoretical investigations and Alikhanyan brothers' idea about a variety of elementary particles became very popular among physicists all over the world, making the Aragats research station one of the most important centers of cosmic ray physics. It should be mentioned that defining the reliability of peaks in one- and two-dimensional distributions is still one of the most important and complicated problems in High Energy Physics and Astrophysics. Also nowadays that are many groups using sophisticated mathematical methods cannot avoid mistakes and reported discoveries based on the fake peaks (see for example discussion about "discovery" of pentaquark in Seife, 2004).

[2] Tina Asatiani, employee of YerPhI since 1943, is emeritus staff member of CRD.

Fig. 3. The memorial magnet of the Alikhanov–Alikhanyan spectrometer, erected on the entrance of the Aragats research station.

## 3. Calorimetric measurements on Mt. Aragats

The second phase of scientific research on Mt. Aragats, calorimetric measurements, covers the period from 1958 to 1970. The mass spectrometric method had reached its energy limit by that time. In 1958 a group of scientists from the Institute of Nuclear Physics of Moscow State University and Yerevan Physics Institute (team leader – Naum Grigorov) installed the first ionization calorimeter at Aragats station (Grigorov et al., 1958). Experiments with ionization calorimeter at Aragats proved the energy-dependence of the effective inelastic cross-section of the hadron interaction with nuclei. This fact was later confirmed by direct measurements on Proton satellites (Grigorov et al., 1970) and accelerator experiments. The ionization calorimeter also detected another interesting result concerning the peculiarities of multiparticle production of high energy pions (Babayan et al., 1965), which was later (1990) registered as a discovery in USSR: in some cases only few $\pi^0$-mesons, generated in the interaction with atmospheric nuclei, "takes away" almost the entire energy of the primary particle. The authors of this discovery were Babayan (deputy-director of YerPhI from 1956–1969), Naum Grigorov, Erik Mamijanyan (head of Cosmic Ray Division of YerPhI in 1969–1992) and Vladimir Shestoperov.

The Nor-Amberd station, which started operation in 1960 (see Fig. 4) at altitude 2000 m, considerably enlarged the possibilities for studying high energy cosmic ray hadrons and their interaction with different nuclei (head of laboratory in 1960–1986 – Gerasim Marikyan).

At that time physicists from various scientific institutions of the Soviet Union participated in the investigations on the Armenian mountains, also scientists from USA,

Fig. 4. Nor-Amberd research station (altitude 2000 m).

France, Japan and Great Britain visited high altitude stations.

The method of wide-gap spark chambers was intensively investigated in YerPhI in late 50-s. The prestigious Lenin Prize was awarded to Artem Alikhanyan and Tina Asatiani (head of muon laboratory of YerPhI in 1960–1987) in collaboration with groups of Russian and Georgian physicists for developing the wide-gap spark chamber techniques.

In 1968–1969 a system of proportional counters was added to the Aragats ionization calorimeter. Using this facility, the neutron component of cosmic rays at mountain altitude was measured by E. Mamijanyan and his colleagues (Azaryan et al., 1977).

Babayan in early 70-s started his research of CR variations by installing neutron supermonitors of 18NM64 type at Aragats and Nor-Amberd research stations, which served as a basis for creating a unique center of cosmic ray monitoring in the "new history" of Aragats.

## 4. High Energy Astrophysics

During the next period (1970–1980) experiments PION (Avakian et al., 1978) and MUON (Asatiani et al., 1980) measured fluxes of secondary cosmic rays and some phenomenological characteristics of strong interactions. The team leaders of the experimental groups were Vahram Avakyan (head of Aragats station from 1963 to 1993) and Tina Asatiani, respectively. PION was a unique facility (Alikhanyan et al., 1974), which included transition radiation detection system for particle identification, created by Albert Oganesian's group (head of laboratory from 1978 to 1996) and an ionization calorimeter for particle energy estimation.

The muon magnetic spectrometer for studying near-horizontal high energy muons was equipped with coordinate measuring systems based on the wire spark chambers and wide-gap spark chambers, thus increasing the range of reliable muon momentum measurement up to $\sim$2.5 TeV/c. Both experiments used modern numerical algorithms and on-line computers for data analysis. One of the first soviet computers M220 was used to calculate horizontal muon energy spectrum. The PION experiment used the first Armenian minicomputer NAIRI-2 for data acquisition.

In 80s it became clear that larger detectors are necessary for the research of primary cosmic ray fluxes. The planned ANI experiment on Mt. Aragats (Danilova et al., 1982) met all these requirements. It was intended to register electrons and muons of Extensive Air Showers (EASs) by a system of surface scintillators; interactions of hadrons from EAS core with the world's largest calorimeter (surface area 1600 $m^2$); high energy muons by a huge underground muon detector and huge magnetic spectrometer (area 40 $m^2$). The ANI experiment was designed in cooperation with the Lebedev Physics Institute of USSR Academy of Science under the guidance of USSR Ministry of Medium Machinery (presently, Federal Nuclear Energy Agency of the Russian Federation). The experiment leaders were Sergey Nikolsky (director of the Division of Nuclear Physics and Astrophysics of Lebedev Physics Institute) and Erik Mamijanyan.

The ANI complex was not completed because of the collapse of the USSR, followed by the collapse of the Armenian economy, but 2 surface particle arrays MAKET-ANI (Fig. 5, experiment leader Gagik Hovsepyan, see details in Chilingarian et al., 2007) and GAMMA (Fig. 6, experiment leader Romen Martirosov, see details in Garyaka et al., 2002) made significant contribution to the "knee" region physics.

For selecting the proper model of the CR origin one has to measure the partial energy spectra of the different groups of primary nuclei, i.e. perform classification of the primary nuclei from largely smeared EAS information content. These very complicated tasks became feasible after the development of the nonparametric multivariate methodology of data analysis by Ashot Chilingarian in 1989.[3]

Event-by-event-analysis of EAS data, using Bayesian and Artificial Neural Network (ANN) information technologies (Chilingarian, 1989, 1994) helped to obtain the energy spectra of light and heavy primary nuclei from MAKET-ANI experiment and also three partial spectra, corresponding to light, intermediate and heavy nuclei groups from KASCADE experiment (Antoni et al., 2003, 2005). MAKET-ANI data (Chilingarian et al., 2004, 2007) demonstrates the existence of a sharp knee in the light component, and no evidence of knee in the heavy component up to $\sim 3 \times 10^{16}$ eV (see Fig. 7). The available data from other experiments confirm these results. In the KASCADE experiment, the position of the knee shifts towards higher energies with increasing mass number (Apel et al., 2006). In HEGRA experiment (Horns and Rohring, 2001) a steepening of the light mass group spectrum was detected. In EAS-TOP (Aglietta et al., 2004) the light nuclei

[3] Head of CRD since 1993.

Fig. 5. MAKET-ANI surface detector, Aragats research station.

Fig. 6. GAMMA surface array, Aragats research station.

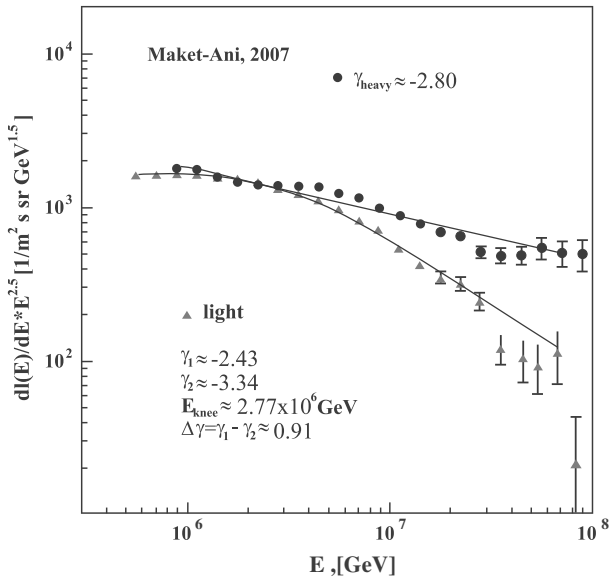


Fig. 7. Differential spectra of light and heavy nuclei groups of primary flux as measured by the MAKET-ANI surface array.

group also demonstrate sharp knee. Therefore, EAS evidence on the galactic CR origin consists in establishing charge proportional to acceleration of CR that is in general agreement with the model of shock acceleration in the blast waves of supernovae explosions. Further observations made by orbiting in space gamma-ray observatories and ground-based Atmospheric Cherenkov Telescopes (ACTs) also point on the Supernovae Remnants (SNR) as one of the major cosmic ray sources.

After publishing the final papers the MAKET-ANI detector ceased operation in 2007. The scintillators are used now for monitoring changing fluxes of low energy charged CRs. Arrangement was made also for making a test facility for the new precise timing system for a new large EAS array for measuring CRs far beyond the knee, now under consideration at CRD.

*Direct evidence* of shock acceleration in SNR shells can be deduced from joint detection of young SNRs in X and $\gamma$-rays. To prove that the young supernovae remnant RX J1713.7-3946 is a very efficient proton accelerator Uchiyama with colleagues (Uchiyama et al., 2007) include in the analysis information on broadband X-ray spectra (from 0.4 to 40 KeV) measured by the Suzaku satellite (Takahashi et al., 2008) and on high energy $\gamma$-ray spectra (extending over 10 TeV) measured by HESS Imagining Atmospheric Cherenkov Telescope (IACT) (Aharonyan et al., 2007). They exclude the inverse Compton origin of detected high energy $\gamma$-quanta, and taking into account the Tev–KeV correlations validate the hadronic model of detected $\gamma$-rays. Thus, the joint analysis of X-ray maps from Chandra and X-ray spectra from Suzaku satellites with high energy $\gamma$-ray spectra measured by HESS ACT provide very strong argument for the acceleration of protons and nuclei of 1 PeV and beyond in young SNR shells.

Armenian physicists have a significant impact in the development of the ACT technique. Pioneering system of IACTs "on the Canary island of La Palma" (HEGRA) followed by large IACTs HESS in Namibia and MAGIC on the Canary island of La Palma designed and operated by international collaborations with the participation of Armenian physicists.

In 1985 design and construction of the first system of five IACTs for the ANI experiment on the mountain Aragats started by YerPhI. The telescopes comprised tessellated reflectors of 3 m diameter and 37-pixel imaging cameras. The pixel construction was based on FEU-130 type Soviet PMTs of bialkali photocathode and GaP first dynode. High quality glass mirrors with quartz protection, equatorial mounts of the telescopes with drive electronics, the imaging cameras and the DAQ electronics also were produced by different workshops of YerPhI. The gamma ray group was lead by Felix Aharonyan and Razmik Mirzoyan. The group started measuring cosmic ray signals at Nor-Amberd research station and calibrating the telescope for the first measurements of the Crab Nebula when the collapse of the former Soviet Union stops experimental activities. Fortunately, the Armenian scientists togethers

with German physicist Alkoffer have developed a program for installing the same system of ACTs on a newly created High Energy Gamma Ray Astronomy (HEGRA) cosmic ray detector on the Canary island of La Palma. Already prepared devices and materials for the construction of the five telescopes have been shifted from Armenia via Germany to La Palma and the construction started in 1991. In 1992 the first HEGRA telescope measured gamma rays from Crab Nebula (see Mirzoyan et al., 1994).

That was the first significant confirmation of the discovery of the 10 m diameter Whipple telescope in Arizona, USA. In 1993 second telescope was build and operated in stereo mode with the first one and later on four more telescopes were added to the system. The HEGRA telescopes were operated until 2002 and provided a rich harvest of gamma sources. The contribution of Armenian physicists in HEGRA was very significant because of their leading role both in the techniques of IACTs as well as their theoretical work on the very frontier of gamma astronomy.

After termination of HEGRA the astrophysicists from the collaboration continued to build new advanced instruments. Already in 1994 the 17 m diameter MAGIC telescope, intending to investigate gamma rays below 300 GeV down to energies of 30 GeV was proposed by Razmik Mirzoyan. An international collaboration was formed and in 1998 it became an official project in Max-Planck-Institute of Physics (MPI) in Munich. YerPhI and several institutions in Germany, Spain, Italy, Switzerland and Finland became member of the MAGIC collaboration. The first MAGIC telescope was built in La Palma in 2001–2003 and has been in operation since 2004. The second MAGIC telescope was built 85 m distance from the first one and since recently is operating together with the first one.

The other part of HEGRA collaboration continues its research with 10 m diameter class telescopes, with advanced optics and electronics. A new array, initiated in 1997 by Felix Aharonyan, under the name H.E.S.S., is comprised of four telescopes of 12 m diameter and was built by an international collaboration, mostly from Germany and France, in Namibia in 2001–2003. Scientists from YerPhI also became member in H.E.S.S. H.E.S.S. collaboration intends to complete their array with one 28 m diameter very large telescope in 2010.

The number of VHE gamma sources increased from $\sim$20 to more than 80 just in 3–4 years and very interesting publications, more than 100 by now, appeared in peer refereed journals, also in such famous ones as Science and Nature. It is expected that both instruments together with VERITAS from USA will increase the number of sources to $\sim$100 just in the next 2–3 years and finally long-standing questions of Cosmic Rays, Astrophysics, and Astroparticle physics can be understood and answered.

## 5. Solar Physics and Space Weather research

Cosmic Rays are accelerated not only in the depths of galaxies but also by our nearest star, the Sun. Strong solar flares sometimes accelerate particles in the Mev–GeV range to intensities more than the total galactic flux reaching terrestrial atmosphere. Solar particles interact with the magnetosphere, ionosphere and the atmosphere, thus influencing the near Earth environment and abruptly changing the "space weather", seriously impacting space-born and Earth-based technologies. Space Storms can harm astronauts in space and cause excessive radiation exposure for aircraft crew. Space weather changes very fast, the intensity of X-ray radiation and particles of high energies can greatly increase in a few seconds. Protons and nuclei, which penetrate microscopic electronic devices create additional currents and change the state of the electronic circuits, generating false commands and damaging on-board management systems. Electron fluxes, rushing through the atmosphere, create polar flares and induce currents in surface conductors, which cause pipeline corrosion and damage transformers at electric stations. Our civilization heavily depends on space-based technologies, including telecommunication, navigation, disaster warning, weather forecasting, military systems, etc. For this reason, Space Weather research attracts more and more scientists. At the end of last century USA, Canada, Europe and Japan adopted national programs to study space weather and to create reliable forewarning services. CRD physicists are contributed to this important endeavor.

Starting in 1996 we have been developing various detectors to measure fluxes of different components of secondary cosmic rays. In 1996 we restarted our first detector – the Nor-Amberd neutron monitor 18NM64. A similar detector started to take data at the Aragats research station in autumn 2000 (Tsuchiya et al., 2001). A Solar Neutron Telescope (SNT) has been in operation at the Aragats research station since 1997, as part of the world-wide network coordinated by the Solar-Terrestrial laboratory of Nagoya University (Chilingarian and Reymers, 2007). In addition to the primary goal of detecting the direct neutron flux from the Sun, the SNT also has the ability to detect charged fluxes (mostly muons and electrons) and roughly measure the direction of the incident muons. Another monitoring system is based on the scintillation detectors of the Extensive Air Shower (EAS) surface arrays, MAKET-ANI and GAMMA, located on Mt. Aragats. The charged component monitoring system at the Nor-Amberd research station started operation in 2002. Our Data Acquisition (DAQ) system was modernized in 2005. Modern electronics was designed to support the combined neutron-muon detector systems as well as measurement of the environmental parameters (temperature, pressure, humidity). Microcontroller-based DAQ systems and high precision time synchronization of the remote installations via Global Positioning System (GPS) receivers are crucial ingredients of the new facilities on Mt. Aragats. Information on changing secondary particle fluxes, measured by hundreds of detecting channels, is used for the enumerating solar modulation effects during large solar explosions.

The Aragats Space Environmental Center (ASEC, Chilingarian et al., 2003, 2005) operating since 2000, provided detailed coverage of the violent events of the 23rd solar activity ending in 2008. One of the most exciting results obtained recently at Mt. Aragats is the discovery of protons of highest energies (greater than 20 GeV) accelerated on the Sun during space-era largest Ground Level Enhancement (GLE) (Bostanjyan et al., 2007; Chilingarian and Reymers, 2007). On 20th of January 2005, during the recovery phase of the Forbush decrease a long lasting X-ray burst occurred near the west limb of the Sun (helio-coordinates: 14N, 67W). The start of the X7.1 solar flare was at 06:36 and maximum of the X-ray flux at 7:01. The fastest (relative to X-ray start time) GLE event of 23rd cycle was detected by space-born and surface particle detectors a few minutes after the flare onset. The start of GLE was placed at 6:48; the maximal amplitude of 5000% recorded by NM at the South Pole is the largest increase ever recorded by neutron monitors. ASEC monitors detected significant excess of count rates at 7:00–8:00 UT. From 7:02 to 7:04 UT, the Aragats Multichannel Muon Monitor (AMMM) detected a peak with a significance of $\sim 4\sigma$. It was the first time that we detected a significant enhancement of the >5 GeV muons coinciding with the GLE detected by the world-wide networks of neutron monitors. Detailed statistical analysis of the peak (Chilingarian, 2009) proves the non-random nature of the detected enhancement. This short enhancement (see Fig. 8) exactly coincides in time with peaks from Tibet neutron monitor (Miyasaka et al., 2005), Tibet solar neutron telescope (Zhu et al., 2005) and the Baksan scintillator surface array (Karpov et al., 2005), see Fig. 8. Another surface array (GRAND, located in Western hemisphere) demonstrated a very large peak ~10 min earlier (D'Andrea and Poirier, 2005).

The differential energy spectrum of the SCR protons at 7:02–7:04 UT measured by the space-born spectrometers and surface particle detectors covers more than 3 orders of magnitude from 10 MeV to 20 GeV and demonstrates very sharp "turn-over" at 700–800 MeV. The energy spectrum remains very hard up to ~800 MeV (with power index ~−1) and extended until tens of GeV with a power index between ~−5.

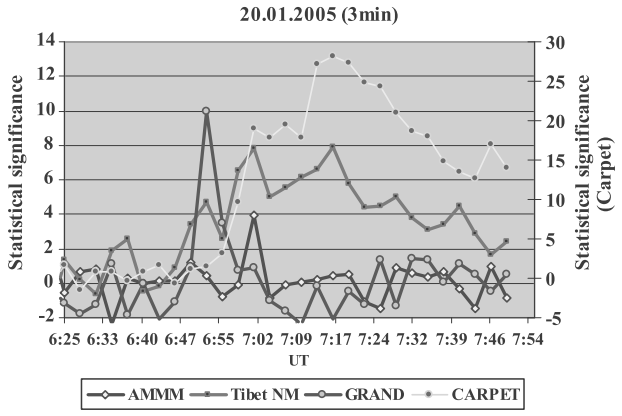


Fig. 8. Time series of muon detectors and neutron monitors detected GLE at 20 January, 2005. Note the peak at 7:02 detected by CARPET surface array, (most probable energy ~10 GeV), Tibet NM (most probable energy ~13 GeV) and AMMM (most probable energy >20 GeV).

## 6. CRD space education center

Artem Alikhanyan, whose 100th anniversary was celebrated on July 9, 2008 at Nor-Amberd station, was not only a brilliant scientist, but also an experienced educator. In early 60s when the international contacts were still suppressed by soviet authorities, he initiated the famous Nor-Amberd schools, where problems of High Energy and Elementary Particle Physics were discussed. Experienced, prominent and young scientists from many countries participated in the activities of these schools. This tradition has been preserved up to the present days. CRD organizes in its Yerevan headquarters the Space Educational Center, where lectures on High Energy Astrophysics, Cosmic Rays and Modeling of Physical processes are followed by experimental work in teaching laboratories, where students work with modern particle detectors and data acquisition electronics.

CRD developed an advanced Space Weather information product: Data Visualization Interactive Network (DVIN) for the Aragats Space Environmental Center. This product aims at visualizing scientific information about radiation conditions on Earth caused by the strong radiation and geomagnetic storms from the sun. DVIN was officially announced as the world's best project in the e-science category at the World Summit on Information Society (WSIS) in Geneva in 2003. On June 10, 2005 DVIN was declared the winner of the Pan-Armenian e-content Mashtots 1600 competition.

Students work with the DVIN package, revealing peaks in time series of Aragats monitors, enumerating the significance of the peaks and decide upon the physical nature of these abrupt enhancements of particle fluxes.

CRD is organising annual international symposia devoted to Solar Physics and Space Weather research. During the week of September 26–30 2005, 75 scientists and students from 11 countries attended the second conference on Solar Extreme Events (SEE-2005) in Nor-Amberd, Armenia. Conference reports included information on consequences of Solar Extreme Events and Super Storms, the most violent explosions in the Solar System. The participants became acquainted with the ASEC monitors and capabilities of the Armenian physicists who created the Aragats Space Environmental Center. In September 28–October 3, 2008 an international symposium on *Fo*recasting of the *R*adiation and *Ge*omagnetic *S*torms by networks of particle detectors (FORGES-2008) took place in Nor-Amberd (Chilingarian, 2008).

## 7. Future plans

Currently Aragats is a modern scientific center, equipped with key scientific equipment and necessary sup-

porting infrastructure, which is constantly being updated. Information on changing fluxes of secondary cosmic rays is distributed world-wide to numerous CRD collaborators. Modern science is impossible without *large-scale* scientific cooperation. This cooperation is especially important for cosmic ray physics, which relies on data obtained with detectors located at different longitudes and latitudes all over the Earth, to develop a model of the solar-terrestrial connections. Aragats and Nor-Amberd Neutron monitors are a part of the world-wide network of neutron monitors, solar neutron telescopes and muon detectors.

Recently 12 countries of Europe decide to form joint data base for 1-min counts from neutron monitors (NMBD), supported by European FP7 programme. The joint project of muon detectors is currently implemented in collaboration with Germany, Switzerland and Israel. CRD initiated the development of a new world-wide particle detector network called "Space Environment Viewing and Analysis Network" (SEVAN) – (Chilingarian and Reymers, 2008; Chilingarian et al., 2009). The United Nations Office of Outer Space Affairs and the International Heliophysical Year (IHY) have launched a small instrument programme as one of United Nations Basic Space Science (UNBSS) activity. SEVAN Network aims to improve the fundamental research on particle acceleration in the vicinity of sun and in space environment conditions. The new type of particle detectors will simultaneously measure changing fluxes of most species of secondary cosmic rays, thus turning into a powerful integrated device for exploration of solar modulation effects. The first SEVAN modules are under test at the Aragats Space Environmental Center in Armenia, in Croatia and Bulgaria. The network will grow in 2009 with detectors deployed in Slovakia and India. Research groups from these countries participated in training on detector operation and data analysis during FORGES-2008 symposium.

The basic detecting unit of the SEVAN network (see Fig. 9) is assembled from standard slabs of $50 \times 50 \times 5\ cm^3$ plastic scintillators. Between two identical assemblies of $100 \times 100 \times 5\ cm^3$ scintillators (four standard slabs) are located two $100 \times 100 \times 5\ cm^3$ lead absorbers and thick $50 \times 50 \times 25\ cm^3$ scintillator assembly (five standard slabs). A scintillator light capture cone and Photo Multiplier Tube (PMT) are located on the top, bottom and in the intermediate layer of the detector. Incoming neutral particles undergo nuclear reactions in the thick 25 cm plastic scintillator and produce protons and other charged particles. In the upper 5 cm thick scintillator charged particles are detected very effectively; however for the nuclear interactions of neutral particles there is not enough substance. When a neutral particle traverses the top thin (5 cm) scintillator, usually no signal is produced. The absence of the signal in the upper scintillators, coinciding with the signal in the middle scintillator, points to neutral particle detection. The coincidence of signals from the top and bottom scintillators indicates the traversal of high energy muons. Lead absorbers microcontroller-based DAQ electronics

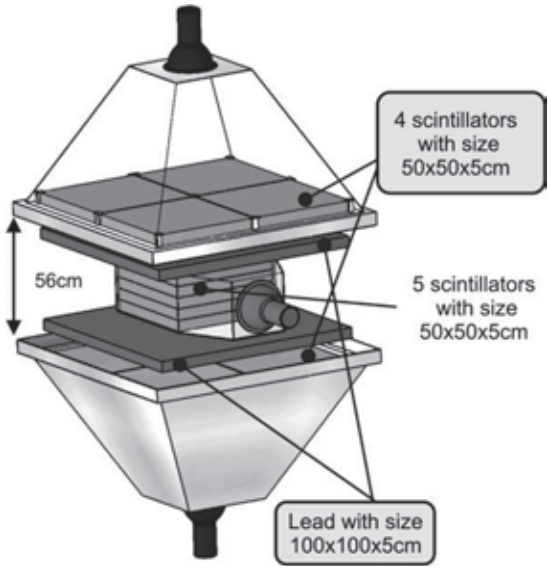


Fig. 9. Layout of basic model of SEVAN network.

and an Advanced Data Analysis System (ADAS) provide registration and storage of all logical combinations of the detector signals for further off-line analysis and for on-line alerts. The special ADAS sub-system allows the remote control of the PMT high voltage and of other important parameters of the DAQ electronics.

The network of hybrid particle detectors, measuring neutral and charged fluxes provide the following advantages over existing detector networks measuring single species of secondary cosmic rays:

- Enlarged statistical accuracy of measurements.
- Probe different populations of primary cosmic rays with rigidities from 7 GV up to 20 GV.
- Reconstruct SCR spectra and determine position of the spectral "knees".
- Classify GLEs in "neutron" or "proton" initiated events.
- Estimate and analyze correlation matrices among different fluxes.
- Significantly enlarge the reliability of Space Weather alerts due to detection of 3 particle fluxes instead of only one in existing neutron monitor and muon telescope world-wide networks.

A new trend in Astrophysics research is in the observation of celestial objects in several wavelengths simultaneously (e.g. in radio, optical, X-ray, and gamma rays). A variety of complementary measurements give sufficient information for building and testing models of the galaxy formation, of supernovae explosions, of accompanying gamma-ray bursts, of accretion disc interactions with super-dense objects, and finally of the evolution of the Universe itself. The additional information about the particles of highest energies arriving at the Solar system significantly

enlarges the information on the most violent processes in the Universe.

Summarising the situation with investigation of the CR spectra in the energy interval lasting from $10^4$ until $10^{20}$ eV we can say:

Lowest energies in keV – tens of TeV region are rather well measured by space-born/air-born spectrometers located at satellites, space stations and balloons.
The "knee" region spectra from $10^{14}$ to $10^{17}$ eV has been well explored during last 40 years by the surface arrays covering thousands of square meters.
The ultra-high energy region – above $10^{19}$ eV – after pioneering research of Haverah Park, Volcano-Ranch, Yakutsk, AGASA and HIGHRES detectors took a mature state with AUGER-South observatory started to present valuable data, to be confirmed in next decade by an expected large volume of data.

This picture contain two obvious gaps in satisfactory well established spectra: $10^{13}$–$10^{14}$ eV; and $10^{17}$–$10^{19}$ eV. If first gap can be filled with planned long-duration balloon flight and experiments on the Space Station, the second can be filled only by several square kilometre size particle arrays.

Recently CRD physicist started to prepare proposal of new large EAS surface array with the *main scientific goal of measuring partial energy spectra of the cosmic rays in the poorly explored energy region of* $10^{17}$–$10^{19}$ eV. The aim of the project is to build a large detector for investigation of the mentioned energy region, using already operating particle detectors on the slopes of Mt. Aragats and by installing new hybrid particle detectors measuring neutral and charged CR secondary fluxes. The main physical task *is* determination of the contribution of the extragalactic CR component to give a consistent description for the entire GCR spectrum after the "knee".

The energy region of $10^{17}$–$10^{19}$ eV is still poorly explored and the origin of the extragalactic cosmic rays is still mystery. To measure partial energy spectra (spectra of "light" and "heavy" nuclei groups) a very large area of EAS detection is required (at least several square kilometers). The optimal altitude (to measure maximal number of particles in EAS) is ~2000 m. above sea level. At these altitudes the EAS from primary proton with energy $10^{18}$ eV will produce $6 \times 10^8$ electrons. Therefore, also taking into account very severe climatic conditions at the altitude of 3200 m. at Aragats station, we propose to build the new large EAS detector in Nor-Amberd – Burakan region. We plan to use new type of hybrid particle detectors measuring electron, muon and neutron contents of EAS at 2 sites, separated by ~3.5 km, at Nor-Amberd research station and in the Antarut village (see Fig. 10).

Project objectives include:

- Development of a new-generation particle detector for measuring neutral and charged CR fluxes and their directions.


Fig. 10. NewANI EAS array planned at slopes of Aragats Mountain.

- Creation of a particle detector network for continuous detection of cosmic rays in the energy range $10^{17}$–$10^{19}$ eV.
- Determination of the characteristics of the "iron knee".
- Search for point sources of cosmic rays.
- Investigation of the "fine structure" of the partial energy spectra.

Two networks of particle detectors will be formed around the central part of ~ 20 $m^2$ hybrid particle detectors (see Fig. 8). Each array will be completed with detectors as soon as particle detectors are commissioned and assembled. The third site will be formed by the particle detectors of MAKET-ANI and GAMMA EAS arrays operating at Aragats research station of Alikhanyan Physics Institute. All three sites have total area ~0.35 $km^2$, and will detect primary particles with energies up to several units of $10^{17}$ eV (trigger conditions and corresponding EAS core collecting area will be obtained via Monte-Carlo simulations).

Huge events triggering 2 arrays out of 3 will indicate primary energies above $10^{19}$ eV. EAS core collection area will be ~15 and 75 $km^2$ correspondingly for 2 and 5 km radii circles.

Basic detectors tests and deployments started in 2008; with appropriate funding in 2011 new EAS detector will

be equipped with enough modules for enlarging the investigated energy range up to $10^{18}$ eV.

Cosmic Ray research in the energy range of $10^{17}$–$10^{19}$ eV is a continuation of the MAKET-ANI and GAMMA arrays energy domain of $10^{14}$–$10^{17}$ eV, thus providing continuous partial energy spectra in the energy range covering 5 orders of magnitudes where almost all the significant features of energy spectra are taking place. No operating or planned surface array is intended to cover this very important and large energy domain: the KASCADE energy limit is $\sim 10^{18}$ eV, the energy range of HiRes and Auger is starting from $5 \times 10^{18}$ eV. Therefore the proposed detector will provide unique information extending the already well investigated low energy domain with the enigmatic highest energy domain.

Among other projects started on Aragats we can mention planned correlated measurements of the disturbances of geomagnetic field and changes of secondary particle fluxes by starting precise measurements of the Earth's magnetic field and electric fields. First measurements are planned in fall of 2009.

The next project is connected with registrations of radio burst on the sun by a network of antennas. Outbursts of plasma and shocks on the sun accelerate electrons, which in turn produce the radio signal. The same strong shock must also accelerate atomic nuclei in the solar wind, which produce the radiation storm. Since the radio signal moves at the speed of light while the particles lag behind, we can radio signals from the sun to give warning that it is generating a radiation storm that will hit us soon. In collaboration with Hartmut Gemmeke from research center Karlsruhe, we started measurements of radio-noise at slopes of Aragts to select the best place to install a network of radio antennas for solar burst monitoring.

## 8. Conclusion

The CRD staff includes approximately 80 people, who work at the Aragats and Nor-Amberd high altitude stations and at the headquarters in Yerevan where most of the data analysis and computation takes place. Many of the staff members are young graduate students or recent postgraduates. Scientific research on Mt. Aragats is constantly searching for new methods and new frontiers as the Armenian physicists do their best in the quest of solving the mysteries of the Universe.

## Acknowledgements

We thank the former and the present CRD employees for their dedicated work at Aragats as well as our collaborators and supporters all over the world.

## References

Aglietta, M., Alessandro, B., Antonioli, P., et al. The primary cosmic ray composition between 10**15 and 10**16 eV from Extensive Air Showers electromagnetic and TeV muon data. Astropart. Phys. 20, 641–652, 2004.

Aharonyan, F.A., Akhperjanian, A.G., Bazer-Bachi, A.R., et al. Primary particle acceleration above 100 TeV in the shell-type supernova remnant RXJ1713. 7 – 3446 with deep HESS observations. Astron. Astrophys. 464, 235–243, 2007.

Alikhanyan, A.I., Alikhanov, A.I., Nikitin, S. Highly ionizing particles in soft component of cosmic rays. J. Phys. 9, 175–182, 1945.

Alikhanyan, A.I., Asatiani, T.L. Investigation of Auger showers. J. Phys. 9, 167–174, 1945.

Alikhanyan, A.I., Alikhanov, A.I. Varitrons. J. Exp. Theor. Phys. 21, 1023–1044 (in Russian), 1951.

Alikhanyan, A.I., Avakian, V.V., Mamidjanyan, E.A., et al. A facility for identification of the hadrons with energy 300 GeV with transition radiation detector. Proc. Soviet Acad. Sci. Phys. Ser. 38, 1993–1995 (in Russian), 1974.

Anderson, C.D., Neddermeyer, S.H. Note on the nature of cosmic-ray particles. Phys. Rev. 51, 884, 1937.

Antoni, T., Appel, W.D., Badea, F., et al. The cosmic-ray experiment KASCADE. Nucl. Instrum. Methods A 513, 490–510, 2003.

Antoni, T., Appel, W.D., Badea, F., et al. KASCADE measurements of energy spectra for elemental groups of cosmic rays: results and open problems. Astropart. Phys. 24, 1–25, 2005.

Apel, W.D., Asch, T., Badea, A.F., et al. The LOPES collaboration. Astropart. Phys. 26, 332–340, 2006.

Asatiani, T.L., Chilingarian, A.A., Kazaryan, K., et al. Investigation of characteristics of high-energy cosmic ray muons. Proc. USSR Acad. Sci. Ser. Phys. 45, 323, 1980.

Avakian, V.V., Mamidjanyan, E.A., Oganessyan, A. Experimental facility for investigation of interaction of cosmic ray hadrons with use of transition radiation detector. Proc. Soviet Acad. Sci. Phys. Ser. 40, 1058 (in Russian), 1978.

Azaryan, M.O., Zazyan, M.Z., Mamidjanyan, E.A. On the albedo particles in hadron–nuclear interactions at energies above 1 TeV. J. Nucl. Phys. 26, 141 (in Russian), 1977.

Babayan, Kh.P., Grigorov, N.L., Mamidjanian, E.A., et al. Investigation of the interactions of hadrons with energy ~1 TeV with ionization calorimeter. Proc. Soviet Acad. Sci. Phys. Ser. 30, 1652–1656 (in Russian), 1965.

Bostanjyan, N.Kh., Chilingarian, A.A., Karap-etyan, G., et al. On the production of highest energy solar protons on 20 January 2005. Adv. Space Res. 39, 1456–1459, 2007.

Chilingarian, A.A. Statistical decisions under nonparametric a priory information. Comput. Phys. Commun. 54, 381–390, 1989.

Chilingaryan, A.A. Neural classification technique for background rejection in high energy physics experiments. Neurocomputing 6, 497–512, 1994.

Chilingarian, A.A., Avagyan, K., Babayan, V., et al. Aragats Space-Environmental Center: status and SEP forecasting possibilities. J. Phys. G Nucl. Part Phys. 29, 939–952, 2003.

Chilingarian, A.A., Arakelyan, K., Avagyan, K., et al. Correlated measurements of secondary cosmic ray fluxes by the Aragats Space Environmental Center monitors. NIM A 543, 483–496, 2005.

Chilingarian, A., Gharagyozyan, G., Hovsepyan, G., et al. Light and heavy cosmic-ray mass group energy spectra as measured by the MAKET-ANI detector. Astrophys. J. 603, L29–L32, 2004.

Chilingarian, A.A., Hovsepyan, G.G., Melkymyan, L.G., et al. Study of extensive air showers and primary energy spectra by MAKET-ANI detector on mountain Aragats. Astropart. Phys. 28, 58–71, 2007.

Chilingarian, A.A., Reymers, A.E. Particle detectors in Solar Physics and Space Weather Research. Astropart. Phys. 27, 465–472, 2007.

Chilingarian, A.A. Statistical study of the detection of solar protons of highest energies at 20 January 2005. Adv. Space Res. 43, 702–707, doi:10.1016/j.asr.2008.10.005, 2009.

Chilingarian, A.A., Reymers, A. Investigations of the response of hybrid particle detectors for the Space Environmental Viewing and Analysis Network (SEVAN). Ann. Geophys. 26, 249–257, 2008.

Chilingarian, A.A. Forecasting of radiation and geomagnetic storms by Networks of Particle Detectors Workshop, Nor Amberd, Armenia, 29 September–3 October, 2008. Space Res. Today 173, 125–127, 2008.

Chilingarian, A., Avakyan, K., Arakelyan, K., et al. Space Environmental Viewing and Analysis Network (SEVAN) Earth, Moon, and Planets, doi: 10.1007/s11038-008-9288-1, 2009.

D'Andrea, C., Poirier, J. Ground level muons coincident with the 20 January 2005 solar flare. Geophys. Res. Lett. 32, L14102, doi:10.1029/2005GL023336, 2005.

Danilova, T.V., Dunaevsky, A.M., Erlykin, A.D., et al. A project of the experiment on the investigation of interactions of hadrons in the energy range$10^3$–$10^5$ TeV. Proc. Armenian Acad. Sci. Phys. Ser. 17, 129–132 (in Russian), 1982.

Garyaka, A.P., Martirosov, R., Eganov, V., et al. The cosmic ray energy spectrum around the knee measured with the GAMMA array at Mt. Aragats. J. Phys. G. Nucl. Part. 28, 231–2328, 2002.

Grigorov, N.L., Murzin, V.S., Rapoport, I.D. The method of measurement of the energy of particles in a region more than $10^{11}$ eV. J. Exp. Theor. Phys. 4, 506–523 (in Russian), 1958.

Grigorov, N.L., Nesterov, V.E., Rappoport, I.D. Measurements of particle spectra on the proton 1,2,3 satellites. J. Nucl. Phys. 11, 1058–1067 (in Russian), 1970.

Horns, D., Rohring, A. For the HEGRA collaboration, measurement of the energy spectrum of light cosmic rays with the HEGRA air shower array, in: Proceedings of the 27th ICRC, Hamburg, vol. 1, pp. 1091–1094, 2001.

Karpov, S.N., Karpova, Z.M., Balabin, Yu.V., Vashenyuk, E.V. Study of the GLE events with use of the EAS-arrays data, in: Proceedings of the 29th ICRC, Pune, India, vol. 1, pp. 193–196, 2005.

Kocharian, N.M. Investigation of the azimuth asymmetry of cosmic rays, in: Scientific studies of Yerevan State University, vol. 12, pp. 23–28, 1940 (in Russian).

Kocharian, N.M., Saakian, G.S., Aivazian, M.T. Energy spectra of μ-mesons on the altitude of 3200 m. Rep. Armenian Acad. Sci. 24, 344–348 (in Russian), 1957.

Mirzoyan, R., Kankanian, R., Krennrich, F., et al. The first telescope of the HEGRA air Cherenkov imaging telescope array. Nucl. Instr. Meth. A 351, 513, 1994.

Miyasaka, H., Takahashi, E., Shimoda, S., et al. The solar event on 20 January 2005 observed with the Tibet YBJ neutron monitor observatory, in: Proceedings of the 29th ICRC, Pune, India, vol. 1, pp. 245–248, 2005.

Seife, C. Rara avis or statistical mirage? Pentaquark remains at large. Science 306, 1281–1982, 2004.

Takahashi, T., Tanaka, T., Uchiyama, Y., et al. Measuring the Broadband X-ray spectrum from 400 eV to 40 keV in the southwest part of the Supernova Remnant RX J1713.7-3946.. Publ. Astron. Soc. Jpn. 60, S131–S162, 2008.

Tsuchiya, H., Muraki, Y., Masuda, K., et al. Detection efficiency of a new type of solar neutron detector calibrated by an accelerator neutron beam. NIM A 463, 183–193, 2001.

Uchiyama, Y., Aharonyan, F., Tanaka, T., et al. Extremely fast acceleration of cosmic rays in a supernova remnant. Nat. Lett. 449 (4), doi:10.1038/nature06210, 2007.

Zhu, F.R., Tang, Y.Q., Zhang, Y., et al. The Solar event on 20 January 2005 observed with the Tibet YBJ neutron monitor observatory, in: Proceedings of the 29th ICRC, Pune, India, vol. 1, pp. 185–188, 2005.

Computer Physics Communications 54 (1989) 381–390
North-Holland, Amsterdam



# STATISTICAL DECISIONS UNDER NONPARAMETRIC A PRIORY INFORMATION

A.A. CHILINGARIAN

*Yerevan Physics Institute, Markarian St., 2, SU-375036, Yerevan 36, Armenia, USSR*

Received 3 April 1988; in revised form 12 September 1988

A program is developed for simular and experimental data handling. The main purposes are: the choice of the model most precisely describing the experiment, classification of particles and interaction processes. Procedures used: Bayes error calculation, K nearest neighbour density estimation, "Leave-one-out-at-a-time" test. Used nonparametric methods provide quantitative comparison of multivariate distributions and distribution mixture classification. Applications: high energy physics, cosmic ray physics.

## PROGRAM SUMMARY

*Title of program*: KNN

*Catalogue number*: ABHS

*Program obtainable from*: CPC Program Library, Queen's University of Belfast, N. Ireland (see application form in this issue)

*Computer*: IBM 3090, EC 1045, PDP 11/70, IBM PC-AT

*Operating system*: VM/CMS, RSX, NORTON

*Programming language used*: FORTRAN 77

*No. of bits in a word*: 32, 16

*No. of lines in combined program and test deck*: 487

*Keywords*: Monte Carlo statistical inference, nonparametric methods, pattern recognition, multivariate analysis, Bayes risk estimation, probability density estimation, classification

*Nature of physical problems*
Choice of theoretical model most precisely describing experimental Data, extraction of events of a definite type, classification of particles and interaction processes.

*Nature of statistical problems*
Quantitative comparison of multivariate distributions, classification of distribution mixture, bump hunting, feature extraction.

*Procedures used*
Bayes decision making, "leave-one-out" test, K nearest neighbours (KNN) density estimation.

## LONG WRITE-UP

### 0. Introduction

The scientific method is characterized by data classification, the study of their interrelations and relations to past experience, summarized in various theories and hypotheses. Usually, it is impossible either to prove or to refute hypotheses by deductive method. The challenge is to draw sensible conclusions from noisy, discrepant information.

The main aspect of applied statistics is collection and interpretation of data, the interpretative aspect being the one that is now regarded as the essence of the subject [1]. The fundamental idea of statistics is that useful information can be acquired from individual small bits of data. Inductive methods lead to empirical statements, that may be connected with theoretical ones by means of rational inductive conclusion rules [2].

However, it is very important to provide the scientist with an objective criterion by which he can judge the claims of hypotheses (models) under investigation. By model we mean a complete probability statement of what currently is supposed to be known a priori about the mode of generation of data and of uncertainty about the parameters [3].

If this statement consists in the existence of an analytic distribution family (like Poisson or Gaussian), appropriate to the problem at hand, we have a prescribed parametric model. For such parametric models a well known concept of statistical inference consists in obtaining estimates of its parameters and verifying the validity of the chosen family [4].

We shall restrict ourselves to the binary comparison case, that is, comparisons of two from many competing hypotheses at a time. Our example concerns a case where we want to realize the choice of one of two well-defined hypotheses-cosmic ray hadron classification by means of a Transition Radiation Detector (TRD) [5].

The classification problem is traditionally described in terms of null and alternative hypothesis, critical and acceptance regions, and level of significance [6].

The best critical region is constructed by means of the Likelihood Ratio (LR),

$$\mathrm{LR}(x) = \frac{p(x/\theta_{\pi}^{*})}{p(x/\theta_{\mathrm{pr}}^{*})}. \tag{0.1}$$

Here $x$ is a many-dimensional observable, in our case the energy release in TRD layers. $p(x/\theta_{\pi}^{*})$ and $p(x/\theta_{\mathrm{pr}}^{*})$ are conditioned on particle type probability density functions, obtained separately for pions and protons. $\theta^{*}$ is a Maximal Likelihood Estimate (MLE)

$$\theta^{*} = \underset{\theta}{\mathrm{argmax}} \sum_{i=1}^{M} \ln\, p(x_i/\theta), \tag{0.2}$$

where set $\{x_i\}$, $i = 1,\ M$, is obtained from TRD callibration or, for superaccelerator energies, by simulation. $M$ is the number of callibration or simulation trials.

Leaving apart the question about effectiveness of MLE for finite samples [7], we want to check, whether the MLE method permits us to do a very powerfull summary of data – we are summarizing a $\{x_i\}$ dataset by a probability density. Maximal Likelihood Summary (MLS) can be used for comparative purposes [8].

But for almost all problems of inference, the crucial question is whether the fitted probability family is in fact consistent with the data. Usually parametric models are chosen for their statistical tractability, rather than for their appropriatness to the real process being studied.

Of course, any statistical inference is conditioned on the model used, and, if the model is oversimplified, so, that essential details are either omitted, or improperly defined, at best only qualitative conclusions may be done. Now, in cosmic ray and accelerator physics very sophysticated models are being used, completely mimicking a stochastic mechanism where by data is generated. An example of such models is the Geant3 system, designed for detector description, simulation and optimization studies [9], and models of cosmic radiation propagation through atmosphere and detectors [10].

Such models are defined on a more fundamental level than parametric models, and provide us with a wide range of outcomes from identical input variable sets- "labled", or "training" samples (TS). These sets of events with known membership representing a general, nonparametric mode of a priori information. For our example, we obtained samples, corresponding to pion and proton traversals through TRD, i.e. $\omega_\pi$ and $\omega_{\mathrm{pr}}$.

So, usually, for experimental physics data handling, the likelihood function cannot be written explicitly, and we deal with implicit, nonparametric models, for which no parametric form of underlying distribution is known, or can be assumed.

Although using simulation to analyse data in high energy physics is wide-spread, we are aware of very few systematic investigations of theoretical aspects about how data may be compared with its simulated counterpart [11,12]. What we need is a well defined technique, what one can call Monte-Carlo Inference.

The term "Monte-Carlo Inference" at first appeared in the discussion of the valuable paper by Diggle and Gratton, where analitically intractable model fitting facilities were established [13].

This present paper considers classification and hypothesis testing problems in the framework of Bayesian paradigm [14]. The inference problem in Baysian approach is similarly described in terms of $[X, \Theta, D, P_\theta, p(x/\theta), L(d, \theta)]$, where $X$ is an event (measurement, feature,...) space-collection of possible outcomes of random experiments, $\theta \ni \Theta$ is a parameter or index of various classes, types, hypotheses (further we shall denote these classes by $w_i$, or explicitely-by $w_{\mathrm{pr}}$ and $w_\pi$), $P_\theta$ is the prior density, $p(x/\theta)$ is the conditional density, $D$ is the decision space, containing possible decisions, and $L(d, \theta)$ is the nonnegative loss function, defined on $D \times \Theta$.

For our example specification of prior density and loss function meets no difficulties: $\Theta$-space includes two values pr and $\pi$, with prior probabilities $P_{\mathrm{pr}}$ and $P_\pi$, $(P_{\mathrm{pr}} + P_\pi = 1)$ which are obtained from a previous most confident experiment. If there is no such experiment, the uniform density can be used: $P_{\mathrm{pr}} = P_\pi = 0.5$.

For classification purposes a simple one to zero loss function is usually used: losses are equal to zero for a correct decision and one for any error.

## 1. Bayes decision rule, the measures of the closeness of empirical data and model

Bayssian approach provides the general method of incorporation of a priori and experimental information. Bayes theorem,

$$p(\omega_j/x) = \frac{P_j p(x/\omega_j)}{\sum_{i=1}^{L} P_i p(x/\omega_i)}, \tag{1.1}$$

gives us a posterior to the $x$-density, i.e. the probability of $w_j$-class(hypothesis) to be truth, if the $x$-value was observed, and before experiment the $P_j$ prior density was assumed. $L$ is the number of hypothesis under investigation.

The decision rule, that assigns observable $x$ to the class with the highest a posteriori density $w^*$ (Bayes decision rule), takes into account all usefull information and all possible losses due to any wrong decision,

$$w^* = \operatorname*{argmax}_i p(w_i/x), \quad i = 1, L. \tag{1.2}$$

For hadron classification Bayes decision rule takes the form

$$p(w_\pi/x) \lesseqgtr p(w_{pr}/x) \xrightarrow{\text{decision}} w^* \equiv \begin{cases} \mathrm{pr} \\ \pi \end{cases}. \tag{1.3}$$

So, the posterior density is the basis of statistical decisions on particle type and on simular and experimental data closeness. The term closeness refers to the degree of coincidence, similarity, correlation, overlapping or any such variable. Examples of these separability measures are the Kolmogorov variational distance (L1-metric) [15],

$$K_j = \int_X | p(\omega_{\mathrm{exp}}/x) - p(\omega_j/x) | \, \mathrm{d}x, \tag{1.4}$$

and the Bhattacharya distance (Hotteling coefficient),

$$B_j = \int_X \left( p(\omega_{\mathrm{exp}}/x) p(\omega_j/x) \right)^{0.5} \mathrm{d}x. \tag{1.5}$$

Another possibility to compare experimental and different model samples is the loglikelihood function estimation,

$$L_j = \sum_{i=1}^{M} \ln\, p(x_i/w_j), \tag{1.6}$$

where $p(x_i/w_j)$ is the probability density obtained with the $w_j$ training sample, corresponding to the $j$th class and $M$ is the number of observations.

The most convinient closeness measure, commonly used in pattern recognition problems for feature extraction [16], is Bayes error (Bayes risk for 0–1 loss function). Bayes classifier provides a minimum probability of error among all classifiers for the same feature set. The probability to misclassify the $x$ observable, using Bayes rule, is equal to

$$r(x) = 1 - p(w^*/x), \tag{1.7}$$

or, for our example,

$$r(x) = \min\{\, p(w_\pi/x),\ p(w_{\text{pr}}/x)\,\}. \tag{1.8}$$

Finally, Bayes error is determined by the expression

$$R = \int_X r(x)p(x)\,\mathrm{d}x, \tag{1.9}$$

where $p(x)$ is a mixture of distributions, representing the denominator of eq. (1.1).

However, it is impossible to calculate $R$ and other distance measures, as the analytic expression of conditional densities and, hence, the posterior ones, is unknown. Therefore, we are obliged to use their nonparametric estimates. Nonparametric in the sense, that the density function is not a particular member of a previously chosen parametric distribution family, but an estimate based only on sample information and on very mild conditions on the underlying density (usually only continuity).

The nonparametric density estimation will be considered further; now we shall gain some insight into the methods of using the training sample in the procedure of Bayes error calculation.

Three main methods are distinguished [17]: the resubstitution–P method: the classifier is both trained and examined on the same sample i.e., first the conditional densities $p(x/w_i)$ are determined by TS, and then classification is carried out with the same sample; the holdout–H method: the TS is divided into two equal parts, with one half for the training and the other for examination. The P-method decreased Bayes risk; the H, on the contrary, increased it. Besides that the H-method does not use the TS effectively.

The leave-one-out–U method is free of such defects. One element is removed from the sample, the training is performed without it, then this element is classified and replaced in the TS and the procedure is repeated, untill all the TS elements have been classified. The U–method (also refered to as the cross-validation method) has been shown to have a much smaller bias than other methods, and it seems to be insensitive to data departure from normality [18].

The empirical error count was one of the first suggested estimation procedures. Let us introduce a random variable,

$$\epsilon(x) = \begin{cases} 0, & \text{if } x \text{ is classified correctly,} \\ 1, & \text{otherwise.} \end{cases} \tag{1.10}$$

The empirical error $R^{\text{e}}$ is determined by

$$R^{\text{e}} = \frac{1}{M}\sum_{i=1}^{M} \epsilon(x_i) = \frac{\#_{\text{err}}}{M}, \tag{1.11}$$

where $\#_{\text{err}}$ is the number of errors, commited during leave-one-out test over TS.

The estimate variance equals

$$\sigma^2_{R^{\text{e}}} = \frac{1}{M} R(1-R). \tag{1.12}$$

Another type of estimate the so called average conditional error $R^{\text{p}}$, is connected with approximation of the expression (1.9),

$$R^{\text{p}} = \frac{1}{M}\sum_{i=1}^{M} \min\{\, p(w_1/x_i),\ p(w_2/x_i)\,\}. \tag{1.13}$$

It is interesting to note, that the variance of this estimate proves to be less, then that of the previous one,

$$\sigma^2_{R^{\text{p}}} = \frac{1}{M} R(1-R) - \frac{R}{2M}. \tag{1.14}$$

This result seems to be paradoxical, as in the second case the information on the $x$ observable true lables is not used. This contradiction is explained by the fact that $R^p$ takes on a continuum of values approaching $R$, while $R^e$ takes on only discrete values, this quantization causing larger spread around $R$.

Comparing of experimental and model data can be considered as a two stage process. At first, relevant features must be selected from all available measerments. The feature selection problem can be viewed as an optimization problem, requiring a criterion function and a search procedure. We do not deal with methods of optimal subset selection in this paper; suppose we have an heuristic procedure to generate probable subsets, then we recomend Bayes error as a criterion function. Of course, one can use any other separability measure, but Bayes error is most straightforward and its estimation methods for high dimensionality spaces are well develop. Calculating Bayes error for different subsets of features, we shall select a subset that provides the maximal value of $R$; this subset will have the maximal differentiation power. With extracted features the tasks of classification, determination of different particle fractions in the mixture distribution, etc., can be carried out.

It must be mentioned, that actual values of both likelihood function and Bayes error have no statistical interpretation; only comparative conclusions may be done. If we want to evaluate statistical significance of our inference, some distribution free test must be used. We can recommend the permutation test [19] and the percentile test, using a bootstrup distribution, providing approximate confidence intervals in small sample nonparametric situations [20].

## 3. The nonparametric probability density estimation

The nonparametric density estimation methods have received a large development efforts in the last decade [see, e.g. ref. [21], mainly due to their simplicity and absence of excessive requirements on the form of the distribution function. Most popular kernel type estimates were introduced by Rosenblatt [22] and studied by Parzen [23]. In the Parzen procedure every point of TS, $w_j$, is substituted by a bell-like function, and the density in arbitrary point $x$ of the feature space is obtained as a superposition of numerous "kernels" centered about each TS point,

$$p_h(x) = \frac{1}{M} \sum_{i=1}^{M} (1/h^N) K\{(x - x_i)/h\}, \qquad (2.1)$$

where $K(z)$ is a kernel function, satisfying $\int K(z)\, dz = 1$, kernel size $h$ is a smoothing factor, determining the "spread" of the kernel (for Gaussian kernels $h \equiv$ mean square deviation), $N$ is the dimensionality of the feature space, $\{x_i\} \ni w_j$.

Very close related to the Parzen estimates, KNN estimates were introduced by Fix and Hodges [24] and studied by Loftsgaarden and Quesenberry [25],

$$p_k(x) = \frac{K - 1}{M V_k(x)}, \qquad V_k(x) = \frac{2^{N/2} d_k^N(x)}{N \Gamma(N/2)}, \qquad (2.2)$$

where $\Gamma(\cdot)$ is Gamma function, $V_k(x)$ is the volume of the $N$-dimensional sphere $S$, containing $K$ elements of TS, nearest, in any convinient metric, to point $x$, $d_k(x)$ is the distance to the $K$th nearest neighbour of point $x$.

Two metrics are usually used: the Euclidean metric and the Mahalonobis metric [26]. For the latter the distance between observable $x$ and TS element $y$ is equal to

$$D^2_{\text{Mah}} = (x - y)^T \Sigma^{-1} (x - y), \qquad (2.3)$$

where $\Sigma$ is the covariance matrix, calculated by means of TS, to which $y$ belongs. The use of the Mahalonobis metric allowes one to take into account the correlation information, moreover, the distances, calculated in this metric, are scale invariant, so, no transformation of initial data is necessarily.

The relationship of KNN to the Parzen estimate is brought out if the kernel function is uniform over region $S$, and zero outside, so only elements of TS within region $S$, centered at point

$x$, equally contributed in the density estimate.

Despite underlying density variations in feature space, in every point the density is estimated by $K$ elements, and in low density regions the cell size is much greater than in high density regions. KNN estimates are "fixed event number in the cell" estimates, in contrast with "fixed cell size" histogram estimates.

If the $K$-value is small relative to TS size $M$, we have nearly the same probabilities for all TS sample points contributing to the estimate, and averaging over the $S$ region, centered at a $x$ point and containing $K$ neighbours, is valid. But, on the other hand, it is desirable to have $K$ as large as possible to reduce the influence of fluctuations in TS and achieve statistical stability. It is very difficult to choose the optimal $K$ value to cohere these two requirments for different dimensionalities of the observation space, various underlying distributions and TS sizes.

Although many theoretical investigations prove the asymptotically unbiasness and consistence of kernel type estimates [27] and many recommandations have been done on kernel type and width and optimal $K$ value, very little is known under finite sample condition. Recently, K. Fukunaga, the pioneer of KNN -and Parzen method developments for pattern recognition problems, claimed that "unrealiability of the estimators in finite conditions is the major obstacle toward their implementation in practice, and theoretically determined values of $h$ or $K$ gave very discouraging and inconsistent results" [28].

We tried to automate the procedure of optimal $K$ value selection by using such a surprisingly powerfull technique as ordered statistics.

In ref. [29] it was suggested to calculate the KNN density estimates for several, IQ (IQ < $M$, usually IQ = $M/2$), different $K$ values simultaneously. By means of a sequence of estimates, $\{p_k(x)\}$, $k = 1$, IQ, the averaged estimate, KNN3, is constructed,

$$p_{\mathrm{IQ}}(x) = \frac{1}{\mathrm{IQ}} \sum_{k=1}^{\mathrm{IQ}} p_k(x). \tag{2.4}$$

This estimate uses more detailed information on the neighbourhood of point $x$ and is more stable. However, in the sequence of estimates $\{p_k(x)\}$ there may be significant deviations from the true density value, due to large variance of the simple KNN estimate, that distorts the average estimate.

To weight effectively every member of the sequence, we introduce a new KNN estimate in the form of a linear combination of ordered statistics,

$$p_{[\mathrm{IQ}]}(x) = \sum_{k=1}^{\mathrm{IQ}} c_i p_{[k]}(x), \qquad \sum_{k=1}^{\mathrm{IQ}} c_i = 1, \tag{2.5}$$

where square brackets [ ] indicate, that the sequence $\{p_{[k]}(x)\}$ is ordered according to the magnitude of the members.

If we heavily weight the members in the middle of the ordered sequence, we shall obtain a stable, with respect to the fluctuations in TS, estimate. An example of such an estimate is the median estimate, $p^{\mathrm{med}}_{[\mathrm{IQ}]}(x)$, for which

$$c_i = \begin{cases} 1, & \text{if } i = |\mathrm{IQ}/2| + 1, \\ & \mathrm{IQ} \text{ is an odd number}, \\ 0, & \text{otherwise.} \end{cases} \tag{2.6}$$

$|\cdot|$ stands for the whole part of a number. If IQ is an even number, two middle order statistics are weighted with 0.5. So, for every $x$ point, there will be done an unique choice of a $K$ value (or two $K$ values for even IQ). In the middle of an ordered sequence it will appear the most stable member of the sequence. This, self-adjusting character of the median estimate, as we shall see further, leads to estimates better, than one can obtain with any fixed $K$ value.

Our $K$-dependence investigations [30] show, that for regions with very low density (so called, peripheral regions) simple KNN estimates with $K = 2/7$ (for TS size 50/400), are preferable. It can be explained by the fact, that for points in this region, whenever NN "enters" a high density region, further increase in $K$ will not lead to any significant increase of the KNN volume. Hence, as one can see from (2.2), values of most terms of the ordered sequence will be overestimated, and median estimate will be optimistically biased. Therefore, at the peripheral points, that are chosen according to the relative size of local region it

will be better to calculate the density by a simple KNN rule.

For every point $x$ a local neighbourhood size is defined as,

$$\rho_{\mathrm{LOC}}(x_i) = \frac{1}{\mathrm{MSQ}} \sum_{j=1}^{\mathrm{MSQ}} d_j(x_j), \tag{2.7}$$

where $d_j(x)$ is the distance to the $j$th nearest neighbour of a point $x_i$ and $\mathrm{MSQ} = \sqrt{M}$. And, if this "local region size" is 3 times greater, than

$$\bar{\rho}_{\mathrm{LOC}} = \frac{1}{M} \sum_{i=1}^{M} \rho_{\mathrm{LOC}}(x_i), \tag{2.8}$$

the density at point $x_i$ is estimated by a simple KNN rule. Median estimates with such peripheral points corrections, we shall call adaptive KNN estimates, $p^{\mathrm{ad}}_{[\mathrm{IQ}]}(x)$.

KNN density estimation enables effective control of the degree of smoothing of empirical distributions. Displaying the same distribution by different modifications of the KNN method, the peaks in the distribution will become more evident.

Recently an evidence of a narrow enhancement in the pp mass distribution from reaction $\gamma d \to pp\pi^-$ was reported [31]. The statistical significance of this enhancement was proved by the KNN density estimation method, showing the observed structure of the mass distribution better, than the Histogram method. So, KNN median and adaptive modifications can also be very usefull for resonance data analysis.

## 4. Information input and output

The tasks of particle classification and Bayes risk estimation, of obtaining smooth estimates of the probability density, etc. are recomplished with the KNN module. Some simple subroutines are used for nearest neighbour distances calculation and ordering, local region size determination (DISTNN,DIST,ORDER,RSLOC). Covariance matrix calculation and inverting is done by MISR, CORINV and SMXINV modules.

The exchange of information with the KNN module is realized by means of formal parameters only (no COMMON blocks are used), though it leads to a rather long list of parameters, the undesirable collateral effects of the module on the main program are practically excluded, and high obviousness of operation of the module is provided [32].

All statistical procedures are carried out simultaneously for different modifications of the density estimator. The computation load, however, increased only slightly, since wasting most time ordering NN distances, is done only once. In the presented version of the program the ordering is carried out by simple DO-loops but it can easily be changed by some fast procedure e.g. FLPSOR from the CERN program library, MO1AJF from the NAG library, or by a special routine for finding NN, based on ordered partition of each projection axis [33].

The control parametres and arrays of the module are:

N is the features space dimensionality; NS is the dimensionality of the subset under investigation; M is the size of the TS; L is the number of classes (for simplicity, it is assumed here, that all classes have the same TS size); MP is the control sample size; IQ is the size of ordered densities sequence; METRIC is the code for choosing the metric in which distances to NN are calculated, the value METRIC = 0 corresponds to the Mahalonobis metric; the IMODE parameter chooses the program is operation regime: IMODE = 1, classification and likelihood function calculation, IMODE = 2, Bayes error calculation, IMODE = 3, density estimation.

D(IQ,L,MP) is the basic neighbourhood information, distances from every point of the control sample to each class of the training sample; NL(N) is the code combination, by means of which the feature subset selection from primary observables is realized; code 1 in the $i$th position signifies the $i$th feature inclusion in the subset under investigation; AP(L) are the prior probabilities of the models being studied; PST(L) are current values of posterior densities; RM(L) is the mean local region size for TS classes; C(IQ) are the coefficients of the order statistics. During the operation in

"leave-one-out" for Bayes error calculation, the number of TS classes L = 2, and in the subroutine DISTNN the control sample CS(MP) is substituted by the training one.

The number of events, separately of the $w_i$, $i = 1$, L, classes, classified as representatives of the $w_j$, $j = 1$, L, classes, by means of the various modifications of the KNN method, are placed in the array CL(L,L,IQ + 2), where

$$\mathrm{CL}(\mathrm{L},\mathrm{L},i) = \begin{cases} i = 1, 2, \ldots, \mathrm{IQ} \\ \quad \text{error rates for simple KNN,} \\ \quad \text{eq. (2.2)} \\ i = \mathrm{IQ} + 1, \\ \quad \text{rates for median estimate,} \\ \quad \text{eqs. (2.4), (2.5)} \\ i = \mathrm{IQ} + 2, \\ \quad \text{rates for adaptive estimate.} \end{cases} \tag{3.1}$$

This information enables calculation of misclassification rates for every model separately, e.g. $R_{\pi \to \mathrm{pr}}$ and $R_{\mathrm{pr} \to \pi}$, where

$$R = P_\pi R_{\pi \to \mathrm{pr}} + P_{\mathrm{pr}} R_{\mathrm{pr} \to \pi}. \tag{3.2}$$

Using these rates, one can reconstruct the true fraction of iron nuclei in the primary flux [34] or the pion fraction in the hadron flux:

$$P_\pi = \frac{P_\pi^* - R_{\pi \to \mathrm{pr}}}{1 - R_{\pi \to \mathrm{pr}} - R_{\mathrm{pr} \to \pi}}, \tag{3.3}$$

where $P_\pi^*$ is portion of experimental events classified as pions by Bayes decision rule, $R_{\pi \to \mathrm{pr}}$ and $R_{\mathrm{pr} \to \pi}$ are error rates obtained from the same TS.

Values of the Bayes error, calculated by averaging the posterior error $R^{\mathrm{p}}$ are returned in the RP(IQ + 2) array. The $R^{\mathrm{e}}$ values, the misclassification rates, are returned in the RE(IQ + 2) array. The order of values in the arrays is analogous to CL.

In the classification regime the class lables, to which the control events are refered, are placed in the array LUM(MP). Likelihood function values are returned in the FLIK(L) array.

In the regime of constructing the density smoothed estimate, density estimates for the L classes of TS, are placed in the DS(MP,IQ + 2) array.

Besides the presented, some operational arrayes are used, PKNN(IQ) and DEN(L,IQ + 2).

## 5. Program testing

Program testing was performed with the use of samples generated according to the normal (Gaussian) distribution. The choice of this distribution is due to its extensive use as a simple test to compare various density estimation methods, as well as due to the simplicity of calculating the true value of Bayes error, allowing a comparison of the estimates with the calculated values,

$$R = \Phi(-D_{\mathrm{mah}}/2), \tag{4.1}$$

where $\Phi$ is the cumulative normal distribution function and $D_{\mathrm{mah}}$ is the Mahalonobis distance between mathematical expectations of the two classes.

From the program output one can see results of the KNN operation in different modes: Bayes classification and likelihood estimation of one of the two normal population's, $N(0, 1)$ and $N(1, 1)$, control sample is from the same population as the first class of the training one, the likelihood function for the "true" class (hypothesis) is much greater than for the second class: Bayes error values for different KNN modifications can be compared with the true value, $R = 0.3085$; density KNN estimates are calculated for 27 different estimation modifications.

For investigations of bias and consistency of KNN estimates several random samples of fixed size were generated from the normal distribution; the density was estimated at 51 points, uniform distributed over an interval $(-5, 5)$, then the mean square error (MSE) was calculated,

$$\mathrm{MSE}\{\hat{p}(x)\} = E\{\{p(x) - \hat{p}(x)\}^2\}, \tag{4.2}$$

where the mathematical expectation is taken over all possible samples of fixed size drawn from

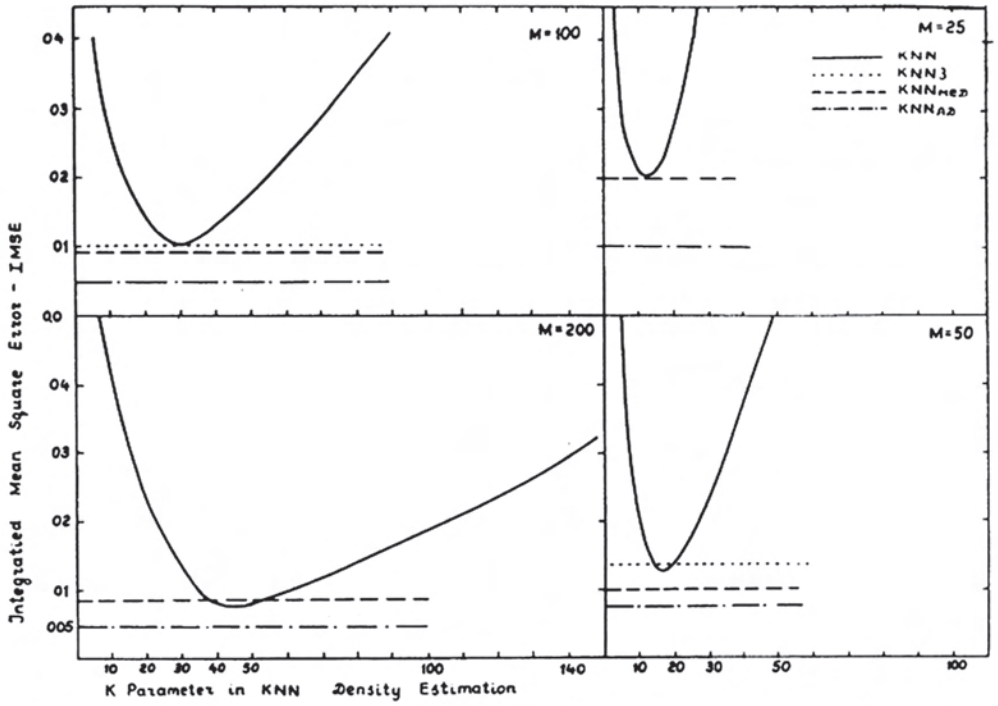


Fig. 1. The test results for the comparison of simple KNN, average, median and adaptive estimates.

general population; $\hat{p}(x)$ is one of considered KNN density estimates.

The integrated mean square error (IMSE) equals

$$\mathrm{IMSE}_{\hat{p}} = \int_X \mathrm{MSE}\{\hat{p}(x)\}\,\mathrm{d}x, \qquad (4.3)$$

where $\mathrm{MSE}(x)$ was obtained by averaging density estimates, calculated with 25 independent samples. This procedure was repeated 10 times to evaluate the mean and standard deviation of IMSE.

Figure 1 showes the results of testing for the comparison of simple KNN, average, median and adaptive estimates. Standard normal density $N(0, 1)$ was estimated. Obviously, the adaptive estimates are much more precise than the ones obtained with any fixed parameter $K$.

Table 1 presents the results of comparing the adaptive KNN method with the Parzen method and MLE with the penalty function (the latter two are taken from ref. [27]. IMSE and its variance (in brackets) are calculated by $25 \times 10$ independent samples from $N(0, 1)$ and bimodal distribution $p(x) = 0.5N(-1.5, 1) + 0.5N(1.5, 1)$. The density was estimated in 51 points on the interval $(-5, 5)$.

The adaptive estimates have shown somewhat worse results. However, it should be noted that the parameters of the Parzen and ML methods have been chosen with the aid of information on the true underlying density, while the adaptive KNN

Table 1
IMSE of various nonparametric density estimators

| Distribution | TS size $M$ | MLM with penalty | Parzen with Gauss. kern. | Adaptive KNN |
|---|---|---|---|---|
| $N(0, 1)$ | 25 | 0.0100(0.0080) | 0.0160(0.0120) | 0.0140(0.0100) |
| $N(0, 1)$ | 100 | 0.0037(0.0021) | 0.0050(0.0027) | 0.0052(0.0020) |
| $N(0, 1)$ | 400 | 0.0015(0.0008) | 0.0020(0.0009) | 0.0032(0.0012) |
| Bimodal | 25 | 0.0100(0.0030) | 0.0090(0.0700) | 0.0012(0.0030) |
| Bimodal | 100 | 0.0036(0.0007) | 0.0036(0.0020) | 0.0048(0.0017) |

Table 2
Comparison of Bayes error estimation $R^e$ and $R^p$ methods

| $N$ | $M$ | $R$ | $\sigma_{R^e}$ | $\sigma_{R^p}$ | $\hat{\sigma}_{R^e}$ | $\hat{\sigma}_{R^p}$ | $\mathrm{MSE}_{R^e}$ | $\mathrm{MSE}_{R^p}$ |
|---|---|---|---|---|---|---|---|---|
| 1 | 100 | 0.3085 | 0.046 | 0.024 | 0.039 | 0.026 | 0.0005 | 0.0013 |
| 1 | 200 | 0.3085 | 0.033 | 0.017 | 0.026 | 0.015 | 0.0003 | 0.0008 |
| 2 | 50 | 0.2340 | 0.048 | 0.031 | 0.044 | 0.027 | 0.0030 | 0.0039 |
| 8 | 50 | 0.5000 | 0.070 | 0.050 | 0.050 | 0.012 | 0.0050 | 0.0044 |
| 10 | 50 | 0.5000 | 0.070 | 0.047 | 0.047 | 0.017 | 0.0040 | 0.0046 |

method uses only the sample information. In processing real data, of course, the analytical density form is unknown, therefore, the slight deterioration of accuracy is compensated with improved procedure stability.

The Bayes risk was calculated for the samples from normal distribution at various feature space dimensionalities and Mahalanobis distances. The calculations were performed with use of 10 independent samples. Table 2 presents the variances, calculated by eqs. (1.12) and (1.14), their estimates and mean square errors. A good agreement of sample and theoretical values of variances is apparent, and although the variances of the $R^p$ values are less than those of $R^e$, their bias leads to their greater mean square deviation. Therefore, the empirical error count estimator is more preferable, especially for feature spaces of large dimensionality.

## References


[1] E. Lederman, Handbook of Applied Mathematics: Statistics (Wiley, New York, 1984).
[2] P. Hajek and T. Havranek, Mechanizing Hypothesis Formation (Springer, Heidelberg, 1979).
[3] G.E.P. Box, Technometrics, 26 (1984) 1.
[4] E.A. Eadie, D. Drijard, F.E. James, M. Roos and B. Sadoulet, Statistical Methods in Experimental Physics (North-Holland, Amsterdam, 1971).
[5] A.A. Chilingarian, in: Proc. of the Symp. on High-Energy Particles Transition Radiation, Yerevan, 1984.
[6] S. Zacks, The Theory of Statistical Inference (John Wiley & Sons, New York, 1977).
[7] J. Berkson, Ann. Stat. 8 (1980) 457.
[8] B. Efron, Ann. of Stat., 10 (1982) 340.
[9] R. Brun, F. Bruyant, M. Maire, A.C. McFerson and P. Zanarini, GEANT3, CERN Preprint, DD/EE/84-1 (1986).
[10] A.M. Dynaevsky et al., in: Proc. FIAN, Moscow, 1984.
[11] J.N. Friedman, Data Analysis Techniques for High-Energy Physics, CERN Yellow Report (1974).
[12] A.A. Chilingarian, VANT, Ser. Tecn. Phys. Exp., Kharkov, 1981.
[13] P.J. Diggle and R.J. Gratton, J. Roy. Statist. Soc. B 46 (1984) 193.
[14] D.V. Lindley, Bayesian Statistics, (Soc. for Indust. and Appl. math., Philadelphia, 1978).
[15] M. Yablon and J.T. Chu, IEEE Trans. on Pattern Analysis and Machine Intelligence, PAMI-2 (1980) 97.
[16] K. Fukunage and R.D. Short, IEEE Trans. on Informormation, IT-26 (1980) 59.
[17] G.T. Toussaint, IEEE Trans. on Information, IT-20 (1974) 472.
[18] S.M. Snappin and J.D. Knoke, Technometrics, 26 (1984) 371.
[19] F. James, Determining the Statistical Significance of Experimental Results, CERN Preprint DD/81-02 (1981).
[20] B. Efron, Canadian J. Statist. 9 (1981) 139.
[21] L. Devroye and L. Gyorfi, Nonparametric Density Estimation. The L1 View, (Wiley, New York, 1985).
[22] M. Rosenblatt, Ann. Math. Stat. 27 (1956) 832.
[23] E. Parzen, Ann. Math. Stat. 33 (1962) 1065.
[24] E. Fix and J.L. Hodges, Project 21-49-004, Report 4, USAF School of Aviation Medicine, Randolf Field, Texas (1951).
[25] D.O. Lofsgaarden and C.D. Quesenberry, Ann. Math. Stat. 36 (1965) 1049.
[26] P.C. Mahalonobis, Proc. of the Nat. Inst. of India 2 (1936) 49.
[27] R.A. Tapia and J.R. Thompson, Nonparametric Probability Density Estimation (The John Hopkins University Press, Baltimore and London, 1978).
[28] K. Fukunaga and D. Himmels, IEEE Trans. on Pattern Analysis and Machine Intelligence, PAMI9 (1987) 634.
[29] L.R. Rabiner, E. Levinson, A.E. Rozenberg and J.G. Wilpon, IEEE Trans. on Acoustics, Speech, Signal Processing, ASSP-27 (1974) 336.
[30] A.A. Chilingarian and S.Kh. Galfayan, Stat. Problems of Control, Vilnius, 66 (1984) 66.
[31] B. Bock, W. Ruhw et al, Nucl. Phys. A 459 (1986) 573.
[32] P.E. Gill, W. Murray and S.M. Piches, ACM Trans. of Math. Software, 5 (1979) 266.
[33] B.S. Kim and S.B. Park, On Pattern Analysis and Machine Intelligence, PAMI-8 (1986) 761.
[34] V.G. Denisova, A.M. Dunaevsky, S.A. Slavatinsky et al., in: Proc. of the 20th ICRC, Moscow, 1987, p. 390.

IL NUOVO CIMENTO VOL. 14 C, N. 6 Novembre-Dicembre 1991

# On the Possibility of Investigation of the Mass Composition and Energy Spectra of Primary Cosmic Ray (PCR) in the Energy Range from $10^{15}$ to $10^{17}$ eV Using EAS Data.

A. A. CHILINGARIAN and G. Z. ZAZIAN
*Yerevan Physics Institute*
*Alikhanian Brother St. 2, 375036 Yerevan 36, Armenia, USSR*

(ricevuto il 19 Aprile 1990; approvato il 2 Gennaio 1991)

**Summary.** — A method allowing one to determine the mass composition of primary cosmic radiation by means of simultaneous analysis of model and experimental data is presented in this paper. The most important part of this work is the quantitative comparison of multivariate distributions and the use of methods of nonparametric statistics for probability density estimation in a multivariate space of features. To check the method offered, events with $E_0 > 500$ TeV were generated by the Monte Carlo method. The showers generated were preliminarily processed by algorithms used in experimental data handling. The apparatus-induced distortions of the measured EAS characteristics have been taken into account. The method allows one to select an experimental event initiated by primary protons and iron nuclei with an efficiency of $(70 \div 80)\%$. Also a new multivariate method of incident particle energy estimation based on the nonparametric regression is described. The method proposed, together with the above-mentioned multivariate EAS classification, allows one to determine the energy spectrum of incident protons and nuclei. Detection and investigation of the products of interaction of these particles with the atmosphere will allow us to study proton-nuclei and nuclei-nuclei interactions at energies from $10^{15}$ to $10^{17}$ eV.

PACS 94.40. – Cosmic-ray interactions with the Earth.

## 1. – Introduction.

The ambiguity of interpretation of the results of experiments with cosmic rays is connected with both significant gaps in our knowledge of the characteristics of hadron-nuclear interactions at superaccelerator energies and indefiniteness of the PCR composition. The extra difficulties are due to indirect experiments and hence, due to the use of Monte Carlo simulations of development and detection of different components of nuclear electromagnetic cascades.

To research into hadron-nuclear interactions in CR, one should know the type of cascade-initiating incident particle. Besides, the investigation of the mass composi-

tion of PCR is of particular interest is connection with the problem of the CR origin.

At present the data available on the mass composition of PCR in the energy range $(10^{15} \div 10^{17})$ eV are obtained by detecting and investigating the different components of EAS and $\gamma$-families detected by X-ray emulsion chambers (X-REC). And if the first data set states a «normal composition»—extrapolation of PCR composition (40% protons and 20% iron nuclei) measured by direct methods in the energy range $(10^{11} \div 10^{14})$ eV [1, 5], then the data on $\gamma$-family fluxes testify to a decrease of the protons fraction in PCR at $E_0 > 10^{16}$ eV down to $(15 \div 20)$% and hence to dominance of iron nuclei [2].

This contradiction, yet inexplicable, may be due to different experimental data handling methods. Besides, the $\gamma$-family characteristics are more sensitive to the model of strong interactions than the EAS ones, hence, variation of model parameters can change the estimate of the proton and iron nuclei fractions. The problem of relative dominance of iron nuclei is very important, because the interpretation of the experimental data obtained in UHE CR is based on the mass composition of PCR [3].

The PCR energy spectrum has been investigated up to energy $10^{15}$ eV in satellite and balloon experiments. The measurements based on detection of EAS mainly fit to the satellite and balloon data in the energy range up to $10^{15}$ eV [4]. The integral spectrum index changes from 1.6 to 2 in the energy range $(5 \cdot 10^{14} \div 5 \cdot 10^{16})$ eV—the so-called spectrum «knee».

A possible step to the description of spectrum breaking is the study of the energy spectra of separate groups of nuclei and protons in the region of the knee, since by them one can judge about the validity of different models of the origin and propagation of CR. The proton energy spectra are studied up to $10^{15}$ eV by the JACEE collaboration [5] and in satellite experiments up to $10^{14}$ eV [6]. Selecting the proton showers via the presence of the high-energy hadrons in the calorimeter ($E_h/E_0 => 0.25$), the energy spectrum of protons with energy $10^{15}$ eV has been obtained in ref. [7]. This method is based on the fact that the incident particle energy dissipation is more intense in the cascades initiated by incident nuclei. But due to large fluctations in the portion of energy transferred to hadrons at a fixed initial energy, such selection may considerably reduce the number of proton showers. In ref. [8] the fractions of different groups of nuclei in PCR were estimated and the energy spectra of the corresponding nuclei in the energy range $(10^{15} \div 10^{16})$ eV were obtained by the method of solving the inverse problem. The results of ref. [7, 8] mainly coincide with the direct experiment data.

In this paper an approach is presented, which allows one to determine the mass composition of PCR by means of simultaneous analysis of model and experimental data. The most important part of the method is the quantitative comparison of multivariate distributions and use of a nonparametric technique to estimate the probability density in a multidimensional feature space. As compared to the earlier used methods of inverse problem solution, with the help of which the mass composition of PCR was first determined in the energy range $E_0 > 10^{15}$ eV with sufficient quantitative certainty [8], in the proposed method the object of analysis is each particular event (a point in the multivariate space of EAS parameters) rather than alternative distributions of model and experimental data. That is why, along with the averaged characteristics, the belonging of each event to a certain class is determined.

This approach was first used to estimate the upper limit of the iron nuclei fraction

according to the $\gamma$-family characteristics [9, 10]. As opposed to ref. [10], where events were classified into two classes ($A > 50$ and $A < 50$), now it is possible to classify events into an unlimited number of classes [11].

After particle identification the new multivariate method of estimation of incident particle energy, used also to estimate the hadron energy according to X-ray emulsion chamber data [12], was applied to recover the energy characteristics of fluxes of different nuclei incident on the atmosphere.

Events with $E_0 > 500\,\text{TeV}$ have been simulated to check the methods proposed. The showers were registered at a depth of $700\,\text{g/cm}^2$. The model data were preliminarily handled according to algorithms used in the data handling at the Tien-Shan station [13]. The finite resolution of the installation measuring EAS characteristics has been taken into account.

## 2. – Simulation of a nuclear-electromagnetic cascade in the atmosphere.

The incident particle energy was drawn according to the energy spectrum given in ref. [4]. A normal CR composition was simulated (40% protons and 20% iron nuclei). Five groups of nuclei were considered: protons (p), $\alpha$-particles ($\alpha$), nuclei with $A = (7 \div 16)$ CNO, $A = (24 \div 27)$ H and $A = (50 \div 56)$ VH. Protons and $\alpha$-particles further were unified into one group.

Strong interactions were simulated by algorithms which reproduce the quark-gluon string model (QGSM) spectra for hA interactions [14]. The algorithm used allows one to simulate nucleon, pion, kaon and $\Lambda$-hyperon interactions with $N^{14}$ at $0.03 < E < 10^6$ TeV. Production of $\mathcal{N}\bar{\mathcal{N}}$ pairs, $\pi$, k, $\Lambda$, $\eta$ was taken into account. In the frame of the Regge theory there were simulated processes of single and double diffraction as well as inelastic recharging of $\pi^{\pm} \to \pi^0$, $\text{p} \to \text{n}$.

The incident nucleus fragmentation was taken into account when simulating $AN^{14}$ interactions. The $hN^{14}$ interaction cross-sections were approximated as

$$(2.1)\qquad \begin{cases} \sigma_{\text{prod}}^{\text{pN}^{14}} = 295 + 23.94 \log(E) + 3.55 \log^2(E), \\ \sigma_{\text{prod}}^{\pi\text{N}^{14}} = 226 + 24.511 \log(E) + 2.31 \log^2(E), \\ \sigma_{\text{prod}}^{\text{kN}^{14}} = 198 + 27.021 \log(E) + 1.81 \log^2(E), \end{cases}$$

where $E$ is the incident particle energy in the laboratory system of coordinates ($E$ is in TeV). Energy dependence of the mean multiplicity of charged particles in $hN^{14}$ interactions was approximated as

$$(2.2)\qquad \langle N \rangle_{\text{ch}} = 0.817 \ln^2 E + 3.127 \ln E + 10.27 \qquad (E \text{ is in TeV}).$$

The number of secondaries was drawn according to KNO distribution. It was taken that the mean transverse momentum of secondaries increased with the energy according to

$$(2.3)\qquad \langle P_{\text{t}} \rangle = 0.36(1 + 0.023 \ln(E/0.1)) \qquad (E \text{ is in TeV}).$$

For different secondaries $\langle P_{\text{t}} \rangle$ and the shape of distribution over $P_{\text{t}}$ differed and corresponded to the existing accelerator data.

Electromagnetic interactions were simulated as in ref. [15]. Pair production,

bremsstrahlung and multiple Coulomb scattering were taken into account. At the same time, it was assumed that transversal development of electron-photon cascades is due to only multiple Coulomb scattering. To calculate the average EAS characteristics, we have used the approximated formulae obtained in ref. [16].

## 3. – Comparison of EAS single characteristics and choice of optimal features.

To choose features most sensitive to the PCR composition, the single characteristics of EAS initiated by primary protons and iron nuclei were compared. The following EAS characteristics have been considered: the total number of electrons $N_e$, the total number of muons with $E_\mu > 5\,\text{GeV}$, the EAS age parameter $S$, the total number, energy, mean energy, average distance to EAS cores and dispersion of spatial and energy distributions of muons with $E_\mu > 200\,\text{GeV}$ and hadrons with $E_h > 200\,\text{GeV}$ in EAS and the linear regression coefficients of spatial and energy distributions of muons and hadrons ($E = C1 + C2R$).

A quantitative comparison of various features is presented in table I, where the $P$-quantiles of statistical tests of comparison of samples from univariate distributions as well as the Bhattacharya probabilistic distance [17] between the samples are given. The Student, Kolmogorov, Mann-Whitney tests have been used. It follows from these data that the most appropriate feature to determine the EAS composition are the high-energy muon characteristics. The hadron component characteristics are less sensitive to the primary particle type (the higher the $P$-quantile of the test, the stronger the difference between the corresponding distributions). In this paper we have used EAS characteristics only ($N_e$, $N_\mu$ ($E > 5\,\text{GeV}$), $S$). Though the sensitivity of $N_e$ and $S$ to the primary particle type is low, however, due to a different degree of correlation between $N_e$, $N_\mu$ and $S$ for events initiated by primary protons and iron nuclei, as is seen from table II and III, the use of all the three EAS characteristics essentially improves the event classification reliability. The choice of these characteris-

TABLE I. – *P-quantiles of statistical tests of comparison of univariate distribution of different characteristics of* EAS *initiated by primary protons and iron group nuclei at* $1 \cdot 10^5 < N_e < 2 \cdot 10^5$.

| | Student | Kolmogorov | Mann-Whitney | Bhattacharya distance |
|---|---|---|---|---|
| $N_e$ | 0.835 | 1.021 | 1.17 | 0.002 |
| $N_\mu(E_\mu > 5\,\text{GeV})$ | 23.647 | 7.329 | 16.12 | 0.433 |
| $S$ | 7.046 | 3.178 | 6.60 | 0.074 |
| $N_\mu(E_\mu > 200\,\text{GeV})$ | 25.435 | 7.553 | 16.34 | 0.451 |
| $\sum E_\mu(E_\mu > 200\,\text{GeV})$ | 15.217 | 5.582 | 12.45 | 0.189 |
| $\langle E_\mu \rangle(E_\mu > 200\,\text{GeV})$ | 6.792 | 5.528 | 11.13 | 0.458 |
| $\langle R_\mu \rangle(E_\mu > 200\,\text{GeV})$ | 18.341 | 6.533 | 14.36 | 0.295 |
| $N_h(E_h > 200\,\text{GeV})$ | 4.717 | 2.400 | 4.88 | 0.248 |
| $\sum E_h(E_h > 200\,\text{GeV})$ | 4.015 | 2.609 | 5.30 | 0.495 |
| $\langle E_h \rangle(E_h > 200\,\text{GeV})$ | 3.503 | 1.658 | 3.44 | 0.128 |
| $\langle R_h \rangle(R_h > 200\,\text{GeV})$ | 5.903 | 3.395 | 6.73 | 0.033 |

TABLE II. – *The coefficients of correlation between the characteristics of the electron-photon and the muon components of* EAS *with* $1 \cdot 10^5 < N_e < 2 \cdot 10^5$ *from primary protons (the quantities marked with* $*$ *correspond to muons with* $E_\mu > 200$ GeV).

| | $N_e$ | $N_\mu$ | $S$ | $N_\mu^*$ | $\sum E_\mu^*$ | $\langle E_\mu^* \rangle$ | $\langle R_\mu^* \rangle$ |
|---|---|---|---|---|---|---|---|
| $N_e$ | **** | 0.393 | −0.132 | 0.145 | 0.108 | 0.01 | −0.180 |
| $N_\mu$ | 0.393 | ***** | 0.443 | 0.838 | 0.717 | 0.044 | 0.516 |
| $S$ | −0.132 | 0.443 | ***** | 0.468 | 0.441 | 0.039 | 0.469 |
| $N_\mu^*$ | 0.145 | 0.838 | 0.468 | ***** | 0.896 | 0.104 | 0.726 |
| $\sum E_\mu^*$ | 0.108 | 0.717 | 0.411 | 0.896 | ***** | 0.476 | 0.658 |
| $\langle E_\mu^* \rangle$ | 0.010 | 0.044 | 0.039 | 0.104 | 0.476 | ***** | 0.093 |
| $\langle R_\mu^* \rangle$ | −0.18 | 0.516 | 0.469 | 0.726 | 0.658 | 0.093 | ***** |

TABLE III. – *The coefficients of correlation between the characteristics of the electron-photon and the muon components of* EAS *with* $1 \cdot 10^5 < N_e < 2 \cdot 10^5$ *from primary iron nuclei (the quantities marked with* $*$ *correspond to muons with* $E_\mu > 200$ GeV).

| | $N_e$ | $N_\mu$ | $S$ | $N_\mu^*$ | $\sum E_\mu^*$ | $\langle E_\mu^* \rangle$ | $\langle R_\mu^* \rangle$ |
|---|---|---|---|---|---|---|---|
| $N_e$ | **** | 0.555 | −0.205 | 0.353 | 0.366 | 0.252 | −0.026 |
| $N_\mu$ | 0.555 | ***** | 0.195 | 0.830 | 0.820 | 0.375 | 0.345 |
| $S$ | −0.205 | 0.195 | ***** | 0.238 | 0.224 | 0.075 | 0.224 |
| $N_\mu^*$ | 0.353 | 0.830 | 0.238 | ***** | 0.978 | 0.391 | 0.633 |
| $\sum E_\mu^*$ | 0.366 | 0.820 | 0.224 | 0.978 | ***** | 0.556 | 0.611 |
| $\langle E_\mu^* \rangle$ | 0.252 | 0.375 | 0.075 | 0.391 | 0.566 | ***** | 0.213 |
| $\langle R_\mu^* \rangle$ | −0.026 | 0.345 | 0.224 | 0.633 | 0.611 | 0.213 | ***** |

tics is also due to their relatively low sensitivity to strong interaction characteristics, which allows one to hope for obtaining a model-independent inference on the PCR mass composition.

## 4. – Classification of the distribution mixture.

Let us consider the stochastic mechanism $(A, \mathscr{P})$ which generates the observation $\boldsymbol{v}$ in a multivariate feature space ($\boldsymbol{v}$ is a $d$-dimensional vector of values measured in experiment, $d$ is dimensionality of the feature space). The basic states space $A$ is a unification of events from different primary nuclei. We know no law of nature like $(A, \mathscr{P})$, that is why, to determine a probability measure on $A$, the total Monte Carlo simulation of the phenomenon under investigation is performed, including experimental data registration and handling.

The set of $d$-dimensional $\boldsymbol{U}$ vectors obtained in simulations is the simular analog of the experimentally measured values of $\boldsymbol{V}$. But, as opposed to experimental data, it is known to which of the alternative classes each of the events belongs. These «labeled» events include *a priori* information about dynamics of the process under investigation, which is given in a nonparametric form, as finite-size samples. The sequence

$\{U_i t_j\}$, where $i = 1, M_{TS}$, $j = 1, L$, $t_j$ is the class index, we usually call a training series or sample (TS) which is also denoted by $(A, \tilde{\mathscr{P}})$.

Since both physical processes of particle production and those of registration are stochastic and the information about the phenomena under investigation is smeared out, the data analysis is uncertain in the sense that one need not wait for event separation into compact nonoverlapping groups corresponding to different primary nuclei. The only thing we can require when classifying experimental data by various primary nuclei is to minimize the losses due to an incorrect classification to some degree and to ensure the use of *a priori* information completely. Such a procedure is the Bayes decision rule with nonparametric estimation of the multivariate probability density function, which, when using a simple loss function (the loss is zero in case of correct classification and is the same at any error), takes the form

$$\hat{A} = \eta(v, A, \tilde{\mathscr{P}}) = \operatorname{argmax}\{\hat{P}(A_i/v)\}, \qquad i = 1, L, \tag{4.1}$$

where $\hat{P}(A_i/v) \sim P_i \hat{P}(v/A_i)$ are *a posteriori* densities, $\hat{P}(v/A_i)$ are conditional densities which are estimated by TS $(A, \tilde{\mathscr{P}})$ using one of many nonparametric methods available [18], $L$ is the number of groups of nuclei.

Initial (*a priori*) values of $P_i$ are taken equal. The monograph [19] is devoted to the interplay of *a priori* and experimental information in fraction estimation problems. Here we shall not go into discussion of competence of the choice of a uniform *a priori* distribution, but only mention that at such a choice the *a posteriori* probability and hence, the results of classification, will be totally defined by experimental information, which seems reasonable to us in the given physical task.

To estimate conditional densities, we used Parzen's method with automatic kernel width adaptation. In this method some probability density values are calculated which correspond to different values of method parameters. Then the sequence obtained is ordered and the median of this sequence is chosen as final estimate. Depending on the value of the probability density in the vicinity of $V$, due to stabilizing properties of the median, each time we will choose an estimate with a width most fitting for that region [20]. The probability density is estimated by

$$P(V/A_i) = 1/(2\pi^{d/2} h^d) \sum_{j=1}^{M_i} \exp[-r_j^2/h^d] W_j, \qquad i = 1, L, \tag{4.2}$$

where $d$ is the feature space dimensionality, $M_i$ is the number of vectors of the $i$-th TS class, $r_j$ is the distance to the $j$-th neighbour in the Mahalanobis metric:

$$r_j = (V - U_j)^T R^{-1} (V - U_j), \tag{4.3}$$

where $R$ is a sampling covariance matrix of class to which $U_j$ belongs, $W_j$ is the event weight, $h$ is the kernel width.

The classification methods, like all the statistical ones, include the procedure quality test as a necessary element. This stage beside all the others is also necessary for the determination of the primary composition. The most natural procedure quality estimate is the error probability which depends on both the degree of overlapping of alternative multivariate distributions and the decision rule being used (Bayes decision rules provide minimum error probability as compared to any other one):

$$R_M^B = E\{\theta[\eta(V, A, \mathscr{P})]\}, \tag{4.4}$$

where

$$\theta[\eta(V, A, \mathscr{P})] = \begin{cases} 0, & \text{at correct classification}, \\ 1, & \text{otherwise}, \end{cases}$$

and $E$ stands for mathematical expectation. The expectation is taken over all possible samples of volume $M$ and over the whole $d$-dimensional space of measured values.

Since we do not exactly know to what class the experimental vectors belong, the estimate of $R_M^{\mathrm{B}}$ we obtain via TS is

$$\hat{R}_M = 1/M_{\mathrm{TS}} \sum_{i=1}^{M_{\mathrm{TS}}} \theta\{t_j, \eta(U_i, A, \tilde{\mathscr{P}})\}, \tag{4.5}$$

*i.e.* we classify the $\{U_i\}$ TS and check the correctness of classification over the index of the class $t_j$, $j = 1, L$. However, as numerous investigations have shown (*e.g.*, [21]), this estimate is systematically biased and hence, a cross-validation estimation is preferable:

$$\hat{R}_M^{\mathrm{e}} = 1/M_{\mathrm{TS}} \sum_{i=1}^{M_{\mathrm{TS}}} \theta\{t_j, \eta(U_i, A, \tilde{\mathscr{P}}_{(i)})\}, \tag{4.6}$$

where $A$, $\tilde{\mathscr{P}}_{(i)}$ is a TS with a removed $i$-th element, which is classified. This estimate is unbiased and has an essentially smaller r.m.s. deviation. The advantage of $R_M^{\mathrm{e}}$ is especially notable when the feature space has a higher dimensionality [22].

Note that we have the possibility to estimate the errors probability of various types by imposing to classification various TS classes, $\{U_i, t_j\}$, $j = 1, L$, $L$ is the number of classes.

By $R_{ij}$ we denote the probability for the classification of the $i$-th class events as belonging to the $j$-th class (misclassification).

Now let us estimate the *a posteriori* fraction of various kernel types in the incident flux.

It is known [23] that the best estimate of *a posteriori* fraction (in case of uniform *a priori* information and absence of classification errors) is the empirical fraction

$$P_i^{\mathrm{e}} = M_i / M_{\mathrm{tot}}, \tag{4.7}$$

where $M_i$ is the number of events classified as initiated by the kernel group $A_i$, $M_{\mathrm{tot}}$ is the total number of events registered during experiment. It can be shown (see [24], where a formula for the case with $L = 2$ is derived) that with account of classification errors the fraction of various kernels can be obtained as the solution of the following set of linear equations:

$$\left(1 - \sum_{j \neq i}^{L} R_{ij}\right) \hat{P}_i + \sum_{k \neq i}^{L} \hat{P}_k R_{ki} = P_i^{\mathrm{e}}, \qquad i = 1, L. \tag{4.8}$$

In the first sum summation goes over $j$, in the second over $k$. All estimates of $R_{ij}$ and $P_i^{\mathrm{e}}$ are obtained over one and the same TS using the same decision rules.

The accuracy of estimates is defined by the TS size and number of experimental data as well as by the value of the classification errors, which present the «quality» of

discrimination in the chosen feature subset. Note that the set (4.8) is a poorly defined system and at large values of classification errors the solutions of the set are unpredictable and hence, the choice of a feature combination providing a high percentage ($\geqslant 60\%$) of correct classification is a necessary preliminary stage.

## 5. – The method of primary flux determination.

As we have shown in the previous section, to estimate the fraction of various nuclei in an incident flux of cosmic radiation, beside classification of an experimental sample by a TS, it is also necessary to calculate any misclassification coefficients, $R_{ij}$. The error in the determination of the fraction of various kernels is a function of the errors both from classification and in determination of $R_{ij}$.

The possibility to decrease the bias and variance of misclassification rates estimates was discussed in ref. [24], where it was mentioned that it is possible to improve the accuracy of $R_{ij}$ estimates, if the TS size is large enough to separate the TS into independent subsamples.

Unfortunately, time consumption per model event generation increases abruptly with energy and we have not to expect much model information in the energy range $E > 10^{15}$ eV.

Thus, the problem of an efficient use of the information contained in simulation results is as never actual for cosmic ray and accelerator physics, since the classical sampling models do not allow us to extract the whole information carried by a sample.

The methods of sample control during handling are widely used in the last few years. One of these is the leave-one-out-for-a-time test considered in the previous section, which allows us to decrease the sample bias.

A more efficient procedure actively developing in both applied and theoretical respects in the last decade is the bootstrap which lies in replication of the initial sample very many times by means of random sampling with replacement [25]. The thus obtained conditionally independent bootstrap-replicas in many respects stand for independent samples from the general population (under the condition of sufficiently large size of the initial sample). In fact, the bootstrap substitutes the unknown general population by a single sample, *i.e.* the ideology described in sect. 4 of this paper is followed.

There are two ways of distribution mixture coefficient estimation: i) to obtain the bootstrap estimate of the misclassification coefficients $R_{ij}^{e}$, then classify and estimate the fraction or ii) carry out fraction estimation over each bootstrap replica, then obtain the fraction and the standard deviation bootstrap expectation. The second way is preferable, because obtaining the standard deviation in the first case is time-consuming. It is enough to say that the errors propagation formulae obtained by the REDUCE symbolic manipulation program occupy several standard sheets in case of classification into four classes.

The bootstrap method of the distribution mixture coefficient estimation takes the following form:

$$\boldsymbol{P} \equiv \boldsymbol{P}\{\hat{P}_1, \ldots, \hat{P}_1\} = f\{V, \tilde{\mathscr{P}}, \eta(V, A, \tilde{\mathscr{P}})\}. \tag{5.1}$$

This solution is a complex function of experimental data and the TS as well as the decision rule $\eta$ being used. By several TS bootstrap replicas we calculate the bootstrap expectation and the bootstrap standard deviation of the mixture coefficients $\hat{P}_i$,

TABLE IV. – *The Bayes error matrix obtained by the leave-one-out method, by* TS *within the range* $1 \cdot 10^5 < N_e < 2 \cdot 10^5$.

| | P | CNO | H | VH |
|---|---|---|---|---|
| P | 0.798 | 0.102 | 0.067 | 0.033 |
| CNO | 0.127 | 0.688 | 0.105 | 0.080 |
| H | 0.072 | 0.113 | 0.691 | 0.124 |
| VH | 0.034 | 0.090 | 0.150 | 0.726 |

which are used as estimates of the fraction of different kernel groups in the primary flux.

To test the method, the generated events were grouped in two. The first were used to create a TS and the second as pseudo-experimental events. The EAS characteristics ($N_e, N_\mu, S$) were used in the events classification, where events in different fixed intervals over $N_e$ were selected. The TS consisted of four classes in accordance with the primary kernel type (p-protons and $\alpha$-particles, CNO-kernels with $A = 7 \div 16$, H with $A = 24 \div 27$ and VH with $A = 50 \div 56$).

Table IV presents the Bayes error matrix obtained as a result of a leave-one-out test over TS. The diagonal elements of this matrix show the probability for a correct events classification and the nondiagonal elements the probability for misclassifications. It is seen from table IV that the correct classifications make about $(70 \div 80)\%$ (classification of «boundary» groups (protons and iron group nuclei) is essentially better than that of the intermediate groups). Note that the accuracy of classification can be improved by selecting events at narrow zenith angles $\vartheta$ ($\vartheta$ varies between 0 and 45°).

Table V shows the recovered nuclei fractions obtained by classification of model events for one interval over $N_e$. The errors presented are obtained by the bootstrap procedure. Fractions of kernel groups given in EAS simulations (true fractions) are presented *ibid.* As is seen from this table, the proposed method allows us to determine the fraction of protons and iron nuclei in the incident flux with quite a good accuracy. To improve the accuracy of determination of the fraction of intermediate nuclei it is necessary to increase the size of TS.

In this work events obtained by the same model are used as control (pseudo-experimental) and training samples. During the experimental data handling the model adequacy test is a necessary stage. The difficulty lies in the fact that the changes both in the strong interaction model and in the mass composition can lead to the same change of the observed values. To overcome this ambiguity one can use the «self-consistency» method developed in ref. [10].

TABLE V. – *Recovered fractions of four groups of nuclei within* $1 \cdot 10^5 < N_e < 2 \cdot 10^5$ ($W_{in}$ *is a «true» fraction,* $W_{out}$ *a recovered one).*

| | $N_{TS}$ | $W_{in}$ | $E_*\{W_{out}\}$ | $\sigma_*\{W_{out}\}$ |
|---|---|---|---|---|
| P | 200 | 0.370 | 0.345 | 0.038 |
| CNO | 188 | 0.272 | 0.229 | 0.067 |
| H | 194 | 0.168 | 0.232 | 0.057 |
| VH | 163 | 0.189 | 0.194 | 0.019 |

## 6. – The nonparametric regression method.

As ground for estimation of the primary particle energy serves the fact of its correlation with the measured EAS parameters. Table VI presents the coefficients of the primary particle energy correlation with various shower parameters. It is seen that though the total number of electrons in a shower ($N_e$) is the main parameter used to estimate the primary energy, the characteristics of the muon component of EAS correlate with $E_0$ somewhat better. That is why our purpose was to investigate the possibility of improvement of the accuracy of estimation of the primary particle energy via the characteristics of the electron-photon and the muon components of EAS.

First, some words about general formulation of the regression problem (we will mainly follow ref. [26]). Suppose a flux of particles is sporadically and independently incident on the atmosphere in accordance with some spectrum $f(E)$. Then these particles, undergoing random collisions and interactions with air atom nuclei, initiate an extensive air shower, the parameters of which are registered by the experimental set-up, *i.e.* each value of $E$ is put into coincidence with some random vector of measurements, $\boldsymbol{X}$, according to some conditional probability density $P(\boldsymbol{X}/E)$.

The peculiarity of solution of the regression problem in the cosmic-ray physics is the fact that neither the true spectrum $f(E)$ nor the conditional density $P(\boldsymbol{X}/E)$ are known in the general case, but there is a training sequence $\{E_i, X_i\}$, $i = 1, M_{TS}$ (obtained by simulation) and it is required to «recover» the regression $E = E(X)$ by this sequence ($M_{TS}$ is the number of events in the training sample).

In the absence of systematic errors (the mathematical expectation of random vector measurement at a fixed independent variable (energy) is equal to the regression function value in that point) this problem is reduced to one of minimization of the average risk:

$$I(\alpha) = \int (E - F(\boldsymbol{X}, \alpha))^2 P(X, E)\, \mathrm{d}X\, \mathrm{d}E\,, \tag{6.1}$$

where $F(X, \alpha)$ is some functional family depending on the parameter $\alpha$, $P(X, E) \sim P(X)\, P(X/E)$ is the probability density function. If there is available *a priori* information about the form of probability function and the chosen functional family $F(\boldsymbol{X}, \alpha)$ is not too complex, then the regression problem can be solved by the least mean squares or the maximal likelihood standard methods.

Due to the complicated stochastic picture of particles and nuclei passing through the atmosphere and the detectors, we have not to expect a standard probability interpretation of all random processes, that is why we have chosen a method

TABLE VI. – *The coefficients of correlation of the characteristics of the electron-photon and the muon components of* EAS *with initial energy* $1 \cdot 10^5 < N_e < 2 \cdot 10^5$.

| | $N_e$ | $N_\mu$ ($E_\mu > 5$ GeV) | $S$ | $N_\mu$ ($E_\mu > 200$ GeV) | $\sum E_\mu$ ($E_\mu > 200$ GeV) |
|---|---|---|---|---|---|
| P | 0.355 | 0.730 | 0.33 | 0.678 | 0.584 |
| Fe | 0.495 | 0.953 | 0.23 | 0.899 | 0.892 |

based on a nonparametric way of treatment of *a priori* information, which does not impose any structure and totally uses the information carried by TS.

The method is based on the obvious fact that the events close to some metric (usually the Mahalanobis metric [27] is used) in the feature space have similar energy: the compactness hypothesis. The method based on the consideration of the «nearest neighbours» is first analysed in ref. [28]. In this work it was shown that when the number of the nearest neighbours, $K$, and the total number of events in TS, $M$, tend to infinity so that $K/M \to 0$, then the risk of the procedure tends to the minimum achievable Bayes risk and even the use of one neighbour increases the risk only twice as compared to the Bayes risk. The uniform consistency of the following estimate is shown in ref. [29]:

$$\hat{E}(X) = \sum_{i=1}^{k} C_i E_{[i]}(X), \qquad \sum_{i=1}^{k} C_i = 1, \tag{6.2}$$

where $E_{[i]}(X)$ is the value of the independent variable (energy) of the $i$-th nearest neighbour of the event $X$ in the feature space.

The weight coefficients $C_i$ are optimized by TS so that some quality function, *e.g.*, the mean-square error (MSE) of estimation, is minimized,

$$\mathrm{MSE} = \sqrt{\sum_{i=1}^{M_{\mathrm{TS}}} (E_i - \hat{E}_{(i)}(X))^2 / M_{\mathrm{TS}}}, \tag{6.3}$$

where the index $(i)$ means that the $i$-th event, the energy of which is estimated, is temporarily removed from TS (leave-one-out test). Despite the fact that the nonparametric procedures are optimal under unlimited sampling, for the case of finite samples there are practically no theoretical and practical recommendations on the choice of the method parameters (*e.g.*, the number of nearest neighbours). That is why we apply the estimate adaptation ideology to the regression analysis, which was developed for multivariate nonparametric estimation of density function [20]. In this approach there are simultaneously calculated several estimates corresponding to different method parameters. The median of the ordered sequence is taken as final estimate.

## 7. – The method of particle energy determination.

To estimate the accuracy of primary particle energy determination by the method of nonparametric regression, there were generated showers with initial energy $E_0 > 500$ TeV. The preprocessing of showers was carried out by the data handling algorithms used in the Tien-Shan experiment [13]. The detector-induced fluctuations were taken into account when determining the characteristics of the electron-photon and the muon components. After preprocessing of showers, part of them were used as TS and another as «experimental» data. Table VII presents the results of estimation of the energy of «pseudo-experimental» events in various ranges of $N_e$ initiated by incident protons and nuclei with $A > 24$. The relative mean-square errors (RMSE) are presented *ibid.*

$$\mathrm{RMSE}_i = (E_i - \hat{E}_i)/E_i, \qquad i = 1, M, \tag{7.1}$$

TABLE VII. – *Mean-square errors of estimation of the energy of protons and nuclei with* $A > 24$.

| | | | | |
|---|---|---|---|---|
| $\langle N_e \rangle / 10^5$ | $0.66 \pm 0.196$ | $1.404 \pm 0.281$ | $2.716 \pm 0.534$ | $9.758 \pm 1.079$ |
| $\langle N_\mu \rangle / 10^3$ | $2.74 \pm 0.258$ | $3.839 \pm 0.335$ | $5.881 \pm 0.667$ | $14.545 \pm 1.01$ |
| $N_{TS}^p$ | 864 | 913 | 484 | 402 |
| $N_{exp}^p$ | 439 | 465 | 256 | 216 |
| $RMSE^p$ (%) | 20 | 24.3 | 25 | 25 |
| $N_{TS}^A$ | 377 | 357 | 184 | 128 |
| $N_{exp}^A$ | 184 | 225 | 102 | 73 |
| $RMSE^A$ (%) | 10.1 | 10.6 | 9.7 | 10.6 |

where $E_i$ is the true energy of the event estimated and $\hat{E}_i$ is its nonparametric estimate. The features used are $N_e$ and $N_\mu$; it is seen from the table that in case of events initiated by incident nuclei, the mean-square error of estimation is 2.5 times smaller than that for proton-induced events, which is due to a stronger correlation of EAS parameters with the initial energy in the case of nuclear events as compared to the proton-initiated events (see table VI).

The «true» integral energy spectra of protons and nuclei with $A > 24$ (the true spectrum corresponds to 100% of correct classification of protons and nuclei and to zero error in the determination of primary particle energy) and the «experimental» spectra obtained as a result of Bayesian classification of «pseudo-experimental» events and then by nonparametric estimation of energy are compared.

There is a satisfactory agreement between the «true» and estimated energy spectra. The energy of events is somewhat overestimated for the «proton» events (the measured EAS characteristics of misclassified nuclei are attributed to protons with high energy) and are underestimated in the case of selected events attributed to heavy nuclei (vice versa). The presence of such distortions leads to some change in the index of the integral energy spectrum of incident protons and nuclei. To obtain a quantitative estimate of the degree of distortion of the index of the integral energy spectrum of protons and heavy nuclei, the corresponding distributions were approximated by power law, with the help of the minimization program «FUMILI» from the CERN program-library. For true proton events the spectrum is approximated by

$$I_p^{tr}(E > 500) = (4.75 \pm 0.36) E^{-1.76 \pm 0.013};$$

for selected proton events it is approximated by

$$I_p^{est}(E > 500) = (4.59 \pm 0.061) E^{-1.70 \pm 0.020}.$$

For the events initiated by heavy nuclei it is approximated by

$$I_A^{tr}(E > 500) = (4.56 \pm 0.075) E^{-1.69 \pm 0.030},$$

$$I_A^{est}(E > 500) = (4.84 \pm 0.099) E^{-1.77 \pm 0.037},$$

respectively.

It follows from these formulae that the relative error at the determination of the

integral energy spectrum index is 3% for incident protons and 5% for incident nuclei with $A > 24$.

## 8. – Conclusion.

The classification method allows one to select experimental events initiated by incident protons and nuclei with an efficiency of $(70 \div 80)\%$ and determine the mass composition of PCR at energies from $10^{15}$ to $10^{17}$ eV. The main advantages of the method proposed are:

i) its being a multivariate one, *i.e.* inclusion of additional EAS parameters in the analysis meet no difficulties;

ii) individual analysis (event by event)—each experimental event is an object of analysis—their belonging to a certain class and the error of statistical solution are determined;

iii) *a priori* chosen probability family is not imposed on data—the results of simulation are used directly during the process of statistical solutions.

We hope that the use of the proposed method when handling the experimental data obtained at complex arrays will allow us to get unambiguous information about the character of strong interactions at superaccelerator energies.

The nonparametric regression method for studying the energy spectra of PCR in the energy range from $10^{15}$ to $10^{17}$ eV via EAS data is based on

i) high reliability of multivariate classification of EAS;

ii) high accuracy of primary particle energy determination by the nonparametric regression method (relative mean-square error is $(10 \div 25)\%$).

By the characteristics of the electron-photon and the muon components of EAS we can determine the parameters of proton and nuclear «beams» incident on the atmosphere.

Detection and investigation of the products of interaction of these particles with the atmosphere (target) will allow us to study PA and AA interactions at energies $(10^{15} \div 10^{17})$ eV.

* * *

We are grateful to A. M. Dunaevsky and N. Stamenov for useful discussions and to E. A. Mamidjanian for stimulating interest in the work.

One of the authors (ZGZ) also thanks A. M. Dunaevsky for provision of EAS simulation algorithms.

## REFERENCES

[1] J. N. STAMENOV: *High energy cosmic ray mass composition on the basis of* EAS *studies at mountain altitudes*, in *V International Symposium on Very High Energy Cosmic Rays Interactions, Lodz, Poland, 1988*.

[2] MT. FUJI EMULSION CHAMBER COLLABORATION: *Apparent decrease of proton fraction*

*around the «Knee» observed in mt. Fuji emulsion chamber experiment*, in *Proceedings of the XX ICRC*, Vol. 1 (Moscow, 1987), p. 382.
[3] J. RICH, D. L. OWEN and M. SPIRO: *Phys. Rep.*, **151**, 1 (1987).
[4] S. I. NIKOLSKY: *Energy Spectrum and Mass Composition of* PCR (Nauka, Moscow, 1987).
[5] JACEE COLLABORATION: *Energy spectra of primary protons and helium nuclei in the energy range* $(10^{12} \div 10^{15})$ eV *from* JACEE, in *Proceedings of the XX ICRC*, Vol. 1 (Moscow, 1986), p. 371.
[6] I. P. IVANENKO *et al.*: *Spectrum and charge composition of cosmic rays with energy from* 2 *to* 100 TeV, in *V International Symposium on Very High Energy Cosmic Rays Interaction* (Lodz, Poland, 1988), p. 197.
[7] A. P. CHUBENKO, N. P. KRUTIKOVA *et al.*: *Primary protons, inclusive cross-section in P-A interaction and their relation to energy spectra of hadrons in the atmosphere*, in *Proceedings of the XX ICRC*, Vol. 1 (Moscow, 1986), p. 373.
[8] I. N. STAMENOV: PCR *mass composition investigation by* EAS, Ph. doctor dissertation, Lebedev Physics Institute (1981).
[9] A. A. CHILINGARIAN: *The* CR *high energy particles investigation with nonparametric statistics*, Ph. doctor dissertation, Yerevan Physics Institute (1984).
[10] A. A. CHILINGARIAN, S. KH. GALFAYAN *et al.*: *Upper boundary of iron nuclei fraction in* PCR, Preprint FIAN 75, 1988.
[11] A. A. CHILINGARIAN and H. Z. ZAZYAN: *A classification method of* PCR *mass composition determination*, Preprint EPI 1204(81), 1989.
[12] A. A. CHILINGARIAN and H. Z. ZAZYAN: *Nonparametric method of hadron energy estimation*, Preprint EPI 1217(3), 1990.
[13] N. M. NIKOLSKAYA and I. N. STAMENOV: *The Tien-Shan* EAS *installation data handling algorithm investigation*, Preprint FIAN 125, 1975.
[14] IU. M. SHABELSKY: *Cross-sections and spectrums of secondary particles in hadron-nuclei collisions*, Preprint LIAF 1224, 1986.
[15] A. M. DUNAEVSKY and A. V. URISON: *Scaling, cross-section increase and simulation of electron-nuclear cascades in the athmosphere*, Preprint FIAN 150, 1975.
[16] A. V. PLYASHESHNIKOV, A. K. KONOPELKO and K. V. VOROBYEV: *The three-dimensional development of high energy electromagnetic cascades in atmosphere*, Preprint FIAN 92, 1988.
[17] S. R. RAO: *Cluster analysis as applied to study of race mixing in human populations*, in *Classification and Clustering* (Academic Press, New York, N.Y., London, 1977).
[18] L. DEVROY and L. GYORFI: *Nonparametric Density Estimation. The* L1 *View* (John Wiley & Sons, New York, N.Y., 1985).
[19] E. E. LEAMER: *Ad Hoc Inference with Nonexperimental Data* (John Wiley & Sons, New York, N.Y., Chichester, Brisbane, Toronto, 1978).
[20] A. A. CHILINGARIAN: *Comp. Phys. Commun.*, **54**, 381 (1988).
[21] C. T. TOUSSAINT: *IEEE Trans. Inf.*, IT-**20**, 472 (1974).
[22] A. A. CHILINGARIAN and S. CH. GALFAYAN: *Calculation of Bayes Risk by KNN Method. Stat. Problem of Control* (Vilnius, 1984), p. 66.
[23] J. D. HEY: *An Introduction to Bayesian Statistical Inference* (Martin Robertson, 1983).
[24] A. A. CHILINGARIAN, S. KH. GALFAYAN *et al.*: *Multidimensional analysis of* EAS *and Roentgen-emulsion data*, Preprint FIAN 332, 1986.
[25] B. EFRON: *The Jackkife Bootstrap and other Resempling Plans* (Society for Industrial and Applied Mathematics, Philadelphia, Penn., 1982).
[26] V. N. VAPNIK: *Dependence Reconstruction by Empiric Data* (Nauka, Moscow, 1974).
[27] P. C. MAHANALOBIS: *Proc. Natl. Inst. Sci. India*, **12**, 49 (1963).
[28] T. M. COVER: *IEEE Trans. Inf. Theory*, IT-**14**, 50 (1968).
[29] A. P. DEVROYE: *IEEE Trans. Inf. Theory*, IT-**24**, 142 (1978).

Pattern Recognition Letters 11 (1990) 781–785
North-Holland

December 1990

# A bootstrap method of distribution mixture proportion determination

A.A. CHILINGARIAN and G.Z. ZAZIAN
*Yerevan Physics Institute, Alikhanian Brothers 2, SU-375036, Yerevan 36, Republica of Armenia, USSR*

Received 23 April 1990
Revised 7 September 1990

*Abstract:* A simulation-based methodology for distribution mixture proportion determination is presented. A Monte Carlo study using Gaussian population data and cosmic-ray-experiments data proved the reliability of the methods proposed.

*Key words:* Bootstrap, classification, multivariate analysis, probability density estimation, distribution mixture, error rate estimation.

## 1. Introduction

The basic goal of this letter is to report development of a unified theory of statistical inference, based on nonparametric models, in which various nonparametric approaches (density estimation, Bayesian decision making, error rate estimation, feature extraction, sample control during handling, etc.) are used.

For a nonparametric model, that is a model in the form of a stochastic mechanism, whereby the data are generated, the underlying log-likelihood function cannot be given explicitly [1]. These, in a convenient way intractable statistical models often arise in modern high-energy physics experiments, where very sophisticated Monte Carlo models are being used.

A cosmic-ray-physics experiment, used as an example for the technique proposed, concerns the Primary Cosmic Rays (PCR) composition determination by the Extensive Air Showers (EAS) data [2].

A Monte Carlo study of the bootstrap method is also presented.

## 2. Classification of the distribution mixture

Let us consider the stochastic mechanism $(A, \mathscr{P})$ which generates the observation $\boldsymbol{v}$ in a multivariate feature space $V$ ($\boldsymbol{v}$ is a $d$-dimensional vector of values measured experimentally, $d$ is the dimensionality of the feature space, $\boldsymbol{v} \in V$). The basic states space $A$ consists of alternative hypotheses or classes (for example, different primary nuclei). We know no law of nature like $(A, \mathscr{P})$, that is why, to determine the mutual probability measure on the direct product of $A$ and $V$ spaces, the total Monte Carlo simulation of the phenomenon under investigation is performed, including experimental data registration and handling.

The set of $d$-dimensional $\boldsymbol{u}$ vectors obtained in simulations is the analog of the experimentally measured values of $\boldsymbol{v}$. But, as opposed to experimental data, it is known to which of the alternative classes each of the events belongs. These 'labeled' events include a priori information about dynamics of the process under investigation, which is given in a nonparametric form, as finite samples. The sequence $\{u_i, t_j\}$, where $i = 1, \ldots, M_{\mathrm{TS}}$, $j = 1, \ldots, L$, $t_j$ is a class index, we usually call a training set or sample (TS) which is also denoted by $(A, \tilde{\mathscr{P}})$.

Since both physical processes of particle production and those of registration are stochastic, only by careful measurement of probabilities can we gain an understanding of the phenomena under investigation. The high energy physics data analysis is uncertain in the sense that the probability distributions concerning the alternative hypotheses usually overlap significantly.

The only thing we can require when classifying a distribution mixture is to minimize the losses due to incorrect classification to some degree and to ensure use of a priori information completely. Such a procedure is the Bayes decision rule with nonparametric estimation of the multivariate probability density function, which, when using a simple loss function (the loss is zero in case of correct classification and it is the same for any error), takes the form:

$$\hat{A} = \eta(\upsilon, A, \tilde{\mathscr{P}}) = \operatorname{argmax}\{\hat{P}(A_i/\upsilon)\}, \quad i = 1, \ldots, L \tag{2.1}$$

where $\hat{P}(A_i/\upsilon) \sim P_i \hat{P}(\upsilon/A_i)$ are a posterior densities, $\hat{P}(\upsilon/A_i)$ are conditional densities which are estimated by TS $(A, \tilde{\mathscr{P}})$ using one of many nonparametric methods available [3], $L$ is the number of classes.

To estimate conditional densities, we used Parzen's method with automatic kernel width adaptation. In this method some probability density values are calculated which correspond to different values of method parameters. Then the sequence obtained is ordered and the median of this sequence is chosen as final estimate. Depending on the value of the probability density in the vicinity of $\upsilon$, due to stabilizing properties of the median, each time we will choose an estimate with a width most fitting for that region [4]. The probability density is estimated by:

$$P(\upsilon/A_i) = 1/(2\pi^{d/2}h^d) \sum_{j=1}^{M_i} \mathrm{e}^{-r_j^2/h^d} W_j, \quad i = 1, \ldots, L \tag{2.2}$$

where $d$ is the feature space dimensionality, $M_i$ is the number of vectors in the $i$th TS class, $r_j$ is the distance to the $j$th neighbor in the Mahalanobis metric:

$$r_j = (\upsilon - u_j)^{\mathrm{T}} R^{-1} (\upsilon - u_j), \tag{2.3}$$

where $R$ is a sampling covariance matrix of the class to which $u_j$ belongs, $W_j$ are the event weights, $h$ is the kernel width.

The classification methods, like all the statistical ones, include a procedure quality test as a necessary element. This stage beside all the others is also necessary for the determination of the mixture proportion. The most natural procedure quality estimate is the error probability which depends on both the degree of overlapping of alternative multivariate distributions and the decision rule being used (Bayes decision rules provide minimum error probability as compared to any other):

$$R_M^{\mathrm{B}} = E\{\theta[\eta(\upsilon, A, \mathscr{P})]\}, \tag{2.4}$$

where

$$\theta[\eta(\upsilon, A, \mathscr{P})] = \begin{cases} 0, & \text{for correct classification,} \\ 1, & \text{otherwise} \end{cases}$$

and $E$ stands for mathematical expectation. The expectation is taken over all possible samples of volume $M$ and over the whole $d$-dimensional space of measured values.

Since we do not know to which class the experimental vectors belong, we obtain an estimate of $R_M^{\mathrm{B}}$ via TS:

$$\hat{R}_M = \frac{1}{M_{\mathrm{TS}}} \sum_{i=1}^{M_{\mathrm{TS}}} \theta\{t_j, \eta(u_i, A, \tilde{\mathscr{P}})\}, \tag{2.5}$$

i.e., we classify the $\{u_i\}$ TS and check correctness of classification over the index of the class $t_j$, $j = 1, \ldots, L$. However, as numerous investigations have shown (e.g., [5]), this estimate is systematically biased and hence, a cross-validation estimation is preferable:

$$R_M^{\mathrm{c}} = \frac{1}{M_{\mathrm{TS}}} \sum_{i=1}^{M_{\mathrm{TS}}} \theta\{t_j, \eta(u_i, A, \tilde{\mathscr{P}}_{(i)})\} \tag{2.6}$$

where $A, \tilde{\mathscr{P}}_{(i)}$ is a TS with a removed $i$th element, which is classified. This estimate is unbiased and has an essentially smaller r.m.s. deviation. The advantage of $R_M^{\mathrm{c}}$ is especially notable when the feature space has a high dimensionality [6].

Note, that we have the possibility to estimate the error probability of various types by classifying various TS classes $\{u_i, t_j\}$, $j = 1, \ldots, L$.

By $R_{ij}$ we denote the probability of classifying the $i$th class events as belonging to the $j$th class (misclassification).

Now let us estimate the a posterior fraction of various classes in the distribution mixture.

It is known [7] that the best estimate of the a posterior fraction (in case of uniform a priori information and absence of systematic errors) is the empirical fraction

$$P_i^e = M_i/M_{tot} \tag{2.7}$$

where $M_i$ is the number of events classified as belonging to the class $A_i$, $M_{tot}$ is the total number of events. It can be shown that with account of classification errors the fraction (proportion) can be obtained as the solution of the following set of linear equations:

$$\left(1 - \sum_{j\neq i}^{L} R_{ij}\right)\hat{P}_i + \sum_{k\neq i}^{L} \hat{P}_k R_{ki} = P_i^e, \quad i = 1, \ldots, L. \tag{2.8}$$

In the first sum summation goes over $j$, in the second sum over $k$. All estimates of $R_{ij}$ and $P_i^e$ are obtained over one and the same TS using the same decision rules.

The accuracy of the estimates is defined by the TS size and the number of control data as well as by the value of the classification errors, which present the 'quality' of discrimination in the chosen feature subset. Note that the set (2.8) is a poorly defined system and at large values of classification errors the solutions of the set are unpredictable and hence, the choice of a feature combination providing a high percentage ($\geqslant 60\%$) of correct classification is a necessary preliminary stage.

## 3. The bootstrap procedure of fraction estimation

As we have shown in the previous section, to estimate the proportion of various classes in a distribution mixture, beside classification of a control sample by a TS, it is also necessary to calculate the misclassification coefficients, $R_{ij}$. The error in determination of the fraction is a function of the errors both from classification and in determination of $R_{ij}$.

The possibility to decrease the bias and variance of misclassification rates estimates was discussed in [8], where it was mentioned that it is possible to improve the accuracy of the $R_{ij}$ estimates, if the TS size is large enough to separate the TS into independent subsamples.

Unfortunately, time consumption per model event generation increases abruptly with primary particle energy and the TS size is always limited for high energy events.

Thus, the problem of an efficient use of the information contained in training samples is very important for cosmic-ray and accelerator physics, since the classical sampling models do not allow to extract the whole information carried by a sample.

The methods of sample control during handling are widely used in the last few years. One of these is the leave-one-out-for-a-time test considered in the previous section, which allows to decrease the sample bias. A more efficient procedure actively developing in both applied and theoretical respects in the last decade is the bootstrap which lies in replication of the initial sample very many times by means of random sampling with replacement. The thus obtained conditionally independent bootstrap-replicas in many respects stand for independent samples from the general population (under the condition of sufficiently large size of the initial sample). In fact, the bootstrap substitutes the unknown general population by a single sample.

The theoretical basis of the bootstrap method is the analog of the central limit theorem (CLT) proved in [9]:

$$P\{\sqrt{B}(\mu_B - \mu_M) < tS_M \mid x_1, \ldots, x_M\} \to \Phi(t), \tag{3.1}$$

when $M, B \to \infty$, $x_1, \ldots, x_M$ are independent, identically distributed (iid) random quantities, $\Phi(t)$ is a normal (Gaussian) distribution, $\mu_M$ and $S_M$ are sample estimates of the first and the second moments,

$$\mu_B = \sum_{j=1}^{B} \mu_j^*/B,$$

and

$$\mu_j^* = \sum_{i=1}^{M} x_i^{(j)}/M$$

is the $j$th bootstrap replica's mean. Moreover, analogies between sampling and the bootstrap are valid also for many other statistics. Referring to [10], we shortly summarize the main idea of the

new procedure: the bootstrap-moments (denoted by $E_*, \sigma_*$) are introduced, which in many cases substitute the statistical moments calculated according to a distribution function (in most cases of interest it is unknown).

Owing to the fact that the bootstrap is very important for high-energy physics, and to investigate its possibilities for finite samples and a limited number of bootstrap replicas, we have carried out an investigation with the purpose to calculate the bootstrap expectation ($\mu_j^* - \mu_M$), a 'butstrap' CLT test, and calculation of bootstrap expectations of the standard deviation of the mean iid random variables, $\delta_*^2 = \sigma_*^2/M$. To do this we used samples from the standard, normal distribution $N(0, 1)$; the sample size varied between 25 and 1000, the number of bootstrap replicas in a series was from 10 to 2000. The mean was calculated for each bootstrap replica, and for each bootstrap series the bootstrap-estimate of the mean standard deviation, $\delta_*$, was calculated.

A round of recalculations including 100 series of the same size has been carried out using different initial samples; the obtained data were averaged and the mean-square deviations were calculated. The results of investigations, which are present in Table 1, illustrate the validity of 'butstrap' CLT and consistency of using the bootstrap expectation. Although the mathematical theorems were proved for the asymptotic cases $M, B \to \infty$, even with small sample sizes and small numbers of bootstrap replicas ($M, B = 50$), the obtained estimates fit to the expected theoretical ones.

There are two ways of distribution mixture coefficient estimation: (i) to obtain the bootstrap estimate of the misclassification coefficients $R_{ij}^e$, then classify and estimate the fraction, or (ii) carry out fraction estimation over each bootstrap

Table 1
Bootstrap expectations and bootstrap standard deviations of sampling statistics

| | $B$ | 10 | 50 | 100 | 200 |
|---|---|---|---|---|---|
| | $E_*\{\mu_B - \mu_M\}$ | −0.0152 | 0.0031 | −0.0048 | −0.0003 |
| $M = 25$ | $\sigma_*\{\mu_B - \mu_M\}$ | 0.0639 | 0.0251 | 0.0174 | 0.0160 |
| $\delta_{25} = 0.2$ | $E\{\delta_*\}$ | 0.1891 | 0.1974 | 0.1929 | 0.1977 |
| | $\sigma\{\delta_*\}$ | 0.0560 | 0.0300 | 0.0031 | 0.0028 |
| | $E_*\{\mu_B - \mu_M\}$ | −0.0024 | −0.0023 | 0.0003 | −0.0001 |
| $M = 50$ | $\sigma_*\{\mu_B - \mu_M\}$ | 0.0402 | 0.0227 | 0.0149 | 0.0097 |
| $\delta_{50} = 0.1414$ | $E\{\delta_*\}$ | 0.1481 | 0.1398 | 0.1396 | 0.1395 |
| | $\sigma\{\delta_*\}$ | 0.0286 | 0.0182 | 0.0167 | 0.0154 |
| | $E_*\{\mu_B - \mu_M\}$ | −0.0171 | −0.0010 | 0.0004 | −0.0008 |
| $M = 100$ | $\sigma_*\{\mu_B - \mu_M\}$ | 0.0323 | 0.0152 | 0.0101 | 0.0066 |
| $\delta_{100} = 0.1$ | $E\{\delta_*\}$ | 0.0897 | 0.0959 | 0.1000 | 0.0988 |
| | $\sigma\{\delta_*\}$ | 0.0212 | 0.0107 | 0.0097 | 0.0086 |
| | $E_*\{\mu_B - \mu_M\}$ | 0.0038 | −0.0017 | 0.0001 | 0.0000 |
| $M = 200$ | $\sigma_*\{\mu_B - \mu_M\}$ | 0.0231 | 0.0107 | 0.0082 | 0.0048 |
| $\delta_{200} = 0.0707$ | $E\{\delta_*\}$ | 0.0593 | 0.0692 | 0.0694 | 0.0700 |
| | $\sigma\{\delta_*\}$ | 0.0154 | 0.0078 | 0.0063 | 0.0049 |
| | $E_*\{\mu_B - \mu_M\}$ | −0.0018 | 0.0007 | 0.0004 | 0.0003 |
| $M = 500$ | $\sigma_*\{\mu_B - \mu_M\}$ | 0.0115 | 0.0072 | 0.0040 | 0.0032 |
| $\delta_{500} = 0.0447$ | $E\{\delta_*\}$ | 0.0430 | 0.0452 | 0.0442 | 0.0446 |
| | $\sigma\{\delta_*\}$ | 0.0095 | 0.0043 | 0.0033 | 0.0024 |
| | $E_*\{\mu_B - \mu_M\}$ | 0.0038 | 0.0001 | 0.0002 | 0.0003 |
| $M = 1000$ | $\sigma_*\{\mu_B - \mu_M\}$ | 0.0079 | 0.0050 | 0.0030 | 0.0022 |
| $\delta_{1000} = 0.032$ | $E\{\delta_*\}$ | 0.0322 | 0.0317 | 0.0316 | 0.0315 |
| | $\sigma\{\delta_*\}$ | 0.0073 | 0.0033 | 0.0022 | 0.0017 |

replica, then obtain the fraction and the standard deviation bootstrap expectation. The second way is preferable, because obtaining of the standard deviation in the first case is time-consuming: the error propagation formulae obtained by the REDUCE symbolic manipulation program occupy several standard sheets in case of classification into four classes.

Finally, let us formalize the bootstrap method of the distribution mixture coefficient estimation. Let us define the solution of the set (2.8) as:

$$\boldsymbol{P} \equiv \boldsymbol{P}\{\hat{P}_1, \ldots, \hat{P}_l\} = f\{\upsilon, \tilde{\mathscr{P}}, \eta(\upsilon, A, \tilde{\mathscr{P}})\}. \quad (3.2)$$

This solution is a complicated function of experimental data and the TS as well as the decision rule $\eta$ being used. By several TS bootstrap replicas we calculate the bootstrap expectation and the bootstrap standard deviation of the mixture coefficients $\hat{P}_i$, which are used as estimates of the fraction of different nuclei groups in the primary flux.

## 4. Results of calculations

To test the method, the generated events were grouped in two. The first were used to create a TS and the second as control events. The EAS characteristics—number of electrons, number of muons, age parameter ($N_e, N_\mu, S$)—were used in the events classification. The TS consisted of four classes in accordance with the primary nuclei type (p: protons, $\alpha$-particles, CNO: nuclei with atomic number $A = 7$–16, H: nuclei with atomic number $A = 24$–27, and VH: nuclei with atomic number $A = 50$–56).

Table 2 presents the Bayes error matrix obtained as a result of a leave-one-out test over TS. The diagonal elements of this matrix show the probability of correct classification and the nondiagonal elements represent the probability for misclassifications. It is seen from Table 2 that the percentage of correct classifications amounts to 70–80%. Classification of 'boundary' groups (protons and iron group nuclei) is essentially better than that of the intermediate groups.

Table 2
The Bayes error matrix obtained by the leave-one-out method

| | p | CNO | H | VH |
|---|---|---|---|---|
| p | 0.798 | 0.102 | 0.067 | 0.033 |
| CNO | 0.127 | 0.688 | 0.105 | 0.080 |
| H | 0.072 | 0.113 | 0.691 | 0.124 |
| VH | 0.034 | 0.090 | 0.150 | 0.726 |

Table 3
Recovered factions of four groups of nuclei ($W_{in}$ is a 'true' fraction, $W_{out}$ is a recovered one)

| | $N_{TS}$ | $W_{in}$ | $E_*\{W_{out}\}$ | $\sigma_*\{W_{out}\}$ |
|---|---|---|---|---|
| p | 200 | 0.370 | 0.345 | 0.038 |
| CNO | 188 | 0.272 | 0.299 | 0.067 |
| H | 194 | 0.168 | 0.232 | 0.057 |
| VH | 163 | 0.189 | 0.194 | 0.019 |

Table 3 shows the recovered nuclei fractions obtained by classification of control events for one interval over $N_e$. The errors presented are obtained by the bootstrap procedure. As is seen from this table, the proposed method allows to determine the fraction of protons and iron nuclei in the incident flux with quite a good accuracy.

## References


[1] Diggle, P.J. and R. Gratton (1984). Monte Carlo methods of inference for implicit statistical models. *J. Roy. Statist. Soc. B* 46, 193.

[2] Rich, J., D.L. Owen and M. Spiro (1987). Experimental particle physics without accelerators. *Phys. Reports* 151 (5,6).

[3] Devroy, L. and L. Gyorfi (1985). *Nonparametric Density Estimation. The L1 View*. Wiley, New York.

[4] Chilingarian, A.A. (1989). Statistical decisions under nonparametric a priori information. *Comp. Phys. Comm.* 54, 381–390.

[5] Toussaint, G.T. (1974). Bibliography of misclassification. *IEEE Trans. Information* 20, 472–478.

[6] Chilingarian, A.A. and S.Ch. Galfayan (1984). Calculation of Bayes risk by KNN method. *Stat. Problem of Control*. Vilnius, 66–76.

[7] Hey, J.D. (1983). *An introduction to Bayesian Statistical Inference*. Martin Robertson.

[8] Jain, A.K., R.C. Dubes and C.-C. Chen (1987). Bootstrap techniques for error estimation. *IEEE Trans. Pattern Anal. Machine Intell.* 9, 628.

[9] Bickel, P.J. and D.A. Freedman (1981). Some asymptotic theory for the bootstrap. *Ann. Stat.* 9, 1198.

[10] Efron, B. (1982). The Jackkife bootstrap and other resampling plans. Society for Industrial and Applied Mathematics, Philadelphia, PA.

Nuclear Instruments and Methods in Physics Research A302 (1991) 522–528
North-Holland

# A multidimensional analysis of the Cherenkov images of air showers induced by very high energy γ-rays and protons

F.A. Aharonian and A.A. Chilingarian
*Yerevan Physics Institute, Alikhanian Brothers 2, 375036 Yerevan, Republic of Armenia*

A.K. Konopelko and A.V. Plyasheshnikov
*Altai State University, Dimitrov st. 66, Barnaul, 656099 USSR*

Received 13 March 1990 and in revised form 8 October 1990

A multidimensional analysis based on Bayes decision rules and nonparametric multivariate density estimation is proposed for classification of the Cherenkov light images of air showers registered by an air Cherenkov detector (ACD) with the multichannel light receiver The differences in the angular size of the image, its orientation and position in the focal plane of the ACD and spectral composition of the Cherenkov light are used in the analysis to distinguish the showers induced by primary γ-rays from showers induced by background cosmic rays (CR). It is shown that the usage of several image parameters together with their correlations can lead to a reduction of the CR background rejection down to a few tenths of a percent while retaining about 50% of useful (γ-ray-induced) events.

## 1. Introduction

One of the most important problems of very high energy (VHE) γ-ray astronomy is related to the improvement of the air Cherenkov technique to effectively reduce the background hadron contamination (see, e.g., ref. [1]). Recent Monte Carlo simulations [2–5] have shown that the differences between Cherenkov light emission from air showers initiated by γ-rays and protons (and other nuclei of CR) are more pronounced than it was supposed earlier. These differences include a greater angular divergence of particles in the CR-initiated showers (p-showers) due to the multiple particle production processes.

The image of the p-shower is therefore broader, and the presence of penetrating particles in the p-shower makes the p-image also longer than the γ-shower image. The differences in the arrival direction cause the γ-shower images to have a characteristic radial alignment relative to the optical axis of the ACD. Finally, due to deeper penetration of the p-showers we expect an ultraviolet light excess for such showers.

The theoretical analysis of the efficiency of the discrimination against the CR background using the differences between p- and γ-shower images mentioned above has been carried out in refs. [2–5]. In particular, it was shown by Hillas [2] that for the 10-m telescope of the Whipple Observatory it is possible to reject up to 97–98% of the background events while retaining 60–70% of the useful events induced by γ-rays from the point source. However, the technique proposed in ref. [2], though using several image parameters simultaneously, is, in fact, a one-dimensional technique, as these parameters are treated separately, and the possible differences in the correlation between parameters for γ- and p-events are not taken into account. Our purpose is to investigate the possibility for an improvement of the background discrimination by using Bayesian decision rules and multivariate probability density estimation.

## 2. Simulation of the cascade development

The numerical analysis carried out in the present work is based on Monte Carlo simulations of development of air showers produced by VHE γ-rays and protons as well as the registration of the Cherenkov light flashes from such showers by a γ-ray telescope. The detailed description of the computational code used for VHE electromagnetic cascade simulations can be found in refs. [3,6]. The quark–gluon strings model [7] was used for the description of hadron and meson interactions. Some of the calculations of the two-dimen-

0168-9002/91/$03.50 

sional Cherenkov light images induced by p-showers were made using the radial scaling model proposed by Hillas [8], but comparison of the data obtained using the two models of strong interactions mentioned above showed no significant differences in the p-shower image parameters.

The data used in subsequent sections of this paper corresponds to a power-law primary energy spectrum ($d\mathfrak{I}/dE \sim E^{-\gamma}$). For $\gamma$-showers the power exponent $\gamma$ was taken as 2.25 in the energy region (0.15–3.0) TeV. For p-showers $\gamma = 2.65$, $E \in (0.3\text{–}6.0)$ TeV.

In our calculations we considered air showers with impact parameters distributed uniformly in the range from 0 to 240 m. The optical axis of the $\gamma$-ray telescope was assumed to be in the vertical direction. The primary $\gamma$-ray arrival direction was assumed to be parallel to the telescope optical axis. The CR background showers were displaced isotropically within the field of view of the telescope.

The main characteristic of the simulated optical reflector camera is its effective area $S_{\text{eff}} = \eta k S \approx 10$ m$^2$ where $S$ is the geometric area, $\eta$ is the reflectivity of the mirror, and $k$ is the quantum efficiency of phototubes. The altitude was taken to be 1000 m above sea level.

Two hexagonal configurations of the multichannel light receiver were considered. The first of them (basic configuration) has 37 pixels with the angular size of each of them 0.5° and the total viewing angle 2.5°. For the second configuration the total number of pixels is 127, the pixel size is 0.25°, and the total field of view is 3.25°.

To reject random flashes from the night sky background we took into consideration (following the recommendations of the experiment [9]) only such events that give signals exceeding 80 photoelectrons (40 electrons for configuration 2) in at least two pixels of the light receiver (excepting the outer pixel ring for configuration 1 and two outer pixel rings for configuration 2). We attributed shower images having the largest signal in one of the pixel rings to so-called ZONEs which were numbered from the central pixel as 0, 1,...,7. In the calculations of two-dimensional shower image parameters we neglected contributions from pixels having values less than 1% from the total Cherenkov light flash intensity.

In the multidimensional analysis presented here we considered a number of the shower image parameters proposed earlier in refs. [2,3,5]. They are LENGTH, WIDTH – the longitudinal and lateral sizes of the Cherenkov light spot in the focal plane of the telescope reflector; ALPHA – the angle between the main axis of the spot and the direction to the focal plane center; MISS = DIST × sin(ALPHA), where DIST is the angular distance of the image centroid from the center of the field; TH = (WIDTH × LENGTH)$^{1/2}$; AZWIDTH = WIDTH/cos(ALPHA); U/V – the ratio of the total flash intensities in ultraviolet (0.2–0.3 μm) and visible (0.3–0.6 μm) spectral regions.

## 3. Bayesian classification of Cherenkov light images

The Bayesian approach formalizes the account of all the losses connected with probable misclassification and utilizes all the differences of alternative classes [10,11]. The decision problem in a Bayesian approach is simply described in terms of the following probability measures defined on metric spaces:

(a) The space of possible states of nature – $\theta = (\text{p}, \gamma)$ where p and $\gamma$ are the indexes of alternative classes (hypotheses);

(b) The space of possible statistical decisions – $\tilde{\theta} = (\tilde{\text{p}}, \tilde{\gamma})$ – the decision that the examined image is caused by a primary proton or a $\gamma$-quantum;

(c) Cost (losses) measure $C_{\theta\tilde{\theta}}$ defined on the direct product of nature states and decision spaces ($\theta \times \tilde{\theta}$). At correct classification the losses are equal to zero:

$$C_{\text{p}\tilde{\text{p}}} = C_{\gamma\tilde{\gamma}} = 0.$$

If we misclassify the signal event, we decrease the efficiency of $\gamma$-event registration. If we attribute hadronic images to $\gamma$-ray ones, we increase the background contamination. As we expect a significant excess of background against signal, we are interested in a strong background rejection. It is not therefore reasonable to take the symmetric loss function $C_{\text{p}\tilde{\gamma}} = C_{\tilde{\text{p}}\gamma} = 0.5$, as we did in our earlier studies concerning the cosmic-ray hadron classification by a transition radiation detector and iron nuclei fraction determination in the primary flux [12].

The determination of $C_{\text{p}\tilde{\gamma}}$ and $C_{\gamma\tilde{\text{p}}}$ values was done by maximization of the ratio of the signal value to the background fluctuations. By such a way we can obtain signal acceptance about 50% and a significant background rejection (greater than 99%);

(d) Event (measurement, feature) space – a set of possible results of a random experiment – image parameter samples obtained by a Monte Carlo simulation. We shall denote these samples by $\omega_{\text{p}}$ and $\omega_{\gamma}$ and call them training samples (TS), as the experimental image handling procedure parameters are determined by these samples;

(e) The prior measure $P_{\theta} = (P_{\gamma}, P_{\text{p}})$. We used for this measure the uniform distribution $P_{\gamma} = P_{\text{p}} = 0.5$. In this case classification results will depend only on the available experimental information and the losses. A more detailed discussion of the prior measure choice can be found in ref. [13];

(f) Conditional density (likelihood function), $\{p(x/\omega_{\text{p}}), p(x/\omega_{\gamma})\}$.

Estimating the conditional (on particle type) density on the basis of a collection of simulations is a typical

problem in cosmic-ray and high-energy physics. The application of nonparametric local density estimation methods (the kernel-type Parzen estimates [14], the K-nearest-neighbors (KNN) estimates [15]) gives the best results. Our development of these nonparametric density estimates [16] makes their use in cosmic-ray physics considerably more simple and increases their precision.

Let us introduce an invariant metric in an $N$-dimensional feature space (Mahalonobis distance):

$$R_{\mathrm{Mah}} = (x' - x)^{\mathrm{T}} \Sigma^{-1} (x' - x), \tag{1}$$

where $\Sigma$ is a covariance matrix calculated by means of the TS to which $x'$ belongs and T denotes matrix transposition. Then the KNN density estimate takes the form:

$$P_K(x/\omega_i) = \frac{K-1}{M_i V_i(x)}, \qquad i = \mathrm{p}, \gamma, \tag{2}$$

where $V_i(x)$ is the volume of an $N$-dimensional sphere containing $K$ elements of the TS nearest to the point $x$; $K$ is the parameter controlling the degree of smoothing of the empirical distribution; $M_i$ is the TS size.

As our Monte Carlo is a weighted one, we modify the KNN method to the so-called "heavy ball" method:

$$P_r(x/\omega_j) = \sum_{i=1}^{K_j} S_i / \sum_{i=1}^{M_i} S_i V_r, \qquad j = \mathrm{p}, \gamma. \tag{3}$$

where $S_i$ is the event weight; $r$ is the ball radius; $V_r$ is the ball volume; $K_j$ is the number of events falling into the ball. Here, instead of counting the number of events, the total weight of the events is calculated, and the ball radius is fixed instead of the parameter $K$. The calculations are carried out for several values of $r$ simultaneously. Then the obtained density estimates are ordered according to their magnitude and the median of the ordered sequence is taken as the final estimates;

(g) The a posteriori density $p(\omega/x) = \{p(\omega_\mathrm{p}/x), p(\omega_\gamma/x)\}$ in which the prior and experimental information is included. As we choose a uniform prior information, the a posteriori density coincides with the conditional one.

Proceeding from the above definitions we can introduce the Bayesian decision rule:

$$P(x/\omega_\gamma) C_{\mathrm{p}\bar{\gamma}} \gtrless P(x/\omega_\mathrm{p}) C_{\gamma\bar{\mathrm{p}}} \rightarrow x \in \begin{cases} \gamma, \\ \mathrm{p}. \end{cases} \tag{4}$$

## 4. Selection of an optimal feature combination

The pattern recognition is a two-stage process. It includes selection of informative variables and construction of a classifier (a decision rule) performing the recognition.

The most important problem in any field is feature extraction. Though this problem can be formalized by a linear (or nonlinear) feature space transformation [17], the feature selection problem depends mostly on the experimenter's intuition.

The quantitative comparison of the distinctive information contained in one-dimensional distributions can be made by the so called $P$-values (and $\sigma_\mathrm{P}$ quantiles) of standard statistical tests.

$$P = \int_{\sigma_\mathrm{P}}^{\infty} f(x)\, \mathrm{d}x,$$

where $f(\cdot)$ is the test function (usually a standard Gaussian distribution), and $\sigma_\mathrm{P}$ is the test statistic, calculated by model or experimental data. $P$ equals the probability of incorrectly rejecting the null hypothesis (the hypothesis that the $\gamma$-sample and p-sample come from the same population). Thus the $P$-values are inversely proportional to the studied image parameters discriminative value. Instead of using $P$-values, which are usually very small, we shall use the $\sigma_\mathrm{P}$ quantile values for comparison purposes.

The Kolmogorov nonparametric test, the Student parametric test and the Mann–Whitney rank test were used for this purpose [18]. The Fisher test was used [19] to determine the significance of correlation differences. Beside that, the so-called Bhatacharia probabilistic distance was used [20].

Table 1
$\sigma_\mathrm{P}$-quantiles of one-dimensional tests, 37 channels, ZONE 2, #$\gamma$/#p = 584/364

| Tests | AZWID | U/V | MISS | LENGTH | WIDTH | TH |
|---|---|---|---|---|---|---|
| Student | 24.86 | 14 37 | 31.76 | 19 04 | 6 85 | 17.08 |
| Kolmogorov | 11 35 | 7 49 | 10.79 | 8 90 | 5 54 | 8.95 |
| Mann–Whitney | 21.54 | 16 33 | 21.64 | 15.84 | 10 35 | 15.81 |
| Bhatacharia | 0 61 | 0.14 | 0.56 | 0.52 | 0.12 | 0.36 |
| Bayes error upper bound | 0.27 | 0 44 | 0.29 | 0.30 | 0.44 | 0.35 |

Table 2
Comparison of correlations between parameters of p- and γ-shower images by means of the Fisher test $P$-value, 37 channels, ZONE 2, #γ/#p = 584/364

| | AZWID | U/V | MISS | LENGTH | WIDTH | TH |
|---|---|---|---|---|---|---|
| AZWID | * | | | | | |
| U/V | 1.968 | * | | | | |
| MISS | 4.298 | 2 271 | * | | | |
| LENGTH | 18.561 | 0 735 | 0.503 | * | | |
| WIDTH | 24 814 | 6.989 | 6.985 | 3 785 | * | |
| TH | 3 102 | 4.628 | 4.559 | 8.655 | 2.974 | * |

The Bhatacharia distance consists of two parts – the difference in the mean values and in covariances:

$$R_{\mathrm{Bha}} = \tfrac{1}{8}(\mu_1-\mu_2)^T\left(\frac{\Sigma_1+\Sigma_2}{2}\right)^{-1}(\mu_1-\mu_2) + \frac{1}{2}\ln\left(\frac{\frac{1}{2}|\Sigma_1+\Sigma_2|}{|\Sigma_1|^{1/2}|\Sigma_2|^{1/2}}\right), \quad (5)$$

where $\mu_1$, $\mu_2$ are the feature mean values; $\Sigma_1$, $\Sigma_2$ are covariance matrices. The Bhatacharia distance is equal to zero if the classes completely overlap and it is equal to $\infty$ if they do not overlap at all. Through the Bhatacharia distance one can express the upper bound of the expected misclassification rate:

$$U_{\mathrm{B}} = 1 - \exp(-2R_{\mathrm{Bha}}). \quad (6)$$

In table 1 we give some results on the application of these statistical tests. The results in this table were obtained using events having the largest value of the signal magnitude in one of the pixels from the second pixel ring (ZONE 2) of the basic light receiver configuration. As can be seen from the table parameters AZWIDTH and MISS have the largest $P$-quantile values and the largest values of the probabilistic distance.

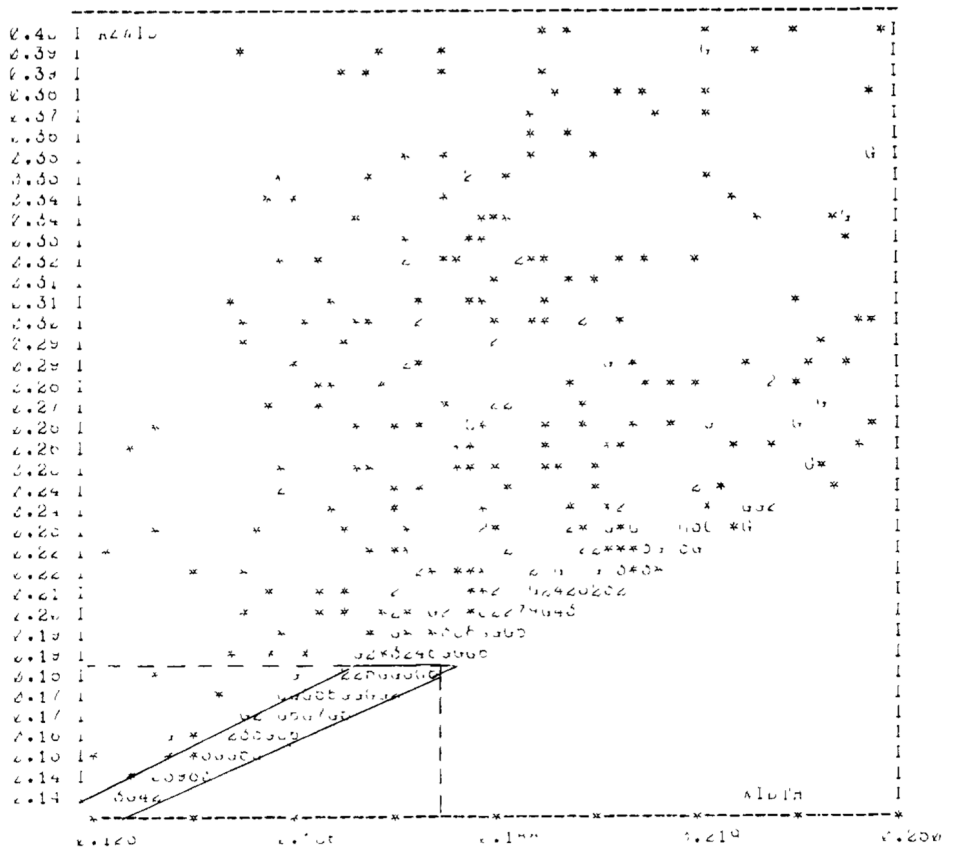

Fig. 1 Scatter plot· WIDTH vs AZWID. * P images, 364 events, correlation 0 369. G: gamma images, 586 events, correlation 0 910

Table 3
Probabilistic distances between parameter distributions of Cherenkov images of p- and γ-showers, 37 channels

| Distance | WIDTH AZWID | LENGTH AZWID | WIDTH LENGTH AZWID | WIDTH LENGTH AZWID U/V |
|---|---|---|---|---|
| Mahalonobis | 0.282 | 0 275 | 0.278 | 0 302 |
| Correlation | 0.812 | 0.530 | 1.046 | 1 070 |
| Bhatacharia | 1 004 | 0.805 | 1.324 | 1.431 |
| Bayes error upper bound | 0.167 | 0.224 | 0 133 | 0 120 |

Therefore, for these parameters the smallest overlapping takes place of the probability distributions corresponding to the alternative classes, and these parameters are the best ones.

The best pairs of features can be chosen by their correlation differences in alternative classes (see table 2). We can select the AZWIDTH–WIDTH pair on the basis that it yields the largest Fisher test value. Such a choice can be explained in the following way. For γ-images the correlation between AZWIDTH and WIDTH parameters is very strong ( ~ 1), because the plane-parallel direction of γ-rays arriving causes a radial alignment of patterns in the telescope focal plane, and AZWIDTH practically coincides with WIDTH. Images from isotropically distributed cosmic-ray protons have no preferable orientation, and the correlation between the these two parameters is not pronounced.

From the scatter plot of values of parameters WIDTH and AZWIDTH (fig. 1) we can see that the γ-domain chosen by a correlation analysis (polygonal region) is considerably better than that obtained in the ref. [2] (rectangular domain in the left lower corner of the plot) without taking into account correlations between WIDTH and AZWIDTH. A more complicated domain obtained from a multidimensional analysis provides much higher levels of signal acceptance and background rejection. On the other hand, the successive one-dimensional analysis ignores the correlation information and thus cannot outline the best γ-domain.

From table 3 it is seen that the "correlation" part of the Bhatacharia distance is about a factor of three larger than its "mean value difference" part. It is another confirmation that consideration of correlations is very important for the imaging technique.

Finally, the features should be selected as follows.

(a) The best single image parameters are selected by one-dimensional tests (table 1);
(b) The best pairs and triples are selected so that at least one of the parameters chosen above is included and their correlations are significantly different for the γ- and p-events (table 2).

Note that there are some restrictions on the possible space dimensionality which are based on the sample size [21] and which prevent increasing the number of parameters in the combination under investigation. For Cherenkov images we expect five independent parameters only – two for the image shape, one for orientation, one for position and one for the ultraviolet fraction (the U/V ratio).

## 5. The results of the multidimensional shower image analysis

To apply the technique developed here to shower image classification we used the so called "leave-one-out-at-a-time" test (the U-method). It has been shown in [22] that the U-method provides much lower bias than other methods.

According to the U-method, one event is removed from the TS, the training (conditional density estimate) is performed without it, then that element is classified and replaced in the TS. This procedure is repeated until all the TS elements are classified. By this the error rates $R_{\gamma\tilde{p}}$ and $R_{p\tilde{\gamma}}$ corresponding to the maximum available value of the signal-to-background-ratio improvement-factor,

$$\eta = \left(1 - R_{\gamma\tilde{p}}\right) / \sqrt{R_{p\tilde{\gamma}}}, \qquad (7)$$

are obtained.

In table 4 we present some results of application of this technique for the case of the a parameter In addition, we present in this table results obtained on the basis of the Monte Carlo calculations of Hillas taken from ref. [23]. It may be seen from the table that there is a good agreement between the data.

Table 4
Data on the discrimination against p-showers in the case of single discrimination parameters usage, 37 channels, ZONE1 and ZONE2

| | LENGTH | WIDTH | DIST | MISS | AZWID |
|---|---|---|---|---|---|
| Our data [a,b] | 0.932 | 0.942 | 0 791 | 0.714 | 0.615 |
| | 0.186 | 0.458 | 0.384 | 0 206 | 0.069 |
| | 2.162 | 1.392 | 1.276 | 1.571 | 2 346 |
| From ref. [23] [a] | 0.826 | 0 858 | 0 935 | 0.676 | 0.768 |
| | 0 210 | 0.367 | 0 683 | 0.231 | 0.121 |
| | 1 802 | 1 416 | 1.132 | 1 408 | 2.204 |

[a] 1st line, acception efficiency for gamma showers $R_{\gamma\tilde{\gamma}}$, 2nd line contributed proton showers background $R_{p\tilde{\gamma}}$; 3rd line: discrimination efficiency improvement $R_{\gamma\tilde{\gamma}} / \sqrt{R_{p\tilde{\gamma}}}$

[b] To obtain these data special calculations were done in which the same observation level and effective mirror surface square as in ref. [23] were used

Table 5
Comparison of different parameters combinations for multidimensional proton background rejection

| ZONE | EVENT (#γ/#P) | TH LENGTH AZWID [a] | WIDTH LENGHT MISS [a] | WIDTH LENGTH AZWID [a] | WIDTH LENGTH MISS U/V [a] | WIDTH LENGTH U/V AZWID [a] | TH LENGTH U/V AZWID [a] |
|---|---|---|---|---|---|---|---|
| *37 channels* | | | | | | | |
| 1 | 639/229 | 0.421 | 0.228 | 0.333 | 0.445 | 0 346 | 0 379 |
| | | 0.016 | 0 008 | 0.008 | 0.004 | 0.003 | 0 003 |
| | | 3.320 | 2 549 | 3.674 | 6.973 | 6 317 | 6 572 |
| 2 | 584/364 | 0.537 | 0.411 | 0.501 | 0.698 | 0 51 | 0.384 |
| | | 0.001 | 0.004 | 0.001 | 0 012 | 0.001 | 0 001 |
| | | 21.820 | 6 766 | 13.077 | 6.299 | 17 652 | 11.410 |
| All | 1797/939 | 0 317 | 0.543 | 0.384 | 0.394 | 0 363 | 0 411 |
| | | 0.004 | 0.047 | 0.010 | 0 018 | 0 013 | 0 018 |
| | | 4 958 | 2 503 | 3.896 | 2.958 | 3 172 | 3.050 |
| 1 & 2 | 1233/593 | 0.477 | 0 315 | 0.414 | 0.565 | 0 429 | 0.381 |
| | | 0.007 | 0 006 | 0.004 | 0.009 | 0 002 | 0.002 |
| | | 5.689 | 4 232 | 6.806 | 6.388 | 10.210 | 9.071 |
| *127 channels* | | | | | | | |
| 3 | 336/156 | 0.605 | 0.722 | 0.584 | 0.552 | 0 654 | 0.628 |
| | | 0.003 | 0.008 | 0.002 | 0.001 | 0 002 | 0.002 |
| | | 10.770 | 8.273 | 12.120 | 15.560 | 14.624 | 14.050 |
| 4 | 345/214 | 0.624 | 0.658 | 0.649 | 0.583 | 0 624 | 0 590 |
| | | 0.004 | 0.004 | 0.004 | 0.004 | 0.004 | 0 004 |
| | | 9.448 | 9.887 | 9.834 | 8.836 | 9.449 | 8 943 |

[a] 1st line: acception efficiency for gamma showers $R_{\gamma\tilde{\gamma}}$; 2nd line. contributed proton showers background $R_{p\tilde{\gamma}}$; 3rd line discrimination efficiency improvement $R_{\gamma\tilde{\gamma}}/\sqrt{R_{p\tilde{\gamma}}}$

The results of multidimensional analysis for several image parameter combinations are presented in table 5. It is seen that background contamination can be rejected down to a few tenths of a percent. For the 37 channel receiver configuration with a pixel size of 0.5° the best background discrimination is attained for the second ZONE. The 127-channel camera with a pixel size of 0.25° provides almost uniform background rejection over all the central ZONEs.

It should be noted that the very large $\eta$ values in table 5 (values in excess of 10) would have large statistical uncertainty due to the limited number of background images.

As you can see in fig. 2 we can choose the value of the losses measure to obtain the desirable relation between the coefficients of the signal acceptance and background rejection. Moving to the left along the $x$ = axis of fig. 2 we can reach the almost background-free region at losses value $< 0.5$. But for small values of losses (this corresponds to low values of background contamination) the signal acceptance level will be quite high (say, about 0.5) only in the case of multidimen-

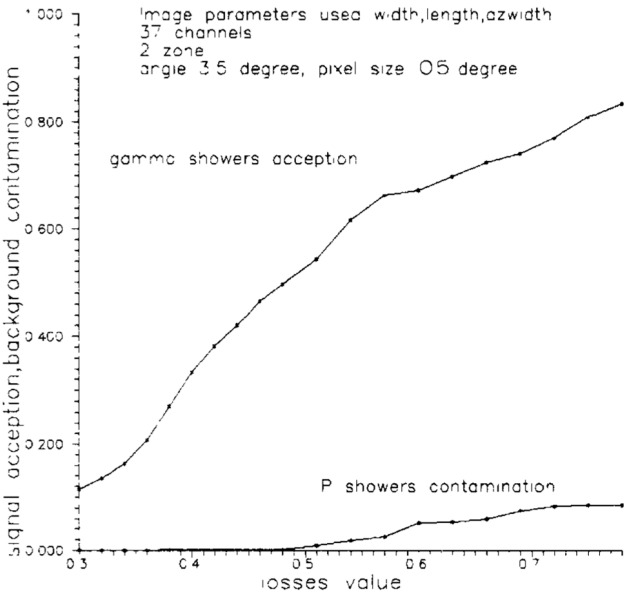


Fig. 2. Bayesian classification.

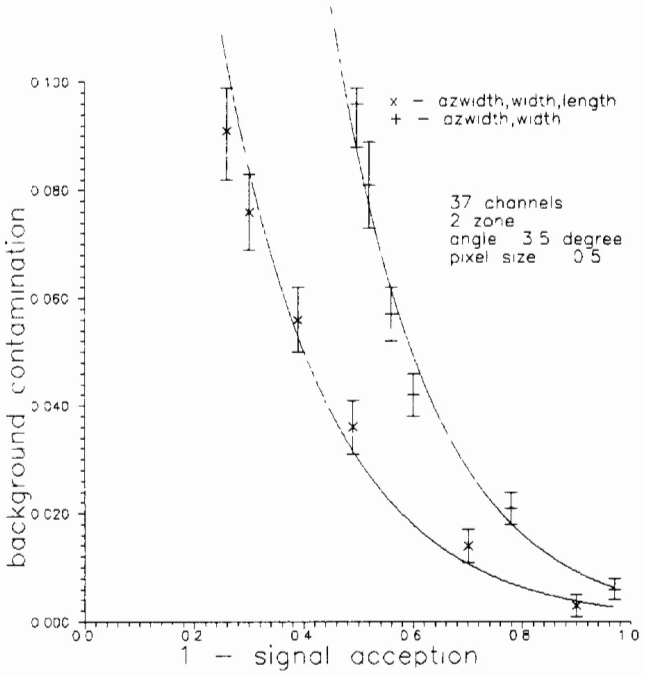


Fig. 3. Preference curves.

sional analysis. This can be seen from fig. 3 where the relations between background rejection and signal detection effectiveness are presented for parameters combinations AZWIDTH + WIDTH + LENGTH, AZWIDTH + WIDTH.

To conclude, multidimensional analysis provides much greater discrimination efficiency compared to the application of several image parameters independently without taking into account their correlations as in ref. [24].

## Acknowledgement

We are grateful to M. Cawley for useful discussions.

## References

[1] T.C. Weekes, Nucl. Instr. and Meth. A264 (1988) 55
[2] A.M. Hillas, Proc. 19th ICRC, USA, 1985, vol. 3, p. 445.
[3] A.V. Plyasheshnikov and G.F. Bignami, Nuovo Cimento 8c (1985) p. 39
[4] T.C. Weekes, R.C. Lamb and A.M. Hillas, Proc. NATO Workshop on VHE γ-Ray Astronomy, Durham, ed. K E Turver (Reidel, Boston, 1987) p. 235.
[5] Y.L. Zyskin, Proc. Worksop of VHE γ-Ray Astronomy, Crimea, 1989, p. 148.
[6] A.V. Plyasheshnikov and A.K. Konopelko, The energy estimation of VHE γ by the Cerenkov teleskope with the multi-channel receiver, Proc workshop of VHE gamma-ray astronomy, Crimea, 1989.
[7] Y.M. Shabelsky, Preprint LIAF, 1986.
[8] A M. Hillas, Proc 16th ICRC, Kyoto, Japan, 1979, vol. 6, p. 13
[9] M.F. Cawley, D.J. Fegan et al, Proc. 19th ICRC, USA, 1985, vol. 3, p. 449.
[10] H. Raiffa and R Schlaifer, Applied Statistical Decision Theory (MIT, Cambridge, MA, 1978)
[11] J D. Hey, An Introduction to Bayesian Statistical Inference (Robertson, 1983).
[12] V.G. Denisova, A M. Dunaevsky, S.A. Slavatinsky et al., Proc. 20th ICRC, Moscow, USSR, 1987, vol. OG 5.1, p. 390.
[13] E.E. Leamer, Ad hoc Inference with Nonexperimental Data (Wiley, New York, NY, USA, 1981)
[14] E Parzen, Ann Math. Stat. 33 (1962) 1065
[15] D.O Lofsgaarden and C.D Quesenberry, Ann. Math. Stat. 36 (1965) 1049.
[16] A.A Chilingarian, Comput. Phys. Commun. 54 (1989) 381.
[17] K Fukunaga, Introducton to Statistical Pattern Recognition (Academic Press, New York, 1972).
[18] System/360 Scientific Subroutine Package (360a-cm-03x) (IBM, Technical Publications Department, New York, NY, USA, 1971).
[19] K Uberla, Faktorenanalysis (Springer, Berlin, 1977).
[20] A. Bhatacharia, Sankhya 7 (1946) 401
[21] S Kh. Galfayan, A.M. Dunaevsky et al., Preprint FIAN no 332 (1986).
[22] A.A. Chilingarian, S.Kh. Galfayan et al., Proc. 20th ICRC, Moscaw, USSR, 1987, v. HE5, p 487.
[23] K.G. Gibbs, Ph.D. thesis, University of Arizona (1986).
[24] A.M. Hillas, J.R. Patterson, Proc. NATO Workshop on VHE γ-Ray Astronomy, Durham (Reidel, Boston, 1987) p. 249

Computer Physics Communications 69 (1992) 347–359
North-Holland

Computer Physics Communications

# Dimensionality analysis of multiparticle production at high energies

A.A. Chilingarian
*Yerevan Physics Institute, Alichanian brothers St. 2, Yerevan 36, Armenia*

Received 10 May 1990; in revised form 1 July 1991

An algorithm for the analysis of multiparticle final states is offered. By the Renyi dimensionalities, which were calculated according to experimental data, either the hadron distribution over rapidity intervals or the particle distribution in an $N$-dimensional momentum space, we can judge the degree of correlation of particles, separate the momentum-space projections and areas where probability measure singularities are observed. The method is tested in a series of calculations with samples of fractal object points and with samples obtained by means of different generators of pseudo- and quasi-random numbers.

## 1. Phenomenological description of multiparticle production

The significant increase of information about multiparticle final states produced in particle collisions with higher and higher energies makes it urgent to develop non-traditional methods of analysis of experimental data. From the parameters of the detected particles one can construct many joint and conditional probability distributions which are much more informative than the averaged characteristics [1].

Since the general theory of strong interactions is not yet complete, a phenomenological approach to ultra-high-energy collisions is widely used. One of the first theoretical generalizations of multiparticle production processes is KNO scaling, which predicts that at sufficiently high energies the distribution of hadron multiplicity $P_n$ obeys the scaling

$$P_n\langle n\rangle = \Psi(z), \quad z = n/\langle n\rangle, \tag{1}$$

where $P_n$ is the probability to observe $n$ hadrons in the final state, and $\langle n\rangle$ is the mean multiplicity at a given energy.

Since the Poisson distribution

$$P_n = \langle n\rangle^n \, \mathrm{e}^{-\langle n\rangle}/n! \tag{2}$$

describes the hadron multiplicity badly, it was proposed to use the negative binomial distribution and the Bose–Einstein distribution, which supposes the presence of $k$ independent random sources with the same intensity:

$$P_n^{\langle k\rangle}\langle n\rangle = \Psi_k(z) = k^k z^{k-1} \, \mathrm{e}^{-kz}/(k-1)!. \tag{3}$$

Carruthers has shown [2] that $\Psi_2(z)$ describes the ISR and SPS data well.

Though the description of the nature of random sources meets difficulties, it has recently been possible, using the Bose–Einstein correlations, to estimate the size of hadron sources [3]. The source size in p–$\bar{\mathrm{p}}$ collisions did not change when the energy changed from 0.9 to 2.2 TeV in the c.m.s. (as was to be expected, if the KNO scaling was satisfied) and was in a linear dependence with the charge density in the pseudorapidity bin $(\Delta n/\Delta\eta)$:

$$R_{\mathrm{Fermi}} = 0.59 \pm 0.05(\Delta n/\Delta\eta). \tag{4}$$

Recently the particle distribution in rapidity windows has become the object of great attention. Large fluctuations in some rapidity bins, which were found in experiments at colliders and in cosmic-ray experiments [4], could not find any description in the frame of earlier suggested phenomenological mechanisms. The conclusion was drawn that the large fluctuations in the rapidity distributions reflect non-trivial fluctuations of hadronic matter during collisions.

Until how the instrument of investigation of non-trivial rapidity correlations has been the study of the dependence of normalized moments of the rapidity distributions on the size of the rapidity bin [5]. Several modifications of the moments method are suggested:

$$C_q = \langle n^q \rangle / \langle n \rangle^q, \quad q = 1, 2, \ldots, \tag{5}$$

$$C'_q = \langle (n - \langle n \rangle)^q \rangle / \langle n \rangle^q, \tag{6}$$

$$C''_q = \langle n(n-1) \cdots (n-q+1) \rangle / \langle n \rangle^q, \tag{7}$$

where $q$ is the order of the normalized momenta and $\langle\ \rangle$ means averaging over the rapidity bins.

Let us write down a more detailed expression of a normalized moment,

$$C_q(M) = \frac{1}{M} \sum_{m=1}^{M} n_m^q / \langle n_m \rangle^q, \tag{8}$$

where $M$ is the number of equal rapidity bins $\delta_y = \Delta/M$, $\Delta$ usually is the interval $(-2, 2)$, i.e. $\delta_y = 4/M$, $n_m$ is the number of hadrons falling into the $m$th bin, and $\langle n_m \rangle$ is the average bin population of events with multiplicity $n$.

Let us consider, following ref. [6], how the normalized moments behave assuming first absence of correlation and then very strong correlation. Consider the uniform bins distribution: $n_m = N/M$, $m = 1, \ldots M$. It is easily seen that for all $q$, $F_q(M) = 1$. And if all the hadrons have fallen into the same bin, $n_m = N$ for some $m = r$, and $n_m = 0$ for the rest of $m$, then

$$C_q(M) = M^{q-1}, \tag{9}$$

i.e. at an extremal fluctuation the moments significantly increase with the number of bins. That is why the moments method sometimes is called a magnifier for exposure of non-uniformities. Rewriting eq. (9) in a somewhat different form and taking its logarithm gives

$$C_q(M) = (\Delta/\delta_M)^{q-1}, \tag{10}$$

$$\ln C_q(M) = -(q-1) \ln \delta_M + (q-1) \ln \Delta. \tag{11}$$

The moments logarithm depends linearly on the logarithm of the bin size. A random quantity with such a behaviour is called *intermittent* and the factor multiplying the logarithm of the bin size is called the *index of intermittency*. An intermittent random quantity in a sense is the opposite of a Gaussian one, for which a considerable deviation from the average value is very improbable.

If even after averaging over all the events (events with both the same and different multiplicity can be averaged), the scaling relation

$$\ln\langle C_q(M) \rangle = -\lambda_q \ln \delta_M + g_q \ln \Delta \tag{12}$$

is satisfied, then the physical process investigated is characterized by *intermittency*.

It is obvious that the experimental growth of normalized moments, revealed in a wide energy range of hadronic and leptonic collisions, is a new main characteristic of multiparticle production, which emphasizes the role of very short-range correlations compared with the usual short-range ones responsible for resonance production.

The first phenomenological mechanism describing the behaviour of factorial moments was the hypothesis of the existence of two types of sources: *luminary*, with a regular signal distribution, and *turbulent*, which is characterized by chaotic bursts [7]. When colliding, the parton, passing through and interacting in hadronic matter, enters high-density regions (narrow channels), emits many particles, also passes through low-density regions (wide channels) and uniformly emits few particles. In such an interpretation, the main attention is drawn to the very complicated trajectory of the partons wandering in the hadronic matter [8]. But we believe a much more natural way to interpret the anomalous behaviour of normalized moments is based on the hierarchy (self-similarity) of the processes of multiparticle

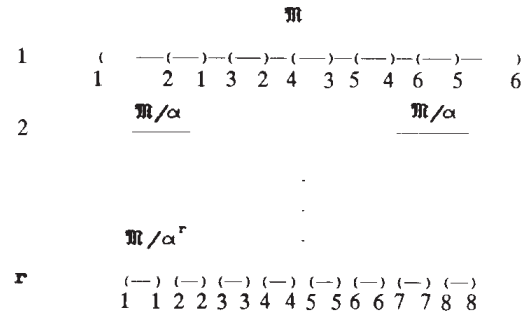


Fig. 1. Self-similar cascade decay of a particle with mass $m$. On the $r$th step of the cascade development there are $2r$ particles with mass $m/\alpha^r$.

production and on the notion of fractal (multifractal) dimensionality, closely connected with self-similarity.

Relations like (12) are a consequence of self-similarity in the structure studied and give ground to carry out a dimensionality analysis. A dimensionality analysis means revealing in a $3N$-dimensional momentum space (or in a one-dimensional rapidity space) lower-dimensional regions where the events are grouped.

At present a number of simulations of quark–gluon cascade development in hadronic matter [9,10] are available. The updating of the LUND program based on the idea of parton–hadron duality [11,12] led to the realization that the unusual behaviour of normalized moments is due to the QCD cascade [12,13].

Before going on to the fractal analysis formalism, we shall show how a non-integer fractal dimensionality can arise in the simplest cascade process of the decay of a particle of mass $m$ [14] (see fig. 1).

On each self-similarity step of the cascade the mass decreases by a factor of $1/\alpha$, with $\alpha \geq 2$. ($\alpha = 2$ if final-state particles are produced with zero kinetic energy). On the $r$th step of the cascade we have $2r$ particles with mass $(1/\alpha)^r m$. The masses of the particles obtained as a result of the cascade constitute the metric set $\mathscr{K}$.

Let us show that at the beginning of the cascade process the topological dimension $d_T\mathscr{K} = 1$, and then later $d_T\mathscr{K} < 1$.

The topological dimension is equal to $\mathscr{T}$, if it is possible to enter the finite open coverage of the multiplicity $\leq \mathscr{T} + 1$ into any finite open coverage of the set $\mathscr{K}$, and if there exist such finite open coverages of $\mathscr{K}$ into which it is impossible to enter finite open coverages of multiplicity $\mathscr{T} + 2$. The coverage multiplicity is the maximum number of coverage elements containing common points of the set $\mathscr{K}$ [15]. For our example, the possibility of entering coverages of multiplicity 2 into any open coverage of $\mathscr{K}$ is a necessary condition for the dimension to be equal to unity.

The open intervals 1–1, 2–2, ..., in fig. 1 form the finite open coverage of the set $\mathscr{K}$. As can be seen from this figure, it is possible to enter the coverage of multiplicity 2 for the incident particle – it is enough to take somewhat shorter intervals of coverage and they will also intersect, i.e. the multiplicity is 2; and for the $r$th step of the cascade it is impossible, since the intersecting intervals cannot be embedded in the non-intersecting ones.

## 2. The technique of dimensionality analysis

Cascade processes, which are frequent in high-energy physics, are due to some characteristic dimensionality. But, in contrast to the ideal self-similar cascades of geometric figures (e.g. Serpinski's carpet), in real physical systems there are possible deviations from self-similarity and, first of all, they contain not a single, but several characteristic scales connected with some dimensionality. The main goal of the dimensionality analysis is to reveal these dimensionalities and to relate them to the dynamic mechanisms responsible for their production.

There exist many different definitions of dimensionality. The following definition can easily be generalized to a non-integer case,

$$d_F = -\lim_{l \to 0} \frac{\ln N(l)}{\ln l}, \tag{13}$$

where $N(l)$ is the coverage of the set under investigation by open $l$-spheres.

It can be shown that $d_F \leq d_T$ and, if $d_F < d_T$, then the object is called a fractal object, i.e.

having a fractional dimensionality. Note that definition (13) has a purely geometric nature.

A set of events recorded in an experiment fill momentum space very nonuniformly, reflecting via the structure the dynamic mechanisms of particle production. That is why the event distribution over $N(l)$ bins will be highly non-uniform and this non-uniformity with a physical meaning is not reflected at all.

To generalize the notion (13), it is necessary to choose a universal measure fit to characterize the momentum-space structure non-uniformities. The subject of measure was discussed for dynamical systems turning to chaos [16]. For such systems, due to the necessity for transition from time averages to spatial ones, invariance of measure is required. There is no such problem for experimental data analysis, since the object (a population of points) can be considered as given, and time is not an essential characteristic. Besides, the object is compact: for any open coverage there exists a finite subcoverage.

Let us consider the $l$-coverage of the compact. In each bin $N_i(l)$ determine probability (cellular) measure (mass),

$$P_i(l) = \int_A \mathrm{d}\rho(x), \tag{14}$$

where $A$ is the volume of a bin with size $l$, $\rho(x)$ is a probability density function determined in the whole space by means of some non-parametric method, by the experimental data or by a Monte Carlo simulation program [17].

From the point of view of experimental resolution it is important to use the cellular measure $P_i(l)$, though $l$ should not be so small that the integral $\int_A \rho(x)$ loses its meaning.

The basic approach to dimensionality analysis lies in characterizing physical systems by the invariant probability measure singularities [18]. To do this, let us determine the scaling of the moments of the random quantity $p_i(l)$ of order $q$ at scale $l$:

$$C_q(l) \equiv \langle p_i(l)^q \rangle \equiv \sum_{i=1}^{N(l)} p_i(l)^{q+1} \sim l^{\phi(q)},$$

$$\phi(q) = qd_{q+1}, \tag{15}$$

where $d_q$ are the Renyi dimensions (generalized dimensions) determined for $-\infty < q < +\infty$. At $q = -1$, the relation (15) determines the capacity dimension $d_F = d_0$, at $q = 0$ the information dimensionality $d_1$, and at $q = 1$ the correlation dimension $d_2$.

If the fractal is uniform (geometric), then

$$p_i \equiv p = 1/N_l, \quad N_l = N(l), \tag{16}$$

and

$$(1/N_l)^{q-1} N_l \sim l^{qd_{q+1}}, \tag{17}$$

hence we obtain for all $q$,

$$\ln N_l \sim -d_0 \ln l, \tag{18}$$

i.e. for uniform fractals the Renyi dimensions of any order are the same and are equal to the fractal dimension, and the scaling of the $q$th order momentum is characterized by the index $qd_0$, which increases linearly with the momentum order. And if the fractal is non-uniform, then all $d_q$ are different (anomalous scaling) and the deviation from the dimensionality can be characterized by:

$$d_q - qd_0. \tag{19}$$

Thus, as in the case of normalized moments (6), the Renyi dimensions can serve as quantitative power indices of non-uniformity of both the rapidity distribution and the hadron distribution in momentum space.

The Renyi dimensions are defined as a slope connecting some values of $\{l_i\}$ with the corresponding values of $\{C_q(l_i)\}$ in a double-logarithmic scale. But the direct application of formula (15) to Renyi dimension calculation is rather time-consuming and, moreover, there are no instructions regarding the choice of the box-size sequence $\{l_i\}$. Algorithms based on nearest-neighbour information (NN-algorithms) are much more efficient than box-counting algorithms and they introduce a natural scale, the sample-averaged distance to NN,

$$\bar{R}_k, \quad k = 1, 2, \ldots, M,$$

where $M$ is total number of events in the sample.

Using the ergodic theorem one can make a replacement [19,20],

$$\sum_{i=1}^{N(l)} p_i(l)^{q+1} \approx \sum_{j=1}^{M} \tilde{p}_j^q \approx Q_l, \tag{20}$$

where $\tilde{p}_j$ is the probability to find the point of the studied set not in the box of size $l$ but inside the hypersphere of radius $l$, centered at some other point of the studied set and $Q_l$ is the total number of $q$-tuples within this sphere.

For a $\bar{R}_k$ sequence the scaling relation takes the form

$$Q_{\bar{R}_k} \sim \bar{R}_k^{\phi(q)}. \tag{21}$$

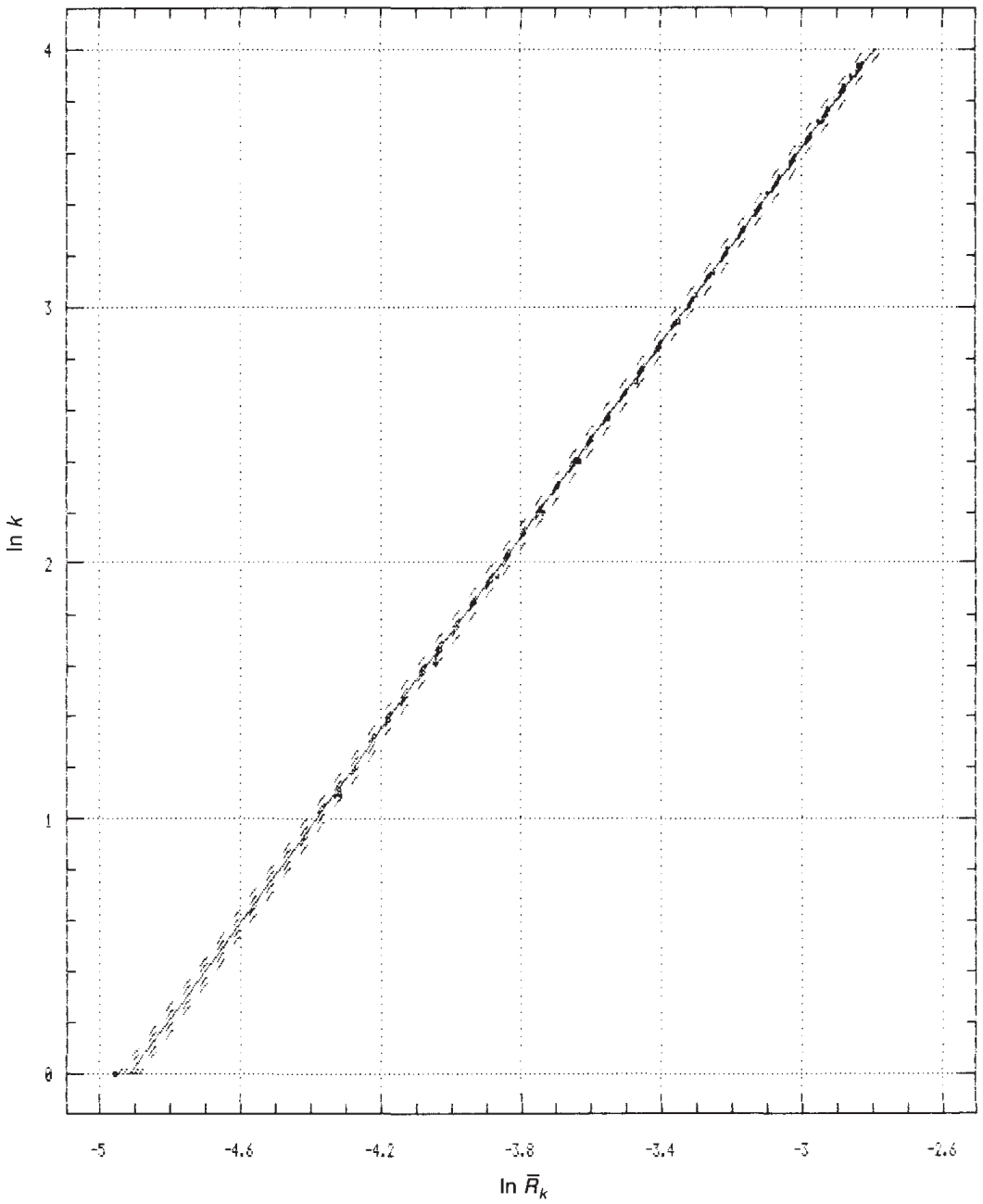


Fig. 2. The straight line slope determination, by which the correlation dimensionality of the Serpinski carpet is determined.

For $q = 1$ (correlation dimension), the number of $q$-tuples is simply equal to the number of sample events within $l$-spheres, and the left-hand side of (21) is equivalent to the mean number of sample points inside a hypersphere with radius equal to the average distance to the $k$th neighbour, i.e. is equal to the number $k$, so

$$k \sim \bar{R}_k^{d_2}. \tag{22}$$

Hence, the modified algorithm defines $d_2$ as a slope of the $k$-dependence of $\bar{R}_k$ in a double-logarithmic scale.

Figure 2 shows such dependence used to define the correlation dimension of the Sterpinski carpet. The dimension was determined by the least-squares method through 25 points: The logarithm of the number of the nearest neighbour 1, 3, ... 49 is approximated by the logarithm of the sample-averaged distance to the nearest neighbour. Of course, the number of events must be large enough; there is a definite relation between the space dimensionality and the minimum number of events needed to draw consistent conclusions.

By the $\phi(q)$ dependence it is possible to classify different events of multiparticle production [21], since a multifractal object can be considered as an interwoven family of uniform fractals, each obeying the scaling law with index $d_0^{\alpha}$.

Note that the dimensionalities of $d_0^{\alpha}$ are not in any way connected with the regions where singularities of the probability measure arise, i.e. it is impossible to recover the spatial structure of the multifractal support from the $d_q$ spectrum. That is why we believe that the local dimensionality

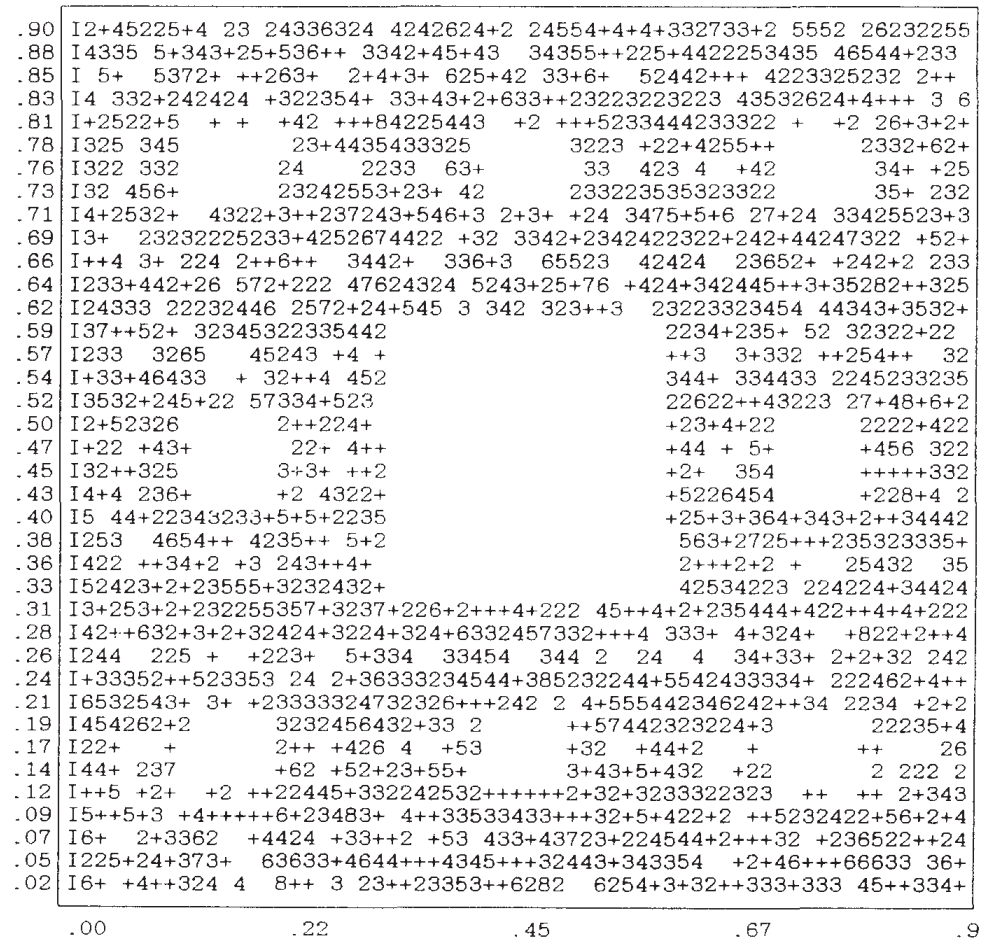


Fig. 3. The 5th generation of the Serpinski carpet, 5000 points.

introduced in ref. [22] may be useful in separating the momentum-space regions where considerable fluctuations of the invariant probability measure are observed.

A description of the algorithm for the local and global correlation dimension calculation is presented in the next section, along with an interesting relation of the fractal dimensions to the *intrinsic dimension*, a notion developed also in the mathematical theory of pattern recognition.

## 3. KNN estimation of probability density. Local and global dimensionality.

Consider the KNN estimation of probability density [23] which is a development of the well-known histogram method,

$$\rho_k(x_i) = \frac{k}{MV_k(x_i)}, \tag{23}$$

where $V_k(x_i)$ is the volume of a $d$-dimensional hypersphere containing the $k$ nearest neighbours to $x_i$.

$$V_k(x_i) = V_d R_k^d, \qquad V_d = \frac{\pi^{d/2}}{\Gamma(d/2+1)}, \tag{24}$$

where $R_k$ is the distance to the $k$th nearest neighbour of $x_i$ and $\Gamma(z)$ is the gamma function. From eqs. (23) and (24) we can readily obtain [24]

$$\ln R_k(x_i) = \frac{1}{d}\ln k + \ln\left[MV_d\rho_k(x_i)\right]^{-1/d}. \tag{25}$$

Equation (25) cannot be solved for $d$, since the estimate of $\rho(x_i)$, as one can see from eq. (23), depends on $k$. Therefore, let us average $R_k$ over the whole sample, according to the distribution function,

$$f_{k,x}(R) = CdR^{d-1}\frac{(CR^d)^{k-1}}{\Gamma(k)}e^{-CR^d}, \tag{26}$$

where $C = M\rho(x)\,V_d$.

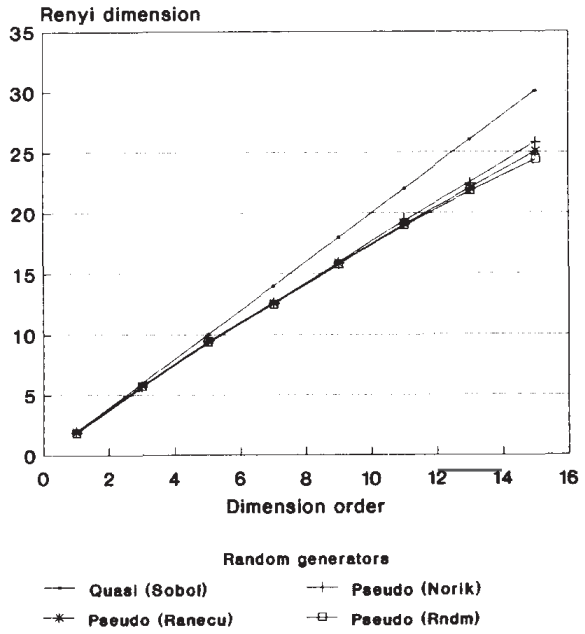


Fig. 4. The $\phi(q)$ curve. For a complete uniformity of quasi-random numbers in a square of side 1, all the Renyi dimensions are the same, the pseudo-random numbers somewhat deviate from uniformity.

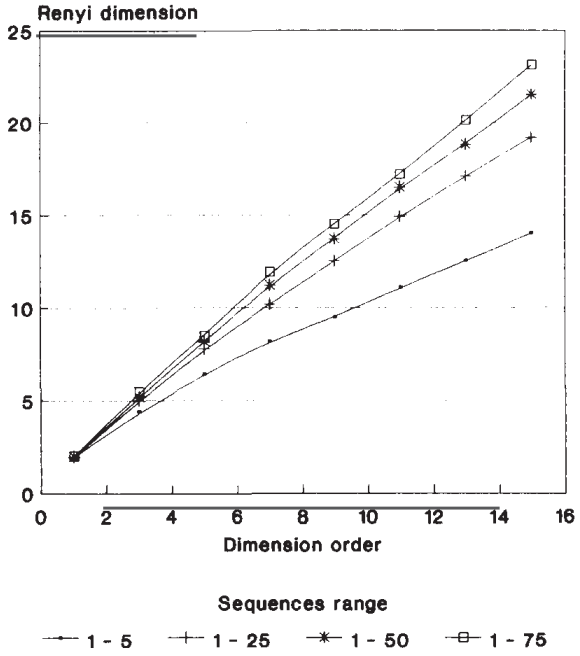


Fig. 5. Comparison of the degree of non-uniformity of the population of a unit square by two-dimensional random numbers (the RNDM generator). The narrower the $\bar{R}_k$ sequence for determination of the Renyi dimension, the higher the nonuniformity.

In the approximation of small $R$ and large $M$ we obtain the following equations:

$$\ln G_{k,d} + \ln \bar{R}_k = \frac{1}{d} \ln k + \text{constant}, \tag{27}$$

$$G_{k,d} = \frac{k^{1/d}\Gamma(k)}{\Gamma(k+1/d)}, \tag{28}$$

where $\bar{R}_k$ is the sample-averaged distance to the $k$th nearest neighbour and the constant is independent of $k$.

The difference between this scaling equation and those we obtained previously by a completely different approach, consists in the so-called iterative addition $G_{k,d}$, which is close to zero for all $k$ and $d$. Therefore, we solve this equation iteratively, first assuming $G_{k,d} = 0$, and then, having obtained $d_i$, we calculate $G_{k,d_i}$ and determine the value of $d_{i+1}$. We stop the iterations when $d$ becomes nearly constant.

Such verification of $d$-estimates is connected with the averaging of the correlation integral. The correlation integral (the number of sample points inside a hypersphere of fixed radius) is a random variable belonging to a binomial distribution with parameter $\rho(x)$ (the probability for the sample point to fall within this hypersphere).

Notice that our estimate is global, i.e. the whole sample is characterized by one number, though local differences are possible. From this point of view, local dimensionality is much more interesting, since it allows us to detect local inhomogeneities corresponding to various dynamical mechanisms.

Consider eq. (25) again. Apart from sample averaging, there is also one more way to get a linear equation for determining the dimension. For this, one must choose the series $\{k_j\}$ such that the density estimates are very close, and hence the dependence of $\rho_k(x)$ on $k$ can be ignored. Following these chosen values $\{k_j\}$ and the corresponding $\{R_{k_j}(x_i)\}$, one can estimate the local dimension at the point $x_i$.

## 4. The simulation study

The Renyi dimension was determined for the samples generated by the algorithm for the Serpinski carpet (fig. 3), the Henon map, and for

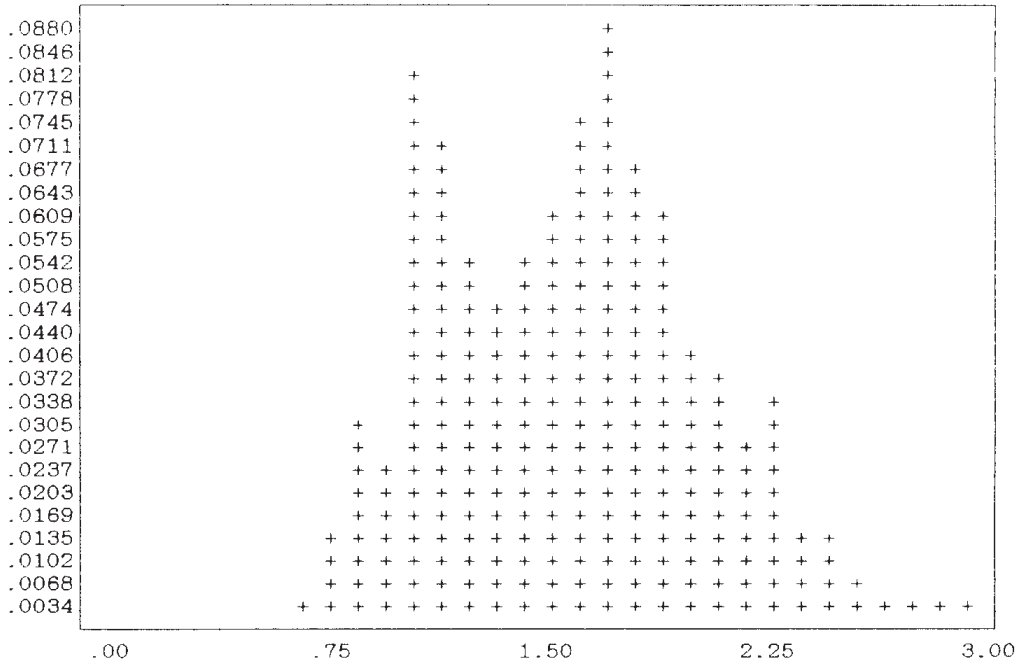


Fig. 6. Histogram of the local dimensionality of a mixed sample – a Serpinski carpet and a Henon map.

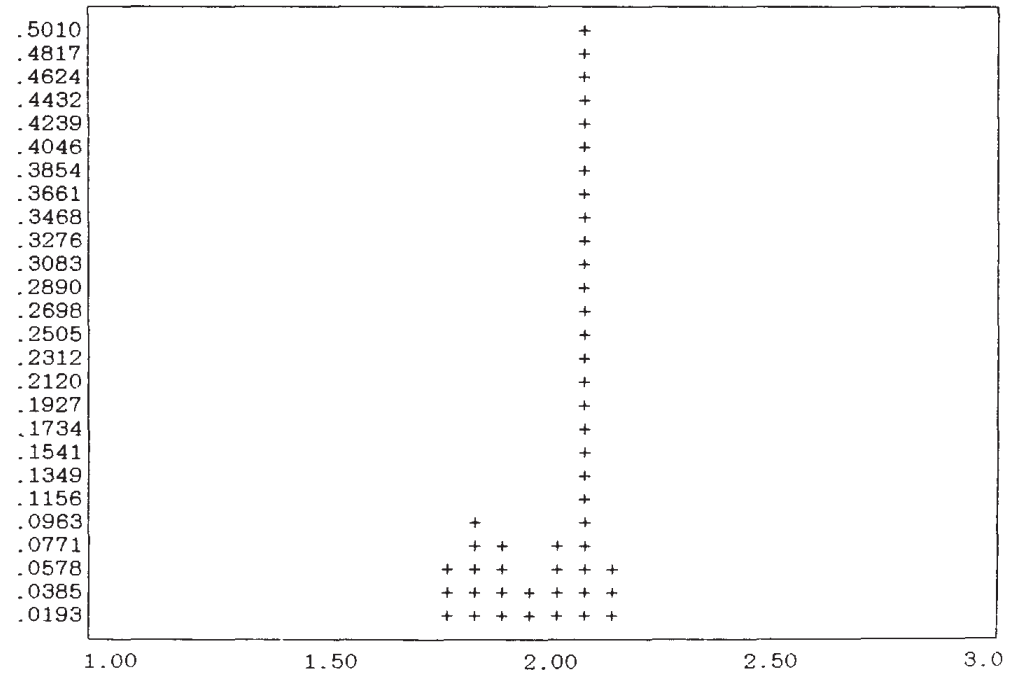


Fig. 7. Distribution (normalized histogram) of the local dimensionalities determined for samples of two-dimensional quasi-random numbers.

samples obtained by different random-number generators.

The experiments were carried out to investigate the sensitivity of the method to the choice of parameters which include the sample size, the sequence of the nearest neighbours and the order

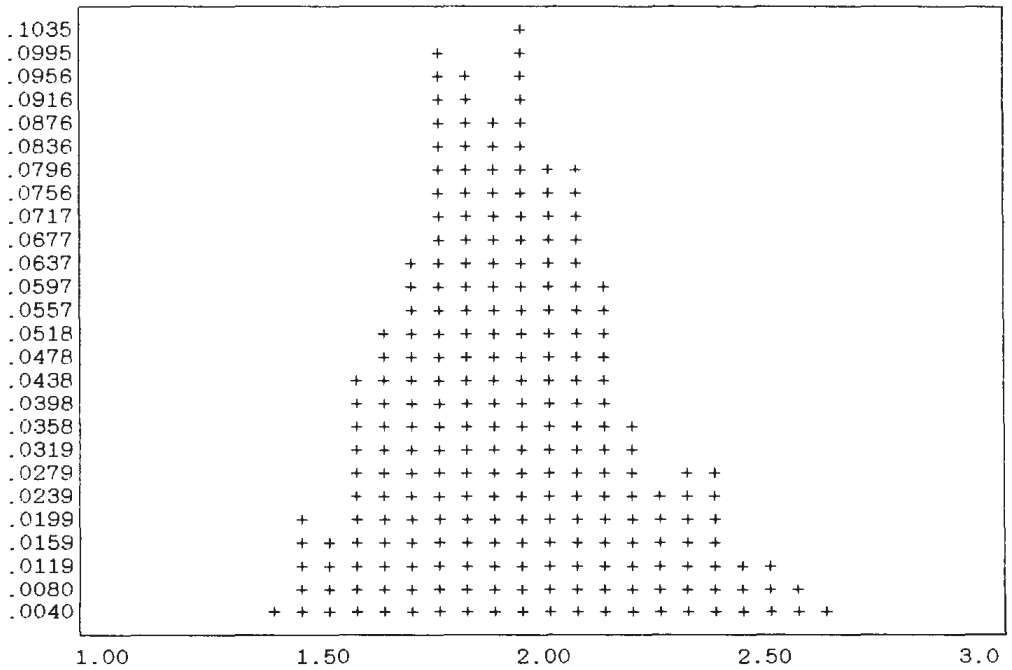


Fig. 8. Distribution (normalized histogram) of the local dimensionalities determined for samples of two-dimensional pseudo-random numbers.

of the Renyi dimensions, and to study the possibilities of separating the regions with anomalous structure. We also considered the quality of the quasi-random-number generators, an important aspect for many applications. For comparison of the uniformity of the population of an $N$-dimensional space by "random" numbers, we used "quasi-random" numbers – LP-sieves, which uniformly fill an $N$-dimensional cube [25].

Figure 4 presents the Renyi dimensions of order from 1 to 15 – the function $\phi(q)$. The three random-number generators being compared are: RNDM, which has been widely used in the past decade; RANECU, a generator recently recommended by F. James [26], and NORIK, a matrix generator designed in the Yerevan Physics Institute [27].

Sets of two-dimensional random quantities distributed in a square of side 1 were considered. The slopes connecting the values of the moments of the invariant probability measure (15) were calculated through 70 points for distances equal to the average distance to the nearest neighbours with numbers from 6 to 75, the orders of dimensions being chosen from 1 to 15. The sample sizes were 1000 and 5000.

For a strictly periodic structure of LP-sieves, all the Renyi dimensions are the same: $\phi(q) = qd_0$ and the random-number generators show some deviation from uniformity, which is due to the limited sample sizes. The matrix generator reveals somewhat better results.

Figure 5 presents Renyi dimensions calculated using different $\overline{R}_k$-sequences (the sequences con-

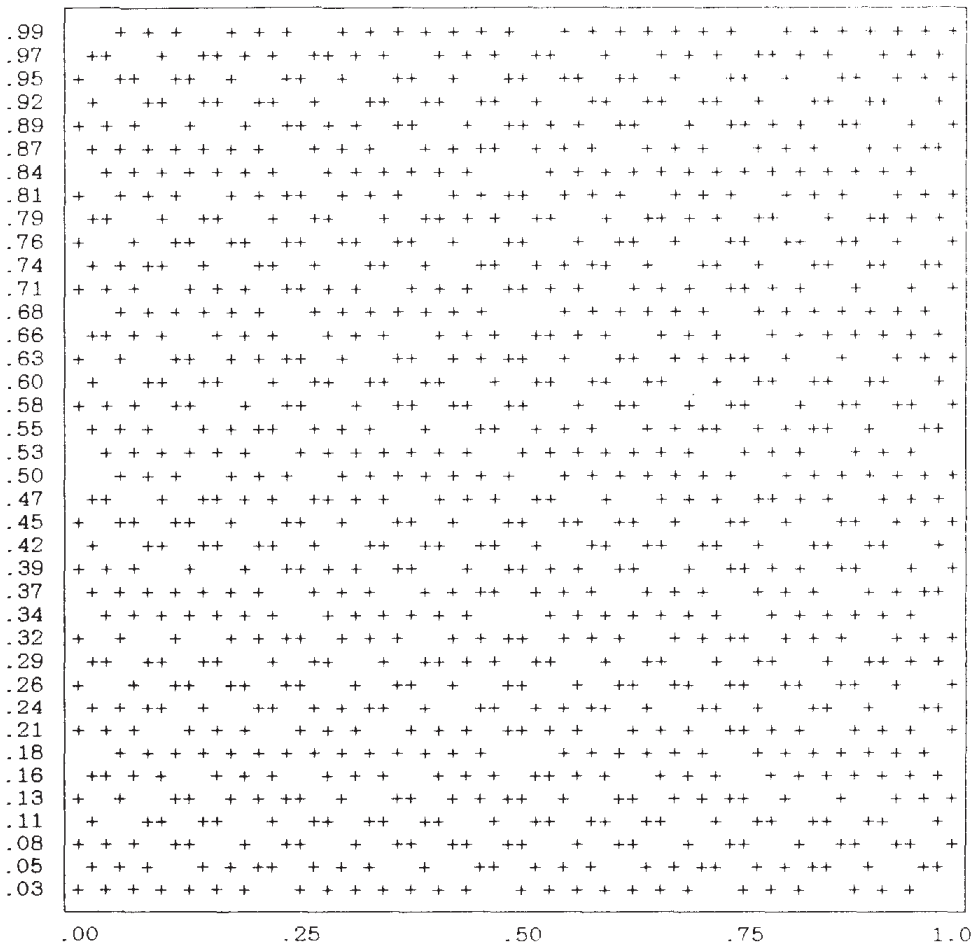


Fig. 9. A planar LP-sieve, 1024 nodes.

sisted of average distances from 1 to 5, 1 to 25,...,1 to 75 nearest neighbours). The smaller the range over which the dimension is determined, the more the random fluctuations and the more the difference between the function $\phi(q)$ and the line $y = qd_0$, which corresponds to complete uniformity.

Figure 6 shows the histogram of the local dimensions of a mixed sample consisting of a mixture of 500 events of Serpinski's carpet ($d_2 \approx 1.9$) and 500 events of Henon's map ($d_2 \approx 1.2$). Two peaks are clearly seen, which correspond to two modes (the correlation dimensionality is binned).

Unimodal distributions corresponding to data of the same type are shown in figs. 7 and 8.

A quasi-periodical distribution was used to "scan" the fractal support with the purpose of determining the anomalous areas: the dimensionality was calculated in the nodes of the LP-sieve (fig. 9). Figure 10 presents the results of scanning a square of side 0.9 where the Serpinski carpet is situated. For the sieve points falling into the empty areas of the carpet the fractal dimension turned out to be greater than 2.2, which allows them to be reliably separated.

The quasi-random sequence itself also turned out to be non-uniform on the boundaries of its support shown in fig. 11.

The program code is written in Fortran 77 for VAX and IBM-compatible computers operating under VM. Some subroutines from the KNN

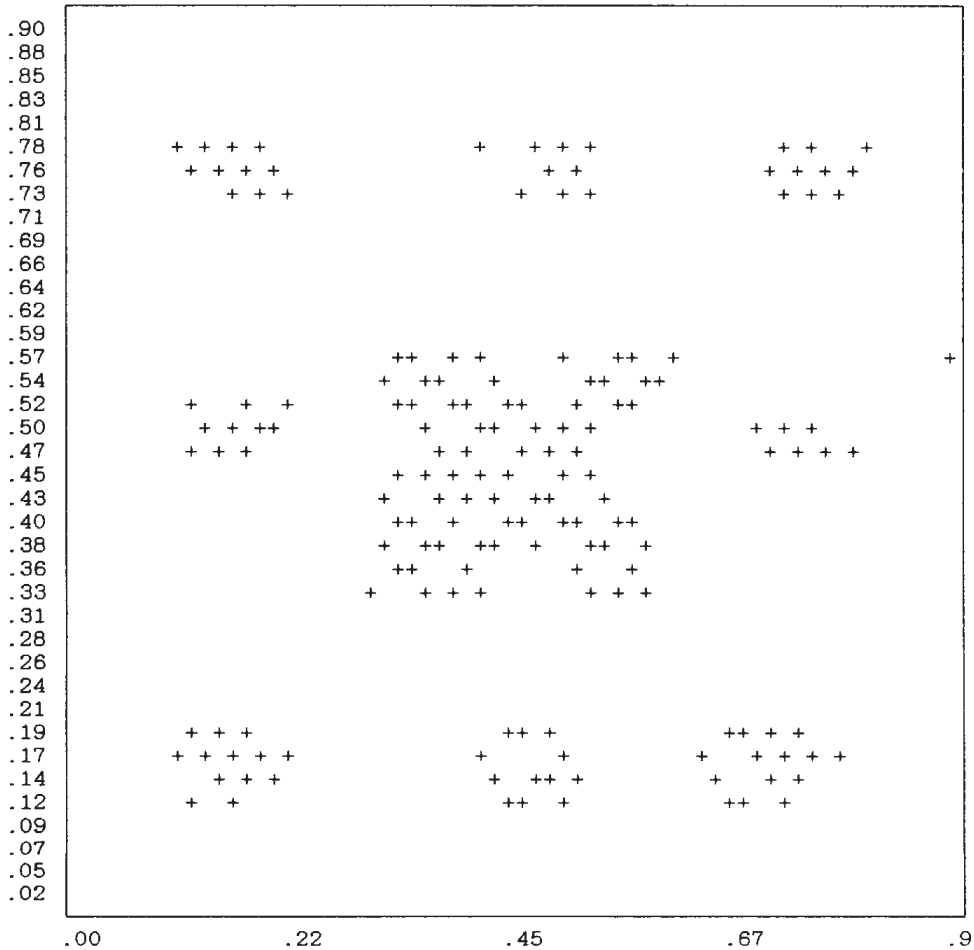


Fig. 10. The results of scanning a Serpinski carpet to denote points where the local dimension is larger than 2.2.

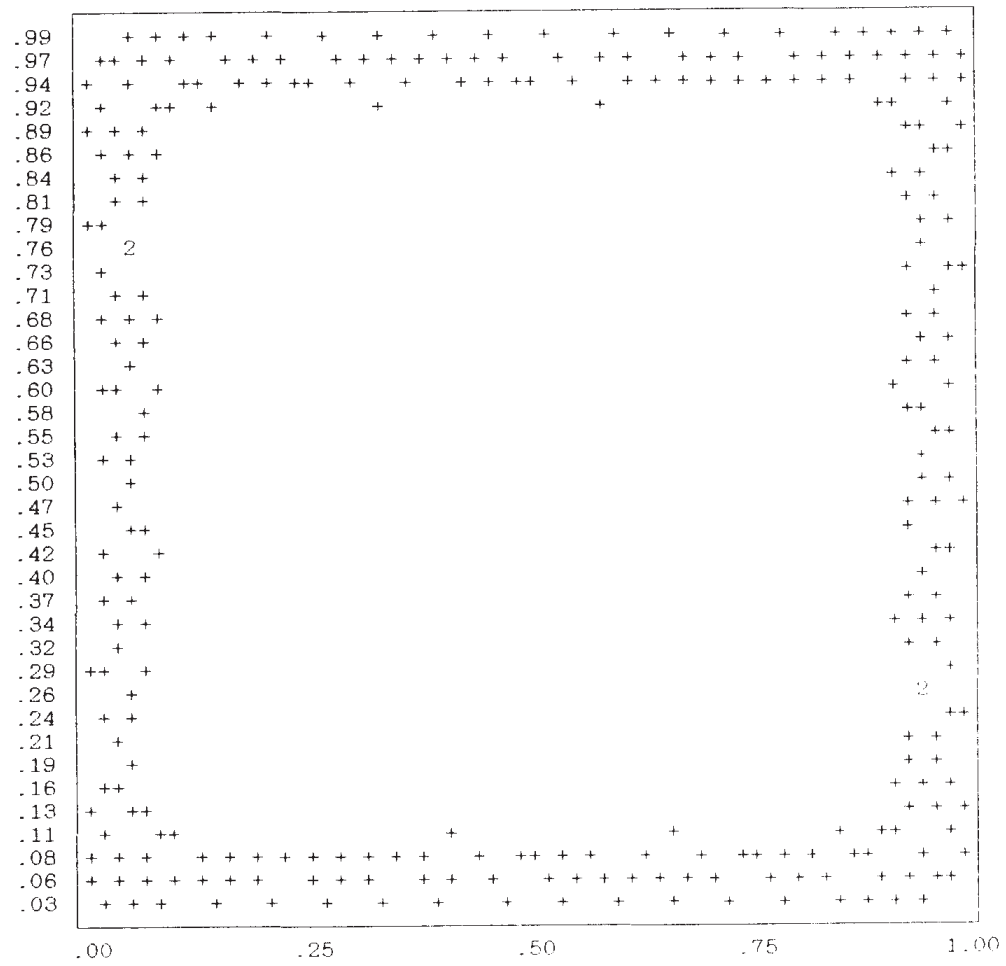


Fig. 11. The results of scanning a planar LP-sieve over the boundaries of its support; + denotes points where the local dimension is larger than 2.2.

multivariate density-estimation package [17] are used for NN distance calculations and $q$-tuple counting. The calculations have been carried out on an EC-1046 computer in the computation center of the Yerevan Physics Institute.

## 5. Conclusion

To summarise, we have investigated a new method of multiparticle data analysis which can deal with the large number of particles produced in modern colliders.

We have demonstrated how the Renyi dimensions can be used as a quantitative measure to outline possible inhomogenieties in a $3N$-dimensional momentum space or in the rapidity (pseudo-rapidity) distributions.

We introduce a simple technique for Renyi dimension calculation. A universal scale – sample-averaged distance to NN – is offered. A $q$-tuple counting algorithm provides an evaluation of Renyi dimensions in a sizeable range of values of $q$. The KNN algorithm for calculating the correlation dimension is much more suitable and precise than box-counting algorithms.

By the local dimension distribution obtained on fractal support we can judge the relative importance of the different mechanisms taking part in the creation of the data.

The application of these ideas to the analysis of multiparticle production dynamics requires in-

tensive Monte Carlo simulations and detailed quantitative comparisons of simulated and experimental data.

## Acknowledgement

I express my sincere gratitude to S.G. Matinyan for helpful discussions.

## References

[1] P. Carruthers and C.C. Shin, Mutual information and forward–backward correlations in multihadron production, Phy. Rev. Let 62 (1989) 2073.
[2] P. Carruthers and C.C. Shin, Correlations and fluctuations in hadron multiplicity distributions, J. Mod. Phys. A 2 (1987) 1447.
[3] UA1 Collaboration, Bose–Einstein Correlations in pp bar interactions at sqrt $S = 0.2$ to 0.9 Tev, Preprint CERN-EP-/89-71 (1989).
[4] T.H. Barnet et al., Extremely High multiplicities in high-energy nucleus–nucleus collisions, Phys. Rev. Lett. 50 (1983) 2062.
[5] A. Bialas and R. Pescansci, Intermittence in multiparticle production at high energy, Nucl. Phys. B 308 (1988) 857.
[6] H. Satz, Intermittence and critical behaviour, Nucl. Phys. B 326 (1989) 613.
[7] J. Dias de Deus, Intermittence model for rapidity particle density fluctuations, Phys. Lett. B 194 (1987) 297.
[8] I.M. Dremin, Fractal behaviour in multiparticle productions, Pis'ma Zh. Eksp. Teor. Fiz. (1987) 505.
[9] L. Lonnblad and U. Petterson, ARIADNE-2, a Monte Carlo for QCD cascades in the colour dipole formulation, Preprint LUTP-88-15, Lund (1988).
[10] G. Marchesini and B. Webber, Herwig – Monte Carlo program for event generation, Nucl. Phys. B 310 (1988) 461.
[11] Y.I. Azimov, Yu.L. Dokshitzer, V.A. Khoze and S.I. Troyan, The string effects and QCD coherence, Phys. Lett. B 165 (1985) 147.
[12] P. Dahlqvist, B. Andersen and G. Gustaffson, Intermittence and multifractal structures in OCD cascades, Nucl. Phys. B 328 (1989) 74.
[13] K. Fialkowski, B. Wosiek and J. Wosiek, Intermittence and OCD jets, Acta Phys. Pol. B 20 (1989) 639.
[14] I. Sarcevic and H. Satz, Self-similar multihadron production of high energies, Phys. Lett. B 194 (1987) 297.
[15] R. Engelking, Dimension Theory (North-Holland, Amsterdam, 1978).
[16] J.P. Eckman and D. Ruelle, Ergodic theory of chaos and strange attractors, Rev. Mod. Phys. 57 (1985) 617.
[17] A.A. Chilingarian, Statistical decisions under nonparametric a priori information, Comput. Phys. Commun. 54 (1989) 381.
[18] C. Paladin, and A. Vulpiani, Anomalous scaling laws in multifractal objects, Phys. Rep. 156 (1987) 4.
[19] K. Pawelzik and H.S. Shuster, Generalized dimensions and entropies from a measured time series, Phys. Rev. A 35 (1987) 481.
[20] J.G. Caputo and P. Atten, Metric entropy: an experimental means for characterizing and quantifying chaos, Phys. Rev. A. 35 (1987) 1311.
[21] I.M. Dremin, The fractal correlation measure for multiple production, Mod. Phys. Lett. 3 (1988) 1333.
[22] A.A. Chilingarian and S.Kh. Harutunyan, On the possibility of a multidimensional kinematic information analysis by means of nearest-neighbour estimation of dimensionality, Nucl. Instrum. Methods, A 281 (1989) 388.
[23] R.A. Tapia and T.R. Thompson, Nonparametric Probability Density Estimation (John Hopkins Univ. Press, Baltimore, 1978).
[24] K.W. Pettis, T.A. Baily, A.K. Tain and R.C. Dubes, An intrinsic dimensionality estimator from nearest neighbour information, IEEE Trans. Pattern Anal. Machine Intel. 1 (1979) 25.
[25] I.M. Sobol, On the systematic search in a hypercube, SIAM J. Number. Anal. 16 (1979) 790.
[26] F. James, A review of pseudorandom number generators, Comput. Phys. Commun. 60 (1990) 329.
[27] N.Z. Akopov, G.K. Savvidy and N.G. Ter-Harutyunian, Matrix generator of pseudorandum numbers, Preprint TPI-MINN-89/13P, University of Minnesota (1989).

# THE SYSTEM OF IMAGING ATMOSPHERIC CHERENKOV TELESCOPES: THE NEW PROSPECTS FOR VHE GAMMA RAY ASTRONOMY.

F.A. Aharonian, A.A. Chilingarian, R.G. Mirzoyan

*Yerevan Physics Institute, Alikhanian Brothers 2, Yerevan, 375036, Armenia.*

A.K. Konopelko, A.V. Plyasheshnikov

*Altai State University, Dimitrov 66, Barnaul, 656099, Russia*

(Received 7 April 1992; accepted 15 October 1992)

Using Monte Carlo simulations the possibilities are investigated for registration of VHE gamma radiation by means of systems of imaging air Cherenkov telescopes (IACT). It is shown that even a system of IACT's with moderate properties (three telescopes with the geometrical area of the optical reflector $\approx 5\,m^2$ and the angular size of the pixel $\approx 0.41^o$) could provide the energy resolution 20–25% and achieve the sensitivity (minimum detectable flux) up to $10^{-12}\,photon/cm^2 s$ at the effective energy threshold $\approx$1 TeV.

## 1. Introduction.

So far all observations of primary gamma rays at E$\approx$ 1 TeV have been made with Air Cherenkov Telescopes (ACT). In the foreseeable future this technique will dominate at least at energies E$\leq$10 TeV.

One of the most remarkable features of the ACT's is their high rate capability. For collection area $S_{eff} \geq 3 \cdot 10^8 cm^2$, easily achieved by simple ACT, the counting rate of VHE gamma rays from the Crab Nebula should be higher than 0.1 events per minute. However, this important feature can acquire its practical significance only in the case of effective suppression of the background induced by the proton-nuclear component of the primary cosmic radiation. Different ways for cosmic ray background rejection were proposed (for review see, e.g., Weekes, 1988); however at present only the so called imaging technique is realized as a powerful method for significant improvement of the sensitivity of detectors in VHE gamma ray astronomy. The application of the multichannel Cherenkov light receiver in the focus of the high quality optical reflector gives a possibility to separate gamma ray- and proton-induced showers, analyzing the

*Experimental Astronomy* **2**: 331–344, 1993.

differences in the shape and orientation of the Cherenkov light spot in the focal plane. High efficiency of such a separation was established on the base of Monte Carlo simulations (Hillas,1985;Plyasheshnikov et.al.,1985) and observations of the Whipple collaboration: $\approx 45\sigma$ signal from the Crab Nebula has been observed recently by the 10m Cherenkov telescope of this collaboration (Lang et.al.,1991).

Further development of the IACT technique seems to be in two principal directions: (i) reduction of the angular size of the cells of multi-channel camera down to $\Delta\Psi \leq 0.1^{O}$. With the aperture $\approx 3^{O}-4^{O}$, which is necessary to provide a collection area $S \geq 3 \cdot 10^{8} cm^{2}$, it means the construction of the camera having about 1000 channels (PMT's). Besides, it means an essential improvement of the optical characteristics of the reflectors; (ii) by coupling several imaging ACT ($\geq$3) in a system, separated with about 50-100 meters.

We hope that forthcoming systems of the imaging ACT equipped with high resolution cameras will raise VHE gamma ray astronomy to the status of HE ($\geq$100 MeV) gamma ray astronomy based on the satelite experiments. With the imaging ACT (IACT) arrays it will be possible to achieve the angular resolution $0.1^{O}-0.2^{O}$, the energy resolution 20-25 % and the sensitivity (minimum detectable flux) up to $10^{-12}$ photon/$cm^{2}s$ at the effective energy threshold $\approx$1 TeV. It should be noted that owing to a high angular resolution and an effective background rejection it becomes real to study the cosmic gamma rays from the point sources under background-free conditions. Consequently, the sensitivity of the detector will be determined only by the statistics of gamma rays.

The aim of this paper is to show that an essensial improvement of the sensitivity is possible even with relatively moderate arrays. The Monte Carlo calculations presented here were realized for the prototype of the Cherenkov telescope which will be used in the HEGRA observatory (Aharonian et al., 1991).

## 2. A Brief Description of the HEGRA System and Its Hardware Logics.

Each multi-mirror optical reflector of 5 HEGRA telescopes has a geometrical area 5 $m^{2}$. The Cherenkov light receiver, placed in the focus of the reflector (F$\approx$ 5 m), consists of 37 PMT's close-packed in a hexagonal arrangement. The full aperture of the telescope (full angle of view) is about $3^{O}$, the angular size of each pixel is $\approx 0.41^{O}$. The mean number of photoelectrons emitted from the cathode of PMT per one Cherenkov photon falling on the reflector surface, taking into account the mirror reflectivity, the light pipe transparency and the quantum efficiency of the PMT, is about 0.1 (Aharonian et al., 1991a).

The HEGRA IACT's will be situated at the altitude of 2200 m above the sea level (Canary Island La Palma).

In the present version of the HEGRA telescopes the following trigger condition will be used: the signal in at least two pixels from 19 inner PMT's should exceed some critical value $q_O$ (in units of number of photoelectrons),

hereafter the criterion «2/19>$q_0$ ». This criterion has been successfully used in observations with the 10m Whipple Cherenkov telescope. It provides rather good precision for determination of basic parameters of the detected Cherenkov images. Besides, this criterion provides quite high gamma ray detection efficiency even at threshold, while for the proton-nuclear component of cosmic rays the detection efficiency is much lower. In other words, this criterion gives a possibility to achieve an essential rejection of background events already at the hardware level.

The choice of the optimum value of $q_0$ depends on several factors (the background rejection efficiency, the gamma ray collection area, the angular resolution). The Monte Carlo calculations show that the optimum value of $q_0$ is within 10-15 photoelectrons. It should be noted here that the minimum acceptable value $q_0$ for the hardware criterion «2/19>$q_0$» following from the requirement of reliable rejection of the night-sky background has to be equal ≈9 photoelectrons (Aharonian et al., 1991a).

The Cherenkov telescopes of HEGRA installation are planned to be placed in the vertices and the center of the rectangle with the length of the side l=50-100 m. At present two possible regimes of IACT system operation are being discussed: mode 1 — the system switches when the hardware condition «2/19>$q_0$» satisfied for central and two neighbouring peripherial telescopes (three fold regime); mode 2 — the information from all the telescopes is registered when the requirement «2/19>$q_0$» takes place at least for one telescope (this regime can be realized by means of so called «two-level» trigger logic).

Mode 1, the simplest one from the point of view of technical realization, provides the best efficiency of CR background rejection due to the high quality of Cherenkov images. Mode 2 has an apparent advantage since this regime provides the largest collection area and high statistics.

## 3. Calculation Technique.

The numerical analysis presented in this paper is based on detailed Monte Carlo simulations of the cascade development of air showers induced by gamma rays and cosmic rays, as well as simulations of the processes connected with the registration of Cherenkov radiation of the showers by IACT system. The description of the simulation algorithms is given by Plyasheshnikov and Bignami (1985), Konopelko (1990) and Konopelko et.al.(1992). It was supposed that the charged component of primary cosmic rays consists only of protons ( 95 % ) and $\alpha$-particles ( 5 % ).

A real layout of the IACT system of HEGRA installation as well as the configuration of the multi-channel Cherenkov light cameras were taken into consideration in accordance with the algorithms described by Aharonian et al. (1990). Here we present the calculations for a system consisting of the 3 IACT placed in the vertices of the isosceles triangle with the length of the side: 50, 100 m. This configuration of the telescopes is considered as the basic one for the system. More complicated

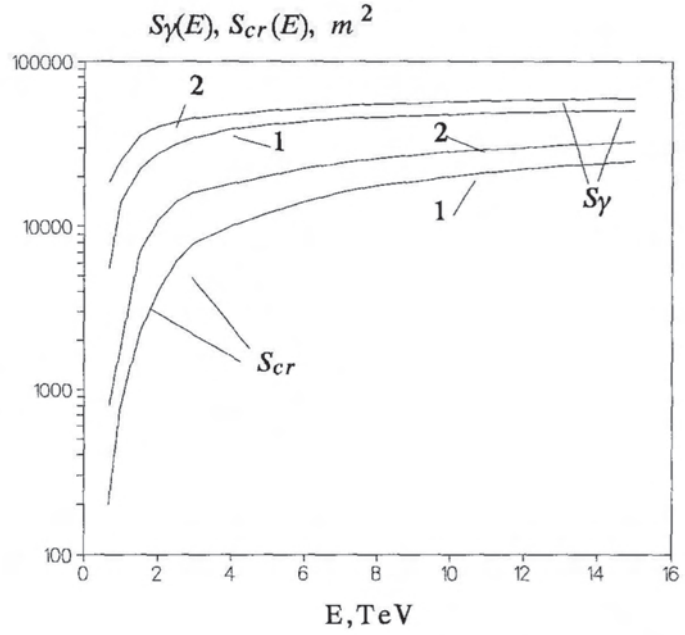


Fig.1. The effective collection area of a single IACT for primary gamma rays and protons. Curve 1— $q_0$ =15 ph.e., curve 2— $q_0$= 9 ph.e.

configurations, coupling more than 3 IACT can be analyzed, in more cases, using the results obtained for this basic configuration.

## 4. Characteristics of the Single Imaging Atmospheric Cherenkov Telescope.

The effective collection areas of detection of the gamma rays and protons ($S\gamma$ and $S_{cr}$) are very important characteristics of the IACT. Particularly, the precise estimation of $S\gamma$ is necessary for the determination of the gamma ray flux from discrete sources. Moreover, the ratio $S\gamma/(S_{cr})^{1/2}$ determines the level of the statistical confidence of observations (before software separation of the registered events on gamma- and proton-induced showers).

So far the detailed quantitative calculations of the effective collection areas of the Cherenkov telescopes have not been carried out. In many works (see,for example,Cawley M.F.,1988) the values $S\gamma$ and $S_{cr}$ are supposed to be the same and independent from the primary energy. In the general case such approximations are rather rough. In particular, in the case of IACT this assumption may lead to an essential error in the estimation of gamma ray fluxes. This is clear from fig. 1, where the energy dependence of $S\gamma$ and $S_{cr}$ for vertical air showers is shown. We see that there is an evident difference between $S\gamma$ and $S_{cr}$ especially near the

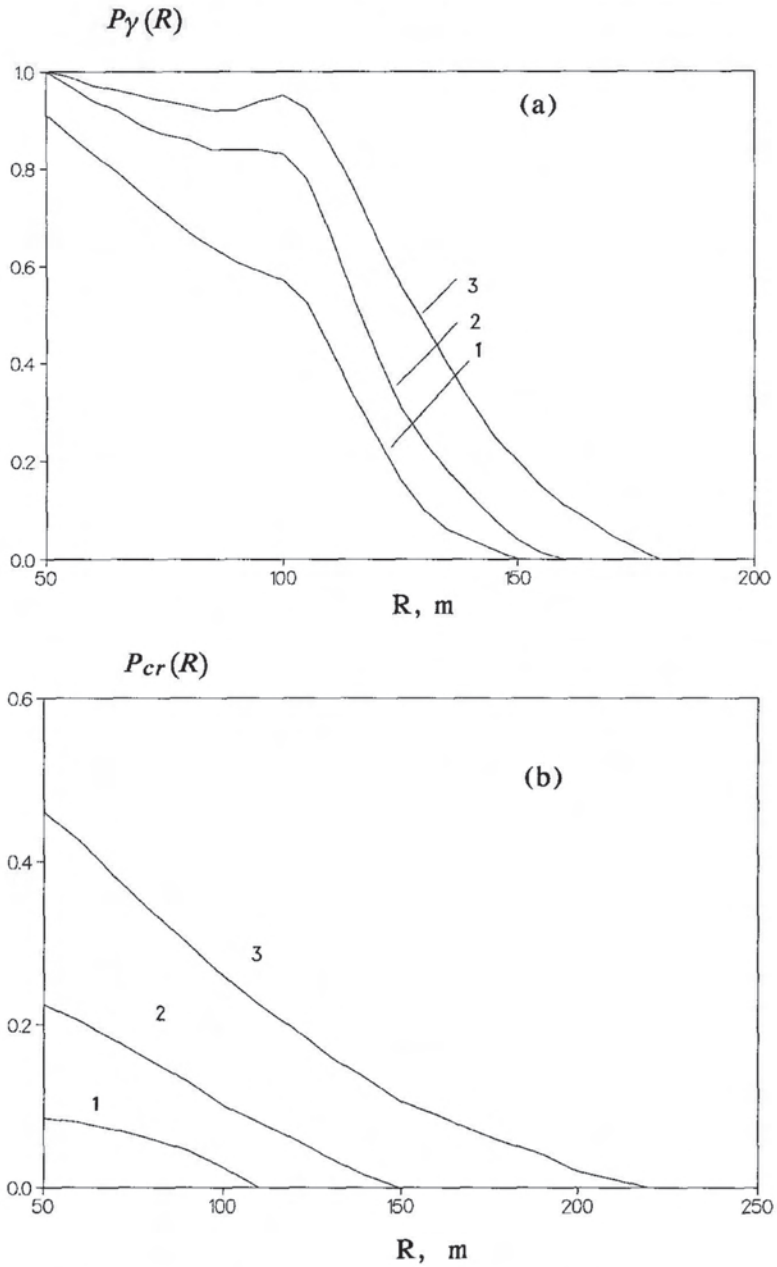


Fig.2. The probability of detection of gamma rays (a) and protons (b) via the impact parameter. The hardware criterion «2/19>$q_0$», $q_0$ = 9 ph.e.. Curve 1 — E = 1 TeV, curve 2 — E=2.5 TeV, curve 3 — E =10 TeV.

threshold energy (E ≈ 1 TeV ). This can be explained by the fact that the hardware condition «2/19>$q_0$» is more suitable for showers initiated by

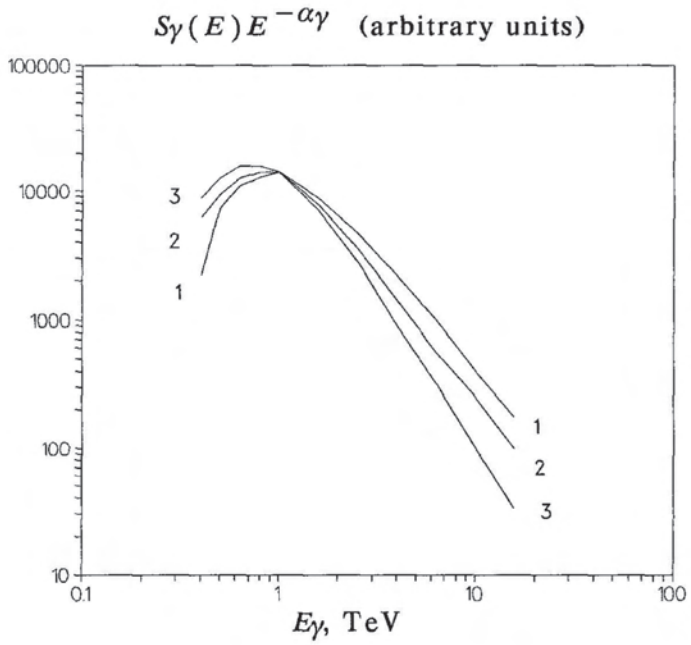


Fig.3. The detection rate of gamma rays $S\gamma E_\gamma^{-\alpha\gamma}$ for the single IACT. Curve 1— $\alpha\gamma = 2$, curve 2— $\alpha\gamma = 2.25$, curve 3— $\alpha\gamma = 2.6$. $q_0 = 15$ ph.e.

the gamma rays than for proton-induced showers. The Cherenkov image of a proton-induced shower is distinguished by its «diffuse-like» spot, consequently, the hardware condition «2/19>$q_0$» (especially near threshold) leads to a low registration efficiency of these showers. On the contrary, the Cherenkov images induced by gamma rays on average have a quite compact spot, therefore the detection probability of the gamma-events remains rather high (at least 50%) for impact parameters up to R $\approx$ 100 m (see fig. 2).

As follows from fig. 1 the collection area for gamma rays becomes large enough ($S\gamma \approx 10^8 cm^2$) already at E $\approx$1 TeV and falls sharply at E< 1 TeV.

To make clear what is the «effective» energy threshold of IACT for gamma rays, we present in fig. 3 the energy dependence of the detection counting rate for gamma-showers defined as $S\gamma I\gamma(E\gamma)$, where $I\gamma(E\gamma)$ is the differential energy spectrum of the gamma rays with different power law indexes $\alpha\gamma$=2; 2.25; 2.6. We can conclude from fig. 3 that the detection rate of the gamma-showers has a maximum value near the energy 1 TeV and this value is practically independent on $\alpha\gamma$. Consequently, we can state that the «effective» energy threshold of the IACT is about 1 TeV. At the same

time Cherenkov images of rather high quality are expected to be at energies ≈2-3 TeV when the total number of photoelectrons in image exceeds 100, and the separation of gamma- and photon-induced showers can be done with high efficiency.

The minimum detectable flux of the gamma rays at the level of confidence of m standard deviations («sigma») for a single IACT may be expressed as

$$F_{\gamma}^{\min}(\geq E) = m \frac{P_{cr\to\gamma}^{1/2} S_{cr}^{1/2}}{P_{\gamma\to\gamma} S_{\gamma}} \left( \frac{I_{cr}(\geq E)\,\Delta\Omega}{t} \right)^{1/2} \qquad (1)$$

where $P_{\gamma\to\gamma}$ is the probability of the right classification of the Cherenkov images produced by gamma ray showers, $P_{cr\to\gamma}$— the probability of missclassification of cosmic ray background events as gamma ray events; $I_{cr}(\geq E) \approx 10^{-5} \left( \frac{E}{1TeV} \right)^{-1.65} cm^{-2} s^{-1} ster^{-1}$ is the flux of the cosmic rays (Linsley,1980); $\Delta\Omega$ — the solid angle of the aperture of the IACT; t — the duration of observations in «ON source» mode.

Probabilities $P_{\gamma\to\gamma}$ and $P_{cr\to\gamma}$ for HEGRA IACT were studied by Aharonian et al., 1990. The efficiency of the cosmic ray background rejection for different Cherenkov image parameters is presented in table 1. For evaluation of the parameters of the two-dimensional air shower image we used technique from Weekes et.al.,1989. The night sky nois was taken into account. The calculations were carried out for the gamma ray spectrum with power law index $\alpha_{\gamma}$=2.25. In contrast to Hillas A.M., 1985, in the software selection criteria we paid no attention to the number of the multichannel receiver ring zone containing the maximum of the Cherenkov light spot. This was done to have a possibility to compare the data corresponding to a single IACT and an IACT system.

As it follows from the table 1 the factor:

$$\eta = \frac{P_{\gamma\to\gamma}}{\sqrt{P_{cr\to\gamma}}}, \qquad (2)$$

which determines the improvements of the signal-to-noise ratio $S/\sqrt{B}$ after the software analysis, has the maximum value in the case of the AZWIDTH parameter. Particularly, for $q_0$ =15 ph.e. the imaging analysis based on the AZWIDTH parameter makes it possible to achieve the background rejection factor $(P_{cr\to\gamma})^{-1} \approx 60$ retaining at the same time more then 40% of the useful (gamma ray) events ($P_{\gamma\to\gamma} \approx 0.41$). As a result the improvement factor $\eta$ is equal 3.4.

It should be mentioned that factor $\eta$ increases with enhancing $q_0$, but after $q_0$ =15 ph.e. this increasing becomes slow. On the other hand the effective collection area decreases with increasing $q_0$. That is why the range of $q_0 \approx$ 10-15 ph.e. seems to be optimal.

For estimation of the optimum value of $q_0$ we consider the following parameter:

$$X = \eta \frac{S_\gamma}{\sqrt{S_{cr}}} \qquad (3)$$

which characterizes the improvement of the signal-to-noise ratio due to the joint application of both the hardware $S_\gamma/(S_{cr})^{1/2}$ and the software $P_{\gamma\to\gamma}/(P_{cr\to\gamma})^{1/2}$ criteria. The results of the calculations realized for different values of the gamma ray spectrum index and for various hardware thresholds $q_0$ are presented in table 2. From this table we can state that for all $\alpha_\gamma$ the parameter X takes the maximum at $q_0$ =15 ph.e.

The minimum detectable flux of gamma rays for a single IACT may be estimated according to the next list of necessary variables: the time of observations in the «on source» mode t=100 h; the parameter $X \approx 6.3 \cdot 10^4 cm$ taken from table 2 for $q_0$ =15 ph.e.; the aperture of the telescope $\Delta\Omega \approx 2\ 10^{-3} (\Delta\Theta_{1/2} \approx 1.5^0)$. Substituting these values in the expression (1) and assuming m=5 we can get

$$F_\gamma^{\min}(\geq 1\ TeV) \approx 2\ 10^{-11} \text{ photon } / cm^2/\text{s}. \qquad (4)$$

By the joint application of several Cherenkov image parameters more effective rejection of the cosmic ray background can be achieved. Such an approach was used in Hillas,1985, but it paid no attention to the correlations between the shower image parameters. Essentially more promising approach to this problem is the method of the multidimensional correlation analysis basing on Bayes decision rules and on the nonparametric estimation of the multidimensional function of the probability density (Aharonian et al., 1991b). The effectiveness of this approach will be discussed below in application to the IACT system.

## 5. The System of Three Imaging Atmospheric Cherenkov Telescopes.

The multidimensional correlation analysis carried out by us (Aharonian et al., 1991b) for a single IACT allowed us to conclude that the simultaneous application of more than 3 Cherenkov image parameters does not give any essential improvement of the discrimination efficency. That is why we take three parameters for each telescope in the IACT system. Earlier (Aharonian et al., 1990) the following combinations were found as the best ones: (WIDTH, AZWIDTH, LENGTH) and (DIST, MISS, WIDTH).

The main results of the multidimensional correlation analysis applied to the classification of the gamma ray and proton-induced showers detected by the 3 IACT system are presented in table 3. The numerical results correspond to different modes of the system operation (called above as mode 1 and 2) and to various basic distances of the telescopes layout l = 50, 100 m. From table 3 some conclusions may be done:

(1) The application of the multidimensional correlation analysis to the three IACT system makes it possible to achieve the background rejection at the level of some decimal parts of a percent, losing only half of the gamma ray events.

**Table 1.** The efficiency of CR background rejection for different values of hardware threshold $q_0$ and different parameters of the Cherenkov light image. Only one Cherenkov image parameter is used for classification of events.

| $q_0$ | | LENG | WIDTH | DIST | ALPHA | MISS | AZWID |
|---|---|---|---|---|---|---|---|
| | $P_{\gamma\to\gamma}$ | 0.442 | 0.871 | 0.890 | 0.842 | 0.867 | 0.249 |
| 9 | $P_{cr\to\gamma}$ | 0.171 | 0.736 | 0.697 | 0.679 | 0.611 | 0.024 |
| | $\eta$ | 1.068 | 1.015 | 1.066 | 1.022 | 1.108 | 1.619 |
| | $P_{\gamma\to\gamma}$ | 0.611 | 0.861 | 0.924 | 0.736 | 0.602 | 0.353 |
| 12 | $P_{cr\to\gamma}$ | 0.231 | 0.591 | 0.653 | 0.409 | 0.252 | 0.018 |
| | $\eta$ | 1.273 | 1.120 | 1.144 | 1.150 | 1.200 | 2.639 |
| | $P_{\gamma\to\gamma}$ | 0.733 | 0.925 | 0.928 | 0.729 | 0.659 | 0.416 |
| 15 | $P_{cr\to\gamma}$ | 0.251 | 0.622 | 0.589 | 0.378 | 0.238 | 0.015 |
| | $\eta$ | 1.461 | 1.173 | 1.209 | 1.186 | 1.349 | 3.390 |
| | $P_{\gamma\to\gamma}$ | 0.783 | 0.827 | 0.967 | 0.719 | 0.735 | 0.496 |
| 20 | $P_{cr\to\gamma}$ | 0.306 | 0.506 | 0.632 | 0.392 | 0.242 | 0.021 |
| | $\eta$ | 1.416 | 1.163 | 1.216 | 1.149 | 1.493 | 3.449 |

**Table 2.** The dependence of the factor X on the hardware threshold $q_0$ and on the power index of the differential spectrum of gamma rays. The AZWIDTH discrimination is used.

| $\alpha_\gamma$ / $q_0$ | 9 | 12 | 15 | 20 | 25 |
|---|---|---|---|---|---|
| 2.00 | 700 | 832 | 948 | 788 | 714 |
| 2.25 | 480 | 563 | 627 | 504 | 442 |
| 2.65 | 268 | 308 | 327 | 247 | 206 |

(2) With increasing the distance between telescopes from 50 m to 100 m the efficiency for separating gamma ray and proton-induced showers is improved. It can be explained in the following way: with increasing the distance between the telescopes the existing correlations in the Cherenkov images detected by different telescopes could be lost and a set of such images becomes more informative. At the same time if the distance between the telescopes is greater than 100 m the probability for simultaneous detection of shower by three IAC telescopes falls down sharply (see fig. 2).

(3) The IACT system operating in mode 1 provides higher efficiency of the cosmic ray background rejection. For mode 1 the Cherenkov images detected by IAC telescopes have on average a higher density of the Cherenkov photons and, consequently, a lower level of fluctuations.

The effective collection areas for the gamma ray showers calculated for two distances between telescopes ( l= 50, 100 m) are presented in fig. 4. The maximum effective collection area is achieved in mode 2 with the basic distance l = 100 m. However in this case the effective collection area $S_{cr}$ is also large, and the factor $S\gamma / \sqrt{S_{cr}}$ characterizing the signal-to-noise ratio at the hardware level depends weakly on the distance between

**Table 3.** The maximum available value of the efficiency of the CR background rejection for system of 3 IACT. Different modes of operation of the system and different distances between telescopes are considered. $q_\sigma$= 15 ph. e., $\alpha_\gamma$=2.25.# $\gamma$ ; # cr - number of images of gamma- and proton-induced showers considered in the analysis.

| l,m | Mode | #$\gamma$ / #cr | | $P_{\gamma\to\gamma}$ | $P_{cr\to\gamma}$ | $\eta$ |
|---|---|---|---|---|---|---|
| 50 | 1 | $\frac{1008}{780}$ | *width azwid length* | 0.360 | 0.002 | 7.28 |
| 50 | 1 | $\frac{1008}{780}$ | *width dist miss* | 0.457 | 0.003 | 8.03 |
| 50 | 2 | $\frac{3161}{2553}$ | *width dist miss* | 0.218 | 0.002 | 5.10 |
| 100 | 2 | $\frac{2964}{2345}$ | *width dist miss* | 0.269 | 0.001 | 8.07 |

telescopes and the mode of the system operation (see fig. 5). Nevertheless, due to the hard trigger condition in mode 2 the parameter $S_\gamma / \sqrt{S_{cr}}$ for this mode is greater than in mode 1.

Thus, if mode 1 provides higher efficiency of the background rejection, the mode 2 makes it possible to achieve a larger collection area for gamma rays. That is why the sensitivity of the IACT system operating in modes 1 and 2, are expected to be comparable.

Let us estimate now the sensitivity of the IACT system operating in mode 2 with l = 100 m. Substituting to the equation (1) the following parameters: $P_{\gamma\to\gamma}$= 0.27, $P_{cr\to\gamma}$ =0.001, $S_\gamma/\sqrt{S_{cr}}$= 8 $10^4$ $cm$ (taken from fig.5 and table 3), the minimum detectable flux of the gamma rays above 1 TeV can be estimated for a $5\sigma$ DC signal from a point source as:

$$F_\gamma^{\min}(\geq 1\,\mathrm{TeV}) \approx 1.7\ 10^{-12}\ \mathrm{photon}/cm^2/\mathrm{s}. \qquad (5)$$

Thus,even for the simplest IACT system the sensitivity is approximately as much as 10 times better than the sensitivity of a single IACT.

It should be noted that for the gamma ray flux $I_\gamma$ ($\geq$1TeV) $\approx 10^{-11}$ photon/$cm^2$ s the detection rate of gamma-events is expected to be about

$$\nu_\gamma \approx P_{\gamma\to\gamma} S_\gamma I_\gamma\ (\geq 1\ \mathrm{TeV}) \approx 2.5\ 10^{-3}\ \mathrm{event/s}, \qquad (6)$$

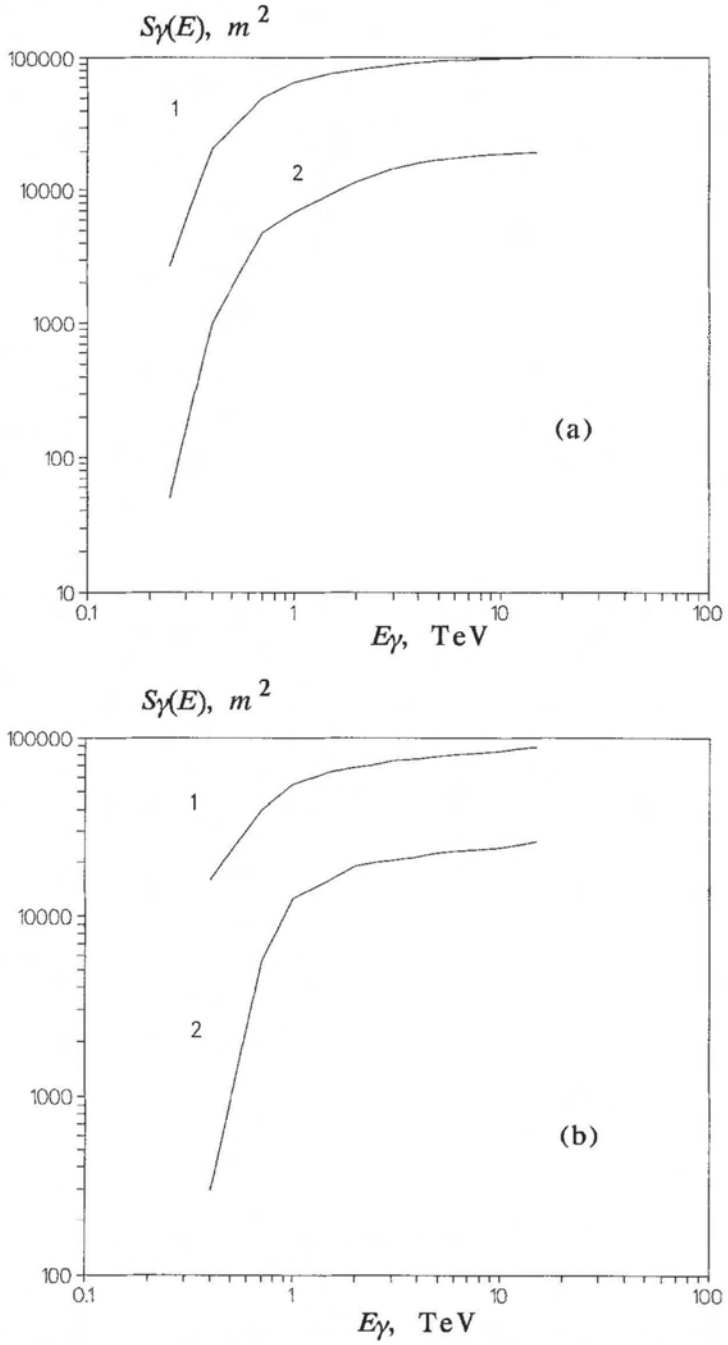


Fig.4. The effective collection area of gamma rays and protons for the system of 3 IACT. (a) l= 100 m, (b) l= 50 m. Curve 1— mode 2, curve 2 — mode 1.

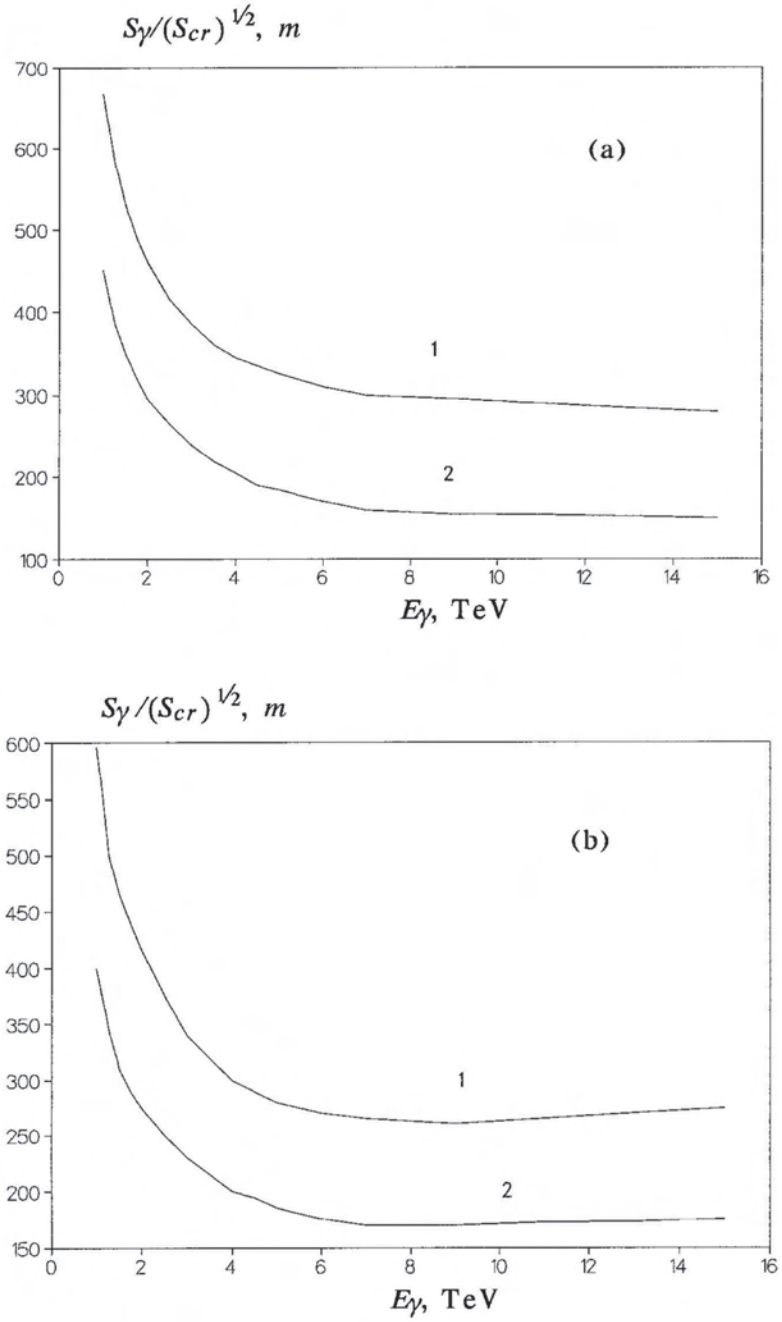


Fig.5. The ratio $S\gamma/\sqrt{S_{cr}}$ for the system of 3 IACT. (a) l = 100 m, (b) l = 50 m. Curve 1— mode 2, curve 2— mode 1.

**Table 4.** The energy resolution for the system of three IACT. Mode 1, l=50 m, $q_0$ = 9 ph.e. The power law index of gamma ray differential spectrum $\alpha_\gamma$=2.25. $E_t$ — the truth value of energy, $E_m$, $\delta E_m$— the mean value and fluctuations of the reconstructed energy, respectively.

| $E_t, TeV$ | 1.0 | 1.5 | 2.5 | 4.0 | 7.0 | 10.0 |
|---|---|---|---|---|---|---|
| $E_m, TeV$ | 1.0 | 1.5 | 2.61 | 4.03 | 7.01 | 10.0 |
| $\delta E_m, \%$ | 18 | 24 | 21 | 23 | 26 | 25 |

and for the cosmic rays

$$\nu_{cr} \approx P_{cr\to\gamma} S_{cr} I_{cr} (\geq 1 \text{ TeV}) \Delta\Omega \approx 2\ 10^{-3} \text{ event/s.} \qquad (7)$$

Thus, if the flux of the gamma-rays above 1 TeV exceeds $10^{-11}$photon/$cm^2$s then the absolute value of the detected gamma ray signal would exceed the cosmic rays background (S>B) and, consequently, it becomes possible to study with the imaging atmospheric technique strong VHE gamma ray sources under conditions practically free from the background.

For determination of the energy spectrum of gamma ray sources with a single IACT or an IACT system the measurement of the individual gamma-induced shower energy is needed (see Plyasheshnikov et.al.,1989; Lewis D.A. et.al.,1991). In the case of a single IACT the technique for such a measurement is developed in Plyasheshnikov et.al.,1989; Lamb,1989. Recently the technique Lamb,1989, has been successfully applied (Vacanti et.al.,1991) for the analysis of the gamma-radiation from the Cram Nebula.

In the case of a single IACT for the energy estimation the total number of registered Cherenkov photons and the shower impact parameter determined on the base of the image centroid position may be used. For several IACT's it is possible (see Konopelko,1990) to use for localization of the shower core a set of the main axis directions of the images registered by IACT's. This allows us to remote an uncertainity in the value of the impact parameter being significant in the case of a single IACT.

In table 4 we present the data on the estimation of the energy resolution of the system of 3 IACT's obtained by Monte Carlo simulations. These data correspond to the technique of the shower energy estimation (Plyasheshnikov et.al.,1989) with usage for the shower core location the method (Konopelko,1990).As can be seen from the table the energy resolution of the system should be about 20-25%.

## 6. Conclusion.

The theoretical predictions concerning the prospects of the imaging atmospheric Cherenkov technique, first of all from the point of view of effective CR background rejection, recently were confirmed in the observations realized by the 10 m Whipple telescope. Further step in the

improvement of the imaging Cherenkov technique is associated with forthcoming systems of IACT's. At least two such installations are under construction now (Akerlof et al., 1990; Aharonian et al., 1991a).

The Monte Carlo simulations applied to the system of three IACT show that a significant progress in improvement of the VHE Cherenkov technique sensitivity could be achieved even with a moderate system of IACT's (several ACT's with limited number of channels of the Cherenkov light receivers and relatively moderate-size reflectors).

A successful application of the IACT systems gives an advance in the understanding of the complicated relativistic processes acting in astrophysical objects.

## References

Aharonian F.A., Chilingarian A.A., Konopelko A.K., Plyasheshnikov A.V. (1990) Preprint YERPHI-1274(60)-90.

Aharonian F.A., Akhperjanian A.G., Kankanian R.S., Mirzoyan R.G., Stepanian A.A., Samorski M., Stamm W., Bot-Bodenhausen M., Lorentz E. and Sawallisch P. (1991a) «Imaging Air Cherenkov Telescopes in the HEGRA Particle Array», Proposal, Kiel.

Aharonian F.A., Chilingarian A.A., Konopelko A.K., Plyasheshnikov A.V. (1991b) NIM in Phisics Research, A302, 522.

Akerlof C.W., Cawley M.F., Fegan D.J., Hillas A.M., Lamb R.C., Lewis D.A., Mayer D.I. and Weekes T.C. (1990) Nucl. Phys. B : Proc. Suppl., 14A, 237.

Hillas A.M.(1985) Proc. 19th ICRC, La Jolla, 3, 445.

Konopelko A.K. (1990) PhD thesis, 1990, 157 p.

Konopelko A.K.,Plyasheshnikov A.V.,Shmidt A.A.(1992) Preprint N6 of P.V.Lebedev Physical Institute, Moscow,48p.

Lamb R.C. (1989) Proc. of Int. VHE Gamma Ray Astron. Workshop, Crimea, 30.

Lang M.J.et.al.(1991) Proc. 22th ICRC,Dublin,1,204.

Lewis D.A. et.al.(1991) Proc. 22th ICRC,Dublin,1,508.

Linsley J.(1980) In: IAU Sump. N94. Origin of Cosmic Rays. D.Reidel Publ. Co., 53.

Plyasheshnikov A.V., Bignami G.F. (1985) Nuovo Cimento, 8C, 39.

Plyasheshnikov A.V., Konopelko A.K. (1989) Proc. of Int. VHE Gamma Ray Astron. Workshop, Crimea, 115; 120.

Weekes T.C. (1988) Phys. Reports, 160, 1.

Weekes T.C. et.al. (1989) Astrophys. J., 342, 379.

ELSEVIER

Neurocomputing 6 (1994) 497–512

NEUROCOMPUTING

# Neural classification technique for background rejection in high energy physics experiments

Ashot Chilingarian *

*Yerevan Physics, Institute, Alikhanian Brothers St. 2, Yerevan 36, Armenia*

Received 16 July 1992; accepted 30 March 1993

**Abstract**

A comparative study of Bayesian and neural classification was done. The mathematical models of neural networks, trained in an evolutionary way, and Bayesian decision rules with Parzen-window multivariate density estimation were applied for background rejection in $\gamma$-ray astronomy experiments.

A weight function was introduced in classification score to control the relative learning 'quality' of alternative classes.

The use of a new quality function, instead of classification score, allows:

- to avoid usage of Monte Carlo events with inherent misleading simplifications and incorrectness;
- to directly optimize the desired quantity: the significance of source detection;
- to obtain the complicated nonlinear boundaries of $\gamma$-cluster.

The proposed technique can be used for background rejection in the constructing experiments of high-energy neutrino point sources identification.

*Keywords:* Neural networks; Multidimensional analysis; Data classification; Background rejection; Decision making

## 1. Introduction

The most difficult and most important part of high energy physic (HEP) data analysis is comparison of competitive hypothesis and decision making on the nature of the investigated physical phenomenon. Modern HEP apparatus consist

* Email: chilin@crd.erphy·armenia.sv


*SSDI* 0925-2312(93)E0017-8

of huge assemblies of electronic detectors that signal the presence and time of passage of ionizing particles or indicate the amount of charge left by a traversing particle. This bulk of diverse information on copious particles is assembled into 'events' that correspond to a single primary particle interaction.

The first decision making problem arises from the necessity of recording events on permanent storage media. The interesting new physics that is expected to embedded from the data analysis is very rare, and in contrast the already well-known noninteresting (background, noise) events are much more frequent. The signal to noise ratio can reach a value of $10^{-9}$.

The so-called experimental triggers are used to make selection and reduce the amount of recorded data for subsequent analysis. In accelerator experiments, several levels (steps) of data reduction are normally used, implemented in electronics, firmware (special purpose processors) and software. Their time scale is limited by the requirement of minimization of the dead time (the time when the apparatus is unable to record events) and usually must not exceed tens of microseconds (for more details see [1,2]).

After triggering, the raw data is converted into physical variables (masses, coordinates, momentums) via the procedures of pattern recognition and estimation, and it is then recorded. Subsequent analysis may involve searching for evidence of new physics, requiring complex decision making and refined noise suppression.

So, the on-line triggering and off-line selection are the key procedures in searching for new physics and are constrained by the enormous data amounts, collection speeds and negligible signal to noise rates expected in the next generation of large accelerators (hadron colliders) known as LHC (large hadron collider, CERN, Geneva) and SSC (superconducting supercollider, Texas).

Modern air shower experiments in cosmic ray physics also are characterized by a significant increase in the volume of data collecting and therefore in the processing time to analyze this event [3]. Thus both in accelerator and cosmic ray experiments new approaches are needed which attempt to reduce the decision time and make the procedure tolerant of noise and missing data.

Another peculiarity of data analysis in high energy physics is the very intensive use of Monte Carlo simulations [4]. At any stage of the off-line analysis the simulated data are widely used; simulated data samples (training samples) are the basis of decision making on the nature of real events. [5]. Thus the proper and complete utilization of simulated data is one of the crucial aspects of data handling procedures. The Neural Network (NN) approach meets all the requirements discussed above and provides promising applications for triggering and pattern recognition at high interaction rates.

Some applications already exist in HEP: the NN method is very efficient for extracting features in hadronic data. World record performance is obtained for quark/gluon separation. The network is able to reduce the QCD background to W/Z jets by a factor of 20–30 [6,7].

Another example is connected with the most exciting discovery in experimental astrophysics of the last decade – the detection of a flux of high energy particles

from point sources. Recently, ground-based experiments have demonstrated the ability to unambiguously detect $\gamma$-rays from the Crab Nebula [8]. The Cherenkov air shower technique detects an electromagnetic cascade in the atmosphere several kilometers long and a few tens of meters wide. The characteristics of the detected shower image (length, width of the flash, the reconstructed ellipsoid axis angles with respect to the optical axis of telescope, etc.) permits rejection of the isotropic background more than two orders of magnitude.

The first successful attempts to utilize the new classification techniques encouraged the physical community to widely incorporate the neural approach in different HEP data analysis.

But further work is needed to enable NN to be properly simulated and used to improve the way the learning process is implemented.

It is hard to derive the global concept of learning from biological observations. However, we believe that in nature the brain has evolved by trial and error and that the coarse structure of the brain is determined genetically.

Our concept consists in the application of the evolutionary methods for NN training, as the most popular backpropagation method of calculation of couplings appears to be unnatural. We suppose that the structure of NN is determined by evolution and is fixed, but the synaptic strengths (couplings) are repeatedly modified in a random search way which hopefully improves the situation until a successful matrix of couplings is found.

The random search is a universal powerful methodology, akin to the trial and error method, and perhaps it forms the basis of the unpredictable efficiency of biological neural nets.

In our previous work, learning was performed in the framework of the Bayesian paradigm, by multidimensional a posteriori probability density estimation. This method was strongly dependent on the choice of a particular nonparametric method of density estimation with its free parameters, and was rather time-consuming.

The NN classifiers can be analyzed as a special class of statistical pattern classifiers which are derived from the training samples, such as Parzen-window classifiers and K Nearest Neighbor classifiers.

The NN and Parzen classifiers are trained on the same samples and, so, for the first time, we compare the two alternative classification techniques on experimental data, thus providing the continuity in development of new information technologies.

## 2. The nonparametric statistical inference

We shall restrict ourselves to the binary comparisons case, that is, comparisons of two, from many competing hypotheses at a time. Our example concerns a case when we want to realize the choice of one of two well-defined hypotheses – the background rejection in $\gamma$-quanta detection with the Cherenkov imaging technique.

If the statistical statement consists in the existence of an analytic distribution family (like Poisson or Gaussian), appropriate to the problem in hand, we have a prescribed parametric model. For such parametric models a well-known concept of statistical inference consists in obtaining estimates of its parameters and verifying the validity of the chosen family [9].

The classification problem is traditionally described in terms of null and alternative hypothesis, critical and acceptance regions, first and second kind errors and level of significance [10].

The best critical region is constructed by means of Likelihood Ratio (LR):

$$\mathrm{LR}(\mathbf{x}) = \frac{p(\mathbf{x}/\theta^*_\gamma)}{p(\mathbf{x}/\theta^*_{pr})}, \tag{1}$$

where $\mathbf{x}$ is a many-dimensional observable, in our case – parameters of Cherenkov flash, $p(\mathbf{x}/\theta^*_\gamma)$, $p(\mathbf{x}/\theta^*_{\mathrm{pr}})$ – are conditioned on particle type probability density functions, obtained separately for $\gamma$-images and proton images, $\theta^*$ is the Maximal Likelihood Estimate (MLE):

$$\theta^* = \underset{\theta}{\operatorname{argmax}} \sum_{i=1}^{M} \ln\, p(\mathbf{x}_i/\theta), \tag{2}$$

where $\mathbf{x}_i$ are obtained from Cherenkov telescope calibration (possible only for background) or simulations (for signal events), and $M$ is the number of calibration or simulation trials.

For almost all problems of inference, the crucial question is whether the fitted probability family is in fact consistent with the data. Usually, parametric models are chosen for their statistical tractability, rather than for their appropriateness to the real process being studied.

Of course, any statistical inference is conditioned on the model used, and, if the model is oversimplistic so that essential details are omitted, or improperly defined, then at best only qualitative conclusions may be obtained. In HEP very sophisticated models are used, completely mimicking a stochastic mechanism whereby data is generated. Such models are defined on a more fundamental level than parametric models, and provide us with a wide range of outcomes from identical input variable sets – 'labeled', or 'training' samples (TS).

Usually, for experimental physics data handling, the Likelihood Function cannot be written explicitly, and we deal with implicit, nonparametric models, for which no parametric form of the underlying distribution is known, or can be assumed.

The Bayesian approach provides the general method of incorporating prior and experimental information and formalizes the account of all the losses connected with probable misclassification and utilizes all the differences of alternative classes [11,12]. The decision problem in a Bayesian approach is simply described in terms of the following probability measures defined on metric spaces:

(a) The space of possible states of nature $\theta = (p, \gamma)$ where $p$, $\gamma$ are indexes of alternative classes (hypotheses);
(b) The space of possible statistical decisions $\tilde{\theta} = (\tilde{p}, \tilde{\gamma})$, the decision that the examined image is caused by a primary proton or a $\gamma$-quantum;

(c) Cost (losses) measure $C_{\theta\tilde{\theta}}$ defined on the direct product of the true states and decision spaces $(\theta \times \tilde{\theta})$. At correct classification the losses are equal to zero: $C_{p\tilde{p}} = C_{\gamma\tilde{\gamma}} = 0$. If we misclassify the signal event (error of the first kind), we decrease the efficiency of the $\gamma$-event registration. If we attribute hadronic images to $\gamma$-ray ones (error of the second kind), we increase the background contamination. As we expect a significant excess of background against signal, we are interested in a strong background rejection. It is therefore not reasonable to take the symmetric loss function $C_{p\tilde{\gamma}} = C_{\tilde{p}\gamma} = 0.5$, as we did in our earlier studies concerning the cosmic-ray hadrons classification by a transition radiation detector and iron nuclei fraction determination in the primary flux [13].

(d) Event (measurement, feature) space – a set of possible results of a random experiment – image parameter samples obtained by a Monte Carlo simulation. We shall denote these samples by $\omega_P$ and $\omega_\gamma$. The experimental image handling procedure parameters are determined by these samples.

(e) The prior measure $P_\theta = (P_\gamma, P_p)$. For this measure we used the uniform distribution $P_\gamma = P_p = 0.5$. In this case classification results will depend only on the available experimental information and the losses.

(f) Conditional density (likelihood function): $\{p(x/\omega_p), p(x/\omega_\gamma)\}$. The estimation of the conditional (on particle type) density on the basis of a collection of simulations (the Bayesian learning) is a typical problem in cosmic ray and high energy physics. The application of nonparametric local density estimation methods (the kernel-type Parzen estimates [14], the K-nearest-neighbors (KNN) estimates [15]) gives the best results. Our development of these nonparametric density estimates [16] makes their use in cosmic ray physics considerably more simple and increases their precision.

(g) The *a posteriori* density $p(\omega_\theta/x) \sim p_\theta p(x/\omega_\theta)$, in which the prior and experimental information is included. As we choose prior information to have a uniform distribution, the *a posteriori* density coincides with the conditional one.

Proceeding from the above definitions we can introduce the Bayesian decision rule:

$$P(\mathbf{x}/\omega_\gamma)C_{p\tilde{\gamma}} \gtrless P(\mathbf{x}/\omega_p)C_{\gamma\tilde{p}} \rightarrow \mathbf{x} \in \begin{cases} \gamma \\ p \end{cases}. \tag{3}$$

## 3. Learning in the feed-forward neural networks

The basic computing element in a NN is a node (neuron). A general $i$th node receives signals from some number of input channels (see *Fig. 1*):

$$\mathrm{IN}_i^{l+1} = \Theta_i + \sum_{j=1}^{\mathrm{NODES}(l)} J_{ij}^l \mathrm{OUT}_j^l, \quad i = 1, \mathrm{NODES}(l+1), \quad l = 1, L, \tag{4}$$

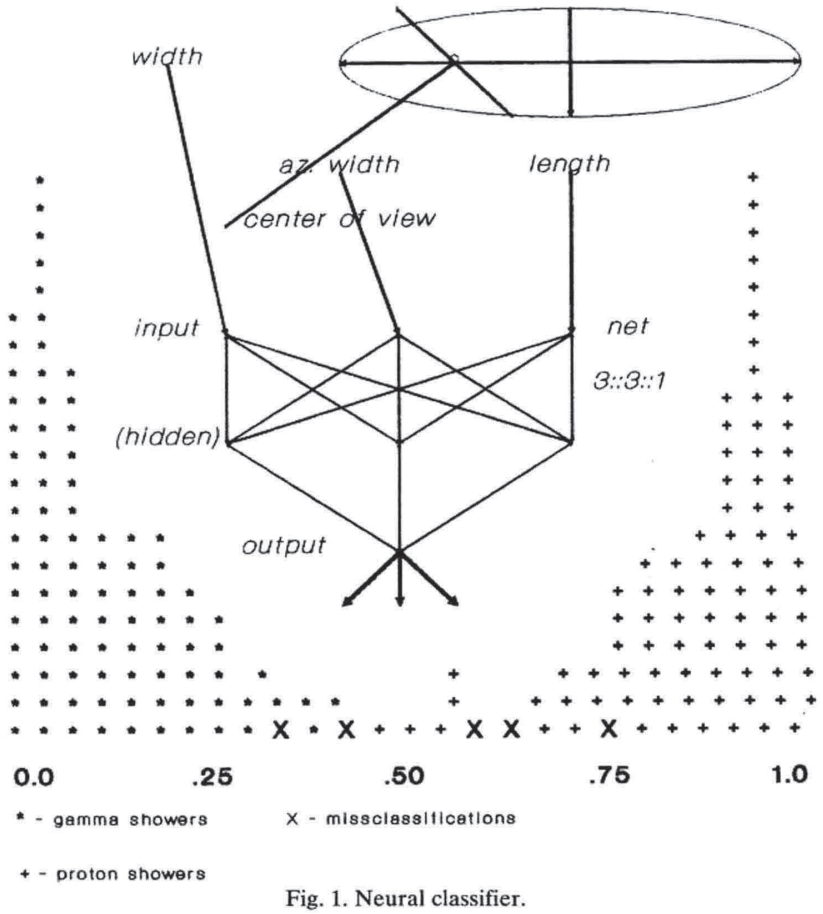


Fig. 1. Neural classifier.

where the threshold $\Theta_i$ and connection strength $J_{ij}^l$ are parameters associated with the node $i$, $l$ is the layer index, $L$ the total number of layers, NODES($l$) the neuron number in the $l$th layer, and $\mathrm{OUT}_j^l$ the output of the $j$th neuron in $l$th layer. The index $j$ always corresponds to the higher layer (the highest layer is the input layer), and the index $i$ to the next layer. The output of the neuron is assumed to be a simple function of this node input; usually it is formed by the nonlinear sigmoid function:

$$\mathrm{OUT}_i^l = 1/\left(1+\exp\left(-\mathrm{IN}_i^l\right)\right), \quad i = 1, \mathrm{NODES}(l), \quad 1 \neq 1, \tag{5}$$

where $\mathrm{IN}_i^l$ is the input of the $i$th neuron in the $l$th layer.

The topology of the NN for event classification purposes usually has a fairly restrictive form [17]:

(1) All nodes are arranged into distinct layers.
(2) The input layer has one node for each measured characteristic.
(3) The output layer has a single node, by which output the classification function is formed.

(4) The feed-forward connectivity: a node in a given layer receives input only from nodes in the preceding layer.
(5) Complete connectivity: each node in a given layer sends its output to all nodes in the next layer.

The trivial case of such an architecture is the linear discriminant function, in which the input nodes are directly connected to the output one. By implementing this topology one can obtain the best linear discriminant, proceeding from the selected input variables.

To obtain a more complicated nonlinear discriminant surface, the transition from input to output proceeds through so-called hidden layers, in which various internal representations of the input are constructed, leading to more complicated decision boundaries.

With an input/output relationship thus defined the multidimensional feature set is translated from input through hidden layers to the output node, where classification is performed. So, the NN provides one-to-one mapping of a complicated input signal to class assignments.

Such a data handling design, combining the linear summation on the nodes input, and nonlinear transformation in the nodes, allows us to take into account all distinctive information, including differences in nonlinear correlations of alternative classes of multidimensional features.

This method is easily generalized to classification with a number of classes (for example, for classification of incident cosmic radiation into 5 distinct nuclei groups). The $M$-node output layer can be used to separate the input stream into $2^M$ classes, if binary representation of the class number is used. The analog signal of the single output node can also be used to classify the events into several categories.

The 'true' output – $\mathrm{OUT}^L_{\mathrm{true}}[k]$ for $k$th category events is determined to maximize the shift of the alternative classes from each other:

$$\mathrm{OUT}^L_{\mathrm{true}}[k] = (k-1)/(K-1), \quad k = 1, K, \tag{6}$$

where $K$ is the total number of classes. In the case of two classes, e.g. the first class being $\gamma$-images and the second being $p$-images (background), the 'true' outputs, as one can easily see, are equal to zero and one. The actual events classification is performed by comparing the obtained output value with the 'true' one.

Thus the network contains a number of free parameters: the thresholds and connection strengths, the total number of which is equal to:

$$\mathrm{NTOT} = \sum_{l=2}^{L} \mathrm{NODES}(l) + \sum_{l=1}^{L-1} \mathrm{NODES}(l)\mathrm{NODES}(l+1). \tag{7}$$

For simple net configurations, e.g. *1*::3::1, NTOT is 10, while for a 3::3::1 NTOT is 18.

The net training consists in determining these parameters using of 'labeled' events (training samples). The figure of merit to be minimized is simply the

discrepancy of apparent and target outputs over all training samples (classification score function):

$$Q = \sum_{k=1}^{K} \sum_{m=1}^{M_k} w(k)\left(\mathrm{OUT}_m^L[k] - \mathrm{OUT}_{\mathrm{true}}[k]\right)^2, \tag{8}$$

where $\mathrm{OUT}_m^k$ is the actual output value of training event, belonging to the $k$th class, and the $\mathrm{OUT}_{\mathrm{true}}[k]$ is the target value of the $k$th class output, where $K$ is the number of categories and $M_k$ is the number of events in the $K$th training set, and $w(k)$ is the weight function, controlling the relative 'quality' of each class training. If we want to suppress the background contamination significantly, the background cluster must be compact and be as near as possible to the $\mathrm{OUT}_{\mathrm{true}}$ [2], i.e. to 1. So the value of $w(2)$ must be somewhat greater than $w(1)$, if the signal cluster may be much more spread near to the 0 point as 50% registration efficiency is good enough.

For feed-forward network training, a standard technique exists, providing the approximate minimization of a classification score function: the changes, initiated by the difference between the expected and predicted output pattern, have propagated back through the network.

The small correction to the network parameters (each correction associated a with particular event) are done by the steepest descent steps:

$$J_{ij}(\mathrm{new}) = J(\mathrm{old}) + \Delta_m J_{ij}, \quad \Delta_m J_{ij} = -\epsilon \partial Q / \partial J_{ij}, \tag{9}$$

where $\epsilon$ is the step size, the distance to move along the gradient, also called the 'learning coefficient'.

The couplings between the last hidden and output units are modified (after proceeding throughout the net of an event) according to

$$\Delta_m J_{1j}^L = \epsilon\left(\mathrm{OUT}_m^L - \mathrm{OUT}_{\mathrm{true}}\right)\mathrm{OUT}_j^{L-1}\mathrm{OUT}_m^L\left(1 - \mathrm{OUT}_m^L\right),$$
$$j = 1, \mathrm{NODES}(L-1), (\mathrm{NODES}(L) = 1), \tag{10}$$

where $\mathrm{OUT}_m^L$ is the actual response of the single output node for the $m$th event, $\mathrm{OUT}_j^{L-1}$ is the output of the $j$th node of the last hidden layer and $\mathrm{OUT}_{\mathrm{true}}$ is the target output of the $m$th event.

The couplings, connected the the hidden layers (or hidden and input layers) are obtained by the formula:

$$\Delta_m J_{ij}^{L-1} = \epsilon J_{i1}^L(\mathrm{new})\left(\mathrm{OUT}_m^L - \mathrm{OUT}_{\mathrm{true}}\right)\mathrm{OUT}_j^{L-2}\mathrm{OUT}_i^{L-1}\left(1 - \mathrm{OUT}_i^{L-1}\right). \tag{11}$$

Thus the error terms, obtained on the output, are evaluated back through the hidden layers to the input layer (hence the name backpropagation).

It is worth remembering that a steepest descent procedure cannot escape from the local minimum region of the quality function once it enters it, and the minimization is not guaranteed to converge to an absolute minimum.

Another strategy introduced recently [18,19], provides the possibility of escaping from the local minimum region and is obviously more biologically realistic. It trains

the net in an evolutionary way, implementing the procedure of trial and error for modification of the values of net parameters.

First, the particular net parameter is randomly chosen (including node thresholds as well as couplings), then the random addition (or subtraction) $\Delta$ is selected:

$$\Delta = \eta f(Q)(\mathrm{RNDM} - 0.5), \tag{12}$$

where RNDM is randomly distributed in the (0–1) interval, $f(Q)$ is the power function controlling the rate of descent when approaching the minimum and $\eta$ is a random 'step' size.

If the random step is successful, i.e. the score function decreases, then the modification survives, otherwise it is subtracted and the random search procedure continues.

The iterations stop when the value of the quality function is stabilized, and no more improvements take place, thus indicating that the theoretical limit of possible classification error reduction has been reached. The resulting set of net parameters can be used for experimental data classification. We expect that data flow passing through the trained net will be divided in two clusters concentrated in the opposite regions of the (0–1) interval. Choosing an arbitrary point in this interval (the so-called decision point $C^*$) the classification procedure can be defined: an event whose output is greater that the decision point is attributed to the second class, while all other events belong to the first class:

$$\mathrm{OUT}^L(\mathbf{x}) \gtrless C^* \rightarrow \mathbf{x} \in \begin{cases} p, \\ \gamma, \end{cases} \tag{13}$$

where $\mathrm{OUT}^L(\mathbf{x})$ is the output node response for a particular experimental image $\mathbf{x}$.

The overlap of clusters caused by the classification errors depends on the discriminative power of the feature subset and on the learning power. By moving the decision point along the (0-1) interval we can change the relation between first and second kind of errors (the position of the decision point is the neural analog of the cost (losses) function in the Bayesian approach).

## 4. Statistical and neural methods of Cherenkov images classification

For a comparative study of statistical and neural classification we used 7000 events from an observation of the Crab nebula at the Whipple observatory [20] (only OFF i.f. background data were used). The training was performed with a combined TS – simulated $\gamma$ – images & experimental hadron images (507 $\gamma$ & 517 p events). Three features were used: LENGTH, WIDTH and AZIMUTHAL WIDTH, the best combination obtained from multidimensional correlation analysis [21].

The Bayesian procedure parameters were: the Parsen width value $-0.35$ for each dimension, the cost value $C_{\tilde{p}\gamma}$ ($C_{p\tilde{\gamma}}$ is equal to $1 - C_{\tilde{p}\gamma}$) varies from 0.01 to 0.1. Leave-one-out-for-a-time procedures were used to estimate classification errors.

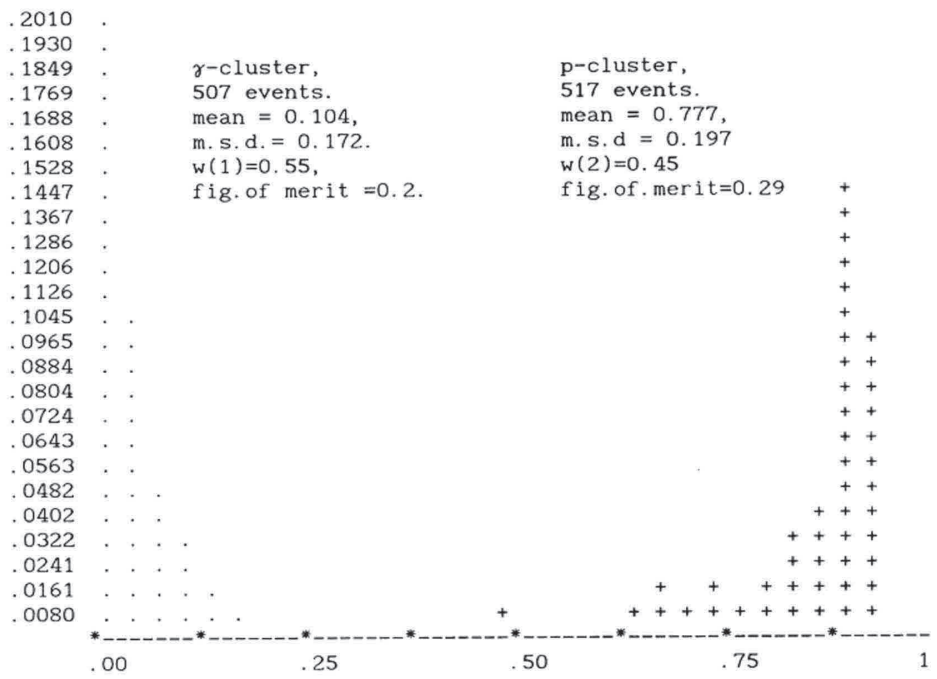


Fig. 2. The NN output after 1000 (148 success steps) trials of random search learning; tough γ-cluster; classification score improoved from 0.5 till 0.24; each sign (•, +) corresponds to 10 events.

The neural classification was performed with a simple three-layered net with 3 hidden and one output nodes. *Fig. 1* shows the Cherenkov image parameters, their input to the net and the output histograms. The decision point was varied in the same interval as the cost function in the Bayesian method. Two variants of weight values were used: 0.45 & 0.55 tight background cluster and 0.55 & 0.45 tight γ-cluster.

As one can see from the normalized histograms (*Figs. 2 and 3*) of net output after 1000 learning iterations, when couplings were modified according to (12), the alternative classes were all well-separated. The differences of the figures prove the ability of controlling the learning 'quality' of each class via altering the weights ratio (see Eq. 8). The output distribution of a well-trained class has mean values close to the target ones and relatively small spread (mean square deviation). As has been mentioned above, we are interested in significant suppression of background *p*-images. Therefore for data classification we use the net with couplings obtained in the learning cycle, corresponding to a 0.45/0.55 weights ratio (*Fig. 3*).

The process of successive improvement of the classification score during the random search is shown in *Figs 4 and 5*. The curves correspond to the histograms on *Figs. 2 and 3*.

From the learning results we can calculate classification errors for both the statistical and neural technique. These training sample errors (apparent errors)

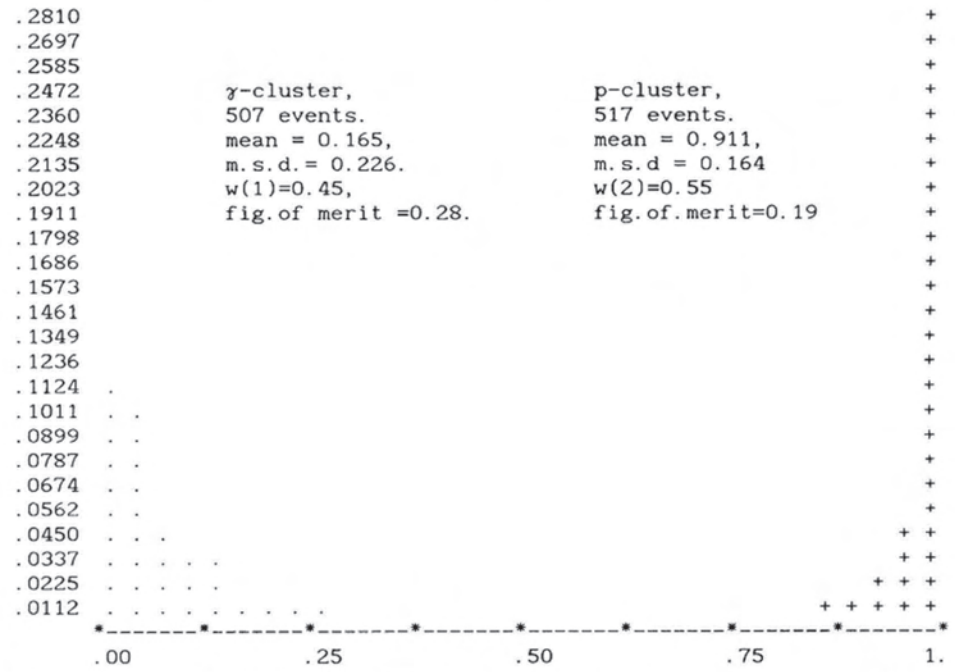


Fig. 3. The NN output after 1000 (189 success steps) trials of random search learning; tough $p$-cluster; classification score improved from 0.5 till 0.23; each sign (•, +) corresponds to 10 events.

usually are optimistically biased and the crucial test is, of course, the control sample test. For the control we used independent (not present in the TS) background observations (7000) events.

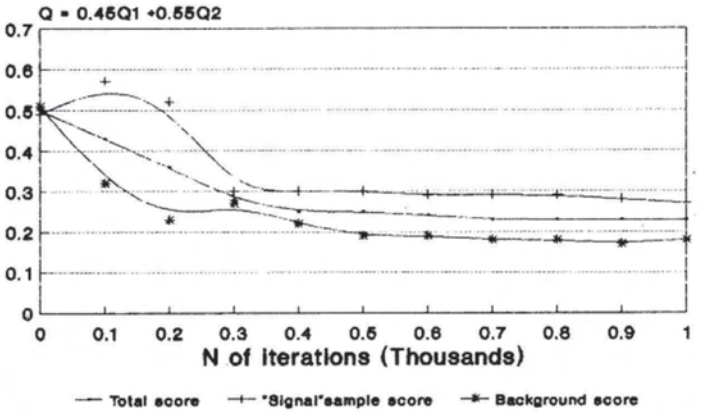


Fig. 4. Random search of net couplings, minimization of classification score.

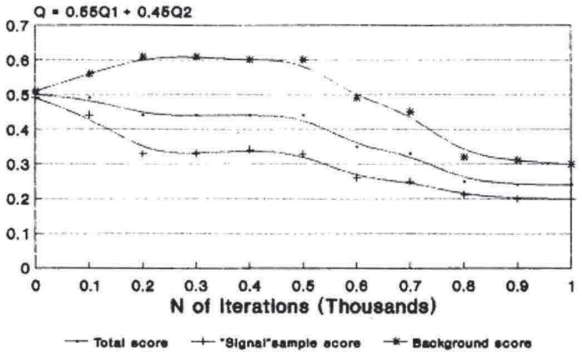


Fig. 5. Random search of net couplings, minimization of classification score.

As one can see from *Table 1*, the apparent and control errors are consistent and the statistical and neural classifications coincide very well. The lack of bias in statistical error rates is explained by use of the leave-one-out method, specially designed to avoid bias effects [22].

By changing the cost function in (3) and the decision point in (13) one can obtain different ratios between errors of the first and second kind (registration efficiency and background contamination). In this way, we obtain so-called 'influence curves' which give us the possibility of choosing the desired errors ratio in classification (remember, that you can't decrease both errors simultaneously).

The influence curves in *Fig. 6* prove again the excellent coincidence of both techniques used, that manifest the agreement of the errors to the theoretical Bayesian error limit and proper construction and learning of nonparametric statistical and neural procedures.

NN training takes $\approx 20$ min. on an IBM PC/AT-386. The time spent for each experimental event classification is 0.001 sec. Bayesian training (multivariate density nonparametric estimation) is repeated for each experimental event again

Table 1
The apparent and control errors obtained by statistical and neural classifiers

| | Apparent (TS) error | Control error |
|---|---|---|
| Bayesian classification | | |
| $\gamma$-image registration efficiency | 0.52 | – |
| background contamination | 0.006 | 0.0058 |
| $C_{\tilde{p}\gamma} = 0.015$ | | |
| Neural classification | | |
| $\gamma$-image registration efficiency | 0.44 | – |
| background contamination | 0.004 | 0.0062 |
| $C^* = 0.05$ | | |

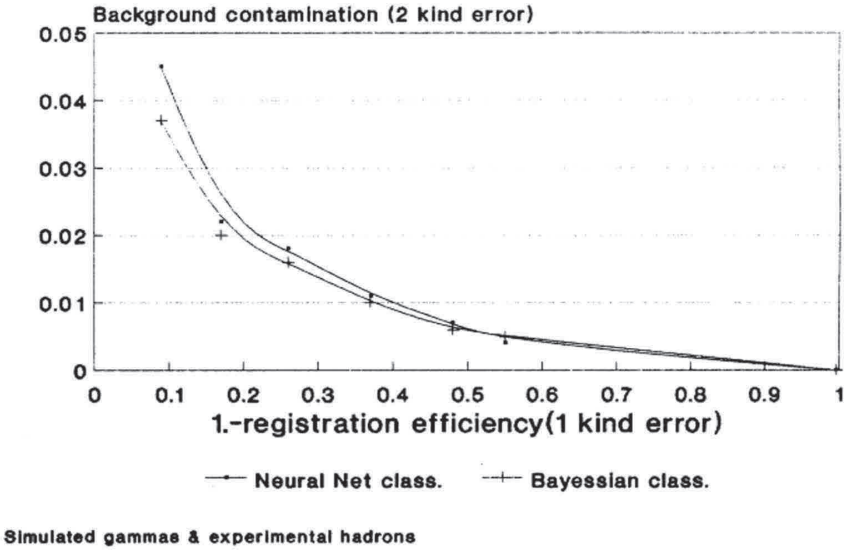


Fig. 6. Influence curve, apparent (training sample) errors.

and again, so an event classification takes $\approx 2$ sec. on the same computer with same the training set and feature space.

## 5. The analysis of the Crab Nebula data

Searches for discrete $\gamma$-ray sources consisted in detection of an abundance $(N_{on} - N_{off})$ of events coming from the direction of a possible source comparing with a control measurement, when pure background is registered. As the expected fluxes are very weak (the signal to background ratio does not exceed 0.01), one question always has to be answered: is the detected abundance a real signal or only background fluctuation? The measure (level) of statistical significance, used in $\gamma$-ray astronomy, is the so-called criterion size (sigma) [23]:

$$\sigma = (N_{on} - N_{off})/(N_{on} + N_{off})^{0.5}. \tag{14}$$

The greater the $\sigma$ value, the lesser the probability, that detected excess is due to background fluctuation, and the equipment construction and new data handling methods development have an aim to enlarge the $\sigma$ value. After selecting the '$\gamma$-like' events from row data (both from the ON and OFF samples), according to some discriminating technique, the criterion takes form:

$$\tilde{\sigma} = \left(\tilde{N}_{on} - \tilde{N}_{off}\right)/\left(\tilde{N}_{on} + \tilde{N}_{off}\right)^{0.5}, \tag{15}$$

where $\tilde{N}_{on}$ $\tilde{N}_{off}$ are the 'survived' events number.

The best discrimination technique, used in Whipple Observatory is the multidimensional cuts ('supercuts') method, proposed in [24] and then improved in [25]

(4 Cherenkov image parameters were used). This method consists in *a posterior* selection of the best $\gamma$-cluster, the multidimensional hypercube, containing '$\gamma$-like' events. The particular coordinates of the cube were selected to maximize the $\sigma$ value on the 1988–1989 Crab Nebula observation database (65 ON, OFF pairs $\sim$ 1 mln. events) [26]. Implementing the supercuts method the initial $\sigma$ value was enlarged from 5 to 34.

However, it is doubtful, that the rectangular shape is the best one, and furthermore Cawley finds significant differences between ON and OFF distributions within the hypercube. We use a simple 4::5::1 neural net to select the better nonlinear shape of the $\gamma$-cluster. A preprocessing was done: events falling in the enlarged hypercube (1.5 times larger than the best ones) were selected. The net was trained on these ON/OFF events. The new quality function was used, instead of classification score (8): the sigma value (15) was maximized.

After several hours of random search the better $\gamma$-cluster was outlined and the $\sigma$ value was enlarged from 27 to 36 (the record value).

The use of new quality function allows one to:

- avoid usage of Monte Carlo events with inherent misleading simplifications and incorrectness;
- direct optimize the desired quantity: the significance of source detection;
- obtain the complicated nonlinear boundaries of $\gamma$-cluster.

This modification of the neural classification method seems to be very promising for the future proton colliders (LHC and SSC) data analysis, intended to detect very rare, as yet unseen physical phenomena [27]. The effects of model dependence of the training are the main obstacles of using standard training with the classification score as quality function. The direct comparison of pure background and an mixture, containing a very small percentage of interesting events, can lead to the discovery of new physical processes and particles.

## 6. Conclusions

The NN classifier forms a special type of statistical classifier and is consistent with other nonparametric classifiers developed within the Bayesian approach.

After a few hundred successful random adjustments of the net parameters, the net is trained to suppress the background contamination down to a desired level, consistent with other sophisticated and time-consuming nonparametric methods.

The great advantage of NN classifiers consists in separation of the learning and the active phase. After the learning phase, all distinctive information contained in the training samples is mapped on the net parameter set. This parameter set can be written to a VLSI neurochip with the aid of a special trainer box [28]. Trained neurochips may be 4 to 5 orders of magnitude faster than software statistical classifiers. Thus we can recommend the NN classifier as a very fast intelligent trigger for on-line analysis in collider and cosmic ray physic experiments and as a sophisticated but also very fast tool for complicated off-line analysis.

The most challenging problem of modern cosmic ray physics seems to be the

identification of high energy neutrino point sources. A recently proposed approach [30] for constructing an above-ground neutrino detector (registering the upward going muons produced by charged interaction of parent neutrino in the rock below the detector), requires a very high rejection power (up to $10^{11}$) to reduce the background due to upward going muons which are produced by cosmic ray interaction in the atmosphere. The proposed classification technique can be used to enlarge the sensitivity of the detector to very weak neutrino fluxes.

## Acknowledgement

The author thanks the Whipple Collaboration for use of the Crab Nebula database and Dr. Michael Cawley for numerous useful discussions and valuable remarks concerning new methods of data analysis.

## References

[1] T. Nash, High energy physics experiment triggers and the trustworthiness of software, FERMILAB-Conf-91/270, Fermi National Accelerator Laboratory, 1991.
[2] L. Gupta, B. Denby et al., Neural network trigger algorithms for heavy quark event selection in a fixed target high energy physics experiment, FERMILAB-Pub-91/117, Fermi National Accelerator Laboratory, 1991.
[3] J.C. Perret and J.T.P.M. van Stekelenborg, The applications of NN in the core location analysis of EAS, *J. Phys. G: Nucl. Part. Phys.* 17 (1991) 1291-1302.
[4] L. Lönnbland and A. Nilsson, The MC$^{++}$ Event generation toolkit, DESY 91-158, LU TP 91-35, University of Lund, Deutsches Electronen-Synchrotron, 1991.
[5] A.A. Chilingarian, Statistical decisions under nonparametric a priori information, *Comp. Phys Comm.* 54 (1989) 381–390.
[6] P. Bhat, L. Lönnbland et. al., Using NN to identify jets in hadron-hadron collisions, Lu TP 90-13, DESY 90–144, University of Lund, Deutsches Electronen-Synchrotron, 1990.
[7] C. Petersen, Using NN to identivy the origin of gets, LU TP 90-14, University of Lund, 1990.
[8] C.W. Akerlof, M.F. Cawley et al., *Proc. 22 Internat. Cosmic Ray Conf.*, OG-sessions, Dublin (1991) 456–459.
[9] E.A. Eadie, D. Drijard, F.E. James, M. Ross and B. Sadoulet, *Statistical Methods in Experimental Physics* (North Holland, Amsterdam, 1971).
[10] S. Zacks, *The Theory of Statistical Inference* (Wiley, New York, 1977).
[11] H. Raiffa and R. Schlaifer, *Applied Statistical Decision Theory* (MIT Press, Cambridge, MA, 1978).
[12] J.D. Hey, *An Introduction to Bayesian Statistical Inference* (Martin Robertson, 1983).
[13] A.A. Chilingarian, and H.Z. Zazyan, On the possibility of investigation of the mass composition and energy spectra of PCR in the energy range $10^{15}$–$10^{17}$ ev using EAS data, *Il Nuovo Cimento* 14C (6) (1991) 555–566.
[14] E. Parzen, On estimation of a probability density function and mode, *Ann. Math. Stat.* 33 (1962) 1065–1087.
[15] D.O. Lofsgaarden and C.D. Quesenberry, A nonparametric estimate of a multivariate density function, *Ann. Math. Stat.* 36 (1965) 1049–1063.
[16] A.A. Chilingarian and H.Z. Zazyan, A bootstrap method of distribution mixture proportion determination, *Pattern Recognition Letters* 11 (1990) 781–785.
[17] T.D. Gottshalk and R. Nolty, Identification of physical processes using NN classifier, DOE REPORT CALT-68-160, California Institute of Technology, 1990.

[18] S. Bornholdt and D. Graudenz, General asymmetric neural networks and structure design by genetic algorithms, Desy 91-046, Deutches Electronen-Synchrotron, 1991.
[19] A.A. Chilingarian, Neural net classification of the $\gamma$- and $p$-images registered with atmospheric Cherenkov technique, *Proc. 22 Internat. Cosmic Ray Conf.*, OG-sessions, Dublin (1991) 540–543.
[20] M.G. Lang, C.W. Akerlof, M.F. Cawley et al., Tev observation of the Crab nebula and other plerions in the epoch 1988–91, *Proc. 22 Internat. Cosmic Ray Conf.*, Dublin (1991) 204–207.
[21] F.A. Aharonian, A.A. Chilingarian et al., A multidimensional analysis of the Cherenkov images of air showers induced by very high energy $\gamma$-rays and protons, *Nuclear Instruments & Methods* A302 (1991) 522–528.
[22] A.A. Chilingarian and S.Kh. Galfayan, Calculation of Bayes risk, *Stat. Problems of Control* 66 (Vilnius, 1984) 66–77.
[23] S.N. Zhang and D. Ramsden, Statistical data analysis for $\gamma$-ray astronomy, *Exp. Astronomy* 1 (1990) 145.
[24] A.A. Chilingarian and M.F. Cawlew, Application of multivariate analysis to atmospheric Cherenkov imaging data from the Crab nebula, *Proc. 22 ICRC*, Vol. 1 Dublin (1991) 460.
[25] M. Punch, C.W. Akerlof, M.F. Cawley, et al., Supercuts: an improved method of selecting gamma-rays, *Proc. 22 ICRC*, Vol. 1 Dublin (1991) 464.
[26] G. Vacanti, M.F. Cawlew et al., Gamma-ray observations of the Crab nebula at Tev energies, *Ap. J.* 377 (1991) 467.
[27] B. Denby, Tutorial on neural network applications in high energy physica: A 1992 perspective, Fermilab-Conf-92/121-E.
[28] C. Lindsdey, B. Denby and H. Haggerty, Real time track finding in a drift chamber with a VLSI neural network, FERMILAB-PUB 92/55, Fermi National Accelerator Laboratory, 1992.
[29] MINI Collaboration, Rejection power of a horizontal RPC telescope for left and right coming cosmic muons, Inst. Naz. Fis. Nucl. [RAPP.] AE-18, 1992.

**Ashot Chilingarian** is the director of the cosmic ray department of the Yerevan Physics Institute. He received the B.S. in experimental physics in 1971 at Yerevan State University, the Ph. D. degree (1984) and Doctor of Science degree (1991) at Yerevan Physics Institute. He is a member of INNS.

He has published more than eighty papers in the areas of his research interests, which include experimental cosmic ray and high energy physics, statistic methods of data analysis, multivariate density nonparametric estimation and dimensionality analysis. The main emphasis of his present research lies in the field of development of new information technologies for high energy physics data analysis, with particular emphasis on recurrent and feed-forward neural networks simulation.

ELSEVIER

April 1995

Pattern Recognition Letters 16 (1995) 333–338

Pattern Recognition Letters

# Detection of weak signals against background (noise) using neural network classifiers

Ashot Chilingarian *

*Yerevan physics institute, Alikhanian Br. 2, Yerevan 36, Armenia*

Received 5 May 1993; revised 10 November 1994

**Abstract**

We introduce a new neural classification technique for background rejection in high energy physics and astrophysics experiments, which permits us to (i) directly optimize the desired quantity, i.e. the significance of signal detection (signal to noise ratio); (ii) obtain the complicated nonlinear boundaries for signal event acceptance. Examples of implementing the proposed technique for background rejection in high energy astrophysics experiments are presented.

## 1. Introduction

In high energy physics and astrophysics experiments the most important task is to separate experimental data into two classes, i.e. the signal (new interesting physical phenomenon) and background (non-interesting, abundant events). Typically in a physical experiment a particular event is described as a point in an $N$-dimensional measurement metric space and a mixture probability density function can be defined.

In a previous paper we considered the problem of distribution mixture classification in the case of the nonparametric type of a priori information (the statistic model is given in the form of a stochastic mechanism, whereby the data are generated and the underlying log-likelihood function cannot be given explicitly) (Chilingarian and Zazyan, 1990). A method of the distribution mixture coefficient estimation was proposed, based on the Bayesian decision rules and bootstrap replicas. The nonparametric probability density estimates used in Bayesian decision rules were obtained with the help of sets of "pseudoexperimental" events obtained in Monte Carlo simulations (training samples).

The normal approach to high energy physics data analysis is to perform precise simulations of particle collisions, determine the detector's response to the passage of the produced particles and to simulate the secondary interactions and showers (Flugge, 1991). But, if one is searching for new, yet unseen phenomena, the simulation can be misleading, and only experimental information can prove the existence of "new physics". Considering that the rate of interesting events expected in colliders of the next generation and astrophysics experiments is negligible as compared to noninteresting (background) events, we can state that the reduction of the data volumes in such a way, that the maximum sensitivity to the new physics is preserved and the maximum immunity to noise is achieved, is the key to the successful analysis (Mapelli, 1991).

* Email: chilin@crd.erphy.armenia.su.


*SSDI* 0167-8655(94)00107-3

Such "cuts" (mostly linear) performed on multidimensional distributions of measurements are usually used in collider experiments analysis to enlarge the significance of statistical conclusions concerning the existence of new phenomena. First of all it is necessary to prove with high significance level the existence of any signal, i.e. that in the mixture distribution:

$$P(x) = \alpha\, P_{\text{signal}}(x) + (1-\alpha)\, P_{\text{background}}(x) \quad (1)$$

(where usually $\alpha < 0.01$ and $P_{\text{signal}}(x)$ is unknown), $\alpha$ is not equal to 0. Then the value of the parameter $\alpha$ has to be estimated.

The fundamental theory of particle physics called the Standard Model predicts almost all of the properties of elementary particles except their masses (so we cannot obtain probability distributions of pure signal events). Determination of the masses of the top quark and the neutrino is currently the highest priority in high energy physics. After an accelerator run during 1992–1993 the D0 collaboration at Fermilab (USA) collected a data file consisting of 13 million events and one cannot expect more than a few dozen events to be the result of top quark production (D0 Collaboration, 1994).

It is difficult to outline the desired "best" signal domain where it is possible to detect the significant abundance of signal events over the background distribution — signal detection problem. The signal domain — multidimensional decision surface — can be nonlinear and its selection without knowing the signal and background distribution shapes is an unsolved problem yet.

We propose to use Neural Networks (NN) for the a posteriori signal detection. The NN technique is widely used in high-energy physics experiments for classification and event reconstruction purposes (Fogelman Soulie, 1992; Peterson and Gvaldsson, 1991; Denby, 1992). The net is usually trained on simulation data, and the so-called "classification score" is used as the objective (quality) function in minimization (best net parameters selection). It is assumed that both background and signal samples are available. But in the case of interest, the pure signal samples obtained from Monte Carlo trials are often either simplified or incorrect, so it will be better not to use "signal" samples at all. The peculiarity of our approach consists in training the net without using pure signal samples. We propose to use mixed signal and background and pure background samples obtained from the experiment for neural net training. A new type of objective function is introduced instead of the classification score.

In Section 2 the NN classification technique is presented. Section 3 describes modification to the technique and uses as an example the detection of very high energy $\gamma$-quanta coming from point sources, registered by imaging Cherenkov telescopes (Lang et al., 1991).

## 2. The neural classification technique

The basic computing element in a multilayered feed-forward NN is a node (formal neuron). A general $i$th node receives signals from all neurons of the previous layer:

$$\text{IN}_i^{l+1} = T_i + \sum_{j=1}^{\text{NODES}(l)} W_{ij}^l \times \text{OUT}_j^l,$$

$$i = 1, \ldots, \text{NODES}(l+1),\ l = 1, \ldots, L-1 \quad (2)$$

where the threshold $T_i$ and connection strength $W_{ij}^l$ are parameters associated with the node $i$, $l$ is the layer index, $L$ is the total number of layers, NODES($l$) is the number of neurons in the $l$th layer and $\text{OUT}_j^l$ is the output of the $j$th neuron in the $l$th layer. The index $j$ always corresponds to the higher layer (the highest layer is the input layer), and the index $i$ to the next layer. The output of the neuron is assumed to be a simple function of this node input, usually it is formed by the nonlinear sigmoid function:

$$\text{OUT}_i^l = 1/(1 + e^{-\text{IN}_i^l}),$$

$$i = 1, \ldots, \text{NODES}(l),\ l = 2, \ldots, L \quad (3)$$

where $\text{IN}_i^l$ is the input of the $i$th neuron in the $l$th layer.

With this defined input/output relationship, the multidimensional feature set is translated from input through hidden layers to the output nodes, where classification is performed. So, the NN provides the mapping of a complicated input signal to the class assignments.

Such a data handling design, combining the linear summation on the nodes input and nonlinear trans-

formation in the nodes, allows us to take into account the whole distinctive information, including differences in nonlinear correlations of alternative classes of multidimensional features.

The "target" output $\mathrm{OUT}^{\mathrm{target}}(k)$ for events of the $k$th category (we restrict ourselves to networks with a single output node) is determined to maximize the separation of the alternative classes from each other:

$$\mathrm{OUT}^{\mathrm{target}}(k) = \frac{k-1}{K-1}, \quad k = 1, \ldots, K \tag{4}$$

where $K$ is the total number of classes. In the case of two classes, i.e. signal and background events, the "target" outputs, as one can easily see, are equal to zero and one. The actual events classification is performed by comparing the obtained output value with the "target" one. We expect, that the data flow passing through the trained net will be divided in two clusters concentrated in the opposite regions of the (0, 1) interval. Choosing an appropriate point in this interval (the so-called decision point $C^*$), the classification procedure can be defined: an event with an output greater than or equal to the decision point is attributed to the background class, while all the other events are assigned to the signal class:

$$\mathrm{OUT}(x)\begin{cases} < C^*, & x \text{ is classified as signal,} \\ \geqslant C^*, & x \text{ is classified as background,} \end{cases} \tag{5}$$

where $\mathrm{OUT}(x)$ is the output node response for a particular experimental measurement $x$. This decision rule is a Bayesian decision rule; therefore the output signal of a properly trained feedforward neural net is an estimate of the a posteriori probability density (Ruck et al., 1990).

The expected minimal classification error caused by the overlap of the distributions (the Bayes error) depends on the discriminative power of the feature subset selected and on the learning power. By moving the decision point along the (0, 1) interval we can change the relation between the errors of the first and second kind (the position of the decision point is the neural analog of the loss function in the Bayesian approach).

The net training consists of determining the neuron couplings using the "labeled" events (training samples). The figure of merit to be minimized is simply the discrepancy of apparent and target outputs over all training samples (classification score):

$$Q = \sum_{k=1}^{K} \sum_{m=1}^{M_k} \left(\mathrm{OUT}_m(k) - \mathrm{OUT}^{\mathrm{target}}(k)\right)^2 \tag{6}$$

where $\mathrm{OUT}_m(k)$ is the actual output value for the $m$th training event, belonging to the $k$th class, and $\mathrm{OUT}^{\mathrm{target}}(k)$ is the target value for the $k$th class output, where $K$ is the number of categories and $M_k$ is the number of events in the $k$th training set.

Our goal is to change the training procedure to avoid the usage of the "signal" sample. In the next section we shall introduce a new type of quality function to perform the best signal domain selection (signal detection).

## 3. The new neural algorithm for background rejection

In high energy astrophysics during the 1980's, significant progress has been made in the unambiguous detection of the Crab nebula at TeV energies by the Whipple collaboration (Lang et al., 1991). At TeV energies gamma rays have been shown to possess such characteristics of the Cherenkov image shape and orientation which permit them to be isolated from a much larger hadronic background. The main technique to reject this huge background consisted in applying multidimensional linear cuts on measured Cherenkov image parameters, first introduced by Hillas (1985).

To search for discrete gamma-ray sources, one looks for an abundance $(N_{\mathrm{on}} - N_{\mathrm{off}})$ of events coming from the direction of a possible source $(N_{\mathrm{on}})$ as compared with the control measurement, when pure background is registered $(N_{\mathrm{off}})$. As the expected fluxes are very weak (the signal to background ratio not exceeding 0.01), one should always answer the following question: is the detected abundance a real signal or only a background fluctuation? The measure (level) of statistical significance used in gamma-ray astronomy is the so-called criterion size $(\sigma)$ (Zhang and Ramsden, 1990):

$$\sigma = \frac{N_{\mathrm{on}} - N_{\mathrm{off}}}{\sqrt{N_{\mathrm{on}} + N_{\mathrm{off}}}}. \tag{7}$$

Table 1
Whipple Crab detection, 1988–1990

| | $N^*_{on}$ | $N^*_{off}$ | $\sigma$ | DIFF | DIFF/$N^*_{off}$ | $N^*_{off}/N_{off}$ |
|---|---|---|---|---|---|---|
| Raw | 506255 | 501408 | 4.8 | 4847 | 0.01 | |
| Azwidth | 14622 | 11389 | 20.4 | 3233 | 0.28 | 0.0227 |
| Wedge cut [a] | 6017 | 3381 | 27.2 | 2636 | 0.78 | 0.0067 |
| Supercut [b] | 4452 | 1766 | 34.3 | 2686 | 1.52 | 0.0035 |
| Neural 4::5::1 | 6278 | 2858 | 35.8 | 3420 | 1.20 | 0.0057 |

[a] (Chilingarian and Cawley, 1991).
[b] (Punch et al., 1991).

The greater $\sigma$, the lesser the probability that the detected excess is due to a background fluctuation. Development of new detector hardware and new data handling methods aim to enlarge the value of $\sigma$. After selecting the "gamma-like" events from raw data (both from the ON and OFF samples), the criterion takes the form:

$$\sigma = \frac{N^*_{on} - N^*_{off}}{\sqrt{N^*_{on} + N^*_{off}}} \tag{8}$$

where $N^*_{on}$, $N^*_{off}$ are the numbers of events surviving data selection cuts.

The best discrimination technique used in the Whipple Observatory is the multidimensional cuts (*supercuts*) method proposed in (Chilingarian and Cawley, 1991) and then improved in (Punch et al., 1991) (four Cherenkov image parameters were used). The method consists of a posteriori selection of the best gamma-cluster (multidimensional box), containing "gamma-like" events. The particular coordinates of the box were selected to maximize the $\sigma$ value on the 1988–89 Crab nebula observation data base (65 ON, OFF pairs $\sim 10^6$ events) (Vacanti et al., 1991). By implementing the supercuts method, the initial $\sigma$ value was enlarged from 5 (raw data) to 34.

For Neural Net analysis, we used the same variables as for Supercut analysis, i.e. Width, Length, Dist, and Alpha (Width and Length specify the angular size of the image, Dist specifies the position of the centroid of the image relative to the source position, and Alpha specifies the orientation of the major axis of the image relative to the source position). We use a simple 4::5::1 neural net to select a more realistic nonlinear shape for the gamma cluster. The net was trained on experimental ON and OFF events (i.e. events taken in the direction of the source and events taken on a background or "control" region).

A new objective function was used: instead of the classification score (6) the $\sigma$ value (8) was maximized. During the iterations each particular ON& OFF event was classified according to decision rule (5) with a prechosen (or also optimized) decision point $C^*$ and after executing all training events a new $\sigma$ value was calculated. After several thousands of iterations the more complicated gamma-cluster shape was outlined and the $\sigma$ value was enlarged up to 35.8 (the minimization was performed on a subsample of data, containing 25% of all events, and the $\sigma$ value extrapolated for the whole data set).

The comparison of different background supression methods is shown in Table 1, where DIFF = $N^*_{on} - N^*_{off}$ is the estimate of the signal, DIFF/$N^*_{off}$ is the estimate of the signal-to-noise ratio, $N^*_{off}/N_{off}$ is the estimate of background supression by the technique used.

The Neural Net classification (multidimensional nonlinear masks method) was also applied to the detection of the Crab Nebula by another Cherenkov telescope located on La Palma (Kanarian, Hegra collaboration).

Table 2
Hegra Crab detection, 1992–1993 (Krennrich et al., 1993)

| | $N^*_{on}$ | $N^*_{off}$ | $\sigma$ | DIFF | DIFF/$N^*_{off}$ | $N^*_{off}/N_{off}$ |
|---|---|---|---|---|---|---|
| Azwidth (< 0.18) | 4083 | 3674 | 4.64 | 409 | 0.11 | 0.05 |

Table 3
Hegra Crab detection, 1992, September–October

| | $N^*_{on}$ | $N^*_{off}$ | $\sigma$ | DIFF | DIFF/$N^*_{off}$ | $N^*_{off}/N_{off}$ |
|---|---|---|---|---|---|---|
| Raw | 30880 | 30857 | 0 | 23 | 0.001 | |
| Azwidth | 1333 | 1146 | 3.76 | 187 | 0.16 | 0.037 |
| Width, Miss | 955 | 784 | 4.1 | 171 | 0.22 | 0.025 |
| Width, Miss, Length | 659 | 492 | 4.99 | 167 | 0.34 | 0.016 |
| Width, Miss, Length, Conc | 638 | 460 | 5.37 | 178 | 0.39 | 0.015 |
| Neural 4::3::1 | 520 | 342 | 6.08 | 178 | 0.52 | 0.011 |

The Azwidth analysis results (Krennrich et al., 1993) on this data set (150000 events) are presented in Table 2.

The new methods were applied only to part of the data (September–October 1992). In Table 3 the results of different background rejection methods as applied to this data are summarized. As one can see, the neural analysis achieves the highest signal-to-noise ratio and the smallest background contamination using 4 image parameters (Width, Length, Miss, Conc) and only 3 nodes in a single hidden layer.

## 4. Conclusions

There are some alternatives to the use of neural networks for background rejection in high energy physics experiments. There exist also many traditional statistical methods which are more mathematically founded, for example, Baysian statistical decisions (one can see examples of the use of this approach in high energy physics data analysis in (Chilingarian, 1989; Chilingarian and Zazyan, 1991)).

Time for training the neural net, tedious selection of network architecture, neuron output function and global learning parameters plus the dependence of results on the initial state of the network leads to the results of which optimality and reliability have to be checked with results obtained using traditional nonparametric statistical methods (Duch and Dierksen, 1994).

Many important theoretical problems of neural calculations are far from being solved. Only very few quantitative results are available. There are several practical problems to be solved:

- Selection of the learning rules for different problems;
- Investigation of the influence of the accuracy of the weights on the NN performance;
- Investigations of the role of the shape of the nonlinear output function and of the number of nodes in the hidden layer on the sensitivity of NN classifier;
- Designing fast training algorithms which minimize the true error (on a test sample) instead of minimizing the apparent error (on the training sample).

Nevertheless for solving mathematically ill-posed multidimensional nonlinear problems with ill-defined conditions (like selection of nonlinear multivariate signal domain), where common statistical methods usually fail, the use of neural techniques seem to be suitable and as one can see from the previous the section, the data analysis results can be comparable with or better than traditional techniques.

## Acknowledgments

We thank the members of the Whipple and Hegra collaborations for the use of the Crab Nebula databases.

We thank Dr. M. Cawley for valuable remarks concerning new methods of data analysis, Prof. W. Hofman, Prof. F. Aharonian, Dr. A. Heusler and M. Halpaap for useful discussions.

## References

Chilingarian, A.A. (1989). Statistical decisions under nonparametric a priory information. *Comp. Phys. Comm.* 54, 381–390.

Chilingarian, A.A. and M.F. Cawley (1991). Application of multivariate analysis to atmospheric Cherenkov imaging data from

the Crab nebula. *Proc. 22nd Internat. Cosmic Ray Conf.*, Dublin, Vol. 1, 460–463.

Chilingarian, A.A. and H.Z. Zazyan (1990). A bootstrap method of distribution mixture proportion determination. *Pattern Recognition Lett.* 11, 781–785.

Chilingarian, A.A. and H.Z. Zazyan (1991). On the possibility of investigation of the mass composition and energy spectra of PCR in the energy range 1–10 eV using EAS data. *Il Nuovo Cimento* 14C (6), 555–568.

D0 Collaboration, S. Abachi et al. (1994). The D0 detector. *NIM* A338, 185.

Denby, B. (1992). Tutorial on neural network applications in high energy physics: a 1992 perspective. Fermilab-Conf-92/121-E.

Duch, W. and G.H.F. Dierksen (1994). Neural networks as tools to solve problems in physics and chemistry. *Comp. Phys. Comm.* 82, 91–103.

Flugge, G. (1991). Physics at the large hadron collider. *Proc. 1991 CERN School of Computing*, 23–50.

Fogelman Soulie, F. (1992). Neural networks for pattern recognition: introduction and comparison to other techniques. In: D. Perret-Gallix, Ed., *Proc. 2nd Internat. Workshop on Soft. Enginer.*, 277–286.

Hillas, M. (1985). Cherenkov light images of EAS produced by primary gamma rays and by nuclei. *Proc. 19th Internat. Cosmic Ray Conf.*, USA, Vol. 3, 445–448.

Krennrich, F., R. Mirzoyan, et. al. (1993). Observation of VHE gamma emission from the Crab nebula with the prototype of the Hegra air Cherenkov telescope array. *Proc. 23rd Internat. Cosmic Ray Conf.*, Calgary, Vol. 1, 251–254.

Lang, M.G., C.W. Akerlof, M.F. Cawley, et. al. (1991). TeV observation of the Crab nebula and other plerions in the epoch 1988–91. *Proc. 22nd Internat. Cosmic Ray Conf.*, Dublin, 204–207.

Mapelli, L. (1991). Collisions at future supercolliders: the first 10 microseconds. *Proc. 1991 CERN School of Computing*, 79–112.

Peterson, C. and T. Gvaldsson (1991). An introduction to artificial neural networks. *Proc. 1991 CERN School of Computing*, 113–170.

Punch, M., C.W. Akerlof, M.F. Cawley, et. al. (1991). Supercuts: an improved method of selecting gamma-rays. *Proc. 22nd Internat. Cosmic Ray Conf.*, Dublin, Vol. 1, 464–467.

Ruck, D.W., K.S. Rogers, et al. (1990). The multilayer perceptron as an approximation to a Bayes optimal discriminant function. *IEEE Trans. Neural Networks* 1, 296.

Vacanti, G., M.F. Cawley, et. al. (1991). Gamma-ray observations of the Crab nebula at TeV energies. *Astroph. J.* 377, 467–475.

Zhang, S.N. and D. Ramsden (1990). Statistical data analysis for g-ray astronomy. *Exp. Astronomy* 1, 145–158.

Nuclear Instruments and Methods in Physics Research A 389 (1997) 242–244

ELSEVIER

NUCLEAR INSTRUMENTS & METHODS IN PHYSICS RESEARCH Section A

# The non-linear signal domain selection using a new quality function in neural net training

A. Chilingarian[a,*], E. Sevinian[a], S. Chilingarian[b]

[a]*Cosmic Ray Division, Yerevan Physics Institute, Alikhanyan Brothres 2, Yerevan 36, Armenia*
[b]*Mathematics Department, Moscow State University, Russia*

**Abstract**

Applying cuts in the space of event parameters is the traditional technique for background rejection in high energy physics. Obtained by considering the simulation of signal and background events, particular values of these cuts are used to reach required balance between efficiency of signal detection and background rejection.

Modern experiments in high energy accelerator physics and astrophysics are operating with multidimensional parametric spaces. Thus, the problem of the best cut selection is of vital interest. Frequently used rectangular cuts are usually too restrictive and can deteriorate the shape of selected multivariate signal distribution. With the aid of the proposed method, it is possible to obtain smooth nonlinear shape of signal cluster which optimizes the ratio of signal to noise. The search of the best $\gamma$-cluster on the data files of Crab nebula detection by Atmospheric Cherenkov Telescope of Whipple collaboration proves the superiority of neural techniques upon traditional methods.

## 1. Introduction

The rates of interesting events, expected at LHC and in astrophysics experiments, are negligible as compared with background events. Therefore, a key to successful analysis is the reduction of the data volumes in such a way that the maximum sensitivity to a new physics is preserved and the maximum immunity to noise is achieved [1].

The "cuts" (mostly linear) performed on multidimensional distributions of measurements are usually used in collider experiments analysis to enlarge the significance of statistical conclusions concerning the existence of new phenomena. Usually, it is difficult to outline the desired "best" signal domain where it is possible to detect the significant abundance of signal events over background distribution. The signal domain, multidimensional decision surface, can be nonlinear and it selection is an unsolved problem yet without knowing the signal and background distribution shapes.

It is proposed to use the neural net training the experimentally obtained pure background and mixed signal and background samples. A new of objective function is introduced instead of the classification score.

## 2. The new neural algorithm for background rejection

Significant processes in high energy astrophysics has been made in the unambiguous detection of the Crab Nebula at TeV energies by the Whipple collaboration [2]. Huge background is caused by isotropically distributed flux of charged cosmic rays in this experiment. The main technique to reject this background is applying multidimensional linear cuts on measured Cherenkov image parameters, as introduced by Hillas [3].

To prove the existence of neutral particles from celestial sources, one looks for an abundance ($N_{on} - N_{off}$) of events coming from the direction of a possible source ($N_{on}$) compared with the control measurement, when pure background is registered ($N_{off}$). As the expected fluxes are very weak (the ratio of signal to background does not exceed 0.01), it is necessary to answer the following question: is the detected abundance a real signal or only a background fluctuation? The measure (level) of statistical significance used in $\gamma$-ray astronomy is so-called criterion size ($\sigma$) [4]:

*Corresponding author. Tel./fax: + 7 374 2 352041, e-mail: chili@yerphi.am.


*PII* S0168-9002(97)00141-1

$$\sigma = \frac{N_{on} - N_{off}}{\sqrt{N_{on} + N_{off}}}, \quad (1)$$

The greater $\sigma$, the lesser the probability that the detected excess is caused by a background fluctuation. After selecting the "$\gamma$-like" events from rat data (both from the ON and OFF samples), the criterion takes the form:

$$\sigma = \frac{N^*_{on} - N^*_{off}}{\sqrt{N^*_{on} + N^*_{off}}}, \quad (2)$$

$N^*_{on}$, $N^*_{off}$ are the numbers of events which passed data selection cuts. As shown in Ref. [5], the use of $\sigma$ as objective function, helps us to outline realistic nonlinear shape of $\gamma$-cluster and enlarge $\sigma$, compared with the technique used in the Whipple Observatory (supercuts), proposed in Ref. [6] and then improved in Ref. [7]. New methods of net training on simplified problem of nonlinear cluster detection and on a new piece of Crab data are illustrated in following section.

## 3. Results

The 2:4:2:1 feed-forward network is used to detect the 2-dimensional cluster with radial symmetry (see Fig. 1). Training samples consist of 450 "background" events, uniformly distributed in a unit square. Fifty "signal" events generated according to radial symmetric Gaussian distribution with mean $= 0.5$ and $\sigma = 0.03$ were added to one of the background samples. The goal of the algorithm is to find a two-dimensional cluster maximising this objective function (2). Fig. 1 presents the results of cluster search for 1 + 1 random search strategy.

Obtained "chromosoms" were used as a "pool" for genetic algorithm, the results of which are presented on Fig. 2. Both "mutations" and "crossoveers" give a rise to the objective function.

Data, obtained on the Crab Nebula in December 1993 using the Whipple Collaboration 10 m Cherenkov Imaging telescope, were used in the analysis. The database consisted of 19 On/Off pairs, with total on-source time of

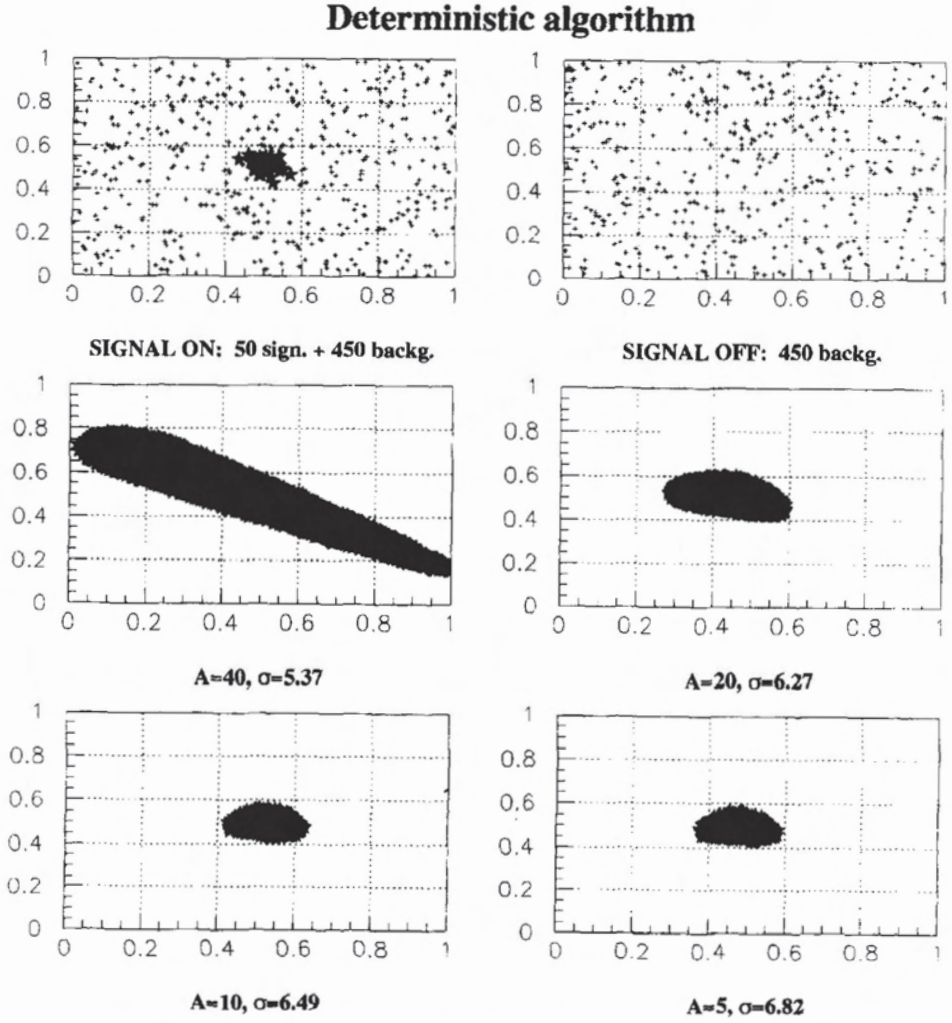


Fig. 1.

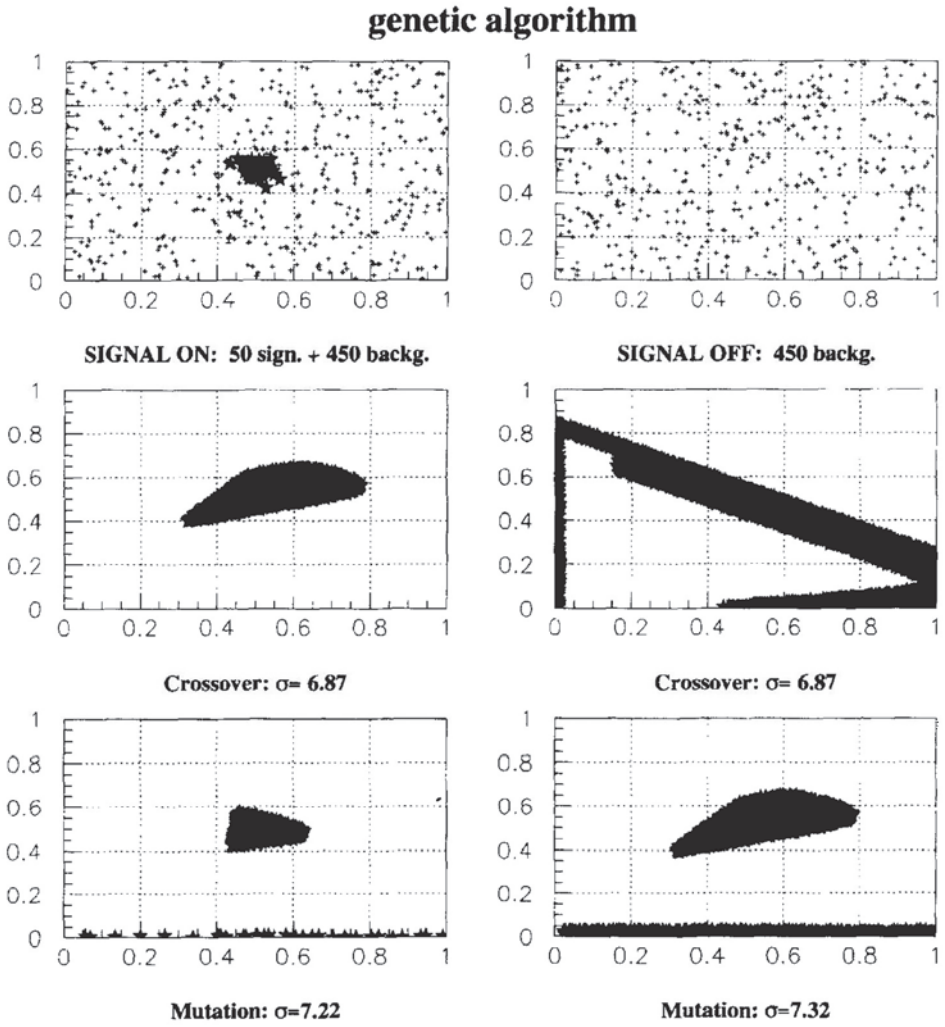


Fig. 2.

Table 1
WHIPPLE Crab detection, 1993

| | $N^*_{on}$ | $N^*_{off}$ | $\sigma$ | DIFF | DIFF/$N^*_{off}$ |
|---|---|---|---|---|---|
| SUPERCUT | 1710 | 866 | 16.6 | 844 | 0.97 |
| NN, 4:3:1 | 1552 | 707 | 17.8 | 845 | 1.2 |

473 min. The standard "supercuts" effect was 16.6$\sigma$ on this database; this increased up to 17.8$\sigma$ after optimization using the neural network (see Table 1). While this is not in itself a very marked improvement in sensitivity, it is, nevertheless, encouraging that some improvement is obtainable, particularly, as the improved shape of the $\gamma$-ray domain can be readily explained [8].

## Acknowledgements

We wish to acknowledge the members of the Whipple collaborations for the use of the Crab Nebula databases. We thank Dr. M. Cawley for valuable remarks concerning new methods of data analysis. This work was partly supported by the research grant number 94694 of Armenian government.

## References

[1] L. Mapelli, Proc. 1991 CERN school of computing, p. 79.
[2] M.G. Lang, C.W. Akerlof, M.F. Cawley et al., Proc. 22 Int. Cosmic Ray Conf., Dublin (1991) p. 204.
[3] M. Hillas, Proc. 19th ICRC, USA, Vol. 3 (1985) p. 445.
[4] S.N. Zhang and D. Ramsden, Exp. Astronomy 1 (1990) 145.
[5] A.A. Chilingarian, Pattern Recognition Lett. 16 (1995) 333.
[6] A.A. Chilingarian and M.F. Cawley, Proc. 22 ICRC, Vol. 1, Dublin (1991) p. 460.
[7] M. Punch, C.W. Akerlof, M.F. Cawley, et al., Proc. 22 ICRC, Vol. 1, Dublin (1991) p. 464.
[8] A.A. Chilingarian and M.F. Cawley, Proc. 24 ICRC, Vol. 3, Rome (1995) p. 742.

Available online at www.sciencedirect.com
SCIENCE DIRECT®
Astroparticle Physics 19 (2003) 715–728
Astroparticle Physics
www.elsevier.com/locate/astropart

# Preparation of enriched cosmic ray mass groups with KASCADE

KASCADE Collaboration

T. Antoni [a], W.D. Apel [b], A.F. Badea [a,1], K. Bekk [b], A. Bercuci [b], H. Blümer [b,a], H. Bozdog [c], I.M. Brancus [c], C. Büttner [a], A. Chilingarian [d], K. Daumiller [a], P. Doll [b], J. Engler [b], F. Feßler [b], H.J. Gils [b], R. Glasstetter [a], R. Haeusler [a], A. Haungs [b,*], D. Heck [b], J.R. Hörandel [a], A. Iwan [a,2], K.-H. Kampert [a,b], H.O. Klages [b], G. Maier [b], H.-J. Mathes [b], H.J. Mayer [b], J. Milke [a], M. Müller [b], R. Obenland [b], J. Oehlschläger [b], S. Ostapchenko [a,3], M. Petcu [c], H. Rebel [b], M. Risse [b], M. Roth [b], G. Schatz [b], H. Schieler [b], J. Scholz [b], T. Thouw [b], H. Ulrich [a], A. Vardanyan [d,*], J.H. Weber [a], A. Weindl [b], J. Wentz [b], J. Wochele [b], J. Zabierowski [e]

[a] *Institut für Experimentelle Kernphysik, University of Karlsruhe, 76021 Karlsruhe, Germany*
[b] *Institut für Kernphysik, Forschungszentrum Karlsruhe, Postfach 3640, 76021 Karlsruhe, Germany*
[c] *National Institute of Physics and Nuclear Engineering, 7690 Bucharest, Romania*
[d] *Cosmic Ray Division, Yerevan Physics Institute, Yerevan 36, Armenia*
[e] *Soltan Institute for Nuclear Studies, 90950 Lodz, Poland*

Received 14 November 2002; received in revised form 6 February 2003; accepted 10 February 2003

**Abstract**

The KASCADE experiment measures a high number of EAS observables with a large degree of sampling of the electron–photon, muon, and hadron components. It provides accurate data for an event-by-event analysis of the primary cosmic ray flux in the energy range around the knee. The possibility of selecting samples of enriched proton and iron induced extensive air showers by applying the statistical techniques of multivariate analyses is scrutinized using detailed Monte Carlo simulations of three different primaries. The purity and efficiency of the proton and iron classification probability is investigated. After obtaining enriched samples from the measured data by application of the procedures the reconstructed number of hadrons, hadronic energy and other parameters are investigated in the primary

* Corresponding authors. Tel.: +49-7247-823321; fax: +49-7247-824075.
*E-mail addresses:* haungs@ik3.fzk.de (A. Haungs), aro@crdlx5.yerphi.am (A. Vardanyan).
[1] On leave of absence from the NIPNE, Bucharest, Romania.
[2] Also University of Lodz, Lodz, Poland.
[3] On leave of absence from Moscow State University, Moscow, Russia.

0927-6505/03/$ - see front matter 
doi:10.1016/S0927-6505(03)00135-X

energy range $10^{15}$–$10^{16}$ eV. By comparing these shower parameters for purified proton and iron events, respectively, with simulated distributions an attempt is made to check the validity of strong interaction models at high energies.


*PACS:* 96.40.Pq; 96.40.De
*Keywords:* Cosmic rays; Air shower; Hadronic interactions; Monte Carlo simulations; Nonparametric methods of statistical data analysis

## 1. Introduction

Above primary energies of a few hundred TeV direct measurements of energy and mass of individual cosmic ray nuclei are unfeasible due to the drastic decrease of the cosmic ray intensity with increasing energy. Hence, one has resort to the measurements of extensive air showers (EAS) which are produced when high energy cosmic ray particles enter into the Earth's atmosphere. Therefore the determination of primary energy and mass from EAS observables depends on the understanding of the high-energy hadronic interaction features of the primary particle, and further on of the shower development in general. Consequently redundant information on the measurements is required to disentangle the problem.

The idea to use advanced statistical techniques of multivariate analyses [1] for enriching certain classes of primaries [2,3] and to prepare enriched samples by mass discriminating event-by-event analyses of EAS observations was first investigated for the ANI experiment [4]. The realization has become feasible by recent measurements of the multi-detector experiment KASCADE [5] which provides an accurate experimental basis by simultaneous measurements of many EAS observables for each individual event. The purpose of this paper is to apply these techniques to KASCADE data and to investigate possibilities of testing high-energy hadronic interaction models.

Such an approach appears to be very promising in view of detailed tests of interaction models currently under debate and for paving the way to a consistent description of the hadronic interaction at extremely high energies by experimental signatures. Still the results of the KASCADE experiment concerning the energy spectrum and mass composition of primary cosmic rays are considerably affected by the uncertainties of the used Monte Carlo models, which are estimated to be much larger than the statistical uncertainties, e.g. for the deduced features of the cosmic ray energy spectrum [6].

The present investigation introduces the preparation of samples of enriched cosmic ray mass groups and their use for studies of hadronic interactions with air nuclei. The concept for the classification is based on multivariate nonparametric methods of statistical inference. Using the information on an event-by-event basis empirical statements can be drawn on the validity of the 'a priori' knowledge of the Monte Carlo simulations. Global event observables like the muon and electron shower sizes are used in order to select event samples with enriched contents of proton and iron primaries, respectively. Additional observables mainly of the hadronic component are subsequently used for the investigation of interaction features of the primaries. It is worthwhile to mention that results obtained by event-by-event analyses are conditional on the particular hadronic interaction models used for the Monte Carlo simulation. The disentanglement of the threefold problem in determining of the primary mass, primary energy and strong interaction features by a combined analysis can be improved by selecting enriched samples of various mass groups. Even within one pre-chosen model some hints are expected which will enable to understand which particular features of the strong interaction models have to be improved in order to reproduce the experimental data in a consistent way.

## 2. Experimental setup and simulation procedures

The KASCADE experiment, located at the laboratory site of Forschungszentrum Karlsruhe, Germany at 8°E, 49°N, 110 m a.s.l., consists of

three main parts—the scintillator array, the central detector and the muon tracking detector. Due to its multi-detector setup, it is able to measure a large number of EAS characteristics for each individual event in the PeV primary energy region. The schematic view of the KASCADE detector installations is shown in Fig. 1.

A scintillator array [5] measures secondary electrons, photons and muons of extensive air showers in 252 detector stations on a grid of 13 m spacing, hence forming an array of $200 \times 200$ m$^2$. The stations contain unshielded liquid scintillation counters and below lead and iron absorbers also plastic scintillators. With this array the reconstruction of the muon and electron size of the EAS is done in an iterative way, e.g. by correcting the electron number by use of the measured muon content [7].

The basic component of the central detector is a finely segmented hadron calorimeter [8]. A $20 \times 16$ m$^2$ iron stack arranged in nine horizontal planes is equipped by liquid ionisation chambers forming 44,000 electronic channels. The calorimeter measures energy, angle and point of incidence of individual EAS hadrons.

Below 30 radiation lengths of absorber the central calorimeter contains a layer of 456 scintillation detectors [8] acting as trigger for the central detector and measuring the arrival time of muons and hadrons. Underneath the calorimeter two layers of multiwire proportional chambers (MWPC) and one layer of limited streamer tubes (LST) reconstruct muon tracks above an energy of 2.4 GeV with an angular accuracy of about 1.0° [9].

North of the central detector in a 50 m long tunnel muons above the threshold energy of

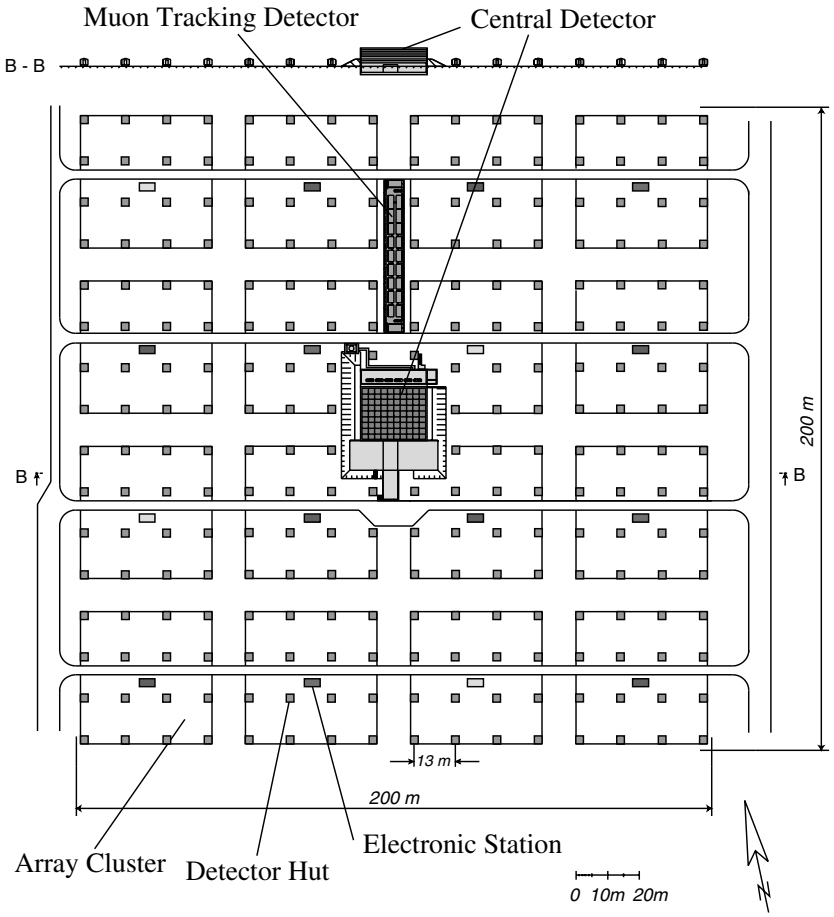


Fig. 1. Layout of the KASCADE experiment.

0.8 GeV are measured with the help of streamer tubes (LST) [10]. On an area of about 128 $m^2$ three layers of LST track muons with an accuracy of 0.5°.

For the present analysis ≈700,000 events registered by the KASCADE field array are used, corresponding approximately to one year data taking. The selection of these showers requires a core distance from the center of the array of less than 91 m and a successful reconstruction of the electron size ($N_e$) and muon size ($N_\mu^{tr}$). The investigated zenith angle range is restricted to 15°–20°. In this sample there are around 6000 events where the shower axis hits the KASCADE central detector, and hence detailed hadronic information of the EAS is available for the analysis.

The simulations for the present analysis use the CORSIKA code version 5.62 [11] with QGSJET [12] as high-energy hadronic interaction model for the EAS development in the atmosphere. The options GHEISHA [13] for the interactions at low energies and EGS4 [14] for the electromagnetic cascades are chosen.

The detailed detector simulation was made on the basis of the GEANT [15] package, taking into account all shower particles, absorber and active materials, energy deposits, and arrival times. More than 20,000 showers are generated for each primary nucleus in the primary energy range of $5 \times 10^{14}$–$3 \times 10^{16}$ eV. The simulations are performed in 10 energy bins with a spectral slope of $\gamma = -2.5$ inside and of $\gamma = -1$ from bin to bin. The simulations cover the angular range of 13°–22°. Three different primaries are taken into account: protons, oxygen nuclei, and iron nuclei.

On this basis different EAS parameters are reconstructed whereby simulated and experimental data are handled with the same algorithms. The EAS core position, arrival direction, electron–muon densities, electron size and muon content from the array, hadronic EAS observables, muon tracks and arrival time distributions observed with the central detector, and many other characteristics are reconstructed. EAS parameters used in the present analysis are compiled in Table 1. For a more detailed description of the reconstruction procedures see e.g. Refs. [6,7].

Table 1
EAS observables of the KASCADE experiment used in the present analysis

| | |
|---|---|
| $N_e$ | Number of electrons in the EAS $\left(N_e = 2\pi \int_0^\infty \rho_e(r) r \, dr\right)$ |
| $N_\mu^{tr}$ | Truncated number of muons $\left(N_\mu^{tr} = 2\pi \int_{40m}^{200m} \rho_\mu(r) r \, dr\right)$ ($E_\mu > 230$ MeV) |
| $N_\mu^{CD}$ | Number of tracked muons in the central detector (MWPC) ($E_\mu > 2.4$ GeV) |
| $N_h$ | Number of reconstructed hadrons at the calorimeter ($E_h > 100$ GeV) |
| $E_h^{max}$ | The energy of the most energetic hadron detected (>100 GeV) |
| $E_{tot}$ | Energy sum of the reconstructed hadrons with $E_h > 100$ GeV |

## 3. Primary energy and mass determination

Multivariate methods are used for the classification of the measured events in mass groups and for energy estimation. These methods take into account the correlations of the used observables. In principle such methods can be applied for any number of observables, but the reconstruction quality is restricted by the statistical accuracy of the reference Monte Carlo sample. For the present analysis a multi-layered feed-forward perceptron neural network algorithm is used to determine the mass and energy of individual primary cosmic rays in the knee region of data registered with KASCADE. It allows to estimate the primary energy and to classify the primary mass into multiple categories using similar procedures. The basics of neural network techniques can be found in [16]. The general procedures for the application of Bayesian and neural network methods at EAS data analysis are given in [6,17].

For estimation and classification, the observables of the electromagnetic and muonic components ($N_e, N_\mu^{tr}$) measured by the KASCADE field array detectors are used. The restriction to these two observables is motivated by following reasons:

- Due to the high statistical accuracy available the uncertainties from EAS fluctuations are smaller as compared with the hadronic information of EAS.
- The information of the KASCADE central detector, especially the hadronic observables, is

intended to be used for subsequent studies of the interactions of the selected subsamples.
- In former studies [18–20] we have found that the electromagnetic and muonic component of EAS are described well by the used high-energy interaction model QGSJET.

The accuracy of the energy estimation, displayed in Fig. 2 by the relative deviation of the reconstructed energy $E_{\rm rec}$ from the true energy $E_0$ results in approximately 25%, with improvements at higher energies and for heavier primaries. It demonstrates the high reliability nearly free from bias eventually arising from the procedure. We use a wider energy interval for the simulated events than for the experimental ones to avoid an over- or underestimation of primary energies at the boundaries of the investigated energy region. Systematic uncertainties of the energy estimation are the composition of the control sample (here three primaries with equivalent contribution in number of events are used), and the high-energy interaction model itself used for the generation of the samples. Of minor influence is the slope of the energy spectrum used at the Monte Carlo sample if the statistics is large enough over the whole energy range.

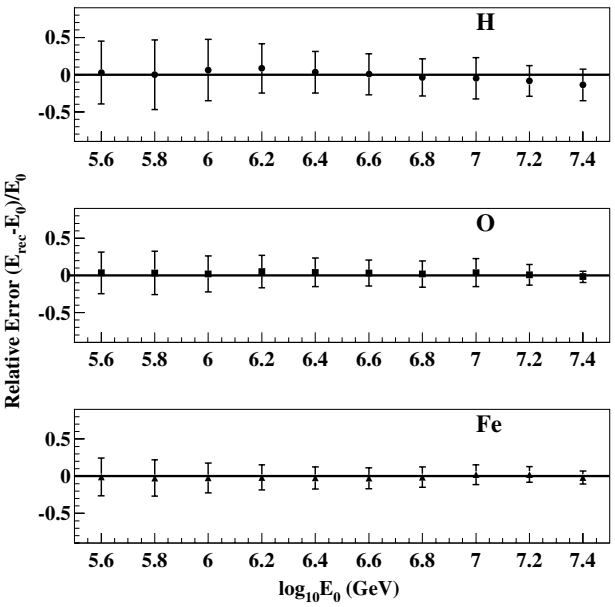


Fig. 2. Accuracy of the energy determination for different classes of primaries (H, O, Fe) displayed by the relative deviation $(E_{\rm rec} - E_0)/E_0$. The error bars indicate the width of the distributions.

Table 2
Classification probabilities obtained by a neural network classification using a control sample. Used observables are the shower sizes $N_e$ and $N_\mu^{tr}$. $W_{i\leftarrow j}$ denotes the abundance of events of type $j$ of the sample classified as $i$

| $W_{i\leftarrow j}$ | $j=$ H (%) | $j=$ O (%) | $j=$ Fe (%) |
|---|---|---|---|
| $i=$ H | 80 | 18 | 2 |
| $i=$ O | 19 | 58 | 23 |
| $i=$ Fe | 2 | 23 | 75 |

After estimating the primary energy each EAS event is classified as being induced by light, intermediate or heavy nuclei. We will refer to these groups as 'proton', 'oxygen', and 'iron'. The classification is performed by a neural network independently trained from the net used for the energy estimation. The results of the classification of the generalized neural network are presented in Table 2. It shows the probabilities of contamination of events of the different classes in each category. The classification matrix is obtained by classifying 4000 control events (not used for the training) per class. A high purity (rather small share of events from alternative classes) of proton and iron events is obvious, while the oxygen class has a lower purity since it contains a significant contamination from both, protons and irons. The classification depends slightly on primary energy with improved accuracy at higher energies by $\approx$10% due to decreasing fluctuations of the observables. The restriction to three mass groups leads to systematic distortions if intermediate primary mass groups are present in control or measured samples. For example, helium nuclei would be classified mainly as protons and a part of them (more than protons) would be attributed to the medium and heavy classes (see Ref. [6]).

After applying the trained neural networks to measurements we combine the energy and mass information of the analyzed KASCADE data sample. Figs. 3 and 4 display the $(N_e, E_{\rm rec})$- and $(N_\mu^{tr}, E_{\rm rec})$-dependence for the three selected samples of primaries. The energy resolution is expected to be $\sim$25% as demonstrated by Monte Carlo simulations (Fig. 2), and the mass discrimination

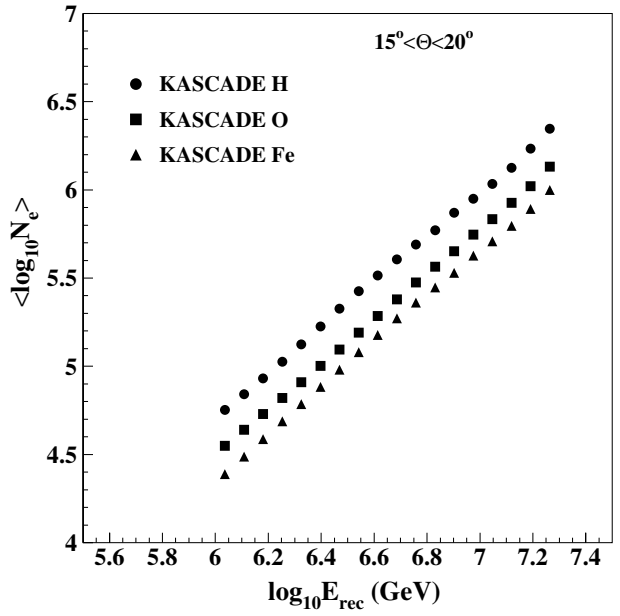


Fig. 3. Mean shower size $N_e$ versus the reconstructed primary energy $E_{\rm rec}$ for the measured KASCADE data set, classified in proton, oxygen, and iron samples.

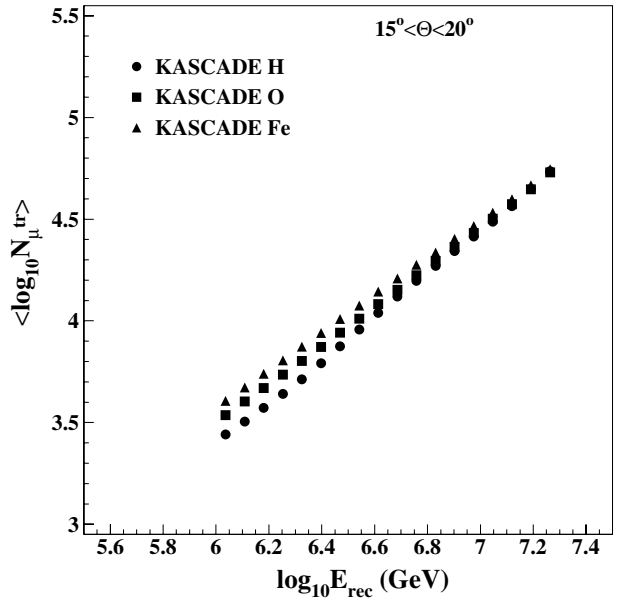


Fig. 4. Mean muon size $N_\mu^{tr}$ versus the reconstructed primary energy $E_{\rm rec}$ for the measured KASCADE data set, classified in proton, oxygen, and iron samples.

power is ~70% as illustrated in Table 2. The discrimination power is defined as the arithmetic mean of the probabilities $W_{i\leftarrow i}$. It is obvious that the mean $N_e$ values are rather close for the intermediate and heavy groups of nuclei, which explains the comparatively strong mixture between these two classes ($W_{\rm Fe\to O} = W_{\rm O\to Fe} = 23\%$). The mean numbers of muons are approximately the same for all primaries in all energy bins. One recognizes small differences from that in the lowest energy bins, but the overall independence of $N_\mu^{tr}$ from the primary mass is obvious, i.e. $N_\mu^{tr}$ dominates (at KASCADE observation level) the energy estimation. The slight deviations at high energies from a pure power law in case of protons are probably due to a small underestimation at highest energies ($E_0 > 2 \times 10^{16}$ eV) (see Fig. 2).

## 4. The purification procedure

The neural network analyses perform a nonlinear mapping of multidimensional characteristics of the EAS to the real number interval [0,1] (Fig. 5). Particular class assignments for the three way classification are the subintervals [0,0.33), [0.33, 0.66] and (0.66,1] for the light, medium, and heavy nuclei, respectively. We characterize the quality of

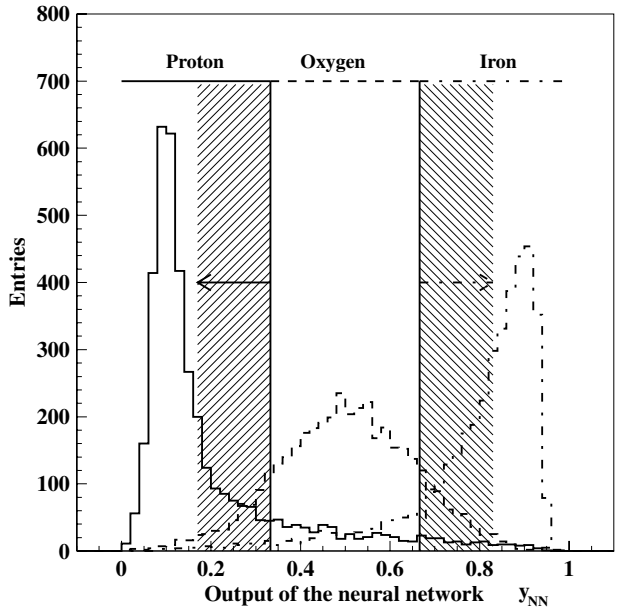


Fig. 5. The distribution of the neural network output for the simulated control sample. Purification can be performed by shifting the boundaries of the subintervals.

the classification procedures by the 'purity' and 'efficiency' variables. The purity of a sample is defined as the fraction of true classified events in an actual number of events assigned to a given class. The classification efficiency is defined as the fraction of true classified events to the initial number of events of a given class. The actual classification procedure results in a purity of 80% for the proton class, and of 70% for the iron class assuming equal total numbers of primaries in each of the three classes. The neural information technique [21] allows now to reduce the contamination of misclassified events in each class of nuclei. Of course, the efficiency of the classification is reduced at the same time. The optimum of purity and efficiency to be chosen depends on the given problem. Investigations of the behavior of definite primaries requires a higher purity at may be efficiency, whereas estimation of chemical composition needs high efficiency. It should be remarked, that for obtaining results on chemical composition of a measured sample the numbers in each class have to be corrected with the misclassification matrix. Changing the boundaries of the class assignments will always result in the same composition after the correction, if no systematic effects are introduced. In this analysis the possibility of the selection of maximally pure samples of cosmic ray mass groups will now be investigated, with respect to the question of the cost we have to pay (in terms of efficiency loss) to get light and heavy nuclei induced showers with higher purity.

When the neural network (NN) is satisfactorily trained, the NN output distributions for the different classes are overlapping at the subinterval boundaries. Therefore, by shrinking the subintervals, one can remove a large proportion of misclassified events. But, simultaneously one looses parts of the correctly classified events. Fig. 5 illustrates this procedure of purification.

Fig. 6 plots purity versus efficiency for two classes. For equal total number of simulated events the purity of proton and iron nuclei can reach more than 90% while the efficiency is still remaining above 50%. The purity and efficiencies are obtained by classifying 4000 simulated control events per class which are not used for the training of the neural network. For a given purity value the

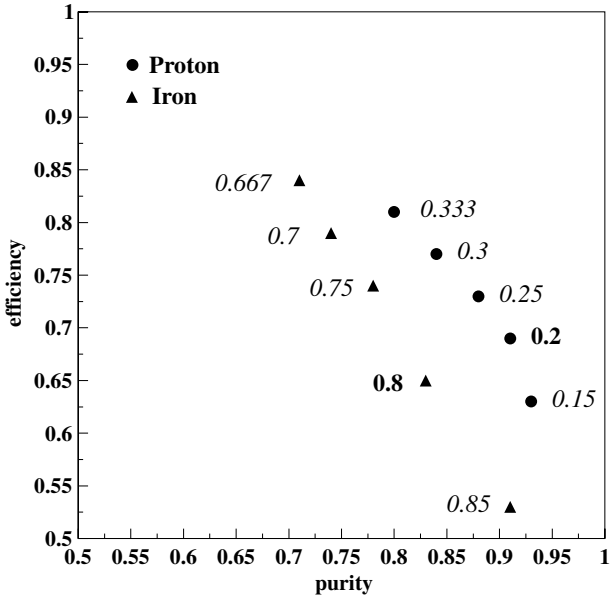


Fig. 6. Efficiency versus purity for proton and iron events by variation of the subinterval boundaries as indicated by the numbers. The values are obtained by classifying a Monte Carlo control sample with equal total numbers of primaries for each mass.

efficiency of proton events is always slightly larger than the efficiency for the iron induced sample, due to the narrower NN output distribution of the protons (Fig. 5), e.g. the separation of oxygen–proton is better than oxygen–iron. The separation of protons from the other classes is good due to the combination of proton and helium nuclei in one class.

For the preparation of the enriched samples to investigate the hadronic interactions the purification procedure has to be scrutinized in order to get the optimal purification not to distort the initial parameter distributions. Hence, first of all we investigate how the shrinking of the interval for the different classes at the NN output affects the corresponding one- and two-dimensional distributions of the selected events, i.e. the bias introduced by the purification. For this we compare the distributions of observables for the measured EAS samples of events selected by the purification with the removed ones. Fig. 7 shows the distributions of EAS parameters of proton and iron classes for two different cuts in the NN output intervals applied to the KASCADE data sample. The upper two plots

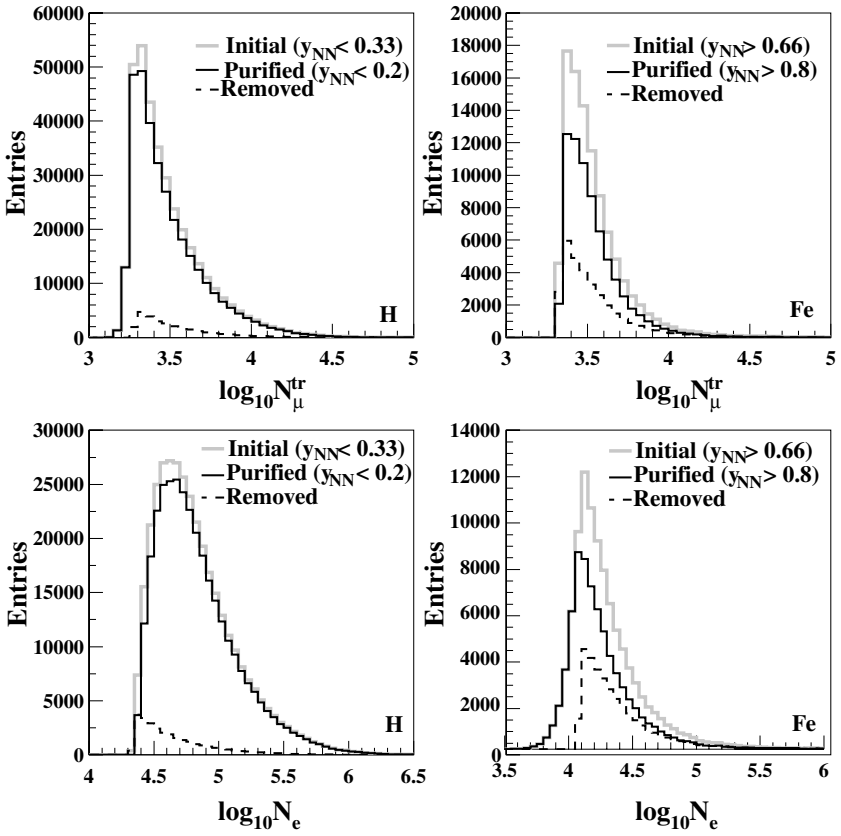


Fig. 7. Distributions of $N_e$ and $N_\mu^{tr}$ for the initial, the purified, and removed proton and iron samples as measured with KASCADE. Details see text.

show the purified and removed distributions compared with the initial ones in case of the muon size, and the lower two plots in case of the electron number. For the shown purification the boundaries are shifted from $y_{\mathrm{NN}} = 0.33$ to $y_{\mathrm{NN}} = 0.2$ and from $y_{\mathrm{NN}} = 0.66$ to $y_{\mathrm{NN}} = 0.8$, respectively. The events are removed over nearly the whole range of the distributions proving the small dependence of the classification on primary energy. A more detailed inspection of Fig. 7 shows that only few events with smallest shower size $N_e$ are removed from the iron sample and only few events with largest size from the proton events distribution. The opposite situation is observed for the $N_\mu^{tr}$ distribution. Fig. 8 illustrates this feature by displaying as example the ratio of the purified to initial sample of the $N_\mu^{tr}$ distributions for the proton sample. The shape (Fig. 7) and the mean values $\mu_{N_i}^j$ with $i \in e, \mu$ and $j \in \mathrm{H}, \mathrm{Fe}$ (Table 3) of the

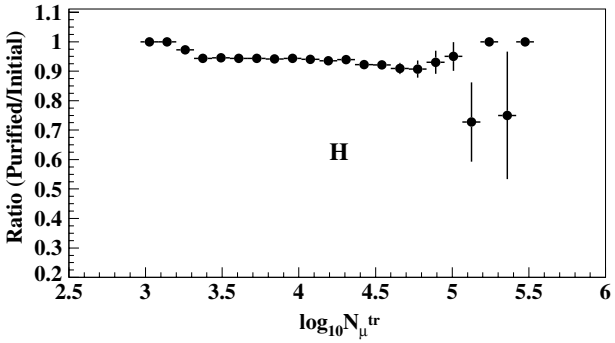


Fig. 8. The ratio of the purified to initial distribution for $N_\mu^{tr}$ of the proton sample as measured with KASCADE.

distributions are only slightly changed by the purification procedure. For further investigations using the purified samples it is important that they still represent the total range of the distributions.

Table 3
The mean values $\mu$ (and its variances) of parameter distributions (Fig. 7) of the initial, purified, and removed proton and iron samples of the KASCADE experimental data set

| | $\mu^{H}_{N_e}(\sigma)$ | $\mu^{Fe}_{N_e}(\sigma)$ | $\mu^{H}_{N^{tr}_{\mu}}(\sigma)$ | $\mu^{Fe}_{N^{tr}_{\mu}}(\sigma)$ |
|---|---|---|---|---|
| Initial | 4.82(0.316) | 4.30(0.311) | 3.49(0.228) | 3.54(0.210) |
| Purified | 4.83(0.313) | 4.26(0.300) | 3.49(0.227) | 3.54(0.202) |
| Removed | 4.67(0.309) | 4.40(0.316) | 3.53(0.237) | 3.55(0.229) |

In order to scrutinize possible systematic distortions of distributions of parameters not used in the classification procedure, one-dimensional statistical tests [22] have been performed comparing the initial and the purified samples. Table 4 displays the results of three different tests for hadronic observables measured with the KASCADE central detector. We perform different tests because they compare the distributions using varying statistical criteria. The presented values are the probabilities of accepting the null hypothesis, which is that these two samples are from one and the same population. In cases of small probabilities the null hypothesis is rejected, i.e. there exists a big difference between the two samples. It was found that all probabilities from Table 4 are above the critical values of these tests to reject the null hypothesis [22]. The initial and purified proton and iron samples belong statistically to the same population demonstrating that the purification does not introduce large systematic distortions. It should be noted that these tests have been done for hadronic observables which are not used for energy estimation and mass classification.

Generally, the one-dimensional distributions are not strongly affected by more detailed cuts in the NN output distribution. Therefore, a cut applied to the NN output distribution is not linearly transferred to the distributions of the input parameters. This feature illustrates that the neural network analysis performs a nonlinear mapping of the multidimensional input vector to an one-dimensional output value, with the observation that the fraction of removed events at the $N_e$- and $N^{tr}_{\mu}$-distributions is nearly independent of the shower sizes. This is demonstrated in Fig. 9, which displays the $(N_e, N^{tr}_{\mu})$-parameters as a two-dimensional distribution. It is obvious that we remove both proton and iron events from the boundary region, where the misclassification probability is high. But by changing the cut values in the NN output different regions of the $(N_e, N^{tr}_{\mu})$ parameter space are involved. The nonlinearity of the mapping is of importance as linear cuts would not do justice to the intrinsic shower fluctuations in $N_e$ and $N^{tr}_{\mu}$ which depend on primary energy and mass.

We conclude that only small systematic uncertainties are introduced to the parameter distributions when 'purifying' the proton and iron samples. But there are still other parameters which may be systematically affected by the cuts. One of these parameters is the height of the first

Table 4
The probability values of different tests (*t*-student, KS-Kolmogorov–Smirnov, MW-Mann–Whitney) comparing the initial and purified proton and iron samples of various hadronic shower observables

| | Proton distributions | | | Iron distributions | | |
|---|---|---|---|---|---|---|
| | *t* | KS | MW | *t* | KS | MW |
| $N_h$ | 0.36 | 0.99 | 0.49 | 0.35 | 0.99 | 0.28 |
| $E_h$ | 0.36 | 0.77 | 0.40 | 0.38 | 0.72 | 0.23 |
| $E_h^{max}$ | 0.30 | 0.81 | 0.29 | 0.40 | 0.84 | 0.26 |

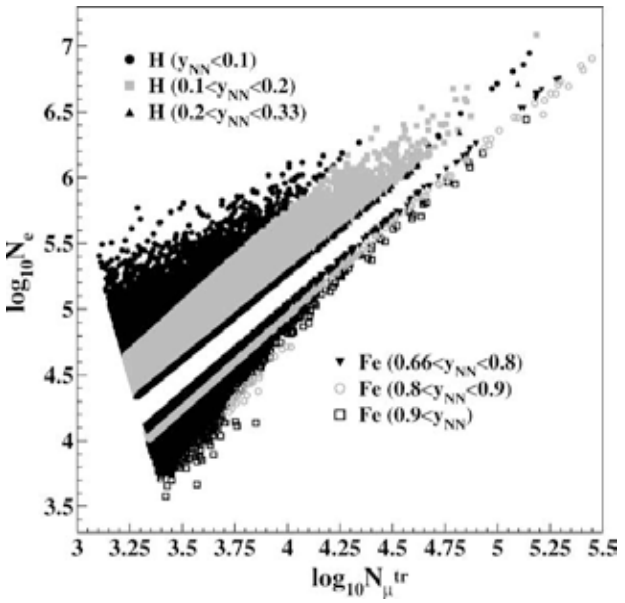


Fig. 9. Two-dimensional distribution of the NN input parameters $N_e$ and $N^{tr}_{\mu}$ with different cuts applied on the NN output parameter. The cut values are indicated.

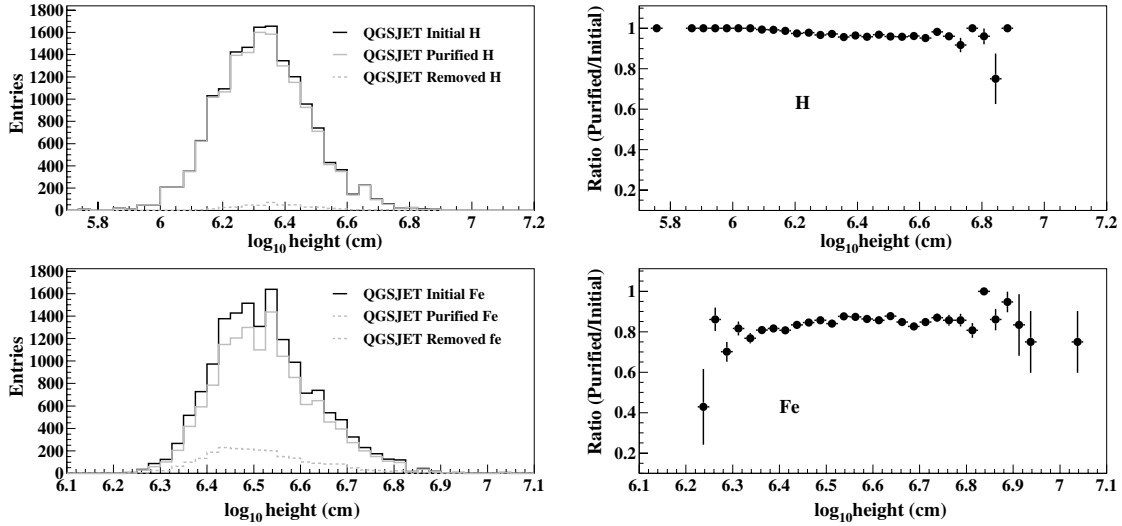


Fig. 10. Same as Fig. 7, but for the height of the first interaction and in case of Monte Carlo simulations. In the right part the ratio of the purified to initial samples are displayed.

interaction of the primary nucleus. Unfortunately this parameter is not accessible by our experimental data. Therefore the distributions of this parameter for initial and purified proton and iron samples have been only investigated for MC data. As the height of the first interaction influences directly the muon and electron shower sizes at observation level, we expect that the purification affects mainly the boundary region (low heights for iron and large heights for proton) of the height distribution. This is confirmed as displayed in Fig. 10. Additionally Fig. 10 shows, that an eventual systematic bias introduced for this parameter remains again small.

## 5. Studies with mass enriched EAS samples

An estimation of the primary energy with ~25% relative error in addition to an accurate classification of the primary particles into three mass categories was performed. The purification technique was applied for preparing the enriched samples using only the KASCADE array information ($N_e, N_\mu^{tr}$) (see also [23]). The procedure facilitates production of enriched samples of proton and iron induced events with the additional knowledge of the primary energy on an event-by-event basis. Some characteristic features of these purified 'light' and 'heavy' samples will now be discussed, especially the behavior of hadronic observables with primary energy. The event selection and reconstruction procedures are done for simulated and experimental data samples in a corresponding way. First, the parameters $N_e$ and $N_\mu^{tr}$ of the experimental events are compared with those from MC simulations (Figs. 11 and 12). A good agreement is displayed, demonstrating the high methodical accuracy, and furthermore, that the electromagnetic and muonic components of EAS are well described by the MC model used. As the method takes also the correlation of the two observables into account, the agreement in both observables suggests the validity of the Monte Carlo model for these gross shower parameters.

The purification of the samples makes it possible to study high-energy muons and hadronic observables detected by the KASCADE central detector separately for showers induced by different primary mass. These parameters are measured independently from the observables used for EAS selection, reconstruction of energy and mass, i.e. independent of producing the enriched samples. In this context a test can be performed on the balance of energy and particle number distributions of the different shower components in the Monte Carlo

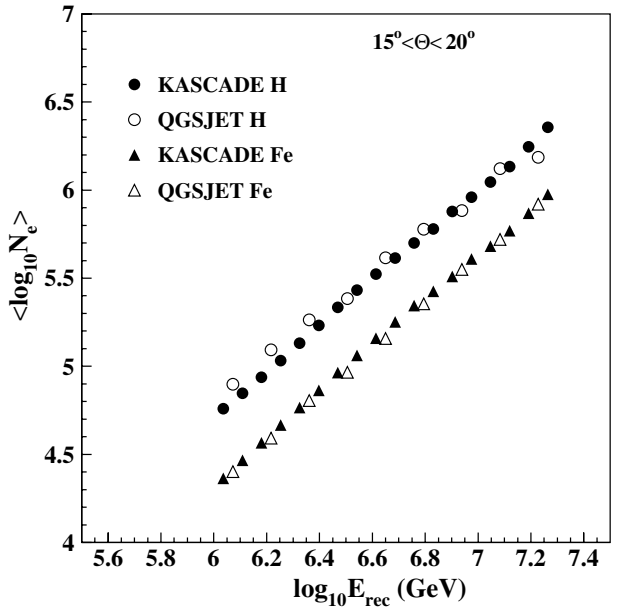


Fig. 11. Shower size $N_e$ versus the reconstructed energy $E_{\rm rec}$ for simulated and experimental proton and iron events. The primary energy is estimated by neural regression method.

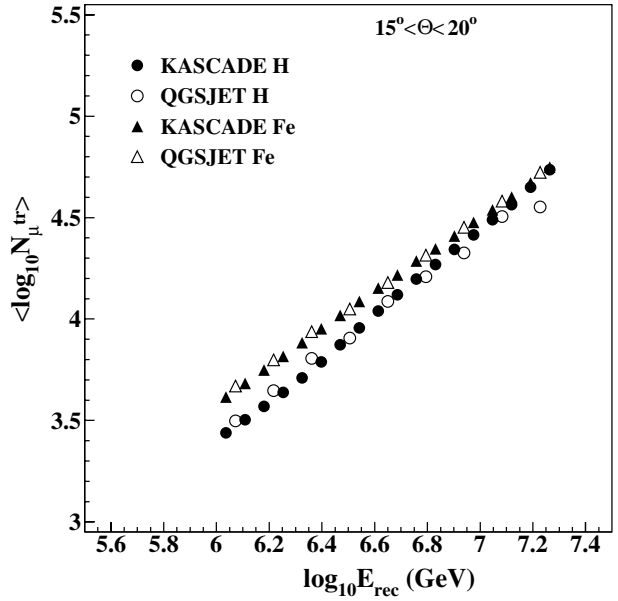


Fig. 12. Muon size $N_\mu^{tr}$ versus the reconstructed energy $E_{\rm rec}$ for simulated and experimental proton and iron events. The primary energy is estimated by neural regression method.

model. For illustration purposes of the presented techniques we consider the energy sum $E_{\rm tot}$ of the hadrons with $E_h > 100$ GeV reconstructed on shower-to-shower basis from calorimeter data of the central detector system. Only EAS with the core inside the area of the central detector have been used. Additionally an electron number of more than 10,000 and at least two reconstructed hadrons ($E_h > 100$ GeV) for a single event were required. Hence, the number of selected events is noticeably reduced.

In Fig. 13 we compare simulations using the QGSJET model [12] with KASCADE data. In the data sample the fraction of showers induced by light nuclei is larger than that of heavy induced showers. Hence the distributions of the proton class are smoother and show smaller statistical fluctuations. For the data points with lowest reconstructed energies the model predicts an increased hadronic energy sum compared to the data. This may be affected by systematic features of trigger or cut efficiencies, but the increase is even more pronounced if instead the total energy sum the energy of the highest energy reconstructed hadron is considered (Fig. 14). This observation together with the information of earlier investigations of KASCADE data [6] suggests that cut and trigger effects are minor sources of the discrepancy. The nonzero contamination of both, proton and

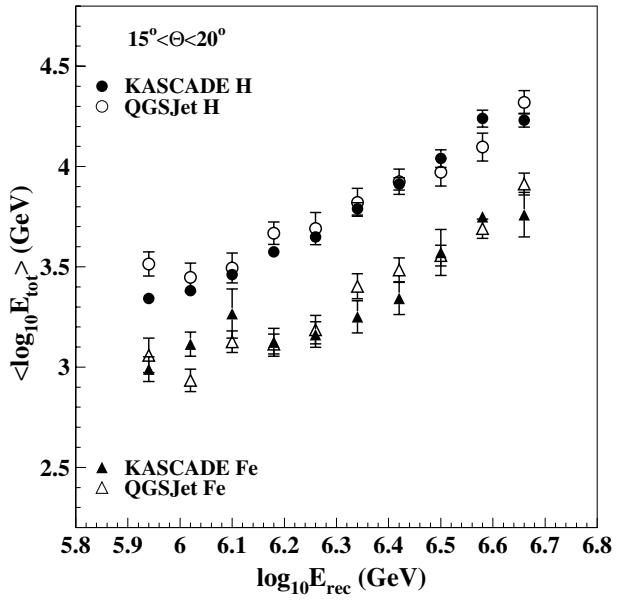


Fig. 13. Dependence of the energy sum of reconstructed hadrons $E_h > 100$ GeV on the reconstructed primary energy for simulated and experimental proton and iron classes.

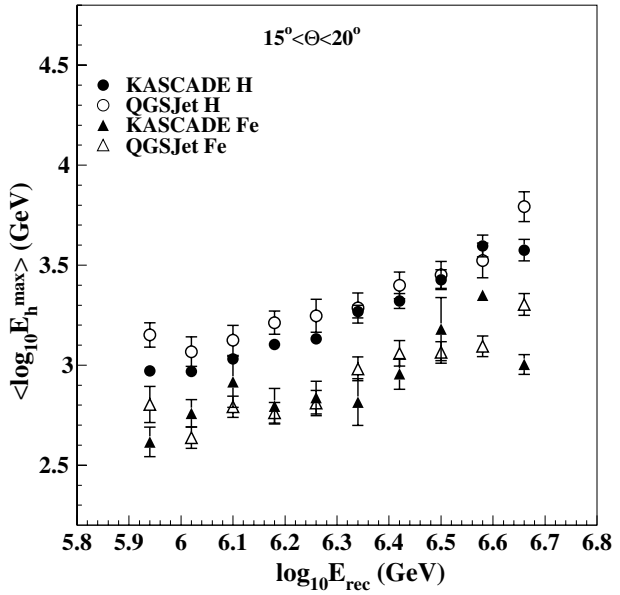


Fig. 14. Dependence of the highest energy reconstructed hadron on the reconstructed primary energy for simulated and experimental proton and iron classes.

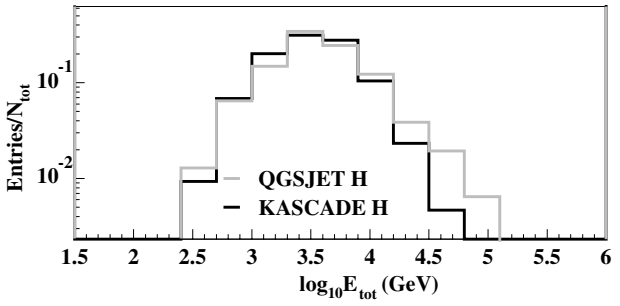


Fig. 15. One dimensional distributions of the reconstructed hadronic energy sum for the proton enriched samples of data and Monte Carlo in the energy range of $6.05 < \log(E_{\rm rec}/\mathrm{GeV}) < 6.25$.

iron induced events by the intermediate nuclei has been ignored in the simulations. This unknown role of primaries of intermediate mass (mostly helium nuclei) at the data sample may lead to the systematic differences in the distributions. Fig. 15 shows the one-dimensional distribution of the reconstructed hadronic energy for the proton enriched sample in the energy range of $6.05 < \log(E_{\rm rec}/\mathrm{GeV}) < 6.25$ for both data and Monte Carlo. Here again a slight overestimation of the hadronic energy at the predictions is visible. It was found that an adaption of the simulated to measured slope of the energy spectrum does not reduce the deviation. But introducing a reasonable part of primary helium nuclei in the simulated sample lead to an overlap of the distributions.

Allowing for the limited accuracy of the method, the distributions shown in Figs. 13 and 14, originating from primary proton and iron nuclei do agree well with the predictions of the Monte Carlo simulations, i.e. the overall dependence of the shower observables are consistent with the simulations using the QGSJET model. This finding is also confirmed by considerations of the numbers of high-energy muons and hadrons reconstructed at the central detector. We therefore conclude that the QGSJET model describes the KASCADE data in a consistent way for the considered energy range of $10^{15}$–$6 \times 10^{15}$ eV. The found behavior of the QGSJET model in the present investigations confirms the findings of an earlier publication of the KASCADE collaboration [18]. Especially the results shown in Fig. 14 are comparable to comparisons of Monte Carlo events with data in Fig. 13 of Ref. [18], but in the present case the hadronic parameter is displayed with respect to the reconstructed primary energy and for enhanced samples of different mass groups.

With a larger sample of higher statistical accuracy this kind of comparisons provides, albeit indirectly, reliable information on strong interaction parameters and will help to tune the hadronic interaction models used as Monte Carlo generators. Studies with distributions based on larger statistical accuracy are foreseen for different energy intervals and various hadronic interaction models in a forthcoming paper. A more sophisticated approach is planned with a neural network trained for a classification in four or five mass groups.

## 6. Summary

The paper presents an approach for the preparation of enriched cosmic ray mass group samples from EAS observations. For that purpose a unified framework of statistical inference has been used, based on nonparametric techniques for the analysis of multivariate parameter distributions. The approach has been demonstrated with

experimental data of the multidetector experiment KASCADE, whose large number of EAS observables, simultaneously measured for each event, enables a successful application and useful investigations of high energy hadronic interactions on an event-by-event basis.

For the preparation of samples enriched with events of a given class (mass of the primary particle) the $(N_e, N_\mu^{tr})$-correlation has been exploited as a potential mass and energy identifier, using reference patterns from Monte Carlo simulations with the QGSJET model as generator of the high-energy hadronic interaction. The classification and misclassification rates have been studied and a purification procedure of the samples has been introduced. Efficiency and purity of the procedure are scrutinized. It has been shown that the purity of the samples (fraction of true classified events in an actual sample allocated to a given class) can be noticeably improved without a drastic reduction of the efficiency (defined as fraction of true classified events of the total number of events of a given class). It should be emphasized that the procedure does remove events over nearly the full range of the distributions, thus avoiding any biasing of the remaining samples. In addition the approach accounts properly for the natural EAS fluctuations, as far as the reference patterns reflect also these fluctuations realistically.

For illustrations, in a second step, the prepared samples have been used to study various EAS observables from the KASCADE experiment and their consistency with the QGSJET model. The electron size and muon content can be fairly well reproduced, as well as hadronic observables measured at the core of showers, though in the latter case the samples are affected by the limited statistical accuracy of the number of events registered with the hadron calorimeter, and of the Monte Carlo simulations. An improvement of the analyses in this direction is a future task with studies of other current hadronic interaction models using the presented distributions.

It is obvious that the demonstrated approach enables a number of interesting investigations of the interaction of such enriched samples with the air nuclei, e.g. studies of the attenuation lengths of specified primary cosmic particles by EAS observations with different zenith angles of incidence and with detector installations on different observation levels.

## Acknowledgements

The authors would like to thank the members of the engineering and technical staff of KASCADE who considerably contributed to the reported measurements. The work has been supported by the Ministry for Research of the Federal Republic of Germany and by a NATO Collaborative Linkage Grant between Armenia and Germany (PST. CLG.978825). The Romanian Ministry of Education and Research provided a grant for supporting the collaborating group of the National Institute for Physics and Nuclear Engineering of Bucharest. The Polish collaborating group of the Cosmic Ray Division of the Soltan Institute of Nuclear Studies in Lodz is supported by the Polish State Committee for Scientific Research (grant no. 5 P03B 133 20). The KASCADE collaboration work was embedded in the frame of scientific–technical cooperation (WTZ) projects between Germany and Armenia (ARM 98/002), Poland (POL-99/005), and Romania (ROM 99/005).

## References

[1] A.A. Chilingarian, Comp. Phys. Com. 54 (1989) 381.
[2] A.A. Chilingarian, H.Z. Zazyan, Sov. J. Nucl. Phys. 54 (1991) 128 (in Russian).
[3] A.A. Chilingarian, H.Z. Zazyan, Il Nuovo Cimento 14C (6) (1991) 555.
[4] ANI Collaboration, NIM A 323 (1992) 104.
[5] H.O. Klages et al., Nucl. Phys. B 52B (1997) 92; KASCADE collaboration, T. Antoni et al., NIM, submitted for publication.
[6] KASCADE collaboration, T. Antoni et al., Astropart. Phys. 16 (2002) 245.
[7] KASCADE collaboration, T. Antoni et al., Astropart. Phys. 14 (2001) 245.
[8] J. Engler et al., NIM A 427 (1999) 528.
[9] H. Bozdog et al., NIM A 465 (2001) 455.
[10] P. Doll et al., NIM A 488 (2002) 517.
[11] D. Heck et al., FZKA-Report 6019, Forschungszentrum Karlsruhe, 1998.
[12] N.N. Kalmykov, S.S. Ostapchenko, A.I. Pavlov, Nucl. Phys. B 52B (1997) 17.
[13] H. Fesefeldt, Report PITHA-85/02, RWTH Aachen, 1985.

[14] W.R. Nelson, H. Hirayama, D.W.O. Rogers, Report SLAC 265, Stanford Linear Accelerator Center, 1985.
[15] CERN, GEANT: CERN Program Library Long Writeups, 1993.
[16] C.M. Bishop, Neural Networks for Pattern Recognition, Oxford University Press, New York, 1995.
[17] A.A. Chilingaryan, Neurocomputing 6 (1994) 497.
[18] KASCADE collaboration, T. Antoni et al., J. Phys. G: Nucl. Part. Phys. 25 (1999) 2161.
[19] KASCADE collaboration, T. Antoni et al., J. Phys. G: Nucl. Part. Phys. 27 (2001) 1785.
[20] KASCADE collaboration, J. Milke et al., Proc. 27th ICRC 2001, Hamburg 1 (2001) 241.
[21] A.A. Chilingarian, Program Package ANI, (Users Manual, unpublished) http://crdlx5.yerphi.am/proj/ani.
[22] K. Fukunaga, Introduction to Statistical Pattern Recognition, Academic Press, Harcourt Brace Jovanovich Publishers, 1990.
[23] A.A. Vardanyan et al., in: A.A. Chilingarian, A. Haungs, H. Rebel, Kh. Sanosyan (Eds.), Proc. Workshop ANI 99, Nor-Amberd, Armenia FZKA-Report 6472, Forschungszentrum Karlsruhe, 1999, p. 23.

ELSEVIER

Mathematical Biosciences 176 (2002) 59–69

Mathematical Biosciences

www.elsevier.com/locate/mbs

# Multivariate approach for selecting sets of differentially expressed genes

A. Chilingaryan [a], N. Gevorgyan [a], A. Vardanyan [a], D. Jones [b], A. Szabo [b,*]

[a] *Cosmic Ray Division, Yerevan Physics Institute, 2 Alikhanian Brothers st., Yerevan 375036, Armenia*
[b] *Huntsman Cancer Institute and Department of Oncological Sciences, University of Utah, 2000 Circle of Hope, Salt Lake City, UT 84112-5550, USA*

Received 21 May 2001; received in revised form 13 June 2001; accepted 20 November 2001

**Abstract**

An important problem addressed using cDNA microarray data is the detection of genes differentially expressed in two tissues of interest. Currently used approaches ignore the multidimensional structure of the data. However it is well known that correlation among covariates can enhance the ability to detect less pronounced differences. We use the Mahalanobis distance between vectors of gene expressions as a criterion for simultaneously comparing a set of genes and develop an algorithm for maximizing it. To overcome the problem of instability of covariance matrices we propose a new method of combining data from small-scale random search experiments. We show that by utilizing the correlation structure the multivariate method, in addition to the genes found by the one-dimensional criteria, finds genes whose differential expression is not detectable marginally. © 2002 Published by Elsevier Science Inc.

*Keywords:* Microarray; Random search; Mahalanobis distance; Simulation study

## 1. Introduction

Microarray technology is rapidly gaining popularity, with a large number of researchers planning experiments and producing data. While there are variations in the exact methodology, the shared goal of microarray technologies is to measure the expression of a *very* large number of genes simultaneously. The activity of a gene manifests itself in its expression level – the abundance of mRNA (messenger RNA), a copy of the information carried by the gene. The role of mRNA is to move the information contained in the DNA to the translation machinery that produces

* Corresponding author. Tel.: +1-801 585 5182; fax: +1-801 585 5357/5337.
*E-mail address:* aniko.szabo@hci.utah.edu (A. Szabo).

0025-5564/02/$ - see front matter © 2002 Published by Elsevier Science Inc.
PII: S0025-5564(01)00105-5

proteins used by the cell. Thus the amount of mRNA of a specific gene reflects how many proteins coded by that gene are actually produced. This principle is the basis of the interest in gene expression microarray methodology despite the caveat that many events that have important consequences for the cell occur during the transcription and translation processes.

In this paper we explicitly consider two-channel spotted cDNA (complementary DNA) microarrays, however similar ideas can be explored with other technologies as well. In this approach mRNA is extracted from two tissues and is labeled separately with fluorescent dyes (usually red and green). The samples are then mixed and hybridized simultaneously to a slide that has cDNA spots corresponding to each of the genes of interest. During the hybridization process each mRNA finds the matching cDNA and binds (hybridizes) to it. If a particular gene is highly expressed, then a large number of mRNAs corresponding to it will hybridize to its cDNA, thus the fluorescence intensity of that spot will be high. The expression level of each gene of a tissue is measured as the fluorescence intensity of its spot in the corresponding (red or green) channel.

One of the common uses of microarrays is the comparison of two tissues of interest with the aim of finding genes that are responsible for biological differences between them. These two tissues might be very distinct phenotypically, like neoplastic and normal tissues, or the difference might be slight, as the same cells during various stages of the cell cycle, before and after applying some treatment, etc. Thus the expected number of genes with different expression level in the two tissues can vary from just a few to hundreds, and the extent of differential expression can vary from slight to very large as well. We consider the experimental design that assigns one of the tissues of interest to the green channel and the other to the red channel on the same microarray slide. We will also assume that several independent samples (slides) are available.

Unfortunately both the intrinsic genomic instability of tumors and measurement instability (poor reproducibility) can obscure actual differences between normal and pathological cells, or introduce fake ones. The extremely large number of genes (the dimensionality of the 'feature space' reaches tens of thousands), the relatively small number of measurements (usually just a few dozen), the complex nature of biochemical pathways and numerous sources of experimental errors prevent rigorous diagnostic inference from microarray data.

Early users of microarrays had only one replicate (slide) available, so their ability to apply statistical methodology was very limited. The usual approach was to set an arbitrary cutoff level for the value of the ratio (say 3) and declare any gene with a higher observed ratio of expression in the two tissues to be differentially expressed [1–3]. Variability was reduced through normalization that used predetermined 'control' spots/genes [4,5] or replicate spots [6,7]. Moreover, the need for independent replicates has been recognized [8], and several methods for combining information from several slides have been proposed. These methods assign a test score to each of the genes and then select those that are 'significant'. The test statistics used include the *t*-statistic [9,10], the ANOVA *F*-statistic [11] and the information theoretic measure known as InfoScore [12,13].

Currently used methods for selecting differentially expressed genes are mostly of a univariate nature, they do not utilize the information on interactions between genes. It is well known that genes do not work independently; activation of one gene usually triggers changes in the expression level of other genes, that is genes are involved in so-called *pathways*. The extent of the changes in the expression level of the genes in a pathway varies, so some of the changes might not be highly 'statistically significant'; however the biological significance of the involvement of many genes of a pathway is high. In this paper we develop an approach that uses both the mean expression levels

and the covariance structure of the data. Our algorithm outputs an ordered list of genes differentially expressed in the two tissues that is enriched by functionally related genes.

Unfortunately, several obstacles prevent the straightforward application of well-established statistical techniques for multidimensional variable selection. Many of them rely on estimates of the covariance matrix; however the small number of independent samples and the presence of outliers make these estimates unstable for large dimensions. In other words, while a relatively large number of genes can be differentially expressed, only small gene sets can be considered. There are other problems that arise when scaling methods of data analysis up into a high dimensional space. First, the number of possible gene combinations is enormously large; therefore it is impossible to compare all gene subsets and find the optimal one. On the other hand, if a global optimum could be found, it would be overly training sample specific, because of the phenomenon of overfitting.

In this paper we propose a solution that to a certain extent remedies the above mentioned difficulties while retaining the benefits of multivariate methods. This gene selection method operates in feature spaces of small dimensionality in which the covariance matrix estimation still makes sense, while allowing sets of differentially expressed genes of larger size to be built.

## 2. Multi-start random search with early stopping

Random search algorithms are well suited for finding optima in complex combinatorial spaces [14]. Here we propose a modification of the basic random search algorithm, the idea of which is to apply a local search procedure multiple times and then use all the selected genes for further analysis. As overfitting is an ever-present danger, we concentrate on short local searches to be able to examine *local maximum regions* and to prevent convergence to a unique global maximum. The method can be applied for a wide variety of parametric and non-parametric quality functions; our choice will be discussed in the next section. The basic structure of the multi-start random search method with early stopping (MRSES) is outlined by the following sequence of steps:

*Step 0*: Randomly select $N_{\text{clust}}$ genes from $N_{\text{all}}$, $N_{\text{clust}} \ll N_{\text{all}}$. Evaluate the quality function.
*Step 1*: Generate a new evaluation point by swapping one or more randomly selected genes between the currently selected set and the rest of the genes.
*Step 2*: Evaluate the quality function for the new combination; if its value has decreased, then return to the previous combination.
*Step 3*: Repeat Steps 1 and 2 until the number of iterations reaches $N_{\text{iter}}$, then save the best configuration.
*Step 4*: Repeat Steps 0–3 until the number of these cycles reaches $N_{\text{cycle}}$.
*Step 5*: Post-process the resultant $N_{\text{cycle}}$ groups of $N_{\text{clust}}$ genes each in the manner described below.

The value of the cluster size parameter $N_{\text{clust}}$ is limited by the number of available training samples (microarray slides). The nature of this limitation depends on the particular choice of the quality function, but generally both parametric and non-parametric criteria are very sensitive to the scarceness of training samples in a high-dimensional feature space. In our colon cancer cell line application only 12 samples per tissue are available so in this study we used $N_{\text{clust}} = 5$, the largest

value that did not cause the quality function estimates to become unstable (specifically, the critical element was the determinant of the covariance matrix). It is important to note that due to the multiple repetition of the search and the post-processing described below, the choice of $N_{\text{clust}}$ does not limit the detectable number of differentially expressed genes, but rather the depth of the estimated interaction structure.

The number of iterations $N_{\text{iter}}$ is crucial to control overfitting; its value should balance between being too small to provide enough time for finding truly differentially expressed genes and being too large. In the latter case one can expect the same maximum attained in many cycles of search because of overfitting. We investigate the role of the choice of $N_{\text{iter}}$ in the search for differentially expressed genes in the simulation study below.

The variability of the algorithm start points for detecting differentially expressed gene clusters depends on the number of search cycles $N_{\text{cycle}}$. Therefore it should be as large as possible and is limited by CPU power only (we have used $N_{\text{cycle}} = 10\,000$).

In the post-processing step the local optima are combined to provide a final, global solution. We proceed from the heuristic argument that strongly differentially expressed genes should appear in many of the local maxima, so that each gene is characterized by the frequency of its occurrence in the suboptimal set selected by each of the $N_{\text{cycle}}$ cycles. A conservative estimate of the $p$-value corresponding to the observed frequency can be calculated. If a gene is not differentially expressed, then the probability that it will be in the selected subset by chance is expected to be equal to $N_{\text{clust}}/N_{\text{all}}$ (and most likely smaller). As the number of repetitions $N_{\text{cycle}}$ is large, the final selection frequency of this gene is well approximated by a Poisson distribution with mean $N_{\text{cycle}}N_{\text{clust}}/N_{\text{all}}$. Based on this null-distribution the corresponding (conservative) $p$-values for each gene can be calculated.

## 3. Optimization criterion

A key component of the search is the quality function to be optimized. It should measure the 'distinctiveness' of the two tissues under comparison based on a set of genes taking into account the correlation structure. Generally, correctly specified parametric methods are more powerful than non-parametric methods due to the utilization of the additional information invested in the model, however they can be sensitive to departures from this model. With microarray data small sample sizes are a persistent problem, so an appropriate parametric quality function will give a gain in power, while the non-parametric random search algorithm will add robustness. Probably the most popular parametric measure of the discrepancy between two multidimensional samples is the Mahalanobis distance [15]

$$R^2_{\text{Mah}} = (\mathbf{v} - \mathbf{u})' \left( \frac{\Sigma_u + \Sigma_v}{2} \right)^{-1} (\mathbf{v} - \mathbf{u}), \tag{1}$$

where $\mathbf{v}$ and $\mathbf{u}$ are the sample means and $\Sigma_u$, $\Sigma_v$ are the two sample variance-covariance matrices. It is a natural extension of the $t$-statistic to a multidimensional setting. At first glance it might appear that the calculation of the Mahalanobis distance at every step of the search ($N_{\text{iter}} \times N_{\text{cycle}}$ times) is prohibitive because of the matrix inverse involved. However the structure of the algorithm that changes the vectors in only one dimension allows for a fast update formula (see [16]).

If differences in both the mean and the covariance structure are of interest, the Bhattacharya distance can be used:

$$R^2_{\text{Bha}} = \frac{1}{8} R^2_{\text{Mah}} + \frac{1}{2} \ln \frac{|(\Sigma_u + \Sigma_v)/2|}{\sqrt{|\Sigma_u||\Sigma_v|}}. \tag{2}$$

Clearly, other parametric or non-parametric dissimilarity measures can be used to concentrate on departures of specific form that are of interest for the researcher.

With the Mahalanobis distance between subvectors of gene expression as the optimization criterion, we used a related adjustment of experimental and simulated data: on each slide the data points $X_{ij}$, $i = 1, \ldots, N_{\text{all}}$, $j = 1, \ldots, N_{\text{slides}}$ were replaced by their normal scores $X^*_{ij}$ using the formula

$$X^*_{ij} = \Phi^{-1}(\text{rank}_j X_{ij}/N_{\text{all}}), \tag{3}$$

where $\Phi^{-1}(\alpha)$ is the $100\alpha$th percentile of the standard normal distribution and $\text{rank}_j X_{ij}$ is the rank of $X_{ij}$ among all of the observations on the $j$th slide. We have also looked at the rank-based adjustment [17,18] and the classical mean-log adjustment (divide by mean and take logarithm), however the results appeared to be very close, and for this reason they are not reported here.

## 4. Simulation model

Appropriate simulation models can be a powerful tool for evaluating and comparing techniques under controlled circumstances. Unfortunately, the problem of developing a simulation model for microarray data has been largely ignored, we are aware of only one attempt [19] in which a highly specific parametric model assuming independent genes is used. As utilizing gene interaction is a primary feature of our approach, we have to develop a more elaborate model incorporating correlated gene groups. Our simulation model for microarray data follows the underlying error process by starting at the 'true' gene expression levels and adding biological sample-to-sample variability and technology-related errors. It is necessarily involved as the biological underpinning is complex and different kinds of error sources need to be incorporated.

*Ideal gene expression:* The genes to be simulated are divided into groups of equal or unequal size; within each group the gene expressions are dependent, however genes in different group are independent. First independent expression levels $a_i$ were generated for each gene from the mixture of log-normal distribution with mean $\mu = 2.5$ and standard deviation (STD) $\sigma = 3$, and uniform distribution on $[0, 190]$. The proportion of the uniform distribution in the mixture was taken to be $\pi = 0.15$. Dependency was introduced in the biological variability step through a frailty variable having a gamma distribution with mean 1 and variance 0.2.

*Biological variability:* For each cluster $c$ and sample $j$ a frailty $\gamma_{cj}$ was generated. To obtain both positively and negatively correlated genes, each gene is marked as 'to be divided by the frailty parameter' with probability 0.5 and 'to be multiplied by this factor' otherwise. We will denote the operation corresponding to a gene by $\divideontimes$. Sample-to-sample variability was introduced by generating $A_{ij}$, the expression of gene $i$ (from cluster $c$) in sample $j$ from a log-normal distribution with mean $a_i \divideontimes \gamma_{cj}$ and coefficient of variation $v = 0.3$. This procedure results in both positively and

negatively correlated gene-pairs in the cluster with expected value $\pm 0.65$ (this value depends on the variance of the frailty and the coefficient of variation $v$).

*Experimental errors:* The next step was to introduce observation errors. Observed expressions in the green channel were generated as $X_{ij} = A_{ij}\alpha_j + v_j$. The slide effect $\alpha$ was taken lognormally distributed with mean 1 and STD 0.2. The additive background effect $v$ is log-normal with mean 1.1 and STD 0.15.

Observed expressions in the red channel were generated in accordance with the model $Y_{ij} = A'_{ij}\alpha_j d_i \rho + \delta_j$. The ideal expression $A'_{ij}$ was generated from the same distribution as $A_{ij}$. The coefficient $\alpha_j$ is the same slide-specific multiplicative error as used for the green channel. The reference intensity ratio $\rho$ is a constant equaling 1.5 (chosen to match data generated by microarray equipment at the Huntsman Cancer Institute) introduced to describe the fact that the red signal is generally different from a comparable green one. Differential expression is modeled through a random variable $d$ which was set at value 1 in the non-differentially expressed clusters and can be regulated as intended in the differentially expressed clusters. Since the red signal is higher than the green one, a higher background is generated for the red channel: $\delta$ was log-normal with mean 2.0 and STD 0.15.

In our simulation study below we used 1000 genes divided into dependent clusters of equal size 20. One of the clusters (of 20 genes) was chosen to be differentially expressed with the gene-specific ratio $d$ randomly generated for each of these genes from a log-normal distribution with mean 1 and variance 0.5; the correlation structure was kept the same in the two hypothetic tissues. Thus in the chosen cluster some of the genes exhibited large over- or under-expression, while others with $d \approx 1$ changed their expression level only slightly. The model was used to simulate 20 slides with one of the tissues on the green channel and the other one on the red channel.

## 5. Results of computer simulations

The main goal of the simulation study is to investigate under controlled conditions whether the multivariate search method really increases the power of detection of differentially expressed genes. We also want to assess the effect of changing the parameters of the proposed MRSES algorithm, with special attention to $N_{\text{iter}}$.

First we simulated one data set as described in Section 5 and applied the search algorithm using the parameters $N_{\text{clust}} = 5$, $N_{\text{cycle}} = 10\,000$ and several values of $N_{\text{iter}}$. In Fig. 1 we compare some characteristics of the algorithm; the left side corresponds to $N_{\text{iter}} = 1000$ and the right side to $N_{\text{iter}} = 100\,000$.

The top graphs display the histogram of the values of the 'last good iteration'—the number of iterations after which no successful steps were encountered (that is when the final set was found). It is clear that 1000 iterations are not sufficient to reach the global maximum, on the other hand 100 000 iterations are more than enough for the random search to converge. The middle pictures illustrate this in another way. In the case of early stopping the distribution of the Mahalanobis distances (the algorithm's quality function) corresponding to the $N_{\text{cycle}}$ suboptimal sets is unimodal with high variability. Therefore, we can conclude that the algorithm explored many different local maxima with a variety of corresponding values of the quality function. When the iterations are continued to reach 100 000, the distribution of the Mahalanobis distances achieved in the sub-

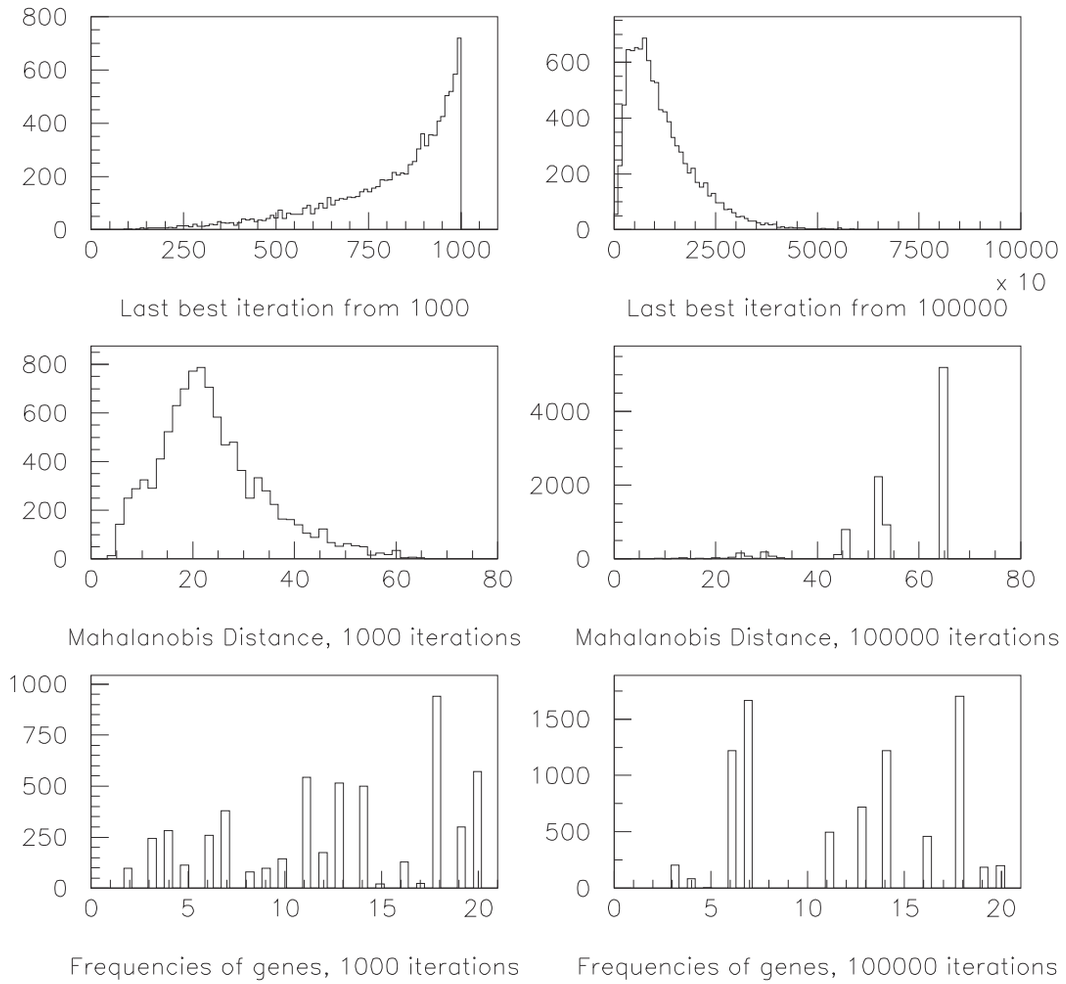


Fig. 1. Comparison of gene selection with early and late stopping of the multi-start random search algorithm. First row: histogram of the value of the 'last best iteration' in the $N_{\text{cycle}}$ searches. Second row: histogram of the estimated Mahalanobis distances for the $N_{\text{cycle}}$ selected sets. Third row: frequency of inclusion of the differentially expressed genes (1–20) in one of the selected sets. One simulated data set.

optimal sets becomes very discrete. In half of the cases the search reaches the global maximum on a unique combination of genes, one of which was not preset as differentially expressed. So we do find the global maximum, but miss many local maxima and the corresponding differentially expressed genes from the predefined cluster. When we stop early at the 1000th iteration none of the 10 000 cycles finds the global maximum, but a variety of genes are selected. This is demonstrated in the bottom pictures, where the frequencies of selection for the 20 genes belonging to the differentially expressed cluster are plotted. In our experiment, 17 from 20 genes pass the selection criteria (to have the frequency of occurrence higher than 0.5%) with the early stop, while only 10 genes are correctly selected when we force algorithm to attain the global maximum.

To further investigate the dependence of the power of the algorithm on the stopping time, we estimated the ROC curves corresponding to values of $N_{\text{iter}}$ ranging from 100 to 10 000 based on 10 independently simulated data sets (other parameters were held constant: $N_{\text{clust}} = 5$,

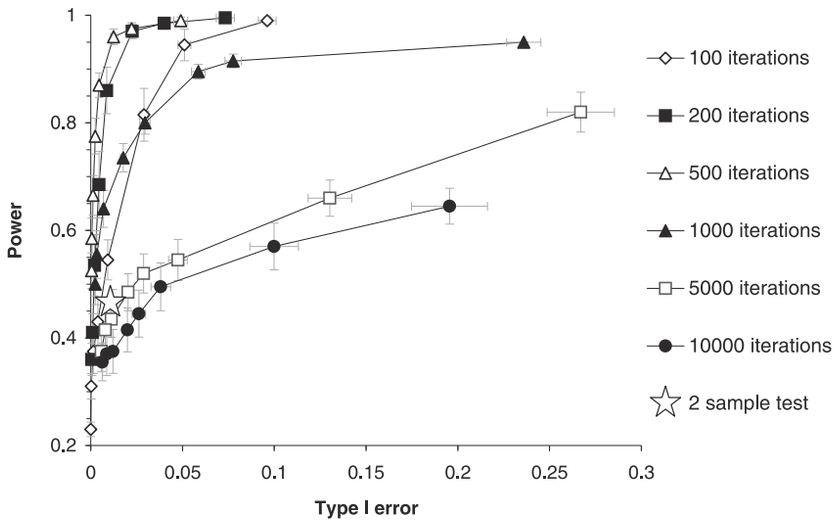


Fig. 2. ROC curves for various values of $N_{\text{iter}}$ controlling the stopping time. Based on 10 simulated data sets; the error bars show the standard errors of the point estimates.

$N_{\text{cycle}} = 10\,000$). For each search we obtained a list of genes with associated frequencies of occurrence in the selected subset and compiled a final selection of differentially expressed genes by applying cutoff values ranging from 0.1% to 10%. Based on the null hypotheses of no differential expression, for each of these sets we estimated the type I error as the proportion among all non-differentially expressed genes of those genes that were included in the selection and the type II error as the proportion among the genes in the differentially expressed cluster that were not included in the final selection. The resulting ROC curves are shown in Fig. 2. As a reference a point representing the type I error and the power of the marginal $t$-test with 5% significance level is also plotted. From Fig. 2 we can see that the choice of $N_{\text{iter}}$ does indeed have a large influence on the performance of the algorithm and long searches are inferior to early stopping. Of course there is a limit on how early one should stop, because very short searches do not have a chance to reach any local maxima. Under our setup $N_{\text{iter}} = 500$ gives the best performance.

## 6. Application: two colon cancer cell lines

We selected two commonly studied colon cancer cell lines for our analyses. HT29 cells represent advanced, highly aggressive colon tumors. They contain mutations in both the APC gene and p53 gene, two tumor suppressor genes that frequently mutate during colon tumorigenesis. As another cell type, we selected HCT116 cells. This cell line models less aggressive colon tumors and harbors functional p53 and APC. However, they show a deficiency of those genetic systems that are responsible for the repair of mismatched regions of DNA. To generate the data, three samples of each mRNA (1 μg each) were labeled by production of first-strand cDNA in the presence of Cy3-dCTP (green) or Cy5-dCTP (red). Cy-3 was used to label HCT116 cells while Cy-5 was used for HT29 cells. Each comparison set was hybridized against two microarray slides (facing each other) containing 4608 minimally redundant cDNAs spotted in duplicate. As a quality control tool, six *Drosophila* genes are always added to the Cy-5 sample, so in a red vs. green comparison they have

to be differentially expressed by design. This experiment resulted in a total of twelve measurements on each channels for each gene on the microarrays. While there is a nested dependence structure of the samples, we used them as independent replicates. From a separate experiment we also have data with ten HCT116 samples hybridized with Cy-5, that is on the red channel. The normal score adjustment (3) was used.

We have performed two comparisons: HCT116 vs. HT29 and HCT116 (green) vs. HCT116 (red), the latter after the exclusion of the six *Drosophila* control genes. Based on our simulation studies and the available sample size we chose $N_{\text{clust}} = 5$ and $N_{\text{iter}} = 500$. In Fig. 3 we compare the two search procedures. The left column corresponds to the comparison of the different cell lines, while the right column to the comparison of the same cell line on different channels. The histogram of the last best iteration is very similar for both cases and looks like the one obtained in our simulation studies where the global maximum was not obtained. Thus in both cases due to the early stopping the algorithm keeps exploring local maxima. However the distribution of the estimated Mahalanobis distance at these local maxima is very different: when different cell lines were compared the Mahalanobis distance $R^2_{\text{Mah}}$ based on the locally optimal subsets tended to be much larger, that is the separation of the two tissues was considerably better.

We also compared the two lists of genes ordered by decreasing frequency of occurrence in the selected subset. The histogram of the first 115 genes on the list is shown in Fig. 4 (white and black columns); the right tails of the histograms are very close to each other. As an additional reference we included the histogram generated by the HCT116 (green) vs. HCT116 (red) comparison with the control genes included (grey columns). It is clear that some of the genes in the HCT116/HT29 comparison (black) are selected more often than expected under the null hypothesis of no

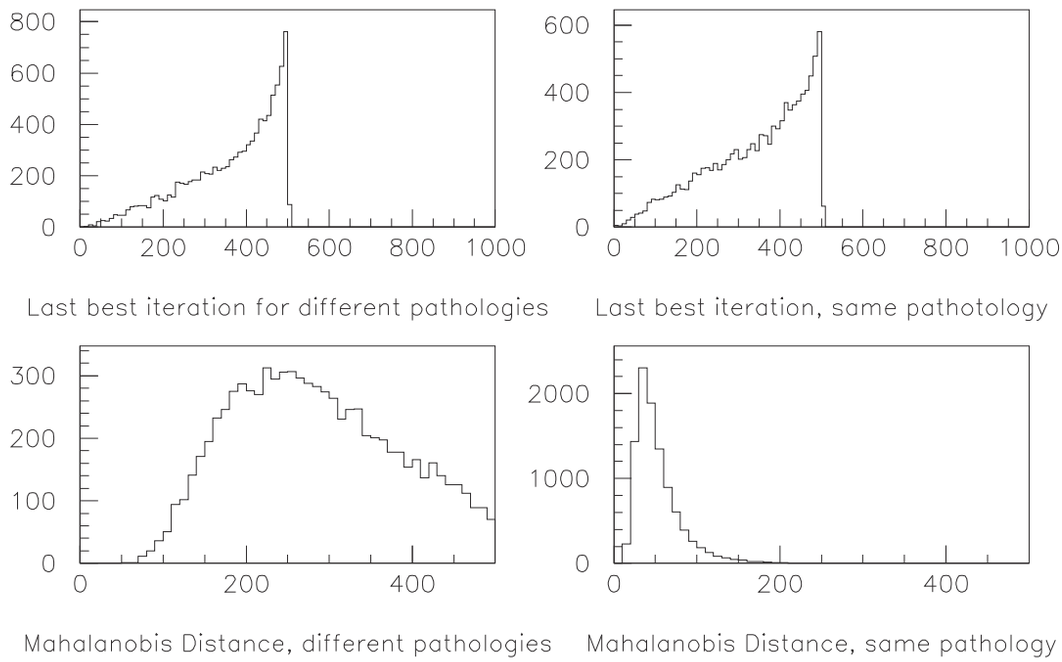


Fig. 3. Comparison of the search procedure used for same and different tissues. First row: histogram of the value of the 'last best iteration' in the $N_{\text{cycle}}$ searches. Second row: histogram of the estimated Mahalanobis distances for the $N_{\text{cycle}}$ suboptimal sets. HCT—HT data.

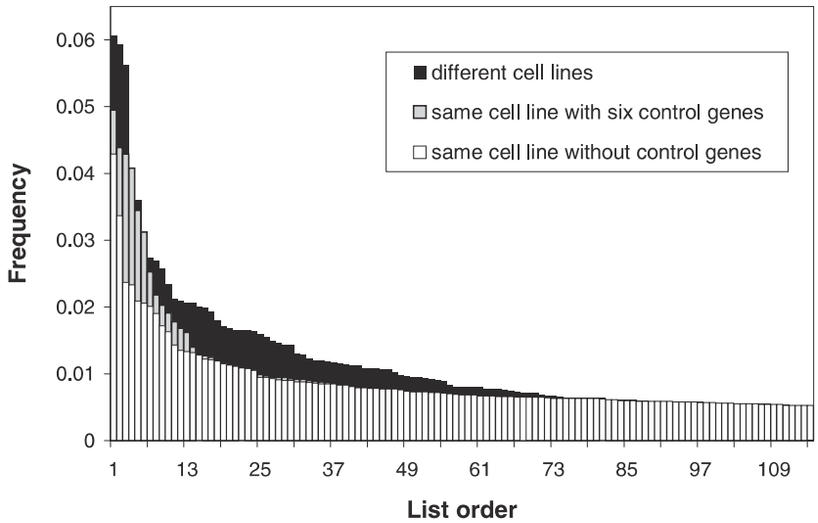


Fig. 4. Comparison of the frequency of inclusion in the selected locally optimal set in the search procedure used for same tissue with (gray) or without (white) the six control *Drosophila* genes on the two channels and for different tissues (black). HCT—HT data.

difference between the two tissues (white). In the no-difference comparison (without control genes) there are just two genes that are selected in more than 3% of the cycles; if the control genes are included, this number increases to six and 4 out of the top 5 genes (#1–3 and 5) are actually the *Drosophila* controls.

Based on the histograms we decided to use 1% as the cutoff for selecting differentially expressed genes, thus selecting 59 cDNA spots. We have compared this list with the top 59 genes selected by values of the $t$-statistic. Almost half of these genes (25 exactly) appear in both lists. However a striking feature of the selection using multivariate random search is its ability to include correlated genes. Some of the genes have several spots that correspond to them, thus their expression level at various spots is known to be correlated. Among the 59 genes selected by the multivariate method 13 have two, and 2 have three spots related to them. Four of these genes have all their replicates in the selected set including one of the genes with three replicates. By comparison, in the list based on the marginal $t$-statistic 17 genes have two or more replicates on the slide, and only one of them has all of its replicates selected. While one would hope to be able to find all the replicates of a gene, in practice localized errors can make it infeasible. Part of the problem is the unreliability of the gene identifications in our dataset, so some cDNAs labeled the same might actually correspond to different genes. Despite the caveat, this finding is encouraging and is in line with what we have seen in the simulation studies: genes with less pronounced differential expression can be selected if they are correlated with more strongly differentially expressed genes.

## Acknowledgements

We would like to thank Andrei Yakovlev for introducing us to the microarray data analysis problems and useful discussions and the two referees for their helpful comments. This research was supported by Grant AB2-2005 awarded by the US Civilian Research and Development

Foundation (CRDF), NCI Cancer Center Support Grant 5P30 CA42014, and the Huntsman Cancer Foundation.

## References

[1] J. DeRisi, L. Penland, P.O. Brown, M.L. Bittner, P.S. Meltzer, M. Ray, Y. Chen, Y.A. Su, J.M. Trent, Use of a cDNA microarray to analyse gene expression patterns in human cancer, Nature Genet. 14 (4) (1996) 457.
[2] M. Schena, D. Shalon, R. Davis, P. Brown, Quantitative monitoring of gene expression patterns with a complementary DNA microarray, Science 270 (5235) (1995) 467.
[3] M. Schena, D. Shalon, R. Heller, A. Chai, P. Brown, R. Davis, Parallel human genome analysis: microarray-based expression monitoring of 1000 genes, Proc. Nat. Acad. Sci. USA 93 (20) (1996) 10614.
[4] C.H. Rhee, K. Hess, J. Jabbur, M. Ruiz, Y. Yang, S. Chen, A. Chenchik, G.N. Fuller, W. Zhang, cDNA expression array reveals heterogeneous gene expression profiles in three glioblastoma cell lines, Oncogene 18 (1999) 2711.
[5] J. Khan, R. Simon, M. Bittner, Y. Chen, S.B. Leighton, T. Pohida, P.D. Smith, Y. Jiang, G.C. Gooden, J.M. Trent, P.S. Meltzer, Gene expression profiling of alveolar rhabdomyosarcoma with cDNA microarrays, Cancer Res. 58 (1998) 5009.
[6] J. Schuchhardt, D. Beule, A. Malik, E. Wolski, H. Eickhoff, H. Lehrach, H. Herzel, Normalization strategies for cDNA microarrays, Nucl. Acids Res. 28 (10) (2000) e47.
[7] H. Herzel, D. Beule, S. Kielbasa, J. Korbel, C. Sers, A. Malik, H. Eickhoff, H. Lehrach, J. Schuchhardt, Extracting information from cDNA arrays, Chaos 11 (1) (2001) 98.
[8] M.-L.T. Lee, F.C. Kuo, G.A. Whitmore, J. Sklar, Importance of replication in microarray gene expression studies: Statistical methods and evidence from repetitive cDNA hybridizations, Proc. Nat. Acad. Sci. USA 97 (18) (2000) 9834.
[9] L. Zhang, W. Zhou, V.E. Velculescu, S.E. Kern, R.H. Hruban, S.R. Hamilton, B. Vogelstein, K.W. Kinzler, Gene expression profiles in normal and cancer cells, Science 276 (5316) (1997) 1268.
[10] U. Alon, N. Barkai, D.A. Notterman, K. Gish, S. Ybarra, D. Mack, A.J. Levine, Broad patterns of gene expression revealed by clustering analysis of tumor and normal colon tissues probed by oligonucleotide arrays, Proc. Nat. Acad. Sci. USA 96 (12) (1999) 6745.
[11] M.K. Kerr, M. Martin, G.A. Churchill, Analysis of variance for gene expression microarray data, J. Computat. Biology 7 (6) (2000) 819.
[12] A. Ben-Dor, N. Friedman, Z. Yakhini, Scoring genes for relevance.
[13] I. Hedenfalk, D. Duggan, Y. Chen, M. Radmacher, M. Bittner, R. Simon, P. Meltzer, B. Gusterson, M. Esteller, O.P. Kallioniemi, B. Wilfond, A. Borg, J. Trent, Gene-expression profiles in hereditary breast cancer, New England J. Med. 344 (8) (2001) 539.
[14] A.A. Zhigljavsky, Theory of global random search, Mathematics and its Applications (Soviet Series), vol. 65, Kluwer Academic, Dordrecht, 1991.
[15] P.C. Mahalanobis, On the generalized distance in statistics, Proc. Nat. Inst. India 12 (1936) 49.
[16] G.J. McLachlan, Discriminant Analysis and Statistical Pattern Recognition, Wiley, New York, 1992.
[17] A. Tsodikov, A. Szabo, D. Jones, Adjustments and tests for differential expression, ENAR conference, Charlotte NC, 2001.
[18] A. Tsodikov, A. Szabo, D. Jones, Adjustments and measures of differential expression for microarray data, Bioinformatics (2002), in press.
[19] M.A. Newton, C.M. Kendziorski, C.S. Richmond, F.R. Blattner, K.W. Tsui, On differential variability of expression ratios: improving statistical inference about gene expression changes from microarray data, J. Computat. Biology 8 (1) (2000) 37.

INSTITUTE OF PHYSICS PUBLISHING JOURNAL OF PHYSICS G: NUCLEAR AND PARTICLE PHYSICS

J. Phys. G: Nucl. Part. Phys. **32** (2006) 2279–2291 doi:10.1088/0954-3899/32/11/019

# Study on cosmic ray background rejection with a 30 m stand-alone IACT using non-parametric multivariate methods in a sub-100 GeV energy range

**A Konopelko[1], A Chilingarian[2] and A Reimers[2]**

[1] Department of Physics, Purdue University, 525 Northwestern Avenue, West Lafayette, IN 47907-2036, USA
[2] Cosmic Ray Division, Alikhanian Physics Institute, Armenia

Received 24 March 2006
Published 9 October 2006
Online at stacks.iop.org/JPhysG/32/2279

**Abstract**

During the last decade ground-based very high-energy $\gamma$-ray astronomy achieved a remarkable advancement in the development of the observational technique for the registration and study of $\gamma$-ray emission above 100 GeV. It is widely believed that the next step in its future development will be the construction of telescopes of substantially larger size than the currently used 10 m class telescopes. This can drastically improve the sensitivity of the ground-based detectors for $\gamma$-rays of energy from 10 to 100 GeV. Based on Monte Carlo simulations of the response of a single stand-alone 30 m imaging atmospheric Cherenkov telescope (IACT), the maximal rejection power against background cosmic ray showers for low-energy $\gamma$-rays was investigated in great detail. An advanced Bayesian multivariate analysis has been applied to the simulated Cherenkov light images of the $\gamma$-ray- and proton-induced air showers. The results obtained here quantitatively testify that the separation between the signal and background images degrades substantially at low energies, and consequently the maximum overall quality factor can only be about 3.1 for $\gamma$-rays in the 10–30 GeV energy range. Various selection criteria as well as optimal combinations of the standard image parameters utilized for effective image separation have also been evaluated.

(Some figures in this article are in colour only in the electronic version)

## 1. Introduction

Development of the instrumentation in the field of very high-energy (VHE) $\gamma$-ray astronomy is nowadays primarily motivated by the physics goals that the astrophysical community seeks to attain (Weekes 2003). Among these goals are: (i) the observation of supernova remnants (SNR), which are the conjectural sources of the VHE $\gamma$-rays; (ii) the continuous study of

0954-3899/06/112279+13$30.00  

the physics of jets in active galactic nuclei (AGN); (iii) investigation of the morphology and spectra of pulsar wind nebulae (PWN); (iv) a wider search for sources of pulsed $\gamma$-ray emission in the VHE range, to name a few. Such a variety of physics topics are difficult to address with a single ground-based instrument. In fact, the physical diversity of the $\gamma$-ray emission mechanisms requires a similar diversity of the observational approaches and instrumentation for different energy ranges. For instance, further observations of AGN and pulsars necessitate the reduction of instrumental energy threshold down to at least 10–20 GeV, whereas for the detection of a SNR a noticeable upgrade of the telescope sensitivity above 100 GeV is more favourable. Ultimately the design of a major ground-based Cherenkov facility for future dedicated $\gamma$-ray observations has to conform to many requirements in order to allow an efficient observational strategy given the expected $\gamma$-ray fluxes from sources of an entirely different nature.

The high energy stereoscopic system (HESS), which is a system of four 12 m imaging atmospheric Cherenkov telescopes, has been operating for three years in the Khomas Highland of Namibia, close to Windhoek, at 1800 m above sea level (Hofmann 2005). This next-generation instrument for ground-based $\gamma$-ray astronomy has an energy threshold of about 100 GeV and a sensitivity of about 1% of the Crab Nebula flux. Such a sensitivity is achieved due to good angular resolution ($0.1^\circ$), good energy resolution (15%) and a stringent rejection of the cosmic ray background using the stereoscopic approach. Similar stereoscopic arrays are currently under construction and final testing in both Arizona, and Woomera, Australia. Two 17 m telescopes are being built by the MAGIC collaboration on the Canary Island of La Palma. One of these has been taking data since fall 2004.

The outstanding physics results obtained with HESS and MAGIC in the first few years of their operation are a strong motivation for the further development of the imaging atmospheric Cherenkov technique and are basically driven by a further reduction of the energy threshold for future $\gamma$-ray observations. Here we are presenting results for such a detector, a 30 m stand-alone imaging atmospheric Cherenkov telescope (IACT) that may potentially achieve an energy threshold as low as 10 GeV and is representative of a prototype for future low energy telescope arrays (see Konopelko (2005)). The performance of such a telescope is basically determined by its efficiency at cosmic ray background rejection in the sub-100 GeV energy range. This important issue will be addressed in this paper using detailed Monte Carlo simulations and advanced statistical analysis methods.

## 2. Simulations

The atmospheric showers induced by the $\gamma$-rays and protons have been simulated using the numerical code described in Konopelko and Plyasheshnikov (2000). The primary energy of simulated showers was uniformly randomized within each of three energy bins, which were chosen to cover the energy range starting from 1 GeV and extending up to 1 TeV. The events were weighted according to a power-law primary spectrum and the reconstructed shower energy. The maximum impact distance of the shower axis with respect to the centre of the 30 m Cherenkov telescope was 300 m. All showers were simulated at the zenith with a random sampling over azimuth. This reduces any systematic bias in the distributions of the image parameters due to the geomagnetic effect, although it noticeably enhances fluctuations in individual showers. The basic parameters of the simulation setup are summarized in table 1. The detailed simulation procedure of the camera response accounts for all efficiencies involved in the process of the Cherenkov light propagation, which starts from the photon emission in a shower and ends with the digitization of the camera photomultiplier tube

**Table 1.** Basic parameters of the simulation setup.

| | |
|---|---|
| Altitude | 1.8 km above sea level |
| Atmosphere | Tropical |
| Reflector size | 30 m |
| Reflector design | parabolic ($F/D = 1.25$) |
| Number of camera pixels | 1951 |
| Pixel size | 0.07° |
| Photon-to-photoelectron efficiency | 0.1 |
| Trigger | Signal in each of 3 PMs exceeds 6 ph.-e. |
| 'Boundary'/'Picture' thresholds | 3/5 ph.-e. |

(PMT) signal. This includes the atmospheric absorption, the mirror reflectivity, the photon-to-photoelectron conversion inside the PMT etc. The overall efficiency of the photon-to-photoelectron conversion is ∼0.1. The standard 'picture' and 'boundary' technique with thresholds of 5 and 3 photoelectrons (ph.-e.), respectively, was applied for image cleaning. The procedure accepts for the computation of the second-moment image parameters all camera PMT signals that exceed the 'picture' threshold, and only those PMT signals that exceed the 'boundary' threshold and are adjacent to any of the 'picture' pixels. The simulated images have been parameterized using the standard measures of their angular extension and orientation in the telescope focal plane. Further details on the simulation procedure can be found in Konopelko (1999, 2005).

The basic parameters of the simulation setup have been chosen to meet the major technical requirements for the effective imaging of the atmospheric showers. The parabolic optical reflector yields a point-spread function of sufficiently narrow width (∼0.06°) in the range of the light incidence angles of 1.75°. This constrains the choice of the minimum angular size of a PMT and the total number of PMT in the camera, which ultimately determines the camera field of view. Note that any increase of the PMT angular size will substantially degrade the image parameterization of the low-energy $\gamma$-rays. At the same time further reduction of the PMT angular size or an increase of the camera field of view will not be beneficial due to significant optical smearing, which is a major limiting factor. All other parameters of the simulation setup such as the atmosphere, the geomagnetic field strength and the observational height have been chosen to match the environmental conditions of the HESS II project (Hofmann 2005), which is a large 28 m IACT under construction in Namibia.

The proton-induced air showers simulated here started at 1 GeV. This energy accounts for all the secondary muons that could trigger the telescope. Here we did not distinguish between the images generated by a single muon or a low energy proton shower that are very similar in shape. That is why, in the sub-100 GeV energy range, the standard anti-muon cut (length/size) does not work effectively against muon events but rather increases the energy threshold for $\gamma$-ray showers.

It is worth noting that the images of simulated $\gamma$-ray- and cosmic-ray-induced atmospheric showers at TeV energies were formerly crosschecked versus the images recorded with the HEGRA (Konopelko 1999) and HESS (Konopelko *et al* 2003) experiments.

The performance of a single 30 m IACT was discussed by Konopelko (2005) in great detail. Thus the expected raw event detection rate for such a telescope is expected to be about 1.7 kHz. Note that such a high rate can still be maintained by conventional data acquisition systems. The cosmic electrons contribute substantially to this high rate, but the rate is still dominated by the cosmic ray protons and nuclei. Even after applying the standard analysis cuts, the remaining proton rate at energies above 20 GeV exceeds the electron rate by a factor of 2.

## 3. Bayesian paradigm

The background rejection strategies can be divided into two major categories:

1. *A priori* strategies derived from the simulations of both the $\gamma$-ray- and cosmic-ray-induced atmospheric showers. For each simulated shower the Cherenkov light image can be generated and parameterized. By varying the energy and impact distance of simulated showers and taking into account all possible distortions in the hardware response, including a trigger decision, image cleaning etc one can obtain the so-called training samples for both the $\gamma$-ray and cosmic ray primaries. It is in fact very difficult to parameterize the multivariate distribution function for a number of image parameters; therefore we deal with simulation results as they are, i.e. with the samples of the simulated images for the proton- and $\gamma$-ray-initiated showers. To represent such a sample of the simulated data we will use, instead of the underlying multivariate distribution function, the special methods of non-parametric statistics.
2. *A posteriori* strategies based on the experimental data: the so-called on-source sample of events, which were recorded when the telescope was tracking a putative $\gamma$-ray source, and the off-source sample, recorded when the telescope was pointed at the same celestial coordinates, but delayed by 28 min after (or before) the source passage. Using these two signal and background samples it becomes possible to pose the problem of searching *a signal domain*: a volume limited by a multi-dimensional nonlinear surface, which includes a majority of the signal events and which is substantially enhancing the signal events content and consequently significantly enlarging the so-called *signal-to-noise ratio*. Further details on *a posteriori* strategy in the $\gamma$-ray signal evaluation can be found, for instance, in Chilingarian and Cawley (1991) or Chilingarian (1993).

A first attempt to develop a statistical theory of cosmic ray background rejection in the framework of the Bayesian approach for the analysis of VHE $\gamma$-ray data was undertaken by Aharonian *et al* (1990, 1991). This statistical theory includes the following:

- selection of the optimal subset of parameters for discrimination purposes;
- introducing the Bayesian decision rules;
- introducing the *P*-values of the statistical tests that indicate the overlap between the parameter distributions of two different event classes;
- correlation analysis revealing the best pairs to be used in the discrimination process;
- estimation of the Bayes risk (probability of misclassification) as a measure of the overlap of the multivariate distributions;
- adaptive models of the Parzen and K-nearest-neighbour non-parametric density estimation; for a detailed discussion of these models see Parzen (1962) and Tapia and Thompson (1978).

Generally, to prove the existence of a $\gamma$-ray source one calculates the excess of events coming from the direction of a possible source, $N_{\rm on} - N_{\rm off}$. Here $N_{\rm on}$ is a number of events in the on-source sample, which has to be compared to the control event sample. This control sample must guarantee that pure background events have been recorded, $N_{\rm off}$ . The expected $\gamma$-ray fluxes are often very weak and the signal-to-background ratio might frequently be very small, less than 0.01. In such a case one should always answer the following generic question: is the detected abundance a real signal or only a background fluctuation? The measure of statistical significance commonly used in VHE $\gamma$-ray astronomy is the so-called signal-to-noise ratio, $\sigma$ (e.g. Zhang and Ramsden (1990)):

$$\sigma = \frac{N_{\rm on} - N_{\rm off}}{\sqrt{N_{\rm on} + N_{\rm off}}}. \tag{1}$$

The larger the signal-to-noise ratio ($\sigma$) the smaller the probability that the detected excess is due to a background fluctuation. Development of new detector hardware and new data handling methods aim to enlarge the value of $\sigma$. After selecting the $\gamma$-like events from the raw data, in both ON and OFF data samples, the criterion takes the form:

$$\sigma^* = \frac{N^*_{\rm on} - N^*_{\rm off}}{\sqrt{N^*_{\rm on} + N^*_{\rm off}}}, \tag{2}$$

where $N^*_{\rm on}$, $N^*_{\rm off}$ are the numbers of the ON and OFF events surviving image selection cuts.

Using the actual values of the image parameters measured for each individual event one has to decide whether this event was initiated by a $\gamma$-ray or cosmic ray. This statistical decision problem in the Bayesian approach can be described in terms of the following probability measures, defined in metric spaces. Let us introduce the set of possible *states of nature* $\tilde{\mathtt{A}} \equiv (\gamma, h)$, e.g. the $\gamma$-rays ($\gamma$) and cosmic ray hadrons ($h$). The set of all possible statistical decisions is $\tilde{\mathtt{A}} \equiv (\tilde{\gamma}, \tilde{h})$, where the tilde sign denotes the statistical decisions for any examined event, which may belong to one of the signal or background samples. Both decision sets contain the same two elements, but they are not identical: in the first case we deal with *a priori* given categories, while the second set reflects the results of applying any specific statistical evaluation procedure, constructed for the classification of the experimentally measured events into two given classes.

By multiplication of these two sets we define the so-called loss measure, $c_{A\tilde{A}}$, which indicates the possible consequences of any applied statistical decision. For the problem of background rejection in VHE $\gamma$-ray astronomy it is logical to define zero losses for correct classification:

$$c_{\gamma\tilde{\gamma}} = c_{h\tilde{h}} = 0. \tag{3}$$

If we misclassify a signal event, we decrease the acceptance efficiency for $\gamma$-ray events. At the same time if we erroneously attribute some cosmic ray event to a $\gamma$-ray event, we increase the background contamination. As we initially expect to observe a significant excess of background events over signal events, we are interested in very strong background suppression. Therefore it is reasonable to introduce a non-symmetric loss function for this case, for example:

$$c_{\gamma\tilde{h}} = 0.01, \qquad c_{h\tilde{\gamma}} = 0.99. \tag{4}$$

The dimension of the event entry space, $\mathcal{V}$ (measurements, features etc), is defined in our case by a number of measured image parameters. For example, one could measure the number of camera pixels with non-zero signal.

A prior measure $P_A \equiv (P_\gamma, P_h)$ is the assumed proportion of the $\gamma$-rays and cosmic rays in the raw data flow. The conditional densities or likelihood functions of image parameters $\mathbf{v} \subset \mathcal{V}$ are denoted as

$$\hat{p}(\mathbf{v}/\gamma), \qquad \hat{p}(\mathbf{v}/h). \tag{5}$$

These probability density functions can be estimated using the training samples and are in fact the main elements of the decision rule. Multivariate probability density estimation is a fundamental problem in data analysis, pattern recognition and even artificial intelligence. Naturally, we find that the estimation of the conditional density using simulations is a key problem in VHE $\gamma$-ray astronomy as well.

## 4. Bayesian decision rules

An optimal decision rule should minimize the mean losses, averaged over all possible statistical decisions. For the special selection of the loss function, equations (3) and (4), the correct

statistical decisions will not introduce any losses; therefore we have to select between two possibilities: to erroneously discard a $\gamma$-ray image, or to erroneously accept cosmic ray h-images as signal. The non-parametric Bayesian decision rule $\eta$ depends on the conditional densities, loss functions and on some prior measures, and has a generic form:

$$\tilde{\mathtt{A}} = \eta(\mathbf{v}, \mathtt{A}, \tilde{\mathtt{P}}) = \arg\{\min_i\{c_i\,\hat{p}(\mathtt{A}_i/\mathbf{v})\}, i = \gamma, h\}, \tag{6}$$

where $c_i$ is the loss connected to the decision $\tilde{\mathtt{A}}$. $\hat{p}(\mathtt{A}_i/\mathbf{v})$ is the non-parametric estimate of *a posteriori* density, which is connected to the conditional density by the Bayes theorem:

$$\tilde{p}(\mathtt{A}_i/\mathbf{v}) = \frac{P_i\,\hat{p}(\mathbf{v}/\mathtt{A}_i)}{\hat{p}(\mathbf{v})}, \tag{7}$$

where $\hat{p}(\mathbf{v}) = \hat{p}(\mathbf{v}/\gamma) + \hat{p}(\mathbf{v}/h)$.

Finally, substituting the *a posteriori* densities with the conditional[3] ones we get the Bayesian decision rule in the form:

$$\tilde{\mathtt{A}} = \arg\{\min_i\{c_i\,P_i\,\hat{p}(\mathbf{v}/\mathtt{A}_i)\}, i = \gamma, h\} \tag{8}$$

As one can easily see from equation (8) the Bayesian statistical decision depends on the product of $c_i\,P_i$. Therefore we cannot separate the influence of loss measure and prior measure on the decision rule. We will treat the multiplication $c_i\,P_i$ as a unique term and ascribe it as *a priori loss*. To investigate the influence of chosen values of *a priori* losses the event type evaluation procedure has been performed simultaneously using various variants of the a *priori* losses (see below). Examining the so-called *influence curves,* obtained for different losses, one can select the preferable regime of the decision rule. For instance, it is easy to control the ratio of the background suppression factor to the signal event acceptance.

## 5. Non-parametric probability density estimators

To estimate conditional densities we used here the Parzen method of the probability density estimation (Devroye and Gyorfi 1985, Parzen 1962) with an automatic choice of the kernel width (Chilingarian and Galfayan 1984). Several estimates of the probability density, which correspond to a number of Parzen kernel widths, were calculated simultaneously. Afterwards the sequence of all derived estimates was ordered according to the magnitude of the signal-to-noise ratio. The median entry of this sequence was chosen as a final estimate. Such an estimator of the probability density function (L-estimator) has apparent stabilizing properties for the final estimate by reason that the best estimate is chosen among a number of calculated ones (Efron 1981).

The Parzen kernel-type probability density is defined as

$$\hat{p}(\mathbf{v}/\mathtt{A}_i) = \frac{|\Sigma_i|^{-0.5}}{(2\pi)^{d/2}s^d}\sum_{j=1}^{M_i} \mathrm{e}^{-r_j^2/2s^2}\omega_j, \qquad i = 1, \ldots, L, \sum_{j=1}^{M_i}\omega_j = 1, \tag{9}$$

where $d$ is the dimension of the multi-parameter space, $M_i$ is the number of events in the $i$th training sample, $w_j$ are the event weights (e.g. the energy spectrum weights), $s$ is the kernel width (this the only free parameter which controls the smoothness of the estimate), $r_j$ is the distance from the experimentally measured event $\mathbf{v}$ to the $j$ th event of the training sample, $\mathbf{u_j}$, in the multi-parameter space using the Mahalanobis metric (Mahalonobis 1936):

$$r_j^2 = (\mathbf{v} - \mathbf{u}_j)^T \sum\nolimits_i^{-1} (\mathbf{v} - \mathbf{u}_j), \tag{10}$$

[3] The conditional density $f(x/A)$ is the density of a variable $x$ given any specific condition $A$, e.g. the type of the primary particle is a hadron.

where $\sum_i{}^{-1}$ is the sampling covariance matrix of the event class ($\gamma$-rays, cosmic rays) to which $\mathbf{u}_j$ belongs.

## 6. Bayes error estimation

The most natural measure of both the selection of a best subset of the features and the performance of the event type evaluation is the classification error probability. It depends in turn on both the degree of overlap of a few alternative multivariate distributions and the quality of the decision rule applied. It is worth noting that the Bayes decision rule provides the minimal classification errors as compared to any other decision rule strategy. Bayes errors can be calculated as follows:

$$R^B = E\{\theta[\eta(\mathbf{v}, \mathbf{A}, \mathbf{P})]\} = \int \theta p(\mathbf{v})\, \mathrm{d}\mathbf{v}, \tag{11}$$

where

$$\theta[\eta(\mathbf{v}, \mathrm{A}, \mathtt{P})] = \begin{cases} 1, & \text{otherwise} \\ 0, & \text{for correct classification} \end{cases} \tag{12}$$

and $\eta$ ($\mathbf{v}$, $\mathtt{A}$, $\mathtt{P}$) is the decision rule defined by equation (8).

The mathematical average is calculated for the whole $d$-dimensional feature space $\mathcal{V}$. In other words, the Bayes error is a measure of the overlap of alternative distributions of different event classes in the feature space $\mathcal{V}$, e.g. it gives a relative contribution of all *incorrectly* classified events. Since we do not know to which event class each particular individual event recorded in the experiment belongs, we can obtain an estimate of $R^B$ exclusively using the training samples $\mathbf{u}_j$:

$$\widehat{R}^B = E\left\{\frac{1}{M_{TS}} \sum_{i=1}^{M_{TS}} \theta[\eta(\mathbf{u}_i, \mathtt{A}, \widetilde{\mathtt{P}})]\right\}, \tag{13}$$

i.e. we classify the simulated events $\{\mathbf{u}_i\}, i = 1, M_{TS}$ and check the correctness of the classification. An average error is calculated over all possible samples of size $M_{TS}$. Many independent investigations have shown (e.g. Toussaint (1974)) that this estimate is systematically biased and hence, the so-called *one-leave-out-for-a-time* estimate is preferable:

$$\hat{R}^e = \frac{1}{M_{TS}} \sum_{i=1}^{M_{TS}} \theta\{\eta(\mathbf{u}_i, \mathtt{A}, \tilde{\mathtt{P}}_{(i)})\}, \tag{14}$$

where $(\mathtt{A}, \tilde{\mathtt{P}}_{(i)})$ is a training sample without the $i$th element, which is classified first and then *returned* back into the sample. This estimate is unbiased and essentially has a smaller mean squared deviation compared to other estimators (Snappin and Knoke 1984). The advantage of $\hat{R}^e$ is especially notable when the feature space is of high dimension. Note that we can estimate the erroneous classification probability by classifying various training sample classes. In this way we can estimate the expected $\gamma$-ray event acceptance efficiency and the cosmic ray contamination.

## 7. Estimates of the background rejection rates

After selecting the best single discriminate out of the image parameters (see figure 1) and the best pairs of discriminates using the technique first developed by Aharonian *et al* (1991), which is implemented in the applied statistical decision package ANI (Chilingarian 1989, 1998), the same parameters used for the image analysis of data taken with the 10 m Whipple

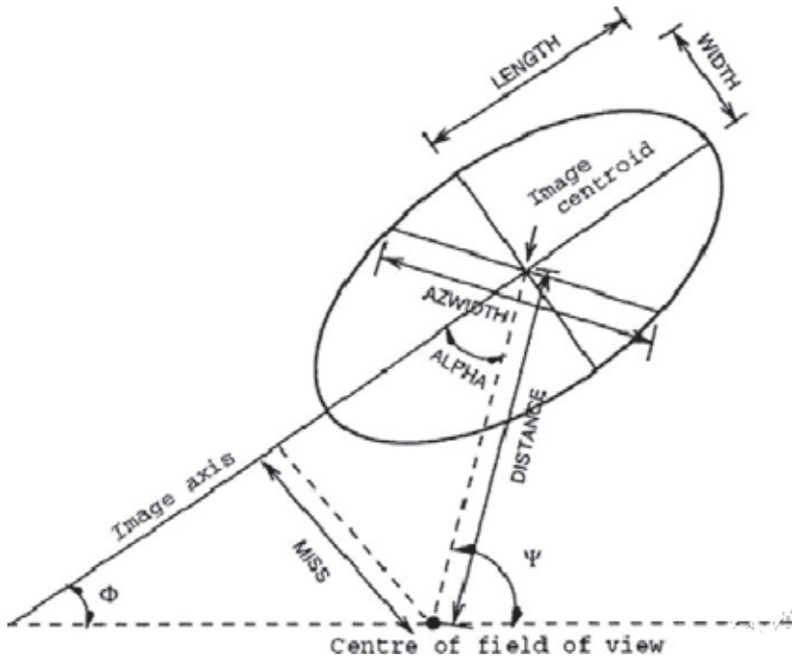


**Figure 1.** The second-moment parameters of the Cherenkov light image.

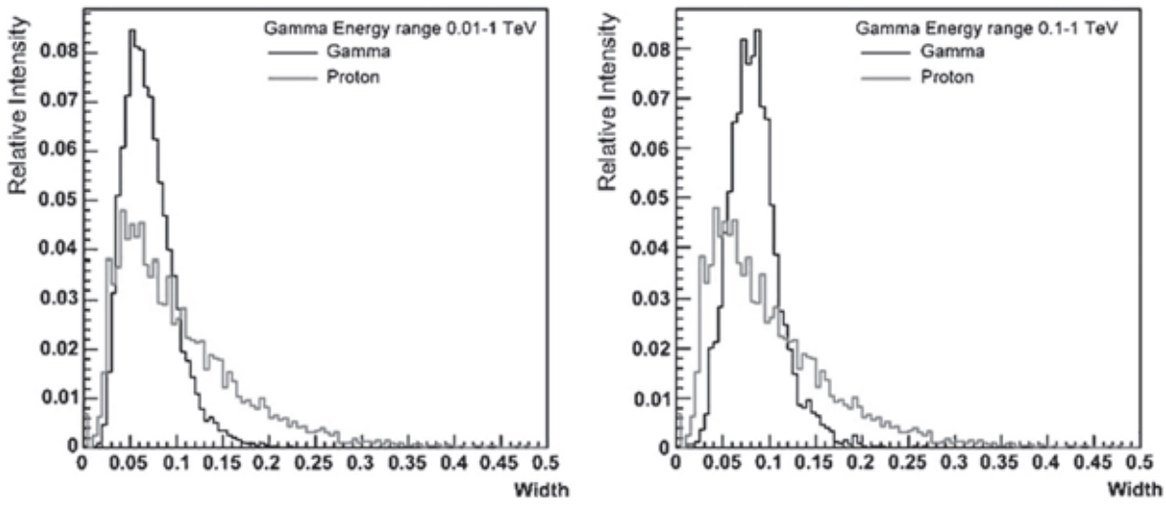


**Figure 2.** Illustration of the discrimination power between $\gamma$-rays and protons using a single image parameter, Width, in two energy intervals.

Collaboration telescope were proven to be the best (Aharonian *et al* 1991). They are the image shape parameters Width, Length, and the combined parameter of image shape and orientation, AzWidth. At the same time, as shown in figure 2, the single shape parameter Width cannot provide any significant discrimination for both the low- and high-energy $\gamma$-rays considered here.

Adding the second shape parameter length significantly improves the situation. One can see in figure 3 that for the images of high-energy events we can outline a two-dimensional domain where most of the $\gamma$-like events are included. Apparently the low-energy interval contains much more discrepant and diffuse images and is widely spread in the parameter

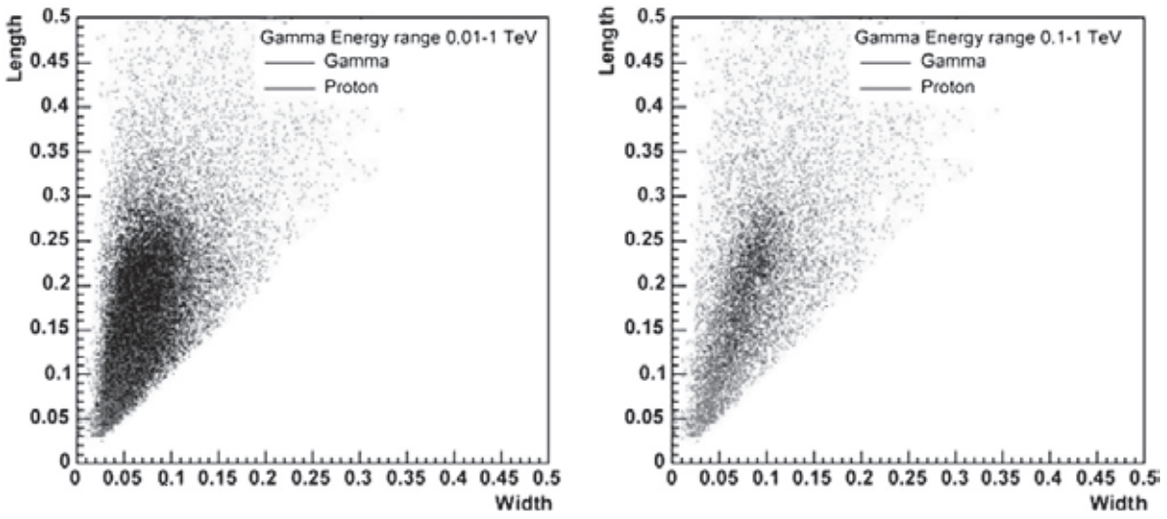


**Figure 3.** Illustration of the discrimination power between $\gamma$-rays and protons using simultaneously two image parameters, Width and Length, in two energy intervals.

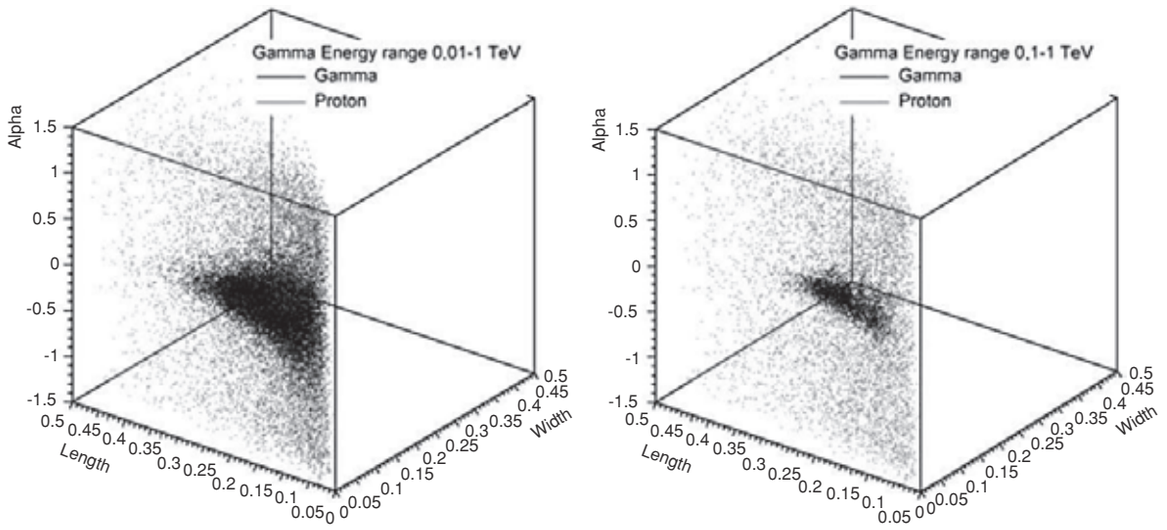


**Figure 4.** The $\gamma$-ray domain in the three-dimensional space of the image parameters.

space. As a result, the discrimination is much worse for those events as compared to the high-energy interval.

An additional orientation parameter, alpha, taken along with the shape parameters, Width and Length, substantially improves the situation and we can see compact $\gamma$-ray domains for both high- and low-energy events (see figure 4). Again the $\gamma$-ray domain for low-energy events is much larger. Nevertheless, the observed concentration of the $\gamma$-ray events might allow a treatment of the background rejection problem even for the low-energy events.

In figure 5 the best set of image parameters is shown. After applying a one-dimensional analysis, correlation analysis and the Bhattacharia distance minimization technique described by Aharonian *et al* (1991) we performed multiple calculations of the Bayes risk given in equation (13). Here we applied the Bayes decision rule equation (8) using the numerical approximation of the probability density function given in equation (9).

The results of calculations using different loss functions and two different energy intervals are summarized in figure 6. In the present analysis we used the overlapping energy intervals

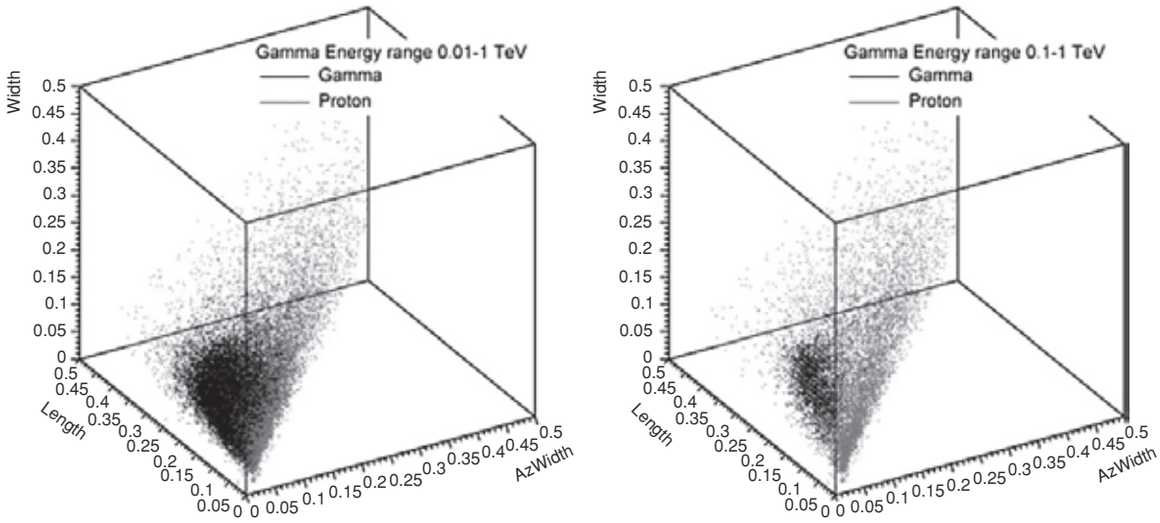


**Figure 5.** The $\gamma$-ray domain in the three-dimensional space of the image parameters. This domain provides a minimal Bayes error.

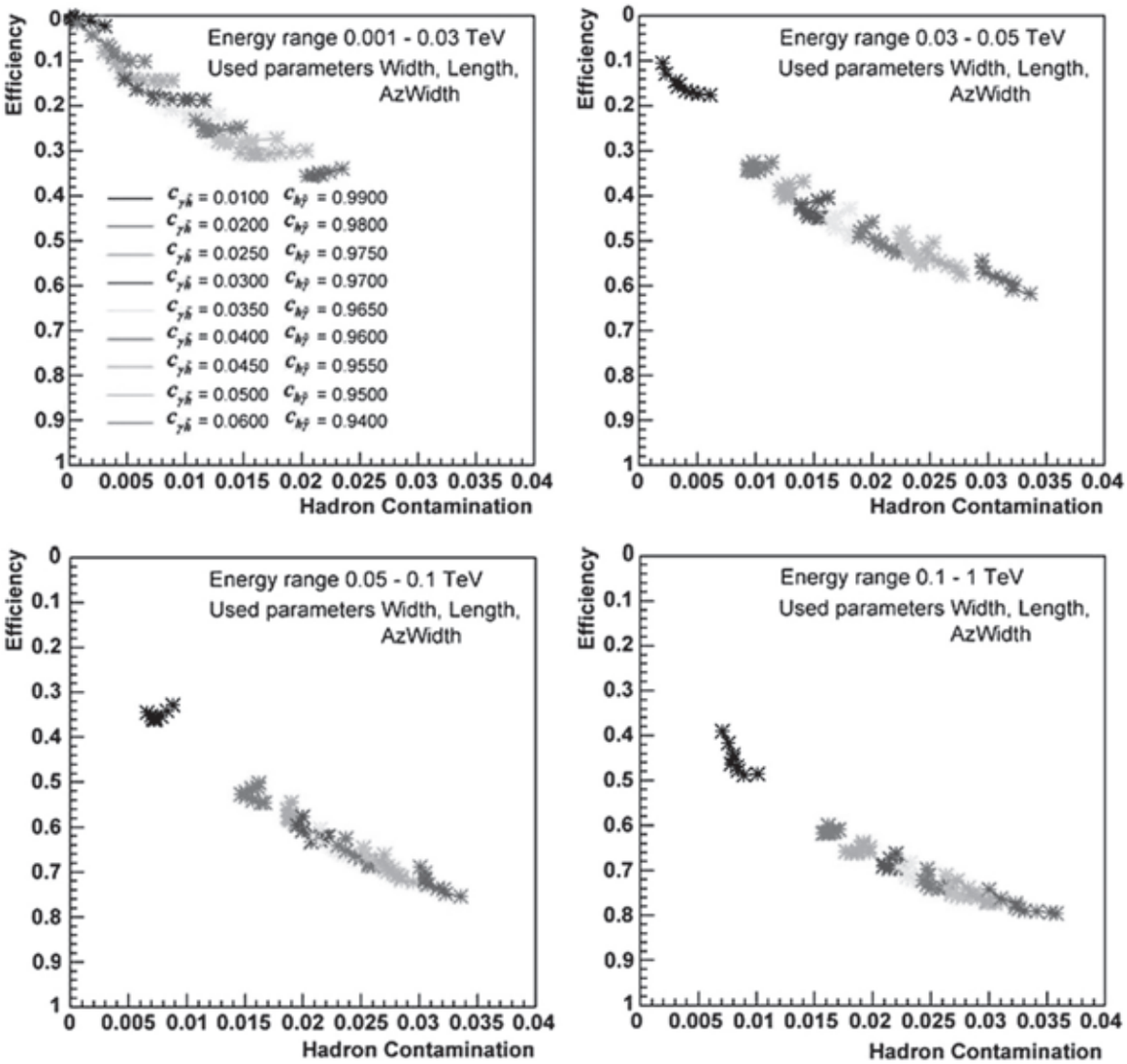


**Figure 6.** Comparison of the Bayesian risk estimates for four different energy intervals.

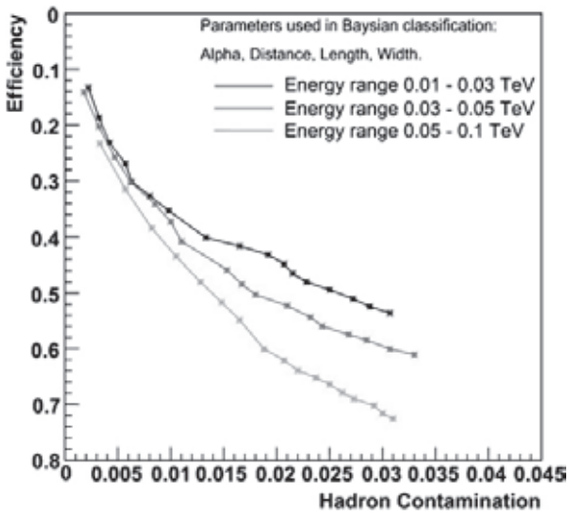


**Figure 7.** The influence curves for three different energy ranges of the simulated $\gamma$-rays.

but we have utilized the reconstructed energy for each individual event. For a power-law spectrum most of the triggered events occur right above the energy threshold, e.g. 10 or 100 GeV, so such an analysis clearly illustrates how the rejection power depends on shower energy. Figure 7 shows the so-called *influence curves*. By varying the $c_i$ parameter in equation (6) one can obtain the classification results for a number of different loss functions. It is the way to obtain the influence curve. The influence curve displays all possible combinations of the $\gamma$-ray acceptance efficiency and the corresponding cosmic ray background contamination. For instance, one can obtain a very high efficiency at the cost of a rather large background contamination or vice versa. For the high-energy interval it is possible to achieve a cosmic ray background rejection much less than 1% while keeping the acceptance of $\gamma$-rays at about 50%. The situation dramatically worsens at low energy. However, the discrimination is still possible even for the lowest energy interval of 10–30 GeV, where we can obtain a so-called $Q$-factor ($Q = \varepsilon_\gamma/\sqrt{\varepsilon_h}$, where $\varepsilon_\gamma$ is the $\gamma$-ray acceptance efficiency and $\varepsilon_h$ is the corresponding cosmic ray hadron contamination) of about 3.1. For higher energy ranges, 30–50 GeV and 50–100 GeV, the $Q$-factors are 3.8 and 4.2, respectively (see figure 7). It is worth noting that the image parameter AzWidth is directly related to the image orientation and the angular resolution of the telescope, which is about 0.3° at low energies. Such a modest angular resolution is a result of the large fluctuations in the development of the low energy shower, the geomagnetic field deflection of shower electrons and the rather low photoelectron content of these images. Note that currently achieved telescope pointing accuracy is less than 1 arc min, which is negligible compared with the actual angular resolution of the low-energy $\gamma$-rays.

## 8. Summary

The construction of a 30 m telescope in Namibia is currently ongoing. Such an instrument is strongly supported by various physics motivations for studying $\gamma$-rays around and above 20 GeV. The performance of this instrument greatly relies on the ability to extract the $\gamma$-ray signal out of the dominant cosmic ray background. Any possible further advancement in the analysis that may improve the performance of future $\gamma$-ray observatories is very important. Here we applied a multivariate analysis to the simulated data for a single stand-alone 30 m

imaging Cherenkov telescope. Despite the fact that we have used a complete Monte Carlo simulation of the telescope response, a few minor effects that might distort the performance of the telescope were not taken into account, such as detailed timing of reflected photons etc. However, the major results on the classification efficiency for a 30 m telescope of a specific hardware design should not largely deviate from the results obtained here.

A single imaging Cherenkov telescope does not allow very accurate measurement of the arrival direction of individual showers. A number of currently existing advanced methods of shower reconstruction for a single telescope become totally ineffective at low energies, such as 10 GeV. This fact can be explained by large fluctuations in the shape and orientation of the low energy images. Motivated by that, we applied here a set of image parameters that utilizes the difference in correlations between two basic parameters, Width and AzWidth, for the $\gamma$-ray and cosmic ray showers. One can directly apply the recommended combination of the image parameters to the forthcoming experimental data.

The results shown in figure 6 demonstrate that the discrimination power against a cosmic ray background substantially worsens at low energies. The maximum quality factor obtained for the $\gamma$-ray events in the energy range of 10–30 GeV is about 3.1. This value is significantly lower than the value achieved for the energy range above 100 GeV, which is about 7. Given a very steep predicted spectrum of $\gamma$-ray emission in the sub-100 GeV energy range for various sources (e.g. pulsars, distant AGN etc) a relatively modest rejection power could be compensated for by the enhanced statistics of the $\gamma$-rays. The situation could be substantially improved for a system of 3–5 identical 30 m telescopes operating in a stereoscopic mode. The discussion of an advanced multi-telescope analysis for observations of low-energy $\gamma$-rays with a system of a few 30 m IACTs will be the subject of a forthcoming paper.

## Acknowledgments

AK and AC are very thankful to Nikolai Pavel[4] for support of this project. AC would also like to thank Nikolai Pavel and all members of his group for hospitality during his stay at Institute of Physics of Humboldt-University of Berlin. AK would like to thank John P Finley for discussions on a subject of this paper.

## References

Aharonian F A, Chilingaryan A A, Konopelko A K and Plyasheshnikov A V 1990 On the possibility of an improvement of background hadronic showers discrimination against $\gamma$-ray coming from a discrete source by a multidimensional Cherenkov light analysis *Proc. 21 ICRC* (Adelaide) vol 4 p 246

Aharonian F A, Chilingarian A A, Konopelko A K and Plyasheshnikov A V 1991 A multidimensional analysis of the Cherenkov images of air showers induced by very high-energy $\gamma$-rays and protons *Nucl. Instrum. Methods* A **302** 522 (1989 *YerPhI preprint* 1171 (48)–79)

Chilingarian A A 1989 Statistical decisions under nonparametric a *priori* information *Comput. Phys. Commun.* **54** 381–90

Chilingarian A A and Cawley M F 1991 Application of multivariate analysis to atmospheric Cherenkov imaging data from the Crab nebula *Proc. 22 ICRC (Dublin)* vol 1 pp 460–3

Chilingarian A A and Galfayan S Kh 1984 Calculation of Bayes risk by KNN method, Stat *Probl. Control* **66** 66 Vilnius

Chilingarian A 1993 On the methods of the enhancement of the reliability of the signal detection with Cherenkov Atmospheric techniques *Izv. AN USSR, Phys.* A **57** 186

Chilingarian A A Analysis and Nonparametric Inference in High Energy Physics and Astroparticle Physics, 1998, program Package A N I (User's Manual, unpublished) http://crdlx5.yerphi.am/proj/ani

Devroye L and Gyorfi L 1985 *Nonparametric Density Estimation: The LI View* (New York: Wiley)

[4] Deceased.

Efron B 1981 Nonparametric standard errors and confidence intervals *Can. J. Stat.* **9** 139
Fix E and Hodges J L 1951 Discriminatory analysis. Nonparametric discrimination, consistency properties *Project 21-49-004, Report 4,USAF School of Aviation Medicine*
Fukunaga K and Himmels D 1987 Bayes error estimation using Parzen and KNN procedures *IEEE Trans.* **9** 634
Hofmann W 2005 *Proc. 29 Int. Cosmic Ray Conference (Pune, India)* vol 10 pp 97–114
Konopelko A 1999 Performance of the stereoscopic system of the HEGRA imaging air Cerenkov telescopes: Monte Carlo simulations and observations *Astropart. Phys.* **10** 275
Konopelko A and Plyasheshnikov A V 2000 ALTAI: computational code for the simulations of TeV air showers as observed with the ground-based imaging atmospheric Cherenkov telescopes *Nucl. Instrum. Methods Phys. Res.* A **450** 419–429
Konopelko A *et al* (for the HESS Collaboration) 2003 *Proc. 28th Int. Cosmic Ray Conf. (Tsukuba) (Tokyo: University of Academy Press)* p 2903
Konopelko A 2005 STEREO ARRAY of 30 m imaging atmospheric Čerenkov telescopes: a next-generation detector for ground-based high energy $\gamma$-ray astronomy *Astropart. Phys.* **24** 191–207
Lofsgaarden D O and Quesenberry C D 1966 A nonparametric estimate of a multi-variate density function *Ann. Math. Stat.* **36** 1049
Mahalonobis P C 1936 On the generalized distance in statistics *Natl Inst. India* **2** 49
Parzen E 1962 On estimation of a probability density function and mode *Ann. Math. Stat.* **33** 1065
Rabiner L R, Levinson E, Rozenberg A E and Wilpon J G 1974 Speaker—independent recognition of isolated words using clustering techniques *IEEE Trans. Acoustics, Speech, Signal Process.* **27** 336
Rosenblatt M 1957 Remarks on some nonparametric estimates of a density function *Ann. Math. Stat.* **27** 832
Snappin S M and Knoke J D 1984 Classification error rate estimators evaluated by unconditional mean squared error *Technometrics* **26** 371
Tapia R A and Thompson J R 1978 *Nonparametric Probability Density Estimation* (Baltimore: Johns Hopkins University Press)
Toussaint G T 1974 Bibliography on estimation of misclassification *IEEE Trans. Inf. Theor.* **IT-20** 472–9
Zhang S N and Ramsden D 1990 Statistical data analysis for $\gamma$-ray astronomy *Exp. Astron.* **1** 147
Weekes T C 2003 *Very High Energy Gamma Ray Astronomy* (Bristol: Institute of Physics Publishing)

The Astrophysical Journal, 603:L29–L32, 2004 March 1


# LIGHT AND HEAVY COSMIC-RAY MASS GROUP ENERGY SPECTRA AS MEASURED BY THE MAKET-ANI DETECTOR

A. Chilingarian, G. Gharagyozyan, G. Hovsepyan, S. Ghazaryan, L. Melkumyan, and A. Vardanyan
Cosmic Ray Division, Yerevan Physics Institute, Alikhanian Brothers 2, Yerevan 36, Armenia; chili@crdlx5.yerphi.am, gagik@crdlx5.yerphi.am, hgg@jerewan1.yerphi.am, ssk@crdlx5.yerphi.am, laura@crdlx5.yerphi.am, aro@crdlx5.yerphi.am
*Received 2003 November 14; accepted 2004 January 21; published 2004 February 12*

## ABSTRACT

Standard models of cosmic-ray origin link the space accelerators of our Galaxy to the supernova remnants (SNRs)—expanding shells driven by very fast blast waves, usually with gamma-ray pulsars near the morphological center. Energy spectra of fully stripped ions with charges from $Z = 1$ to $Z = 26$ can provide clues to the validity of the standard model. Unfortunately, smeared data from the extensive air shower experiments do not provide enough information for such ion "spectroscopy." Nonetheless, the measurement of energy spectra of two or three broad mass groups (so-called light, intermediate, and heavy) will allow us to prove or disprove the "rigidity-dependent" acceleration. Recently, using multidimensional classification methods, the "all-particle" spectra from the MAKET-ANI experiment on Mount Aragats, in Armenia, was categorized into two distinct primary mass groups. We present, for the first time, the light and heavy nuclei spectra from the MAKET-ANI experiment.

*Subject headings:* acceleration of particles — cosmic rays — supernova remnants

## 1. COSMIC RAYS IN THE VICINITY OF EARTH

The detected nonthermal radio emission from supernova remnants (SNRs), which led to the natural assumption of the presence of accelerated electrons, made SNRs the main candidate engine for particle acceleration (Koyama et al. 1995). Recent *Chandra* measurements of the X-ray distributions, obtained to very small spatial scale (Long et al. 2003), indicate a very large effective magnetic field of ~100 $\mu$G in SN 1006. In Berezhko, Ksenofontov, & Volk (2003), the authors conclude that such a large field could be generated only as a result of the nonlinear interactions of the accelerated protons and stripped heavier nuclei with self-generated Alfvén waves in a strong shock. Therefore, the SN 1006 data confirm the acceleration of the nuclear component at least until a few units of $10^{14}$ eV. Gamma-ray pulsars usually located near the SNR center are another candidate for the cosmic-ray acceleration (Bednarek & Protheroe 2002). As mentioned in Bhadra (2003), pulsar-accelerated cosmic rays are expected to have a very flat spectrum. Therefore, the impact of the nearest pulsar to energies higher than $10^{14}$ eV can be tremendous and can explain the fine structure of the energy spectrum, which may reflect acceleration of the specific groups of nuclei.

To investigate various scenarios of particle acceleration in SNRs, we still have to use indirect information contained in cosmic-ray spectra in the vicinity of Earth. The cosmic-ray flux incident on the terrestrial atmosphere consists mostly of protons and heavier stripped nuclei. Entering the atmosphere, primary cosmic rays initiate a cascade of secondary particles of lower energies, the so-called extensive air showers (EASs), covering a sizable surface on the Earth. Assuming a definite shape of the EAS electron lateral distribution function and measuring the density of electrons on some rectangular or circular grid of distributed particle detectors, we determine the overall number of EAS electrons (shower size). Simultaneously measuring the time delay of the arriving particles, we can calculate the zenith and azimuth angles of the inclined "shower particle disk," which is a very good estimate of the primary particle angles of incidence on the terrestrial atmosphere. The shower size is correlated with the particle energy but also with several unknown parameters, such as the particle type and the height of the first interaction. The functional form of size-energy dependence introduces additional uncertainty, because it is obtained from a particular model of the strong interaction of protons and ions with atmospheric nuclei. At PeV energies, there are no man-made accelerators to produce the data to check this model.

Nevertheless, during the last 50 years, some important characteristics of the particle spectra were established thanks to numerous measurements with EAS surface detectors. For the list of detectors and their operational characteristics, see Haungs, Rebel, & Roth (2003).

The most intriguing features are the slight bend or the "knee" of the spectra, the power index changing from $\gamma \sim -2.7$ to $\gamma \sim -3.0$ at 3–4 PeV, and the "ankle," occurring near $10^{18}$ eV. The MAKET-ANI installation (Avakian et al. 1986), owing to its modest size, has effectively collected the cores of EASs initiated by primaries with energies up to $(2–3) \times 10^{16}$ eV; therefore, we will constrain our analysis to the energy range $10^{15}$–$2 \times 10^{16}$ eV. Another modern experiment measuring the EASs in the knee region—KASCADE (Antoni et al. 2003b)—introduced the CORSIKA simulation code (Heck et al. 1998) as a universal tool for comparisons of simulations and experimental data. Developing the nonparametric multivariate methodology of data analysis (Chilingarian 1989), we solve the problem of event-by-event analysis of EAS data (Chilingarian & Zazyan 1991) using Bayesian and neural network information technologies (Chilingarian 1995; Bishop 1995). Proceeding from the MAKET-ANI energy spectra, we discuss the cosmic-ray origin model supported by our experimental evidence.

## 2. ENERGY SPECTRA

The MAKET-ANI experiment is located 3200 m above sea level. Therefore, the quality of the reconstruction of EAS size and shape is reasonably good, and we can use for EAS classification both shower size (Ne) and shape, adapting the so-called shower age ($s$) parameter. Our earlier studies of the $s$-

TABLE 1
POPULATION OF DIFFERENT NUCLEI IN LIGHT AND HEAVY GROUPS

| Group | H | He | O | Si | Fe |
|---|---|---|---|---|---|
| Light ..... | 0.407 | 0.298 | 0.137 | 0.111 | 0.047 |
| Heavy ..... | 0.162 | 0.167 | 0.208 | 0.255 | 0.208 |

parameter demonstrate that by choosing the appropriate *s* intervals, we can divide size spectra into two distinct classes, one demonstrating a very sharp knee and the second without the knee (Chilingarian et al. 1999). The distinctive information contained in the distributions of these two parameters allows us to classify the EASs with a high level of accuracy into only two distinct groups, initiated by "light" or "heavy" nuclei.

For neural network (NN) classification and energy estimation, we generate "training samples," i.e., Ne-*s* pairs, generated by the CORSIKA code (Heck et al. 1998) and the QGSJet strong interaction model (Kalmykov, Ostapchenko, & Pavlov 1997), taking into account the MAKET-ANI response function described by G. G. Hovsepyan.[1] In the light mass group, we include showers initiated by protons and helium nuclei; in the heavy mass group, by silicon and iron nuclei. We did not include intermediate O nuclei in the NN training procedure because distinctive values of our measurements did not allow classification of registered showers in three groups; the contamination of showers initiated by the oxygen nuclei was investigated (see Tables 1 and 2).

Before the neural classification of the MAKET-ANI data, we investigate the expected purity[2] and efficiency[3] of the data analysis procedures. The purification of the selected light and heavy groups was done by selecting the appropriate domain in the entire range of the network output. The feed-forward NN performs a nonlinear mapping of the multidimensional characteristics of the EASs to the real number interval [0, 1], called the output of the NN. Figure 1 shows the network output histogram. The network was trained to shift the heavy group to the right and the light group to the left of the histogram. The 0.5 point of the NN output is the so-called decision point. The particular class assignments for the two-way classification are the subintervals [0.0, 0.5] and [0.5, 1.0] for the light and heavy class, respectively. If the NN is satisfactorily trained to have generalization capabilities, the output distributions for the different classes will overlap at the subinterval boundaries. Therefore, by shrinking the subintervals—i.e., moving the interval boundary to the left and right of the decision point 0.5—it is possible to remove a large proportion of the misclassified events. Of course, simultaneously we lose parts of the true classified events, i.e., decrease the efficiency. Thus, instead of one decision point in the middle of the NN output interval, we will have two "decision intervals" for accepting light and heavy nuclei and a third interval in between where we reject the classification. Figure 1 demonstrates this "purification" procedure. Figure 2 shows the results of the purification. The values next to the symbols indicate the selected decision interval used for obtaining a particular purity-efficiency relation. For example, if we select the [0.0, 0.3] and [0.7, 1.0] intervals for classification of the light and heavy nuclei, we obtain 96% purity and 56% efficiency for the light class and 78% purity and 55% efficiency for the heavy class. Therefore, we can enhance the purity of the light nuclei up to 95% and the purity of the heavy nuclei up to 80%, while still holding the efficiency above 50%. The purity and the efficiencies are obtained by

[1] See the ANI collaboration report 3 at http://crdlx5.yerphi.am/ani/ani_collab.html.

[2] The fraction of the true classified events in the actual number of events assigned to a given class.

[3] The fraction of the true classified events in the total number of events of a given class.

TABLE 2
POPULATION OF DIFFERENT NUCLEI IN LIGHT AND HEAVY GROUPS (AFTER PURIFICATION)

| Group | H | He | O | Si | Fe |
|---|---|---|---|---|---|
| Light ..... | 0.459 | 0.310 | 0.115 | 0.084 | 0.032 |
| Heavy ..... | 0.115 | 0.131 | 0.207 | 0.278 | 0.268 |

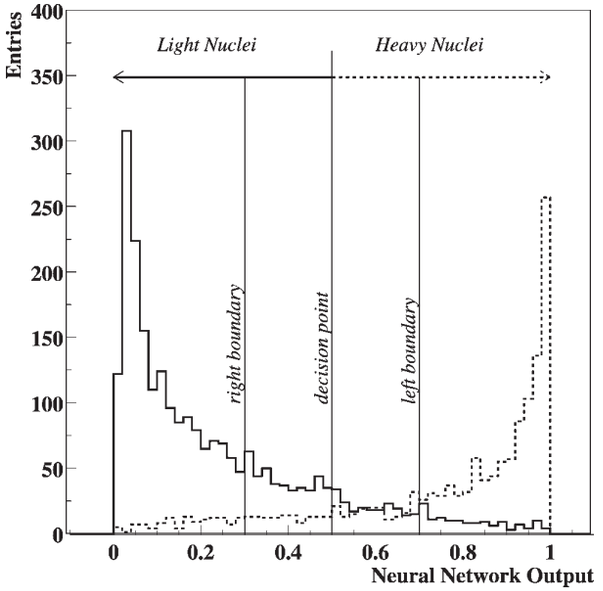


FIG. 1.—Output of the NN trained to distinguish light and heavy nuclei

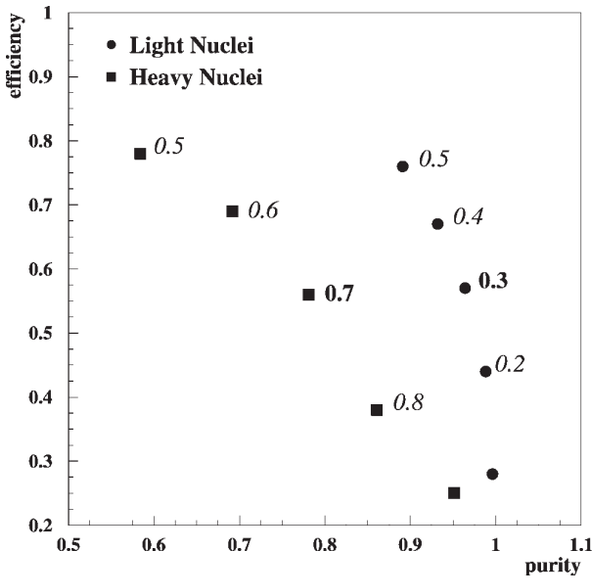


FIG. 2.—Efficiency vs. purity for the classification of EASs initiated by light and heavy nuclei. The numbers near the symbols designate the decision intervals.

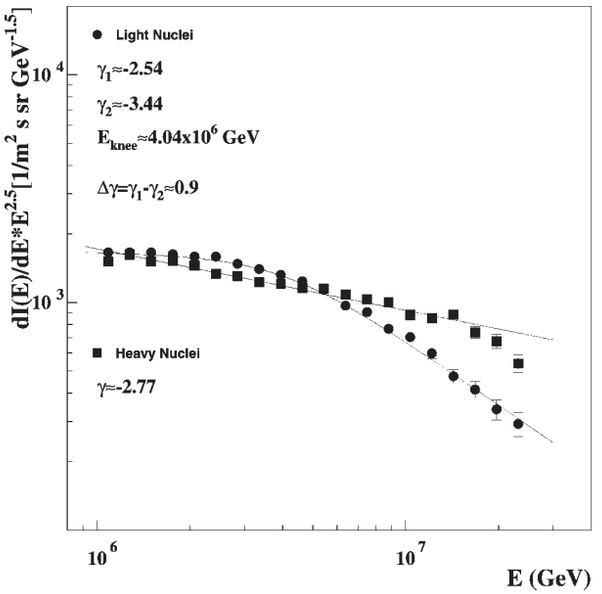


FIG. 3.—Energy spectra of light and heavy nuclei obtained by neural classification and energy estimation. The EAS characteristics used are shower size and shape (age).

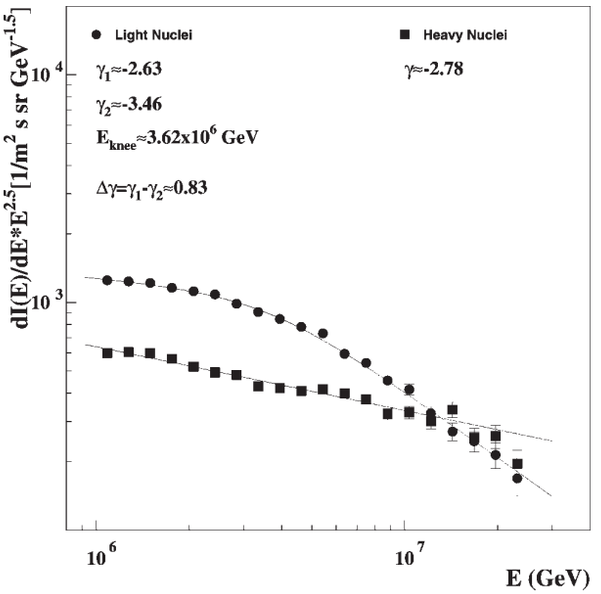


FIG. 4.—Same as Fig. 3, but obtained with purified light and heavy data samples. Purification intervals are [0.0, 0.3] and [0.7, 1.0].

classifying ~35,000 light (H, He) and ~17,000 heavy (Si, Fe) control events, which are not used for the training of the NN.

To understand how the light and heavy classes are "populated" by different nuclei, we assume an arbitrary mass composition of 30% H, 24% He, 17% O, 17.5% Si, and 11.5% Fe. The results of the classification of this mixture are posted in Tables 1 and 2. From the Tables, we see in more detail how the purification procedure works and how the intermediate oxygen nuclei is distributed among light and heavy classes. Also, we can estimate the "mean charge" of the alternative classes:

$$\frac{Z_{\rm heavy}}{Z_{\rm light}} = \frac{11.14}{4.87} \sim 2.29, \quad (1)$$

and after purification,

$$\frac{Z^p_{\rm heavy}}{Z^p_{\rm light}} = \frac{12.9}{4.0} \sim 3.23. \quad (2)$$

Of course, the obtained relations are model-dependent and can be used only as a first approximation.

After checking for the purity and the efficiency, each of the near 1 million showers registered by the MAKET-ANI installation in 1999–2002, with shower size greater than $10^5$, was classified according to the techniques described in Chilingarian & Zazyan (1991) and Antoni et al. (2003a). The energy of the two distinct classes of showers was estimated for each group separately using again the CORSIKA simulations and neural estimation techniques. In Figure 3, we present the obtained energy spectra of the light and heavy mass groups. The spectrum of the light group shows a knee in the region of (3–4) $\times$ $10^{15}$ eV. The knee feature is not observed for the spectrum of the heavy component at least until energies of $10^{16}$ eV. The number of light and heavy nuclei at ~$10^{15}$ eV are approximately equal, and the number of heavy nuclei gets larger at energies greater than the knee energy.

The purified spectra shown in Figure 4 demonstrate the lower flux intensities for both classes of particles due to the lower efficiency. The knee position shifts to lower energies, as we expect that after purification the proportion of protons is enlarged. In addition, the slope of the spectrum (spectral index) of the purified light component becomes steeper: $\gamma = -2.63$, compared to $\gamma = -2.54$ before purification. Both results are consistent with the rigidity-dependent acceleration and consequent fading of the proton flux at high energies.

Another important feature of the obtained spectra is the very large difference between spectral indices before and after the knee: $\Delta\gamma(\text{light}) = \gamma_2 - \gamma_1 \sim 0.9$. It is well known that the same parameter for the all-particle spectra is $\Delta\gamma(\text{all-particle}) \sim 0.3$ (Haungs et al. 2003). Erlykin & Wolfendale, in their simulations, failed to reproduce the actual shape of the all-particle spectrum by averaging the proton and nuclei fluxes produced by nearly 50,000 distant supernovae in our Galaxy (Erlykin & Wolfendale 2001). Therefore, they propose that the nearby young supernova (<500 pc and <110 kyr) is responsible for approximately 60% of the detected cosmic-ray flux in the vicinity of Earth (Erlykin & Wolfendale 2003). The very large difference of the spectral indices before and after the knee of the light component (~0.9) confirms the proposal of Erlykin & Wolfendale regarding the huge impact of the nearest supernova on the cosmic-ray flux in the vicinity of Earth. It suggests the necessity of making detailed calculations of the influence of the nearest supernova on the detected cosmic-ray fluxes, i.e., obtaining the partial spectra of the nuclei accelerated by the single source (for candidates of such source, see Thorsett et al. (2003).

## 3. CONCLUSIONS

The MAKET-ANI data allow us to summarize the experimental evidence in the following statements:

1. The energy spectrum of the heavy mass group of cosmic rays shows no knee in the energy interval of $10^{15}$–$10^{16}$ eV. Fine structure of the energy spectrum above $10^{16}$ eV is con-

sistent with that estimated from the "second knee" position of equations (1) and (2), although for a firm conclusion we need to prolong the energy spectrum until $5 \times 10^{16}$ eV.

2. The estimated energy spectrum of the light mass group of nuclei shows a very sharp knee: $\Delta\gamma \sim 0.9$, compared to $\sim$0.3 for the all-particle energy spectra.

Proceeding from the experimental evidence, we conclude that:

1. The SNR acceleration model is supported by the MAKET-ANI data on partial energy spectra.

2. The nearest SNR produces a significant portion of the high-energy cosmic rays in the knee region.

The data collected by the MAKET-ANI detector from 1997 to 2002 is the property of the ANI collaboration. We thank the ANI collaboration members for their fruitful cooperation over many years. This work was supported by Armenian government grant 1465, by the ISTC grant A216, and by the INTAS grant IA-2000-01.

REFERENCES

Antoni, T., et al. 2003a, Astropart. Phys., 19, 715
———. 2003b, Nucl. Instrum. Methods Phys. Res., 513, 409
Avakian, V. V., et al. 1986, Vopr. Atomnoj Nauki Tekh. Ser. Tech. Phys. Exp., 5(31), 1
Bednarek, W., & Protheroe, R. J. 2002, Astropart. Phys., 16, 397
Berezhko, E. G., Ksenofontov, L. T., & Volk, H. J. 2003, A&A, 412, L11
Bhadra, A. 2003, Proc. 28th Int. Cosmic Ray Conf. (Tsukuba), 303
Bishop, C. M. 1995, Neural Networks for Pattern Recognition (New York: Oxford Univ. Press)
Chilingarian, A. A. 1989, Comput. Phys. Commun., 54, 381
———. 1995, Pattern Recognition Lett., 16, 333
Chilingarian, A. A., & Zazyan, H. Z. 1991, Nuovo Cimento C, 14, 555
Chilingarian, A. A., et al. 1999, in Proc. Workshop ANI 99, ed. A. A. Chilingarian, A. Haungs, H. Rebel, & H. Z. Zazian, FZK preprint (6472)
Erlykin, A. D., & Wolfendale, A. W. 2001, J. Phys. G, 27, 941
———. 2003, in Proc. 28th Int. Cosmic Ray Conf. (Tsukuba), 2349
Haungs, A., Rebel, H., & Roth, M. 2003, Rep. Prog. Phys., 66, 1145
Heck, D., Knapp, J., Capdevielle, J. N., Shatz, G., & Thouw, T. 1998, CORSIKA: A Monte Carlo Code to Simulate Extensive Air Showers (FZKA 6019; Karlsruhe: Forschungszentrum Karlsruhe)
Kalmykov, N. N., Ostapchenko, S. S., & Pavlov, A. I. 1997, Nucl. Phys. B, 52, 17
Koyama, K., Petre, R., Gotthelf, E. V., Hwang, U., Matsuura, M., Ozaki, M., & Holt, S. S. 1995, Nature, 378, 255
Long, K. S., Reynolds, S. P., Raymond, J. C., Winkler, P. F., Dyer, K. K., & Petre, R. 2003, ApJ, 586, 1162
Thorsett, S. E., Benjamin, R. A., Brisken, W. F., Golden, A., & Goss, W. M. 2003, ApJ, 592, L71

The Astrophysical Journal, 597:L000–L000, 2003 November 10


# DETECTION OF THE HIGH-ENERGY COSMIC RAYS FROM THE MONOGEM RING

A. Chilingarian, H. Martirosian, and G. Gharagyozyan
Cosmic Ray Division, Yerevan Physics Institute, Alikhanian Brothers 2, Yerevan 36, Armenia;
chili@crdlx5.yerphi.am, hmart@crdlx5.yerphi.am, gagik@crdlx5.yerphi.am
*Received 2003 August 25; accepted 2003 September 30; published 2003 October 21*

## ABSTRACT

The MAKET-ANI detector reveals significant excess of extensive air showers with arrival directions pointed to the Monogem ring, a supernova remnant located at a distance of ≈300 pc from the Sun with ≈100 kyr old radio pulsar PSR B0656+14 near the center. The chances that this excess is due to the fluctuations of an isotropic flux is 2 per million. For the search of the cosmic-ray source, we use the MAKET-ANI detector data from years 1997 to 2003. The best signal bin coordinates, right ascension $7^h.5$, declination 14° (750+14), significantly deviate from the ring morphological center, shifted in the direction of the most intensive X-ray emission from the supernova remnant's limb, now located 66 pc from the supernova remnant center and 27 pc from the candidate source.

*Subject headings:* acceleration of particles — cosmic rays — supernova remnants

## 1. INTRODUCTION

The most exciting problem connected with cosmic rays is the exploration of a particular accelerating astrophysical source. Unfortunately, owing to the bending in Galactic magnetic fields, charged particles lose information about parent sites during the long travel and arrive at Earth highly isotropic. The supernova (SN) explosions are the most popular candidates for acceleration sites. The problem is in understanding how the Galactic "ensemble" of SNe maintains the cosmic-ray flux in the vicinity of Earth. The fine structure of all-particle spectra at the "knee" suggests the hypothesis that one or several recent nearby SNe are responsible for the observed spectra structures (Erlykin & Wolfendale 1997, 1998). Therefore, identifying such an SN and measuring the flux of particles from its direction will be the best proofs of the most popular model of hadron acceleration.

Very long baseline interferometric measurements of the ≈100 Kyr old pulsar PSR 656+14 (Brisken et al. 2003) locate the pulsar near the center of the supernova remnant (SNR) called the Monogem ring at ≈300 pc from the Sun. It was logical to assume that the Monogem ring, the shell of debris from an SN explosion, was the remnant of the blast that created the pulsar (Thorsett et al. 2003). The position and age of the SNR perfectly fit the single source (SS) model (Erlykin & Wolfendale 2003), and following the recommendation in Thorsett et al. (2003), we "scanned" the Monogem ring with high-energy cosmic rays detected by the MAKET-ANI detector (Chilingarian et al. 1999) at Mount Aragats in Armenia (N40°30′, E44°10′).

We choose high-energy particles, not deflected significantly by the Galactic magnetic fields. More than 2,000,000 extensive air showers detected by the MAKET-ANI experiment with size greater than $N_e > 10^5$ [primary energy >(3–4) × $10^{14}$ eV] were selected for the search of the cosmic-ray point source. Two-dimensional grids were generated in equatorial coordinates with the bin center tuned in the direction of the Monogem ring center (circle of $9^\circ.2$). The best signal was obtained with bin center coordinates of 750+14 and bin size 3° × 3°. The selected direction corresponds to the detector looking at the zenith coordinates of ≈28°, where the MAKET-ANI zenith angular accuracy is ≈1°.5 and azimuth angle estimation accuracy is about 3° (Chilingarian et al. 2001). Shower cores were collected from an area of 18 × 36 $m^2$ around the rectangular central area of the detector. The shower age parameter was selected in the range of 0.3–1.7.

## 2. SIGNAL FINDING AND SIGNIFICANCE TESTS

After analyzing more than 2 million events with $N_e > 10^5$, we test different locations of the source within the Monogem ring using different cuts on shower size. Results are summarized in Figures 1 and 2 and Tables 1 and 2. From the analyses, we determine the declination band where the candidate source is located ($\delta_j$ = $12^\circ.5$–$15^\circ.5$). In the right ascension (R.A.) bin distribution (Fig. 1), we see a large peak corresponding to the R.A. bin of 7.4–7.6 hr.

We use the R.A. scan method for confirming the existence of the cosmic-ray point source. The background events were taken from the mean value of other R.A. bins in the same declination band (in our case, 120 rectangular R.A. bins in each of 20 declination bands of 3°). The significance of the source was calculated by

$$\sigma_{i,j} = \frac{N_{i,j} - \bar{N_j}}{\sqrt{\bar{N_j}}}, \quad i = 1, N_\alpha, 3, \quad j = N_{\delta 1}, N_{\delta 2}, 3, \quad (1)$$

where $N_{i,j}$ is the number of events in the equatorial coordinates bin (window), $N_\alpha$ = 360 is the range of R.A., $N_{\delta 1}$ = 6 is the first declination, and $N_{\delta 2}$ = 66 is the last declination, for a total of 20 declination "bands;" $N_j$ is the band-averaged number of events in the bin.

We are looking for SS candidates in the two-dimensional $\Delta\alpha \times \Delta\delta$ (3° × 3°) grid, covering a 360° × 60° equatorial coordinate range with 2400 bins. We assume that for $j$th declination belt, the number of events that fall in each R.A. bin is a random variable obeying the Gaussian distribution with parameters $N[N_j, (N_j)^{1/2}]$. We calculated the R.A. bin average (over 120 bins) and used its square root as a measure of the background variance for this particular declination. To integrate information from all declination bands, we perform normalization transformation (eq. [1]) and obtain joint distribution for all declination bins. As is usual in statistical hypothesis testing, the main hypothesis we want to check (named $H_0$) exists in opposition to the hypotheses in which we are interested; i.e., we will check the hypothesis that the arrival of the particles detected by the MAKET-ANI detector is isotropic ("no-signal"

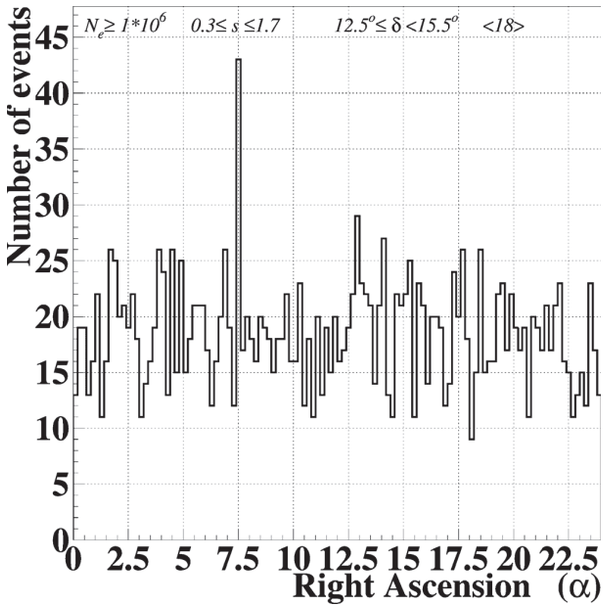


FIG. 1.—Distribution of the number of events in each of 120 R.A. bins for the declination band of 12°.5–15°.5.

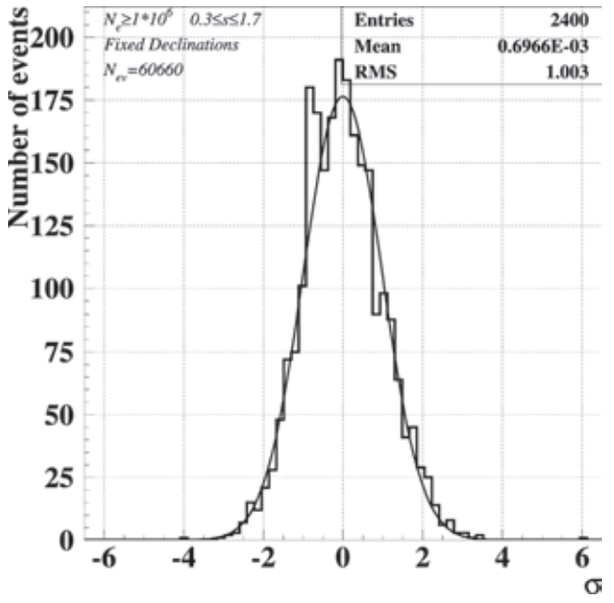


FIG. 2.—Signal significance test with full equatorial coverage with 2400 3° × 3° bins; $N_e > 10^6$.

hypothesis) and, therefore, that the detected enhancement in the "signal bin" is simple random fluctuation of the isotropic background. We are interested in the rejection of $H_0$ with the maximal possible confidence. Detecting a large peak, we estimate a very low probability of $H_0$ being true, but, of course, it does not imply that the opposite hypothesis is automatically valid. As was mentioned by Astone & D'Agostini (1999), behind the logic of standard hypothesis testing is hidden a revised version of the classical proof by contradiction. "In standard dialectics, one assumes a hypothesis to be true, then looks for a logical consequence which is manifestly false, in order to reject the hypothesis. The slight difference introduced in classical statistical tests is that the false consequence is replaced by an improbable one." If the experimental histogram will not differ significantly from test distribution, we will have no reason to reject $H_0$ and, therefore, our results will support the hypothesis that the detected peak is statistical fluctuation only. If the experimental histogram significantly deviates from the test distribution, we will be able to reject $H_0$ and accept with a high level of confidence that detected enhancement is due to the additional cosmic rays from the Monogem ring. According to the logic described above, we calculate the test statistics by applying equation (1) to the experimentally detected showers and using the equatorial grid covering all directions seen by the MAKET-ANI detector. As we can see from Figure 2, the shape of the cumulative distribution is very close to the standard Gaussian distribution $N(0, 1)$; the $\chi^2$ test value is 1.5 per degree of freedom. Only one point from 2400 (corresponding to the Monogem ring direction) deviates from the $N(0, 1)$ distribution. Proceeding from this experimental result, we adopt the hypothesis of isotropic background in 2399 bins and signal mixed with background in one bin. From the obtained value of $\sigma = 6.04$ for this particular signal bin, we calculate the corresponding probability of obtaining this value under the $H_0$ hypothesis to be $2 \times 10^{-6}$. The null hypothesis could be true only in two cases out of a million; therefore, we have good reason to reject the null hypothesis and conclude that the MAKET-ANI detector detected high-energy cosmic rays from the direction of the Monogem ring.

For more details about signal dependence on shower size, we calculate the number of events that fall in the signal bin for different $N_e$ cuts. The best estimate of the number of signal events equals the difference between the number of events in the signal bin and the mean number of events in the considered declination band ($N_s \approx N_{750+14} - N_{\text{background}}$). This estimate is a random variable with variance controlled by the variance of the background. Table 1 demonstrates that the estimated number of signal events remains approximately constant after shower size cuts from $N_e > 5 \times 10^5$ up to $N_e = 10^6$ and fades rapidly thereafter.

TABLE 1

DEPENDENCE OF THE SIGNAL VALUE ON SHOWER SIZE CUT

| $N_e$ | Number of Events in Declination Band $\delta_j$ = 12°.5–15°.5 | Mean Number of Events in R.A. = 3° Bin (Background) | Number of Events in R.A. = $7^h.4$–$7^h.6$ Signal Bin | Number of Signal Events |
|---|---|---|---|---|
| $>10^5$ ..... | 73382 | 611 | 663 | 52 ± 35 |
| $>5 \times 10^5$ ..... | 7123 | 58 | 84 | 26 ± 11 |
| $>8 \times 10^5$ ..... | 3282 | 26 | 57 | 31 ± 7 |
| $>10^6$ ..... | 2225 | 18 | 43 | 25 ± 6 |
| $>2 \times 10^6$ ..... | 573 | 4 | 13 | 9 ± 3 |

TABLE 2
COSMIC-RAY SOURCE LOCALIZATION AROUND THE CENTER OF THE SIGNAL BIN

| Bin Size ($\alpha \times \delta$) | Number of Events in the Chosen Declination Band | Mean Number of Events in R.A. = 3° Bin (Background) | Number of Events in Signal Bin | Number of Signal Events |
|---|---|---|---|---|
| 1 × 1 ..... | 744 | 2 | 11 | 9 ± 2 |
| 2 × 2 ..... | 1468 | 7 | 22 | 15 ± 4 |
| 3 × 3 ..... | 2225 | 18 | 43 | 25 ± 6 |
| 4 × 4 ..... | 2952 | 32 | 48 | 16 ± 8 |
| 5 × 5 ..... | 3739 | 51 | 71 | 20 ± 10 |

Another test concerns the influence of the chosen bin size on the signal significance. From Table 2, we can conclude that the 3° × 3° bin size provides the best coverage of the signal domain. Enlarging the bin size leads to the reduction of the signal due to the enlarged fluctuations of background, but the number of signal events remains approximately constant. The statistical errors in Table 2 illustrate that the number of signal events obtained in the "best confidence" bin and equal to 25 is consistent with both enlarging the bins and lowering the shower size cut. Nevertheless, we did not claim that 25 is the best estimate of the signal; for checking the statistical hypothesis on the best signal value we need to tune more precisely the shape of the signal domain using neural network techniques described in Chilingarian (1995).

## 3. CONCLUSIONS

The MAKET-ANI experiment detects significant excess of particles from the direction of the Monogem ring with a chance fluctuation probability of 2 per million. Position of the cosmic-ray source, 750+14, is consistent with the SN shock propagation. These conclusions lead us to accept the Monogem ring SNR as the universal source of particles with energy up to at least $3 \times 10^{15}$ eV. For estimating the source energy spectra, we need a more precise estimation of the type and energy of the SS particles, now underway with methodology proposed in Chilingarian (1989) and Chilingarian & Zazian (1991).

The data collected by the MAKET-ANI detector from 1997 to 2003 are the property of the ANI collaboration. This publication primarily reflects the opinion of its authors. We thank ANI collaboration members for multiyear fruitful cooperation and scientific discussion. The authors also thank Gagik Hovsepyan for numerous cross-checks of the reported results. Work was supported by the Armenian government grants, by grant ISTC A216, and by grant INTAS IA-2000-01.

## REFERENCES

Astone, P., & D'Agostini, G. 1999, preprint (hep-ex/9909047)
Brisken, W. F., Thorsett, S. E., Golden, A., & Goss, W. M. 2003, ApJ, 593, L89
Chilingarian, A. A. 1989, Comput. Phys. Commun., 54, 381
———. 1995, Pattern Recognition Lett., 16, 333
Chilingarian, A. A., & Zazian, H. Z. 1991, Nuovo Cimento C, 14, 555
Chilingarian, A. A., et al. 1999, Proc. 26th Int. Cosmic Ray Conf. (Salt Lake City), 1, 240
Chilingarian, A. A., et al. 2001, Proc. 27th Int. Cosmic Ray Conf. (Hamburg), 2, 540
Erlykin, A. D., & Wolfendale, E. W. 1997, J. Phys. G, 23, 979
———. 1998, Astropart. Phys., 8, 265
———. 2003, Proc. 28th Int. Cosmic Ray Conf. (Tsukuba), 2349
Thorsett, S. E., Benjamin, R. A., Brisken, W. F., Golden, A., & Goss, W. M. 2003, ApJ, 592, L71

Available online at www.sciencedirect.com
SCIENCE DIRECT®
Astroparticle Physics 25 (2006) 269–276
Astroparticle Physics
www.elsevier.com/locate/astropart

# Statistical methods for signal estimation of point sources of cosmic rays

A. Chilingarian *, G. Gharagyozyan, G. Hovsepyan, G. Karapetyan

*Cosmic Ray Division, Alikhanyan Physics Institute, Alikhanyan Brothers 2, 375036 Yerevan 36, Armenia*

Received 3 November 2005; received in revised form 3 February 2006; accepted 20 February 2006
Available online 20 March 2006

**Abstract**

The estimation of the significance of the peaks in one- and two-dimensional distributions is one of the most important problems in high-energy physics and astrophysics. The physical inference from low-statistics experiments usually is biased and many discoveries lack further confirmation. One of the typical mistakes in physical inference is the use of non-adequate statistical models. We analyze the significance of the experimental evidence in the on-going efforts of detecting the point source of cosmic rays. We found that simple statistical models (Gaussian or Poisson) did not adequately describe the experimental situation of point source searches. To avoid drawbacks related to usage of the incorrect statistical model, we introduce new extremum statistical models appropriate for the point source searches. The analysis is conducted in the framework of two models utilizing extremum statistics: first – using the fixed grid of celestial coordinates, and second – using the tuned grid (introducing more degrees of freedom in the search). The test distributions for the significance estimation are obtained both from simulation models and from the analytical model of extremum statistics. We show that the second model gives adequate physical inference, while the first model can lead to the positively biased conclusions of the point source significance.


*Keywords:* Statistical inference; Extremum statistics; Cosmic rays; Point sources

## 1. Introduction

Searches of the cosmic ray sources is one of the most promising ways to gain insight in the long-standing problem of the origin of these particles. While many experiments have shown that the distribution of arrival directions are isotropic [2 and references therein, 3], existence of the small-angle anisotropies has been claimed by several groups in the "knee" energy region $10^{14}$–$10^{16}$ eV [18,7] and the ultrahigh energy range $>10^{19}$ eV [20].

Physicists usually attribute considerably greater than statistically expected positive fluctuation to a "source". However, experience has shown that large excesses, up to $6\sigma$, are more common than were expected [14]. When consistent and reliable statistical tests are applied we cannot obtain convincing proof for point sources. It was demonstrated in 1973 that the evidence for many of the claimed $\gamma$-ray sources, when properly treated, is rather weak [16]. Another striking illustration of the importance of accurately assessing the significance of peaks embedded in the low statistics, high background experiments is the "discovery" of the so-called pentaquark particle, which contains four quarks and one antiquark, according to the claims. In 2003 physicists from many laboratories around the world made headlines, announcing that they had found a new particle. There were above 10 particle detections reported with very high confidence level of 5 and even $6\sigma$. Unfortunately, new experiments with better statistics do not confirm existence of the new particle. The "overwhelming body of negative evidence" indicates that the pentaquark might be an artifact [19].

Therefore, in the search of the point sources or new particles, the most important is to prove that observed excess is not background fluctuation only or systematic effect introduced by the detector. Positive excess of counts is compared with mean value of background count rate and

* Corresponding author. Tel.: +374 1 344 377.
*E-mail address:* chili@crdlx5.yerphi.am (A. Chilingarian).

0927-6505/$ - see front matter © 2006 Elsevier B.V. All rights reserved.
doi:10.1016/j.astropartphys.2006.02.004

its variance. It is also necessary to take into account the number of attempts physicist made to reveal the signal more effectively. Any re-binning and shifting of the grid, superimposed on the data, changes the statistical model used for estimating the significance of the source [16]. It is often very difficult to account on all specific experimental procedures applying for the revealing signal. Therefore, the significance obtained using inadequate assumptions usually lead to positively biased significances and observations supported by significances which are unlikely to be chance fluctuations, have not been able to be verified in later experiments. It is due to the overall problem related to the choice of the appropriate statistical model. The ascribed physical inference could be valid within a chosen model, but tell nothing about the validity of the model itself.

In this publication we use both analytical approach and Monte-Carlo method to obtain the statistical model, adequately describing the signal searches. The sources for possible erroneous physical inference based on biased models are clearly stated and discussed. As an example for comparing the different statistical models we consider the observations of the Monogem Ring (MR) by surface particle detector arrays [7]. The MR is a supernova remnant (SNR), located at a distance of ~300 parsec from the Sun, with an ~100K year-old radio pulsar, PSR B0656+14, near the center [21]. Recently, three new observations of MR were published. Two of them [15,6] confirm a signal from MR, while the third one [2] report no signal from MR with very large significance. Nonetheless, the MR continues to be considered as a candidate source for cosmic rays [12,13]. Therefore, we consider the rigorous clarification of the point source search methodology as a very up-to-date and important point, which can help to solve the long-standing problem of the cosmic ray (CR) origin.

## 2. Monogem Ring observation by the MAKET-ANI detector

In 2003 we reported significant excess of Extensive Air Showers (EAS) whose arrival direction pointed to the Monogem Ring [7]. In the search for the source of the cosmic rays (CR), we used data from the MAKET-ANI detector on Mt. Aragats in Armenia [4,8], from years 1997 to 2003. In the experiment we measure the horizontal coordinates of the incident primary particle, by calculating the axes of the Extensive Air Shower (EAS), namely, zenith angle $\theta$ and azimuth $\phi$, and then transforming them to equatorial coordinates – Right Ascension (RA) and declination $\delta$, according to the transformation equations [17]. To do this we need to know the angle formed by the detector axes with respect to the direction to the North Pole and the time of event registration, in addition to the horizontal coordinates. After measuring the geographic alignment of the MAKET-ANI array in the summer of 2004, we found an error in the conversion of the measured EAS directions from the horizontal coordinates to equatorial (celestial) coordinates [9], which significantly altered our original conclusion.

As can be seen in Fig. 1, the actual angle between the MAKET-ANI detector axis and the North–South geographic axis of the earth is 17°, while in the MAKET-ANI data base, formed in 2001, zero degrees was assumed. This erroneous assumption resulted in an apparent excess of showers in the histogram bin pointed to the MR direction (signal bin with 43 EAS pointed on the MR direction) as is seen in (Fig. 2(a)). After the correction of the event's equatorial coordinates the excess of the points in the "signal" bin reduced as presented in Fig. 2(b) (only 28 EAS remain). The "migration" of points from the "signal" bin to the neighboring bins is demonstrated in Fig. 3. Compact cluster of showers in the signal bin shown in Fig. 3 as dia-

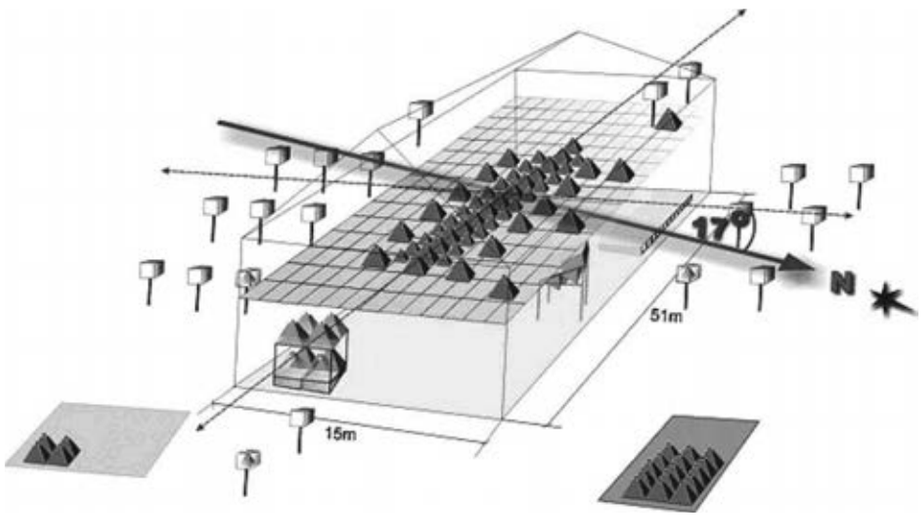


Fig. 1. MAKET-ANI detector, Aragats, Armenia.

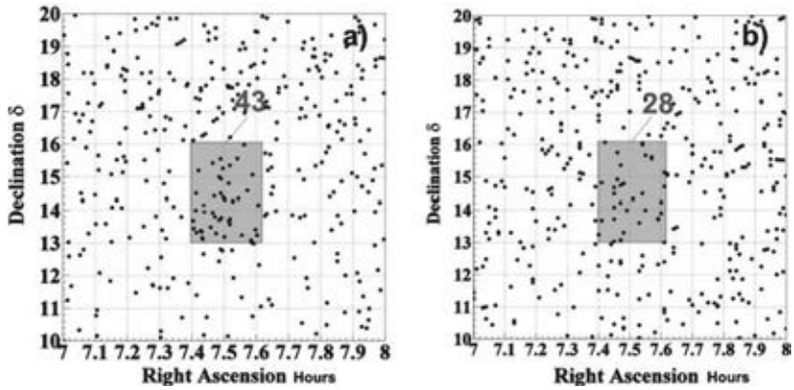


Fig. 2. A part of the sky map (the "signal" bin) obtained from MAKET-ANI EAS data, before (a) and after (b) the correction of the coordinate conversion. Each point in the map represent shower coming from the definite direction.

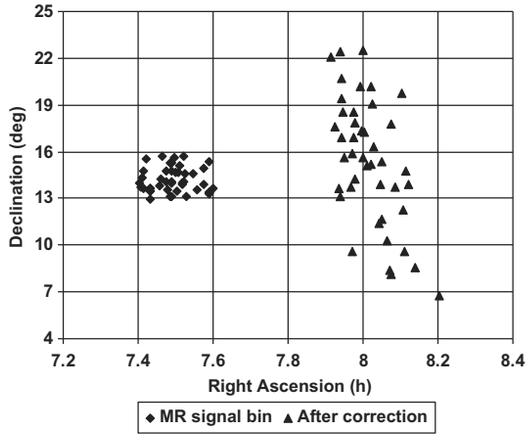


Fig. 3. Migration of events as measured by the MAKET-ANI detector from the "signal" bin to neighboring bins after correction of celestial coordinates.

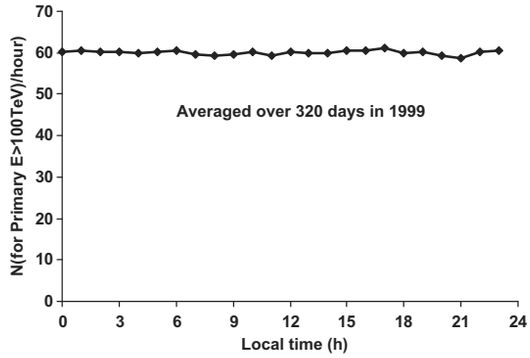


Fig. 4. Averaged daily distribution of MAKET-ANI detector triggers for EAS initiated by primary particles with energies $E > 10^{14}$ eV shows no time dependence.

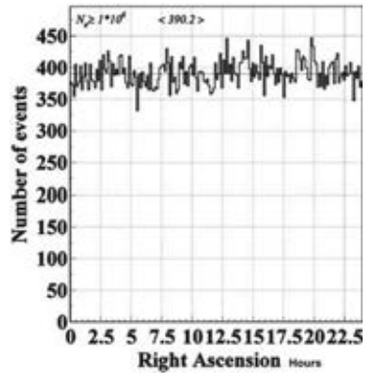


Fig. 5. Distribution of MAKET-ANI EAS data by Right Ascension (RA) for the year 1999.

monds is redistributed among 12 another same size bins shown in same figure as triangles.

By examining the MAKET-ANI EAS database, we found that the detector does not introduce any bias in time, because there was no preferable time or season of particle detection. Fig. 4 shows that the time distribution of the detected particles averaged over 320 days in 1999 is uniform, which leads to uniform distribution by the Right Ascension, as shown in Fig. 5. The analogous distributions of other years are also highly uniform.

However, the distribution by zenith angle in horizontal coordinates is highly anisotropic, because of the different effective thickness of atmosphere for each angle, which incident particles have to pass to reach the detector [1]. For the MAKET-ANI EAS data this anisotropy is well described by a $\cos^6\theta$ dependence, so the distribution of detected particles by zenith angle is described by the function $\sin\theta \cos^6\theta$, having maximum at $\theta \sim 22°$ (as shown in Fig. 6).

When we transform the horizontal coordinates into celestial coordinates, the uniform time distribution is transformed to an isotropic RA distribution, and the anisotropic zenith angle distribution is reflected in the form of

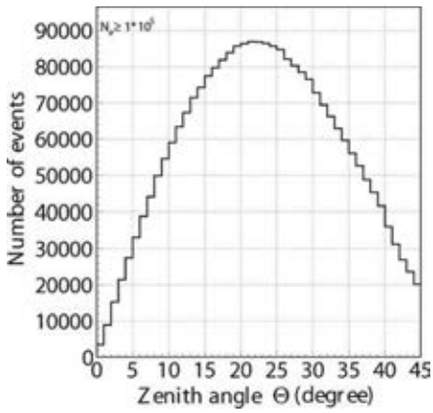


Fig. 6. Distribution of MAKET-ANI EAS data by zenith angle.

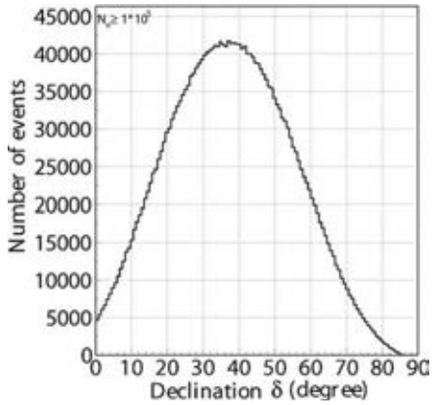


Fig. 7. Distributions of MAKET-ANI EAS data by declination.

anisotropic declination distribution. Since the declination of the zenith is equal to the latitude (40.5° for the Aragats research station), the maximum in the distribution of declinations appears at $\delta \sim 40°$ as shown in Fig. 7. This strong dependence of the number of events upon the declination angle implies that when searching for uniformity in celestial coordinates we have to choose narrow intervals – declination "belts", within which the distribution of events can be treated as approximately uniform.

Proceeding from the detector angular accuracies and available EAS data we choose the bin size as $\Delta\alpha \times \Delta\delta$ $(3° \times 3°)$, covering a $360° \times 60°$ equatorial coordinate range, with 20 declination belts in total, each divided into 120 bins.

The cosmic ray point source should manifest itself as an excess number of counts in one, or several adjacent bins, in comparison with the corresponding belt-average value. In our analysis the Right Ascension Scan (RAS) method [1] was implemented, where not only one, but all declination belts are used to form statistical test distribution. The grid with bin (cell) size of $(3° \times 3°)$ is superimposed on the two-dimensional distribution of the actual values of the celestial coordinates of detected showers, i.e. on the, so-called, sky map. We then examined the distribution of the events within each cell and made further analysis according to the $H_0$ probabilistic model described below.

As is usual in statistical hypothesis testing, the main hypothesis ($H_0$) we need to check is in opposition to the hypothesis we are interested in, i.e. we check the hypothesis that the arrival of the CR on the MAKET-ANI detector is isotropic ("no-signal" hypothesis). In this case it means to determine: is the detected enhancement in the "signal bin" a simple random fluctuation of the isotropic distribution? If we see a large deviation of number of events fallen in particular bin from the value expected assuming the validity of $H_0$, then we will have a very low probability of $H_0$ being true. Therefore, we can reject $H_0$. But, of course, it does not imply that the opposite hypothesis is automatically valid. As was mentioned by Astone and D'Agostini [5], a revised version of the classical proof-by-contradiction is hidden in the logic of standard hypothesis testing – "in standard dialectics, one assumes a hypothesis to be true, then looks for a logical consequence which is manifestly false, in order to reject the hypothesis. The 'slight' difference introduced in 'classical' statistical tests is that the false consequence is replaced by an improbable one".

## 3. Gaussian approximation

The number of events falling in each bin is independently and identically distributed random variables obeying multinomial law. Multinomial process consists of the random realization of one of $N_\delta$ possibilities; in our case – classes, representing the division of the range of all declinations into 20 fixed declination "belts". In our probabilistic treatment of the problem we convolute the uniform distribution of RA and treat the number of events hitting different bins as realizations of the multinomial random process with $\bar{N}_j,\ j = 1, 20$ fixed means. Then, by normalizing each bin content by the mean and variance of the corresponding declination belt we obtain standard Gaussian distribution $N(0,1)$ to be used further as the test statistics:

$$\sigma_{i,j} = \frac{N_{i,j} - \bar{N}_j}{\sqrt{\bar{N}_j}}, \quad i = 1, N_\alpha, 3, \ \ j = N_{\delta 1,\delta 2,3} \tag{1}$$

where $N_{i,j}$ is the number of events in the rectangular bins, $\bar{N}_j$ and $\sqrt{\bar{N}_j}$ are the RA averaged mean and mean square deviation of number of events within the bin of $j$th belt, $N_\alpha = 360$ is the number of RA divisions; $N_{\delta 1} = 6.6$ is the first declination, $N_{\delta 2} = 66.6$ is the last declination for a total 20 declination belts, each of 3°. We were looking for single source candidates in the two-dimensional $\Delta\alpha \times \Delta\delta(3° \times 3°)$ grid, covering a $360° \times 60°$ equatorial coordinate range with $M = 2400$ bins. The rectangular equatorial coordinate system (grid) origin was taken at $(0°, 6.6°)$.

Of course, the multinomial significances are different from the Gaussian ones [11] specially for the large significance values. Nevertheless, first we will present results with the commonly used Gaussian distribution. The bias, intro-

duced due to the slow convergence of Gaussian approximation toward the correct multinomial (Poisson) values, will be discussed in other paper.

More than 2 million showers with sizes starting from $N_e > 10^5$ electrons, detected by the MAKET-ANI detector, were distributed among the $M = 2400$ angular bins. The "signal" was revealed when we examined the sub-sample of $\sim 6 \times 10^4$ events with $N_e > 10^6$. According to the logic of hypothesis testing, we calculate the test statistics by applying Eq. (1) to the experimentally detected showers and using a fixed equatorial grid. As we can see from Fig. 8, the shape of the cumulative distribution of the particles was very close to standard Gaussian distribution N(0, 1), with a $\chi^2$ test value of $\sim$1.5 per degree of freedom. Only one direction from the 2400 demonstrates significant deviation from standard Gaussian distribution $N(0, 1)$. Therefore, we concluded, that the obtained distribution supports the model of isotropic "background" and "signal" mixed with "background" in one of 2400 equatorial bins.

From the obtained value of 6.04 in the "signal bin", as noted by a circle in Fig. 8, we calculated the corresponding probability of obtaining this value under $H_0$ hypothesis.

We assumed that maximal obtained value for the signal in bin 6.04 belongs to the $N(0, 1)$ distribution. Based on this assumption, the probability density distribution function of obtaining this value as the maximal value among $M$ possibilities is straightforward [10]:

$$P_M(x) = M \cdot g(x)(1 - G_{>x})^{M-1} \quad (2)$$

where $g(x)$ is standard Gaussian probability density for the signal bin; $G_{>x} = \int_x^\infty g(t)\mathrm{d}t$ is the so-called test statistics $p$-value: the probability to obtain the value of the test statistics in the interval greater than $x$.

To obtain the probability of observing number of events equivalent to or more than 6.04 standard deviations in one out of 2400 bins (meaning the $p$-value of the distribution

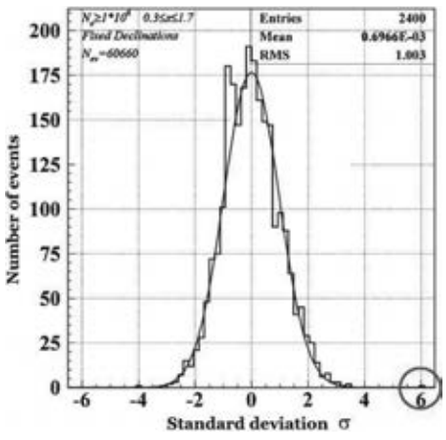


Fig. 8. Signal significance test with full equatorial coverage with 2400, $3° \times 3°$ bins; $N_e > 10^6$, before correction of coordinates conversion. Note the $6.04\sigma$ point in the circle.

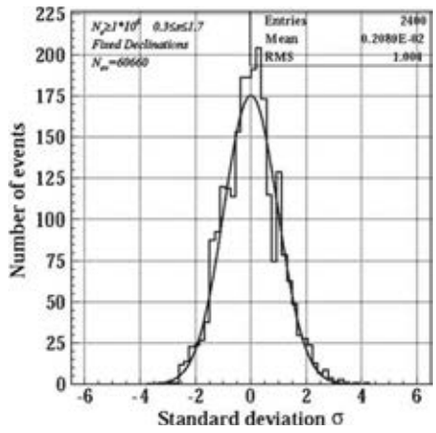


Fig. 9. Signal significance test with full equatorial coverage with 2400, $3° \times 3°$ bins; $N_e > 10^6$, after correction of coordinates conversion. Note that event at $6.04\sigma$ has disappeared.

$P_M(x)$), we need to integrate $P_M(x)$ in the interval [6.04, $+\infty$). For $M = 2400$ we obtain $\int_{6.04}^\infty P_M(x)\mathrm{d}x \sim 2 \times 10^{-6}$. Proceeding from this very small value, we rejected the null hypothesis and concluded that the MAKET-ANI has detected signal from the direction of the Monogem Ring.

After correcting the error in the transformation of the MAKET-ANI geographic coordinates to celestial coordinates we found no significant deviation from $H_0$, as it is seen from Fig. 9. Note that the events at $6.04\sigma$, which existed before the coordinate system correction in Fig. 8, have now disappeared in Fig. 9.

However, the question arises: how did we obtain such low chance probability. Can we explain it as a simple random coincidence, or was it due to the wrong statistical model? We found it very improbable that we were so unlucky that a chance probability of two out of a million was realized. Therefore, we put the statistical model itself under question. In the next sections we will analyze the sources of our error and will develop new methodology for analysis, which will give adequate inference.

## 4. Bin regrouping effects

The statistical model we use for estimating the chance probability, is dependent not only on the chosen distribution function, but also on the methods of grouping of experimental data. "Where one is looking for deviation from uniformity in a continuum, one cannot escape from the multiplicity of possible groupings" [14]. Usually the physicists adjust the grid superimposed on the sky map slightly, to include the "signal" events in the selected bin as much as possible. The logic of such an adjustment is the following: if a randomly chosen, fixed grid divides the signal between neighboring bins, why not try to shift the grid to contain the entire signal in one bin?

In this logic one random grid is changed to another and it seems that nothing essential happens in the process, but as we will see, such a simple operation dramatically

changes the estimate of chance probability. Each regrouping leads to the increase of $M$ in Eq. (2), thus changing the chance probability. Usually, the regrouping effect is not taken into account. Physicists make conclusions on the signal significance by calculating the chance probability according to a simple Gaussian model, often obtaining positively biased significances. To demonstrate that the extremum statistics (2) accounts for the re-binning and provides correct chance probabilities we developed two numerical models.

Our first model generates the random Gaussian variables in 120 RA bins in each of the 20 declination belts according to the belt-specific means and variances as obtained in the experiment, thus generating random sky maps, analogous to that shown in Fig. 2, but for the entire sky seen by the MAKET detector. After applying the normalizing transformation (1) to the generated random map we obtained $M = 2400$ random variables distributed according to the standard Gaussian $N(0,1)$. Then the maximum positive deviation from the $N(0,1)$ was stored as the value of the test statistics.

Our second model generates a number of events in the same way as the first one. Then the origin of the equatorial coordinate system (right ascension and declination) is shifted by 0.1° in the range equal to one bin size ($3° \times 3°$). Thus, instead of one grid $30 \times 30 = 900$ different

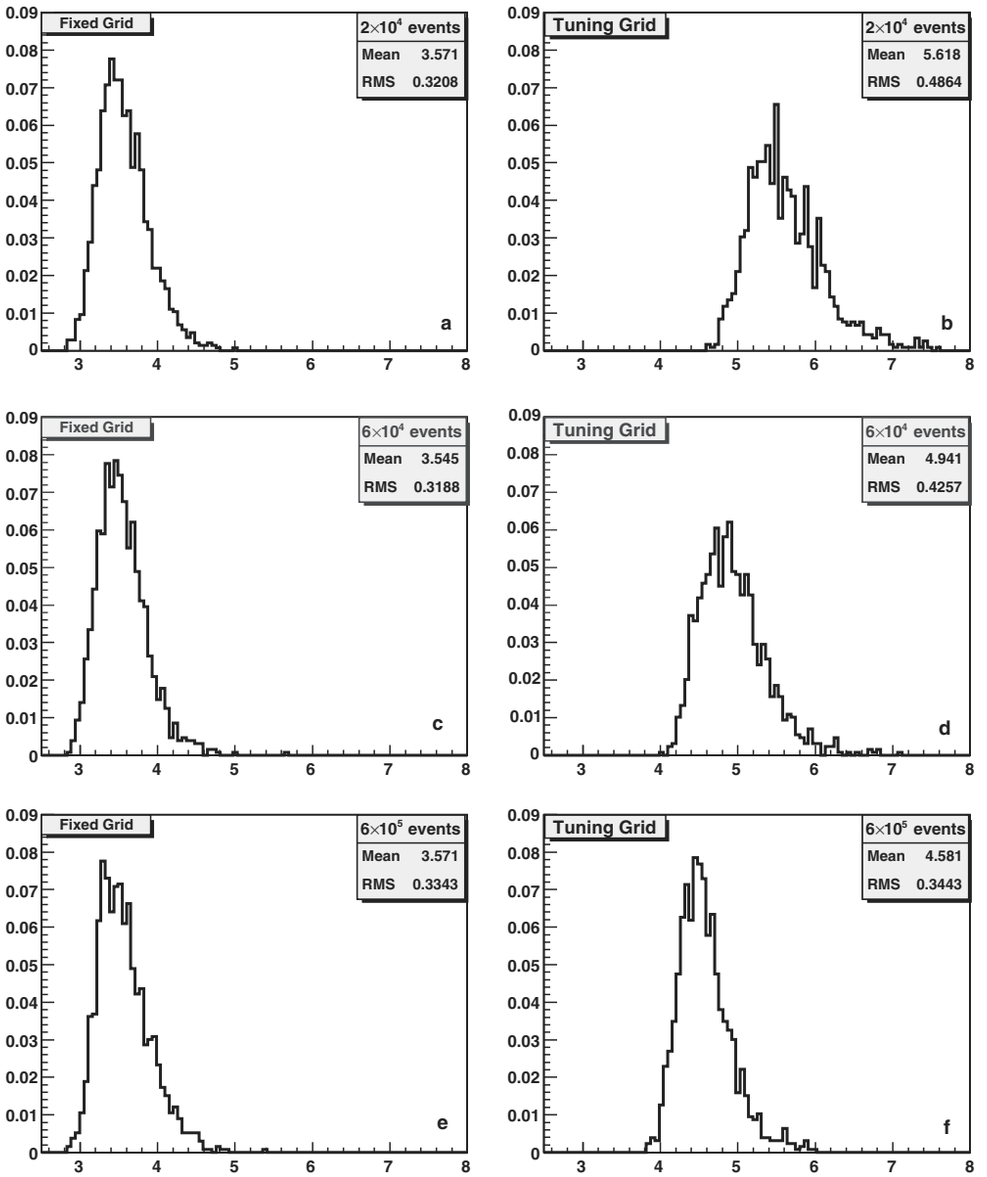


Fig. 10. Distribution of the extremum test statistics values for the first simulation model – one fixed grid with $M = 2400$ bins – (a), (c), (e), and for second simulation model – with tuning the grid to contain maximal signal – (b), (d), (f).

grids are tested. The goal of this procedure is to obtain maximum possible "signal" for given distribution of events. After the shift, the current value of maximum is compared with the previous best one, and if the new one is larger, it is saved as the best. The largest-obtained value of maximum is stored. This value is just the largest positive deviation for the given sky map and grid size obtained in the grid tuning procedure.

The fixed grid model is usually assumed when calculating chance probabilities; nonetheless the tuned grid model describes realistically the experimental situation in peak searching. Our numerical experiment is designed to illustrate how the chance probabilities are changed and why we can obtain very high significances if there is no signal at all.

We generate the random sky map 1288 times, to obtain the distribution of extremum statistics for fixed and tuned grids. As we can see from Fig. 10 the large significance values (large $\sigma$) occurred much more often for the tuned grids (Fig. 10(b), (d) and (f)), as compared to the fixed grid model Fig. 10(a), (c) and (e). Therefore, when calculating chance probabilities we are at risk to make optimistically biased inference: to get much higher significance than experiment allows. We also can see in Fig. 10, that by changing the number of experimental points (showers) filling the grid, the "$\sigma$" distribution for the tuned grid changes dramatically. For the number of events $2\times10^4$ the mean of "$\sigma$" distribution equals 5.6, while for $6\times10^5$ events it is 4.5. This demonstrates that if the number of events is small, and bin-to-bin differences are large, then via tuning it is possible to find the combination of event numbers which correspond to very rare fluctuation. When the number of events is enlarged, the corresponding bin-to-bin differences became smaller and it is much more difficult to find large fluctuations.

Therefore, in low-statistics experiments it is possible to find "fake" signal with very large significance. In Fig. 11 we demonstrate how we can obtain a realistic chance probability for the MAKET-ANI experiment. We perform numerical simulations of the MAKET-ANI's detection of the Monogem Ring with both fixed and tuned grid statistical models.

By the solid line in Fig. 11(a) and (b) we denoted the analytical curve obtained from Eq. (2) for the $M=2400$ (Fig. 11(a)), and $M=2400*600$ (Fig. 11(b)). The histogram on the same figures are obtained with simulations with fixed (Fig. 11(a)) and tuned (Fig. 11(b)) models as described above. The number of events was equal to the one from the MAKET-ANI experiment $\sim6\times10^4$ and 1288 independent random sky maps were generated. From the fixed grid model (Fig. 11(a)) we can see that $6\sigma$ (for simplicity we use the $6\sigma$ value, instead of $6.04\sigma$ obtained in MAKET-ANI experiment) is really very rare fluctuation. The frequency of obtaining $6\sigma$ from histogram equals to 0, because we perform only 1288 trials, and, we can expect only $\sim2.5$ events from million according to analytical calculations.

The frequency of obtaining $6\sigma$ calculated from the "tuned grid" histogram (Fig. 11(b)) equals $\sim2$ from hundred. The analytic calculation gives an order of magnitude smaller value compared with frequency obtained from the histogram. However, the difference between the fixed and tined grid models is striking: at least three orders of magnitude!

When we test many grids, probability to obtain large "$\sigma$" values is dramatically enlarged. For the MAKET-ANI statistics of $\sim6\times10^4$ events with $N_e>10^6$, we can easily obtain significance values exceeding 6 and even 7. Therefore, we do not have enough evidence to reject the $H_0$ hypothesis, if measuring 6.04 value in MAKET-ANI experiment. Remember, that $H_0$ is the statement that the distribution of cosmic rays is isotropic.

The cause of shift of "$\sigma$" distribution mean to larger values when tuning the grid can be explained by enlarging of the number of the tested grids, and, consequently – the number of different bins.

The $M$ multiplier in Eq. (2) represents number of all-possible bins in which the maximum can occur. In the first model we test single fixed grid $M=2400$. In the second model when we shift the grid, we test $M$ new bins for each

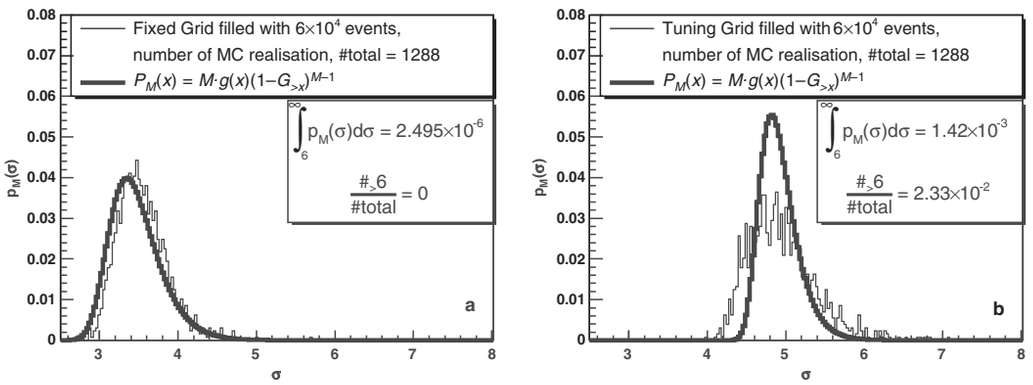


Fig. 11. The comparisons of the two ways of point signal searches, (a) with one fixed grid and (b) with tuned grid to maximize the extremum statistics.

particular shift, enlarging total number of bins to $M * K$, where the $K$ is the number of different grids tested.

Thus the complexity of the second model is $\sim K$ times larger compared to the first one. To check this assumption we enlarge the $M$ value in Eq. (2) till the mode of analytical function (2) comes close to the histogram mode. This occurs at $M = 2400 * 600$, as shown in Fig. 11(b). We reached rather good agreement of the analytic distribution (2) and the tuned grid simulated distribution by the Monte-Carlo method at value of $K \sim 600$, instead of 900 as expected, because not all 900 grids result in different data coverage. Some small shifts leave the distribution of the events in 2400 bins the same. Therefore, such shifts should not be count and value of $K$ is smaller than 900.

## 5. Conclusions

- In estimating the significance of signal detection, we are looking for the maximum value of deviation of the "signal bin" from the background, and statistical inference is drawn based on the value of this maximum. Therefore, the extremum statistics distribution (2), should be used as the test statistics for estimating the significance of signal.
- Both analytical model (2) and simulated distribution obtained with the tuned grid Monte-Carlo method give very consistent results, proving the necessity to account on all choices of data grouping aimed at revealing the signal.
- Performed statistical analysis of the MAKET-ANI sky maps by the use of the tuned grid model does not support the hypothesis of anisotropy of CR flux; therefore, we withdraw the conclusion of paper [7] which claims the existence of a cosmic ray point source within the Super Nova Remnant Monogem Ring.

## Acknowledgements

We thank Suren Chilingarian for writing the code and performing simulations with the first and second models of point source detection, Artur Reimers for calculating significance levels and making Figs. 10 and 11 and Akopov Norair for the discussion of the pentaquark searches.

## References

[1] D.E. Alexandreas, D. Berley, et al., Point source search techniques in ultra high energy gamma ray astronomy, Nucl. Instrum. Methods A 328 (1993) 570.
[2] M. Amenomori, S. Ayabe, et al., Astrophys. J. 635 (2005) L53–L56.
[3] T. Antony et al. KASCADE Collaboration, Astrophys. J. 608 (2003) 865.
[4] V.V. Avakian, E.B. Bazarov, et al., VANT, Ser. Tech. Phys. Exp. 5 (31) (1986) 1.
[5] P. Astone, G. D'Agostini, Inferring the intensity of Poisson processes at the limit of the detector sensitivity, CERN-EP/99-126, 1999.
[6] G. Benko et al., Izv. RAN Ser. Fiz. 68 (2004) 1599 (in Russian). Available from: <astro-ph/0502065>.
[7] A. Chilingarian, H. Martirosian, G. Gharaghoyzyan, Detection of the high-energy cosmic rays from the Monogem Ring, Astrophys. J. 597 (2003) L129–L131.
[8] A. Chilingarian, G. Gharagyozyan, G. Hovsepyan, S. Ghazaryan, L. Melkumyan, A. Vardanyan, Light and heavy cosmic-ray mass group energy spectra as measured by the MAKET-ANI detector, Astrophys. J. 603 (2004) L29–L32.
[9] A. Chilingarian et al., On the detection of the signal from the Monogem Ring by the MAKET-ANI detector, Int. J. Mod. Phys. A 20 (29) (2004) 6753–6765.
[10] S.C. Chapman, G. Rowlands, N.W. Watkins, Extremum statistics – a framework for data analysis, Nonlinear Process. Geophys. 9 (2002) 409–418.
[11] H. Ebeling, Improved approximation of Poissonian errors for high confidence levels. Available from: <astro-ph/0301285> 2003.
[12] A.D. Erlykin, A.W. Wolfendale. Available from: <astro-ph/0510680> 2005.
[13] A.D. Erlykin, A.W. Wolfendale. Available from: <astro-ph/0510016> 2005.
[14] M. Hillas, Proc. 14th ICRC 9 (1975) 3439.
[15] G.V. Kulikov, M.Yu. Zotov, Izv. RAN Ser. Fiz. 68 (2004) 1602 (in Russian). Available from: <astro-ph/0407138>.
[16] E. O'Mongain, Application of statistics to results in gamma ray astronomy, Nature 241 (1973) 376.
[17] J. Meeus, Astronomical Algorithms, Willmann-Bell, 1991.
[18] M. Samorski, W. Stamm, Detection of $2 \times 10^{15}$–$2 \times 10^{16}$ eV gamma-rays from CYGNUS X-3, Astrophys. J. 268 (1983) L17.
[19] C. Seife, Science 306 (2004) 1281.
[20] M. Takeda et al., Astrophys. J. 522 (1999) 225.
[21] S.E. Thorsett, R.A. Benjamin, W.F. Brisken, A. Golden, W.M. Goss, Astrophys. J. 592 (2003) L71.

Available online at www.sciencedirect.com
ScienceDirect
Advances in Space Research 39 (2007) 1454–1457
ADVANCES IN SPACE RESEARCH (a COSPAR publication)
www.elsevier.com/locate/asr

# On the production of highest energy solar protons at 20 January 2005

N.Kh. Bostanjyan *, A.A. Chilingarian, V.S. Eganov, G.G. Karapetyan

*Cosmic Ray Division, Alikhanyan Physics Institute, Alikhanyan Brothers St. 2, Yerevan 36, Armenia*

Received 13 September 2006; received in revised form 12 March 2007; accepted 14 March 2007

**Abstract**

On January 20, 2005, 7:02–7:05 UT the Aragats Multidirectional Muon Monitor (AMMM) located at 3200 m a.s.l. registered enhancement of the high energy secondary muon flux (threshold ~5 GeV). The enhancement, lasting for 3 min, has statistical significance of $\sim 4\sigma$ and is related to the X7.1 flare seen by the GOES, and very fast (>2500 km/s) CME seen by SOHO, and the Ground Level Enhancements (GLE) #69 detected by the world-wide network of neutron monitors and muon detectors. The energetic and temporal characteristics of the muon signal from the AMMM are compared with the characteristics of other monitors located at the Aragats Space-Environmental Center (ASEC) and with other neutron and muon detectors. Since secondary muons with energies >5 GeV are corresponding to solar proton primaries with energies 20–30 GeV we conclude that in the episode of the particle acceleration at 7:02–7:05 UT 20 January 2005 solar protons were accelerated up to energies in excess of 20 GeV.


*Keywords:* Solar Cosmic Rays; Ground Level Enhancement; Particle detectors

## 1. Introduction

On January 20, 2005 NOAA reported an X7 importance flare with helio-coordinates (14N, 61W), which started at 6:36 UT with maximal X-ray flux at 7:01 UT. The associated CME had the largest sky-plane speed, exceeding 3000 km (Gopalswamy et al., 2005). The first results on the unleashed Solar Energetic Particle (SEP) event reported by space-born particle spectrometers (Mewaldt et al., 2005) pointed to very hard energy spectra of accelerated protons. It stimulated detailed investigation of the correspondent Ground Level Enhancement (GLE) #69, having one of the goals to estimate the maximum energy of the solar accelerators.

Available experimental data on the Ground Level Enhancements (GLEs) confirm proton acceleration up to 20 GeV (Toptigin, 1983; Dorman, 2004). The stochastic acceleration in the flares (Petrosian, 2006) and shock acceleration in corona and interplanetary space (Gang and Zank, 2003) are the two theories aimed to explain the origin and mechanisms of the particle acceleration at the Sun.

Middle and high-latitude neutron monitors can not be used for the reconstruction of the primary energy spectra above 5 GeV due to very weak fluxes and relatively small sizes of the detectors. Therefore, recent years surface particle detectors measuring Extensive Air Showers (EAS) were implemented for the investigation of the highest energy solar protons and ions (Ryan, 1999; Ding, 2001; Poirier and D'Andrea, 2002; Chilingarian et al., 2003a). Due to their large surface area and solid angle and high efficiency of the registration of the charged particles, these detectors provide valuable information about the solar proton fluxes above 5 GeV.

The *Aragats Multidirectional Muon Monitor* (AMMM) is located at (40.25°N, 44.15°E) and on altitude 3200 m above sea level (ASL) with cutoff rigidity 7.6 GV and relative accuracy of measuring 3-min time series of ~0.17%, more sensitive than the neutron monitor 18NM64, located at the same altitude.

The AMMM consists of 45 (in 2006 enlarged to 100) plastic scintillators with detecting surface of 1 $m^2$ and

* Corresponding author.
*E-mail address:* bostan@crdlx5.yerphi.am (N.Kh. Bostanjyan).

0273-1177/$30 
doi:10.1016/j.asr.2007.03.024

thickness of 5 cm each. The detector AMMM is located in the underground hall of the ANI experiment (Chilingarian et al., 2003b) under 15 m of soil and concrete, plus 12 cm. of iron bars. Only muons with energies greater than 5 GeV can reach this underground detector. These muons are efficiently produced by primary protons of energy 35–50 GeV if we assume the power-law differential energy spectrum with spectral index of $\gamma = -2.7$ for Galactic Cosmic Rays, and proton energies of ~20–30 GeV if we assume spectral index $\gamma = -4$ to $-5$ (Chilingarian et al., 2005; Zazyan and Chilingarian, 2006).

During GLE #69 on January 20, 2005 from 7:02 to 7:05 UT, AMMM detects a peak with significance $\sim 4\sigma$. We compare this with observations of the other Aragats Space-Environmental Center (ASEC) monitors (Chilingarian et al., 2006a) and other world-wide monitors, see parameters of the monitors in Table 1, where types, heights above sea level, area, cutoff rigidity and geographic coordinate of monitors are presented. Statistical significance is given for peaks occurred at 7:02 UT.

## 2. GLE #69 as detected by the ASEC monitors

GLE #69 was detected by several ASEC monitors on January 20, 2005, during the solar flare X7.1. The 1-min time series of the AMMM is presented in Fig. 1. Enhancement of the count rate is seen from 7:02 till 7:04 UT with maximum at 7:03 UT. Three out of the 45 one $m^2$ scintillators of the AMMM were not operational at the time, therefore only 42 $m^2$ of muon detectors were in use to measure the high energy muon flux. The estimated mean count rate of the Galactic Cosmic Rays (GCR) as measured by the 42 $m^2$ of the AMMM detector is 123,818 particles per min. The additional signal at 7:03 UT equals to 863 particles or enhancement of 0.70%. Taking into account that the standard deviation of 1 min data is 352 (0.29%) the significance of the 1 min peak at 7:03 UT is $2.5\sigma$.

To emphasize the peak in the AMMM time series we group the 1 min date in 3-min time-intervals (see Fig. 2). As expected the 3-min time series demonstrates a more pronounced peak of $3.93\sigma$. The mean count rate of GCR equals 371,454 particles per 3 min. The additional signal at 7:02 equals 2394 or enhancement of 0.644%. If we adopt the Poisson standard deviation for the 3-min time series 0.164% (see detailed discussion on the determination of the significance of detected enhancement in Chilingarian et al., 2006b) we come to the significance of $3.93\sigma$ for the 3 min peak at 7:02–7:05 UT. The excess count rate registered at AMMM during the interval 7:02–7:05 UT corresponds to the flux $(3.1 \pm 0.8) \times 10^{-5}$ muons/cm$^2$/s.

Due to the very short enhancement time span no corrections for the atmospheric pressure and temperature variations are necessary.

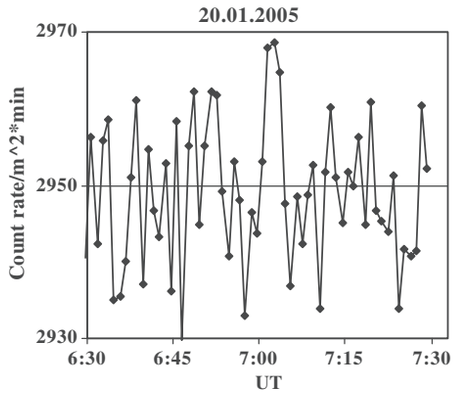


Fig. 1. Time series of the 1 min count rates of secondary muons with energies greater than 5 GeV measured by AMMM. Count rates are normalized to the flux fallen on 1 $m^2$.

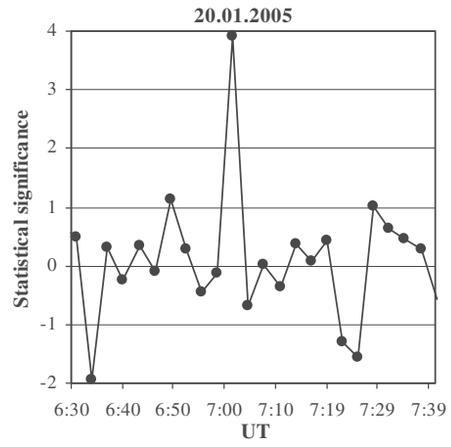


Fig. 2. Time series of the 3 min count rates of secondary muons with energies greater than 5 GeV measured by the AMMM, expressed in the units of the standard deviations. Significance of the peak at 7:02 equals $4\sigma$.

Table 1
Characteristics of the particle detectors registered the GLE #69 at 20 January 2005

| Detectors | Altitude (m) | Surface ($m^2$) | Rigidity GV | Statistical significance | Geographic coordinate |
|---|---|---|---|---|---|
| NANM 18NM64 | 2000 | 18 | 7.6 | 3.7 | 40.25°N, 44.15°E |
| ANM 18NM64 | 3200 | 18 | 7.6 | 1.2 | 40.25°N, 44.15°E |
| ASNT-8 channels | 3200 | 4 (60 cm thick) | 7.6 | 0.2 | 40.25°N, 44.15°E |
| | | 4 (5 cm thick) | | 1.5 | |
| AMMM | 3200 | 42 | 7.6 | 3.93 | 40.25°N, 44.15°E |
| CARPET/Baksan | 1700 | 196 | 5.7 | 19 | 43.28°N, 42.69°E |
| Tibet YBJ NM 28NM64 | 4300 | 28 | 14.1 | 12 | 30.11N 90.53E |

The statistical significance of peaks is calculated by 3-min time series.

The 20 January GLE was detected by several EAS detectors, measuring shower charge particles (mostly muons and electrons) (D'Andrea and Poirier, 2005; Ryan, 2005) and by Tibet YBJ neutron monitor (Miyasaka, 2005); all ensuring registration of highest primary proton energies of 10–15 GeV.

We can see in Fig. 3 rather good agreement of the time series profiles. CARPET and YBJ NM demonstrate high significance peaks in the same time at 7:02, those proving that AMMM $\sim 4\sigma$ peak is not rare fluctuation, but is initiated by the primary protons with energies greater than 20 GeV. Smaller significance values of AMMM comparing with CARPET and YBJ NM is explained by the much higher threshold of AMMM and large index of the proton flux energy spectra $\gamma = -4, -5$ (Bieber et al., 2005; Miyasaka, 2005).

In Figs. 4 and 5 the count rate enhancements measured by the Aragats Neutron Monitor (ANM), located at 3200 m ASL and Nor-Amberd Neutron Monitor (NANM) located at 2000 m ASL are presented (both neutron monitors are 18NM64 type). From the figures we can see that the enhancement at the neutron monitors started $\sim 3$ min earlier than the peak detected by the AMMM and in the interval 6:59–7:45 both ANM and NANM show at least two peaks having significance higher than $3\sigma$.

The 5 cm thick plastic scintillators of upper layer of the Aragats Solar Neutron Telescope (ASNT) is sensitive to charged particles with energies greater $\sim 7$ MeV. As we can see in Fig. 6 in the same interval of 6:59–7:45 ASNT also detect several significant peaks. Analogous patterns were detected by the neutron monitors from the worldwide network (Flueckiger et al., 2005).

The energies of the primary solar protons giving rise to the secondary neutrons (registered by the neutron monitors) and low energy charged particles (registered by surface scintillator detectors) are smaller than the energies of the primary proton that create the 5 GeV muons in the atmosphere.

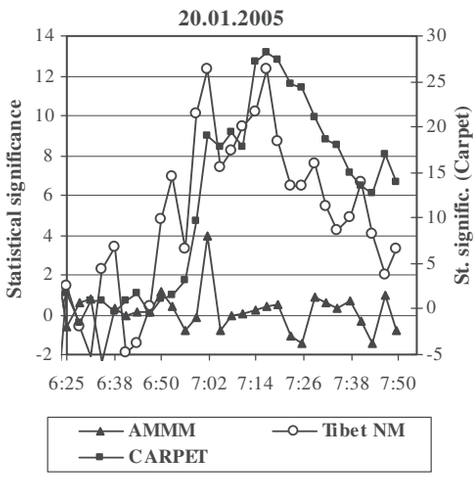


Fig. 3. Comparison of the time series of the particle detector sensitive to the highest energies of solar particles: CARPET (energy range >6 GeV), Tibet NM (>13 GeV) and AMMM (>20 GeV).

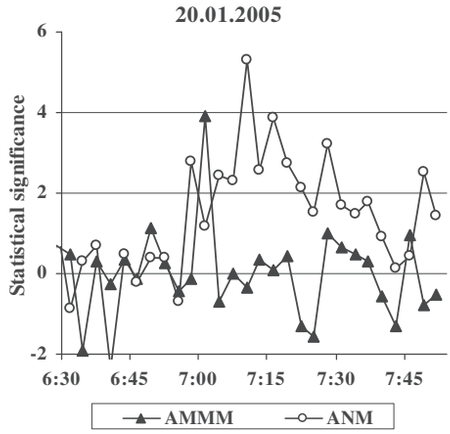


Fig. 4. Comparison of the time series of the 3 min count rates measured by NANM and AMMM detectors expressed in the units of the standard deviations. Duration of the peak measured by AMMM is ~3 min, whereas excess of ANM count rate is much longer ~45 min.

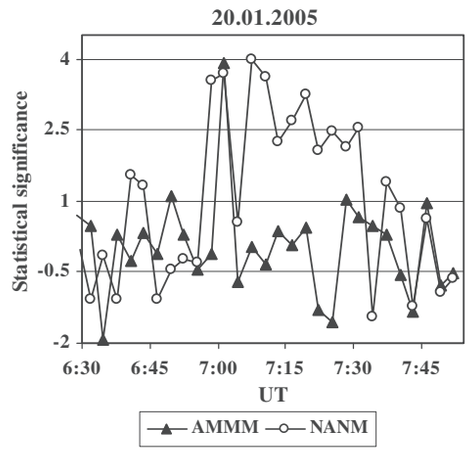


Fig. 5. Comparison of the time series of the 3 min count rates measured by ANM and AMMM detectors expressed in the units of the standard deviations. Duration of the peak measured by AMMM is ~3 min, whereas excess of ANM count rate is much longer ~45 min.

Therefore, we conclude that maximal solar proton energy at 7:12–7:45 was less comparing with 7:02–7:05 when pronounced peak in >5 GeV muon time series was detected. Of course, absence of signal in the AMMM also can be due anisotropic solar protons flux. However, despite the 20 January event was extremely anisotropic at the GLE onset, very soon after onset solar proton flux became rather isotropic (Plainaki et al., 2007; Moraal et al., 2005).

## 3. Conclusions

As mention A. Tylka in (http://creme96.nrl.navy.mil/20Jan05/) "the January 20, 2005 solar event was in many

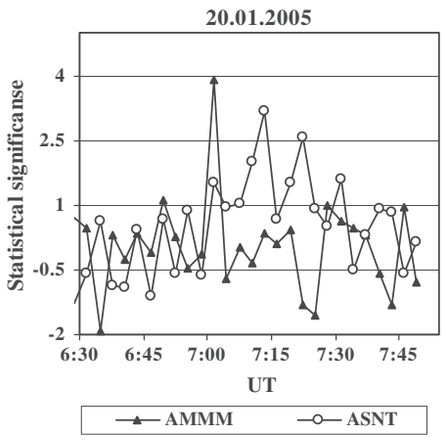


Fig. 6. Comparison of the time series of the 3 min count rates measured by ANM and ASNT detectors expressed in the units of the standard deviations.

ways one of the most spectacular of the Space Age''. Regardless of discussing peculiarities of this event at numerous conferences and workshops the exceptional characteristics of the event are not well understood yet.

Proceeding from the favorable geographical location and high resolution of the AMMM detector at Aragats we add to the corpus of measurements the evidence on the highest proton energies.

On January 20, 2005 at 7:02–7:05 UT the Aragats Multidirectional Muon Monitor registered additional flux of high energy muons equal to $(3.1 \pm 0.8) \times 10^{-5}$ particle/cm$^2$/s, which corresponds to $\sim 4\sigma$ statistical significance. If we assume that the spectral index of the solar protons at this time equals to $\sim -4$ to $-5$, the energy of ''parent'' protons should be 20–30 GeV. Thus we conclude that the protons during this event were accelerated to energies 20–30 GeV.

Particles forming the next peaks of the GLE #69 observed by ASEC monitors at 7:12–7:45 UT has less energy compared with the first peak.

## Acknowledgements

We thank F. Zhu, The Laboratory of Cosmic Ray and High Energy Physics, IHEP, Beijing, China for providing neutron monitor data and S.N. Karpov, Institute for Nuclear Research of RAS, Baksan Neutrino Observatory for providing CARPET detector data. Authors thank the scientific and technical staff of the Aragats and Nor-Amberd research stations for the assistance in the experiment and Hamlet Martirosyan for useful discussions. Work was supported by the ISTC project A1058.

## References

Bieber, J., Clem, J., Evenson, P., et al. Largest GLE in half a century: neutron monitor observations of the January 20, 2005 event, in: Proceedings of the 29th International Cosmic Ray Conference (Pune), vol. 1, pp. 237–240, 2005.

Chilingarian, A., Babayan, V., Bostandjyan, N., et al. Monitoring and forecasting of the geomagnetic and radiation storms during the 23rd solar cycle: Aragats Regional Space Whether Center. Adv. Space Res. 31, 861–865, 2003a.

Chilingarian, A., Avakyan, K., Babayan, V., et al. Aragats Space-Environmental Center: status and SEP forecasting possibilities. J. Phys. G Nucl. Partic. Phys. 29, 939–952, 2003b.

Chilingarian, A., Arakelyan, K., Avakyan, K., et al. Correlated measurements of secondary cosmic ray fluxes by the Aragats Space Environmental Center monitors. NIM A543, 483–496, 2005.

Chilingarian, A., Gharagyozyan, G., Karapetyan, G., et al. Statistical methods for signal estimation of point sources of cosmic rays. Astropart. Phys. 25, 269–276, 2006a.

Chilingarian, A., Bostandjyan, N., Eganov, V.S., et al. On the highest energies of proton acceleration at the Sun on January, in: Proceedings of the 2nd International Symposium on Solar Extreme Events, Nor-Amberd, Armenia, TIGRAN METZ, pp. 180–185, 2006b.

D'Andrea, C., Poirier, J. Ground level muons coincident with the 20 January 2005 solar flare. Geophys. Res. Lett. 32, L14102, doi:10.1029/2005GL023336, 2005.

Ding, L. Variations in cosmic ray intensity observed with the L3 + cosmics shower array detectors and the intense solar flare on 14 July 2000, in: 27th ICRC, SH1.07, 3372. Hamburg, 2001.

Dorman, L.I. Cosmic Rays in the Earth's Atmosphere and Underground. Kluwer Academic Publishers, P. 3, 2004.

Flueckiger, H., Butikofer, R., Mozer, M.R., et al. The cosmic ray ground level enhancement during the Forbush decrease in January 2005, in: Proceedings of the 29th International Cosmic Ray Conference, vol. 1, pp. 225–228, 2005.

Gang, L., Zank, G.P. Energetic particle acceleration and transport at coronal mass ejection-driven shocks. J. Geophys. Res. 108, 1082, doi:10.1029/202JA009666, 2003.

Gopalswamy, N., Xie, H., Yashiro, S., Usoskin I. Coronal mass ejections and ground level enhancements, in: Proceedings of the 29th International Cosmic Ray Conference, vol. 1, pp. 169–173, 2005.

Mewaldt, R.A., Looper, M.D., Cohen, C.M.S., et al. Solar-particle energy spectra during the large events of October–November 2003 and January 2005, in: Proceedings of the 29th International Cosmic Ray Conference (Pune), vol. 1, pp. 101–104, 2005.

Miyasaka, H., and the YBJ NM collaboration. The Solar Event on 20 January 2005 observed with the Tibet YBJ Neutron monitor observatory. Official CD of 29th I.C.R.C., Pune, India, 2005.

Moraal, H., McCracken, K.G., Schoeman, C.C., et al. The ground level enhancement of 20 January 2005 and 28 October 2003, in: Proceedings of the 29th International Cosmic Ray Conference, vol. 1, pp. 221–224, 2005.

Petrosian, V., Liu, S. Stochastic particle acceleration in solar flares, in: Proceedings of the 2nd International Symposium on Solar Extreme Events, Nor-Amberd, Armenia, TIGRAN METZ, pp. 3–19, 2006.

Plainaki, C., Belov, A., Eroshenko, E., et al. Modeling ground level enchancements: the event of 20 January 2005. J. Geophys. Res. 112, doi:10.1029/2006JA011926, 2007.

Poirier, J., D'Andrea, C. Ground level muons in coincidence with the solar flare of April 15, 2001. Geophys. Res. 107 (A11), 1376, doi:10.1029/2001JA009187, 2002.

Ryan, J.M. for Milagro collaboration. Detection of 6 November 1997 ground level event by Milagrito, in: 26th ICRC, Salt Lake City 6, p. 378, 1999.

Ryan, J.M., and the Milagro Collaboration. Ground-level events measured with Milagro, in: Proceedings of the 29th International Cosmic Ray Conference, vol. 1, pp. 245–248, 2005.

Toptigin, I.N. Cosmic rays in the interplanetary magnetic fields. Moscow, 108, in Russian, 1983.

Zazyan, M., Chilingarian, A. On the possibility to deduce solar proton energy spectrum of the 20 January 2005 GLE using Aragats and Nor-Amberd neutron monitor data, in: Proceedings of the 2nd International Symposium on Solar Extreme Events, Nor-Amberd, Armenia, TIGRAN METZ, pp. 200–202, 2006.

Available online at www.sciencedirect.com
ScienceDirect
Astroparticle Physics 28 (2007) 58–71
Astroparticle Physics
www.elsevier.com/locate/astropart

# Study of extensive air showers and primary energy spectra by MAKET-ANI detector on mountain Aragats

A. Chilingarian [a], G. Gharagyozyan [a], S. Ghazaryan [a], G. Hovsepyan [a,b,*], E. Mamidjanyan [a,b], L. Melkumyan [a], V. Romakhin [b,✠], A. Vardanyan [a], S. Sokhoyan [a,b]

[a] *Alikhanyan Physics Institute, Cosmic Ray Division, Armenia*
[b] *Lebedev Physics Institute, Moscow, Russia*

Received 20 November 2006; received in revised form 17 April 2007; accepted 20 April 2007
Available online 27 April 2007

**Abstract**

Small and middle size surface detectors measuring extensive air showers (EAS) initiated by primary cosmic rays (PCR) incident on terrestrial atmosphere have been in operation for the last 50 years. Their main goal is to explore the "knee" in all particle spectrum to solve the problem of cosmic ray (CR) origin and acceleration. The recent achievements of atmospheric Cherenkov telescopes and X-ray space laboratories, establishing the supernova remnants (SNRs) as a source of hadronic cosmic rays, pose stringent conditions on the quality of EAS evidence. After establishing the existence of the "knee" itself, the most pronounced result from EAS studies is the rigidity dependent shift of the knee position to the highest energies. This feature was first observed by separation of the primary flux in different mass groups in MAKET-ANI, EAS-TOP and KASCADE experiments. The MAKET-ANI detector is placed on Mt. Aragats (Armenia) at 3200 m above the sea level (40°25′N, 44°15′E). More than $1.3 \times 10^6$ showers with size greater than $10^5$ particles were registered in 1997–2004. The detector effectively collected the cores of EAS, initiated by primaries with energies of $10^{14}$–$10^{17}$ eV. After proving that the quality of the EAS size and shape reconstruction was reasonably high, we present the lateral distribution function (LDF) for distances from 10 to 120 m from EAS core and EAS size spectra in 5 zenith angle intervals. We use CORSIKA simulations to present the energy spectra. The results from the MAKET-ANI experiment on the energy spectra of the "light"(p + He) and "heavy" (O + Si + Fe) nuclear groups are compared to the spectra obtained by balloon experiments and to other available spectra.


*Keywords:* EAS installation; Lateral distribution function (LDF); EAS size spectra; Cosmic ray energy spectra; "Light" and "heavy" components

## 0. Introduction

A new paradigm in astrophysics research consists of the detection of celestial objects in radio, optical, X-rays, and gamma rays. A variety of compatible measurements provide sufficient information for building realistic models of physical processes of supernovae explosions, of accompanying gamma-ray bursts, of accretion disc interactions with super-dense objects, and, finally, of the evolution of Universe itself. In this case additional information about the particles of highest energies arriving in the Solar system will significantly enrich the information about the most violent processes in the Universe.

Cosmic ray (CR) flux incident on terrestrial atmosphere consists mostly of protons and heavier stripped nuclei accelerated at numerous galactic and extragalactic sites. One of the most exciting questions to be explored by cosmic rays research is that of identifying the accelerating sources and acceleration mechanisms. Due to the bending in galactic magnetic fields, charged particles lose information about the parent sites during their long travel and arrive on the Earth being highly isotropic. Galactic cosmic

* Corresponding author. Address: Alikhanyan Physics Institute, Cosmic Ray Division, Armenia. Tel./fax: +374 10 344 377.
*E-mail address:* hgg@crdlx5.yerphi.am (G. Hovsepyan).
✠ Deceased.

0927-6505/$ - see front matter © 2007 Elsevier B.V. All rights reserved.
doi:10.1016/j.astropartphys.2007.04.005

rays cannot map the objects where they were born, therefore, only integrated information from all sources is available from measurements of cosmic ray fluxes on the surface of Earth. This information consists of the shape of the energy spectra of the the different species of cosmic rays and of the CR arrival anisotropy.

The energy spectrum is of non-thermal origin and follows a power law over many orders of magnitude. The spectrum steepens at energies around 3–5 PeV. This feature is commonly called the knee and its explanation is generally believed to be a corner stone in understanding the origin of cosmic rays [1].

Presently, cosmic rays above ~0.1 PeV are experimentally accessible in ground-based detectors only. These detectors do not measure the primary particles; secondary particles produced in high-energy interactions in the atmosphere and forming extensive air showers (EAS) are measured instead. This makes the interpretation of the indirect measurements very difficult and the results obtained depend on the understanding of high-energy interactions in the atmosphere. However, regardless of considerable differences of the applied methods analyzing the EAS observables, different simulation procedures, and different observation levels, the compiled experimental results agree quite well (see review [2]). After compiling the world data (14 spectra), the average values and their variances result in a slope below the knee $\gamma = -(2.68 \pm 0.06)$ and above the knee to $-(3.06 \pm 0.08)$ with the knee position at $E_k = (3.2 \pm 1.2) \times 10^{15}$ eV. Nevertheless, to understand the CR origin, the knowledge of the all-particle spectra is not enough. As [1] demonstrates, the majority of 17 different particle acceleration models yield very similar all-particle spectra. On the other hand, the predictions of the behavior of the individual element spectra are quite different.

The implementation of the non-parametric multivariate methodology [3] allows for the event-by-event-analysis of EAS data [4], using Bayesian and neural network statistical models [5–7]. These methods also allow control of the quality of statistical decisions. At each stage of the analysis, we estimate the value of the information content of the variables used for EAS classification and energy estimation and restrict the complexity of the physical inference (number of different mass groups) according to this value.

The MAKET-ANI setup is located at 3200 m above the sea level on Mt. Aragats, Armenia. At this altitude the shape of the showers is not distorted by the attenuation in the terrestrial atmosphere and it is possible to reliably reconstruct EAS size and shape. The distinctive information contained in the distributions of these two parameters allows us to classify the EAS with a high level of accuracy only into two distinct groups: initiated by "light" (p + He) or "heavy" (O + Si + Fe) nuclei. The previously published MAKET-ANI data [8] demonstrated the existence of a sharp knee in the light component, and no knee in the heavy one up to about $3 \times 10^{16}$ eV. The available world data confirm these results. In the KASCADE experiment, the position of the knee shifted towards higher energies with increasing element number [9]. In HEGRA [10] a different experimental methodic was used, nevertheless the result also shows steepening of the light mass group and a shift of the knee position to lower energy as compared to the all particle spectra. In EAS-TOP [11], the light component was separated using information from the EAS electrons and TeV muons. The results could again be interpreted in the standard framework of a rigidity-dependent acceleration/propagation process.

To summarize the situation with EAS experiments around the knee, the limiting factors of a more detailed analysis and "mass spectroscopy" in the knee region include the uncertainty of the parameters of high-energy interaction models required for the complicated "unfolding" techniques [12]. See also the discussion in [13]. More robust non-parametric statistical analysis models [14] proceeding from less sophisticated simulations and classifying EAS only into two groups allow to derive rigidity-dependent knee position [8,15–17], as expected from the diffusive shock acceleration by Supernova (SNR) blast waves (see review [18]). We think that this is the *final physical inference* on partial energy spectra that can be drawn from small to middle size EAS experiments. This inference is supported by different experiments, statistical methods, hard interaction models and EAS parameters included in the analysis.

Another *indirect strong evidence* of the proton and ion acceleration in SNR is the strong amplification of the magnetic field. The precise measurements of the X-rays from SN 1006, by CHANDRA [19] imply a very large effective magnetic field of >100 μG in the Supernovae remnant. In [20] the authors conclude that such a large field could be generated only by the non-linear interactions of the accelerated protons and stripped heavier nuclei with self-generated Alfven waves in a strong shock. Therefore, the SN 1006 data confirm the acceleration of the nuclear component at least up to several units of $10^{14}$ eV. Further morphological measurements of young SNRs (Cas A and Tycho, Kepler,...) prove that they all exhibit the amplification effect as a result of the very efficient acceleration of nuclear cosmic rays at the outer shock [21].

The *direct evidence* of the shock wave acceleration in SNR shells was achieved by the atmospheric Cherenkov telescopes (ACT). The measured γ-ray maps of SNR shells RX J1713.7-3946 and RX J0852.0-4622 [22] (both discovered in TeV γ-rays by CANGAROO [23]) demonstrate that the shock wave accelerates particles to multi-TeV energies, generating photons via hadron interactions with gas. This direct evidence provided by the ACT imaging technique is supported by the indirect evidences provided by the detailed X-ray maps of SNR shells and partial spectra of high-energy cosmic rays measured by the surface particle detectors. The theoretical models of shock acceleration assuming shocks with various velocities propagating in the exited random magnetic fields can accelerate even particles up to $10^{17}$ eV (see review [24]). To reach these high energies, the particles should be trapped near the shock

wave to gain energy during numerous shock traversals. The proton and striped nuclei confinement near the shock is accounted for by scattering on the self-excited Alfven waves [25].

We believe that the same mechanisms, operating at a much smaller scale, accelerate the solar cosmic rays [26] reaching the Earth and detected by the space-born and surface particle detectors. These direct relations of the acceleration mechanisms of solar and galactic cosmic rays and the growing understanding of the importance of solar–terrestrial connections contribute to the interest towards ground-based particle detection in Solar physics and Space Weather research [27–29].

It remains, however, very important to summarize and confirm the surface detectors findings to solve the CR source problem. In the presented paper, we clarify and check the EAS registration technique used for the MAKET-ANI data analysis. The most important quantity calculated from EAS measurements is the shower lateral distribution function (LDF). The shower size – $N_e$ and shape (age) – $s$ parameters are derived from the interpolated LDF and used for the primary particle type and energy estimation. We present the procedures used for calculating these parameters and discuss the accuracies and biasness of the estimates. We also present the size distribution of the measured showers, obtained with minimal assumptions about the strong interaction model.

The MAKET-ANI detector has been in operation for ~10 years and its experimental database contains more than 1.3 million showers with $N_e \geqslant 10^5$ and zenith angles $\leqslant 47°$. The EAS database can be accessed from the home page of the Cosmic Ray Division of Yerevan Physics Institute (http://crdlx5.yerphi.am).

## 1. Experimental procedures for obtaining EAS parameters

The MAKET-ANI surface array [30], see Fig. 1, includes 92 particle density detectors consisting of 5 cm thick plastic scintillators. Sixty eight detectors have 1 $m^2$ area, the remaining 24 are 0.09 $m^2$. The central part of the detector consists of 73 scintillators and is arranged in a rectangle of $85 \times 65$ $m^2$. Fifteen and four 1 $m^2$ scintillators of the same type are placed at two remote locations at a distance of 95 m and 65 m from the center of the array. In order to estimate the zenith and azimuth angles, the 19 (9 of them participate in timing trigger) detectors out of 92 are equipped with timing readouts to measure the timing of the appearance of the EAS front with an accuracy of ~5 ns. The photomultiplier tubes (PM-49) of the detectors are placed in the light-tight iron boxes. Logarithmic analog to digital converters (ADC) and constant fraction discriminators (CFD) are assembled just above the photomultiplier tube (see Fig. 2). The dynamic range of the registered particle number is $\sim 5 \times 10^3$.

Three types of detector triggers are used:

1. The hardware trigger: at least 7 of 11 central density detectors must be hit by more than three particles.
2. The timing trigger: at least 4 from 9 preselected timing detectors, symmetrically arranged relative to the center of array, should be hit.
3. The software trigger adding several additional restrictions was used off-line.

If the first two conditions are fulfilled, the information from all 92 channels is stored. The trigger and data readout systems are implemented in the CAMAC standard. The simulations prove that the trigger system selects EAS with sizes $N_e \geqslant 10^5$ with cores located within the rectangle of $44 \times 20$ $m^2$ around the geometrical center of the detector with efficiency no less than 95% [31].

### 1.1. Accuracies of the EAS parameters determination

The EAS axis is assumed to follow the primary CR direction. In turn, the EAS direction is usually derived from the arrival time measurements applying fast-timing technique. In MAKET-ANI array 19 detectors are equipped with two PMs (see Fig. 2). One of them is used for particle density estimation, and the second – for the precise timing. The output signal from the timing channel (in the NIM standard) triggers the 200 MHz frequency generator. The signal of the timing trigger is used as a STOP signal. The quantification level for the timing infor-

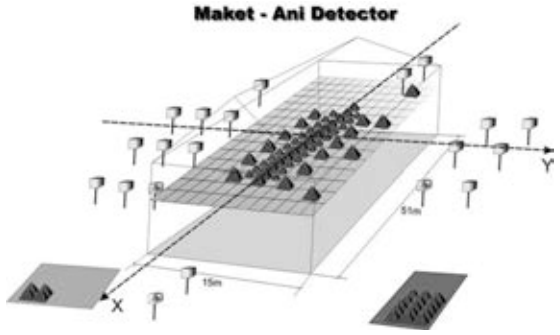


Fig. 1. The layout of the MAKET-ANI detector.

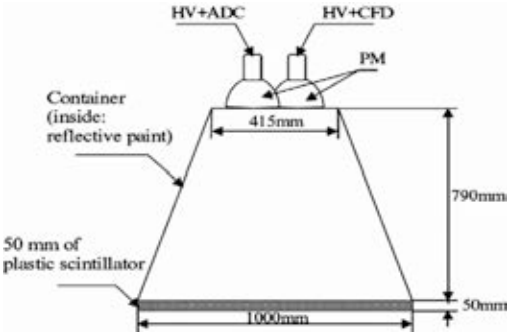


Fig. 2. The MAKET-ANI scintillator–PMT configuration for the 19 detectors with timing.

mation is 5 ns. A more detailed description of the fast-timing system can be found in [32].

The zenith $\theta$ and azimuth $\varphi$ angles are defined by solving the following system of equations:

$$c \cdot \Delta t_i = (x_i \cdot \mathrm{Cos}(\varphi) + y_i \cdot \mathrm{Sin}(\varphi)) \cdot \mathrm{Sin}(\theta) + z_i \cdot \mathrm{Cos}(\theta), \quad i = 1, \ldots, M \tag{1}$$

where $c$ is the speed of light, $\Delta t_i$ is the delay of the signal in the $i$th scintillator compared to a reference scintillator placed in the geometrical center of the array, $x_i, y_i, z_i$ are the space coordinates and $M$ is the number of timing detectors.

The estimates of angular accuracies were obtained by simulation of detector response (taking into account the triggers conditions, EAS size spectrum, etc.), assuming that the particles arrival time can be described by Gaussian distribution [33]. An independent method uses different possible combinations of timing detectors for calculating the angles of incidence. Then, from a variety of alternative estimates, the non-parametric estimate of variance was constructed according to [34]. Both methods give consistent results: angular accuracy no worse than $\sim$1.5° for zenith angles and no worse than $\sim$5° for the azimuth ones for the showers within $15° < \theta < 45°$ (see Fig. 3). The accuracy of the azimuth angle strongly depends on the zenith angle and becomes very poor at small zenith angles.

The analog signal from PM is converted to code using logarithmic ADC; the relative uncertainty introduced by the transition from analog signal to discrete code is $\sim$10% [35].

The logarithmic ADC provides the linearity of the transformation (see Fig. 4), therefore we can write

$$K = \mathrm{int}(d \cdot \ln A_{\mathrm{PM}}) + K_0 \tag{2}$$

where $K$ is the registered code (output of ADC), $d$ is the scale factor of ADC (the so-called "decrement"), tuned

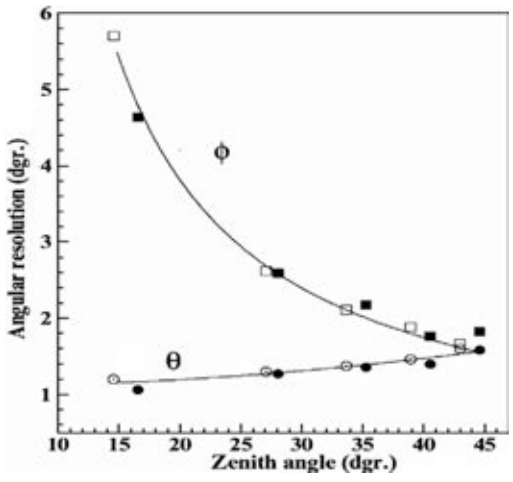


Fig. 3. The angular accuracies of the EAS axes determination. Rectangles – azimuth angles; circles – zenith angles. Open symbols – non-parametric method, closed symbols – simulation.

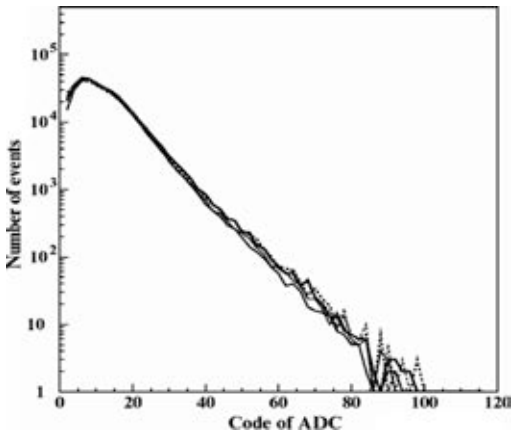


Fig. 4. The distribution of the registered ADC codes by four scintillators of the MAKET-ANI array.

with special electronics to be $d = 10 \pm 0.2$, and $A_{\mathrm{PM}}$ is the output signal of the PM. To give physical meaning to the registered code $K$, we define an arbitrary constant $K_0$ to be equal to the mean energy deposit of electrons in 5 cm thick scintillator. In this case, the quantity $e^{(K-K_0/d)}$ will be equal to the number of particles in the scintillator.

The simulations of EAS electrons traversal through the 5 cm thick scintillator with GEANT3 [80] code and calibration measurements of $K_0$ [36] provide very close value, $\sim$10.8 MeV, of the mean energy release of the EAS electrons. Proceeding from this value, the conversion from the energy release to the detected code was done according to the methodology described in [37]. Using the detected code values, we determine the number of particles (density) at each 92 scintillator location. Then, using interpolation and integration procedures, we estimate the total number of electrons in the shower. We also have to correct the observed particle number registered by the scintillator to various effects such as the contamination of the electron–positron pairs borne by the traversing gamma ray in the scintillator, and nuclear interactions in the scintillator. The ratio between experimentally observed density $\rho_{\mathrm{sc}}(r)$ and EAS electron density $\rho_{\mathrm{ch}}(r)$ depends on the distance from the EAS axes and can be described as follows [38]:

$$R_{\mathrm{sc/ch}}(r) = \rho_{\mathrm{sc}}(r)/\rho_{\mathrm{ch}}(r) = (r/r_{\mathrm{m}})^{-\alpha} \tag{3}$$

where $r$ is the distance from the EAS core, $r_{\mathrm{m}}$ – Moliere radius, equal to 118 m on the MAKET-ANI array location and $\alpha$ is the parameter controlling the steepening of the function (3). We determine $\alpha$ from the measurements of particle densities by the 1.0, 1.5 and 5 cm thick scintillators located in the one and the same position [39]. For the EAS with the number of particles $N_{\mathrm{e}} \geqslant 10^5$, we obtain value $\alpha \sim 0.18$–$0.19$ which agrees well with [40,41]. The accuracy of the measured particles density also depends on the fluctuations of the light collection in the scintillator, PM quantum efficiency, amplifier fluctuation, the accuracy of the scale factor estimation, etc. [37]. Influence of these effects on the density estimates was checked by comparing output

signals of two measuring channels (PM + ADC) attached to the same scintillator. Finally the total relative error of the particle number estimate comes to ~11% for five particles, ~13% for 500 particles and reaches ~18% at a maximal number of 5000 particles.

### 1.2. Detectors calibration and stability

It is necessary to periodically check the stability of array channels during multiyear observations. The drift of the characteristics of the components used for assembling the PM high voltage and ADC electronic devices leads to a bias in the particle density measurements, and, therefore, in EAS size and shape estimation. The MAKET-ANI detector was commissioned in the late 80s. The characteristics of the electronic components significantly degraded and need continuous check and replacement. The idea to use the fluxes of secondary cosmic rays produced by primaries in terrestrial atmosphere for the detector calibration is straightforward. It was much more complicated to choose the appropriate parameter of the secondary flux, stable enough to be used as a reference for at least 10 years. The problem is that our nearest star, the Sun, is modulating the low-energy CR flux. The modulation effects can be broadly categorized into three types. The first one relates to the acceleration of protons and ions in solar flares and by chock waves. If the energy of the accelerated particles is high enough, the solar cosmic rays produce additional muons and electrons enhancing the mean intensity measured by the surface particle detectors (the so-called ground level enhancement – GLE). These events are rather rare and their duration is usually no more than few tens of minutes at Aragats latitude. Other solar modulation effects relate to the transport of the huge magnetic cloud, ejected from Sun during violent explosions (coronal mass ejection – CME). Reaching the Earth, this cloud disturbs the terrestrial magnetic field and makes the intensity of the incident GCR decrease. The consequent decrease of the secondary cosmic rays is known as Forbush decrease (Fd) and can come close to 20% at Aragats latitudes [42]. At the recovery phase of Fd lasting for about a week, the intensity of secondary particles can show a peak lasting for several hours and coinciding with the sudden beginning of a severe geomagnetic storm (GMS). GMS originates due to the decrease of the terrestrial magnetic field interacting with CME magnetic field. This decrease leads to the entrance of additional low-energy protons and ions in the atmosphere and the generation of the additional secondary particles. Therefore, solar modulation effects, mostly long lasting Fd, can significantly change the intensity of the secondary cosmic ray flux, which cannot be used for detector calibration purposes. On the other hand, the spectra of the energy releases in scintillators measured by the ADC prove to be stable quantity, not influenced by even the strongest Fd.

Examining the change of the intensity of the secondary cosmic rays (see Fig. 5a), we detect that during the huge

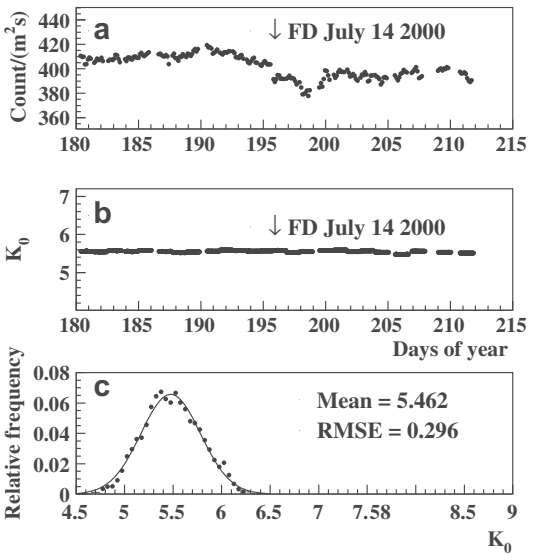


Fig. 5. Time series and histogram of the registered count rates of MAKET-ANI scintillators in July 2000. (a) Count rate of secondary particles per second. There is an abrupt decrease of intensity during Fd which started on July 14, 2000. (b) The time history of the mode of the energy releases spectra $K_0$, note that during the huge Fd on July 14 there are no changes. (c) Distribution of the obtained $K_0$ taken for all 92 scintillators of the array including $N_{tot} \approx 10^4$ measurements of $K_0$.

Forbush decrease on July 14 the intensity decreased by ~8% and it took more than a week to recover its previous value. At the same time (see Fig. 5b) the mode of the spectra of secondary cosmic rays detected by 5 cm scintillator was very stable and did not change during Fd. Fig. 5c confirms the high stability of the chosen parameter. Therefore, the mode values of the spectra of energy release $K_0^i$ (the so-called "single particle" spectrum) were monitored during the whole operation of MAKET-ANI for all 92 channels. After the regular examination of these parameters, if, for example, we find the value of $K_0^i$ of the $i$th scintillator out of the acceptable limits of $5.5 \pm 3\sigma$ (see Fig. 5c), this particular scintillator signal did not enter EAS analysis procedures and its PM high voltage was tuned. In this way, the continuous check of the MAKET-ANI measuring channels provided high stability of array operation in 1997–2004.

### 1.3. Reconstruction of the EAS electron number

From the particle densities measured by the grid of array scintillators, it is possible to derive the total number of particles (the EAS size $N_e$), the center of gravity of the 2-dimensional particle density distribution (EAS core location), and, the so-called, $s$ shower shape (age) parameter, correlated with the height of the first interaction of primary ion with the nuclei of terrestrial atmosphere. The functional form of the EAS lateral distribution was suggested by Nishimura, Kamata and Greizen (NKG) [43,44]:

$$\rho_{sc}(r) = N_e/r_m^2 \cdot C(s) \cdot R_{sc/ch} \cdot (r/r_m)^{s-2} \cdot (r/r_m + 1)^{s-4.5}, \quad (4)$$

where $\rho_{sc}(r)$ is the observed density at distance r from the EAS core position, $N_e$ is the EAS size, $r_m = 118$ m (for the MAKET-ANI altitude) is the Moliere radius, $s$ is the age of shower, $R_{sc/ch}$ – the correction factor (see Eq. (3)) and $C(s) = 0.366s^2(2.07 - s)^{1.25}$ is the normalization constant [45,46]. First, the iteration procedure is used to determine the EAS shape parameter $s$ and core co-ordinates by least squares method (MINUIT [81]), then the shower size $N_e$ is estimated by maximum likelihood method (see details in [47]).

Many authors [48,49] mention that the NKG function does not satisfactorily fit the electron density distribution at the large distances from the EAS core. It is not the case for MAKET-ANI, because the modest sizes of array allowed us to estimate the lateral distribution function at rather small distances not exceeding 120 m.

One of the checks of the EAS parameters reconstruction soundness is the uniformity test. Fig. 6 demonstrates that the reconstructed co-ordinates of EAS axes rather uniformly fill the surface occupied by the MAKET-ANI array. There are no pronounced gaps or peaks in the 2-dimensional distribution of the shower axes.

The event frequency (counts per minute) is also a very important parameter demonstrating the stability of the trigger condition during multiyear operation. Fig. 7 presents the 5-year time series of the frequencies of the detected EAS. The average frequencies of the selected EAS are very stable and equal to $0.234 \pm 0.013$ min$^{-1}$ for $N_e \geqslant 1.6 \times 10^5$; $0.056 \pm 0.006$ min$^{-1}$ for $N_e \geqslant 4 \times 10^5$ and $0.013 \pm 0.003$ min$^{-1}$ for $N_e \geqslant 10^6$.

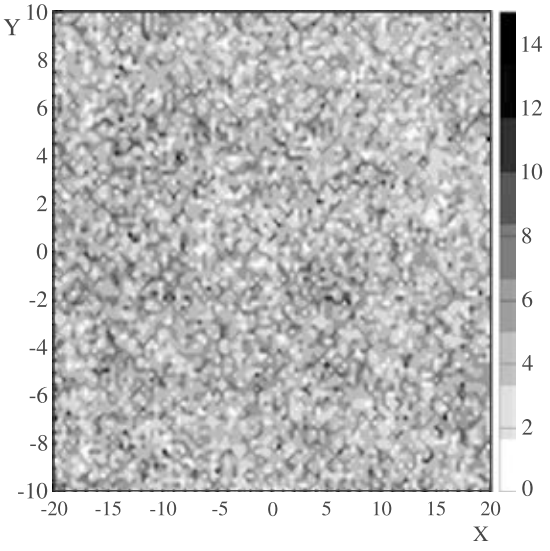


Fig. 6. A two-dimensional histogram of the EAS hits of MAKET-ANI array ($1.5 \times 10^5$ events).

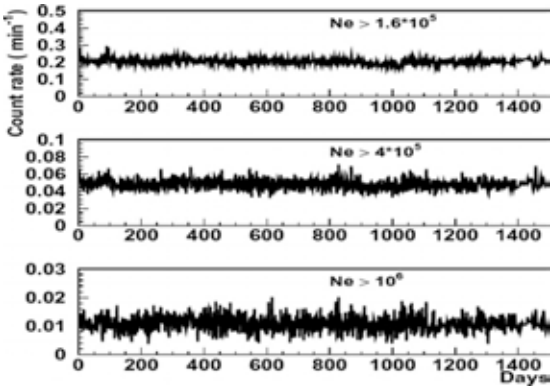


Fig. 7. The count rate of registered EAS versus exposition time since 1st June 1997 for different EAS sizes; core position is within the area of 880 m$^2$.

### *1.4. The efficiency of EAS registration and array response to primary protons and iron nuclei*

For a reliable reconstruction of the CR flux incident on the atmosphere, it is necessary to investigate the efficiency of the trigger. A simple event-generator (for details see [37,50]) simulates the EAS falling randomly on the rectangular area of $44 \times 80$ m. The shower sizes were simulated using the power law with constant power index $\gamma = -2.5$ for the EAS sizes starting from $N_e = 3.8 \times 10^4$. The zenith angle is assumed to follow $\mathrm{Cos}^{\beta}(\theta)$ form, where $\beta = (X_0/\lambda), X_0 = 700$ g/cm$^2$, and $\lambda = 140$ g/cm$^2$, the azimuth angle was simulated by the uniform distribution in 0–360°. Approximately $10^8$ events were generated. For each event the number of shower particles at 92 detector locations was determined using NKG function. The shower age parameter was randomly chosen from the parameterized function obtained from the showers measured by MAKET-ANI. After obtaining NKG particle densities at all 92 array scintillator locations, they were distorted according to the experimental accuracies. Then the data analysis procedures adopted by the MAKET-ANI experiment were used (see points 1.1–1.3). The comparisons of the number ''input'' EAS and the ''registered'' EAS allow us to estimate the array efficiency to detect EAS with different sizes.

After obtaining the efficiencies for each shower size $N_e$, we determine the appropriate core selection areas (rectangles around the array geometrical center) to guarantee high ($\varepsilon \geqslant 0.95$) efficiency of the EAS registration. This allowed to define the so-called effective area $S_{eff}$, ensuring preselected registration efficiency for each shower size. Using appropriate $S_{eff}$ areas for each $N_e$, the size spectra for different angles of incidence were obtained (see Section 4). The additional restriction requires the maximal allowable distortion of age parameter to be less than 0.03.

We also perform simulations to check the array response to the EAS initiated by primary proton, He, Si and iron nuclei. To avoid biases due to attenuation of EAS in terrestrial atmosphere and due to different responses of array to

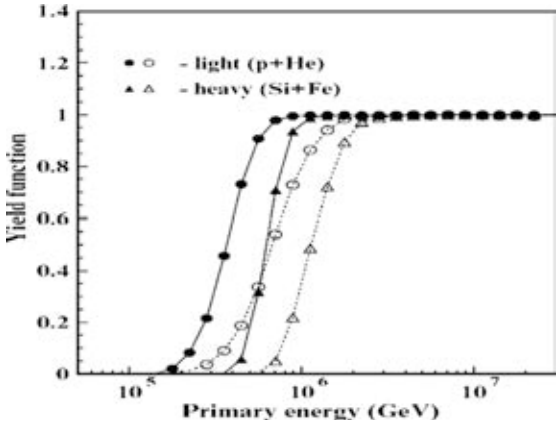


Fig. 8. The response of the MAKET-ANI detector on simulated "light" (p + He) and "heavy" (Si + Fe) induced showers, versus primary energy; shower selection criteria: $N_e \geqslant 10^5$, $\theta \leqslant 30^\circ$ (closed symbols), $N_e \geqslant 10^5$, $30^\circ \leqslant \theta \leqslant 45^\circ$ (open symbols).

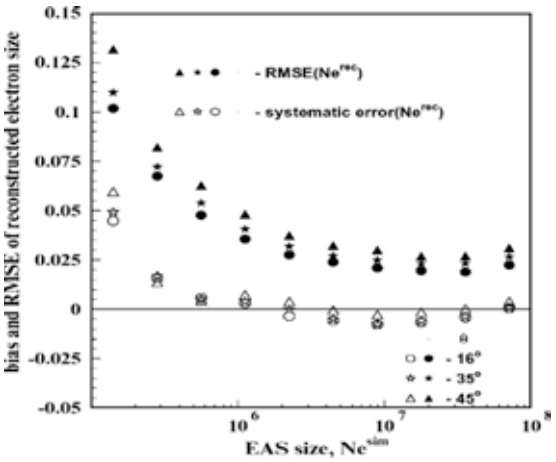


Fig. 9. The systematic errors and RMSE of shower size $N_e^{rec}$ for different zenith angles of incidence.

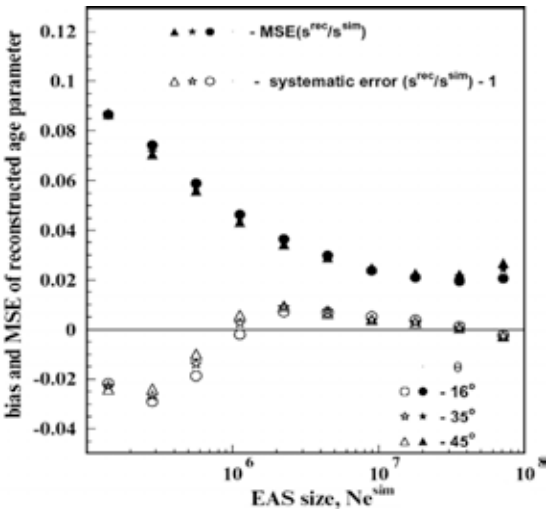


Fig. 10. The average difference (systematic error) and RMSE of ratio of reconstructed and simulated age parameter for the same zenith angles of incidence as in Fig. 9.

"light"(p + He) and "heavy" (O + Si + Fe) primaries, the core selection area was limited to $20 \times 44\ m^2$ around the geometrical center of the array and showers with $N_e \geqslant 10^5$ coming from near vertical direction ($0^\circ \leqslant \theta \leqslant 30^\circ$) were selected. This made us lose some events. However (see Fig. 8, closed symbols), by making small corrections (<10%) to estimated intensities it is possible to obtain the unbiased "recovered" intensity of the "light" nuclei flux starting from $\sim 6 \times 10^{14}$ eV and from $\sim 8 \times 10^{14}$ eV for the "heavy" nuclei, respectively. For the inclined showers ($30^\circ \leqslant \theta \leqslant 45^\circ$), (see Fig. 8, open symbols), much larger corrections should be done. As a result, the reliability of the spectra reconstruction becomes debatable.

### *1.5. The accuracy of the EAS parameters estimation*

The same event generator, as described in Section 1.4, was used for the estimation of the distortions of estimated shower parameters such as particles number $N_e$, shower age $s$ and shower core position. The differences of the "input" EAS parameters $(N_e^{sim}, s^{sim}, R^{sim}(X,Y))$ and calculated $(N_e^{rec}, s^{rec}, R^{rec}(X,Y))$ ones are presented in Figs. 9 and 10. The reconstructed shower size errors (including systematic) are less than ~13% at $N_e = 10^5$ and quickly decrease with the rise of shower size. The systematic errors lead to the overestimation of the EAS size by ~5–6% at $N_e = 10^5$ and near 1% at $N_e \geqslant 10^6$.

The errors of reconstructed age parameter are less than ~9% at $N_e = 10^5$. The underestimation of $s$ parameter is ~0.03 at $N_e \sim 10^5$. It turns to overestimation less than 0.01 at $N_e \sim 10^6$ and becomes vanishingly small at higher shower sizes. The accuracy of the reconstructed EAS core position within the collected area $S_{eff} = 880\ m^2$ is less than 1 m for all simulated age parameters and zenith angles of incidence. Shower parameters reconstruction errors (see Figs. 9 and 10) only slightly depend on the zenith angles of incidence.

## 2. The EAS lateral distribution function (LDF)

From 1997 to 2004 $\sim 1.2 \times 10^7$ shower triggers were registered. The total exposition time was $\sim 1.42 \times 10^8$ s. Only a small portion of the initial data was used for the investigation of the LDF and size and energy spectra in the presented analysis. We have already described how we selected the shower cores from the compact area around the geometrical center of the MAKET-ANI detector, ensuring large efficiency of EAS registration and high values of the "yield" function. This and additional restrictions on the EAS triggers

- $N_e \geqslant 10^5$,
- $0.3 < s < 1.7$,
- $\theta \leqslant 46.8^\circ$,

reduce the total number of events by an order of magnitude to a value of $\sim 1.3 \times 10^6$. Nonetheless, more than one million events with $N_e \geqslant 10^5$ are included in one of the largest data sets obtained by the EAS arrays operating at mountain altitudes.

The LDF functions were estimated in the five zenith angular intervals (bins), uniformly distributed according to Sec($\theta$) in [0–46.8°] and in nine logarithmically uniform intervals in shower size $\mathrm{Lg}\,N_e$[5–7.7] with step $\Delta \mathrm{Lg}(N_e) = 0.3$. To avoid saturation effects, we did not use scintillators located at distances nearer than 10 m from EAS axes.

The analytical form of the LDF function is the major factor influencing the correct reconstruction of the shower size. The reconstructed size of EAS and the energy of primary particle are heavily dependent on the accepted assumption about LDF. Therefore, we first have to check the consistency of the chosen LDF shape by comparing the measured particle densities to those from the LDF best fit at detector location. The bias of density estimates is less than 5% for the core distances up to 80 m; it reaches ~10% at large distances ~120 m and large $N_e$ ($\sim 10^7$) (see Fig. 11).

To compare the experimentally obtained LDF functions to the theoretical ones, we assume the following mass composition and energy spectra of the primary galactic cosmic rays (the so called "normal" mass composition [51]): (35%H, 25%He, 14%O, 15%Si, 10%Fe);

knee position $E_{\mathrm{knee}} = Z \cdot E_0$, $E_0 = 3 \times 10^{15}$ eV, $Z$ is the primary nuclei charge;
energy spectra index $\gamma_1 = -2.7$ before knee and, $\gamma_2 = -3.1$ after knee for all nuclei.

By simulating the EAS development in the atmosphere with the CORSIKA 562 (QGSJet01, NKG mode) code [52], we obtain the "pseudo-experimental" particle densities at scintillator locations. Using the experimental analysis procedures, we obtain the "theoretical" LDF functions.

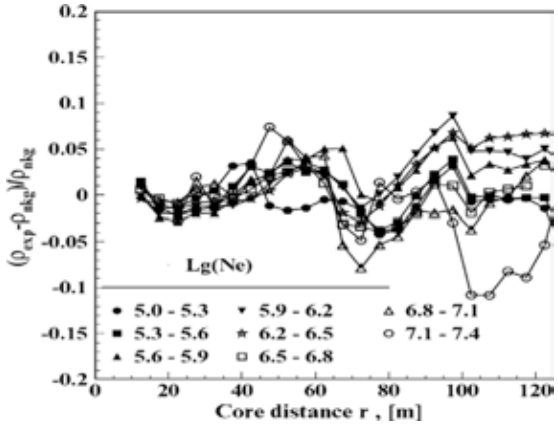


Fig. 11. The relative deviations of the experimentally observed showers particles LDF and expected by the NKG approximation for different EAS sizes.

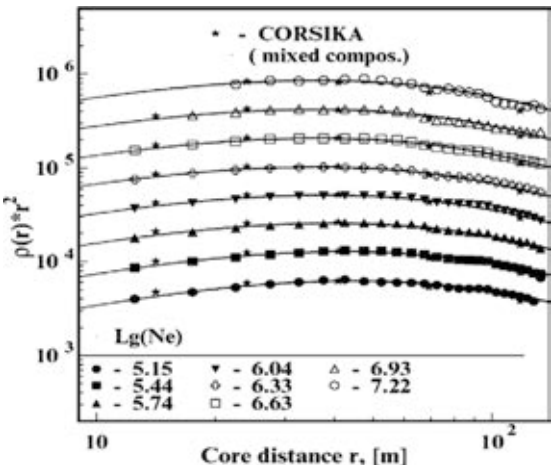


Fig. 12. The experimentally measured LDF in comparison to CORSIKA 562 (QGSJet01, NKG) simulations. The asterisks are "theoretical" values of the LDF function, the lines are LDF corresponding to the "averaged" EAS.

LDF functions are presented for different shower sizes in Fig. 12 for the near vertical EAS incidence [$0° < \theta \leqslant 23.8°$]. The experimental and "theoretical" values of LDF function agree quite well for all distances and for all shower sizes. The lines in Fig. 12 correspond to the LDF function obtained with the averaged EAS parameters measured in the experiment.

The high accuracies of the EAS parameters estimation (Figs. 9 and 10), the good agreement of the LDF obtained by CORSIKA simulations and the interpolation of the measured particle densities (Fig. 12) point to the soundness of using the experimental methodic to calculate

- array response;
- transition effects in the scintillators;
- EAS parameters.

## 3. Physical inference from the measured LDF

As we demonstrated in the previous section, the agreement of the measured LDF with CORSIKA, 562 simulations based on QGSJet01/NKG is quite good. The recently reported [12] disagreement of the measured LDF with that obtained by more sophisticated CORSIKA simulation modes (EGS mode with SIBYLL2.1 and with QGSJet01) can be explained by the drawbacks of strong interaction and electromagnetic cascading processes simulations. The better agreement of LDF measured by MAKET-ANI with that from NKG CORSIKA mode can be explained by the high latitude location of array (at the sea level the showers initiated by primaries of $10^{15}$–$10^{16}$ eV are already attenuated and do not show "classical" NKG shape) and by much smaller EAS core collecting area. In this concern we want to mention once more that the used data analysis methods should be coherent

with (a) the information content of measurements and (b) the physical inference we want to derive from the experiment. We cannot treat simulations of EAS development in terrestrial atmosphere as a precise tool, therefore we have to restrict ourselves to robust physical inference which is efficient for deciding on the alternative physical hypothesis, but not too detailed and, as a result, not too heavily dependent on a particular simulation scheme and on the strong interaction model used.

The dependence of the measured age parameter on shower size in comparison to several models of primary flux composition is presented in Fig. 13. To outline the boundaries of the extreme cases we use pure proton and pure iron nuclei fluxes. More realistic assumptions about energy dependence of the primary composition are between these extreme assumptions:

1. Rigidity dependent "normal" composition with knee position at $E_{\text{knee}} = Z \cdot 3 \times 10^{15}$ eV – [51].
2. The same as in point 1, but with fixed knee position at $E_{\text{knee}} = 3 \times 10^{15}$ eV for each group of nuclei.
3. "Heavy" composition (5% P, 5% He, 10% O, 10% Si, 70% Fe) [53], knee position at $E_{\text{knee}} = Z \cdot 3 \times 10^{15}$ eV.

For all three models the energy spectra index $\gamma_1 = -2.7$ before knee and $\gamma_2 = -3.1$ after knee for all nuclei.

The first model ("normal" composition) fits experimental data quite well (the value of the test equals $\chi^2 = 1.23$). At the same time we can exclude the options 2 ($\chi^2 = 8.8$) and 3 ($\chi^2 = 31.1$). The observed dependence of the age parameter on the EAS size (proxy of the energy of primary proton/nuclei) after knee can be understood as a result of the CR mass composition transition from light to heavy nuclear composition.

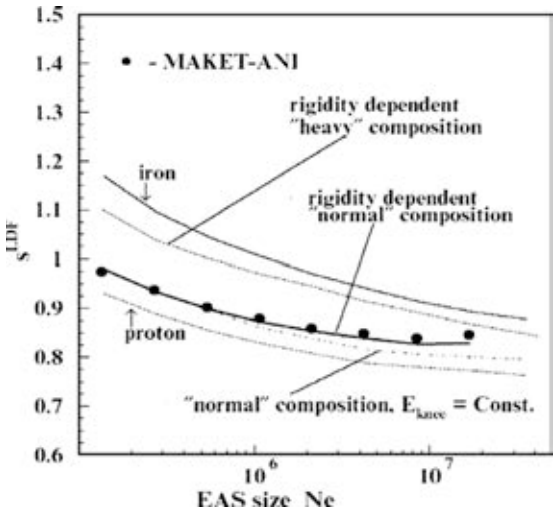


Fig. 13. The comparison of the $s(N_e)$ dependence measured by the MAKET-ANI array with different assumptions about primary flux composition.

## 4. Differential EAS size spectra

The size spectra presented in Table 1 are obtained with EAS collected from the area $S_{\text{eff}}$, providing a chosen level of the trigger efficiency (>95%). We also keep the condition of the maximal allowable distortion of age parameter (<0.03) [31]. To check the detector response obtained with simple model (see Section 1.3), we use CORSIKA code to generate EAS for different nuclei, slopes of energy spectra and knee positions. The obtained results pointed to the model-independence of the used detector response function and to a correct account of the experimental distortions – the accuracy of the reconstructed spectral index was no worse than 0.01. In Table 1, the size spectra for five angular intervals uniform in Sec($\theta$) and 25 logarithmically uniform intervals in shower size are presented. The observed intensities were approximated by the equation suggested in [54]:

$$\frac{\mathrm{d}J(N_e,\theta)}{\mathrm{d}N_e} = A(\theta) \cdot N_e^{-\gamma} \cdot \left[1 + \left(\frac{N_e}{N_e^{\text{knee}}}\right)^{\delta}\right]^{\Delta\gamma/\delta}, \qquad (5)$$

where $A(\theta)$ is the angular dependence of the spectrum; $\Delta\gamma = \gamma_1 - \gamma$ is the change of power index; $\gamma$ and $\gamma_1$ are the spectral indexes before and after knee; $N_e$(knee) is the knee position, and $\delta$ is the sharpness of the knee.

The parameters of approximation (5) of the size spectra, measured by MAKET-ANI, are listed in Table 2. From small values of goodness of fit $\chi^2/n$ df, we can conclude that Eq. (5) describes the size spectra quite well.

In Fig. 14, we present the size spectra measured by the MAKET-ANI detector along with the size spectra measured by the KASCADE experiment [55]. The numbers near the lines indicate the effective atmosphere depth, corresponding to different zenith angles of incidence. Knee positions for both MAKET-ANI and KASCADE data were calculated by Eq. (5). The change of the position of the knee with altitude, indicated by the solid line, demonstrates consistency of the major EAS parameters for both arrays located at sea level and at 3200 m above the sea level.

The remarkable coincidence of the size spectra measured by both detectors mentioned by Stanev [56] and large slant-depth available from joint data provide a well-established ground for attenuation length estimation. The longitudinal development of the electromagnetic fraction of EAS is characterized by the approximately exponential decrease in particle numbers for atmospheric depth far behind the shower maximum. Assuming a direct connection between the primary energy spectra and the electron number spectra, application of equal intensity cuts to integral electron number spectra in different angular bins selects showers with approximately equal primary energy. Measuring the attenuation of the electron number with increasing zenith angles yields the estimate of the attenuation length $\Lambda_{N_e}$. Proceeding from the knee positions indicated in Fig. 14 and the methodology described in [57], the attenuation length estimated by joint KASCADE–MAKET-ANI data

Table 1
The EAS intensities measured by the MAKET-ANI detector in 1997–2004

| $N_e$ | $S_{eff} \cdot T \times 10^{11}$ ($m^2$ s) | $dJ(\theta)/dN_e$ ($m^2$ s sr $\cdot N_e)^{-1}$ 0–23.8° | $dJ(\theta)/dN_e$ ($m^2$ s sr $\cdot N_e)^{-1}$ 23.8–32.4° | $dJ(\theta)/dN_e$ ($m^2$ s sr $\cdot N_e)^{-1}$ 32.4–38.5° | $dJ(\theta)/dN_e$ ($m^2$ s sr $\cdot N_e)^{-1}$ 38.5–43° | $dJ(\theta)/dN_e$ ($m^2$ s sr $\cdot N_e)^{-1}$ 43–46.8° |
|---|---|---|---|---|---|---|
| $1.12 \times 10^5$ | 1.06 | $(1.03 \pm 0.01) \times 10^{-10}$ | $(6.56 \pm 0.01) \times 10^{-11}$ | $(3.96 \pm 0.02) \times 10^{-11}$ | $(2.50 \pm 0.02) \times 10^{-11}$ | $(1.54 \pm 0.02) \times 10^{-11}$ |
| $1.41 \times 10^5$ | – | $(5.70 \pm 0.01) \times 10^{-11}$ | $(3.64 \pm 0.01) \times 10^{-11}$ | $(2.24 \pm 0.01) \times 10^{-11}$ | $(1.40 \pm 0.01) \times 10^{-11}$ | $(8.81 \pm 0.10) \times 10^{-12}$ |
| $1.77 \times 10^5$ | | $(3.18 \pm 0.01) \times 10^{-11}$ | $(2.02 \pm 0.01) \times 10^{-11}$ | $(1.27 \pm 0.01) \times 10^{-11}$ | $(7.96 \pm 0.08) \times 10^{-12}$ | $(4.93 \pm 0.07) \times 10^{-12}$ |
| $2.23 \times 10^5$ | – | $(1.77 \pm 0.01) \times 10^{-11}$ | $(1.14 \pm 0.01) \times 10^{-11}$ | $(7.27 \pm 0.06) \times 10^{-12}$ | $(4.51 \pm 0.06) \times 10^{-12}$ | $(2.85 \pm 0.05) \times 10^{-12}$ |
| $2.81 \times 10^5$ | 1.29 | $(1.00 \pm 0.04) \times 10^{-11}$ | $(6.45 \pm 0.04) \times 10^{-12}$ | $(4.06 \pm 0.04) \times 10^{-12}$ | $(2.55 \pm 0.03) \times 10^{-12}$ | $(1.62 \pm 0.03) \times 10^{-12}$ |
| $3.53 \times 10^5$ | | $(5.61 \pm 0.03) \times 10^{-12}$ | $(3.65 \pm 0.03) \times 10^{-12}$ | $(2.33 \pm 0.03) \times 10^{-12}$ | $(1.45 \pm 0.02) \times 10^{-12}$ | $(9.19 \pm 0.20) \times 10^{-13}$ |
| $4.45 \times 10^5$ | – | $(3.15 \pm 0.02) \times 10^{-12}$ | $(2.05 \pm 0.02) \times 10^{-12}$ | $(1.31 \pm 0.02) \times 10^{-12}$ | $(8.46 \pm 0.15) \times 10^{-13}$ | $(5.38 \pm 0.14) \times 10^{-13}$ |
| $5.60 \times 10^5$ | | $(1.77 \pm 0.01) \times 10^{-12}$ | $(1.14 \pm 0.01) \times 10^{-12}$ | $(7.51 \pm 0.11) \times 10^{-13}$ | $(4.69 \pm 0.10) \times 10^{-13}$ | $(2.85 \pm 0.09) \times 10^{-13}$ |
| $7.05 \times 10^5$ | 1.55 | $(1.01 \pm 0.08) \times 10^{-12}$ | $(6.60 \pm 0.07) \times 10^{-13}$ | $(4.33 \pm 0.08) \times 10^{-13}$ | $(2.68 \pm 0.06) \times 10^{-13}$ | $(1.61 \pm 0.05) \times 10^{-13}$ |
| $8.87 \times 10^5$ | 1.83 | $(5.62 \pm 0.05) \times 10^{-13}$ | $(3.61 \pm 0.05) \times 10^{-13}$ | $(2.40 \pm 0.04) \times 10^{-13}$ | $(1.45 \pm 0.04) \times 10^{-13}$ | $(8.48 \pm 0.32) \times 10^{-14}$ |
| $1.12 \times 10^6$ | 2.13 | $(3.12 \pm 0.03) \times 10^{-13}$ | $(2.03 \pm 0.03) \times 10^{-13}$ | $(1.27 \pm 0.03) \times 10^{-13}$ | $(7.63 \pm 0.21) \times 10^{-14}$ | $(4.58 \pm 0.20) \times 10^{-14}$ |
| $1.41 \times 10^6$ | 2.46 | $(1.73 \pm 0.02) \times 10^{-13}$ | $(1.12 \pm 0.02) \times 10^{-13}$ | $(6.80 \pm 0.16) \times 10^{-14}$ | $(4.19 \pm 0.14) \times 10^{-14}$ | $(2.38 \pm 0.12) \times 10^{-14}$ |
| $1.77 \times 10^6$ | 2.82 | $(9.05 \pm 0.19) \times 10^{-14}$ | $(5.78 \pm 0.11) \times 10^{-14}$ | $(3.72 \pm 0.11) \times 10^{-14}$ | $(2.14 \pm 0.09) \times 10^{-14}$ | $(1.24 \pm 0.08) \times 10^{-14}$ |
| $2.23 \times 10^6$ | – | $(5.06 \pm 0.08) \times 10^{-14}$ | $(2.93 \pm 0.07) \times 10^{-14}$ | $(1.95 \pm 0.07) \times 10^{-14}$ | $(1.13 \pm 0.06) \times 10^{-14}$ | $(6.41 \pm 0.47) \times 10^{-15}$ |
| $2.81 \times 10^6$ | – | $(2.48 \pm 0.05) \times 10^{-14}$ | $(1.59 \pm 0.05) \times 10^{-14}$ | $(1.00 \pm 0.04) \times 10^{-14}$ | $(5.95 \pm 0.38) \times 10^{-15}$ | $(3.08 \pm 0.28) \times 10^{-15}$ |
| $3.54 \times 10^6$ | | $(1.30 \pm 0.03) \times 10^{-14}$ | $(8.09 \pm 0.31) \times 10^{-15}$ | $(5.06 \pm 0.28) \times 10^{-15}$ | $(2.91 \pm 0.23) \times 10^{-15}$ | $(1.76 \pm 0.21) \times 10^{-15}$ |
| $4.43 \times 10^6$ | – | $(6.76 \pm 0.22) \times 10^{-15}$ | $(4.08 \pm 0.19) \times 10^{-15}$ | $(2.54 \pm 0.17) \times 10^{-15}$ | $(1.50 \pm 0.15) \times 10^{-15}$ | $(1.01 \pm 0.14) \times 10^{-15}$ |
| $5.59 \times 10^6$ | | $(3.47 \pm 0.13) \times 10^{-15}$ | $(2.07 \pm 0.13) \times 10^{-15}$ | $(1.11 \pm 0.10) \times 10^{-15}$ | $(8.38 \pm 0.10) \times 10^{-16}$ | $(4.39 \pm 0.78) \times 10^{-16}$ |
| $7.03 \times 10^6$ | – | $(1.58 \pm 0.08) \times 10^{-15}$ | $(1.07 \pm 0.08) \times 10^{-15}$ | $(6.04 \pm 0.66) \times 10^{-16}$ | $(3.17 \pm 0.61) \times 10^{-16}$ | $(2.39 \pm 0.57) \times 10^{-16}$ |
| $8.87 \times 10^7$ | – | $(8.36 \pm 0.53) \times 10^{-16}$ | $(5.03 \pm 0.48) \times 10^{-16}$ | $(4.28 \pm 0.51) \times 10^{-16}$ | $(2.60 \pm 0.43) \times 10^{-16}$ | $(1.26 \pm 0.38) \times 10^{-16}$ |
| $1.12 \times 10^7$ | – | $(3.87 \pm 0.34) \times 10^{-16}$ | $(2.97 \pm 0.35) \times 10^{-16}$ | $(1.59 \pm 0.28) \times 10^{-16}$ | $(1.41 \pm 0.30) \times 10^{-17}$ | $(6.20 \pm 2.29) \times 10^{-17}$ |
| $1.39 \times 10^7$ | – | $(2.31 \pm 0.22) \times 10^{-16}$ | $(1.42 \pm 0.21) \times 10^{-16}$ | $(1.03 \pm 0.10) \times 10^{-16}$ | $(5.50 \pm 1.78) \times 10^{-17}$ | $(4.89 \pm 1.61) \times 10^{-17}$ |
| $1.78 \times 10^7$ | – | $(1.17 \pm 0.14) \times 10^{-16}$ | $(9.30 \pm 1.39) \times 10^{-16}$ | $(4.65 \pm 1.19) \times 10^{-17}$ | $(1.58 \pm 0.79) \times 10^{-17}$ | $(1.98 \pm 1.10) \times 10^{-17}$ |
| $2.20 \times 10^7$ | | $(6.04 \pm 0.92) \times 10^{-17}$ | $(3.87 \pm 0.84) \times 10^{-17}$ | $(3.26 \pm 0.92) \times 10^{-17}$ | $(2.28 \pm 0.85) \times 10^{-18}$ | $(2.10 \pm 0.99) \times 10^{-17}$ |
| $2.75 \times 10^7$ | | $(2.77 \pm 0.58) \times 10^{-17}$ | $(2.77 \pm 0.59) \times 10^{-17}$ | $(1.52 \pm 0.52) \times 10^{-17}$ | $(8.20 \pm 4.80) \times 10^{-18}$ | $(7.46 \pm 4.28) \times 10^{-18}$ |

The error bars are statistical. The systematic errors are presented in Figs. 9 and 10. The corrections according to calculated response function are made.

Table 2
Parameters of the size spectra measured by MAKET-ANI array

| $\Delta\theta$ (degree) | $\gamma$ | $\Delta\gamma$ | $N_e^{knee}$ | $A$ | $\delta$ | $\chi^2$ ($n$ df) |
|---|---|---|---|---|---|---|
| 0.0–23.8 | $2.53 \pm 0.002$ | $0.45 \pm 0.02$ | $1.58 \times 10^6 \pm 8 \times 10^4$ | $641.79 \pm 11$ | $7.1 \pm 1.7$ | 1.1(19) |
| 23.8–32.4 | $2.52 \pm 0.002$ | $0.43 \pm 0.02$ | $1.33 \times 10^6 \pm 6 \times 10^4$ | $333.32 \pm 8.5$ | $11.6 \pm 3.0$ | 1.9(17) |
| 32.4–38.5 | $2.47 \pm 0.003$ | $0.47 \pm 0.03$ | $1.08 \times 10^6 \pm 8 \times 10^4$ | $114.37 \pm 3.8$ | $3.9 \pm 0.8$ | 1.2(19) |
| 38.5–43.0 | $2.45 \pm 0.003$ | $0.45 \pm 0.03$ | $0.86 \times 10^6 \pm 7 \times 10^4$ | $53.60 \pm 2.6$ | $4.36 \pm 1.6$ | 0.8(17) |
| 43.0–46.8 | $2.44 \pm 0.006$ | $0.48 \pm 0.04$ | $0.70 \times 10^6 \pm 6 \times 10^4$ | $29.18 \pm 2.2$ | $4.7 \pm 1.4$ | 0.9(16) |

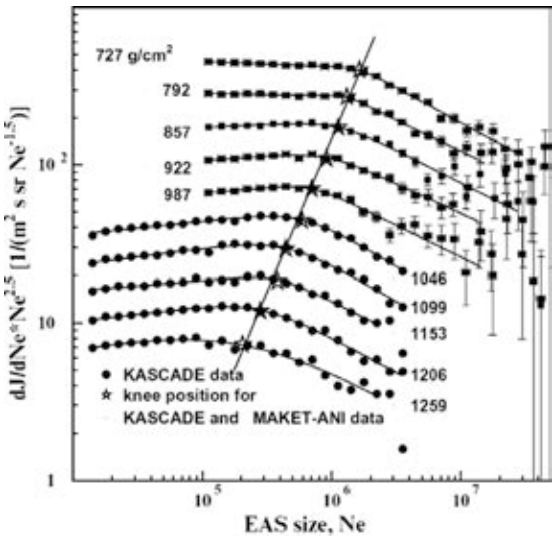


Fig. 14. The size spectra measured by MAKET-ANI and KASCADE experiments. The slant depth covered by experiments comprises 720–1250 g/cm$^2$. The solid line illustrates the EAS attenuation versus slant depth in the atmosphere.

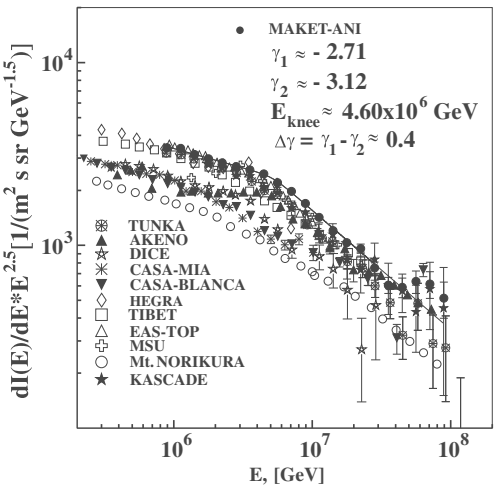


Fig. 15. The all particle spectrum from MAKET-ANI data compared to the world data. The line shows the fit to MAKET-ANI data according to Eq. (5) (integrated into 0–30° zenith angle interval). KASCADE [9], EAS-TOP [59], TIBET [60], HEGRA [61], AKENO [62], CASA-MIA [63], CASA-BLANCA [64]), DICE [65], Mt. NORIKURA [66], MSU [67], and TUNKA [68].

covering the slant depth of 720–1250 g/cm$^2$ is equal to $\Lambda_{N_e} = 194 \pm 14$ g/cm$^2$, while by the MAKET-ANI data only it equals $\Lambda_{N_e} = 211 \pm 38$ g/cm$^2$, and by KASCADE–$\Lambda_{Ne} = 197 \pm 13$ g/cm$^2$ [58], accordingly. All estimates coincide within the error bars.

Taking into account the MAKET-ANI results when selecting light and heavy primary enriched EAS samples [8,34], we can pose the problem of estimation of attenuation length and other phenomenological parameters of strong interaction of primary nuclei with atmosphere for energies till $10^{16}$ eV.

## 5. The primary energy spectra

### 5.1. All particle energy spectrum

All particle energy spectrum is one of the major astrophysical parameters. Regardless of low sensitivity of its shape to models of the origin and acceleration of CR [1], the all particle spectrum is important as a commonly accepted benchmark for comparing different experiments or/and strong interaction models.

Size spectra and energy spectra are related to each other via sophisticated simulation, invoking nuclear-electromagnetic cascade propagation in the atmosphere. As it was demonstrated in numerous KASCADE collaboration

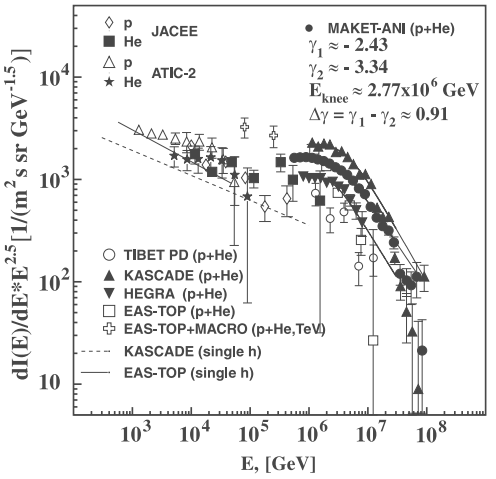


Fig. 16. Primary light component (p + He) measured by the MAKET-ANI detector in comparison to the results from KASCADE [9], EAS-TOP [72], HEGRA [10], EAS-TOP + MACRO [73], TIBET [74] and primary protons spectra approximations obtained by the single hadrons fluxes EAS-TOP [75] and KASCADE [76]. The direct balloon measurements by ATIC-2 [77] and JACEE [78] at $10^2$–$10^5$ GeV are also presented.

papers (see [9]), the resulting energy spectrum depends on the particular high interaction model used in the simulation. Therefore, we should specify that the energy spectrum presented in Fig. 15 is obtained with CORIKA code (QGSJet01, NKG) mode. The very good agreement of spectra measured at the sea level and the mountain altitudes seen in Fig. 15 once more proves the maturity of the EAS experiments. It also proves reliability of the procedures used for the inverse problem solving.

The differential flux values of the primary particles energy spectra were obtained using the database of the simulated events obtained with CORSIKA 562 (QGSJet01, NKG) code [52] and applying the analysis and non-parametric inference (ANI) program package (described in [16,17]).

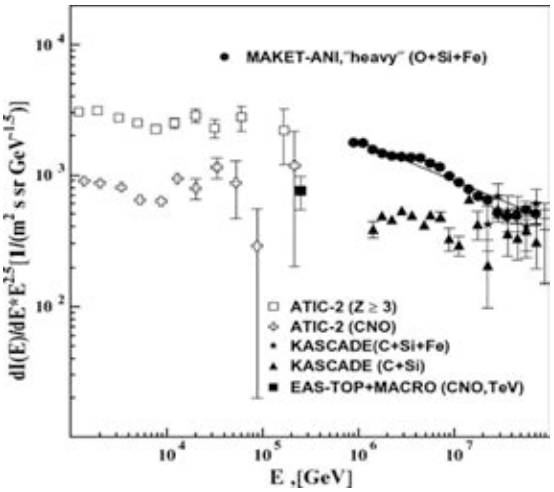


Fig. 17. The energy spectrum of the "heavy" nuclei group measured by the MAKET-ANI detector along with spectra from KASCADE [9], EAS-TOP + MACRO [73] and ATIC-2 [79]. The solid line is a power function approximation.

### 5.2. Partial energy spectra

The spectra of different mass groups were reported by MAKET-ANI and KASCADE data in 1999 [15]; and by EAS-TOP [69], HEGRA [10], TIBET ASγ [70], and KASCADE [71] at Hamburg ICRC in 2001. In [8], we present the spectra of light and heavy nuclei groups and come to the definite physical inference about a very sharp knee for the light component and the absence of knee at least up to $2 \times 10^{16}$ eV for the heavy component. Now, after performing new checks of all possible experimental distortions (see above), we present the updated results on partial energy spectra with the enlarged data sample. For the energy estimation and EAS classification in "light" and "heavy" groups, we use the same statistical models from the "ANI" package as in 2004. The neural network models prove to be very powerful interpolation tool for data analysis in sophisticated multidimensional experiments (see references in [14]). Bayesian methods of classification also prove to be very powerful when model description cannot be supported by the definite analytical shape. By exposing the EAS parameters with known primary and energy to the classifying algorithm, we "train" the algorithm to recognize the experimental EAS without known primary and energy. As alternative classes (states of Nature) we include the "light" mass group showers initiated by the protons

Table 3
The intensities of all CR, light and heavy nuclei groups

| Energy (GeV) | $dJ/dE \pm$ stat.errors ($m^{-2}\,s^{-1}\,sr^{-1}\,GeV^{-1}$) All particles | $dJ/dE \pm$ stat.errors ($m^{-2}\,s^{-1}\,sr^{-1}\,GeV^{-1}$) Light | $dJ/dE \pm$ stat.errors ($m^{-2}\,s^{-1}\,sr^{-1}\,GeV^{-1}$) Heavy |
|---|---|---|---|
| $5.62 \times 10^5$ | $(8.620 \pm 0.022) \times 10^{-12}$ | $(6.920 \pm 0.019) \times 10^{-12}$ | $(1.700 \pm 0.010) \times 10^{-12}$ |
| $7.07 \times 10^5$ | $(6.716 \pm 0.017) \times 10^{-12}$ | $(3.937 \pm 0.013) \times 10^{-12}$ | $(2.779 \pm 0.011) \times 10^{-12}$ |
| $8.91 \times 10^5$ | $(4.587 \pm 0.012) \times 10^{-12}$ | $(2.224 \pm 0.009) \times 10^{-12}$ | $(2.362 \pm 0.009) \times 10^{-12}$ |
| $1.12 \times 10^6$ | $(2.582 \pm 0.008) \times 10^{-12}$ | $(1.236 \pm 0.005) \times 10^{-12}$ | $(1.346 \pm 0.006) \times 10^{-12}$ |
| $1.41 \times 10^6$ | $(1.342 \pm 0.005) \times 10^{-12}$ | $(6.707 \pm 0.038) \times 10^{-13}$ | $(6.722 \pm 0.038) \times 10^{-13}$ |
| $1.77 \times 10^6$ | $(7.157 \pm 0.035) \times 10^{-13}$ | $(3.638 \pm 0.025) \times 10^{-13}$ | $(3.520 \pm 0.025) \times 10^{-13}$ |
| $2.23 \times 10^6$ | $(3.821 \pm 0.023) \times 10^{-13}$ | $(1.936 \pm 0.016) \times 10^{-13}$ | $(1.886 \pm 0.016) \times 10^{-13}$ |
| $2.81 \times 10^6$ | $(2.050 \pm 0.015) \times 10^{-13}$ | $(1.004 \pm 0.010) \times 10^{-13}$ | $(1.046 \pm 0.011) \times 10^{-13}$ |
| $3.54 \times 10^6$ | $(1.104 \pm 0.010) \times 10^{-13}$ | $(5.238 \pm 0.067) \times 10^{-14}$ | $(5.810 \pm 0.070) \times 10^{-14}$ |
| $4.46 \times 10^6$ | $(5.908 \pm 0.063) \times 10^{-14}$ | $(2.676 \pm 0.043) \times 10^{-14}$ | $(3.232 \pm 0.047) \times 10^{-14}$ |
| $5.62 \times 10^6$ | $(2.986 \pm 0.040) \times 10^{-14}$ | $(1.323 \pm 0.027) \times 10^{-14}$ | $(1.664 \pm 0.030) \times 10^{-14}$ |
| $7.07 \times 10^6$ | $(1.501 \pm 0.025) \times 10^{-14}$ | $(6.253 \pm 0.163) \times 10^{-15}$ | $(8.761 \pm 0.194) \times 10^{-15}$ |
| $8.91 \times 10^6$ | $(7.305 \pm 0.158) \times 10^{-15}$ | $(3.073 \pm 0.102) \times 10^{-15}$ | $(4.233 \pm 0.121) \times 10^{-15}$ |
| $1.12 \times 10^7$ | $(3.459 \pm 0.097) \times 10^{-15}$ | $(1.323 \pm 0.059) \times 10^{-15}$ | $(2.136 \pm 0.076) \times 10^{-15}$ |
| $1.41 \times 10^7$ | $(1.640 \pm 0.059) \times 10^{-15}$ | $(5.770 \pm 0.351) \times 10^{-16}$ | $(1.064 \pm 0.048) \times 10^{-15}$ |
| $1.77 \times 10^7$ | $(7.888 \pm 0.037) \times 10^{-16}$ | $(2.623 \pm 0.211) \times 10^{-16}$ | $(5.265 \pm 0.299) \times 10^{-16}$ |
| $2.23 \times 10^7$ | $(4.073 \pm 0.235) \times 10^{-16}$ | $(1.326 \pm 0.134) \times 10^{-16}$ | $(2.748 \pm 0.193) \times 10^{-16}$ |
| $2.81 \times 10^7$ | $(1.827 \pm 0.140) \times 10^{-16}$ | $(6.020 \pm 0.804) \times 10^{-17}$ | $(1.226 \pm 0.115) \times 10^{-16}$ |
| $3.54 \times 10^7$ | $(8.368 \pm 0.845) \times 10^{-17}$ | $(1.622 \pm 0.372) \times 10^{-17}$ | $(6.746 \pm 0.759) \times 10^{-17}$ |
| $4.46 \times 10^7$ | $(4.409 \pm 0.547) \times 10^{-17}$ | $(7.461 \pm 2.249) \times 10^{-18}$ | $(3.663 \pm 0.499) \times 10^{-17}$ |
| $5.62 \times 10^7$ | $(2.747 \pm 0.385) \times 10^{-17}$ | $(4.310 \pm 1.524) \times 10^{-18}$ | $(2.317 \pm 0.353) \times 10^{-17}$ |
| $7.79 \times 10^7$ | $(1.540 \pm 0.257) \times 10^{-17}$ | $(2.995 \pm 1.132) \times 10^{-18}$ | $(1.241 \pm 0.230) \times 10^{-17}$ |
| $8.91 \times 10^7$ | $(6.799 \pm 1.520) \times 10^{-18}$ | $(3.399 \pm 3.399) \times 10^{-19}$ | $(6.459 \pm 1.482) \times 10^{-18}$ |

and Helium nuclei and the "heavy" mass group showers initiated by Silicon and Iron nuclei. Before the Neural classification of the MAKET-ANI data, we investigate the expected purity and efficiency of the data analysis procedures. The purity and the efficiencies are obtained by classifying ~35,000 light (p, He) and ~17,000 heavy (O, Si, Fe) control events, which are not used for the training of the neural network. Neural classifier selects the "light" component with the efficiency ~75%, purity ~85% and the "heavy" component with efficiency ~75%, purity ~57%. To understand how the "light" and "heavy" classes are "populated" by different nuclei, we assume a "normal" mass composition. The results of the classification of this mixture are as following:

Light group: 40% protons, 30% He, 14% O, 11% Si and 5% Fe;
Heavy group: 16% protons, 17% He, 20% O, 26% Si, and 21% Fe.

The energy of the two distinct classes of showers was estimated for each group separately, once more using CORSIKA simulation and neural estimation procedures.

From Fig. 16 it is apparent that the proton acceleration mechanism starts to fade after $10^{15}$ eV. The MAKET-ANI spectrum demonstrated this effect rather clearly, because of its pretty low threshold at $\sim 6 \times 10^{14}$ eV. The lower energy spectra of light nuclei obtained by the balloon experiments JACEE [78] and ATIC-2 [77] are consistent with the spectra obtained in EAS experiments, proving stability of the power index before the "knee" feature.

Fig. 17 presents the energy spectra of the "heavy" nuclei group obtained by MAKET-ANI, KASCADE [9] and EAS-TOP + MACRO [73] detectors along with direct measurement of ATIC-2 [79]. In contrast to "light" nuclei group energy spectra (Fig. 16), at least up to $10^{16}$ eV we did not see any feature demonstrating weakening of heavy nuclei acceleration. All particle spectrum and partial energy spectra measured by MAKET ANI experiment are posted in Table 3.

## 6. Conclusions

From 1997 up to the end of 2004, the MAKET-ANI experiment has taken data with exposition time of $\sim 1.46 \times 10^8$ s. The total number of the registered shower events was $\sim 1.2 \times 10^7$. A smaller sample of the data ($\sim 1.3 \times 10^6$) with $N_e \geqslant 10^5$ and $\theta \leqslant 46.8°$ was used for the in-depth analysis of the LDF and size spectra. By $7.2 \times 10^5$ near the vertical EAS ($\theta \leqslant 30°$), the energy spectra of light and heavy nuclei groups were obtained.

The experimental procedures of physical inference from the MAKET-ANI surface array have been considerably improved, due to the redundant data which allow for important consistency checks. Regular calibrations and cross calibrations, tests of efficiency and uniformity in detector response proved to be essential for retaining data stability and reliability. The published papers on the size and energy spectra usually do not report the methodical errors, which leads to rather large discrepancies in the results. To overcome this drawback and to present methodical procedures with details allowing to judge about the achievable accuracies, we present all relevant procedures used when treating the MAKET-ANI data.

The extension of the experimental statistics, as compared to the previously reported analysis, allows us to present the size spectra and energy spectra of light and heavy components of primary cosmic ray flux in tables and graphs available for the physical inference about the CR origin and acceleration mechanisms.

- The obtained dependence of the shower age on shower size pointed to the weighting of the primary flux mass composition after the knee of the "all particle" spectrum.
- The size spectra show evidence of a "knee" at shower size $\sim 10^6$ particles. As the zenith angle enlarges, the knee position moves to smaller sizes, according to the EAS attenuation length $\Lambda_{Ne} = 211 \pm 38$ g/cm$^2$.
- The difference of the power low spectra before and after the knee is constant with high precision $\Delta\gamma = 0.45 \pm 0.02$.

The following experimental results from partial energy spectra of light and heavy mass groups measured in the MAKET-ANI experiment provide evidence in favor of the rigidity-dependent acceleration at the outer boundaries of SNR:

- The estimated energy spectrum of the light mass group of nuclei shows a very sharp knee: $\Delta\gamma \approx 0.9$, compared to $\Delta\gamma \approx 0.4$ for the all-particle energy spectra.
- The energy spectrum of the heavy mass group of cosmic rays shows no knee in the energy interval of $10^{15}$–$10^{16}$ eV.

The mentioned results are consistent with the non-linear kinetic theory of CR acceleration in SNR shells [20].

## Acknowledgements

We thank the staff of Mt. Aragats Cosmic Ray Observatory who contributed to the MAKET-ANI experiment implementation. We also thank ANI collaboration members for their fruitful cooperation over many years. This work was supported by Armenian Government grants and the ISTC A – 1058 grant.

## References

[1] J. Hoerandel, Astropart. Phys. 21 (2004) 241.
[2] A. Haungs, H. Rebel, M. Roth, Rep. Prog. Phys. 66 (2003) 1145.
[3] A. Chilingarian, Comput. Phys. Commun. 54 (1989) 31.
[4] A. Chilingarian, M. Zazyan, IL Nuovo Cimento 14C (6) (1991) 555.

[5] A. Chilingarian, Neorocomputing 6 (1994) 497.
[6] A. Chilingarian, Pattern Recog. Lett. 16 (1995) 333–338.
[7] C.M. Bishop, Neural Networks for Pattern Recognition, Oxford Univ. Press, New York, 1995.
[8] A. Chilingarian, G. Hovsepyan, et al., ApJ 603 (2004) L29.
[9] T. Antoni et al., (KASCADE), Astropart. Phys. 24 (2005) 1.
[10] D. Horns et al., (HEGRA), in: Proc. 27th ICRC, Hamburg, vol. 1, 2001, p. 101.
[11] M. Aglietta, B. Alessandro, et al., (EAS-TOP + MACRO), Astropart. Phys. 20 (2004) 641.
[12] W.D. Apel et al., (KASCADE), Astropart. Phys. 24 (2006) 467.
[13] A.M. Hillas, Cosmic Rays: Recent Progress and some Current Questions, arXiv:astro-ph/0607109, vol. 1, 2006.
[14] A. Chilingarian, A. Vardanyan, et al., NIMA 502 (2003) 787.
[15] A. Vardanyan, A. Chilingarian, M. Roth, (KASCADE), in: Proc. of the Workshop ANI 99, Nor-Amberd, Preprint FZK 6472, 2000, p. 23.
[16] T. Antoni et al., Astropart. Phys. 16 (2002) 245.
[17] T. Antoni et al., (KASCADE), Astropart. Phys. 19 (2003) 715.
[18] M.A. Maljkov, L.O'C. Drury, Rep. Prog. Phys. 64 (2001) 429.
[19] K.S. Long, S.P. Reynolds, J.C. Raymond, ApJ 586 (2003) 1162.
[20] E.G. Berezhko, L.T. Ksenofontov, H.J. Volk, A&A 412 (2003) 11.
[21] H.J. Volk, E.G. Berezhko, L.T. Ksenofontov, in: Proc. 29th ICRC, Pune, vol. 3, 2005, p. 233.
[22] F.A. Aharonian et al., Science 307 (2005) 1938.
[23] H. Katagiri et al., ApJ 619 (2005) L163.
[24] V.S. Ptuskin, in: Proc. 29th ICRC, Pune, vol. 10, 2005, p. 317.
[25] A. Marcowith, G. Pelletier, M. Lemoin, Proc. 29th ICRC, Pune, vol. 3, 2005, p. 221.
[26] M.J. Aschwanden, in: N. Gopalswamy (Ed.), AGU Monograph of AGU Chapman Conference, Turku, Finland, 2–6 August 2004.
[27] A. Chilingarian et al., in: Proc. of the European High Energy Physics School, ESHEP, Tcakhkadzor, Armenia, 2003.
[28] S.N. Karpov, Z.M. Karpova, Yu.V. Balabin, E.V. Vashenyuk, in: Official CD of 29th ICRC, Pune, 2005.
[29] J. Poirier, C.J. D'Andrea, Geophys. Res., Space Phys. 107 (A11) (2002) 1376.
[30] E.V. Bazarov et al., VANiT, Ser. Nucl. Phys. Reser. 5 (31) (1986) 3 (in Russian).
[31] G. Hovsepyan, A. Chilingarian et al., in: Proc. 29th ICRC, Pune, vol. 6, 2005, p. 93.
[32] A.D. Yerlikin et al., VANiT Ser. Nucl. Phys. Reser. 4 (4) (1998) 3 (in Russian).
[33] J. Linsley, in: Proc. 19th ICRC, vol. 7, 1985, p. 359.
[34] A. Chilingarian et al., in: Proc. 27th ICRC, Hamburg, vol. 2, 2001, p. 590.
[35] A. Daryan et al., Preprint YerPhI, vol. 1485(2)-97, 1997, p. 13 (in Russian).
[36] E.A. Mnatsakanyan et al., Preprint YerPhI, N 1610(8)-06, 2006 (in Russian).
[37] G. Hovsepyan, in: Proc. of the Workshop ANI 98, FZKA 6215, Forschungszentrum Karlsruhe, 1999, p. 41.
[38] V.S. Murzin, Introduction to Cosmic Ray Physics, Moscow, 1979, 275p. (in Russian).
[39] S. Blokhin et al., Proc. of the Workshop ANI 99, FZKA 6472, 2000, p. 111.
[40] T.P. Amineva et al., Izv. AN, Ser. Phys. 33 (1968) 1508 (in Russian).
[41] J.H. Weber et al., (KASCADE), in: Proc. 25th ICRC (Durban), vol. 6, 1997.
[42] A. Chilingarian, K. Avagyan, et al., Adv. Space Res. 31 (2003) 861.
[43] K. Greisen, Prog. Cosmic Ray Phys., vol. 3, North Holland Publ., 1956.
[44] K. Kamata, J. Nishimura, Progr. Theoret. Phys. 6 (Supp.) (1958) 93.
[45] S. Hayakawa, Cosmic Ray Physics, Cosmic Ray Physics, Interscience Monographs and Texts in Physics and Astronomy, vol. 22, Wiley-Interscience, 1969.
[46] V.S. Aseykin et al., Lebedev Inst. Proc. 109 (1979) 3 (in Russian).
[47] G. Gharagyozyan, in: Proc. of the Workshop ANI 98, FZKA, preprint 6215, 1999, p. 51.
[48] S. Yoshida et al., Phys. G: Nucl. Part. Phys. 20 (1994) 651.
[49] A.V. Glushkov et al., in: Proc. 25th ICRC, Durban, vol. 6, 1997, p. 233.
[50] G. Hovsepyan, ANI collab. report No. 5, 2001, http://crdlx5.yerphi.am/ani-collab.html.
[51] G.B. Khristiansen et al., Astropart. Phys. 2 (1994) 127.
[52] D. Heck et al., FZKA report 6019, Forschungszentrum, Karlsruhe, 1998.;
N. Kalmikov, S. Ostapchenko, A. Pavlov, Nucl. Phys. B (Proc. Suppl.) 52B (1997) 17.
[53] E. Juliusson, in: 13th ECRC, Genev, vol. OG-6, 1993, p. 11.
[54] S. Ter-Antonyan, L. Haroyan, hep-ex/0003006, 2000.
[55] R. Glasstetter et al., (KASCADE), in: Proc. 25th ICRC, Durban, vol. 2, 1997.
[56] T. Stanev, in: American Institute of Physics (AIP), Conference Proceedings, vol. 516, 2001, p. 247.
[57] S. Sokhoyan et al., in: Proc. 27th ICRC, Hamburg, vol. 1, 2001, p. 165.
[58] G. Maier et al., (KASCADE), in: Proc. 27th ICRC, Hamburg, vol. 1, 2001, p. 161.
[59] M. Aglietta et al., (EAS-TOP), Astropart. Phys. 10 (1999) 1.
[60] M. Amenomori et al., (TIBET), Astrophys. J. 461 (1996) 408.
[61] F. Arqueros et al., (HEGRA), Astron. Astrophys. 359 (2000) 682.
[62] M. Nagano et al., (AKENO), J. Phys. G: Nucl. Part. Phys. 10 (1984) 1295.
[63] M.A.K. Clasmacher et al., (CASA-MIA), Astropart. Phys. 10 (1999) 291.
[64] J.W. Fowler et al., (CASA-BLANKA), Astropart. Phys. 15 (2001) 49.
[65] S.P. Swordy, D.B. Kieda, (DICE), Astropart. Phys. 13 (2000) 137.
[66] N. Ito et al., (Mt. NORIKURA), in: 25th ICRS, Durban, vol. 4, 1997, p. 117.
[67] Y.A. Fomin et al., (MSU), in: 22nd ICRC, Dublin, vol. 2, 1991, p. 85.
[68] N.M. Budnev et al., (TUNKA), in: Proc. 29th ICRC, Pune, vol. 6, 2005, p. 257.
[69] B. Alessandro et al., (EAS-TOP + MACRO), in: Proc. 27th ICRC, Hamburg, vol. HE1.02, 2001, p. 124.
[70] M. Amenomori et al., (TIBET), in: Proc. 27th ICRC, Hamburg, vol. HE1.02, 2001, p. 148.
[71] H. Ulrich et al., (KASCADE), in: Proc. 27th ICRC, Hamburg, vol. HE1.02, 2001, p. 97.
[72] M. Aglietta et al., (EAS-TOP), Astropart. Phys. 21 (2004) 583.
[73] M. Aglietta et al., (EAS-TOP + MACRO), Astropart. Phys. 21 (2004) 223.
[74] M. Amenomori et al., (TIBET), Phys. Lett. B 632 (2006) 58.
[75] M. Aglietta et al., (EAS-TOP), Astropart. Phys. 19 (2003) 329.
[76] T. Antoni et al., (KASCADE), ApJ 24 (2004) 1.
[77] J.P. Wefel et al., (ATIC-2), in: Proc. 29th ICRC, Pune, vol. 3, 2005, p. 105.
[78] K. Asakimori et al., (JACEE), ApJ 502 (1998) 278–283.
[79] A.D. Panov et al., (ATIC-2), arXiv:astro-ph/0612377, vol. 1, 2006.
[80] GEANT: CERN Program library Long Writeup W5013, CERN, 1993.
[81] MINUIT: CERN Program Library Long Writeup, D506, CERN, 1993.

Available online at www.sciencedirect.com
ScienceDirect
Advances in Space Research 43 (2009) 702–707
ADVANCES IN SPACE RESEARCH (a COSPAR publication)
www.elsevier.com/locate/asr

# Statistical study of the detection of solar protons of highest energies at 20 January 2005

Ashot Chilingarian

*Alikhanyan Physics Institute, Yerevan, Armenia, Alikhanyan Brothers 2, Yerevan 375036, Armenia*

Received 12 December 2007; received in revised form 10 June 2008; accepted 5 October 2008

**Abstract**

On January 20, 2005, 7:02–7:04 UT the Aragats Multichannel Muon Monitor (AMMM) registered enhancement of the high energy secondary muon flux (energy threshold ~5 GeV). The enhancement, lasting 3 min, has statistical significance of $\sim 4\sigma$ and is related to the X7.1 flare seen by the GOES satellite and the ground level enhancement detected by the world-wide network of neutron monitors and by muon detectors. The most probable proton energy corresponding to the measured 5 GeV muon flux is within 23–30 GeV. Due to upmost importance of the detection of solar particles of highest energies in presented paper we perform detailed statistical analysis of the detected peak. The statistical technique introduced in the paper is also appropriate for the searches of sources of ultra-high energy cosmic rays.


*Keywords:* Solar cosmic rays; Neutron monitors; Ground level enhancements

## 1. Introduction

Measurements of the energy spectra of the solar cosmic rays (SCR) up to several tens of GeV will significantly enlarge the basic knowledge on the universal processes of particle acceleration at the Sun and in the Universe and will provide important information for the timely warnings on Space Weather severe conditions. Experimental investigation of the SCR of highest energies is a very difficult problem, requiring large surfaces of the particle detectors located at middle and low latitudes. Solar cosmic rays are electrons, protons and stripped nucleus accelerated in vicinity of Sun in flaring processes and by shock waves driven by the coronal mass ejections (CME).

Solar energetic particles (SEP) sometimes are energetic enough to generate cascades of particles in terrestrial atmosphere. Cascade particles can reach surface and enlarge count rates of particle monitors normally detecting rather stable flux of cascade particles generated by much more energetic galactic cosmic rays (GCR). Such abrupt count rate changes due to SCR are called ground level enhancements (GLE), encountered not more than 10 times during ~11 years of solar activity cycle.

On 20 January 2005, during the recovery phase of the Forbush decrease a long lasting X-ray burst occurred near the west limb of the Sun (helio-coordinates: 14 N, 67 W). The start of X7.1 solar flare was at 06:36 UT and maximum of the X-ray flux at 7:01 UT. The fastest (relative to X-ray start time) SEP/GLE event of 23-cycle (GLE No. 69) was detected by space-born and surface particle detectors few minutes after the flare onset. The start of GLE was placed at 6:48; the maximal amplitude of 5000% recorded by neutron monitor (NM) at the south pole is the largest increase recorded by neutron monitors ever.

Particle detectors of the Aragats Space-Environmental Center (ASEC, see Chilingarian et al., 2003, 2005) detected significant excess of count rates at 7:00–8:00 UT. From 7:02 to 7:04 UT, the Aragats Multichannel Muon Monitor (AMMM) detected a peak with significance $\sim 4\sigma$. It was the first time that we detected a significant enhancement of the >5 GeV muon flux. This short enhancement at 7:02–7:04

*E-mail address:* chili@aragats.am

0273-1177/$34.00 © 2008 COSPAR. Published by Elsevier Ltd. All rights reserved.
doi:10.1016/j.asr.2008.10.005

exactly coincides in time with peaks from Tibet NM (Miyasaka et al., 2005), Tibet Solar Neutron Telescope (Zhu et al., 2005) and Baksan surface array (Karpov et al., 2005).

AMMM is located under 14 m of soil and concrete in the underground hall of former ANI experiment (see details in Chilingarian et al., 2005) and include 42 1 $m^2$ area and 5 cm thick plastic scintillators; the mean count rate of the detector was ~126,000 per minute and relative root mean square error of 1-min time series (RRMSE, usually used measure of particle monitor performance) equals to 0.28%. Therefore, rather large area of detector and corresponding high accuracy allows detection of additional flux due to very weak flux of highest energy SCR.

Flux of the muons with energies above 5 GeV detected by the AMMM as we can see from Fig. 1 (Zazyan, 2008), is generated by the primary protons with energies above 15 GeV. The energy distribution of the "parent" protons giving rise to the energetic muons depends on the power index of the primary proton energy spectra. Energy spectrum of protons, accelerated in Galaxy is very well fitted in wide energy range by power function with index $\gamma = -2.7$; the power index of energy spectra of "solar" protons varies from $\gamma = -4$ till $\gamma = -7$ and less for GeV energies. Our study of energy spectra of GLE No. 69 (Chilingarian and Reymers, 2007) estimates power index between $-4$ and $-5$ around 7:00 UT, 20 January 2005, therefore, most probable energy of primary protons, as we can see from Fig. 1, is between 23 and 30 GeV. To gain an insight into distribution of primary energies we calculate also 10% and 90% quartiles (energy regions containing lowest and greatest 10% of distribution) outlining the "improbable" energy regions. Our calculations prove that the most stable distribution parameter is the mode – energy value at biggest histogram bin. This value remains rather stable when we change simulation model.

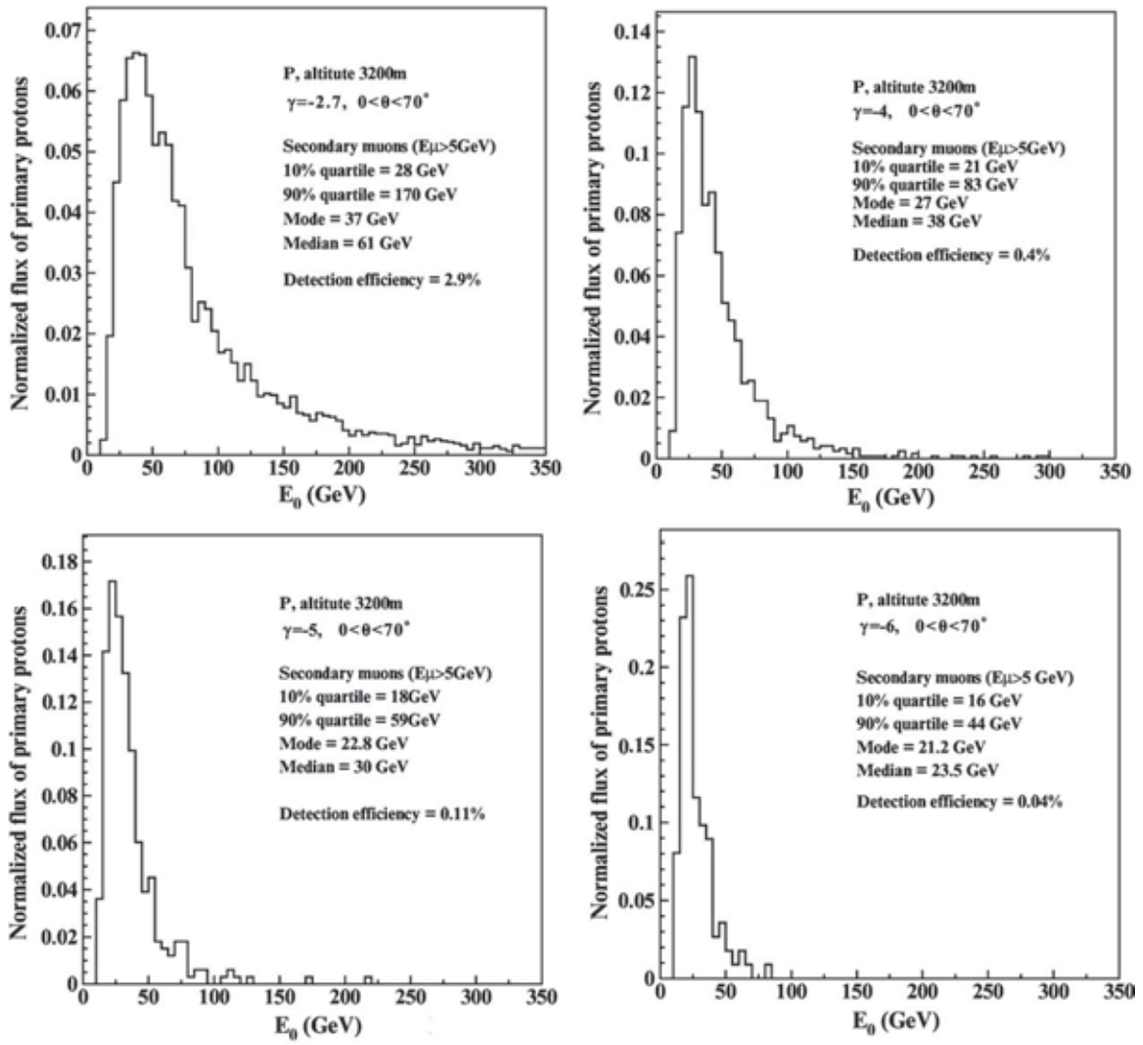


Fig. 1. Energy distribution of the primary protons that generate >5 GeV muons present at 3200 m altitude.

The details of AMMM detection of GLE No. 69, are discussed in Bostanjyan et al. (2007). In present paper due to upmost importance of the detection of solar particles with highest energies we discuss statistical methods used to reveal peak in the time series of AMMM. In the second section of paper we check the hypothesis that fluctuations of the count rates are well described by the Gaussian model, in the third section we introduce extreme statistical distribution, in forth we describe the computational experiment for checking obtained results.

## 2. Analysis of the residuals (checking the Gaussian model)

The difficulty of testing hypothesis of Gaussian nature lies in the slow drift of the mean count rate of time series due to systematic changes of several geophysical and interplanetary parameters. Disturbances of the interplanetary magnetic field (IMF) in the end of January 2005 (triggered by passage of several Interplanetary CMEs at 16–20 January) modulate cosmic ray flux, introducing trend in the secondary cosmic ray fluxes.

To account for the changing mean of the greater than 5 GeV muon flux we calculate the hourly mean count rates and corresponding residuals (fitting errors, differences between observed hourly means and values of 3-min count rates in this hour; 20 numbers for each hour):

$$X_{i,j} = \frac{C_{i,j} - \bar{C}_j}{S_j}, \qquad i = 1,20 \quad j = 1,N_h \tag{1}$$

where $X_{i,j}$ are normalized residuals, $C_{i,j}$ are 3 min count rates of the AMMM at $j$th hour, $\bar{C}_j$ are hourly means of the 3-min time series and

$$S_j \approx \sqrt{\bar{C}_j}, \quad j = 1,N_h \tag{2}$$

are proxies of root mean square errors and $N_h$ is number of hours.

Statistical distribution (1) represents, so called, multinomial process. Multinomial process consists of sum of $j$ Gaussian random processes; in our case – time series of count rates corresponding to Gaussian process with same variance and different means. In our probabilistic treatment of the problem we normalize time series by the "moving" means $\bar{C}_j$ and variances $S_j^2$, estimated each hour. In this way we plan to obtain a proxy of the standard Gaussian distribution $N(0,1)$ to use later on as a test statistics.

To check our assumptions on Gaussian nature of the distribution (1) we perform calculation of residuals for 20 January 2005 and for whole January 2005. As we describe in Bostanjyan et al. (2007) we prepare 3-min time series from the 1 min ones. Joining 1 min time series in 3, 5, 10 or 60 min time series is ordinary operation used by the all groups running the neutron and muon monitors. To account for the arbitrary choice of the start minute we integrate other all three possibilities of different starts of the 3-min time series, therefore number of events in histograms is three times more than number of 3-min count rates.

The resulting histograms of the normalized residuals are shown in Figs. 2 and 3. We see rather good agreement with standard normal distribution $N(0,1)$; values of the $\chi^2$ test are $\sim$1 for degree of freedom. The maximal values of 3.77[1] (see the right tail of histogram in Fig. 2) corresponds to a peak at 7:02–7:04 UT. The same maximal value remains maximal also for the 1-month histogram (Fig. 3). The second maximal value for a month histogram is 3.64.

Proceeding from good agreement of histogram with Gaussian curve and from rather large value of the biggest residual, we can accept the hypothesis that there is additional signal superimposed on the galactic cosmic ray background. Of course, within validity of the Gaussian hypothesis this and larger values can encounter by chance, therefore we'll need additional statistical tests proving that detected peak is caused by the highest energy solar protons.

## 3. Calculation of the chance probability

As usually in statistical hypothesis testing, the hypothesis we want to check (named $H_0$) consists in the opposition to the hypotheses we are interested, i.e., we will check the hypothesis that there is no additional muons in 3-min time series ("no-signal" hypothesis) and, therefore, that detected peak is random fluctuation only. To prove the existence of signal, we have to reject $H_0$ with the maximal possible confidence. Detecting large deviations from $H_0$, i.e., very low probability of $H_0$ being true, do not imply that the opposite hypothesis is automatically valid. As was mentioned by Astone and D' Agostini (1999) behind logic of standard hypothesis testing is hidden a revised version of the classical proof by contradiction. "In standard dialectics, one assumes a hypothesis to be true, then looks for a logical consequence which is manifestly false, in order to reject the hypothesis. The "slight" difference introduced in "classical" statistical tests is that the false consequence is replaced by an improbable one".

If the experimental data will not differ significantly from test distribution obtained under assumption of "no-signal" hypothesis there will be no reason to reject H0 and therefore we cannot claim that AMMM detected high energy muons of "solar origin". And if we will be able to reject $H_0$, we can accept with definite level of confidence that there are high energy protons coming from the sun. Usually confidence level is enumerated as "chance probability", the probability of $H_0$ hypothesis to be true.

The statistical test for accepting or rejecting hypothesis is based on the maximal deviation from most probable value (3.77 in our case) observed in time series. The probability to obtain this or another maximal deviation depends on the number of events considered, i.e., on the time series

[1] We obtain maximal value 3.77 instead of, reported in Bostanjyan et al. (2007), 3.93 due to slightly different procedure of residual calculation.

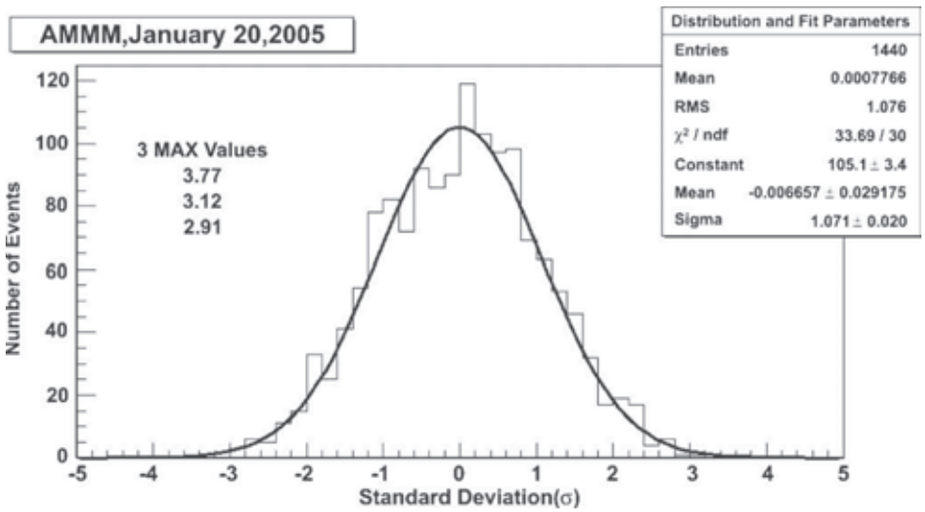


Fig. 2. Normalized residuals calculated by 3-min AMMM time series at 20 January 2005. In the picture legend are posted the histogram mean and RMS and also fitted curve mean and variance, as well as number of degrees of freedom in the $\chi^2$ test.

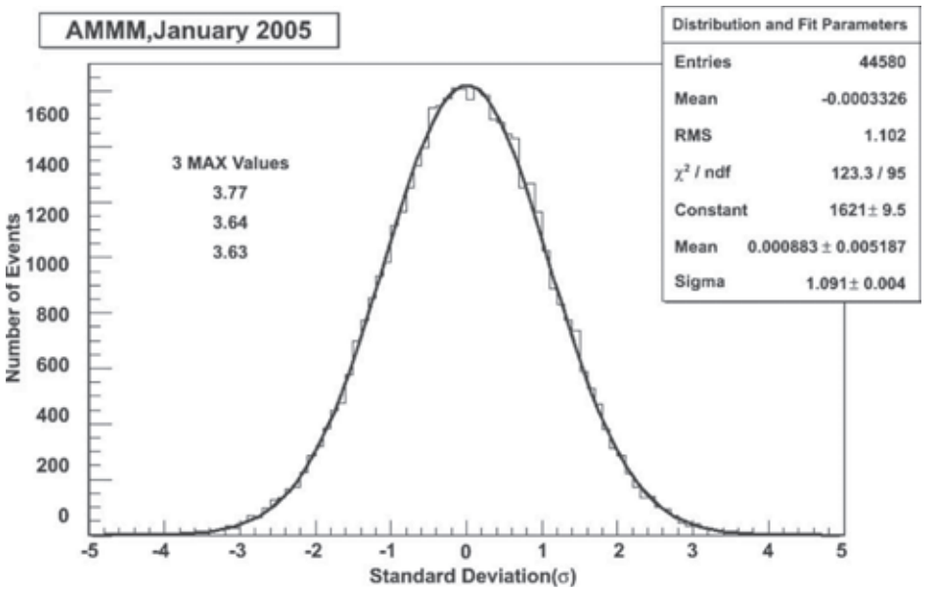


Fig. 3. Normalized residuals calculated by 3-min AMMM time series at January 2005. In the picture legend are posted the histogram mean and RMS and also fitted curve mean and variance, as well as number of degrees of freedom in the $\chi^2$ test.

length. Therefore, the most appropriate test provides the extreme statistics distribution (Chapman et al., 2002; Chilingarian et al., 2006):

$$c^M(x) = M \cdot g(x)(1 - G_{>x})^{M-1} \tag{3}$$

where g(x) is standard Gaussian probability density $N(0,1)$.

$$G_{>x} = \int_x^{\infty} g(t)dt \tag{4}$$

is, so called, standard Gaussian distribution's $p$-value: the probability to obtain the value of test statistics greater than $\boldsymbol{x}$; $M$ is number of attempts we made to find the biggest deviation from $H_0$ (number of elements of considered time-series multiplied by number of attempts we made to find greatest deviation).

To obtain the probability to observe extremely deviation equal to $\boldsymbol{x}$ among $M$ identically distributed random variables ($p$-value of the distribution $c^M(x)$) we have to integrate $c^M(x)$ in the interval $[x, +\infty)$:

$$C_x^M = \int_x^{\infty} c^M(t)dt \tag{5}$$

$C_x{}^M(x)$, $p$-value of the distribution (3), equals to probability that observed test statistics $\boldsymbol{x}$ maximally deviates from

the most probable value under assumption that $H_0$ is valid. And if this probability is low enough we can reject $H_0$ and accept alternative hypothesis that observed deviation is not fluctuation, but a contamination of the distribution of different statistical nature, i.e., a signal.

The probability to observe in one from 480 (i.e., during the day) of 3-min time-series count rate enhancement of 3.77 equals according to Eqs. (3) and (5) to:

$$C_{3.77}^{1440} = 0.1045$$

It means that in absence of any signal when examining daily variations of the 3-min count rates in one case from 10 it is expected to detect the deviation of the mean value equal to 3.77. Equivalent statement: approximately once in 10 days only we will detect 3.77 enhancements in the 3-min time series of AMMM.

However, we have to correlate the expected signal from protons, accelerated at Sun with time of X-ray flare and CME launch. Of course, we cannot expect the signal from solar protons before X-ray flare and an hour after the X-ray flare or/and CME launch occurs. The chance probability to detect a deviation equals to 3.77 in 1 h equals to $C_{3.77}^{60} = 0.0049$, i.e., only once in 200 cases we can expect such enhancement.

As we can see in Fig. 3 the second maximal monthly deviation equals to 3.64. If we accept hypothesis that 3.77 value was due to solar protons, we have to check if 3.64 is typical monthly maximal deviation. Calculated according (3)–(5) value of $C_{3.64}^{14340} = 0.2768$ is rather large and we have no reasons to reject $H_0$; i.e., at January 2005 the residual distribution (Fig. 3) was Gaussian with only one outlier attributed to high energy solar protons.

## 4. Effect of the multiple attempts in searches of "biggest deviation from $H_0$"

To check assumption that when calculated significance of signal we should take into account three possible starts of time series we perform simulations with simple model of time series.

The model can be described as following:

(i) generate 1440 numbers from the standard normal distribution $N(0, 1)$;

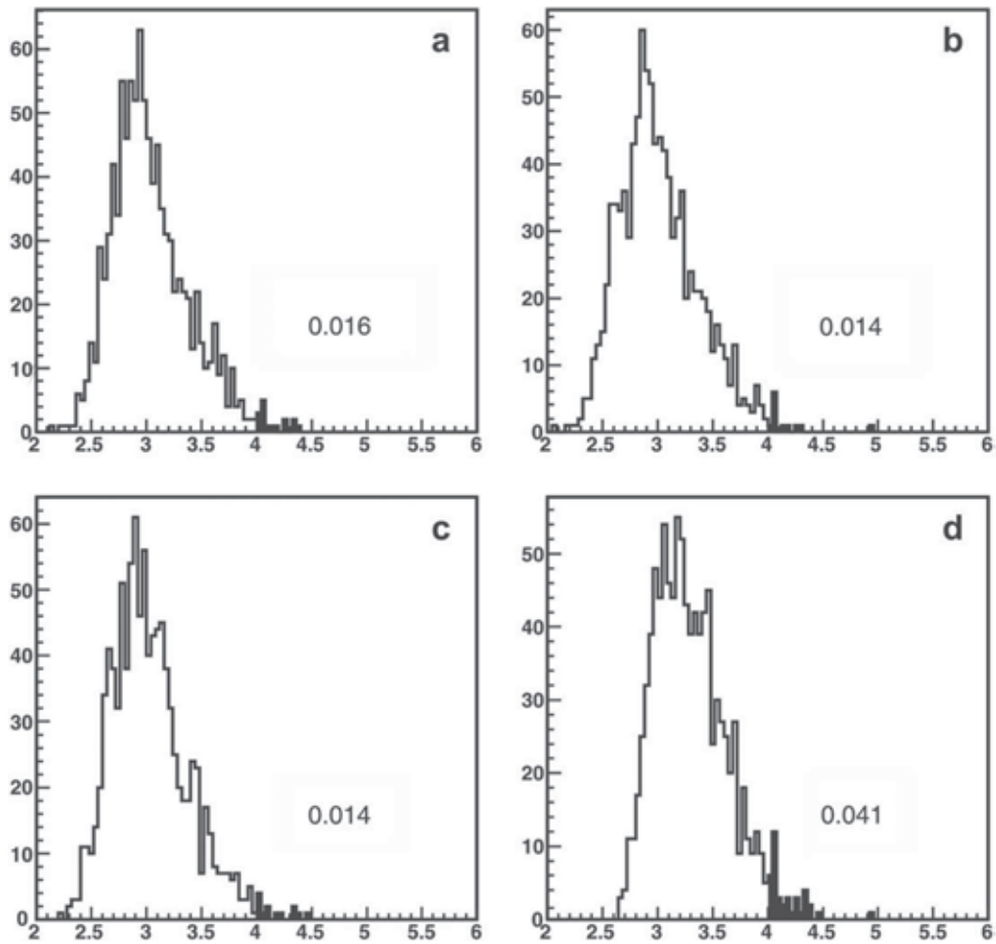


Fig. 4. Histograms of the extreme statistics. (a–c) selecting extreme statistics for three independent time series (iv); and (d) selecting maximal value among three extreme statistics – (v). Black area in the histograms denotes the summation region and number the integral (sum) value from 4 till infinity.

(ii) prepare three time series summing three consequent numbers of the raw, starting from the first, second and the third elements;
(iii) perform according to Eq. (1) normalization procedure (subtract the mean and divide to root of variance);
(iv) determine and store the maximal element of each of three normalized time series;
(v) determine and store the maximal element among three time-series maximums;
(vi) repeat (i)–(vi) 1000 times and consider four histograms of extreme values;
(vii) calculate the frequencies of obtaining values equal or greater than 4 (for simplicity we take 4 instead of 3.77).

Intuitively, when having three possibilities physicist will choose one that emphasis the presence of signal (the situation (v)). But as we can see from Fig. 4d, the probability to obtain the fake signal is dramatically enhanced (approximately by three times). From the same picture we can see that obtained in (d) chance probability 0.041 is in good agreement with value calculated according to Eqs. (3) and (5): $C_4^{1440} = 0.0436$.

## 5. Conclusion

On January 20, 2005, 7:02–7:04 UT the Aragats Multichannel Muon Monitor registered enhancement of the high energy secondary muon flux. The enhancement, lasting 3 min, has statistical significance of $\sim 4\sigma$ and chance probability – less than 0.5%.

Proposed statistical methodology of signal significance estimation can be recommended for the treatment of GLE events, especially for revealing weak signals of solar cosmic rays of the highest energies. The extreme statistics are useful tool for the enumeration of the significance of detected peaks in time series. When making different attempts to reject $H_0$ the probability of obtaining "fake" signal during a given time period increases approximately proportional to number of attempts.

## Acknowledgments

Author is grateful to N. Bostanjyan, G. Karapetyan, A. Hovhannisyan, A. Reymers and Zazyan Meri for useful discussions and fruitful collaboration. Work was partly supported by the INTAS Grant 8777.

## References

Astone, P., D'Agostini, G. Inferring the intensity of Poison processes at the limit of the detector sensitivity, CERN-EP/99-126, 1999.
Bostanjyan, N.Kh., Chilingarian, A.A., Eganov, V.S., Karapetyan, G.G. On the production of highest energy solar protons on 20 January 2005. Adv. Space Res. 39, 1454–1457, 2007.
Chapman, S.C., Rowlands, G., Watkins, N.W. Extremum statistics – a framework for data analysis. Nonlin. Process. Geophys. 9, 409–418, 2002.
Chilingarian, A., Avakyan, K., Babayan, V., et al. Aragats Space-Environmental Center: status and SEP forecasting possibilities. J. Phys. G Nucl. Part. Phys. 29, 939–952, 2003.
Chilingarian, A., Arakelyan, K., Avakyan, K., et al. Correlated measurements of secondary cosmic ray fluxes by the Aragats Space Environmental Center monitors. NIM A543, 483–492, 2005.
Chilingarian, A., Gharagyozyan, G., Karapetyan, G., Hovsepyan, G. Statistical methods for signal estimation of point sources of cosmic rays. Astropart. Phys. 25, 269–276, 2006.
Chilingarian, A., Reymers, A. Particle detectors in Solar Physics and Space Weather Research. Astropart. Phys. 27, 465–472, 2007.
Karpov, S.N., Karpova, Z.M., Balabin, Yu.V., Vashenyuk, E.V. Study of the GLE events with use of the EAS-arrays data, in: Proceedings of the 29th ICRC, Pune, India, vol. 1, pp. 193–196, 2005.
Miyasaka, H., Takahashi, E., Shimoda, S., et al. The solar event on 20 January 2005 observed with the Tibet YBJ neutron monitor observatory, in: Proceedings of the 29th ICRC, Pune, India, vol. 1, pp. 245–2248, 2005.
Zhu, F.R., Tang, Y.Q., Zhang, Y., et al. The Solar Event on 20 January 2005 observed with the Tibet YBJ Neutron monitor observatory, in: Proceedings of the 29th ICRC, Pune, India, vol. 1, pp. 185–188, 2005.
Zazyan, M.Z. Private communication, 2008.

Available online at www.sciencedirect.com
ScienceDirect
Advances in Space Research 45 (2010) 614–621
ADVANCES IN SPACE RESEARCH (a COSPAR publication)
www.elsevier.com/locate/asr

# On the relation of the Forbush decreases detected by ASEC monitors during the 23rd solar activity cycle with ICME parameters

A. Chilingarian, N. Bostanjyan *

*Cosmic Ray Division, Alikhanyan Physics Institute, Alikhanyan Brothers 2, Yerevan 375036, Armenia*

Received 22 April 2009; received in revised form 2 September 2009; accepted 2 September 2009

**Abstract**

To improve the physical understanding of the Forbush decreases (FD) and to explore the Space Weather drivers, we need to measure as much geospace parameter as possible, including the changing fluxes of secondary cosmic rays. At the Aragats Space Environmental Center (ASEC) are routinely measured the neutral and charged fluxes of secondary cosmic rays. Each of species has different most probable energy of primary "parent" proton/nuclei. Therefore, the energy range of the Galactic Cosmic Rays (GCR) affected by Interplanetary Coronal Mass Ejection (ICME) can be effectively estimated using data of the ASEC monitors. We presented relations of the magnitude of FD observed in different secondary particle fluxes to the most probable energy of the primary protons. We investigate the correlations between the magnitude of FD with the size, speed, density and magnetic field of the ICME. We demonstrate that the attenuation of the GCR flux incident on the Earth's atmosphere due to passing of the ICME is dependent on the speed and size of the ICME and the magnetic field strength.


*Keywords:* Neutron monitor; Forbush decrease; Interplanetary coronal mass ejection

## 1. Introduction

The Forbush decreases are the attenuations of the flux of the Galactic Cosmic Rays (GCR) measured by particle detectors on the Earth, on other planets' surfaces and in the interplanetary space before, during and after passage of the Interplanetary Coronal Mass Ejection (ICME). FD takes place in the course of a few hours; over the following several days the GCR intensity returns to pre-FD value.

Using cosmic-ray and magneto-metric measurements Scott Forbush established in 1930s the correlation of worldwide decreases in cosmic-ray intensity with Geomagnetic Storms (GMS, Forbush, 1937). Later he formulated a common geocentric cause for both effects (westward-flowing equatorial ring current as cause of FD (Forbush, 1939)). In 1954 it was recognized that FDs were not produced by the geomagnetic field variations (Simpson, 1954). He claimed on the existence of common mechanism which produces both the accelerating process for cosmic-radiation particles and, indirectly, the geomagnetic disturbances. Examining the relationships among solar activity, GMS, and cosmic-ray intensity, Philip Morrison in 1956 claimed that sporadic emission of clouds of magnetized plasma (now named ICMEs) can modulate the cosmic-ray intensity in interplanetary space and produce terrestrial geomagnetic storms (see Van Allen, 1985 for details).

After establishing that the origin of the non-recurrent FDs are ICMEs and recurrent FDs are caused by the co-rotation of high speed solar wind streams, numerous theoretical and experimental papers were devoted to the possible mechanisms of FD. One of the most intriguing problems was the magnitude of FD. In the paper (Burlaga and Chang, 1988) authors concluded that relatively large decreases in the cosmic-ray intensity are associated with magnetic clouds that are preceded by shocks, whereas only small decreases in CR intensity are associated with magnetic clouds that are not preceded by shocks. Cane

* Corresponding author.
*E-mail address:* nikolai@yerphi.am (N. Bostanjyan).

0273-1177/$36.00 © 2009 COSPAR. Published by Elsevier Ltd. All rights reserved.
doi:10.1016/j.asr.2009.09.001

(2000) also pointed that 80% of FD with magnitude greater than 4% (in secondary neutron flux) are connected with passage of shock and ejecta. She also claimed that there should be at least two different mechanisms of FD corresponding to the interaction of the GCR with shock and ejecta.

In this paper we made an attempt to research the dependence of the FD magnitude not only on the CME launch helio-coordinates, or existence of the fast shock, but also on the energy of the primary cosmic rays, ICME speed, and ICME density and magnetic field.

In ASEC (Chilingarian et al., 2003, 2005), we measure neutral and charged fluxes by particle detectors located at three different altitudes. Each of the measured secondary fluxes has a different most probable energy of primary "parent" proton/nuclei. As we can see from Fig. 1 (Zazyan and Chilingarian, 2009), these energies range from 7 (mode of distribution of primary protons generated neutrons) to 40 GeV (the same for muons with energies greater than 5 GeV). New particle detectors now starting to operate in ASEC will prolong this maximal energy up to 200 GeV (Chilingarian and Hovsepyan, 2008). Therefore, from the ASEC monitor data we can estimate the GCR energy range affected by ICME and reconstruct actual spectra of the GCRs incident on terrestrial atmosphere, thus revealing the energy-dependant pattern of the ICME modulation effects. Recently analogical techniques were developed for the study of the GCR energy and the FD recovery time (Usoskin et al., 2008), with the difference that data was taken from world-wide networks of Neutron Monitors and three ground level muon telescopes. Measurements of all the secondary fluxes at one and the same location are preferable due to effects of the longitudinal dependence of the FD magnitudes (Haurwitz et al., 1965).

Also we introduce several parameters enumerating the "FD-efficiency" of IMCE, for instance, correlation coefficients between time series of different species of secondary cosmic rays. For small FDs the correlation between changing fluxes of neutrons and 5 GeV muons is small or moderate. We expected that large FDs will influence primary protons of much greater energies comparing with small ones, therefore correlations between fluxes of secondary neutrons and 5 GeV muons will be much greater for large FDs.

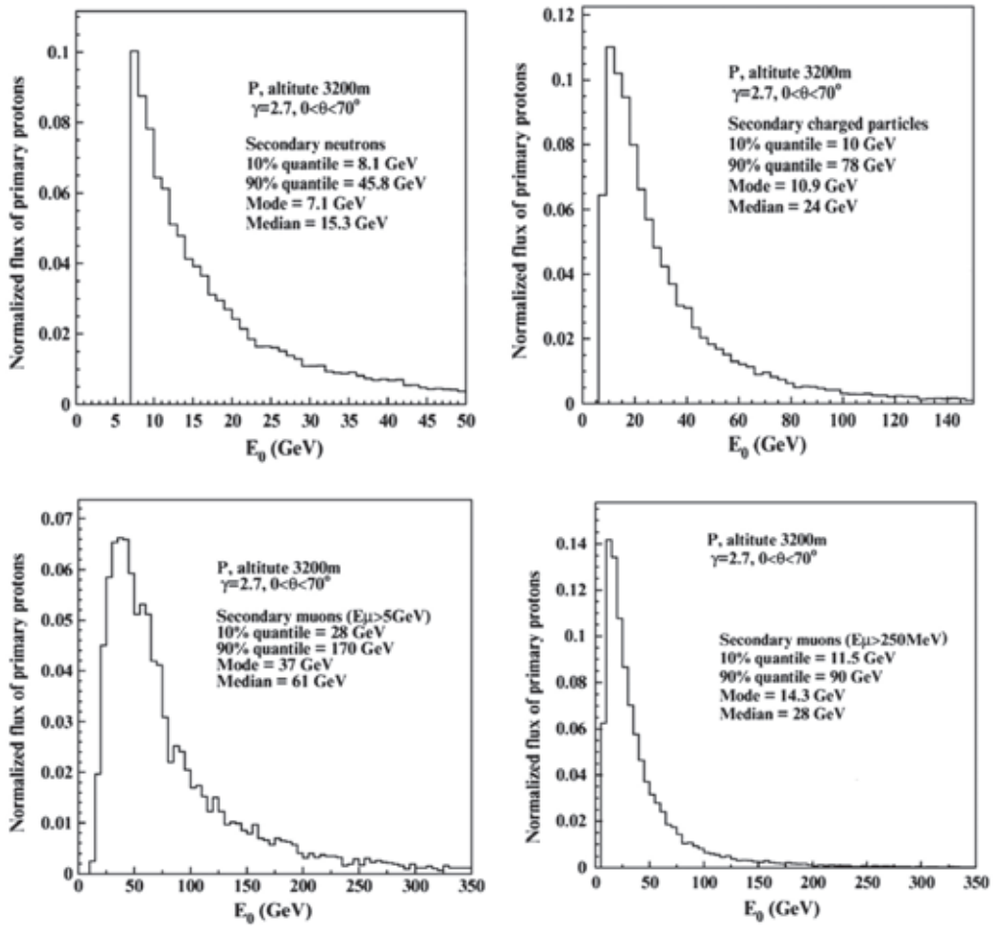


Fig. 1. Energy distribution of the GCR protons initiated various secondary particles at Aragats, 3200 m altitude. The characteristic of the distributions (quintiles, mode, median) helps to estimate most probable energy of each of secondary particle species; the detection efficiency equals to the ratio of primary protons to detected particles.

Another parameter possibly sensitive to ICME modulation strength is the power index of dependence of FD magnitude (percent of flux decrease) on energy of primary protons. Proceeding from a variety of particle detectors at ASEC we can reliably estimate the energy dependence of the attenuation of primary particle flux.

In presented paper we use simple regression model to:

1. Point-up the inter-relations of the FD amplitudes detected in the fluxes of neutrons, low energy charged particles (mostly muons and electrons) and high energy muons. Deduce from it obvious effect that the less is energy of primary particle initiated detected specie of the secondary cosmic ray the greater should be the amplitude of FD.
2. Illustrate the adequateness of the two introduced measures of the FD "strength" based on the detection of FD in different fluxes of secondary particles.
3. Demonstrate the existence or absence of relations between measured FD magnitude and several parameters of the ICME measured by space born facilities.

We still miss the theory and detailed operational models of the propagation of the ICME in the interplanetary space. The interactions of ICME with GCR and magnetosphere can hardly be unfolded in simple models and the observed magnitude of FD is due to complicated interplay of several unknown, or hard to measure parameters, as the ICME size, speed, and magnetic field, as well as conditions of the interplanetary magnetic field and magnetosphere, and other. On present stage of our understanding of these phenomena, simple one-parametric linear models can, at least, outline the relevant characteristics, to be used in future more complicated and more adequate models.

Therefore, the reliability of the obtained relations are done in the terms of values of the determination coefficients $R^2$, showing how well the regression line represents the data and correlation coefficient $R$ demonstrating the strength of linear connections between two variables. Also the 95% confidence intervals of the correlation coefficients are posted in the figures in the brackets. To prove absence of correlation we post in the figures the, so-called, $p$-value of the statistical test (particularly Student two-tailed test), which tells us how likely it is that we would get sample correlation coefficient $r$, just by chance, if there is no correlation at all in the population. If that $p$-value is very small (usually chosen with a threshold of 0.05), we conclude that the sample correlation is *not* due to chance and the population does have some correlation. If it is not very small (for instance >0.05) we cannot reject hypotheses of "no correlation" and can claim that there is no causal relations between examined variables.

The main disadvantages of linear models is strong sensitivity to the presence of unusual data points in the data used to fit a model. Unfortunately, we are not performing controlled experiments and we are obliged to use the scarce data the nature present us. And, sure, there is some extent of arbitrariness in deciding which correlation is significant and which – not. In the paper the graphicall assess to the data is widely used to demonstrate whether or not linear fits are consistent. In the analysis we accept that a correlation greater than 0.7 is generally described as *strong*, whereas a correlation less than 0.4 is generally described as *weak*. We think that systematically applying the one and the same criteria to rather complicated FD & ICME data we present useful information on the dependences and causal connections of the parameters crucial for the investigated problem.

In the second section we present the selection criteria of the FD events detected by ASEC particle detectors. In the third section the comparison of the ASEC data with muon data from Moscow engineering-physics institute detectors is performed. The forth section is devoted to correlations of FD magnitude with ICME various parameters.

## 2. Selection of the FD events detected by ASEC

In Table 1 we present selected FD events detected by the ASEC particle detectors during 2002–2006 and introduce indices reflecting the "modulation strength" of the

Table 1
Relative decreases of neutrons, low energy charged particles and high energy muons with energies greater than 5 GeV during FD and the corresponding ICME parameters.

| | Relative decrease of neutrons (%) | Relative decrease of charge component (%) | Relative decrease of muons >5 GeV | Correlation coefficient between 1 min time series of neutrons and muons >5 GeV | Power index of the fit of FD magnitude vs primary energy | Maximum speed of solar wind km/s (by ACE, SOHO) |
|---|---|---|---|---|---|---|
| 2002.09.07 | 3.6 | 2.6 | 1 | 0.64 | −0.99 | 570 |
| 2003.10.29 | 20 | 15 | 6 | 0.97 | −0.89 | >1000 |
| 2003.11.20 | 3.8 | 2.8 | 1 | – | – | 730 |
| 2004.01.22 | 7.5 | 4 | 1.3 | 0.88 | −1.26 | 690 |
| 2004.07.27 | 10 | 7 | 3 | 0.97 | −0.88 | 1000 |
| 2004.11.09 | 6 | 2.5 | 1.2 | 0.45 | −1.11 | 800 |
| 2005.01.17 | 5.1 | 3.6 | 1 | 0.65 | −1.21 | 800 |
| 2005.05.15 | 6.7 | 4 | 1.4 | 0.7 | −1.13 | 875 |
| 2005.09.11 | 10 | 5.5 | 1.7 | 0.93 | −1.28 | 1000 |
| 2006.12.14 | 4.7 | 1.7 | 0.7 | 0.84 | −1.4 | 900 |

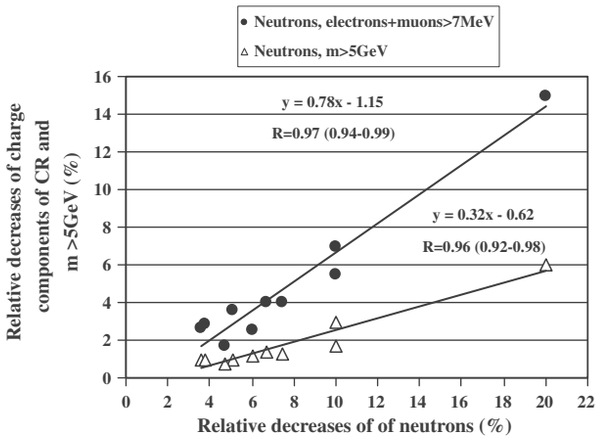


Fig. 2. Relative decreases of the charged CR compared with neutrons.

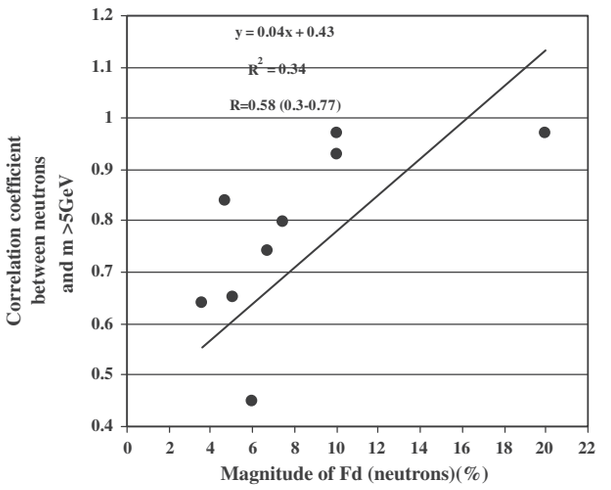


Fig. 3. Dependence of FD magnitude (neutrons) and correlation coefficient between Neutron Monitors and Aragats Multichannel Muon Monitor (>5 GeV muons) time series.

corresponding ICMEs. We select data from three ASEC monitors covering a large range (7–40 GeV, columns 2–4) of the primary proton energies. Correlation coefficients are calculated at FD attenuation phase by 1-min time series for intervals of 5–10 h (by 300–600 points), column 5. In column 6 we post the index of the fitted power function dependence of FD magnitude on the primary energy. The power function fit was done for three points correspondent to FD magnitude in fluxes of neutrons, low energy charge particles and muons with energies above 5 GeV, as it is demonstrated in the Fig. 5. In the last seventh column the maximal solar speed from 1-min data measured by instruments SWEPAM, ACE and SOHO is posted.

In Fig. 2 we can see the relative decreases in different secondary fluxes (neutrons, low energy charged particles, muon with energies greater than 5 GeV) for selected FD events. As it is expected, the relative decrease of definite species of secondary cosmic rays is inversely proportional to the most probable energy of primary generating this species. The most pronounced FD is observed on October 29, 2003 in neutron flux (~20%) and lowest – in >5 GeV muon flux (~6%).

The correlation matrix of the largest detected FD of cycle #23 on October 29, 2003 is posted in Table 2. We can see strong correlations between the neutrons and >5 GeV muon fluxes (most probable energies of primary protons ~7 and ~40 GeV, respectively). ICME having originated the FD on October 29, 2003 was so huge that it equally influenced the GCR flux at least till energies up to 40 GeV. In the scatter plot of the FD magnitude and the correlation coefficient between neutron and >5 GeV muon fluxes (Fig. 3) we can notice a trend, showing growing correlation coefficients for FDs with large magnitudes.

Another possible parameter characterizing the FD strength is the functional dependence of the relative magnitude on the most probable primary energy. In Fig. 4 the dependence of the FD magnitude (for events of 29 October 2003 and 27 July, 2004) of the different secondary cosmic-ray species (neutrons, charged particles and muons with energies greater than >5 GeV) was approximated by the power function. We can see that quality of fit is very high, that allows to use the power index of the dependence as a parameter to characterize the FD strength. In Fig. 5 we post the scatter plot of spectral indices calculated for the FDs from Table 1 vs magnitude of FD in charged component (we use only events in which all the three mentioned fluxes were observed). Although scattering of points is rather large, obviously larger FDs are correspondent to the biggest indices (weaker dependence of FD magnitude on the primary energy).

Table 2
Correlation matrix of time series of different secondary fluxes measured by ASEC on 29 October 2003.

| Type of facility | ANM | NANM | SNT Thr0 | SNT Thr 1 | SNT Thr 2 | SNT Thr 3 | SNT Thr 4 | Muons >5 GeV |
|---|---|---|---|---|---|---|---|---|
| ANM | 1 | | | | | | | |
| NANM | 1.00 | 1 | | | | | | |
| SNT Thr 0 | 0.99 | 0.99 | 1 | | | | | |
| SNT Thr 1 | 0.99 | 0.99 | 1.00 | 1 | | | | |
| SNT Thr 2 | 0.99 | 0.99 | 0.99 | 1.00 | 1 | | | |
| SNT Thr 3 | 0.98 | 0.98 | 0.99 | 0.99 | 0.99 | 1 | | |
| SNT Thr 4 | 0.98 | 0.98 | 0.99 | 0.99 | 0.99 | 0.99 | 1 | |
| Munos > 5 GeV | 0.97 | 0.97 | 0.97 | 0.97 | 0.97 | 0.96 | 0.95 | 1 |

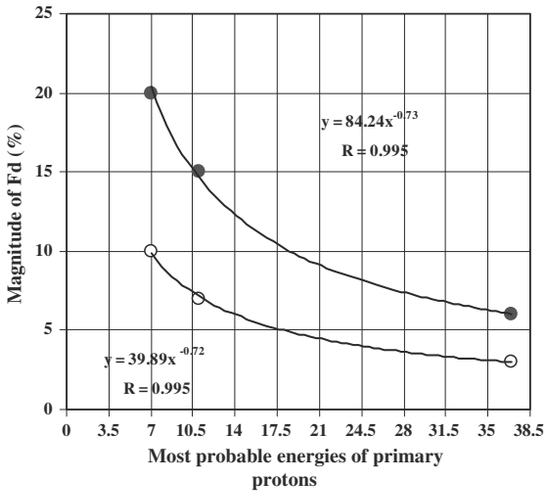


Fig. 4. Dependence of the magnitude of Forbush decrease on the primary energy.

## 3. Joint analysis of FD with the Moscow Engineering – Physics Institute Muon Detector data

The muon count rate variations during some of the FDs of the 23rd solar cycle were registered by muon detectors DECOR, TEMP and URAGAN operating in the experimental complex NEVOD (MEPhI, Moscow, Barbashina et al., 2007). MEPhI data can path the gap between low energy charged particles and high energy muons (>5 GeV) measured by ASEC. In Table 3 and Fig. 6 we present the data on a FD, which occurred on May 15, 2005. In Fig. 6 we see good agreement for data obtained by detectors located at different latitudes and altitudes. It is evident that FD magnitude in the high energy muon flux measured on the Earth's surface is global characteristic, approximately the same for the different detector locations.

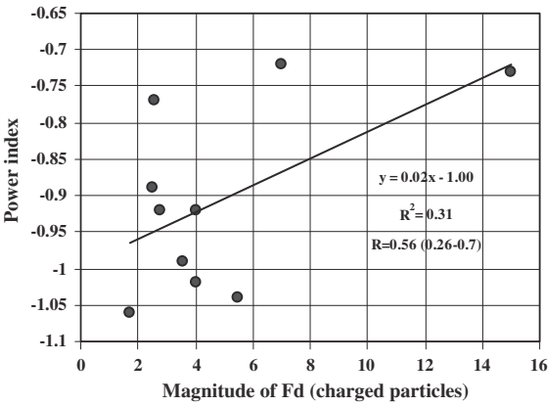


Fig. 5. Dependence of the FD magnitude (in charged secondary flux) and the value of the power index.

Table 3
Magnitudes of FD detected at15 May 2005 by MEPhI and ASEC.

| | Median energies of primary (GeV) | Magnitude of FD (%) |
|---|---|---|
| Moscow NM | 10 | 7.3 |
| ANM | 15 | 6.7 |
| Charged ANI | 24 | 3.8 |
| URAGAN | 23 | 3.3 |
| TEMP | 28 | 2.8 |
| DÉCOR | 50 | 2.2 |
| AMMM | 60 | 1.34 |

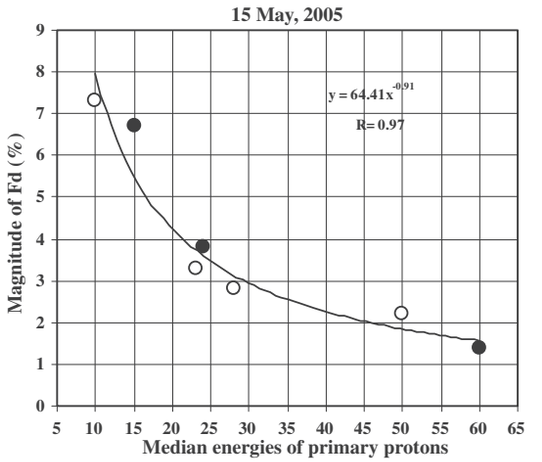


Fig. 6. Observation of the FD from 15 May 2005 by MEPhI. Open symbols – MEPhI data, close symbols – ASEC data.

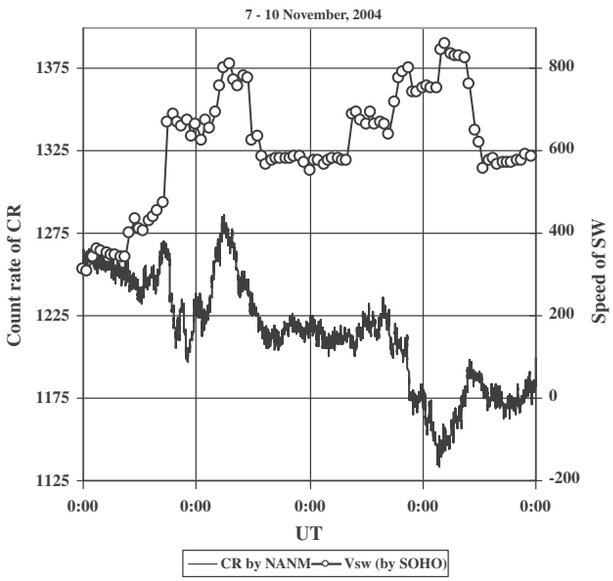


Fig. 7. Several successive ICMEs and geomagnetic storm prevents reliable estimation of the ICME siz.

## 4. Relation of the FD magnitude to the ICME parameters

The attenuation of the GCR flux due to approaching ICME is dependent on its speed, size, the field strength, and the orientation as well as on the pre-shock conditions of the Interplanetary Magnetic Field (IMF). Most of these parameters are rather difficult to measure and interpret; therefore, the explanation of the FD still lacks many details. For instance, it is rather difficult to estimate the spatial elongation of the ICME. The standard technique of measuring ICME thickness is based on the detection of the region with low proton temperature in solar wind passing ACE and SOHO spacecraft and simultaneously – the mean speed of solar wind ($V_{sw}$, see Richardson and Cane, 1995; Gopalswamy, 2007). However, this method is not applicable for the multiple colliding ICMEs; cases of the disturbed IMF by previous ICMEs, etc. The method we use is similar to the described one, with the difference that the time of ICME passage is estimated by the duration of FD decreasing phase (from the start of count rate decrease until maximal decrease). Both methods meet difficulties to distinguish successive ICMEs, as an example let's consider the FD occurred at ~18:00 on November 7, 2004, see Fig. 7. At this time the solar wind speed enhanced by ~200 km/s and the neutron count rate started to decrease. However, both count rate and solar wind speed changes are rather complicated, showing several peaks and dips. Therefore, estimation of the size of the ICME is not a simple arithmetic and for reliable estimation we need "clear" events involving a single ICME. The selected standalone ICMEs that generated FDs and allowing estimation of the sizes of ICME are posted in the Table 4. The heliocoordinates of the CME are posted in first column, the date in the second; in the third column we posted the FD magnitude in neutron flux. In columns 3–6 are posted the ICME parameters as measured by ACE spacecraft facilities. Maximal speed of Solar Wind ($V_{sw}$) and density of solar wind protons are estimated by data from instrument SWEPAM; strength of the magnetic field $B_{total}$ is measured by the MAG facility.

Table 4
"Single" ICMEs generating FD.

| The Solar Source of CME | Years, months, days | Relative decrease of neutrons (%) | Maximum speed of SW km/s (by ACE, SOHO) | Jump of density of SW | Jump of $B_{total}$ (nT) by ACE | Durations of decrease phase (h) | $L$ – size of clouds, associated with decrease phase of FD |
|---|---|---|---|---|---|---|---|
| ? | 2000.11.26 | 1.2 | 435 | 5 | 5 | – | * |
| ? | 2000.11.06 | 1.3 | 590 | 2 | 7 | 5 | 1.1E+07 |
| S15,W15 | 1998.05.04 | 1.5 | 835 | 13 | **36** | – | * |
| ? | 2000.08.10 | 1.6 | 460 | 7 | 5 | 12 | 1.9E + 07 |
| N07,W56 | 2000.02.11 | 1.7 | 520 | 2 | 6 | 5 | 8.4E + 06 |
| N14,W12 | 2001.03.31 | 1.9 | 730 | 25 | **67** | – | * |
| S07,E89 | 2003.06.17 | 1.8 | 540 | 2 | 10 | – | * |
| S17,W40 | 2000.02.12 | 2 | 590 | 20 | 18 | 6 | 1.2E + 07 |
| N20,E70 | 1999.09.15 | 2.4 | 615 | 3 | 11 | 10 | 2.1E + 07 |
| N16,W18 | 2001.10.21 | 3.1 | 650 | 17 | 12 | 7 | 1.4E + 07 |
| N26,W10 | 2001.08.17 | 3.8 | 500 | 30 | 28 | 7 | 8.8E + 06 |
| N00,E18 | 2003.11.20 | 3.8 | 730 | 17 | **47** | 7 | 1.7E + 07 |
| N10,E08 | 2004.11.7 | 3.9 | 650 | 40 | 33 | 5 | 1.1E + 07 |
| N17,W31 | 2001.04.28 | 4.4 | 750 | 9 | 18 | 9 | 2.2E + 07 |
| S21,E31 | 2001.04.08 | 4.6 | 750 | 13 | 15 | 8.5 | 2.2E + 07 |
| S06,W24 | 2006.12.14 | 4.7 | 900 | 4 | 10 | 4.5 | 1.4E + 07 |
| N09,W28 | 2002.09.7 | 4.8 | 580 | 11 | 20 | 13 | 2.4E + 07 |
| S23,E17 | 2001.10.11 | 5 | 550 | 27 | 20 | 8 | 1.5E + 07 |
| N15,W05 | 2005.01.17 | 5.2 | 800 | 40 | 33 | 8.5 | 2.2E + 07 |
| N19,W85 | 2001.04.04 | 5.4 | 790 | 6 | 15.5 | 5.5 | 1.4E + 07 |
| N18,E09 | 1998.09.24 | 5.6 | 810 | 14 | 25 | 6.5 | 1.40E + 07 |
| N20, E18 | 2000.06.08 | 5.5 | 780 | 10 | 19 | 7 | 1.9E + 07 |
| N22,W07 | 2000.07.15 | 5.9 | 1000 | 25 | 37 | 7.5 | 2.7E + 07 |
| N08,W28 | 2004.11.9 | 6.4 | 800 | 23 | 29 | 7 | 2.0E + 07 |
| N12,E12 | 2005.05.15 | 6.7 | 870 | 20 | 42 | 6 | 1.8E + 07 |
| S18,E27 | 2001.04.11 | 6.7 | 750 | 25 | 29 | 7.5 | 1.9E + 07 |
| S16,W12 | 2001.09.25 | 6.8 | 740 | 22 | 25 | 11 | 2.6E + 07 |
| S23,W09 | 2004.01.22 | 7.5 | 690 | 15 | 19 | 9 | 2.1E + 07 |
| N06,W18 | 2001.11.06 | 9.4 | 790 | 30 | 60 | 13 | 3.3E + 07 |
| N04,W30 | 2004.07.27 | 10 | 1035 | 5 | 22 | 5 | 1.8E + 07 |
| S01,E70 | 2005.09.11 | 10 | 1000 | 5 | 20 | 6 | 2.2E + 07 |
| S16,E04 | 2003.10.29 | 20 | 1900** | – | 52 | 11.5 | 5.8E + 07 |

? – The Solar Source of CME and Solar Wind parameters, impossible to determine.
* Overtake CME.
** Master Data Table of Major Geomagnetic Storms (1996–2005). http://cdaw.gsfc.nasa.gov/geomag_cdaw/Data_master_table.html.

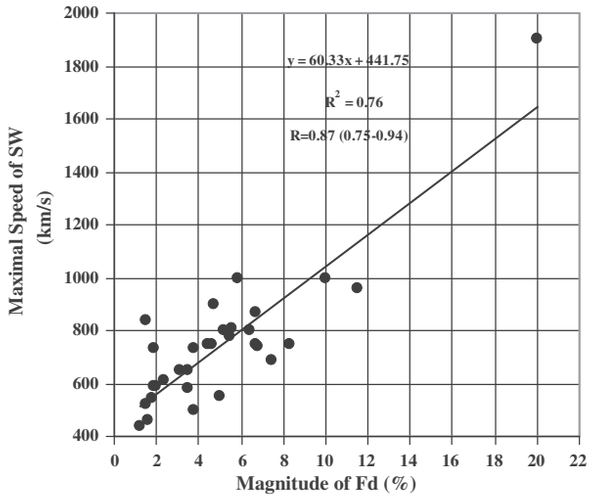


Fig. 8. Dependence of the magnitude of the Forbush decrease on the maximal solar wind speed.

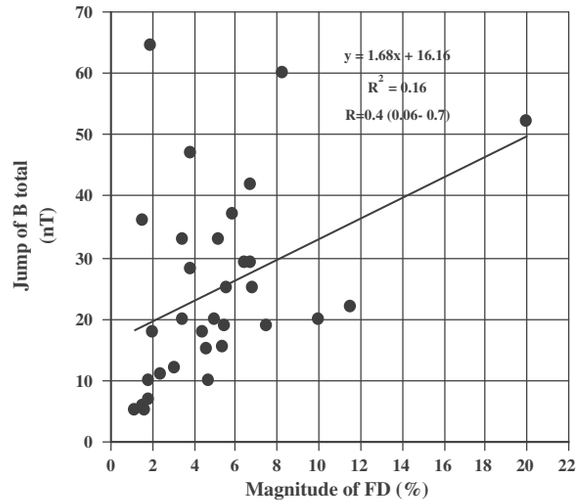


Fig. 10. Dependence of the magnitude of Forbush decrease on the "jump" of the total magnetic field of ICME.

The one and the same procedure was applied to all ICMEs that unleash FD to calculate sizes of ICME; the estimated duration of the FD decreasing phase is posted in the seventh column and corresponding calculated size of IMCE – in the eighth.

Data from Table 4 (total 32 events) was used to investigate correlations between magnitude of FD and ICME parameters. As we can see in Figs. 8 and 9 there is a pronounced dependence between the FD magnitude and ICME speed and size. The dependence of the FD magnitude on the ICME magnetic field (its "jump" at ICME pass) is much weaker (Fig. 10). However, if we exclude the FDs accompanied by strong geomagnetic storms (the depression of CR intensity is someway masked by the reduced cutoff rigidity leading to CR flux enhancement) the discrepancy of points on scatter plot reduces. In Fig. 11 we post the same events as in Fig. 10, excluding events occurred on May 5, 1998, March 31, 2001, and November 20, 2005. The correlation between FD magnitude and change (jump) of total magnetic field measured by MAG facility of ACE spacecraft are notably enlarged. And we did not observe any correlation between FD magnitude and Solar Wind density (Fig. 12).

## 5. Conclusion

We perform a statistical study of FD decreases detected by the ASEC particle detectors during 23rd solar activity cycle. We present relations of the measured magnitude of FD in different secondary particle fluxes to the most probable energy of the primary protons of GCR that initiated these fluxes. The FD magnitude measured in ASEC during

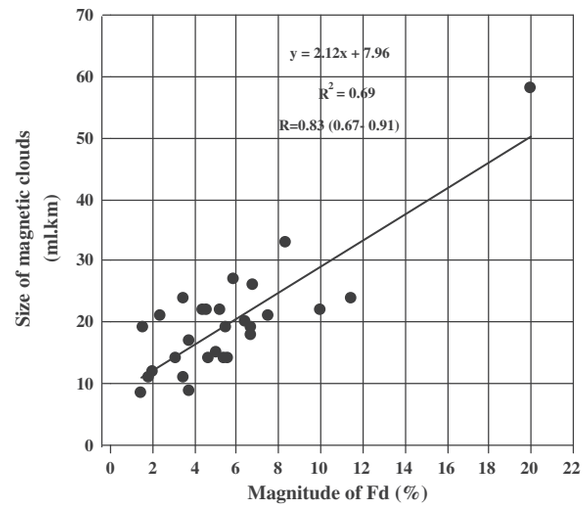


Fig. 9. Dependence of the estimated ICME linear size on the FD magnitude for 28 events.

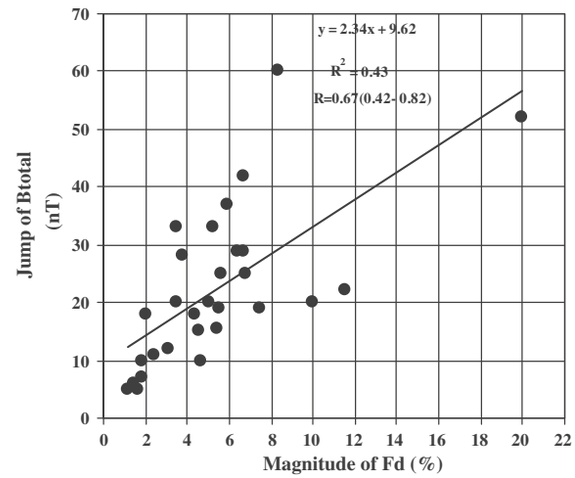


Fig. 11. The same as Fig. 10 without three events excluded (accompanied by severe geomagnetic storms).

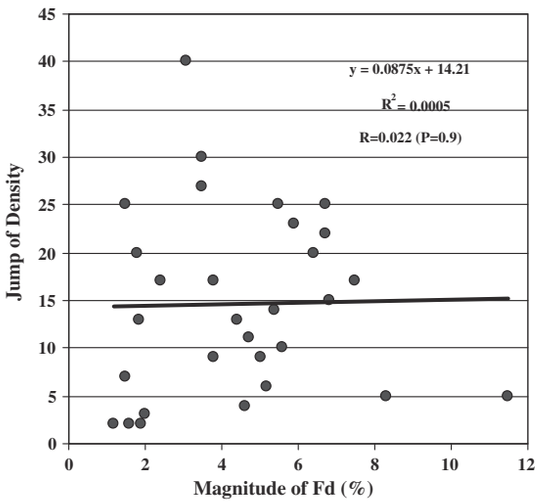


Fig. 12. Dependence of the magnitude of Forbush decrease on the density of solar wind (SW density corresponds to the ICME sheath region.

the 23rd solar activity cycle ranges from about 1.5% to 20% in the secondary neutron flux, 1–15% in the charged low-energy particle flux and 0.6–6% in the >5 GeV muon flux. We introduce two indices to enumerate the ICME "modulation strength", namely: the correlation coefficient of time series of two secondary CR species (neutrons and muons with energies greater than 5 GeV), corresponding to the highest and lowest primary proton energies;

- The power index of the estimated power dependence of the FD magnitude on the most probable energy of primary protons.

Both indices demonstrate apparent positive trend, proving obvious fact that if FD magnitude is large, both low and high energy primaries will be affected by ICME. However, rather large scattering pointed that proposed indices should be calculated by subsamples of events, after applying more specific selection criteria.

Neutron Monitor data was only used for analysis of characteristics of single ICMEs causing Forbush decreases. The modulation strength of the ICMEs is correlated with the speed and size of ICMEs. The correlation with ICME magnetic field can be significantly enlarged if we exclude events accompanied with strong geomagnetic storms. On the base of detected data we cannot claim of existence of any correlation of FD magnitude with density of solar wind.

## Acknowledgement

This work was partly supported by ISTC A1554 grant and INTAS 8777 grant. Authors thank N. Gopalswamy and G. Karapetyan for useful discussions and the ASEC staff for providing continuous operation of the particle detectors during the 23rd solar activity cycle.

## References

Barbashina, N.S., Dmitrieva, A.N., Borog, V.V. Investigation of Forbush effects in muon flux measured in integral and hodoscopic modes, in: Proc. 30th Intl. Cosmic Ray Conf., vol. 1, pp. 315–318, 2007.

Burlaga, L.F., Chang, G. J. Gephys. Res. 93, 2511–2518, 1988.

Cane, H.V. Coronal mass ejections and Forbush decreases. Space Sci. Rev. 93, 55–77, 2000.

Chilingarian, A., Avakyan, K., Babayan, V., et al. Aragats Space-Environmental Centre: status and SEP forecasting possibilities. J. Phys. G: Nucl. Part. Phys. 29, 939–951, 2003.

Chilingarian, A., Arakelyan, K., Avakyan, K., et al. Correlated measurements of secondary cosmic ray fluxes by the Aragats Space-Environmental Center monitors. NIM A543, 483–492, 2005.

Chilingarian, A., Hovsepyan G. New type of particle detectors for Space Weather research, in: Intl. Symp. on Forecasting of the Radiation and Geomagnetic Storms, Nor Amberd, Armenia, pp. 92–97, 2008.

Forbush, S.F. On the effects in cosmic-ray intensity observed during the recent magnetic storm. Phys. Rev. 51, 1108–1109, 1937.

Forbush, S.F. World-wide changes in cosmic-ray intensity. Rev. Mod. Phys. 11, 168–172, 1939.

Gopalswamy, N. Properties of interplanetary coronal mass ejections. Space Sci. Rev., 2007.

Haurwitz, M.W., Yoshida, S., Akasofu, S.I. Interplanetary magnetic field asymmetries and their effects on polar cap absorption effects and Forbush decreases. J. Geophys. Res. 70, 2977–2988, 1965.

Richardson, I.G., Cane, H.V. Regions of abnormally low temperature as signatures of ejecta in the solar wind and their solar cycle dependence, in: Proc. of the 24th ICRC, vol. 4, p. 868, 1995.

Simpson, J.A. Cosmic-radiation intensity-time variations and their origin. Phys. Rev. 94, 426–440, 1954.

Usoskin, I.G., Braun, I., Gladisheva, O.G., et al. Forbush decrease of cosmic rays: energy dependence of recovery phase. J. Geophys. Res. 113, A07102, doi:10.1029/2007JA012955, 2008.

Van Allen, J.A. Scott Ellsworth Forbush, biographical memoirs. Available from: <http://books.nap.edu/html/biomems/sforbush.html>, 1985.

Zazyan, M., Chilingarian, A. Calculations of the sensitivity of the particle detectors of ASEC and SEVAN networks to galactic and solar cosmic rays. Astroparticle Phys., doi:10.1016/j.astropartphys.2009.08.001, 2009.

PHYSICAL REVIEW D **82,** 043009 (2010)

# Ground-based observations of thunderstorm-correlated fluxes of high-energy electrons, gamma rays, and neutrons

A. Chilingarian,* A. Daryan, K. Arakelyan, A. Hovhannisyan, B. Mailyan, L. Melkumyan, G. Hovsepyan, S. Chilingaryan, A. Reymers, and L. Vanyan

*Artem Alikhanyan National Laboratory, Alikhanyan Brothers 2, Yerevan 36, Armenia*

(Received 28 April 2010; published 23 August 2010)

The Aragats Space Environmental Center facilities continuously measure fluxes of neutral and charged secondary cosmic ray incidents on the Earth's surface. Since 2003 in the 1-minute time series we have detected more than 100 enhancements in the electron, gamma ray, and neutron fluxes correlated with thunderstorm activities. During the periods of the count rate enhancements, lasting tens of minutes, millions of additional particles were detected. Based on the largest particle event of September 19, 2009, we show that our measurements support the existence of long-lasting particle multiplication and acceleration mechanisms in the thunderstorm atmosphere. For the first time we present the energy spectra of electrons and gamma rays from the particle avalanches produced in the thunderstorm atmosphere, reaching the Earth's surface.

DOI: 10.1103/PhysRevD.82.043009 PACS numbers: 92.60.Pw, 13.40.−f, 94.05.Dd, 96.50.S−

## I. INTRODUCTION

Charles Thompson Rees Wilson in 1924 [1] realized that a ''particle started with suitable velocity in the electrical field of the thundercloud may be expected to continue to acquire kinetic energy at the rate of many thousand volts per cm.'' In 1992 Alexander Gurevich, Gennady Milikh, and Robert Roussel-Dupre [2] introduced the theory of the generation of fast ''runaway'' electrons from the MeV electrons of the extensive air showers (EAS) initiated by the energetic proton or nuclei incident on the top of the atmosphere. However, the nature of seed particles is still under debate; an alternative source of the seed particles is connected with the lightning leaders [3,4]. Although there is no exact measurements yet of the possible strength of the electric field, in [5] it was suggested that streamer heads can produce fields up to several tens of millions volts per meter. The electrical fields in the thunderstorm atmosphere gave the cosmic ray shower and/or electrons from the lightning leaders a boost by increasing the number of energetic particles through a multiplication process initially called runaway breakdown (RB), and now referred to as relativistic runaway electron avalanche (RREA) [6–8]. The RREA mechanism can create large amounts of high-energy electrons and subsequently the gamma rays, as well as x rays and neutrons. Unfortunately, this model has not yet been able to demonstrate the creation of the hot plasma channel and lightning itself.

Astonishingly, the physical processes in the low atmosphere were observed by the orbiting gamma observatories at 400–600 km above the Earth's surface. Terrestrial gamma flashes (TGF), very short (tens of $\mu$ sec ) bursts of high-energy gamma rays, have been routinely observed by satellite gamma ray detectors during the last 20 years (see Ref. [9]). Recently the TGF have been observed in correlation with strong thunderstorms in the equatorial regions [10]. The spectra of the flashes are roughly expressed by a power-law function with an exponential decaying term; some of them extending up to several tens of MeV. In Ref. [7] these events were interpreted as by-products of the massive number of runaway electrons being generated within thunderclouds.

Surface detections of the RREA process, although having a long history, are discrepant and rare. Early measurements [11,12] discovered the existence of electron flux simultaneously, or earlier, than lightning located 30 kms apart. Atop Mt. Lemmon (altitude 2800 m) at the lightning research facility of the University of Arizona, the simultaneous detection of the cosmic ray flux (by the 10-cm diameter and 10-cm length plastic scintillator) and electrical field (by an electrical field mill) demonstrate $\sim$10% enhancement of the 1-minute count [13]. The average excess duration was $\sim$10 minutes; the threshold energy of the particle detector $\sim$100 keV. The Italian EAS-TOP surface array [14] measures significant excesses in the air shower counting rate lasting 10–20 minutes. The enhancements with maximum amplitude of 10%–15% were attributed mostly to highest energy EAS (large shower sizes, $>10^6$ electrons), and to zenith angles of incidence smaller than 20°; ''thickness'' (time distribution of the EAS particles arrival) of shower was slightly larger than in normal conditions [15].

A radiation monitoring post in a nuclear power plant in Japan reports on a comprehensive observation of a gamma ray burst emission lasting less than 1 min—correlated with snow and lightning activity. Enhancements were detected only during winter time, when thunderclouds are as low as several hundred meters [16]. The summer thunderstorm was observed by the same group at the top of Mt. Fuji (3776 m high). The flux of high-energy gamma rays had a

*chili@aragats.am

 

continuous energy spectrum up to 10 MeV, prolonged up to 20 min. The authors of [17] claim that the bremsstrahlung photons generated by the energetic electrons were produced continuously due to an intense electric field in the thundercloud rather than having originated in the process of lightning discharge.

A Japanese group on another Japanese power plant also detected short (less than 1 min) gamma bursts during winter thunderstorms [18]. The same authors reported a simultaneous detection of gamma rays and electrons at a mountain observatory Norikura located 2770 m above sea level [19]. Two emissions, lasting 90 sec, were associated with thunderclouds. At the same research station, Norikura in the Japanese Alps operates a large multilayered particle detector, primarily intended to register solar neutron events. In August 2000 on account of thunderstorms, particle flux enhancement was detected in 3 layers of a 64 $m^2$ area detecting system [20].

In experiments at the Baksan Neutrino Observatory of the Institute for Nuclear Research, the time series of cosmic rays are continuously measured along with precise measurements being taken of the electric field and monitoring of thunderstorms [8]. Intensity changes of the soft cosmic rays (below 30 MeV) and hard cosmic rays ( $>$ 100 MeV) were studied [21]. It was shown that the critical field and particle energy for this process are $\sim$300 kV/m and $\sim$10 MeV, respectively [8].

The network of the NaI detectors along with EAS triggering system is located at Tien-Shan Cosmic Ray station of the Lebedev Physics Institute, at altitude 3340 m. The goal of the research is to detect runaway breakdown initiated by EAS with energy above 1000 TeV—so-called RB-EAS discharge. Based on short gamma flashes (less that 200 $\mu$ sec ) detected by the network of gamma detectors, the authors of [22] claim that RB-EAS is a rather rare event ( $\sim$ 1% of all EAS registered during thunderstorms) requiring coincidence of several conditions, the most important of them being that the strong electrical field should be located not higher than 400–500 m above the detector.

The neutron production was claimed to correlate with the lightning process [23]; however, the mechanism by which neutrons can be generated by the lightning plasma are not well understood or even formulated [24]. The photonuclear reactions caused by gamma rays originated by bremstrahlung of the RREA electrons can be the origin of the neutron enhancements. On the other hand, absorption of neutrons in the dense lower atmosphere is so strong that the photonuclear neutron yield seems to be insufficient to account for the increase of neutron flux observed on the Earth's surface [25].

From the brief review above, it is apparent that many major problems connected with particle multiplication and acceleration in the thunderstorm atmosphere remains unsolved. Usually only one of the secondary cosmic ray species is measured; the additional particle flux is not too large and the number of detected ''thunderstorm particle events'' is very modest. Available experimental data cannot yet provide sufficient information to confirm the RREA theory. The energy spectra of RREA electrons and gamma rays are derived from a number of simulations; however, the experimental evidence is lacking till now.

Ground-based observations by a variety of the surface particle detectors systematically and repeatedly measuring the gamma rays, electrons, muons, and neutrons from atmospheric sources are necessary for answering these and other questions concerning high-energy phenomena in the atmosphere. Energy spectra and correlations between different particle fluxes, measured on the Earth's surface, address the important issues of where this radiation and particles come from and what kind of role they play in the lightning initiation.

The particle detectors of the Aragats Space Environment Center (ASEC) [26,27] observe charged and neutral fluxes of secondary cosmic rays by the variety of particle detectors located in Yerevan (1000 m a.s.l.) and on slopes of Mt. Aragats at altitudes 2000 and 3200 m. ASEC detectors measure particle fluxes with different energy thresholds and angles of incidence as well as EAS initiated by primary proton or stripped nuclei with energies greater than 50–100 TeV. Numerous thunderstorm-correlated events, detected by the ASEC facilities, constitute a rich experimental set to investigate the high-energy phenomena in the thunderstorm atmosphere. In this paper we will discuss the largest ever measured enhancement of cosmic ray fluxes on the Earth's surface, which occurred on September 19, 2009, at Mt. Aragats in Armenia.

## II. PARTICLE DETECTORS OF THE ARAGATS SPACE ENVIRONMENTAL CENTER

The Aragats Space Environmental Center [26,27] of the Yerevan Physics Institute is located on the highland 3250 m above sea level, 5 km from the southern peak of Aragats (3750 m), near a large lake. The thunderstorm activity on Aragats is extremely strong in May–June. Sometimes, lightning continuously hits the ground in the vicinity of the station during an hour or longer. Thunderstorm clouds are usually below the southern peak (i.e., not higher than 500 m above) and sometimes 100–200 m above the station.

Along with solar modulation effects, ASEC detectors register several coherent enhancements associated with thunderstorm activity. Nearly 50 such events detected in 2007–2009, at solar cycle minimum, unambiguously pointed on the thunderstorm-correlated particle acceleration and multiplication. The experimental techniques used allowed for the first time to simultaneously measure fluxes of the electrons, muons, gamma rays, and neutrons correlated with thunderstorm activity[28].

Most of particle detectors are located in the MAKET building (see Fig. 1) and nearby. Along with 16 plastic

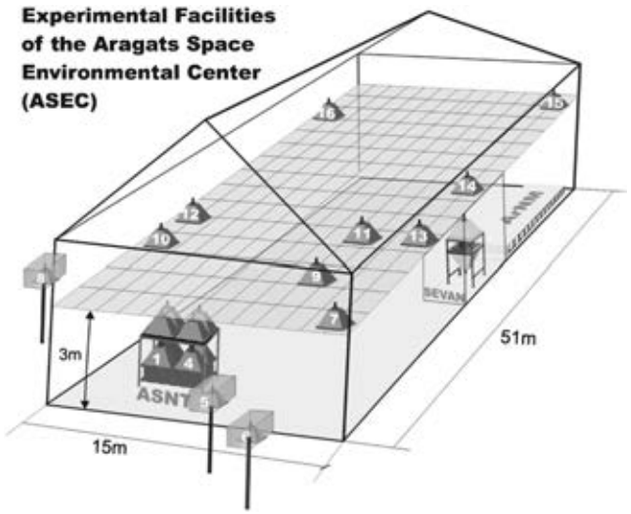


FIG. 1 (color online). The MAKET building at Aragats station, now hosting also ASNT, SEVAN, ArNM detectors, 3250 m above sea level.

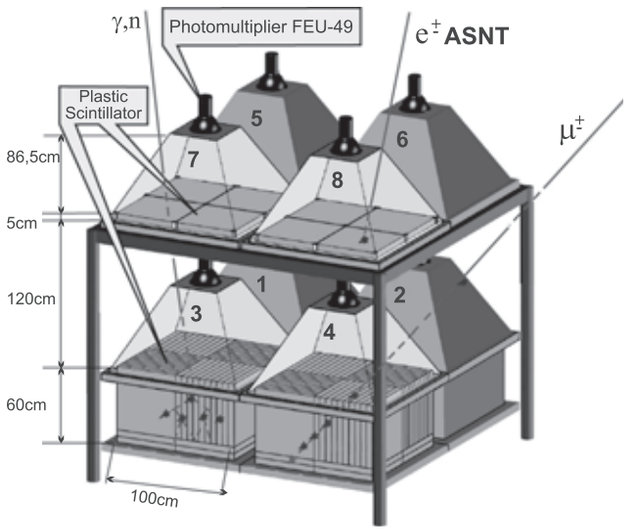


FIG. 2 (color online). Aragats Solar Neutron Telescope (ASNT).

scintillators belonging to the already finished MAKET-ANI surface array, in operation are Aragats Solar Neutron Telescope (ASNT); Aragats Neutron Monitor (ArNM) of 18NM64 type; and SEVAN (Space Environmental Viewing and Analysis Network) particle detectors. ArNM is detecting neutrons and ASNT and SEVAN are both neutral and charged species of the fallen secondary cosmic ray flux. Detailed descriptions of these particle detectors and appropriate references are presented in the following subsections.

### A. Aragats Solar Neutron Telescope

Aragats Solar Neutron Telescope (ASNT, see Fig. 2) is part of the worldwide network coordinated by the Nagoya University (see details in [29]) aiming primarily to measure the fluxes of the neutrons born in the violent solar flares. In 2006, after setting up new data acquisition electronics [30], ASNT measures stopping particle energy in the range 7–120 MeV.

Histograms of the energy releases in the thick scintillators are measured and stored each minute, providing the exact pattern of the energy releases during solar transient events and during thunderstorms. The ASNT consists of 4 up and 4 bottom scintillators, each having the area of 1 $m^2$. The distance between layers is $\sim$1.2 m. The data acquisition system can register all coincidences of detector signals from the upper and lower layers, thus, enabling measurements of the arrival of the particles from different directions. The signals ranging from 0.5 mV to 5 V, from each of 8 photomultipliers, are passed to the programmable threshold discriminators. The output signals are fed in parallel to the 8-channel logical OR gate triggering device and to a buffer. If there is a signal in the channel we will denote it by 1 and the channels that were not fired within the ''opening'' of the gate ( $\sim 1$ $\mu$ sec ) by 0. The ASNT trigger condition is defined by detecting at least one signal in the 8 data channels. The trigger rate of the entire detector system does not exceed 10 kHz. The duration of the entire data readout and signal processing procedure is less than 10 $\mu$ sec . There are 23 different possibilities of so-called ''basic states.'' Sixteen of them carry information about the direction of the incident particle. For example, the state configuration 0010 for the upper layer and 0010 for the lower layer corresponds to the charged particle traversal through the third upper and third lower scintillators (zenith angle between 0° and 30°). Combination 0010 and 1000 corresponds to the traversal through the third upper and the first lower scintillator (zenith angle between 20° and 40°). The other 7 possibilities give additional valuable information on the particle flux incident on the detector. For instance, the combination 01, i.e., no signal in the upper and the signal in the lower layer can be attributed to the traversal of a neutral particle. However, due to small sizes of the anticoincidence shielding (see Fig. 2), several charged particles can hit the detector from the side. Nonetheless, if the particle beam is near vertical (it is just the case of electron-gamma avalanche hitting ASNT), we can measure the energy release spectrum of the thunderstorm-correlated gamma rays. The combination 01 selects neutral particles, and viceversa the combination 10 selects low-energy charged particles (due to energy losses in the roof the threshold energy is $\sim$15–17 MeV). The top scintillators have the thickness of 5 cm (energy release for the vertical electrons and muons is $\sim$10 MeV) the combination 11 will select charged particles with energy greater that 25–27 MeV. The advanced data analysis system (ADAS) provides registration and storage of all logical combinations of the detector signals for further

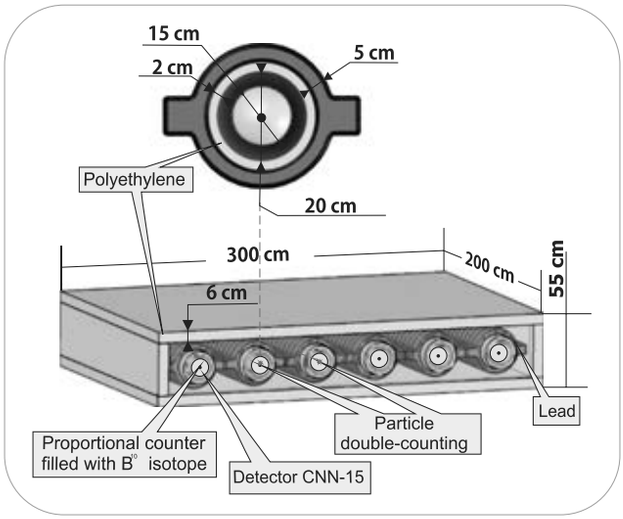


FIG. 3 (color online). Section of Aragats Neutron Monitor 18NM64 type; ArNM consists of 3 separate sections with 6 proportional chambers in each.

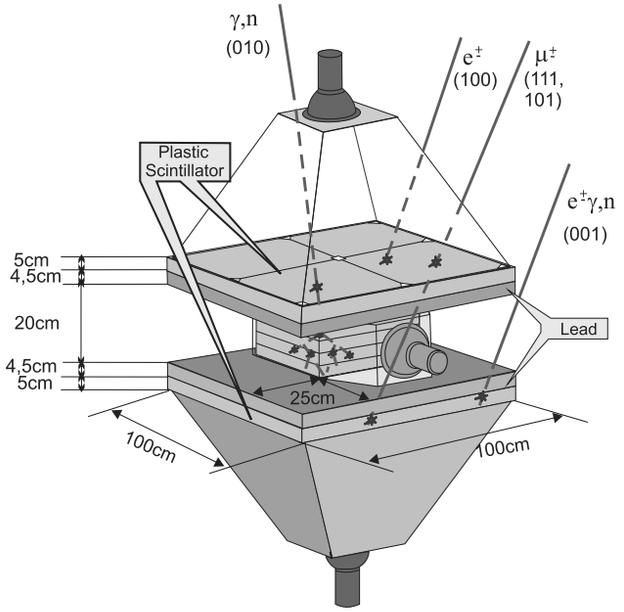


FIG. 4 (color online). SEVAN detector measuring charged and neutral secondary cosmic rays.

offline analysis and for issuing warnings and alerts on the dangerous space weather conditions [31].

### B. Aragats Neutron Monitor (ArNM)

The standard neutron monitor (NM) of 18NM-64 type, see Fig. 3, consists of 18 boron-filled proportional chambers, located below 5 cm of lead (producer) and 10 cm of polyethylene (moderator).

Secondary protons and neutrons interacting with the lead producer give birth to numerous neutrons of smaller energies which release energy in polyethylene (thermalized) and enter the proportional counter filled with gaseous boron. A small fraction of these neutrons ( $\sim 5\%$), are absorbed by $^{10}$B isotope and generate alpha-particles detected by the proportional chamber. The neutron monitors are equipped with DAQ electronics, providing 3 different values of the detector dead time—0.4, 250, and 1250 $\mu$s. Only incident hadrons can be detected by the neutron monitor; the sensitivity of ArNM to electrons, muons, and gamma rays is vanishingly small.

### C. SEVAN particle detectors

The new particle detector system, named SEVAN (Space Environmental Viewing and Analysis Network [32,33]), simultaneously measures fluxes of most species of secondary cosmic rays, thus representing an integrated device used for the exploration of the solar modulation effects.

The basic detecting unit of the SEVAN module (see Fig. 4) is assembled from standard slabs of $50 \times 50 \times 5$ cm$^3$ plastic scintillators. Between two identical assemblies of $100 \times 100 \times 5$ cm$^3$ scintillators (4 standard slabs) are located two $100 \times 100 \times 5$ cm$^3$ lead absorbers and thick $50 \times 50 \times 20$ cm$^3$ scintillator stacks (4 standard slabs). A scintillator light capture cone and photomultiplier tubes (PMTs) are located on the top, bottom, and intermediate layers of the detector. Incoming neutral particles undergo nuclear reactions in the thick 20 cm plastic scintillator and produce protons and other charged particles. In the upper 5-cm thick scintillator, charged particles are registered very effectively; however, for the nuclear or photonuclear interactions of neutral particles there is not enough substance. When a neutral particle traverses the top thin (5 cm) scintillator, usually no signal is produced. The absence of the signal in the upper scintillators, coinciding with the signal in the middle scintillator, points to neutral particle detection (gamma ray or neutron). The coincidence of signals from the top and bottom scintillators indicates the traversal of high-energy muons, traversing 10 cm of lead (minimal energy $\sim$250 MeV).

### D. Surface arrays: Aragats Multichannel Muon Monitor and MAKET ANI

Two detector assemblies measuring the extensive air showers operate on the Aragats research station. The main goal of the GAMMA [34] and MAKET-ANI [35] detectors is to measure the energy spectra of cosmic rays to understand their origin and particle acceleration mechanisms. Both detectors use the plastic scintillators overviewed by photomultipliers to determine the number of electrons in the shower and infer the energy and type of the primary particle. About 300 detecting channels formed from 5-cm thick plastic scintillators with area 1 m$^2$ each are located at the highland of Mt. Aragats at altitudes

3200–3250 m. EAS detectors are triggered arrays; however, each detector counts all incident particles measuring the time series of the changing fluxes of cosmic rays. High count rate ( $\sim 30,000$ counts per $m^2$ per minute), combined with the large area of the detector assembly makes surface arrays ideal detectors for measuring additional electron flux correlated with thunderstorms. We select several detectors from both surface arrays and implement special trigger conditions for detecting additional fluxes of cosmic rays and large particle bursts in correlation with thunderstorm activity. Twenty-six of 1 $m^2$, 5-cm thick scintillators, located in iron boxes, comprise the surface array of the Aragats Multichannel Muon Monitor (AMMM). Another 16 same type scintillators comprise a surface array named MAKET, located inside and in the vicinity of the building where most of the other particle detectors are located, see Fig. 1. AMMM and MAKET detectors measure the charged species of secondary cosmic rays with very high accuracy: the relative error of the mean 1-minute count rates are 0.13% and 0.18% correspondingly. Each of MAKET standalone detectors provide measurements of the incident particles and the array on the whole also provides count of, so-called, EAS triggers (''firing'' of more than 8 detectors of array within the time window of 400 nsec). From the collected triggered events we can select other firing combinations of detector channels (for instance, events with all 16 channels firing). These 2 selections ( $> 8$ and all 16 firing channels) routinely collect EAS with sizes $\sim 10^4$ and $\sim 2^* 10^4$ electrons correspondingly. However, when thunderstorm clouds are ''sitting'' on Mt. Aragats, the RREA process triggers the array and the stable count rate of EAS events goes up abruptly.

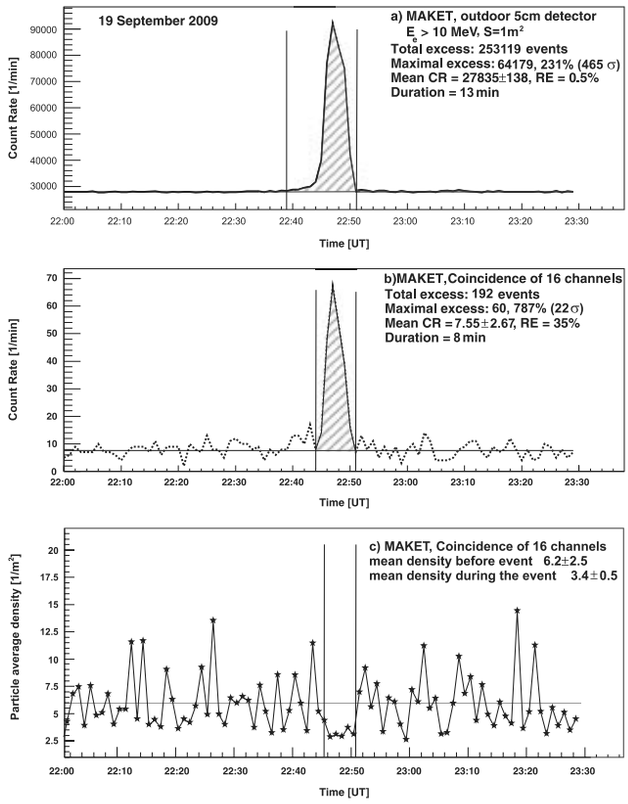


FIG. 5. One-minute time series detected by the MAKET array. (a) Count rate of the standalone outer detector. (b) Count rates of the ''EAS triggers''—all 16 scintillators give signal within 400 nsecs. (c) The mean density of the particles generating the MAKET trigger conditions.

## III. DETECTION OF THE THUNDERSTORM-CORRELATED COSMIC RAY FLUXES

On September 19, 2009 all ASEC detectors measured large enhancements, seen as huge peaks in the 1-minute count rates (see Figs. 5, 6, and 8). According to the staff report and information from the Armenian meteorological service, the thunderstorm clouds height was 100–200 m and lightning accompanied with snow and rain were seen at ~21–22 UT, a half an hour before the particle event.

In the legends of Figs. 5, 6, and 8, we depict a total enhancement during the event, the maximal enhancement occurred during 1 min, and statistical significance of the detected peaks in percents and numbers of standard deviations ($\sigma$). The mean count rate and variance of the count rate and the relative error were estimated by the 1-hour data before the start of enhancement when the mean and variance of the count rate corresponds to the detector typical operation.

In Fig. 5(a) one can see the enhancement of the count rate measured by the outdoor 5-cm thick scintillator of MAKET array (energy threshold 7–8 MeV, scintillator N 5 in Fig. 1. The observed enhancement above the background is really huge—10 times more than any reported ''thunderstorm particle'' flux by the other groups. The count rates of ''triggered'' events (signals in all 16 plastic scintillators within a time window of 400 nsec) although is only 0.1% of the 1-minute total count rate, enhanced ~8 times compared with the background value. The background for the triggered events is EAS generated by the primary proton or stripped nucleolus entering terrestrial atmosphere. From the mean background count rate we can estimated the threshold energy of the primary proton to be 50–100 TeV. During the ''thunderstorm event'' the nature of the additional triggers is completely different from the EAS events. The mean value of the particle density is considerably lower as we can see in Fig. 5(c). A huge number of particles born in a very short time covering large surfaces on the ground possibly pointed on the new source of seed particles, different from the ambient population of the MeV secondary cosmic rays. Possibly seed particles come from the electrons accelerated by very large electrical fields in the plasma of intracloud lightning [4,36].

Also in Fig. 5 we can see that the duration of the particle enhancement measured by the standalone scintillator is much larger than the duration of the ''short flashes'' of particles—13 and 7 min correspondingly. The duration of the event was determined by visually examining the time series; the enhancement is demonstrating itself as a characteristic peak in the time series. Usually we do not need a more formal definition for very large events. However, the peak searching algorithm defines the start as the initial point in the time series starting from which 3 consequent enhancements are greater than $2.5\sigma$. Nonetheless, the big variety of the peaks requires visual check as a final procedure.

## IV. ELECTRONS AND GAMMAS DETECTED BY ASNT

In Fig. 6 we present the excess measured by the ASNT detector at the same time, on September 19, 2009. The statistical significances of the peaks are extremely high. We assume that additional flux was due to the RREA process and additional particles are mostly electrons and gamma rays. Plastic scintillators can register both electrons and gammas and first of all we performed GEANT4 [37] simulations of the detector response to estimate the probability of detection of particles of different types by selecting various ASNT operation options (namely, 01, 10, and 11 combinations).

For each combination we calculate the efficiencies of the registration of the particle of a definite type and contaminations of its counterparts. Gamma rays can be registered by a 5-cm scintillator, with efficiency less than 10% (imitating electron) and in a 60-cm scintillator with efficiency $\sim$20%.[1] The electron can be registered in the top scintillator with efficiency above 95% or miss detection in the top scintillator and be detected in the lower one (imitating gamma ray) with efficiency less than 5%. Taking into account the energy of the minimal ionizing particle, giving a signal in the scincillator, and amount of the matter above the scintillator (roof, scintillator housing), we estimate the threshold energy to detect electron or gamma ray by the top layer of the ASNT to be equal $\sim$15–17 MeV. Several indoor MAKET detectors located near walls of the building have energy thresholds of 11–13 MeV. The energy of electrons detected in both layers of ASNT (11 combination) is above 25 MeV).

The start of the enhancement of gamma rays (energy above 7 MeV) is 4 min earlier compared to the start of the enhancement of electrons with energy above 15 MeV; see Figs. 6(a) and 6(b).

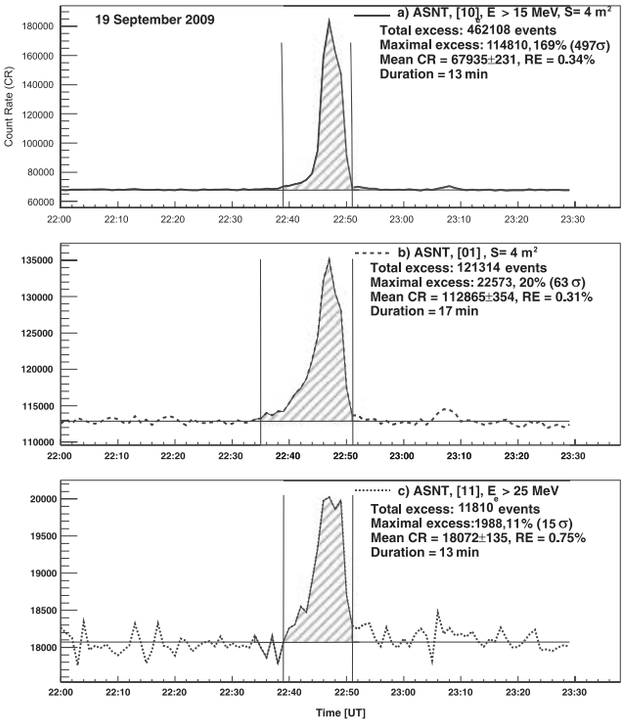


FIG. 6. One-minute time series of the particle fluxes measured by ASNT. (a) 10 combination, signal only in top layer, mostly electrons with energy greater than 15 MeV. (b) 01 combination—mostly gamma rays with contamination of neutrons and electrons. (c) 11 combination—electrons and/or gamma rays with energy above 25 MeV. Additional particles are demonstrated by the dashed areas.

## V. RREA ELECTRON AND GAMMA-RAY ENERGY SPECTRA

By the 60-cm thick scintillator of the ASNT we measure not only count rates but also spectra of energy releases [the distribution of the PMT amplitude heights enumerated as ADC (amplitude-to-digital converter) codes]. However, we are interested not in the energy release spectrum, which is dependent on the detector response, but in the flux of gamma rays before entering the roof and detector. Thus, we have to solve the inverse problem of cosmic ray physics—reconstruct by the measured spectrum of energy releases the spectrum that is fallen on the detector or on the roof of the building where the detector is located. We solve the inverse problem and ''unfold'' the gamma ray energy spectrum by multiple solutions of the direct problem: assuming the analytic form of the RREA gamma ray spectra (power, exponential, or power with cutoff), we tune free parameters (normalizing coefficients, spectral indexes) by minimizing the ''quality'' function describing the closeness of simulated with GEANT4 energy releases histogram to an experimentally measured one. As a quality function we use the sum of the square differences between bin values of 2 histograms. The electrons and gamma rays

[1]Neutrons also are detected by the thick scintillator with considerable efficiency. However, the cross section of the neutron photoproduction is not large and additional neutrons can comprise only very few percents of the gamma rays.

were traced through the material of the roof above the detector and through the substance of the detector. Light absorption in the plastic scintillators was also taken into account in GEANT 4 simulation. Light attenuation coefficients were taken from [29]. We use the random search procedure for selecting the parameters of the energy spectra (see, for example, [38]).

The RREA electron spectrum was obtained using count rates measured by 5-cm thick scintillators of MAKET, ASNT, and SEVAN detectors. From Fig. 1 you can see that the MAKET 5th, 6th, and 8th scintillators are located outdoors and ASNT, SEVAN, and other 13 MAKET scintillators are located indoors. These detectors are of the same type; however, their energy thresholds are different due to different electronics thresholds and a various amount of substance above. Using enhancements (peaks) detected in these 18 5-cm thick scintillators, we select groups corresponding to 4 diverse energy thresholds. The energy thresholds were determined by comparing the mean count rates of scintillators with ''theoretical'' values, obtained from simulations of the EAS propagation in the atmosphere.

The electron integral spectrum is shown in Fig. 7 along with a gamma ray spectrum. The electron spectrum in the energy range 7–20 MeV is fitted by exponential function—$A \bullet e^{b \bullet E}$. The spectral index is $-0.18 \pm 0.06$; corresponding fit quality—$\chi^2/\mathrm{ndf} = 0.34$. The horizontal error bars in the electron energy spectrum reflect uncertainties in determination of the energy thresholds, due to the complicated structure of the roof substance. The electron spectrum abruptly ended at ~30 MeV, as there is no evidence of additional electrons detected by 11 coincidence of ASNT. The peak seen in Fig. 6(c) was found to be caused by the gamma rays giving signals both in the top 5-cm and bottom 60-cm thick scintillators.

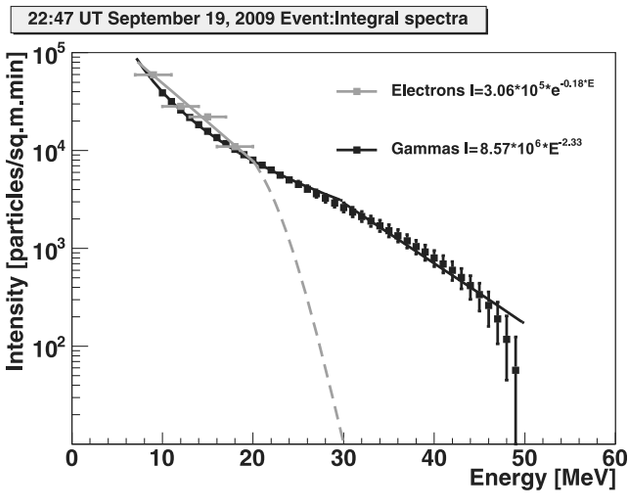


FIG. 7. Unfolded electron and gamma ray spectra fitted by exponential and power functions.

Using obtained electron spectrum, we estimate the number of electrons contaminating the energy release spectrum measured by the 60-cm thick scintillator and afterward correct the gamma ray energy spectrum. In turn, after reconstructing the gamma ray spectrum we correct the electron spectrum. The efficiency of gamma ray detection was checked by GEANT4 simulation; the probabilities of gamma rays to be detected in outer MAKET and ASNT 5-cm detectors are ~3.5% and ~10%, respectively. There is significant roof substance (metallic tilts, wood) above ASNT in which gamma rays create additional electron-positron pairs, increasing the probability of gamma rays to be detected in the 5-cm thick detector under the roof. The reconstructed energy spectrum of the incident gamma rays described by power function is continued till ~50 MeV. The gamma ray energy spectrum is fitted by power function—$A \bullet E^b$ in the range 7–30 MeV ($\chi^2/\mathrm{ndf} \sim 2.4$); in the energy range 30–45 MeV, the gamma ray spectrum is rather well described by the exponential function with slope equal to $-0.14$ and afterwards abruptly vanished near 50 MeV; see Fig. 7. Error bars of the gamma ray energy spectrum are statistical ones.

Details of the electron and gamma ray energy spectra at 3250 m are posted in Table I.

## VI. NEUTRONS IN THE RREA: ARNM EVIDENCE

In Figs. 8(a) and 8(b) we compare the enhancements of the neutrons detected by the ArNM and all neutral particles in the SEVAN detector (signal only in the middle scintillator, combination 010). Placed in a few meters from SEVAN, ArNM's enhancement is consistent with neutral

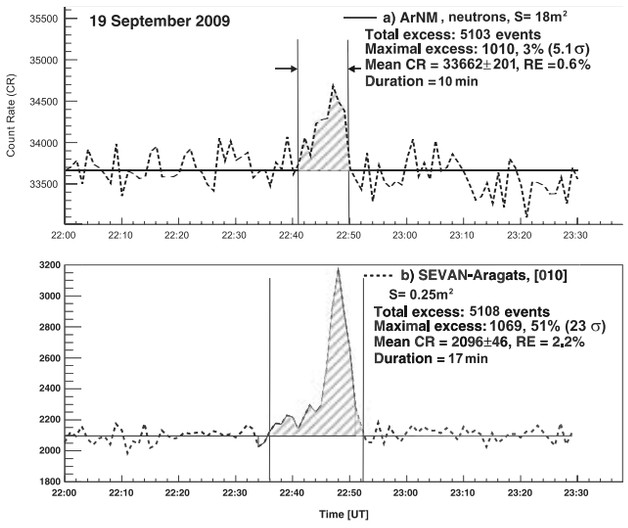


FIG. 8. One-minute time series of the particle flux detected by the SEVAN and ArNM detectors (a) 1-minute time series of ArNM. (b) 1-minute time series of SEVAN (010 combination). The additional particles are demonstrated by the dashed areas.

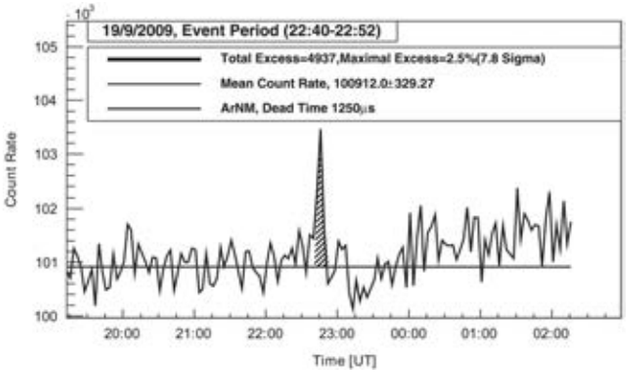


FIG. 9. 3-minute time series of ArNM on September 19, 2009.

fluxes registered by ASNT and SEVAN detectors. ASNT and SEVAN measure all neutral particles; there is no possibility of distinguishing between gamma rays and neutrons. The neutron monitor is a device with suppressed efficiency to measure leptons (see [39,40]).

Additional protons of the cosmic ray flux can also generate an enhancement in NM; however, the conditions of interplanetary magnetic fields were very stable on September 19 and there is absolutely no reason to expect extra proton flux. Therefore, although the enhancement of neutrons in ArNM is not so significant as detection of neutral particles by ASNT and SEVAN ($5.1\sigma$ against $63\sigma$ and $23\sigma$), nonetheless, the peak in ArNM time series proves the detection of neutrons. The source of additional neutrons is located in the atmosphere; the high-energy gamma ray flux generates neutrons in photonuclear reactions with air atoms (see details in [41]). A simultaneous measurement of electrons and gammas on September 19 provides unambiguous confirmation of the photonuclear mechanism for neutron production and is another demonstration that RREA was developing very close to the ASEC detectors on September 19, 2009.[2] The duration of a neutron event is 7 min shorter as compared with the duration of a gamma enhancement. The start time and duration of the gamma ray enhancement detected by the SEVAN detector coincide with the ones detected by the ASNT detector, located 30 m from SEVAN in the same building.

Taking into account the importance of proving neutron production, we form 3-minute time series from initial 1-minute ones, summing counts of the 3 succeeding minutes (a standard practice in time series statistical analysis; see Fig. 9). Obtained significance of the 3-minute neutron peak, equal $\sim 7.8\sigma$, is overwhelming. Calculating the chance probability of obtaining a peak in the 3-minute time series, we take into account the number of attempts we made to obtain the maximal peak significance. Three-minute time series can be obtained by 1-minute time series in 3 ways. Taking only one time series from 3 possible ones, we alter the statistical distribution used for calculation of chance probability (see details of statistical techniques used in [42,43]; see Web calculator in [44]). Final obtained chance probabilities of order $\sim 10^{-14}$ leave absolutely no doubts of the neutron detection on September 19, 2009.

## VII. DISCUSSION

For the quantitative description of the RREA process in the thunderstorm atmosphere the most difficult problem is to determine the height of the cloud and structure and value of the electrical field in it. Nonetheless, despite the fact that we do not measure the height of the thundercloud and the structure of the electrical field in it, we can make rough estimates of some phenomenological parameters of the RREA process based on the measured particle energy spectra and neutrons. The energy spectra of the RREA electrons and gamma rays, as well as the measured flux of the neutrons, contain information on the strength and elongation of the electrical field in the thunderstorm cloud and on the height of the cloud above the detector.

To estimate the multiplication rate of the electrons in the thundercloud and overall number of electrons in it, we first have to estimate the height of the thundercloud on September 19, 2009, above the ASEC detectors. From the measured electron energy spectrum we can conclude that at least 20 MeV electrons reached ground level and were detected by the 5-cm scintillators inside the MAKET building. We can assume that maximal energy of the RREA electrons reached 40–50 MeV.[3] Therefore, assuming the average ionization losses of these electrons at $\sim$3500 m altitude equal to $\sim$200 KeV per meter, the most probable height of the cloud will be 100–150 m, well coinciding with the observations of the Armenian meteorological service. Taking for granted the height of 130 m, we estimate the RREA electrons spectrum just at the entrance from the thundercloud by selecting the trial electron spectrum at 3380 m and simulating with GEANT4 the electron-gamma avalanche till 3250 m. By trying different trial spectra (analogically to recovery of the gamma ray energy spectrum above the roof), evaluating the avalanche from 3380 till 3250 m and comparing each obtained spectrum with an experimental one (shown in Fig. 7 and Table I) we have found that the best approximation of the spectrum at 3380 m have again a exponential functional form; the spectral index is $-0.15 \pm 0.2$. The number of electrons with energies greater than $\sim$30 MeV at 3380 m is $350,000/\mathrm{sq\,m}$ min only $90,000/\mathrm{sq\,m}$ min electrons with energy greater than 7 MeV ( minimal ionizing particle energy of the 5-cm thick scintillators) survive traveling

[2]Neutrons attenuate very fast in dense atmosphere and survival probability of neutrons born high above the detector is very low.

[3]At least the AGILE gamma observatory detects one gamma ray with energy 40 MeV [10].

TABLE I. Parameters of the electron and gamma ray energy spectra fits measured on September 19, 2009, (maximal minute intensities) at altitude 3250 m above sea level.

| Spectra fit function | A (coeff.) | b (slope) | Mean Energy (MeV) |
|---|---|---|---|
| Electron $A^{*}e^{-b^{*}E}$ (from 7 till 20 MeV) | $(3.1 \pm 0.3) \bullet 10^5$ | $-0.18 \pm 0.06$ | $5.6 \pm 0.2$ |
| Gamma $A^{*}E^{-b}$ (from 7 till 30 MeV) | $(8.57 \pm 0.53) \bullet 10^6$ | $-2.33 \pm 0.02$ | $4 \pm 0.8$ ($E_{min} = 1$ MeV) |

till 3250 m. The mean electron energy is estimated to be $\sim 6.7 \pm 0.8$ MeV at the lower edge of the thundercloud at 3380 m. This value is in rather good agreement with that obtained from simulations of value 7.3 MeV [45]. From the measured RREA electron spectrum and spectrum of secondary cosmic ray electrons at 3380 m [46], we have calculated the multiplication rate (avalanche growth factor) in the thundercloud electric field. The obtained RREA energy spectrum on the 3380 m height (assumed end of the thundercloud and large electrical field in it) was extrapolated until 7 MeV; the number of electrons above 7 MeV was calculated and divided by the secondary cosmic ray electron number calculated according to [47]. Obtained multiplication factor equals $\sim 330$, corresponding to $\sim 6$ e-folding. Assuming a cross section area of electric field with radius 500 m (maximal distance between ASEC detectors measuring the thunderstorm-correlated particle enhancements), we will get a total number of electrons above 7 MeV $\sim 3.8^{*}10^{12}$.

The maximal energy gain of electrons per one avalanche length is approximately independent of the atmosphere density and electrical field value and equals $\sim 7$ MeV [45]. Thus, based on the calculations of the multiplication rate we obtain maximal energy of electrons $\sim 40$ MeV in good agreement with our assumptions and measurements.

To calculate the value of the e-folding length we need to know the elongation of the electrical field in the thundercloud. This length we estimate taking into consideration the neutron detection by the Aragats Neutron Monitor; see Figs. 8 and 9. The nuclear fusion origin of the thunderstorm-correlated neutrons was ruled out in [27]. Assuming the flux of the gamma rays with a spectrum stretching up till 50 MeV, well above the photonuclear reaction threshold for nitrogen ($\sim 10.5$ MeV), the $(\gamma, n)$ reaction becomes the best candidate for the neutron generation [25]. On September 19, 2009, ArNM detected $\sim 70$ additional neutrons per square meter at a maximal intensity minute. In the GEANT4 simulation, after the passage of 1500 m, bremsstrahlung photons had generated $\sim 2250$ neutrons. The number of gammas in simulation was taken to be $1 \times 10^6$, which corresponds to the 100 000 gammas after the passage of 1500 m (close to the experimental value). The obtained neutron energy spectrum can be fitted by the exponential function with slope $-0.45$; the maximal energy of neutrons was 14 MeV. The probability of the photonuclear reactions of gamma rays with atmosphere nucleus is rather low ($\sim 1\%$) in comparison with the probability of electromagnetic interactions. That is why the neutron flux is smaller in comparison with the gamma ray flux. Besides, the efficiency of the neutron monitor to register neutrons with energy below 15 MeV is much smaller than the efficiency of detecting neutral particles by ASNT and SEVAN. However, according to [48,49], even neutrons with energy less than 1 MeV still can be detected by the NM 64 neutron monitor. According to their estimates of the neutron detecting efficiency, we calculate the number of the neutrons expected to be registered by the ArNM to be $\sim 20$. The discrepancy between experiment and simulation can be due to other sources of neutron production [24] not taken into account in simulation or by greater than assumed efficiency of the NM 64 to detect low-energy neutrons, or by a too simplified model used for simulation. From the multiple trials of simulations started at the different heights in the atmosphere, we found that the maximal neutron yield was obtained when the starting point was $\sim 1500$ m above the detector. Therefore, from the estimate of the electrical field elongation of 1500 m, we can estimate the e-folding length as 250–300 m and the electrical field strength (if we assume its uniform distribution), according to equation (1) in [45] will be 180–200 kV/m.

A very long duration of the electron and gamma ray fluxes detected on the ground ($\sim 10$ orders of magnitude greater than duration of the terrestrial gamma ray flashes) requires a permanent stable source of the seed particles, and secondary cosmic rays fulfill this condition. On the other hand, we do not decline that the intracloud lightning leader can provide another source of the seed particles. Detection of very short (within 400 nsec) flashes of the electrons detected by the MAKET air shower array is just a demonstration of this possibility. Existence of the alternative seed particle source did not put under question our calculations because a fraction of particles from this source does not exceed 0.1% of the total observed enhancement.

## VIII. CONCLUSION

During the particle event on September 19, huge enhancements of the electrons, gamma rays, and neutrons, as well as short particle bursts, counting millions of the additional particles and distributed over a large area, were detected. The observations of ASEC monitors prove the existence of the long-lasting electron-photon avalanches developing in the atmosphere during thunderstorms.

Simultaneous measurements of the gamma rays and neutrons provide confirmation of the photonuclear mechanism for neutron production.[4]

For the first time we measured the electron and gamma ray energy spectra and made quantitative estimates of some phenomenological parameters of the RREA process based on detected particle fluxes. The exponential spectrum of the RREA electrons is in good agreement with simulations [45], and gamma ray power energy spectrum do not contradict recent observations of the TGF by orbiting gamma observatories [10]. However, we recognize that we measure only high-energy tails of the energy spectra of electrons and gamma rays; to measure bulk of particles of lower energies we need new particle detectors with much lower energy thresholds, under construction now.

[4]However, only ~20% of the detected neutrons can be explained by the photonuclear reaction according to our simulations

## ACKNOWLEDGMENTS

This work was partly supported by the Armenian government grants and by ISTC Grant No. A1554. Authors are grateful to Arnold Wolfendale for his stimulating interest to the applied cosmic rays field.

[1] C. T. R. Wilson, Proc. Cambridge Philos. Soc. **22**, 534 (1925).
[2] A. V. Gurevich, G. M. Milikh, and R. A. Roussel-Dupre, Phys. Lett. A **165**, 463 (1992).
[3] Z. Saleh, J. Dwyer, J. Howard, M. Uman, M. Bakhtiari, D. Concha, M. Stapleton, D. Hill, C. Biagi, and H. Rassoul, J. Geophys. Res. **114**, D17210 (2009).
[4] B. E. Carlson, N. G. Lehtinen, and U. S. Inan, J. Geophys. Res. **114**, A00E08 (2009).
[5] G. D. Moss, V. P. Pasko, N. Liu, and G. Veronis, J. Geophys. Res. **111**, A02307 (2006).
[6] L. P. Babich, E. N. Donskoi, I. M. Kutsyk, and A. Yu. Kudryavtsev, Phys. Lett. A **245**, 460 (1998).
[7] J. R. Dwyer, Phys. Plasmas **14**, 042901 (2007).
[8] N. S. Khaerdinov, A. S. Lidvansky, and V. B. Petkov, Atmos. Res. **76**, 346 (2005).
[9] D. M. Smith *et al.*, Science **307**, 1085 (2005).
[10] M. Marisaldi *et al.*, J. Geophys. Res. **115**, A00E13 (2010).
[11] B. F. J. Schonland, Proc. R. Soc. A **130**, 37 (1930).
[12] B. F. J. Schonland and J. P. T. Viljoen, Proc. R. Soc. A **140**, 314 (1933).
[13] G. E. J. Shaw, Geophys. Res. Bull. **72**, 4623 (1967).
[14] M. Aglietta *et al.*, Nucl. Instrum. Methods Phys. Res., Sect. A **277**, 23 (1989).
[15] S. Vernetto (EAS-TOP Collaboration), *Proceedings of the 27th International Cosmic Ray Conference (ICRC)* (Copernicus Gesellschaft, Hamburg, Germany, 2001), Vol. 10, pp. 4165–4168.
[16] T. Torii, M. Takeishi, and T. Hosono, J. Geophys. Res. **107**, 4324 (2002).
[17] T. Torii, T. Sugita, S. Tanabe, Y. Kimura, M. Kamogawa, K. Yajima, and H. Yasuda, Geophys. Res. Lett. **36**, L13804 (2009).
[18] H. Tsuchiya *et al.*, Phys. Rev. Lett. **99**, 165002 (2007).
[19] H. Tsuchiya *et al.*, Phys. Rev. Lett. **102**, 255003 (2009).
[20] T. Takami1 *et al.*, *Proceedings of the 27th International Cosmic Ray Conference (ICRC)* (Copernicus Gesellschaft, Hamburg, Germany, 2001), Vol. 10, pp. 4027–4030.
[21] A. S. Lidvansky and N. S. Khaerdinov, Izvestiya Rossiiskoi Akademii Nauk. Seriya Fizicheskaya **73**, 418 (2009) [Bulletin of the Russian Academy of Sciences: Physics **73**, 400 (2009)].
[22] A. V. Gurevich *et al.*, Phys. Lett. A **373**, 3550 (2009).
[23] G. N. Shah, H. Razdan, C. L. Bhat, and Q. M. Ali, Nature (London) **313**, 773 (1985).
[24] L. P. Babich and R. A. Roussel-Dupre, J. Geophys. Res. **112**, D13303 (2007).
[25] L. P. Babich, L. I.Bochkov, I. M.Kutsyk, and R. A.Roussel-Dupré, J. Geophys. Res. **115**, A00E28 (2010).
[26] A. A. Chilingarian *et al.*, J. Phys. G **29**, 939 (2003).
[27] A. A. Chilingarian *et al.*, Nucl. Instrum. Methods Phys. Res., Sect. A **543**, 483 (2005).
[28] A. A. Chilingarian *et al.*, *Proceedings of the International Symposium on Forecasting of the Radiation and Geomagnetic Storms by Networks of Particle Detectors ( FORGES 2008)* [Nor Amberd, Armenia, (Alikanyan Physics Institute, printed by Tigran Mets, Yerevan) 2009], pp. 121–126.
[29] A. Chilingarian, L. Melkumyan, G. Hovsepyan, and A. Reymers, Nucl. Instrum. Methods Phys. Res., Sect. A **574**, 255 (2007).
[30] K. Arakelyan *et al.*, *Proceedings of the International Symposium on Forecasting of the Radiation and Geomagnetic Storms by Networks of Particle Detectors ( FORGES 2008)* [Nor Amberd, Armenia, (Alikanyan Physics Institute, printed by Tigran Mets, Yerevan) 2009], pp. , pp. 105–116.
[31] S. Chilingaryan, A. Chilingarian, V. Danielyan, and W. Eppler, Adv. Space Res. **43**, 717 (2009).
[32] A. A. Chilingarian and A. Reymers, Ann. Geophys. **26**, 249 (2008).
[33] A. Chilingarian *et al.*, Earth Moon Planets **104**, 195 (2009).
[34] A. Garyaka *et al.*, J. Phys. G **28**, 2317 (2002).
[35] A. Chilingarian *et al.*, Astropart. Phys. **28**, 58 (2007).
[36] J. R. Dwyer, M. A. Uman, and H. K. Rassoul, J. Geophys. Res. **114**, D09208 (2009).
[37] S. Agostinelli *et al.*, Nucl. Instrum. Methods Phys. Res., Sect. A **506**, 250 (2003).
[38] A. A. Chilingarian, N. Gevorgyan, A. Vardanyan, D.

Jones, and A. Szabo, Math. Biosci. **176**, 59 (2002).
[39] J. M. Clem and L. I. Dorman, Space Sci. Rev. **93**, 335 (2000).
[40] S. Shibata *et al.*, Nucl. Instrum. Methods Phys. Res., Sect. A **463**, 316 (2001).
[41] L. P. Babich, JETP Lett. **84**, 285 (2006).
[42] A. Chilingarian, G. Hovsepyan, G. Gharagyozyan, and G. Karapetyan, Int. J. Mod. Phys. A **20**, 6753 (2005).
[43] A. Chilingarian, Adv. Space Res. **43**, 702 (2009).
[44] A. Chilinarian, http://se.crd.yerphi.am/chapman_calculator
[45] J. R. Dwyer, J. Geophys. Res. **113**, D10103 (2008).
[46] We accept here that RREA seed particles are electrons from the EAS initiated by primary proton and stripped nuclei. The seed electrons were simulated by the WEB generator of secondary cosmic rays (http://phits.jaea.go.jp/expacs/).
[47] T. Sato, EXPACS: Excel-based Program for calculating Atmospheric Cosmic-Ray Spectrum. User's Manual, http://phits.jaea.go.jp/expacs/, 2009.
[48] C. J. Hatton, *Progress in Elementary Particle and Cosmic-Ray Physics*, edited by J. G. Wilson and S. A. Wouthuysen (North Holland, Amsterdam, 1971), Vol. 10, Chap. 1.
[49] E. A. Maurchev *et al.*, ''*Simulation of the Neutron Monitor Response Function, Report to the 31st All Russian Cosmic Ray Conference, GEO_29, Moscow, MSU*, 2010 (unpublished).

PHYSICAL REVIEW D **83,** 062001 (2011)

# Particle bursts from thunderclouds: Natural particle accelerators above our heads

Ashot Chilingarian,* Gagik Hovsepyan, and Armen Hovhannisyan
*Artem Alikhanyan National Laboratory, Alikhanyan Brothers 2, Yerevan – 36, Armenia*
(Received 13 November 2010; published 1 March 2011)

Strong electrical fields inside thunderclouds give rise to fluxes of high-energy electrons and, consequently, gamma rays and neutrons. Gamma rays and electrons are currently detected by the facilities of low orbiting satellites and by networks of surface particle detectors. During intensive particle fluxes, coinciding with thunderstorms, series of particle bursts were detected by the particle detectors of Aragats Space Environmental Center at an altitude of 3250 m. We classify the thunderstorm ground enhancements in 2 categories, one lasting microseconds, and the other lasting tens of minutes. Both types of events can occur at the same time, coinciding with a large negative electric field between the cloud and the ground and negative intracloud lightning. Statistical analysis of the short thunderstorm ground enhancement bursts sample suggests the duration is less than 50 $\mu$s and spatial extension is larger than 1000 m$^2$. We discuss the origin of thunderstorm ground enhancements and its connection to the terrestrial gamma flashes detected by orbiting gamma-ray observatories.

DOI: 10.1103/PhysRevD.83.062001 PACS numbers: 92.60.Pw, 13.40.−f, 94.05.Dd

## I. INTRODUCTION

High-energy particles and radiation of an atmospheric nature is registered in space and on the Earth's surface. Terrestrial gamma-ray flashes (TGFs)—brief bursts of gamma rays[1] produced in the atmosphere—have been firmly established during the last decades by the gamma-ray observatories aboard low-Earth orbit satellites [2–5]. It is generally accepted that the gamma rays in TGFs come from the bremsstrahlung radiation of energetic electrons. Inside thunderclouds, the electric fields can grow large enough to force fast electrons to gain energy from the field larger than the braking force and ''run away.'' As the runaway electrons travel through air, they undergo hard elastic scattering with atomic electrons, producing additional electrons that can also run away. In this way the electrical fields in the thunderstorm atmospheres give the ambient population of the MeV electrons from the cosmic-ray showers a boost by increasing the number of energetic particles through a multiplication and acceleration process called relativistic runaway electron avalanche (RREA) [6,7]. The source of TGFs is located in the space just above or even within thunderclouds (12–20 km above Earth's surface; see [1]). The RREA mechanism can create large amounts of high-energy electrons and subsequently the gamma rays. The nature of seed particles is still under debate; an alternative source of the seed particles could be connected with the lightning step leaders [8–10]. As we will demonstrate in this paper, the very short time span of the discovered thunderstorm ground enhancement (TGE) events supports their lightning origin. However, it is possible that some other mechanisms are responsible for the high-energy phenomena in thunderclouds. Until now there were surprisingly few observations on the electric field dynamics in the thunderstorm atmospheres.

The amount of the surface detection of the electron and gamma-ray fluxes correlated with thunderstorms is not too large (see the review in [11]). Only at the Baksan Neutrino Observatory of the Institute for Nuclear Research [12] and at the Tien-Shan Cosmic Ray Station of the Lebedev Institute, both Russian Academy of Sciences, have surface particle enhancements correlated with thunderstorms been studied for many years in a systematic way. Unfortunately, the location of the surface array in the Baksan valley did not allow registration of large fluxes. The array is located in a deep narrow valley, and thunderclouds are rather high. The Tien-Shan group has concentrated mostly on the research of the very rare process—runaway breakdown initiated by an extensive air shower (EAS) with energy above 1000 TeV, so-called runaway breakdown-EAS discharge [6].

However, if electron and gamma-ray fluxes are unambiguously detected by orbiting gamma-ray observatories ~500 km from the source, we can expect the intensive particle and radiation fluxes on the highland altitudes from thunderclouds located a few hundred meters above. The particle detectors of the Aragats Space Environment Center (ASEC) [13,14] continuously measure the time series of the charged and neutral fluxes of the secondary cosmic rays. ASEC detectors measure 1 min and 10 sec time series starting from the minimal energy of 3 until 250 MeV, as well as time series of numbers of the EASs initiated in the atmosphere by primary protons or stripped nuclei with energy greater than ~50 TeV. Numerous thunderstorm correlated enhancements of electrons, gamma rays, and neutrons, detected by the ASEC facilities at the minimum of the solar activity years, constitute a rich

*chili@aragats.am
[1]Recently, Ref. [1] reported that a substantial fraction of TGF events are not gamma rays but high-energy electrons; see also [2].

 

experimental set to investigate the high-energy phenomena in the thunderstorm atmospheres. The Aragats High-Mountain Research Station of the Artem Alikhanyan National Laboratory (former Yerevan Physics Institute) is located 3250 m above sea level near the southern peak of Aragats (3750 m above sea level); the other 3 peaks of Aragats are located from 10 to 15 km away. The thunderstorm activity on Aragats is strongest in May–June and September–October. Thunderclouds are usually below the southern peak and sometimes 100–200 m only above the station. In 2009–2010 we measured several long TGEs of tens of minutes duration. During the two most intense of these, on 19 September, 2009 and 4 October, 2010, the Maket surface array [15] also detected a series of electron/gamma-ray bursts—short TGEs—extended showers of the coherent particles simultaneously detected in the scintillators of the surface array within a time window of 1 $\mu$s. In this paper, we discuss the short TGEs detection by the surface facilities and its relation to the TGFs detected by satellite facilities. We will demonstrate that TGEs have a duration not greater than 50 $\mu$s and will discuss their origin.

## II. DETECTION OF THE THUNDERSTORM CORRELATED COSMIC-RAY BURSTS ON 4 OCTOBER, 2010

Most of the ASEC particle detectors and field meters are located in the Maket building (see Fig. 1) and nearby. Along with 16 plastic scintillators belonging to the Maket surface array, in operation are the Aragats Solar Neutron Telescope (ASNT), the Aragats neutron monitor of type 18NM64, and the Space Environmental Viewing and Analysis Network (SEVAN) particle detectors

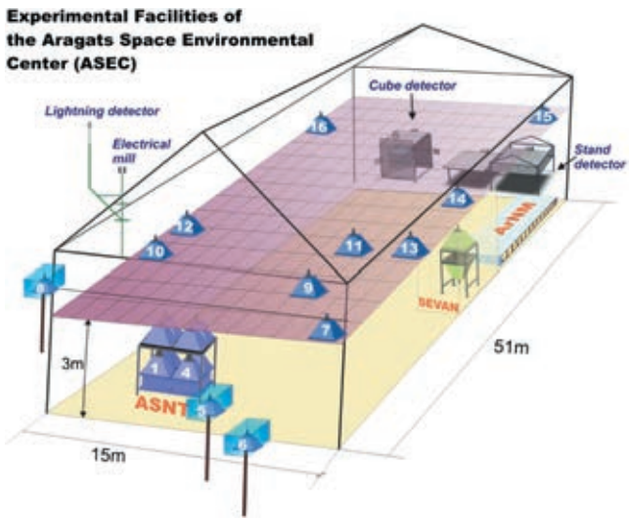


FIG. 1 (color online). Particle detectors and field meters of the Aragats Space Environmental Center operation during the 2010 measurement campaign.

(see the detailed description in [11]). In 2010, especially for the detection of low-energy electrons and gamma rays from thunderclouds, two new outdoor facilities were installed near the Maket building, namely, the Stand and Cube scintillation detectors. The Stand detector is a 3-layered pile of 1 cm thick and 1 m$^2$ area molded plastic scintillators with fiberglass wavelength shifters, fabricated by the High Energy Physics Institute, Serpukhov, Russian Federation. The same type of 3 cm thick scintillator is located also outdoors. The energy thresholds of the 1 cm thick scintillators are ~2, 6, and 10 MeV correspondingly from the top to the bottom: The energy threshold of the 3 cm thick scintillator is ~5 MeV. The energy thresholds of the rest of the ASEC scintillators range from 7 to 18 MeV (dependent on the amount of matter above); therefore in 2009 we reconstructed the energy spectra of RREA electrons and gamma rays starting from 7 MeV. The energy spectra of the 2010 campaign were reconstructed starting from 2 MeV. The aim of the Cube detector is to measure both charged and neutral fluxes separately, with enhanced purity of the neutral flux. For it the assembly of two 20 cm thick and 0.25 m$^2$ area plastic scintillators is fully surrounded by six 1 cm thick 1 m$^2$ area plastic scintillators, forming the veto for charged particles to enter the sensitive volume and hit the thick scintillators. The detector measures count rates of the neutral particles if there is at least one signal from the two inner scintillators without any signal from the surrounding veto scintillators. The histograms of the energy deposits in the two inner thick scintillators are stored every minute. The one-minute count rates of the surrounding 6 scintillators are measured and stored as well.

In 2010 we installed in the Maket building the magnetotelluric station LEMI-417, designed and commissioned by Lviv Center of the Space Research Institute of Ukrainian Academy of Science. One-second time series of the three-dimensional measurement of the geomagnetic field enter the ASEC database, which will highly improve the research of correlations of the geomagnetic parameters and changes of the fluxes of cosmic rays. The same device is measuring also components of the electric field. Additionally, on the roof of the building we installed an electrical field mill for measuring electrical fields between clouds and the ground and a lightning detector, measuring the broadband radio emissions by the intracloud, intercloud, and cloud-ground lightning (see Figs. 1 and 10).

In 2009–2010 we detected simultaneously large fluxes of electrons, gamma rays, and neutrons correlated with thunderstorm activity [11]. During the period of the count rate enhancements lasting tens of minutes, millions of additional particles were detected (see the appendix for discussion on the possible interferences with electronic or natural induced signals).

On October 4, 2010, all ASEC particle detectors measured a large enhancement of count rates seen as huge

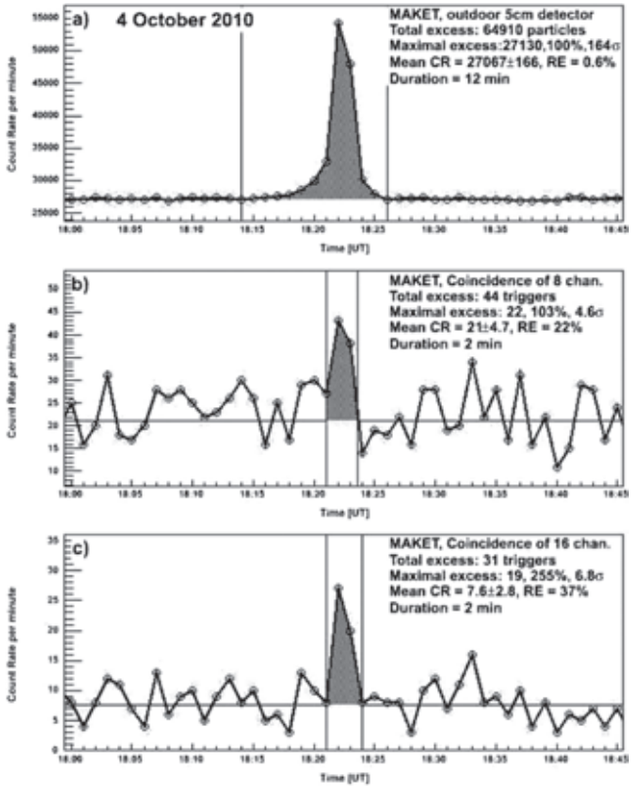


FIG. 2. One-minute time series detected by the Maket array. (a) Count rate of the standalone outer detector (energy threshold ~7 MeV); (b) count rates of the ''EAS hardware trigger''—9 scintillators give a signal within 1 $\mu$s); (c) count rate of the EAS software triggers—off-line selection of events where all 16 scintillators give a signal within 1 $\mu$s.

peaks in the time series (see Fig. 2). In the legend of Fig. 2, we depict a total enhancement during the event, the maximal enhancement that occurred during 1 min, and the statistical significance of the detected peak in percents and numbers of standard deviations ($\sigma$). The mean count rate (CR), the variance, and the relative error (RE) of the time series were estimated by the 1-hour data before the start of enhancement when the mean and variance of the count rate correspond to the detector typical operation.[2] In Fig. 2(a), one can see the huge enhancement of the count rate measured by the outdoor scintillator of the Maket array (energy threshold 7 MeV) with maximal enhancement at 18:23 (100%, 164$\sigma$). In the time series of the number of the Maket hardware triggers (as minimum 9 ''fired'' scintillators), the maximal enhancement of the count rate can be seen during the same minute [Fig. 2(b)]—the peak of ~103% magnitude and ~4.6$\sigma$ significance.[3] When we apply software trigger and select events with all 16 scintillators fired, this enhancement magnifies up to ~250% and ~7$\sigma$ [Fig. 2(c)]. It is indirect evidence that the TGE events cover much larger space than ''background''[4] EAS events (we will discuss the size of the EAS and TGE events in more detail in the following section).

## III. CLASSIFICATION OF THE EAS AND TGE EVENTS

Based on the expected systematic difference of the EAS and TGE event densities, we perform a two-way classification of showers detected on 19 September and 4 October, 2010[5] We select the 10-minute sample of the pure background—EAS events measured during quiet weather. Having 2 samples, one containing the pure background and the other a signal contaminated by background, we can pose the problem of the signal ''purification,'' i.e. selecting the decision boundary in the measured parameter space and performing cuts of the experimental sample containing signal and background. The boundary in the space of measured characteristics (decision boundary) should be optimized in such a way as to keep as many as possible of the signal events and suppress as many as possible of the background events. Obviously, we cannot keep 100% of the signal and reject all background events, because of the overlapping signal and background distributions; therefore, we have to select a compromise. The typical particle density distribution of the EAS hitting Earth's surface is a bell-like two-dimensional distribution with a large fraction of the shower particles near the core of EAS. The TGE event that originated from multiple avalanches of electrons with maximal energy not exceeding 50 MeV [11] is expected to be uniform without any significant particle density peaks.

Almost all of the additional Maket triggers [Figs. 2(b) and 2(c)] have mean density not exceeding 7–8 particles/m$^2$, and we can restrict ourselves by the one-dimensional classification scheme, using only the mean density of an event. However, as we can see in Fig. 3, to the right from the decision line in the region of low density there is a population of events with rather large maximal density. We treat these events as background small EAS events with their shower axes fallen in the array.

[2]Mean count rates and variances of the ASEC particle detectors were very stable in 2009–2010 due to continuous maintenance and the absence of the solar modulation effects during an unusual long period of a quiet Sun.

[3]The coherent short bursts of the thunderstorm correlated particle fluxes were first detected during the event of 19 September, 2009 (see details in [11]).

[4]The background for the triggered events is extensive air showers routinely generated by primary protons or stripped nuclei entering the atmosphere. Comparing the mean background count rate with the intensity of the primary cosmic rays, we estimate the threshold energy of the primary proton flux detected by the Maket array to be 50–100 TeV.

[5]We form a joint sample of events (total 613) containing background—EAS—and ''signal''—TGE—events.

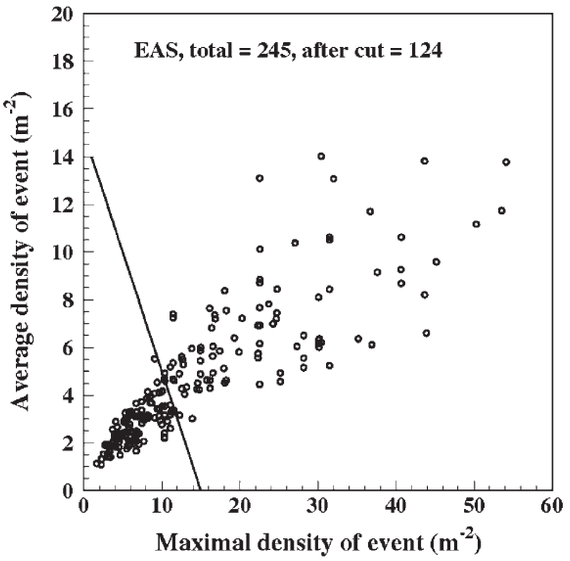


FIG. 3. Scatter plot of the registered at quiet weather Maket triggers; pure EAS events.

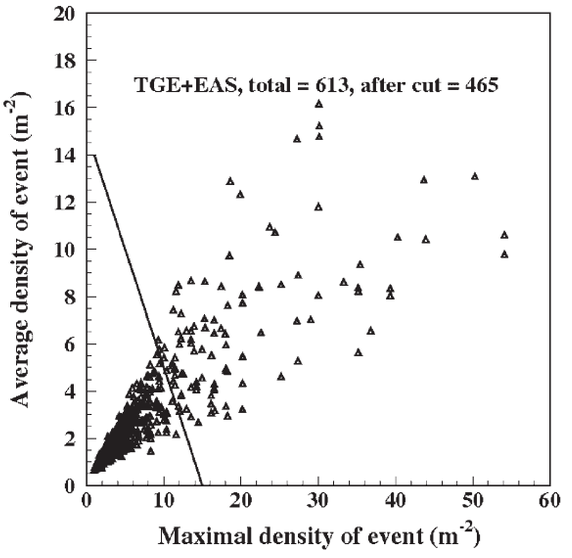


FIG. 4. Two-way classification of the showers detected on 19 September, 2009, and 4 October, 2010, during thunderstorms.

To additionally suppress such events we add the second discriminator—the maximal density within an event. Thus, the mean and maximal densities of Maket scintillators that detected the shower were used for classification. The selection procedure is visualized in Figs. 3 and 4. The showers with parameters in the region to the left from the linear decision boundary are classified as TGE events and the events to the right as EAS events.

Selected classification criteria suppress ~50% of the EAS events (121 from 245; see Fig. 3) but only losing ~25% of the joint EAS and TGE events (148 from 613; Fig. 4). Among the selected 465 signal events we expect about 121 background events; therefore, the expected purity of the selected TGE sample is rather high: ~75%. The 25% of contamination could not be significantly reduced due to large EAS with axes far from the Maket array. The long tails of EASs generate events with low mean and maximal densities and could not be distinguished from TGEs.

Further evidence of the difference of the two classes of events is apparent from Fig. 5. The density distribution of EAS events follows a power law as many other distributions generically connected with population of the galactic cosmic rays falling on the atmosphere. In contrast, the density distribution of the TGE events (obtained by subtraction of the pure EAS sample from the joint TGE + EAS sample) follows an exponential curve, as expected from an avalanche process. The average value of the mean density of EAS and TGE classes is ~6 and 2.5 particles/$m^2$, correspondingly. The density spectra of the TGE + EAS and pure EAS events are drastically different in the region of small densities (less than 7–8 particles/$m^2$) and identical for higher densities.

The comparison of the spatial extension of both classes is shown in Fig. 6. All 16 Maket array scintillators used for the detection of particle showers are located on the area of ~1000 $m^2$.

If in the off-line analysis we require more than 9 scintillators (hardware trigger condition) to be fired, the number of events diminishes with enlarging the number of scintillators participating in the software trigger. However, the speed of the decrease of events significantly differs for the EAS and TGE classes. In Fig. 6, we can see that the

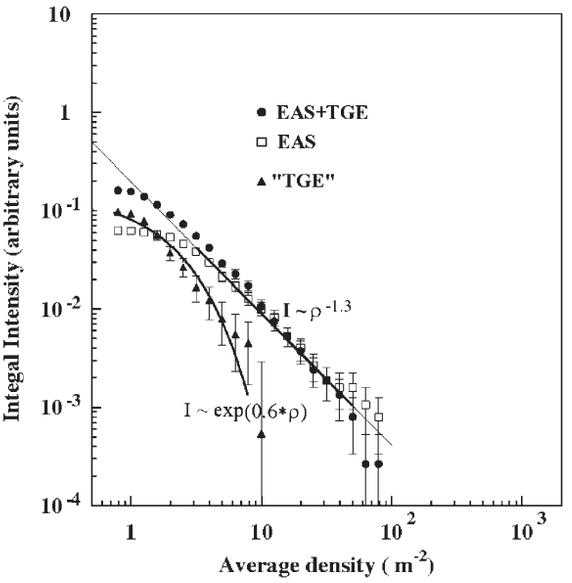


FIG. 5. Integral density distribution of the events from the joint TGE + EAS, statistically reconstructed TGE, and pure EAS classes.

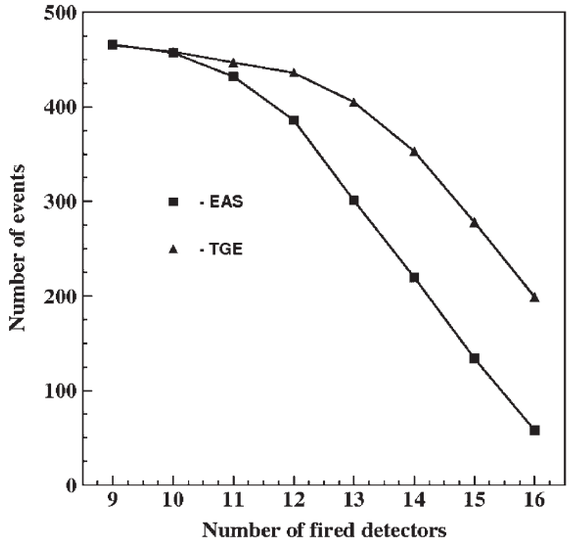


FIG. 6. Numbers of events detected with 9–16 scintillators of the Maket array for the two classes of events, both containing 465 events at hardware trigger conditions (9 scintillators fired).

number of EAS events is fast decreasing (from 465 at the trigger to 50 when all 16 scintillators are required). This can be explained by the small sizes of the EASs at rather low Maket array threshold energies ~50 TeV. The number of events of the TGE class is decreasing much slower. There are two possible reasons for the detected decrease in the number of events: the smaller than array dimension size of the event and the non-100% efficiency of the scintillators. We model the second possibility with 90% scintillator efficiency to register a charged particle.[6] Obtained trigger frequencies rather well coincide with the binomial law assuming a probability of success of 0.9. Therefore, we can state that there is no experimental evidence that the spatial elongation of the TGE events is less than 1000 $m^2$ (limit caused by the finite size of the Maket detector). Most of the EAS events are more compact.

## IV. ESTIMATION OF THE MAXIMAL DURATION OF THE SHORT TGE EVENTS

The duration of the TGF events detected by gamma observatories on board low elevation satellites varies from several tens of microseconds to a few milliseconds, with a mean value of ~0.5 ms. At the present time we did not install megahertz flash amplitude-to-digital converters to measure the duration of the short TGE events directly; however, we establish the limits on the duration of the surface events by statistical analysis of the TGE event temporal distribution. The maximal duration of the surface particle bursts was estimated by exploiting the measured distribution of the TGE events in each of the seconds within a minute of the maximal flux (124 triggers at 22:47, 19 September, 2009). The data acquisition (DAQ) electronics and software operates as described below (see details in [16]):

(i) The Maket trigger system opens the window of ~1 $\mu$s after receiving the signal above the discriminator level from each of 16 channels.
(ii) If trigger conditions are fulfilled (8 selected +1 arbitrary scintillators are fired), 16 energy deposits are written in the temporary memory of the filled programmable gate arrays.
(iii) The duration of operations 1 and 2 is at most 50 $\mu$s, and it is the dead time of the Maket DAQ system.
(iv) The events (strings of 16 energy deposits) are collected during a second and then are transferred to permanent memory in an on-line ADAS personal computer.[7] Each event has a time stamp reporting when it was written in the temporary mass storage.
(v) ADAS joins the events collected in 1 s and transforms them to a 1-minute time series, storing them along with other information for sending to an MSQL database, where the ASEC time series are permanently stored.
(vi) If the duration of the event will exceed 50 $\mu$s after finishing of the dead time, another event will be generated and stored.

In Fig. 7, we present the distribution of the TGE triggers for the 3 selected minutes according to how many triggers were detected in a second. If, say, there is continuous detection of particles (discharge between a thundercloud and the ground) during a second, we can detect ~20 000 triggers (because of the 50 $\mu$s dead time of the DAQ electronics). If the TGE events have a duration exceeding the dead time of the detector, then several events will be detected within the same second; i.e. the detected events will be highly correlated and a very large number of events will fall in the particular second. However, even for the minute when the largest count rate occurred, at most 6 triggers per second were registered. It gives us a hint that the burst events are not correlated; however, we have to prove it formally by using the Neyman-Pearson technique of statistical hypothesis testing. As is usual in statistical hypothesis testing, we have to formulate the null hypothesis ($H_0$). It must be numerically exact—if it is valid, the distribution of the experiment outcomes (the distribution of the number of bursts in a second) should have a very definite shape close (within statistical errors) to the well known analytic distribution, thus allowing us to calculate the measure of the difference. If the calculated difference is

[6]Because of the aging of the scintillators (they have been in operation for ~20 years), the assumed efficiency is a realistic estimate.

[7]The Advanced Data Analysis System (ADAS) is a special software developed for on-line analysis and storing data from ASEC particle detectors; see details in [15].

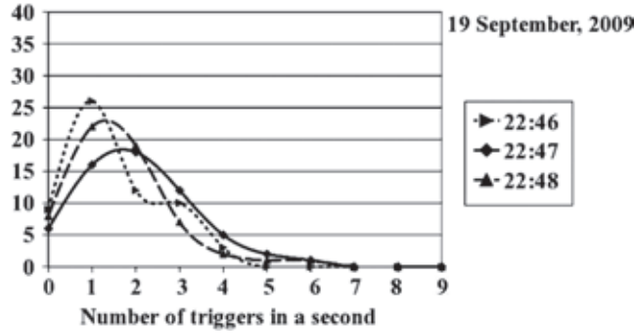


FIG. 7. Distribution of the Maket hardware triggers by the number of triggers per second at 3 minutes of 19 September, 2009.

greater than the preselected threshold value, we can state that the experimental results do not support $H_0$ and reject it ($H_0$ is rejected only for a first kind error—reject $H_0$ when it is true—is very unlikely). If the experimental distribution is close to the theoretical one, we accept $H_0$ stating that there is no evidence to reject it. Therefore, we formulate $H_0$ in the following way:

$H_0$ = there is no correlation between particle bursts measured by the Maket surface array.

The alternative hypothesis consists in the statement that particle bursts are correlated.

As we will see below, if $H_0$ is valid, we can numerically calculate the probabilities of having 1, 2, 3... bursts in a second using binomial, multinomial, and $\chi^2$ analytical distributions. It is why we did not invert our procedure of the hypothesis testing and do not accept as $H_0$ the alternative hypothesis (bursts correlated). It will be very difficult (if even possible) to find the analytical distributions for arbitrary correlation of the bursts (TGEs).

The statistical hypothesis we have testing, the $H_0$ hypothesis (no correlation), consisted in several substatements. The distribution of the number of TGEs in a second can be described by the binomial distribution:

$P(X = r) = C^n{}_r p^r (1\text{-}p)^{n\text{-}r}$, where the combinatorial coefficient is $C^n{}_r = (n!/(n\text{-}r)!)/r!$.

The binomial model is valid when there are exactly two mutually exclusive outcomes of a trial. These outcomes are appropriately labeled success (TGE occurs in the selected second) and failure (TGE occurs during one of the other 59 seconds). The binomial distribution is used to obtain the probability of observing **r** successes in **n** trials, with the probability of success on a single trial denoted by **p** (in our case, $\mathbf{p} = 1/60$). The most important assumption of the binomial statistical model is the independent and identically distributed assumption: Trials (outcomes) of the experiment (TGEs) are independent, identically distributed variables, i.e. the assumption of no correlation between TGEs. To check this assumption we first will calculate binomial probabilities with a Web calculator [17] for the minute 22:47, 19 September, 2010; see column 3 in Table I.

For each minute we have a string of numbers. At the minute 22:47 of 19 September, 2009, we have, from 60 seconds, 6 seconds with no TGEs, 16 seconds with 1 TGF, 18 seconds with 2 TGFs, etc. To deal with the statistical experiment producing not only 2 outcomes as the binomial model but several outcomes, we have to adopt another statistical model, i.e. a multinomial model that has the following properties:

(i) The model consists of $n$ repeated trials.
(ii) Each trial has a discrete number of possible outcomes (0 TGEs in a second, 1 TGE in a second, 2 TGEs in a second, ..., 124 TGE in a second).
(iii) On any given trial, the probability that a particular outcome will occur is constant.
(iv) The trials are independent; that is, the outcome of any of the trials does not affect the outcome of other trials.

To check the validity of the multinomial model, we have to compare the numbers of the experimentally obtained frequencies (column 3 of Table I) and expected frequencies calculated by binomial low (column 4 of Table I).

TABLE I. Comparison of the multinomial ($H_0$), simulated, and measured frequencies.

| $N$ of TGEs | Binomial probability $-\pi_i$ | Experimental frequency at 22:47 ($x_i$) | Theoretical frequency $E_i = \pi_i * 60$ | $(x_i - E_i)^2/E_i$ | Simulated averaged frequency if TGE $< 50$ $\mu$s |
|---|---|---|---|---|---|
| 0 | 0.124 | 6 | 7 | 1/7 | 7.5 |
| 1 | 0.261 | 16 | 16 | 0 | 15.8 |
| 2 | 0.273 | 18 | 17 | 1/17 | 16.2 |
| 3 | 0.188 | 12 | 11 | 1/11 | 11 |
| 4 | 0.096 | 5 | 6 | 1/6 | 5.6 |
| 5 | 0.039 | 2 | 2 | 0 | 2.3 |
| 6 | 0.013 | 1 | 1 | 0 | 1.4 |
| >6 | 0.004 | 0 | 0 | 0 | 0.3 |
| Sum | 1.0 | 60 | 60 | 0.46 | 59.7 |

The validity of the null hypothesis was tested by using Pearson's chi-square test

$$\chi^2 = \sum_{i=1}^{k} \frac{(x_i - E_i)^2}{E_i},$$

where $E_i = N\pi_i$, $N = 60$, is the expected theoretical frequency. The normalized sum of deviations converges to a chi-square distribution with $k - 1$ degrees of freedom when the null hypothesis is true. From Table I we estimate the Pearson's $\chi^2$ test value of 0.46 for 6 degrees of freedom. The corresponding chance probability of $H_0$ being false we can get from another Web calculator [18]. The chance probability of $H_0$ being false is 0.2% only; therefore, we do not have enough evidence to reject $H_0$, and we have to accept it; i.e. the particle bursts detected at 22:47, 19 September, 2010, are independent and identically distributed. From the physical analysis point of view it means that the TGE duration does not exceed 50 $\mu$s. We perform also a Monte Carlo study of the problem, generating trials of the short burst with durations less than 50 $\mu$s, greater than 50 $\mu$s, and less than 100 $\mu$s. If the duration of TGE events is greater than 50 $\mu$s and less than 100 $\mu$s, we can detect only even numbers of TGEs per second: 2, 4, 6, … And, of course, the $\chi^2$ test will rocket to very high values, thus signaling that events are correlated. Obtained frequencies (averaged by 100 independent trials) are posted in the last column of Table I. Frequencies are in very good agreement with analytical calculations proving the independence of the TGE events with the confidence level 99%. Frequencies of the greater than 50 $\mu$s and less than 100 $\mu$s trials do not agree with both experimental and analytically obtained frequencies.

## V. THE ELECTRICAL FIELD STRUCTURE DURING TGE EVENT ON 4 OCTOBER

The static electric field between the thunderclouds and the ground was measured with the Boltek EFM-100 electrical mill installed on Aragats research station at altitude 3250 m just on the Maket building where particle detectors are located. The electrical field measurements were taken 2 times in a second. In Fig. 8, we see the disturbance of the electrical field at Aragats station during the thunderstorm on 4 October, 18:00–18:40 UT. After a period of ~10 minutes of a large positive electrical field (~30 kV/m), the electrical field changed polarity and during another ~10 minutes reached values of about −30 kV/m (right vertical axes). The large negative field was accompanied by a huge flux of particles measured by the ASEC detectors [the 250% enhancement of the Maket triggers, left vertical axes; see, for details, Fig. 2(c)]. The zoomed pattern of the 2 minutes of the maximal flux, namely, 18:22—18: 24, is shown in Fig. 9 along with gamma-ray time series measured by the 01 combination of the ASNT (10 second time series) and lightning occurrence times.

In Fig. 9, we can see the correlations of electrical field, particle flux, and lightning occurrence in much more detail compared with the 1 minute time series. The decreasing of the electrical field is strongly correlated with the rising gamma-ray flux. Flux is reaching the maximal values near the maximum of the absolute value of the negative electrical field.

By the rectangles the intracloud-lightning occurrence time is denoted, measured by the Boltec storm tracker located on the Maket building. All lightnings within a radii of 5 km around the Maket building are depicted in Fig. 9.

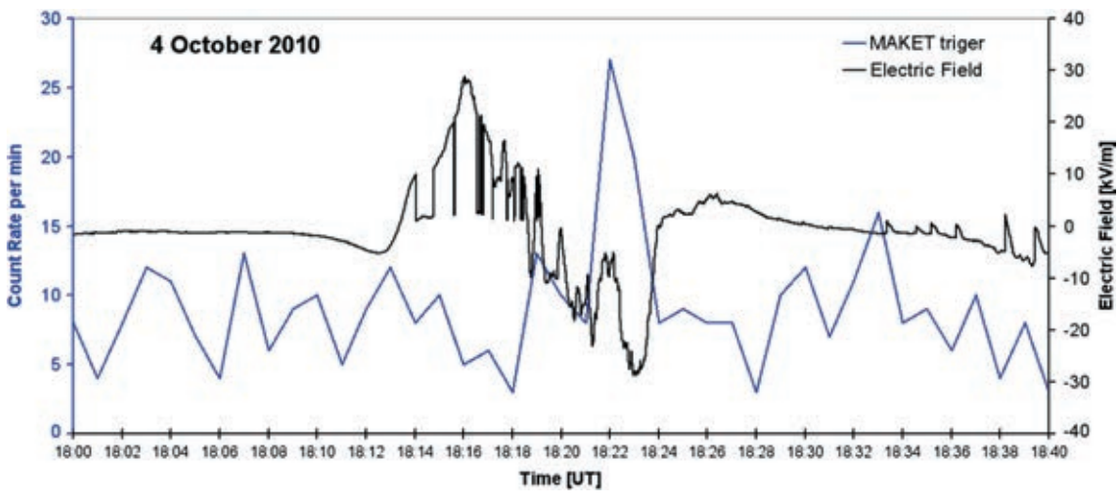


FIG. 8 (color online). The temporal structure of the electrical field disturbances and the time series of the Maket triggers detected on 4 October, 2010.

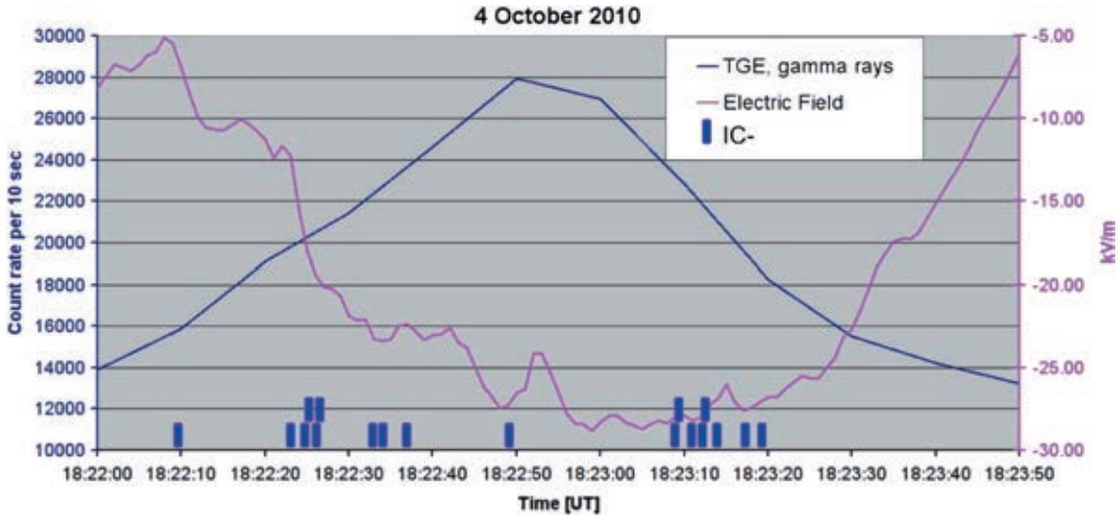


FIG. 9 (color online). Disturbed electric field and count rate of the gamma rays (energy >10 MeV) measured by the 01 combination of the Aragats Solar Neutron Telescope: 4 October, 2010, 18:22–18:24.

Remarkably, only 18 negative intracloud lightnings were detected during the maximal flux of the TGE, no intracloud positive, and no cloud-ground lightning was detected.

## VI. DISCUSSION

We report the new observed phenomenon of the short TGEs (duration less than 50 $\mu$s) detected by the surface particle detectors at mountain altitudes. Short particle bursts occur during a large negative electrical field measured between cloud and the ground accompanied by numerous negative intracloud lightnings. In two episodes on September 19, 2009, and October 4, 2010, lasting totally 10 minutes, $(8 + 2) \sim 340$ short TGE events were detected. Observed short TGEs, in contrast to prolonged ones (described in detail in our previous paper, Ref. [11]) can be compared with TGFs routinely detected by orbiting gamma-ray observatories [3,5].

(i) The origin of the TGFs was estimated to be in (or just above) thunderclouds in the upper troposphere and lower stratosphere, at altitudes 15–21 km [19,20].

(ii) The mean duration of a TGF is $\sim$500 $\mu$s and mean fluence $\sim$1 particle/cm$^2$ [Ramaty High Energy Solar Spectroscopic Imager (RHESSI) observations].

(iii) Maximal energy—up to 50 MeV by Fermi [2] and AGILE observations [4] and even 100 MeV [21].

(iv) Cummer *et al.* [22] based on a subsample of RHESSI TGFs establish TGF correlation with lightning discharges: 50% of analyzed 26 TGFs are found to occur within $-3/+1$ ms of the positive intracloud ( + IC) lightning discharges inside a $\sim$300 km radii circle around the RHESSI subspacecraft position.

(v) Fermi gamma burst monitor data [23] confirm this finding, establishing an association of the 15 from a total of 50 TGFs with individual discharges. Surprisingly, both associations did not establish the time order of lightning-TGF occurrence.[8]

The observed rich phenomenology of the TGFs shortly presented above poses rather stringent constraints on the physical process responsible for TGF generation. According to analysis in [8,20] the huge upward ($\sim 10^{17}$) flux of the gamma rays is responsible for the observed TGFs. A sufficient amount of the seed electrons necessary for the production of $10^{17}$ gamma rays by the RREA developing (see Fig. 10) is provided by the streamers and stepped lightning leaders [8–10] in the intracloud positive lightning ( + IC [20]; see Fig. 10). The proposed mechanism also naturally supported the harmony of the time scales of the electron emission and TGF duration (see Table 2 in [8]).

Downward development of the RREA requires a positive electrical field in the cloud and, therefore, a negative field between clouds and the ground (see Fig. 10). The posed limit on the event maximal duration of 50 $\mu$s also puts severe restrictions on the physical mechanism responsible for the short TGEs. And again stepped leader propagation fits best to submit seed particles in the time scale adequate to the short TGEs. Consequently, the negative intracloud lightning ( − IC) could provide seed particles for the TGEs detected by the Maket detector. As we can see in Fig. 9, the measured electrical field and observed negative intracloud lightnings support the model depicted in Fig. 10.

Thus, the generation mechanisms of the space TGFs and short TGEs are close to each other and symmetric: *RREA*

[8]The estimated mean delay of the RHESSI TGFs relative to lightning is −1.24 ms [22].

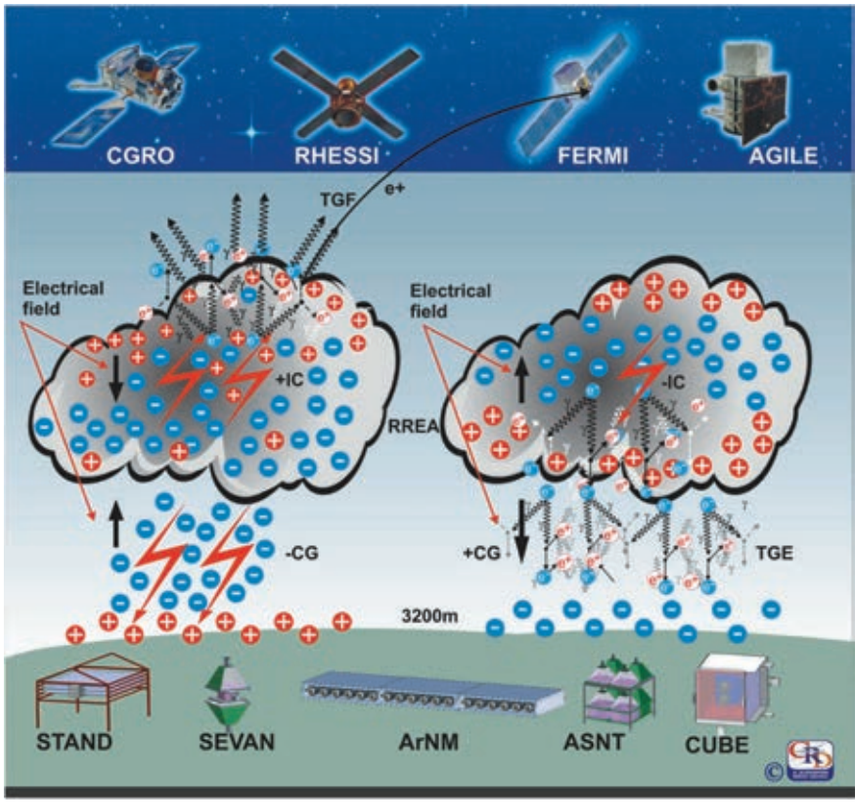


FIG. 10 (color online). Symmetry of the TGFs and TGEs.

*uses as the seeds the electrons from the current pulses along the step leaders* ( $\pm$ IC) *and developing in consequent negative and positive electrical fields.*

Seed electrons for the long TGEs are provided by the ambient population of MeV electrons from the secondary cosmic rays. As we show in [11] the population of the secondary electrons from the particle showers initiated by the primary hadron entering the terrestrial atmosphere is sufficient to generate via the RREA process enough particles to explain the huge surface enhancement on 19 September, 2010.

However, there are significant differences in TGE and TGF events.

(i) Short TGEs are very rare events (detected at Aragats about once a year); the Maket array observes the sky just above the detector ($\sim 10^6$ m$^2$). Fermi and AGILE are observing huge areas reaching $\sim 10^{12}$ m$^2$; therefore, the number of detected TGFs is much larger, reaching hundreds per year.

(ii) Nonetheless, because of the closeness of the particle beam, the number of detected TGEs in 2 series of detection is rather large: $\sim$325. TGE develops in a rather dense atmosphere; only the close location of the thundercloud to the ground and rather large elongation of the strong electrical field in the thundercloud can provide unique possibilities of detection of TGE electrons and gamma rays (see details in [11]).

(iii) The duration of the TGE is more than an order of magnitude shorter than the ones of TGF. Gamma rays arriving at satellite altitude are covering at least 3 orders of magnitude longer path length compared to TGEs and arrive spread over a pulse of $\sim$500 $\mu$s. TGEs come from thunderclouds just above our heads and cover less than 500 m; therefore, they come in pulses with a duration less than 50 $\mu$s.

## VII. CONCLUSION

We discover new energetic atmospheric phenomena, namely, short TGEs tightly connected with the ones detected by orbiting gamma-ray observatories, i.e. TGFs. The basis of high-energy emissions from the thunderstorm atmospheres is believed to be large electrostatic fields within thunderclouds, the mechanism—RREA); seed particles—ambient population of MeV electrons from EAS (for long TGEs) and electrons from current pulses of step leaders of intracloud lightning.

## ACKNOWLEDGMENTS

This work was partly supported by the Armenian government grants and by ISTC Grant No. A1554.

The authors are grateful to participants of the conference TEPA-2010 and to members of the seminar of the cosmic-ray division of Alikhanyan national lab for useful discussion.

## APPENDIX: DISCUSSION ON THE POSSIBILITY OF INTERFERENCES AND ELECTRONIC OR NATURAL INDUCED SIGNALS TO GENERATE PEAKS IN TIME SERIES OF THE ASEC PARTICLE DETECTORS

There are numerous sources of natural and electronics emissions that can mimic the peaks in the time series of particle detector count rates. To answer if the peaks apparent in the time series of the ASEC particle detectors during thunderstorms can be fake, we performed an in-depth analysis of the enhancements of the ASEC detectors and collected evidence demonstrating the existence of the indisputable additional particle fluxes responsible for the detected peaks.

400 m apart at Aragats are in operation same type detectors (AMMM—Aragats Multichannel Muon Monitor—and Maket) with fully independent cabling and DAQ electronics demonstrate similar time-coherent peaks (see Fig. 11).

The enhancements detected by the ASNT are concentrated only in the region of the small energy deposits; the large energy deposits remain unchanged (see Fig. 12).

The ASNT detector measures the incoming directions of the detected particles. The count rates of the near vertical and inclined particles are dramatically different. If we observe huge enhancement in the near vertical direction (expected arrival direction of the RREA particles), at the same time on the same detector using the same DAQ electronics and analysis software we measure a deficit in the inclined particle flux (maybe due to stopping positive muons; see Fig. 13).

The SEVAN particle detector measured 3 types of particle fluxes: low-energy charged particles, neutral particles, and high-energy particles (above 250 MeV, mostly muons). In Fig. 14, we can see a deficit of high-energy muons ($E_\mu > 250$ MeV) and a huge peak in the time series of neutral particles (there is also a peak in the time series of the low-energy charged particles). All 3 types of particle fluxes are detected by the SEVAN detector with one and the same cabling and DAQ electronics.

Nonetheless, we detect some induced signals in a few from hundreds of the ASEC detectors due to radio emission of the lightning. Lightning is a powerful broadband radio signals emitter. The pulse power of the radio signals can reach 100 GW. And if the detector is poorly grounded, or some of the cables have bad isolation, the radio signals induced peaks in these channels. We systematically monitor and repair failure equipment. However, lightning-induced signals in the poorly grounded counters have a very specific shape and follow the pattern of the lightning activity, now also monitored by the ASEC facilities. Therefore, it is not very difficult to outline fake peaks and repair the malfunctioning channels.

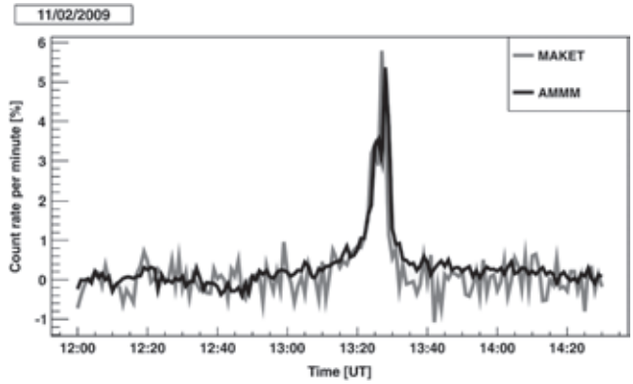


FIG. 11. Time series of the AMMM outdoor 5 cm scintillator and the Maket outdoor 5 cm scintillators located at a distance of 400 m from AMMM; TGE on 2 November, 2009.

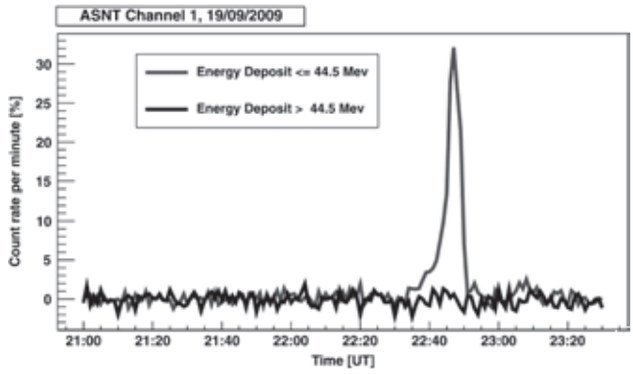


FIG. 12. Time series of the ASNT corresponding to different energy releases during TGE on 19 September, 2009.

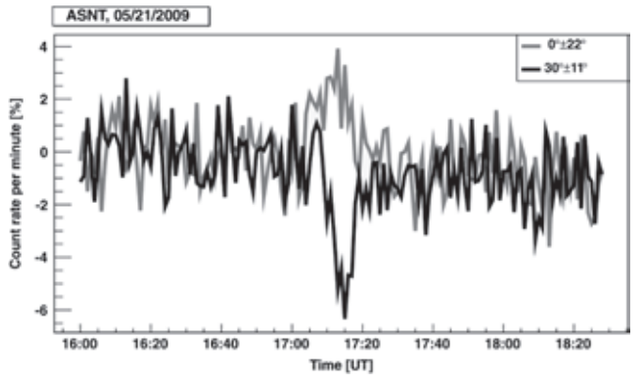


FIG. 13. Time series of ASNT corresponding to different directions of the incoming particle flux; TGE on 21 May, 2009.

[1] J. R. Dwyer, B. W. Grefenstette, and D. M. Smith, Geophys. Res. Lett. **32**, L22804 (2005).
[2] M. S. Brigs *et al.*, J. Geophys. Res. **115**, A07323 (2010).
[3] G. J. Fishman *et al.*, Science **264**, 1313 (1994).
[4] M. Marisaldi *et al.*, J. Geophys. Res. **115**, A00E13 (2010).
[5] D. M. Smith *et al.*, Science **307**, 1085 (2005).
[6] A. V. Gurevich, G. M. Milikh, and R. A. Roussel-Dupre, Phys. Lett. A **165**, 463 (1992); A. V. Gurevich *et al.*, Phys. Lett. A **373**, 3550 (2009).
[7] C. T. R. Wilson, Proc. Cambridge Philos. Soc. **22**, 534 (1925).
[8] B. E. Carlson, N. G. Lehtinen, and U. S. Inan, J. Geophys. Res. **114**, A00E08 (2009).
[9] G. D. Moss, V. P. Pasko, N. Liu, and G. Veronis, J. Geophys. Res. **111**, A02307 (2006).
[10] Z. Saleh, J. Dwyer, J. Howard, M. Uman, M. Bakhtiari, D. Concha, M. Stapleton, D. Hill, C. Biagi, and H. Rassoul, J. Geophys. Res. **114**, D17210 (2009).
[11] A. Chilingarian *et al.*, Phys. Rev. D **82**, 043009 (2010).
[12] N. S. Khaerdinov, A. S. Lidvasky, and V. B. Petkov, Atmos. Res. **76**, 346 (2005).
[13] A. Chilingarian *et al.*, J. Phys. G **29**, 939 (2003).
[14] A. Chilingarian *et al.*, Nucl. Instrum. Methods Phys. Res., Sect. A **543**, 483 (2005).
[15] A. Chilingarian *et al.*, Astropart. Phys. **28**, 58 (2007).
[16] K. Arakelyan *et al.*, in *Proceedings of the Third International Conference Solar Extreme Events, National & Kapodistrian University of Athens, Greece* (National & Kapodistrian University of Athens, Athens, 2009), pp. 363–367.
[17] http://stattrek.com/Tables/Binomial.aspx.
[18] http://www.physics.csbsju.edu/stats/chi-square_form.html.
[19] J. R. Dwyer, B. W. Grefenstette, and D. M. Smith, Geophys. Res. Lett. **35**, L02815 (2008).
[20] E. Williams *et al.*, J. Geophys. Res. **111**, D16209 (2006).
[21] M. Tavani *et al.*, Phys. Rev. Lett. **106**, 018501 (2011).
[22] S. A. Cummer, Y. Zhai, W. Hu, D. M. Smith, L. I. Lopez, and M. A. Stanley, Geophys. Res. Lett. **32**, L08811 (2005).
[23] V. Connaughton *et al.*, J. Geophys. Res. **115**, A12307 (2010).

Atmospheric Research 114–115 (2012) 1–16

Contents lists available at SciVerse ScienceDirect

Atmospheric Research

journal homepage: www.elsevier.com/locate/atmos

# Recovering of the energy spectra of electrons and gamma rays coming from the thunderclouds

Ashot Chilingarian, Bagrat Mailyan *, Levon Vanyan

*A. Alikhanyan National Laboratory, Yerevan Physics Institute, Alikhanyan Brothers 2, Yerevan, Armenia*

ARTICLE INFO

*Article history:*
Received 9 October 2011
Received in revised form 25 April 2012
Accepted 11 May 2012

*Keywords:*
Thunderclouds
Atmospheric electricity
Lightning

ABSTRACT

Strong electric fields inside thunderclouds give rise to enhanced fluxes of high-energy electrons and, consequently, gamma rays and neutrons. During thunderstorms at Mount Aragats, hundreds of Thunderstorm Ground Enhancements (TGEs) comprising millions of energetic electrons and gamma rays, as well as neutrons, were detected at Aragats Space Environmental Center (ASEC) on 3200 m altitude. Observed large TGE events allow for the first time to measure the energy spectra of electrons and gamma rays well above the cosmic ray background. The energy spectra of the electrons have an exponential shape and extend up to 30–40 MeV. Recovered energy spectra of the gamma rays are also exponential in energy range 5–10 MeV, then turns to power law and extends up to 100 MeV.



## 1. Introduction: Thunderstorm ground enhancements (TGEs)

The attempts to discover high-energy phenomena in the atmosphere, so called, Thunderstorm Ground Enhancement (TGE), in spite of a long history since prediction of C.R.T. Wilson in 1924 (Wilson, 1925), were discrepant and rare. Early measurements (Schonland, 1930; Schonland and Viljoen, 1933) reported the existence of electron flux simultaneously, or earlier, than lightning located 30 km apart. Atop Mount Lemmon (altitude 2800 m) at the lightning research facility of the University of Arizona, the simultaneous detection of cosmic ray flux (by the 10-cm diameter and 10-cm length plastic scintillator) and electric field (by an electric field mill) demonstrates ~10% enhancement of the 1-minute count (Shaw, 1967). The average excess duration was ~10 min; the threshold energy of the particle detector was ~100 keV. The Italian EAS-TOP surface array (Aglietta et al., 1989) measures significant excesses in the air shower count rate lasting 10–20 min. The enhancements with maximum amplitude of 10%–15% were attributed mostly to the highest energy Extensive Air Showers (EAS; large shower sizes, $>10^6$ electrons), and to zenith angles of incidence smaller than 20°; "thickness" (time interval of the EAS particles arrival) of shower was slightly larger than in normal conditions (Vernetto et al., 2001).

A radiation monitoring post in a nuclear power plant in Japan reports on a comprehensive observation of a gamma ray burst emission lasting less than 1 min—correlated with snow and lightning activity. Enhancements were detected only during wintertime, when thunderclouds are as low as several hundred meters (Torii et al., 2002). The same group observed a summer thunderstorm at the top of Mount Fuji (3776 m high). The flux of high-energy gamma rays had continuous energy spectrum up to 10 MeV, prolonged up to 20 min. The authors of Torii et al. (2009) claim that the bremsstrahlung photons generated by the energetic electrons were produced continuously due to an intense electric field in the thundercloud rather than having originated in the process of lightning discharge.

A Japanese group on another Japanese power plant also detected short (less than 1 min) gamma ray bursts during winter thunderstorms (Tsuchiya et al., 2007). The same authors reported a simultaneous detection of gamma rays and electrons at a mountain observatory Norikura located 2770 m above sea level (Tsuchiya et al., 2009). Two emissions, lasting 90 s, were associated with thunderclouds. At the same research station at Norikura in the Japanese Alps a large multilayered particle

* Corresponding author.
*E-mail address:* mbagrat@gmail.com (B. Mailyan).

0169-8095/$ – see front matter © 2012 Elsevier B.V. All rights reserved.
doi:10.1016/j.atmosres.2012.05.008

detector operates, primarily intended to register solar neutron events. In August 2000 on account of thunderstorms, particle flux enhancement was detected in 3 layers of a 64 $m^2$ area detecting system (Muraki et al., 2004).

In experiments at the Baksan Neutrino Observatory of the Institute for Nuclear Research, the time series of hard and soft components of secondary cosmic rays are continuously measured along with measurements of the electric field and monitoring of thunderstorms. Intensity changes of the soft cosmic rays (below 30 MeV) and hard component (>100 MeV) were studied (Lidvansky and Khaerdinov, 2009). It was shown that the critical field and particle energy for this process are ~300 kV/m and ~10 MeV respectively (Khaerdinov et al., 2005).

A network of the NaI detectors along with EAS triggering system is located at Tien-Shan Cosmic Ray station of the Lebedev Physics Institute, at altitude of 3340 m. The goal of the research is to detect runaway breakdown initiated by EAS with energy above 1000 TeV—so-called RB-EAS discharge. Based on short gamma flashes (less that 200 μs) detected by the network of gamma ray detectors, the authors of Gurevich et al. (2009) claim that RB-EAS discharge is a rather rare event — occurring in only ~1% of all EAS registered during thunderstorms, requiring coincidence of several conditions. The most important of them being that the strong electric field should be located not higher than 400–500 m above the detector.

Recently Japanese groups perform new measurements of gamma ray emission and detect the source of the radiation in thundercloud moving across locations of several nuclear power plants (Torii et al., 2011; Tsuchiya et al., 2011).

Facilities of the Aragats Space Environment Center (ASEC) (Chilingarian et al., 2003, 2005) observe charged and neutral fluxes of secondary cosmic rays by the variety of particle detectors located in Yerevan and on slopes of Mount Aragats at altitudes 1000, 2000 and 3200 m. ASEC detectors measure particle fluxes with different energy thresholds as well as EAS initiated by primary proton or stripped nuclei with energies greater than 50–100 TeV (Chilingarian et al., 2010). Abrupt enhancements of particle detector count rates correlated with thunderstorm activity, so called Thunderstorm Ground Enhancements (TGEs) detected during 2008–2011 bring vast amounts (243 TGE events) of small and very few large TGEs (only 6 TGE events with amplitude exceeding 20%) allowing the detailed analyses and taxonomy of the new high-energy phenomena in the atmosphere.[1] The flux enhancement is presented in percent relative to rather stable background of the ambient population of secondary cosmic rays. As we can see in the left corner of the histogram (Fig. 1), majority of TGE events have amplitude less than 10%. These small TGEs and analogical TGEs reported by other groups can be explained by the modification of the energy spectra of charged particles in the electric field of thunderclouds. Due to asymmetry of positive-to-negative flux of secondary cosmic rays in the terrestrial atmosphere, peaks and dips can arise in time series of count rates of surface particle detectors. These effects have been theoretically analyzed in Dorman and Dorman (2005) and detected on Mount Norikura (Muraki et al., 2004) and in Baksan, Russia (Alexeenko et al., 2002). Measurements at ASEC and simulations with GEANT4 package (Agnsotelli et al., 2003) confirm additional flux of gamma rays up to 1000% in the energy range of 2–20 MeV and up to 10% in the energy range up to 100 MeV. Simultaneously dips in the muon flux at energies above 200 MeV were obtained by GEANT4 simulations and detected by ASEC detectors.

Few very large enhancements seen in the right corner of Fig. 1 can be explained only by invoking the Runaway Breakdown (RB) process (Gurevich et al., 1992), also referred as Relativistic Runaway Electron avalanche (RREA, Dwyer, 2003, 2007; Carlson et al., 2008). Ambient population of secondary cosmic ray electrons in the electric fields with strength greater than the critical value[2] unleashes the electron-gamma ray avalanches and total number of particles on the exit from cloud can be multiplied by several orders of magnitude. Proceeding from the measurements of the charged and neutral fluxes as well as from the energy deposit of particles in thick scintillators, we recover the energy spectra of TGE electrons and gamma rays for the 2 largest TGE events of September 19, 2009 and October 4, 2010. Installation of Aragats field meters (Boltek firm electric mill EFM100, http://www.boltek.com/efm100.html) and lightning detectors (LD250 powered by the software from Astrogenic systems, http://www.boltek.com/ld250.html) allows correlating the measured particle fluxes with near-surface electric field disturbances and with occurrences of lightning of different types.

In Fig. 1, we present the histogram of the 243 TGE amplitudes (relative enhancements above cosmic ray background) measured by the MAKET detector in 2008–2011; the dates of 4 largest TGE events are displayed as boxed text. Lightning occurrences, as well as sketch of the RREA process in upper and lower dipoles also are depicted. The indispensible condition of TGE initiation is the creation of the lower dipole accelerating electrons downward. The temporarily emerging lower positive charge region (LPCR, Qie et al., 2009) is smaller than the mid-level negative and upper positive layers of the main upper thundercloud dipole (Williams, 1989). Therefore TGE phenomena are local and its duration coincides with the duration of the LCPR, which is usually ~10 min.

The critical electric field strength for the conventional discharge in thunderclouds is very large (~10 times more than RREA critical field) and was never measured in thunderclouds. Therefore, electron-gamma ray avalanches could initiate lightning by creating the initial conductive channel (Gurevich et al., 1999; Dwyer, 2005). Lightning in turn can provide the RREA process with additional seed electrons from the current pulses along developing lightning leader channels (Carlson et al., 2009; Lu et al., 2010, 2011; Cummer et al., 2011).

For the Terrestrial Gamma-ray Flashes (TGFs, Fishman et al., 1994) the physical model is symmetric. The electrons are accelerated upward by the negative field between main negative layer in the middle of the cloud and main positive layer near the top of the cloud. The additional seed electrons are provided by the positive intracloud lightning occurrences usually accompanying the detection of TGFs by the orbiting

[1] Time series of changing particle fluxes registered from ASEC monitors, as well as magnetometer and electrical mill measurements are available from http://adei.crd.yerphi.am/adei/.

[2] The critical electric field $E_t = 1.534$; 1.625, and 1.742 kV/cm at 4500, 4000 and 3400 m respectively. $E_t$ dependence on altitude follows the air density dependence on altitude.

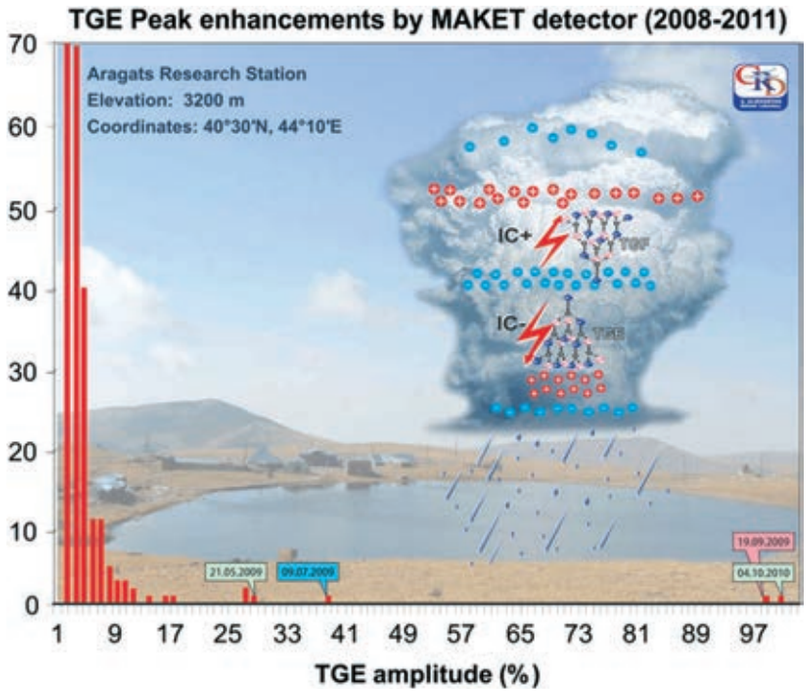


**Fig. 1.** The histogram of the amplitudes of TGE events detected by ASEC detectors in 2008–2010. The peak values of the cosmic ray flux increase above rather stable secondary cosmic ray background were measured by the outdoor plastic scintillators.

gamma ray observatories (Stanley et al., 2006; Cummer et al., 2005).

## 2. Dynamics of TGE events

Despite big varieties of measurements in the thundercloud electric field profiles the following basic structure of the electric field in thunderclouds is widely accepted: from the ground up to the cloud base there is usually a low magnitude field (both positive or negative); relatively small positively charged "pocket" (comprising only ~20% of negative charge higher) is responsible for the larger positive field prolonged up to negatively charged layer at 1–2 km above cloud base; and the negative field is extended about 1–4 km above the negative layer where the main positive charge is located (Stolzenburg et al., 1998). In presence of the positive electric field (pointed upward)[3] within the cloud, the electrons are accelerated downward and, dependent on the strength of the field, the flux of electrons and gamma rays reaching earth surface may exhibit significant amplification. As shown in Fig. 1, most of TGE events have rather small amplitudes; sometimes (less often than once per year) under yet fully unknown conditions the RREA process is unleashed and surface detectors measure huge TGEs surpassing rather stable cosmic ray background flux several times. The necessary condition for the RREA process is the creation of the considerably large positively charged layer in the bottom of the cloud. The manifestation of the existence of such layer is the absence of the cloud-to-ground lightning occurrences (leader attempts) due to the "blocking" of descending negative leader from reaching the ground. Simultaneously, significant enhancement of the intracloud negative lightning (Cui et al., 2009) occurrences took place due to the "converting" potential of the cloud-to-ground flash to an intracloud one (Nag and Rakov, 2009). On May 27, 2011, we detected a large TGE event by the 5 NaI crystals of size $30\times12.5\times12.5$ cm$^3$ newly installed at Aragats.

In Fig. 2, we can see the abrupt increase of the near-surface electric field at 13:07 UT caused by the negative cloud to ground (−CG) lightning flash that contained several strokes to the ground; thereafter the polarity of the electric field starts to reverse.[4] After 13:08 UT the TGE started (green curve) and −CG lightning occurrences stopped after 13:10 UT. At 13:12–13:15 UT we detect numerous intracloud negative discharges (−IC) in radii of 3 km, suggesting the screening of the ground by lower positive charge region (LPCR). The lightning stepped leader may provide the RREA process with additional seed electrons (by the "cold" runaway process, Moss et al., 2006) and at 13:12–13:15 UT the gamma ray intensity peaked at ~70% level above the background when the near surface electric field reaches its minimum.

The LPCR with main negative layer in the middle of the cloud forms lower dipole, responsible for the downward electron acceleration and also playing major role in initiation of cloud-to-ground (−CG) and intracloud (−IC) lightning

[3] We adopt the "atmospheric electricity" sign convention: the positive field (E kV/m) accelerates electrons downward in the direction of the Earth; the negative field (−E kV/m) vice-versa accelerates electrons upward in the direction of space.

[4] The rapid changes of the near-surface electric field usually are accompanied also with rapid change of the electric field within thundercloud (Standler and Winn, 1979).

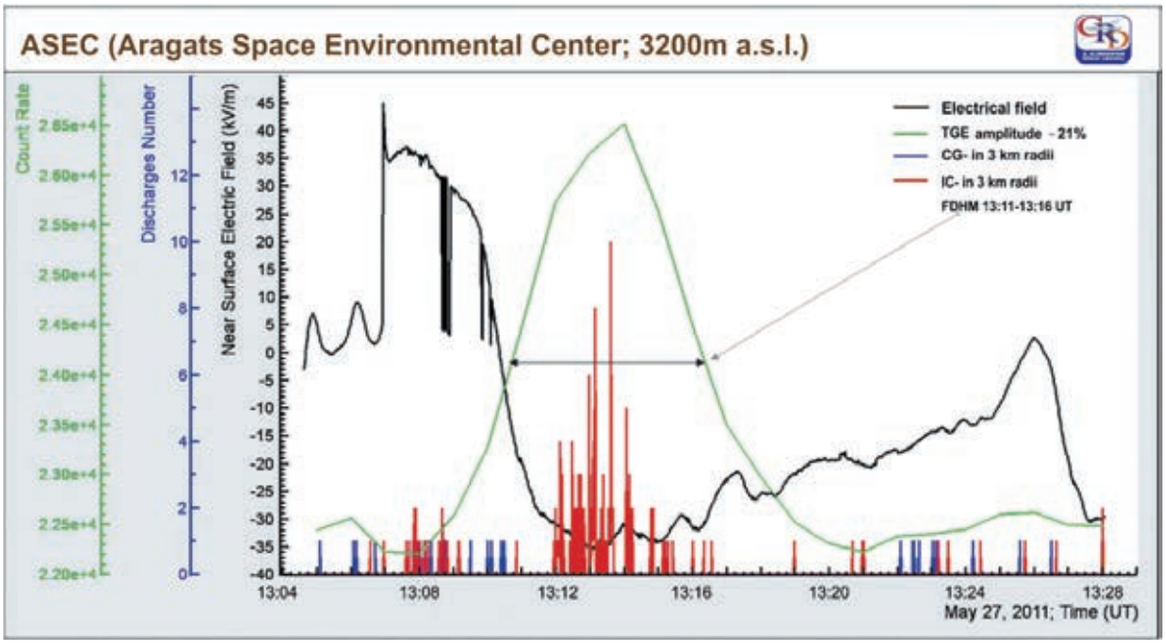


**Fig. 2.** The near-surface electric field (black curve) and frequency of lightning occurrences measured by the Bolter detector each second (2 left vertical axes). 143-CG — lightning occurrences were detected at 13:05–13:10 UT in the radii of 10 km (blue) and 139 IC — lightning occurrences — at 13:12–13:15 UT, radii of 3 km (red). Time series of the NaI crystals count rate (green curve, right vertical axes) demonstrate ~70% enhancement on May 27, 2011 at Aragats, 3200 m a.s.l.

occurrences. Many researchers outline the dominant role that LCPR plays in initiating/triggering an intracloud and cloud-to-ground lightning discharges (Pawar and Kamra, 2004; Nag and Rakov, 2009; Qie et al., 2009). We suggest that development of the LCPR also has a major role in TGE initiation. The locality of the RREA can be explained by the small sizes of the lower positive charge region and the transient character of LCPR can explain the duration of the TGE. Based on the detection of the winter thunderstorms by Japanese authors of Tsuchiya et al. (2011), they estimate the radii of the circle of intense RREA radiation to be 600 m. Another Japanese group (Torii et al., 2011) detects moving at the speed of 7 m/s energetic radiation source at the height of 300 m along with the negatively charged region within the thundercloud at the height of around 1 km. The radiation was emitted from a downward hemispherical surface with radii of 700 m. These findings demonstrate the locality of the RREA process and imply that the number of additional gamma rays can vary significantly depending on the "impact parameter" of the thundercloud relative to the detection site (see also Babich et al., 2010).

Therefore, it is not always the lower dipole that initiates TGE; an evidence of the emerging LPCR without initiated TGE can be seen in Fig. 3. On June 8, 2011, the fair weather field was changed by moderate positive field at 11:29 UT; then electric field reversal happened at ~11:33 UT and field reach negative value was ~−30 kV/m. At 11:55 UT, electric field abruptly changes the polarity and simultaneously the (−CG) lightning occurrences stopped and the intracloud negative lightning (−IC) occurrence started. From Figs. 2 and 3, using the model sketched in Fig. 1, we can conclude that the creation of LCPR stopped −CG lightning occurrences and initiated −IC lightning occurrences. At the same time, near surface electric field changes the polarity and turns from positive to negative. It is also worth mentioning that during this thunderstorm we do not observe any significant TGE in charged and neutral fluxes. The reason of it can be the much higher intensity of the −IC lightning occurrences, comparing with May 27 TGE, which does not allow the development of the mature RREA process. Another reason can be the distant location of the positive bottom layer; only if the positive layer is above the detectors the RREA process can accelerate electrons downward in the direction of the observer.

Continuous measurements of the lightning activity, near-surface electrical field and particle fluxes give a possibility for the first time to investigate the interrelations of these geophysical parameters and estimate the intracloud (IC-) to cloud-to- ground (CG)-lightning flash ratio (Z, Pinto et al., 2007; De Souza et al., 2009) during thunderstorms at Aragats. The Z ratio gives information about the electrical activity in thunderstorms and can be a clue about how the centers of the charge are disposed in the clouds. Our finding that Z is peaked at the minimal near-surface electrical field and the maximum of RREA particle flux confirms that Z is directly correlated with LPCR development.

In Fig. 4, we demonstrate another type of the TGE event: relatively small near-surface electric field and absence of any kind of lightning occurrences accompanied by the moderate count rate enhancement. At 8:35 UT, October 16, 2010 we observe abrupt decrease of the electric field, followed after 2 min by a ~7% enhancement of the count rate of the outdoor plastic scintillators. No lightning occurrence within 10 km was observed during ~10 min of negative field duration and TGE detection.

As the strength of the near-ground electric field was 2 times less than at 27 May and there were no lightning occurrences we can assume that the LCPR was not well developed, and

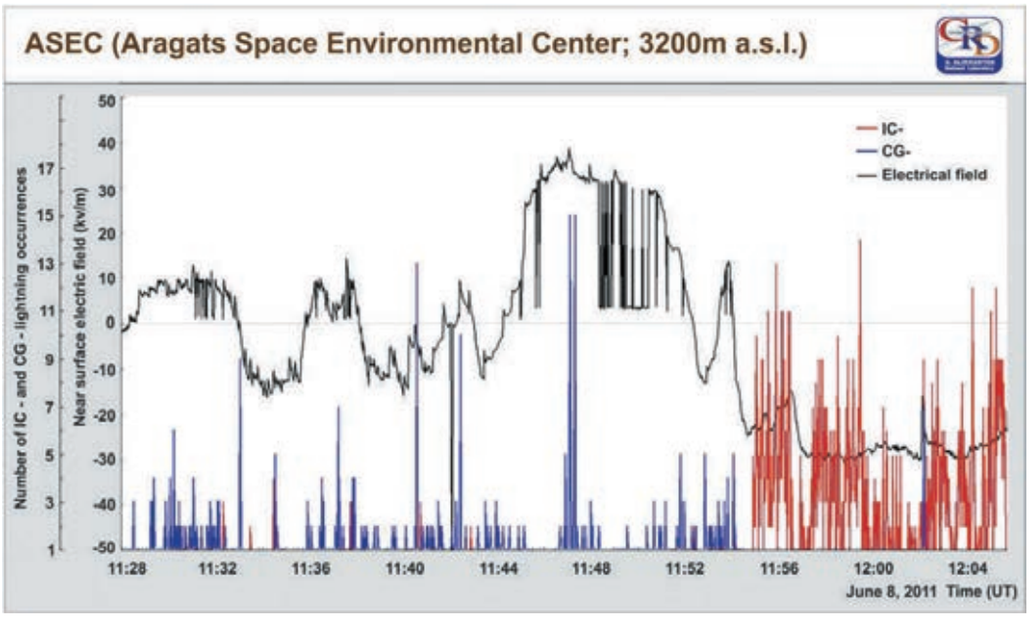


**Fig. 3.** The disturbances of near-ground electric field and frequency of cloud to ground (−CG) lightning occurrence at Aragats, 3200 m on June 8, 2011.

RREA process was not started.[5] The TGE initiation at 16 October can be connected with Modification Of the energy Spectra (MOS) of charged cosmic rays entering the region of the strong electric field within the thundercloud. Thus we introduce 2 types of the TGE origin: RRE avalanches responsible for very rare huge particle multiplication in the thunderclouds (up to 1000%) and MOS process — responsible for much often but small and modest (less than 10%) TGEs.

## 3. Acceleration and deceleration of the secondary charged cosmic rays in weak electric fields

From the consideration of the three thunderstorm events above, we can conclude that by no means electric fields in thunderclouds ultimately result in TGE, and far not all TGEs are due to RREA process. In the database of ASEC time series, we can find significant non-random variations of cosmic ray intensity in the absence of any lightning occurrences, indicating that the electric field strength in the cloud is below the RREA threshold. In Dorman and Dorman (2005), the theory of the modulation of the secondary cosmic ray by the various meteorological effects, including strong electric fields within thunderclouds is developed. Electrons and negative muons are accelerated downwards by a lower dipole before reaching particle detector. The positrons and positive muons as well as protons will be decelerated in the lower dipole. The positive charge of primary cosmic rays (mostly protons and stripped nuclei) introduces several asymmetries between particles and antiparticles born in atmospheric cascades. The intensity of the MeV electrons is larger than the intensity of positrons of the same energies in energy range of 1–50 MeV; the intensity of positive muons above 100 MeV is larger than the intensity of the negative muons, see Figs. 5 and 6 (obtained by EXPACS package, Sato et al., 2009).

We can see in Fig. 5 that the number of electrons with energies below 50 MeV at 5000 m altitude is significantly larger than the positrons. It means that positive electric field in the thundercloud will significantly alter the total intensity of low energy charged particles registered by scintillators at the Earth surface. The changes of intensity will manifest themselves as peaks and dips in the time series of count rates of particles registered by the scintillators located on the Earth surface. The energy spectrum of electrons will be shifted to the right (mean energy becoming larger) leading to the additional bremsstrahlung gamma rays; energy spectrum of positions shifted to the left is not sufficient to compensate these enhanced counts. The attenuation of the electrons in the atmosphere is much larger than the one of the gamma rays. Therefore, most TGE events are detected in the fluxes of gamma rays born by accelerated electrons.

Interestingly, positive fields have opposite influence on counts of muons at energies above 200 MeV. Among ASEC particle detectors there are scintillators with energy threshold greater than 200 MeV and the electron acceleration described above will not influence their count rate. Due to the abundance of the positive muons over the negative muons (1.2–1.3 times, at 100–500 MeV energies, Wentz et al., 2003, see Fig. 6) the braking of positive muons in the positive electric field cannot be compensated by the acceleration of the negative muons in the same field. The consequences of this asymmetry are indicated in Fig. 7. On October 4, 2010, we detected ~5% deficit in the flux of muons with energies greater than ~200 MeV, which concurred with a huge excess of low energy gamma rays and electrons.

[5] Of course, the combination of measurements on the microsecond scale of the lightning occurrences of different types and of the TGE in electron and gamma ray fluxes, as well as the electric field strength within the thundercloud is needed for the definite conclusion on the interrelations of these phenomena.

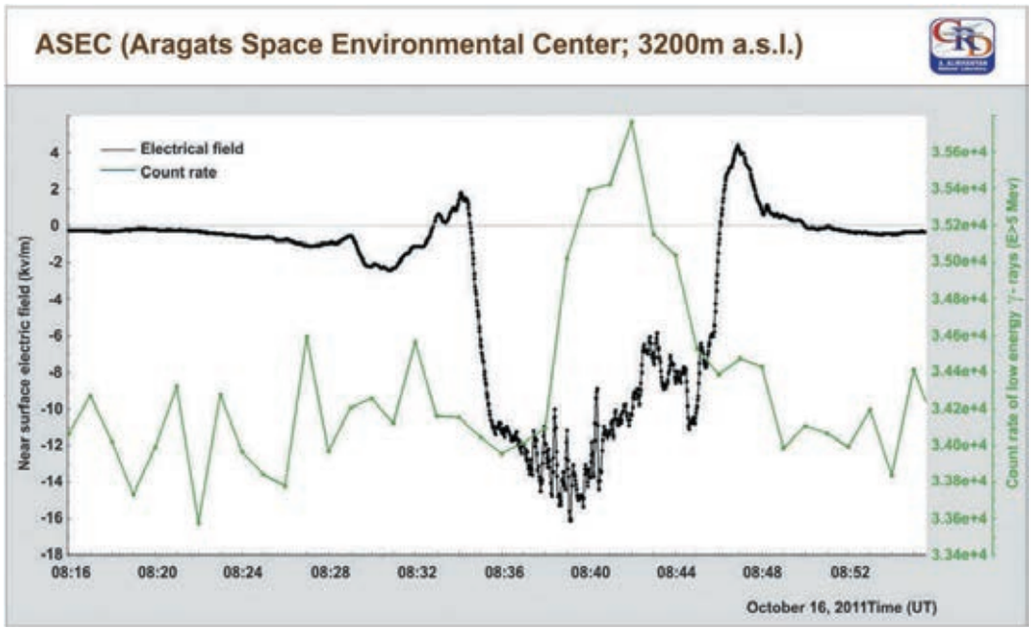


**Fig. 4.** The TGE event on 16 October 2010, the bold black line is the near-surface electric field strength; the gray line is the minute count rate of the 3 cm thick outdoor scintillator (energy threshold 4 MeV).

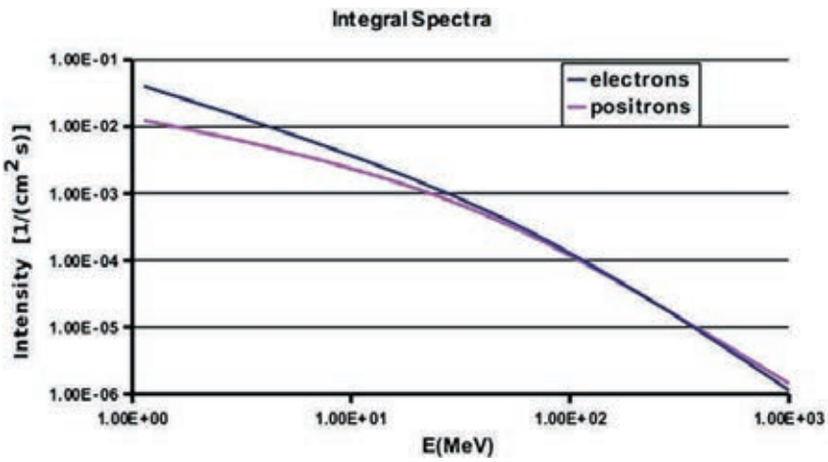


**Fig. 5.** The energy spectra of electrons and positrons at altitude of 5000 m a.s.l.

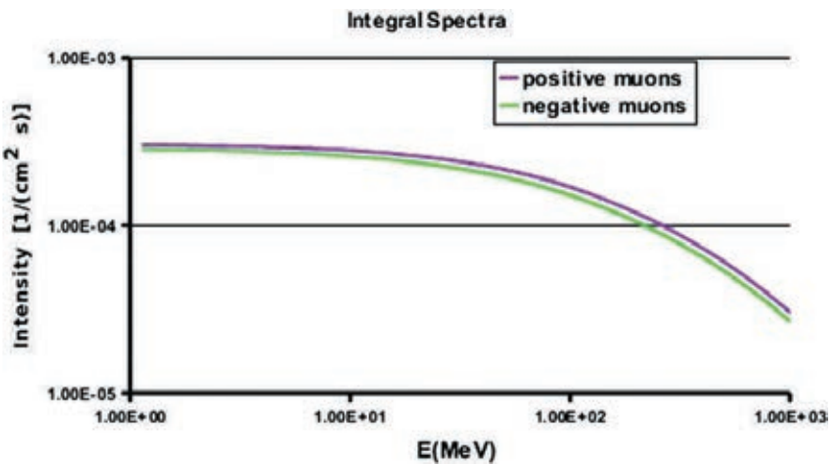


**Fig. 6.** Energy spectra of muonsat altitude 5000 m a.s.l.

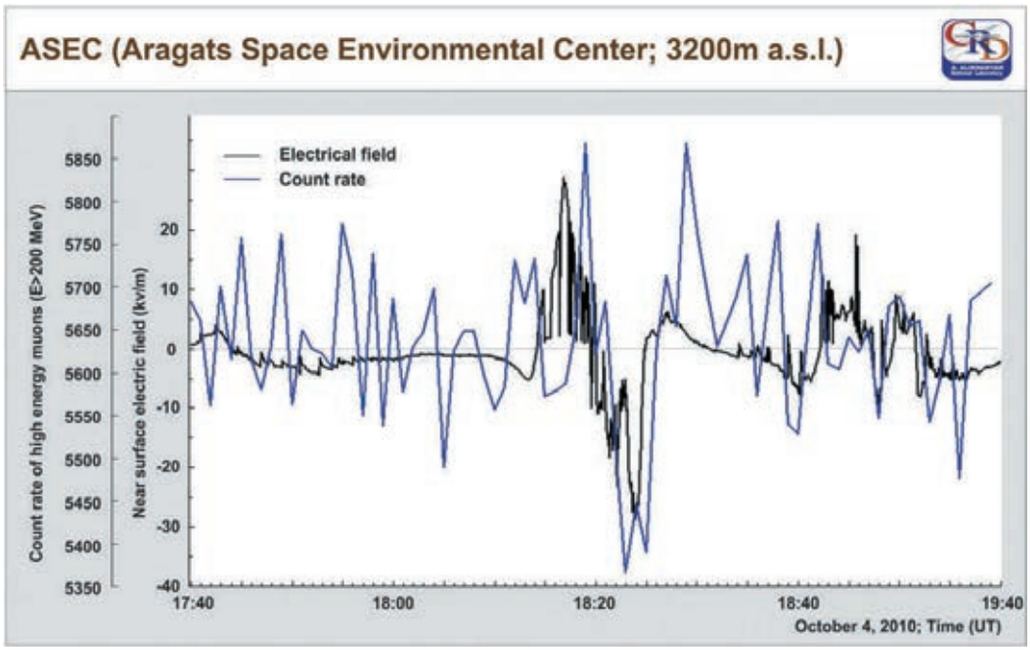


**Fig. 7.** The positive field in the thundercloud (electrons are accelerated downwards) stops positive muons; charge ratio of positive-to-negative muons is ~1.2–1.3, therefore we detect ~5% deficit of the flux of high-energy muons (energy > 200 MeV); simultaneously huge TGE in gamma ray and electron fluxes were measured.

## 4. GEANT4 simulations of particle propagation in strong electrical fields of thunderclouds

To get clues in the mechanisms of electron acceleration in the thunderclouds we implement simulations using a simple model of the electric fields in the thundercloud. GEANT4 simulations of the particle propagation in thunderclouds were performed with an electric field of 1.8 kV/cm spread uniformly from 5000 m till 3600 m a.s.l. Secondary Cosmic Ray (CR) electrons as seed particles in the energy range of 1–300 MeV and with fixed energy 1 MeV (simulating "pure" RREA process, ~1 MeV electrons commit minimal ionization losses in the atmosphere) were used. We chose the uniform electrical field strength above the critical energy of the RREA process at altitudes from 5000 m to 3400 m (1.7 kV/m) and fields below this threshold to illustrate the influence of the modification of secondary CR particle spectra (MOS process), as was described in the previous section.

In Fig. 8, we can apparently see 2 modes of particle generation. The RREA mode with maximal energy of electrons is 30–40 MeV and gamma rays — 20–30 MeV and MOS mode accelerating electrons up to 60–70 MeV; gamma ray spectrum prolonged up to 80–90 MeV. The electron and gamma ray energy spectra in the energy range of 1–10 MeV demonstrate large multiplication of electrons in the RREA process and huge amplitudes of the TGEs. MOS regime is fast fading after 50 MeV and needs large surfaces of particle detectors to be measured above the background of ambient population of secondary cosmic rays.

The high-energy tail of the gamma ray spectrum is due to enhanced bremstrahlung radiation of the higher energy electrons traversing the electric field of the cloud. Because of the highly enlarged radiation losses, high energy electrons cannot unleash the RREA, however, the additional flux of gamma rays radiated by these electrons can reach the mountain altitudes and be registered as small and modest enhancement over CR background — see the histogram in Fig. 1.

To prove our hypothesis on 2 component origin of TGE, we perform the same simulation with a fixed flux of 1 MeV seed electrons. The shape of electron and gamma ray spectra coincides with spectra obtained with 1–300 MeV electron seeds (exponential function — reflecting the particle multiplication in the avalanche process), however there are no high energy tails, see Fig. 9. Thus, pure RREA process with chosen electrical field parameters cannot produce TGE electrons with energies above 30–40 MeV and gamma rays with energies above 20–30 MeV.

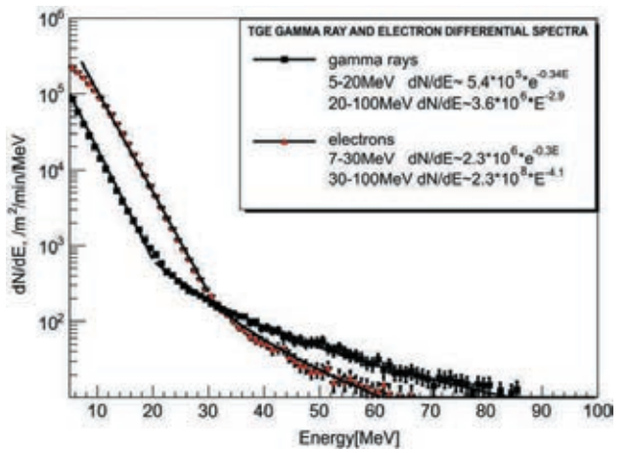


**Fig. 8.** TGE electron and gamma ray spectra obtained from GEANT4 simulation of RREA process in an electric field of 1.8 kV/cm with seed electrons of 1–300 MeV.

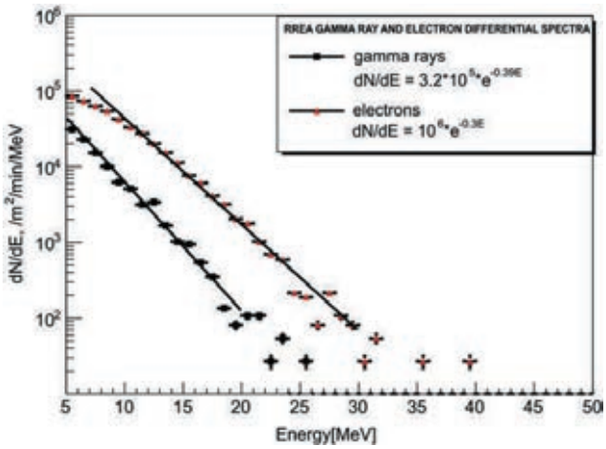


**Fig. 9.** The electron and gamma energy spectra obtained in electric field of 1.8 kV/m prolonged from 5000 till 3400 m with 1 MeV electron as seeds.

To prove that MOS process can provide high-energy gamma rays we perform simulations of the electron propagation in the moderate electric field below RREA initiation threshold (1.5 kV/m). In Fig. 10 we see that only the modification of the energy spectra of electrons can significantly enlarge the yield of the gamma rays reaching the earth surface. Electrons attenuate in the atmosphere after exiting from the cloud; however, as we can see from Fig. 10, the gamma rays survive.

## 5. The energy spectra of TGEs

### 5.1. TGE electron spectrum

The ultimate check of the RREA process detected on the ground is the measuring of the energy spectra of electrons and gamma rays well above the background of cosmic rays. Among hundreds of TGE events detected at ASEC only September 19, 2009 and October 4, 2010 TGEs allow the electron energy spectra recovering. After the estimation of the gamma ray flux, we subtract the obtained gamma-ray contamination, taking into account the efficiencies to register gamma rays by the particular detector and recover electron integral energy spectrum using several detectors with different energy thresholds. In Fig. 9, electron spectra of September 19, 2009 and October 4, 2010 TGEs are presented. The spectrum of September 19, 2009 TGE was obtained by additional counts of plastic scintillators with energy threshold of 9, 12, 15, 18 and 25 MeV (52, 826, 21,773, 15,967, 6750 and 506 electrons per minute per $m^2$, were registered respectively). The spectrum was approximated with exponential function (see fit parameters in the legend of Fig. 9); corresponding exponential mean energy equals to ~3.3 MeV. Scintillators with thresholds of 2, 7 and 12 MeV (36,089, 3896 and 459electrons per minute per $m^2$,was registered correspondingly) were used to recover the October 4, 2010 TGE electron integral spectrum; for this event the mean energy equals to ~2.3 MeV; both values are significantly smaller comparing with estimates based on simulations of the RREA (Lehtinen et al., 1999; Dwyer, 2004, ~7.2 MeV); however the 7.2 MeV value was obtained for the electrons just exiting the electrical field and for rather large electrical field strengths, 2 considered measurements at Aragats were made according to our estimates 50–150 m below the thundercloud (Fig. 11). For the details of separation of electrons and gamma rays and October 4, 2010 TGE electron spectrum recovery, see Appendix A.

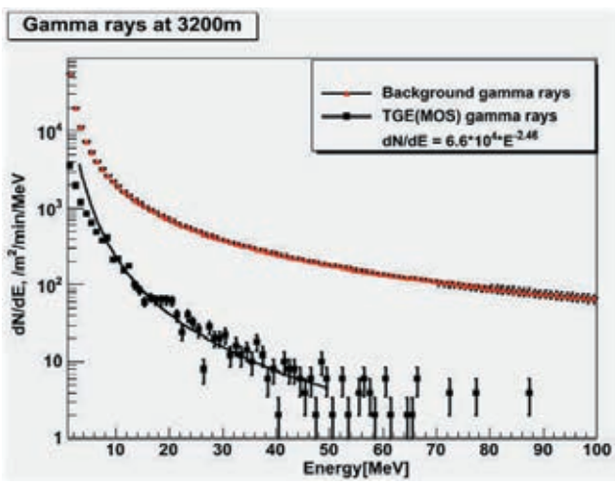


**Fig. 10.** Comparison of background gamma ray spectrum with the surplus gamma ray spectrum generated by electrons accelerated in the field of strength 1.5 kV/m below the critical field for the RREA initiation; the background cosmic ray gamma ray flux and TGE gamma ray flux are calculated at 3200 m altitude after exiting from the uniform electrical field at 3350 m altitude.

### 5.2. The energy spectra of the TGE gamma rays

The energy spectra of September 19, 2009 and October 4, 2010 TGE gamma rays are recovered based on the energy deposit spectra measured by Cube and ASNT detectors (see details of detector operation in Chilingarian et al. (2010) and details of spectra recovery in the Appendix B). Both Cube and ASNT detectors are measuring the energy deposit histograms and store them each minute. These histograms reproduce the

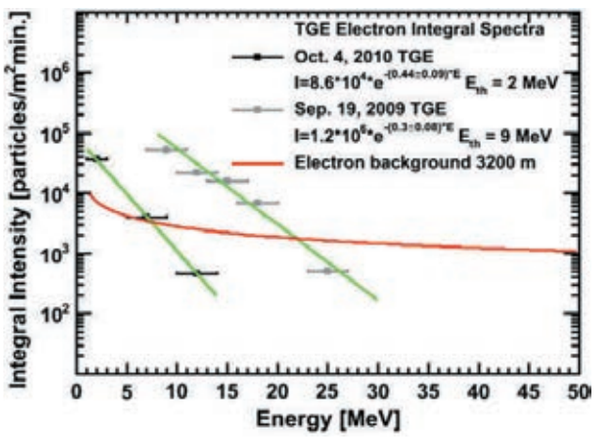


**Fig. 11.** Electron integral energy spectra of the September 19, 2009 and October 4, 2010 TGEs measured at 3200 m compared with the energy spectrum of the ambient population of the cosmic ray electrons at the same altitude (background).

energy spectrum of gamma rays, however they are folded by the detector response very differently for Cube and ASNT detector assemblies. Recovering the energy spectrum by the energy deposit histograms, i.e. solving the inverse problem of cosmic ray physics is rather a complicated task and we use multiple trial spectra for solving it (see for details Appendix B). The outdoor Cube detector was installed at Aragats in Spring 2010, near MAKET building, providing lower threshold of detected particles than indoor detector ASNT. Thus, only for October 4, 2010 TGE, we recover the gamma ray energy spectrum in the range of 5–10 MeV. The spectrum was approximated by both exponential and power law functions. Exponential function with mean energy of ~3.8 MeV provides slightly better approximation of the measured energy deposit with simulated one, than power law fit with index −1.8. $\chi^2$/ndf were ~2 and ~3 for the exponential and power functions respectively.

Since the maximal energy deposit in Cube detector is less than 40 MeV (the scintillator thickness is only 20 cm, comprising ~0.5 radiation lengths), we can reliably recover the spectrum at energies higher than 40 MeV with the ASNT detector assembly only (4 independent detectors comprising scintillators of 60 cm thickness, ~1.5 radiation length).

We use the Cube energy deposit spectra for the calibration of ASNT detector response. By the energy deposit spectra measured by Cube detector we cannot estimate the maximal energy of the gamma rays. We use the energy deposit spectra measured by ASNT to decide on the maximal energy of the gamma ray spectra (see Appendix B). Above 10 MeV the energy spectra are better approximated with power law. The spectral indices of gamma ray differential energy spectra were estimated to be $3.3 \pm 0.7$ and $3.4 \pm 0.25$.

The recovered gamma ray energy spectra posted in Fig. 12 have no error bars due to the spectra recovering method; we chose a particular power index (the power was found to be the best model), which provides simulated energy deposit histogram (obtained by simulation of the detector response) closest to the experimentally measured one (see details in Attachment B). The uncertainties of the procedure, including the possible errors in estimating detector response are included in the errors of the estimated power law indices.

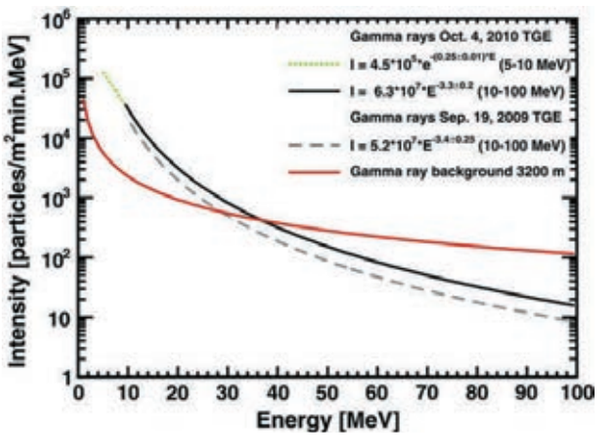


**Fig. 12.** The differential energy spectra of the gamma rays detected on September 19, 2009 and October 4, 2010.

## 6. Discussion and conclusion

The high elevation (~3200 m) of ASEC provides a good opportunity to detect thunderstorm-correlated particles, which attenuate rapidly in the atmosphere. We measure fluxes of the RREA electrons and gamma rays with intensities ~10 times above the cosmic ray background, thus, proving the existence of the runaway mechanism in thunderstorm atmospheres theoretically predicted by Gurevich et al. (1992). Both electron spectra measured on September 19, 2009 and October 4, 2010 are exponential. The gamma ray spectrum in the energy range 5–10 MeV (4 October 2010 TGE) also is better fitted with exponential function, in agreement with our simulations, see Fig. 9.

The estimated mean energies of the electron integral spectra are equal to ~2.3 and 3.3 MeV for October 4, 2010 and September 19, 2009 TGEs. The mean energy of the gamma ray differential energy spectrum in the energy range of 5–10 MeV is estimated to be 3.8 MeV.

It is less than derived from the simulations that the values of mean equal to 7.2 MeV (Dwyer, 2004). However, these values are in good agreement with values obtained from our simulations. Values of the mean energy of the 3 brightest electron/positron Terrestrial gamma flashes (TGFs) measured by the GBM, Fermi also are less than 7.2 varying from 2.3 to 4.6 MeV (Briggs et al., 2011).

Power law describes gamma-ray spectra at energies higher than 10 MeV. The energy spectra of the gamma rays extend till 100 MeV and demonstrate no exponential cutoff at high energies as obtained in many simulations of the RREA process (Dwyer and Smith, 2005). We suggest that the modification of the cosmic ray electron energy spectra in the electric field of the thundercloud leads to additional bremsstrahlung radiation reaching the Earth and sustaining the tail of TGE gamma ray spectra (the MOS process). As the cosmic ray spectra are power law, the high-energy tail of TGE gamma ray spectra is also a power law.

In the discussion section of Chilingarian et al. (2010), we estimate the height of thundercloud on September 19, 2009 TGE by assuming the maximal energy of RREA electrons ~50 MeV and calculating the distance in the air in which these electrons will lose 20–25 MeV (the maximal energy of measured electrons of September 19, 2009 TGE was estimated to be 25–30 MeV). After simulating the RREA process we come to the estimate of maximal energy of RREA electrons to be 30–40 MeV. Therefore we have to re-estimate the thundercloud elevation above detectors on September 19, 2009. Also we introduce a parameter, namely the ratio of electron to gamma ray flux, for estimation of the cloud (electric field) height, see Appendix C. With newly estimated thundercloud height, we re-estimate several phenomenological parameters of the RREA process as the following: the most probable height of thundercloud (and electrical field therein) is ~50 m. The number of electrons with energies above 1 MeV at the exit from the cloud is $1.97 * 10^7$ electrons/m$^2$/min; if we assume that the radiation region in the thundercloud has a radius of 1 km the total number of electrons crossing this region in a minute is $\sim 6 * 10^{13}$.

The same method applied to October 4, 2010 TGE gives the thundercloud height of 130 m. Taking into account that maximal energy of the detected electrons on October 4 was

12–14 MeV, we come to the estimate of the maximal energy of the RREA electrons to be 30–40 MeV, which is in good agreement with our simulations (Fig. 9). The most probable height of thundercloud (and electrical field therein) is ~130 m. The number of electrons with energies above 1 MeV on the exit from the cloud is $\sim 1.5*10^9$ electrons/m$^2$/min; if we assume that the radiation region in the thundercloud has a radius of 1 km the total number of electrons crossing this region in a minute is $\sim 5*10^{15}$.

The dynamics of the TGE increase (shown in Fig. 2) suggests that the largest TGE started by RREA having as seed particles the secondary cosmic ray MeV electrons; the particle avalanche developing in the direction to the Earth from the main negative charge layer in the middle of the thundercloud may create the initial conductive channel for the negative intracloud lightning discharge (Babich et al., 2011). The −IC lightning in turn may provide RB process with additional seed electrons from the current pulses along developing lightning leader channels thus enhancing the intensity of the electron and gamma ray fluxes.[6] Detection of the −IC lightning occurrences during the TGE events supports the suggested model. However, we recognize that the time scales of the lightning and TGE are drastically different and for definite conclusions on the possible seeds from the stepping leader we should compare on microsecond time scale the particle fluxes and lightning occurrences. Nonetheless the discovery of very short (less than 50 μsec) particle bursts within TGEs, coinciding with minute of the maximal flux (see for details, Chilingarian et al., 2011), illustrates the possible link between TGE and lightning.

The scenario of the TGF initiation is symmetric to the TGE: the electron-gamma avalanche is developing upward from the main negative charge layer to the main positive charge layer; coming out of the cloud, gamma rays are moving by straight lines to be detected by the orbiting gamma ray observatories. TGF gamma rays on their way to orbiting gamma observatories generate by Compton scattering and pair production high-energy electron-positron beams (TEBs, Dwyer, 2012), which follow the geomagnetic field line in the inner magnetosphere and may be observed thousands of kilometers away. The RREA developed in the upper dipole usually initiates positive intracloud lightning IC+ (Cummer et al., 2005; Shao et al., 2010; Lu et al., 2010) and the stepping leader of lightning may provide the RREA process with vast numbers of seed electrons.

## 7. Possible systematic errors

We do not measure the electric field within the thundercloud; near surface electric field is not a good proxy of the intracloud fields accelerating electrons downward. We also do not measure vertical extension of the field and only estimate the height of the cloud. Therefore, simulations of the RREA process in the atmosphere with chosen parameters, although are in an agreement with the available measurements of electric fields in the thunderclouds, cannot be used for direct comparisons with TGE measurements. However, these simulations give us understanding of the RREA scale and MOS processes and expected behavior of the energy spectra.

The radiation length of the ASEC electromagnetic calorimeters is 0.5 for Cube and 1.5 for ASNT, light attenuation in the thick scintillator significantly decreases the light incident on the PM cathode, and consequently the PM output pulse. Nonetheless, due to large gamma ray fluxes, energy deposit histograms collected during 1 min of peak intensity give a possibility to recover differential energy spectra of the gamma rays. To check the obtained gamma ray spectra and used attenuation coefficients several calorimeters were used for inter-calibration.

Due to particle bursts (Chilingarian et al., 2011) incident on colorimeter several large energy deposits may be because of multiple particle traversals. These effects are difficult to simulate and our method of the multiple spectra testing can give optimistically biased maximal energy of TGE gamma rays. Therefore, we do not include in the energy spectra recovering procedure 2 largest bins of the energy deposit histogram.

The electron/gamma separation is made by using veto scintillators with non-zero efficiency to detect charged flux. Nonetheless multilayered detectors with dedicated coincidence logic help to check the estimated fraction of TGE electrons and gamma rays and make appropriate corrections.

Several detecting devices are placed at high altitude, under snow and strong winds and it is very difficult to keep stable detecting channel parameters (high voltage, electronics thresholds and other) influencing the operation of detectors. However, high altitude station staff maintained detector operation 24 h daily for 12 months yearly and on-line visualization programs ADAS (Chilingaryan et al., 2008) and ADEI (Chilingaryan et al., 2010) provide possibilities of the remote monitoring and control of the key parameters of detectors.

## 8. Conclusions

We introduce 2 component model of the TGE origin: the RRE avalanches in energy domain up to 30–40 MeV and Modification Of energy Spectra (MOS) process operating on all energy scales and providing extension of gamma ray energy spectra up to 100 MeV. The RREA process can multiply particle flux up to 10 times above ambient background of secondary cosmic rays; the MOS process can provide several percent excess above cosmic rays, however for the much higher energies.

The TGE process is well correlated with near-surface electrical field and with lightning occurrences. All TGEs occur at the large negative near-surface electrical field and particle flux is accompanied with intracloud lightning occurrences (IC−) and suppression of cloud-to-ground lightning occurrences (CG−)). Measured structure of lightning occurrences supports creation of developed lower positive charge region (LPCR) as a fundamental condition of TGE origination.

## Acknowledgements

This work was partly supported by the Armenian government grants, NFSAT-CRDF-ECSP-09-69 grant and by ISTC A1554 grant. Authors thank Karen Arakelyan, Karen Avagyan,

[6] Calculations of the flux of runaway electrons produced by the lightning streamers suggests that stepped leaders produce a considerable number of energetic electrons, which is in an agreement with the number of energetic photons observed from satellites in terrestrial gamma ray flashes (Celectin and Pasko, 2011).

David Pokhsraryan, Arthur Reymers and David Sargsyan for assembling and launching Cube and STAND detectors. Authors are grateful to the members of the seminar of the cosmic ray division of Alikhanyan national lab for useful discussions and to S. Chilingaryan for developing ADEI multivariate visualization tool (Chilingaryan et al., 2010) for the treatment of the ASEC data flow. Gagik Hovsepyan helped in understanding asymmetries of the secondary cosmic ray flux and Laura Melkumyan made the histogram of the TGE events. Authors thank them for collaboration.

## Appendix A. Disentangling of charged and neutral fluxes by ASEC detectors

The largest TGEs measured by the ASEC detectors originated from RREA process in thunderclouds located above Aragats research station. The electrons and gamma rays from the RREA are continuing their path in direction of the Earth after avalanche growth stopped reaching LPCR. Depending on the distance from LPCR to particle detectors the relative fraction of electrons to gamma rays is changing. Measured huge enhancement of count rates is due to electrons and gamma rays, because both neutral and charged particles can generate signals in plastic scintillators, although with different efficiencies. Therefore, to estimate energy spectra of electrons and gamma rays we need to disentangle the mixture of electrons and gamma rays. Special experimental facilities were designed and installed at Aragats for separating electron and gamma ray fluxes. Two 20 cm thick plastic scintillators located inside the Cube detector are completely surrounded by 1 cm thick molded plastic scintillators, which are shown in Fig. 13. Thick scintillators detect charged flux with very high efficiency (99%) and also neutral flux with efficiency of 20–30%. Thin scintillators also detect charged flux with very high efficiency (98–99%), though the efficiency of detecting neutral flux is highly suppressed and equals to 1–2%. Using advanced coincidence technique it is possible to purify the neutral flux detected by inside scintillators, rejecting the charged flux by signals from surrounding thin scintillators. The calibration of Cube detector proves that veto system (preventing counting signal in the thick scintillator if there is a signal in at least one of surrounding six thin scintillators) can reject 98% of the charged flux. Number of TGE particles detected by upper thick scintillator (detector surface 0.25 $m^2$, see Fig. 13) at 18:23, October 4, 2010 was $N(20\ cm) = 43{,}439$ with veto and $N^v(20\ cm) = 44{,}956$ without veto, the difference is $N - N^v = 1517$. By these counts we can recover the flux (number of particles per $m^2$ per minute) of electrons $N_e$ and gamma rays $N_g$ above the detector.

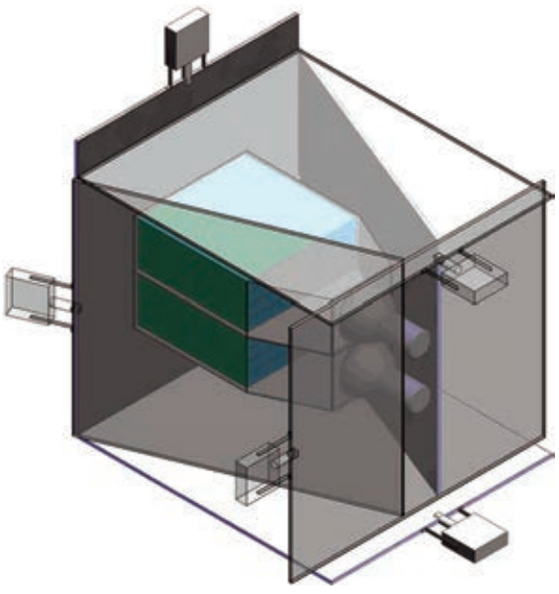

**Fig. 13.** Cube outdoor detector; thick scintillators located inside are measuring neutral flux with purity 98%.

$$\begin{aligned} N(20\,cm) &= N_e p(20\,cm/e) + N_g p(20\,cm/g) \\ N^v(20\,cm) &= N_e p^v(20\,cm/e) + N_g p^v(20\,cm/g), \end{aligned} \quad (1)$$

where p(20 cm/e) and p(20 cm/g) are the conditional probabilities to register electron or gamma ray by 20 cm scintillator. Accordingly $p^v$(20 cm/e) and $p^v$(20 cm/g) are the conditional probabilities to register electron or gamma ray by Cube 20 cm scintillator with veto switched on. By calibration, confirmed with detector response simulations, we estimate these conditional probabilities as follows:

$$\begin{aligned} &p(20\,cm/e) = .99 \\ &p(20\,cm/g) = 0.2 \\ &p(1\,cm/e) = 0.98 \\ &p(1\,cm/g) = 0.02 \\ &p^v(20\,cm/e) = (1 - p(1\,cm/e))p(20\,cm/e) = (1–0.98)0.99 = 0.0198 \\ &p^v(20\,cm/g) = (1 - p(1\,cm/g))p(20\,cm/g) = (1–0.02)0.2 = 0.196. \end{aligned} \quad (2)$$

Solving the system of Eq. (1) with coefficients (2) we readily get: $N_e = 1560$ and $N_g = 215{,}000$. Thus, on October 4, most of TGE particles were gamma rays, the fraction of electrons was less than 1%. From additional 1560 particles detected by 20 cm thick Cube scintillators only 31 can be electrons, i.e. less than 2%. Therefore, by examining the histograms of the energy deposits released in the thick scintillators of Cube we can recover the energy spectrum of the gamma rays of the TGE that happened on October 4, 2010 (see the techniques of the energy spectra recovering in the Appendix B). Of course, our calculations did not include the energy dependence of the efficiencies to detect gamma ray or electron by plastic scintillators; we assume that conditional probabilities are constant, according to Eq. (2). However, estimation of the energy dependence of these efficiencies by detector response function calculation with GEANT 4 code does not significantly alter our results. The ultimate check of the particle classification and energy spectra recovering will be an independent estimate of the particle enhancements registered with other ASEC detectors using those obtained by Cube energy spectra. The energy spectrum of gamma rays (Eq. (3)) obtained by the Cube detector was used to calculate the detector response of the STAND detector.

$$\begin{aligned} &dE/dN = 5.4e + 07{*}\exp(-0.25{*}E) \\ &\quad \text{for the energy range of 5–10 MeV;} \\ &dE/dN = 1.93e + 08{*}E^{-3.3} \text{ for the energy range of } 10-50\,MeV; \end{aligned} \quad (3)$$

Another outdoor detector STAND, see Fig. 14, consists of three 1 cm thick scintillators of the same type as Cube veto scintillators. STAND detector DAQ electronics stored statistics of all possible coincidences of the 3 scintillator “firings”.

Denoting the scintillator, which detected a particle by "1" and the scintillator, which has not registered a particle by "0" we get 7 meaningful combinations (combination 000 has no sense). For instance, combination "100" corresponds to the case when low energy particle stops in the upper layer and does not reach the layers below; "111" combination corresponds to high-energy particle generating signal in all 3 scintillators.

In Table 1 we compare the measurement at 18:23 4 October 2010 coincidence statistics with simulated detector response on reconstructed by Cube gamma ray energy spectrum (3).

Rather good coincidence of the sum of the simulated electrons and gamma rays with measured particle confirms that used gamma ray energy spectrum (3) is valid. Furthermore, by the electron fraction of the total counts we can recover integral spectrum of the TGE electrons.

**Table 1**
Measured and simulated STAND statistics; 18:23, 4 October 2010.

| | 100 | 110 | 111 |
|---|---|---|---|
| Experiment | 95,025 | 7366 | 1836 |
| Simulated gamma rays | 62,832 | 3929 | 1377 |
| Simulated electrons | 32,193 | 3437 | 459 |

## Appendix B. The method of TGE gamma ray and electron spectra recovery

The data acquisition (DAQ) electronics of the ASNT and Cube detectors stores each minute energy deposit histograms, digitized by Amplitude to digital converter (ADC) output analog signals of the photomultipliers (PM) overviewed the 60 cm and 20 cm thick scintillators located in the lightproof housings. On the basis of these histograms, using Monte Carlo techniques we recover differential energy spectra of the gamma rays. We solve the inverse problem and "unfold" the gamma-ray spectra by multiple solutions of the direct problem and comparisons of simulated and measured energy deposit histograms. Assuming the analytic form of the RREA gamma-ray spectra (power, exponential, or power with exponential cutoff) we tune free parameters (number of gamma-rays fallen on the roof and spectral indices) by minimizing the "quality" function describing the closeness of simulated with GEANT4 energy deposit histogram with the experimentally measured one. Gamma rays were traced through the material of the roof above the detector and trough the detector itself. The following steps were performed for the unfolding of the ASNT gamma ray spectrum above the roof of the MAKET building at an altitude of 3200 m:

- An energy spectrum with initial parameters randomly chosen from predetermined interval is generated;
- This spectrum is used to simulate the traversal of gamma rays through roof and ASNT detector components to finally obtain the energy deposit in thick scintillator;
- The obtained histogram of simulated energy deposits is compared with experimental one; the discrepancy (quality function) and initial spectrum parameters are stored;
- The simulations are continued till obtaining the histograms of energy releases corresponding to the whole interval of chosen spectrum parameters.

Having the dependence of the quality function on the test gamma ray spectra parameters, we fit these data by a second order polynomial function and find the minimum corresponding to the test gamma-ray spectrum, which generates an energy deposit spectrum closest to the experimentally measured one. For estimating the bias and accuracy of the above formulated procedure we simulate 150,000 gamma rays with energies distributed by power law with chosen spectral index equal to 3, i.e., $f(E) \sim E^{-3}$. Each gamma ray was followed by GEANT4 code, traversing the roof and detectors, and energy deposit in the scintillators was enumerated and stored. The obtained energy deposit histogram was taken as an "experimental" one and was further used for the energy spectrum recovery procedure. The gamma-ray spectra with power indices from −2 to −4 with step −0.01 were generated and corresponding energy deposit histograms were

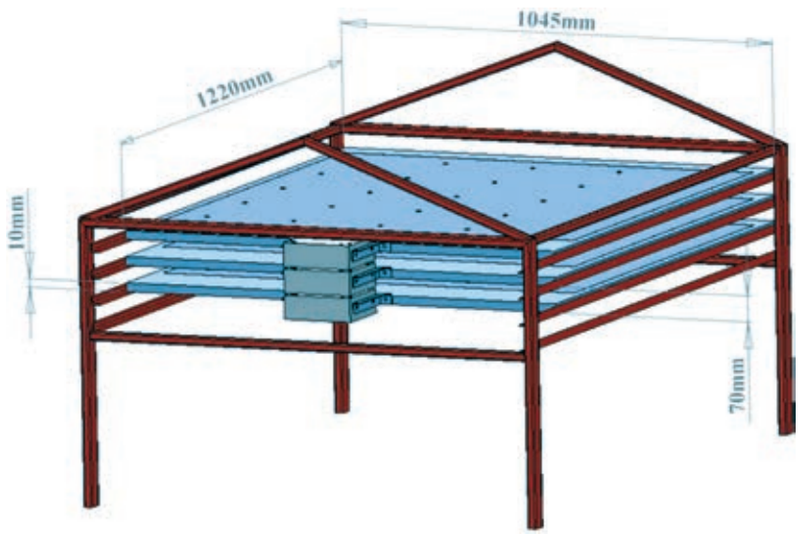


**Fig. 14.** STAND detector consisting of three layers of 1 cm thick scintillators.

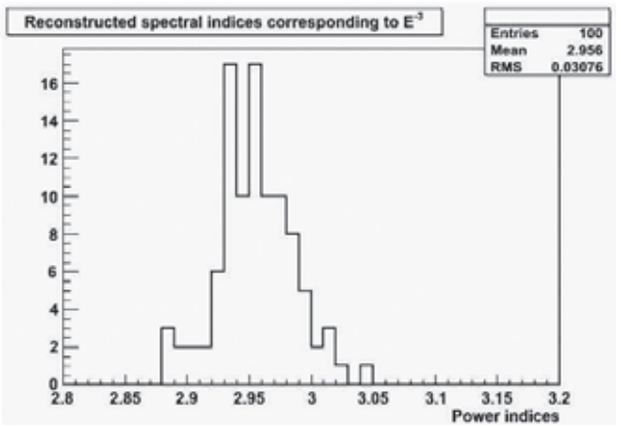


**Fig. 15.** Test of the spectral index recovery using a simulated spectrum as $f(E) \sim E^{-3}$.

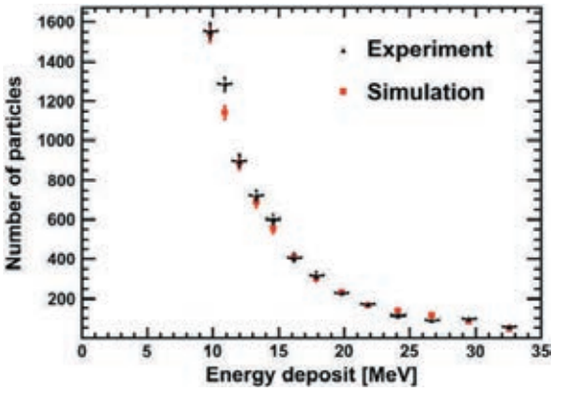


**Fig. 17.** Measured and simulated energy deposit histograms of Cube upper scintillator.

generated. Quality functions between "measured" and simulated spectra were calculated; the value of power index corresponding to the minimum of the quality function was obtained. We have repeated this procedure with hundred independent random samples, which serve as experimental ones and for each of hundred we repeated the spectra recovery procedure. As we can see from the legend of Fig. 15 the negative bias of the method is 0.044 and RMS is ~0.031. The corresponding relative error of the power index estimate is ~2%, which is 3 times less than the statistical error.

The test spectra for the recovering of the gamma ray spectrum of October 4, 2010 TGE were simulated according to power law with spectral indices varying in the range of −2 to −4 with step 0.01. Simultaneously, both spectra measured by top and bottom 20 cm thick Cube scintillators were simulated. Two hundred trials were performed and quality functions were calculated each time to describe the closeness of the energy deposit obtained in simulation with the experimental one. In Fig. 16, the dependence of the quality function on spectral index is shown for upper and lower Cube scintillators. For the quality function the $\chi^2$/ndf was chosen. The power spectra were found to give closer results to the experiment. The values of the quality functions corresponding to the different indices of the power function are approximated by the second order polynomial and as the final estimate the power index corresponding to the minimum of the curve was chosen (see Fig. 16). The $\chi^2$/ndf for the best-fit parameters is less than 1.

The obtained gamma-ray spectra by both Cube 20 cm detectors are in very good agreement with each other. The estimated gamma-ray spectrum by Cube upper scintillator for October 4, 2010 TGE is $\sim E^{-3.3\pm0.2}$in the energy range >10 MeV; the gamma ray flux is ~150,000 particles/m$^2$/min at 18:23 UT on 4 October, 2010, at altitude of 3200 m above sea level. The recovered spectrum by Cube lower scintillator is $\sim E^{-3.3\pm0.2}$. The October 4, 2010 TGE gamma-ray spectrum at energies 5–10 MeV is flatter and can be better described by the exponential function with index ~−0.25, the intensity is equal to ~400,000 particles/m$^2$/min. The "theoretical" (obtained by simulation, assuming power law spectrum of gamma rays above the outdoor Cube detector) and the measured energy deposit histograms of upper Cube scintillator are shown in Fig. 17.

However, the high-energy gamma rays will deposit small fraction of its energy in 20-cm thick scintillator and it will lead to possible biases in the high-energy spectra recovering.

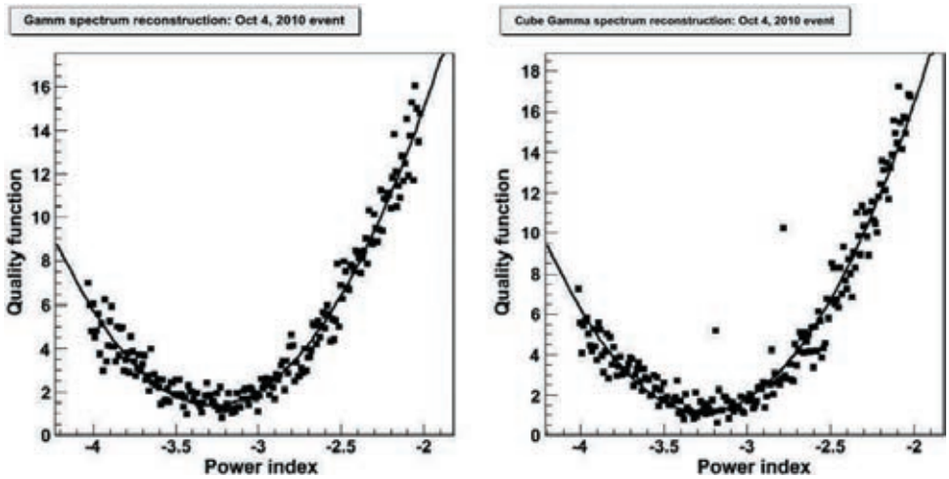


**Fig. 16.** The 200 trial spectra fitted by the second order polynomial (2 cube detectors data on 4 October, 2010).

As we are interested in proving the existence of high-energy tail, for gamma ray spectra recovering above 10 MeV we use 60 cm thick ASNT scintillators, more sensitive for high energies. The energy deposit histogram measured by one of the four ASNT scintillators with the best performance at low threshold (calibrated with spectra measured by Cube detector) was used for energy spectra recovering in high-energy domain. The gamma ray differential energy spectra above detector were estimated by multiple tests of propagation of the trial spectra through detector using GEANT4 code. Simulations in the energy range above 10 MeV were performed with power-law spectra in 2 versions: with maximal gamma-ray energy equal to 50 MeV and 100 MeV. In Fig. 18, the simulated energy deposit spectra obtained with assuming 50 MeV and 100 MeV along with the measured one are presented. The higher value of gamma ray maximal energy made the simulated spectrum closer to the experimental one. The error bars include the uncertainty in determination of the light attenuation coefficients in thick scintillator of ASNT detector. The quality function ($\chi^2$/ndf) describing the closeness of simulated and measured histograms has a smaller value in case of 100 MeV maximal energy of incident gamma rays — ~3 instead of ~250 for 50 MeV.

Large values of $\chi^2$/ndf reflect both possible errors in the used light attenuation coefficients and 2 modes of TGE origin. The fast decrease of experimental energy deposit spectrum at 17 MeV maybe is the illustration of the mode change of the TGE particle initiation.

The recovered gamma ray energy spectrum was checked by SEVAN detector, which can also distinguish neutral and charged fluxes. SEVAN DAQ electronics stores all possible combinations of signals (denoted by 1), and absence of signal (denoted by 0) in 3 layers. Combination "100" selects the low energy charged particles; coincidence "010" selects neutral particles, and combination "111" selects high-energy muons (see details in Chilingarian and Reymers, 2008). Simulating the passage of the recovered gamma-ray flux through the roof above and detector and taking into account the detector response to gamma rays and electrons, we have estimated the expected number of gamma rays detected by the "010" combination to be 1459 respectively. This value is in good agreement with experimentally measured value of $1452 \pm 42$.

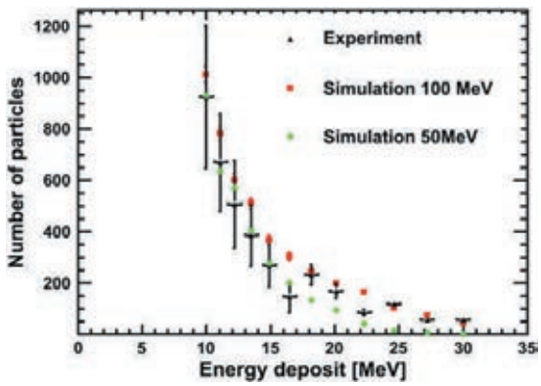


**Fig. 18.** Simulated and measured energy deposit spectra in the 60 cm thick scintillator of ASNT detector. Test power law spectra above detector were simulated in 2 versions: with maximal energy of 50 and 100 MeV.

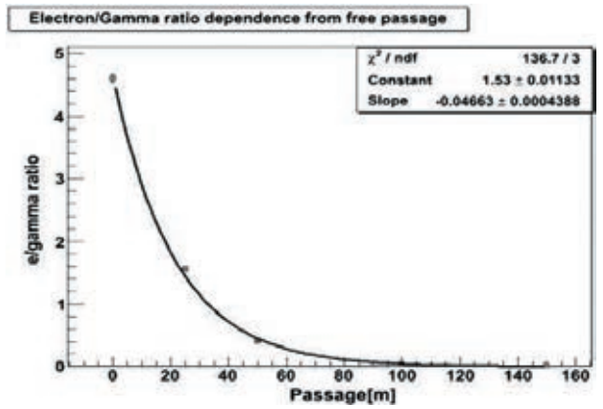


**Fig. 19.** Dependence of the electron/gamma ray ratio on the free passage distance after quitting the electrical field region.

## Appendix C. Thundercloud height estimation; electron number estimation

From the estimated integral energy spectra of electrons and gamma rays of October 4, 2010, we can estimate the approximate altitude of the thundercloud (the altitude from where the electron flux is not accelerated anymore, but only attenuated). This distance can be estimated by the dependence of the electron/gamma ray ratio on these particles' passage in the atmosphere obtained by the simulations of the RREA process followed by the passage of particles in the air. Using the GEANT 4 code we simulate the electron-gamma ray avalanche in an electric field of 1.8 kV/cm prolonged 1.6 km and then — obtain the electron/gamma ray ratio for various passage distances. In Fig. 19, the electron/gamma ray ratio dependence on the passage distance is presented for particles with energies greater than 7 MeV.

From Fig. 20, where we presented integral energy spectra of electrons and gamma rays with energies higher than 1 MeV, along with cosmic ray background electrons and gamma rays at 3200 m, we readily get the electron/gamma ray ratio of 0.0135 for 7 MeV particles. From Fig. 18, we find that the passage distance value corresponding to the observed electron/gamma ray ratio equals ~130 m. The maximal energy of the detected electrons on October 4 was 12–14 MeV, therefore we

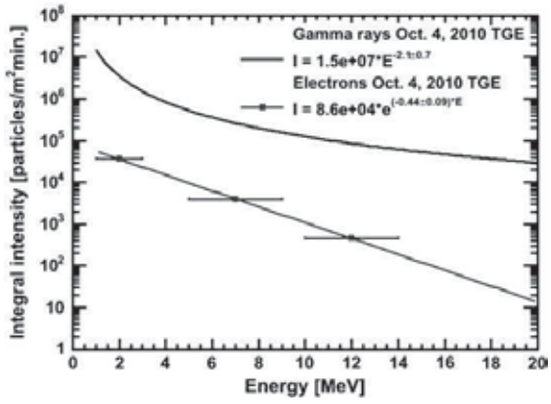


**Fig. 20.** Electron and gamma ray integral energy spectra of 4 October 2010 TGE as measured on 3200 m.

can estimate the maximal energy of the RREA electrons to be 30–40 MeV.

## References


Aglietta, M., et al., EAS-TOP Collaboration, 1989. The EAS-TOP array at E0 = 1014–1016 eV: stability and resolutions. Nucl. Instrum. Methods Phys. Res., Sect. A 277, 23–28.

Agnsotelli, S., Allison, J., Amako, K., et al., 2003. GEANT4—a simulation toolkit. Nucl. Instrum. Methods Phys. Res., Sect. A 506, 250–303.

Alexeenko, V.V., Khaerdinov, N.S., Lidvansky, A.S., Petkov, V.B., 2002. Transient variations of secondary cosmic rays due to atmospheric electric field and evidence for pre-lightning particle acceleration. Phys. Lett. A 301, 299–306, http://dx.doi.org/10.1016/S0375-9601(02)00981-7.

Babich, L.P., Bochkov, L.I., Kutsyk, I.M., Roussel-Dupre, R.A., 2010. Localization of the source of terrestrial neutron bursts detected in thunderstorm atmosphere. J. Geophys. Res. 115, A00E28.

Babich, L.P., Bochkov, E.I., Kutzyk, I.M., 2011. Lightning initiation mechanism based on the development of relativistic runaway electron avalanches triggered by background cosmic radiation: numerical simulation. Russ. J. JETF 139, 1028–1036.

Briggs, M.S., Fishman, G.J., Connaughton, V., et al., 2011. Electron-positron beams from terrestrial lightning observed with Fermi GBM. Geophys. Res. Lett. 38, L02808.

Carlson, B.E., Lehtinen, N.G., Inan, U.S., 2008. Constraints on terrestrial gamma ray flash production from satellite observation. J. Geophys. Res. Lett. 34, L08809.

Carlson, B.E., Lehtinen, N.G., Inan, U.S., 2009. Terrestrial gamma ray flash production by lightning current pulses. J. Geophys. Res. 114, A00E08, http://dx.doi.org/10.1029/2009JA014531.

Celectin, S., Pasko, V.P., 2011. Energy and fluxes of thermal runaway electrons produced by exponential growth of streamers during the stepping of lightning leaders and in transient luminous events. J. Geophys. Res. 116 (A03315), 14, http://dx.doi.org/10.1029/2010JA016260.

Chilingarian, A., Reymers, A., 2008. Investigations of the response of hybrid particle detectors for the Space Environmental Viewing and Analysis Network (SEVAN). Ann. Geophys. 26, 249–257.

Chilingarian, A., Avagyan, K., Babayan, V., et al., 2003. Aragats Space-Environmental Center: status and SEP forecasting possibilities. J. Phys. G: Nucl. Part. Phys. 29, 939–952.

Chilingarian, A., Arakelyan, K., Avakyan, K., et al., 2005. Correlated measurements of secondary cosmic ray fluxes by the Aragats Space-Environmental Center monitors. Nucl. Instrum. Methods Phys. Res., Sect. A 543 (2–3), 483–496.

Chilingarian, A., Daryan, A., Arakelyan, K., et al., 2010. Ground-based observations of thunderstorm-correlated fluxes of high-energy electrons, gamma rays, and neutrons. Phys. Rev. D 82, 043009.

Chilingarian, A., Hovsepyan, G., Hovhannisyan, A., 2011. Particle bursts from thunderclouds: natural particle accelerators above our heads. Phys. Rev. D 83, 062001.

Chilingaryan, S., Chilingarian, A., Danielyan, V., Eppler, W., 2008. The Aragats data acquisition system for highly distributed particle detecting networks. J. Phys. Conf. Ser. 119, 082001.

Chilingaryan, S., Beglarian, A., Kopmann, A., Voekling, S., 2010. Advanced data extraction infrastructure: web based system for management of time series data. J. Phys. Conf. Ser. 219, 042034.

Cui, H., Qie, X., Zhang, Q., Zhang, T., Zhang, G., Yang, J., 2009. Intracloud discharge and the correlated basic charge structure of a thunderstorm in Zhongchuan, a Chinese Inland Plateau region. Atmos. Res. 91, 425–429.

Cummer, S.A., Zhai, Y., Hu, W., Smith, D.M., Lopez, L.I., Stanley, M.A., 2005. Measurements and implications of the relationship between lightning and terrestrial gamma ray flashes. Geophys. Res. Lett. 32, L08811, http://dx.doi.org/10.1029/2005GL022778.

Cummer, S.A., Lu, G., Briggs, M.S., Connaughton, V., Xiong, S., Fishman, G.J., Dwyer, J.R., 2011. The lightning–TGF relationship on microsecond timescales. Geophys. Res. Lett. 38, L14810, http://dx.doi.org/10.1029/2011GL048099.

De Souza, P.E., Pinto Jr., O., Pinto, I.R.C.A., Ferreira, N.J., Dos Santos, A.F., 2009. The intracloud/cloud-to-ground lightning ratio in Southeastern Brazil. Atmos. Res. 91, 491–499, http://dx.doi.org/10.1016/j.atmosres.2008.06.011.

Dorman, L.I., Dorman, I.V., 2005. Possible influence of cosmic rays on climate through thunderstorm clouds. Adv. Space Res. 35, 476–483.

Dwyer, J.R., 2003. A fundamental limit on electric fields in air. Geophys. Res. Lett. 30, 2055.

Dwyer, J.R., 2004. Implications of X-ray emission from lightning. Geophys. Res. Lett. 31, L12102, http://dx.doi.org/10.1029/2004GL019795.

Dwyer, J.R., 2005. The initiation of lightning by runaway air breakdown. Geophys. Res. Lett. 32, L20808.

Dwyer, J.R., 2007. Relativistic breakdown in planetary atmospheres. Phys. Plasmas 14, 042901.

Dwyer, J.R., 2012. The relativistic feedback discharge model of terrestrial gamma ray flashes. J. Geophys. Res. 117, A02308, http://dx.doi.org/10.1029/2011JA017160.

Dwyer, J.R., Smith, D.M., 2005. A comparison between Monte Carlo simulations of runaway breakdown and terrestrial gamma-ray flash observations. Geophys. Res. Lett. 32, L08811.

Fishman, G., Bhat, P.N., Malozzi, R., et al., 1994. Discovery of intense gamma-ray flashes of atmospheric origin. Science 264, 1313–1316.

Gurevich, A.V., Milikh, G.M., Roussel-Dupre, R., 1992. Runaway electron mechanism of air breakdown and preconditioning during a thunderstorm. Phys. Lett. A 165, 463–468.

Gurevich, A., Zybin, K., Roussel-Dupre, R., 1999. Lightning initiation by simultaneous effect of runaway breakdown and cosmic ray showers. Phys. Lett. A 254, 79–87.

Gurevich, A.V., Mitko, G., Antonova, V., et al., 2009. An intracloud discharge caused by extensive atmospheric shower. Phys. Lett. A 373 (39), 3550–3553.

Khaerdinov, N.S., Lidvansky, A.S., Petkov, V.B., 2005. Cosmic rays and the electric field of thunderclouds: evidence for acceleration of particles (runaway electrons). Atmos. Res. 76, 346–354.

Lehtinen, N.G., Bell, T.F., Inan, U.S., 1999. Monte Carlo simulation of runaway MeV electron breakdown with application to red sprites and terrestrial gamma ray flashes. J. Geophys. Res. 104 (A11), 24,699–24,712.

Lidvansky, A.S., Khaerdinov, N.S., 2009. Strong variations of cosmic ray muons during thunderstorms. Izv. Ross. Akad. Nauk, Ser. Fiz. 73, 415–417 [Bulletin of the Russian Academy of Sciences: Physics 73, 400 (2009)].

Lu, G., Blakeslee, R.J., Li, J., Smith, D.M., Shao, X.-M., McCaul, E.W., Buechler, D.E., Christian, H.J., Hall, J.M., Cummer, S.A., 2010. Lightning mapping observation of a terrestrial gamma-ray flash. Geophys. Res. Lett. 37, L11806, http://dx.doi.org/10.1029/2010GL043494.

Lu, G., Cummer, S.A., Li, J., Han, F., Smith, D.M., Grefenstette, B.W., 2011. Characteristics of broadband lightning emissions associated with terrestrial gamma ray flashes. J. Geophys. Res. 116, A03316, http://dx.doi.org/10.1029/2010JA016141.

Moss, G.D., Pasko, V.P., Liu, N., Veronis, G., 2006. Monte Carlo model for analysis of thermal runaway electrons in streamer tips in transient luminous events and streamer zones of lightning leaders. J. Geophys. Res. 111, A02307, http://dx.doi.org/10.1029/2005JA011350.

Muraki, Y., Axford, W.I., Matsubara, Y., et al., 2004. Effects of atmospheric electric fields on cosmic rays. Phys. Rev. D 69, 123010.

Nag, A., Rakov, V.A., 2009. Some inferences on the role of lower positive charge region in facilitating different types of lightning. Geophys. Res. Lett. 36, L05815, http://dx.doi.org/10.1029/2008GL036783.

Pawar, S.D., Kamra, A.K., 2004. Evolution of lightning and the possible initiation/triggering of lightning discharges by the lower positive charge center in an isolated thundercloud in the tropics. J. Geophys. Res. 109, D02205.

Pinto Jr., O., Pinto, I.R.C.A., Naccarato, K.P., 2007. Maximum cloud-to-ground lightning flash densities observed by lightning location systems in the tropical region: a review. Atmos. Res. 84, 189–200.

Qie, X., Zhang, T., Chen, C., Zhang, G., Zhang, T., Kong, X., 2009. Electrical characteristics of thunderstorms in different plateau regions of China. Atmos. Res. 91, 244–249.

Sato, T., Endo, A., Zanki, M., Petoussi-Henss, N., Niita, K., 2009. Fluence-to-dose conversion coefficients for neutrons and protons calculated using the PHITS code and ICRP/ICRU adult reference computational phantoms. Phys. Med. Biol. 54, 1997.

Schonland, B.F.J., 1930. Thunder-storms and the penetrating radiation. Proc. R. Soc. Lond. A 130, 37.

Schonland, B.F.J., Viljoen, J.P.T., 1933. On a penetrating radiation from thunderclouds. Proc. R. Soc. Lond. A 140, 314.

Shao, X.M., Hamlin, T., Smith, D., 2010. A closer examination of terrestrial gamma-ray flash-related lightning processes. J. Geophys. Res. 115, A00E30, http://dx.doi.org/10.1029/2009JA014835.

Shaw, G.E.J., 1967. Cosmic count increase associated with thunderstorms. Geophys. Res. Bull. 72, 4623.

Standler, R.B., Winn, W.P., 1979. Effects of coronae on electric field beneath thunderstorms. Quart. J. Roy. Meteor. Soc. 105, 285–302.

Stanley, M., Shao, X.M., Smith, D., et al., 2006. A link between terrestrial gamma-ray flashes and intracloud lightning discharges. Geophys. Res. Lett. 33, L06803, http://dx.doi.org/10.1029/2005GL025537.

Stolzenburg, M., Marshall, T.C., Rust, W.D., 1998. Electrical structure in thunderstorm convective regions 2. Isolated storms. J. Geophys. Res. 103, 14079.

Torii, T., Takeishi, M., Hosono, T., 2002. Observation of gamma-ray dose increase associated with winter thunderstorm and lightning activity. J. Geophys. Res. 107, 4324, http://dx.doi.org/10.1029/2001JD000938.

Torii, T., Sugita, T., Tanabe, S., Kimura, Y., Kamogawa, M., Yajima, K., Yasuda, H., 2009. Gradual increase of energetic radiation associated with

thunderstorm activity at the top of Mt. Fuji. Geophys. Res. Lett. 36, L13804, http://dx.doi.org/10.1029/2008GL037105.
Torii, T., Sugita, T., Kamogawa, M., et al., 2011. Migrating source of energetic radiation generated by thunderstorm activity. Geophys. Res. Lett. 38, L24801, http://dx.doi.org/10.1029/2011GL049731.
Tsuchiya, H., Enoto, T., Yamada, S., et al., 2007. Detection of high-energy gamma rays from winter thunderclouds. Phys. Rev. Lett. 99, 165002.
Tsuchiya, H., Enoto, T., Torii, T., et al., 2009. Observation of an energetic radiation burst from mountain-top thunderclouds. Phys. Rev. Lett. 102, 255003.
Tsuchiya, H., Enoto, T., Yamada, S., et al., 2011. Long-duration gamma ray emissions from 2007 and 2008 winter thunderstorms. J. Geophys. Res. 116, D09113, http://dx.doi.org/10.1029/2010JD015161.
Vernetto, S., for EAS-TOP Collaboration, 2001. The EAS counting rate during thunderstorms. Proceedings of the 27th International Cosmic Ray Conference (ICRC) (Copernicus Gesellschaft, Hamburg, Germany, 2001), 10, pp. 4165–4168.
Wentz, J., Brancus, I.M., Bercuci, A., Heck, D., Oehlschlager, J., Rebel, H., Vulpescu, B., 2003. Simulation of atmospheric muon and neutrino fluxes with CORSIKA. Phys. Rev. D 67, 073020.
Williams, E.R., 1989. The tripole structure of thunderstorms. J. Geophys. Res. 94, 13151–13167.
Wilson, C.T.R., 1925. The acceleration of b-particles in strong electric fields such as those of thunderclouds. Proc. Camb. Philos. Soc. 22, 534–538, http://dx.doi.org/10.1017/S0305004100003236.

PHYSICAL REVIEW D **85,** 085017 (2012)

# Neutron bursts associated with thunderstorms

A. Chilingarian,* N. Bostanjyan, and L. Vanyan

*A. Alikhanyan National Laboratory (Yerevan Physics Institute), Armenia*

(Received 14 June 2011; revised manuscript received 23 January 2012; published 16 April 2012)

The basis of our analysis is the observation of the simultaneous enhancements of the gamma ray and neutron fluxes detected in 2009–2010 during thunderstorm ground enhancements at the mountain altitude of 3200 m. We investigate the correlated time series of the gamma rays and neutrons measured by the surface particle detectors of Aragats Space Environmental Center. The photonuclear reactions of the gamma rays born in the runaway breakdown (RB, now referred to as relativistic runaway electron avalanche, RREA) process with air were considered as the main process responsible for the copious neutron production. We consider also the mesoatom nuclei decay as a possible source of the additional neutrons registered by the neutron monitor due to enhanced population of the negative muons accelerated in the thunderclouds.

DOI: 10.1103/PhysRevD.85.085017 PACS numbers: 92.60.Pw, 13.40.−f, 94.05.Dd

## I. INTRODUCTION

The idea of neutron production during thunderstorms comes from the experimentation with fibers exploded after applying high voltage pulses. Neutron production in high voltage discharges forcing the explosion of fibers containing hydrogen or deuterium is reported in several papers (see [1], and references therein). An average neutron yield approached $\sim 10^{10}$ and neutron energy spectra peaked at 2.48 MeV. Based on these investigations, it was postulated that natural lightning discharges could produce neutrons as a mixture of deuterium contained in the atmospheric water vapor. However, the attempt to measure these neutrons in correlation with lightning strokes gives fluxes consistent with the cosmic ray background [2].

The first evidence of neutron generation in lightning discharges comes from Gulmarg, India, altitude 2743 m [3]. Neutrons were detected by the low-energy lead-free neutron monitor (GNM) comprising 21 proportional counters filled with $BF_3$ gas enriched by the $B^{10}$ isotope ($\sim 3\%$ registration efficiency for 2.5 MeV neutrons). The counters were arranged in the form of a pile and were placed over 28 cm thick paraffin wax slabs 8 m above the ground. The counters were also covered by 7.5 cm thick paraffin wax. During the 3-year operation of the detector several lightning correlated neutron events were detected, the biggest one comprising 60 neutrons. The authors suggest a nuclear fusion [deuterium-deuterium, $(^2H, n)^3He$] mechanism for producing 2.45 MeV neutrons occurring in the lightning channel. The neutron counting timing accuracy ($> 300\ \mu$ sec) was large compared to the duration of a lightning stroke, though, and there was no possibility to establish a one-to-one relation between lightning and detected neutrons.

Another Indian group running a neutron detection system at Mumbai (sea level) by statistical analysis also claims correlation of neutron bursts with lightning [4]. The experimental device consisted of 16BF3 detectors of 0.05 m diameter, embedded in polyethylene neutron slowing-down material. The neutron burst was identified by the multiplicity greater than 2 (more than 2 neutrons detected by the system of 16 tubes within $\sim$1 millisecond). During the low-altitude lightning occurrences the frequency of counts was significantly higher and multiplicities of 6 and 7 were observed (which were not observed during other weather conditions, including rain). The counts obtained during lightning were $4.8\sigma$ higher than the background. Therefore, the authors stated that neutron bursts were associated with lightning.

Recently the data acquisition electronics of the GNM has been significantly modified to record the time profiles of the neutron bursts with microsecond accuracy [5]. Despite a rather small amount of detected neutrons (the biggest event comprises 63 neutrons) and large millisecond delays of neutrons relative to lightning, the authors confirm the previous GNM claim of the production of neutrons in atmospheric discharges.

In the city of Sao Jose dos Campos, Brazil, at sea level a standard lead- and moderator-free $He^3$ tube (area 70 $cm^2$; type 25291; Ludlum, USA) detected a burst of neutrons which coincided with a lightning strike within a short distance of the detector ($< 0.5$ km). The minute count of 690 (the mean minute count rate was $\sim$0.8) corresponds to the flux $\sim$20 neutrons/$cm^2$, which in turn corresponds to about $10^{12}$–$10^{13}$ neutrons produced by the lightning discharge [6].

A less exotic neutron source is associated with the excitation by gamma rays of natural oscillations of protons relative to neutrons, the so-called giant dipole resonance. When the gamma ray energy exceeds the energy of a giant resonance (the binding energy of the nucleon in the nucleus), neutrons that absorb the gamma rays escape from the nucleus [7].

*chili@aragats.am

 

Whether neutrons observed in correlation with lightning are produced by nuclear fusion or by photonuclear reaction remains uncertain. According to [8], though, the maximum bulk plasma temperature attained in lightning discharge is far too low to initiate fusion reactions. Photonuclear reactions in the air initiated by the gamma rays generated in the relativistic breakdown (RB, [9]), now referred as runaway electron avalanches (RREAs, [10]) seem to be a more probable process. Nonetheless, authors of Ref. [5] claim that there are some hot spots in the lightning channel where the pinch effect could create plasma configurations in which ions may have competing peak energies to induce fusion reactions.

Therefore, the problem of the neutron origin still is challenging. We need simultaneous detection of the gamma rays, neutrons, and lightning occurrence to disentangle this complicated problem. During last year's campaign at Aragats Space Environmental Center (ASEC, 2003, 2005) numerous thunderstorm ground enhancements (TGEs) were detected; some of them also include significant enhancements of the count rate of the Aragats Neutron Monitor (ANM). In this paper we present analysis of the simultaneous gamma ray and neutron enhancements and discuss possible explanations of the peaks in the ANM time series coinciding in time with gamma ray intensity increases.

### A. Neutron enhancements detected by Aragats Neutron Monitor during thunderstorm ground enhancements

Registration of high-energy neutrons at ASEC was performed with the standard neutron supermonitor (NM-64, [11]), located at the slopes of Mt. Aragats near a lake at altitude of 3200 m. The neutron monitor registers basically the atmospheric neutrons in a wide range of energies, although with various efficiency, going down at low energies [12]. Eighteen cylindrical proportional counters of type CHM-15 (length 200 cm, diameter 15 cm) are filled with $BF_3$ gas enriched by a $B^{10}$ isotope. The proportional chambers are surrounded by 5 cm of lead (producer) and 2 cm of polyethylene (moderator). The neutron supermonitor consists of 3 sections, 6 chambers in each. The cross section of lead producer above each section has a surface of $\sim 6\ m^2$, and a total surface of 3 sections—18 $m^2$. The atmospheric hadrons produce secondary neutrons in nuclear interactions in lead; then the neutrons get thermalized in a moderator, enter the sensitive volume of the counter, and in interactions with boron gas bear $L_i^7$ and the $\alpha$ particle. The $\alpha$ particle accelerates in the high electrical field inside the chamber and gives a pulse registered by the data acquisition electronics. The NM response to incident hadrons can contain several pulses depending on the number of secondary low-energy neutrons entering the volume of the counter and reacting with boron gas. Usually high-energy hadrons generate a larger number of secondary neutrons and have greater chances to generate more than one pulse. If we want to count all pulses initiated by the incident hadron (i.e., estimate so-called multiplicities) we have to keep the dead time of the NM very low (the ANM has a minimal dead time of 0.4 $\mu$s); if we want to count incident hadrons only (a one-to-one relation between count rate and hadron flux) we have to keep the dead time as much as all secondary neutron collecting time to avoid double counting (for ANM—1250 $\mu$s).)

For the detection of the thermal atmospheric neutrons on top of the ANM we install two proportional chambers without moderator and producer, only "bare" proportional counters. The 1 min time series of two chambers as well as 18 chambers of ANM are being entered in the MSQL database at CRD headquarters in Yerevan (available online from http://adei.crd.yerphi.am/adei/), and the database of the Euro-Asian consortium of neutron monitors (NMDB@.eu.org).

Other particle detectors of the ASEC [13,14] are continuously registering charged and neutral species of the secondary cosmic rays. The main building blocks of the particle detectors are plastic scintillators (both polished and molded pressed) located in the lightproof housings; the scintillation light is collected directly or via fiberglass light-shifting wires and overviewed by the photomultipliers. From the standard scintillation pieces of 5 cm thickness were assembled scintillator slabs from 20 to 60 cm thickness. The thin scintillators have very high efficiency to detect charged particles (mostly electrons and muons); the thick ones to detect neutral particles (gamma rays and neutrons). Thick detectors register also the energy deposit of traversing particles, thus giving the possibility to recover the energy spectra of the gamma ray flux. The coincidence technique allows significantly suppressing charged particle contamination to counts of thick scintillators and significantly purifying detected gamma ray flux. We use a 01 combination of the Aragats Solar Neutron Telescope (ASNT, 01 combination means no signal in the upper 5 cm thick scintillator and a signal in the 60 cm thick bottom scintillator) and 010 combination of the SEVAN[1] three-layered detector (signal only in the middle 20 cm thick scintillator). Details on detector operation can be found in [16].

In contrast to thick plastic scintillators, sensitive to both neutrons and gamma rays, the neutron monitor is sensitive only to incident hadrons (registration efficiency of electrons and gamma rays is negligible). The relative standard error of the particle detector 1 min time series is rather small (see Table I), ranging from 0.56% to 2%; therefore few percent peaks are significant and if the neutron peaks are correlated with electron and gamma ray peaks the chance probability of random coincidences is vanishingly

[1]SEVAN is the worldwide network of hybrid particle detectors measuring neutral and charged components of the secondary cosmic rays, primarily aimed at space weather research and forecasting (see [15]).

TABLE I. Characteristics of ASEC particle detectors and parameters of the 4 October 2010 TGE.

| Detector | Mean count rate per minute | Standard deviation ($\sigma$) and relative standard deviation | Percent of enhancement at 18:23, 4 October 2010 | Number of standard deviations in peak at 18:23, 4 October 2010 |
|---|---|---|---|---|
| SEVAN 010 | 2040 | 45 (2%) | 73% | $66\sigma$ |
| ASNT 01 | 31750 | 178 (0.56%) | 32% | $57\sigma$ |
| ANM | 37700 | 285 (0.76%) | 5.8% | $7.6\sigma$ |

small. We are also monitoring possible interferences and radio induced fake peaks and cleanup data from the suspicious channels.

The neutron event selection criteria consist of detection of the significant peaks in the neutron monitor 1 min time series coinciding in time with large peaks in gamma ray and electron fluxes measured by other ASEC particle detectors. An example of such an event is posted in Fig. 1.

At 18:23, 4 October 2010, all ASEC particle detectors registered large enhancements; see Fig. 1 and Table I.

Aragats neutron monitors were well maintained and corrected to atmospheric pressure changes and electronics aging [17]. In 2009–2010 when there were no interferences with peaks due to solar modulation effects (ground level enhancements and geomagnetic storms), we detected 12 peak enhancements of the neutron count rate observed by the ANM in coincidence with the enhanced gamma ray flux measured by other ASEC detectors; see Table II.

The first column of Table II provides the date of the TGE event.

In the second column we display the number of additional neutrons in the peak normalized to 1 $m^2$.

In the third column we display the relative enhancement of neutrons in percent of the mean background, estimated by 1 h data before the start of the TGE,[2] and in the number of standard deviations.

In the fourth column we provide the neutron intensity at 3200 m obtained by the NM counts using the shape of the energy spectrum of the photonuclear neutrons and energy dependence of NM efficiency. The simulations were made by GEANT4 code; the primary gamma ray source was located at a height of 5000 m. The obtained neutron energy spectrum (see Fig. 2) coincided well with the spectrum presented in [18], Fig. 1. The energy dependence of the neutron monitor efficiency was taken according to Refs. [19–21].

In the fifth column we put the number of additional gamma rays in the peak detected by the ASNT. Also, we put in the fifth column the values of the reconstructed integral energy spectrum of gamma rays above 10 MeV. Only the two largest TGE events allow reliable gamma ray spectra recovering; for the rest of the events the histograms of energy deposits in the 60 cm thick plastic scintillates of the ASNT detector (see details in [16]) are too scarce to allow reliable retrieving of the gamma ray energy spectra.

In the sixth column we put the relative enhancement of gamma rays in percent of the mean background and in number of standard deviations.

In the seventh column we put the recovered intensities of gamma rays for the 2 largest TGE events.

In the column 8 we put the ratio of neutron-to-gamma rays (for the largest two events also, the ratio of neutron-to-gamma ray intensities), which reveals some important features of neutron and gamma ray propagation in the atmosphere. As we see in column 8 for the 2 largest events the ratio of detected neutrons to detected gamma rays is substantially smaller compared with 10 other events. Thus, TGE events by gamma ray content fall in two groups: events detected on 19 September 2009 and 4 October 2010 and 10 other events.

In Fig. 3 we put the scatter plot of detected additional neutrons ($x$ axis, from column 2 of Table II) vs number of additional gamma rays ($y$ axis, from column 5 of Table II). In the scatter plot the existence of 2 distinct groups introduced above is apparent.

The existence of 2 distinct groups in the TGE events with different gamma ray content suggests that the parent gamma rays generated by the bremsstrahlung of the electrons accelerated in the RREA process have rather narrow lateral distribution. Only TGEs initiated by the RREA

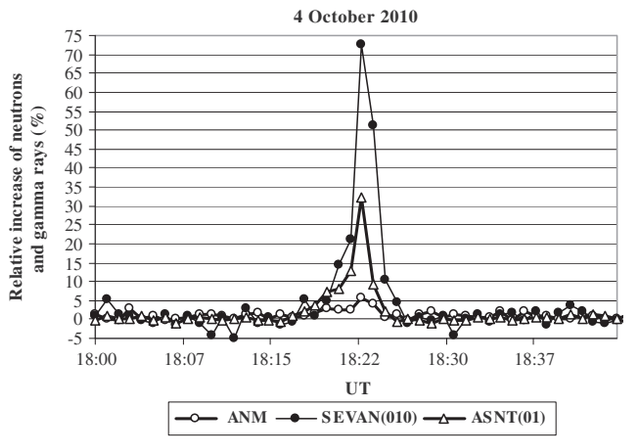


FIG. 1. The count rates of the ANM, SEVAN, and ASNT (01) combination on 4 October 2010.

[2]See for instance the mean count rate, standard deviation, and relative standard deviation of the background on 4 October 2010 in Table I.

TABLE II. The list of the parameters of the 12 TGE events with neutron content (2009–2010).

| Day/month/year | Number of additional neutrons detected by ANM at minute of maximal excess ($min^{-1}$, $m^{-2}$) | Relative increase of neutrons detected by ANM (%)/$N(\sigma)$ | Recovered neutron intensity at 3200 m ($min^{-1}$, $m^{-2}$) | Number of additional gamma rays detected by ASNT (combination 01) at minute of maximal excess $min^{-1}$, $m^{-2}$ | Relative increase of gamma rays in (%)/$N(\sigma)$ | Recovered gamma ray intensity at 3200 by ($min^{-1}$, $m^{-2}$) | Ratio of neutron to gamma ray flux/ ratio of intensities for largest TGE events |
|---|---|---|---|---|---|---|---|
| 21/05/09[a] | 83 | 3.8/5 | 3420 | 1920 | 7/12 | | 0.043 |
| 21/05/09[a] | 94 | 4.3/5.7 | 3847 | 1921 | 7/12 | | 0.049 |
| 03/06/09[a] | 88 | 3.9/5.2 | 3613 | 1215 | 4/7 | | 0.072 |
| 03/06/09[a] | 89 | 3.9/5.2 | 3666 | 1076 | 3.6/6 | | 0.083 |
| 08/07/09[a] | 63 | 2.7/3.5 | 2591 | 1116 | 3.3/5.3 | | 0.056 |
| 08/07/09[a] | 64 | 2.7/3.6 | 2624 | 1290 | 4.1/6.5 | | 0.050 |
| 09/07/09 | 74 | 3.2/4.2 | 3050 | 1690 | 5.3/9.5 | | 0.044 |
| 20/08/09 | 51 | 2.3/3.2 | 2110 | 940 | 3/4.8 | | 0.054 |
| 02/09/09 | 50 | 2.5/3.3 | 2032 | 900 | 3/5.2 | | 0.055 |
| 19/09/09 | 63 | 2.8/3.7 | 2574 | 7452 | 23/41 | 104 000 | 0.008/0.025 |
| 02/11/09 | 50 | 2.3/3.1 | 2041 | 1101 | 3.3/6 | | 0.045 |
| 04/10/10 | 124 | 5.8/7.7 | 5091 | 10280 | 32/58 | 153 000 | 0.012/0.033 |

[a]Events occurred during 1 d but different times.

process above the particle detectors can sustain large gamma ray fluxes. The majority of the TGE events originate due to either modification of the energy spectra of cosmic ray electrons or the RREA process being launched outside the detector location site; in both cases the number of detected gamma rays will be significantly less.

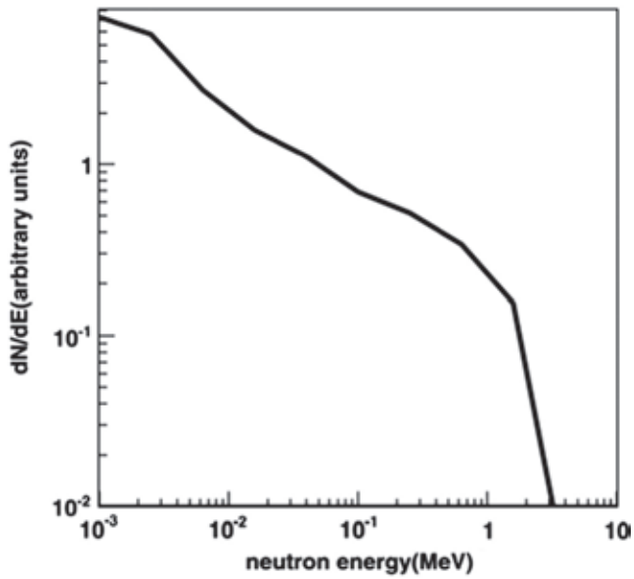


FIG. 2. Energy spectrum of neutrons born in photonuclear reaction; gamma ray source is located at 5000 m, and neutron detectors at 3200 m.

### B. Contribution of the negative muons to ANM counts

The shift of the energy spectrum of the electrons/positrons and negative/positive muons entering a large electrical field region in thunderclouds can lead to dips and peaks in the time series of the count rates of surface particle detectors (see the theory of meteorological effects in [22] and numerical calculations in [23]). The charge ratio of positive-to-negative muons above 200 MeV equals ~1.3 [24,25]. Therefore, if an electrical field in the thundercloud is positive and accelerates electrons and negative muons downward, the same field will also decelerate positive muons. And, due to significant enhancement of the

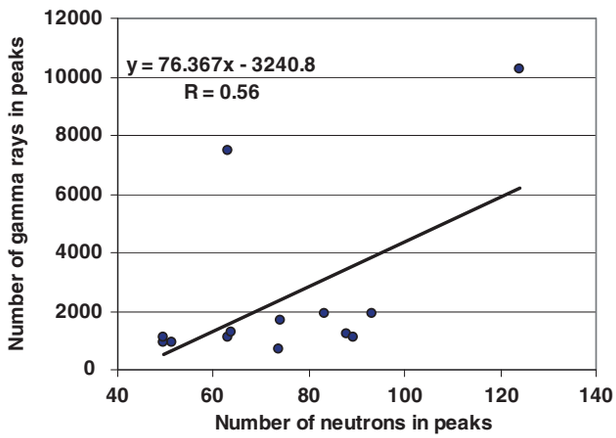


FIG. 3 (color online). Scatter plot of 12 TGE events detected in 2009–2010. $R$ is correlation coefficient.

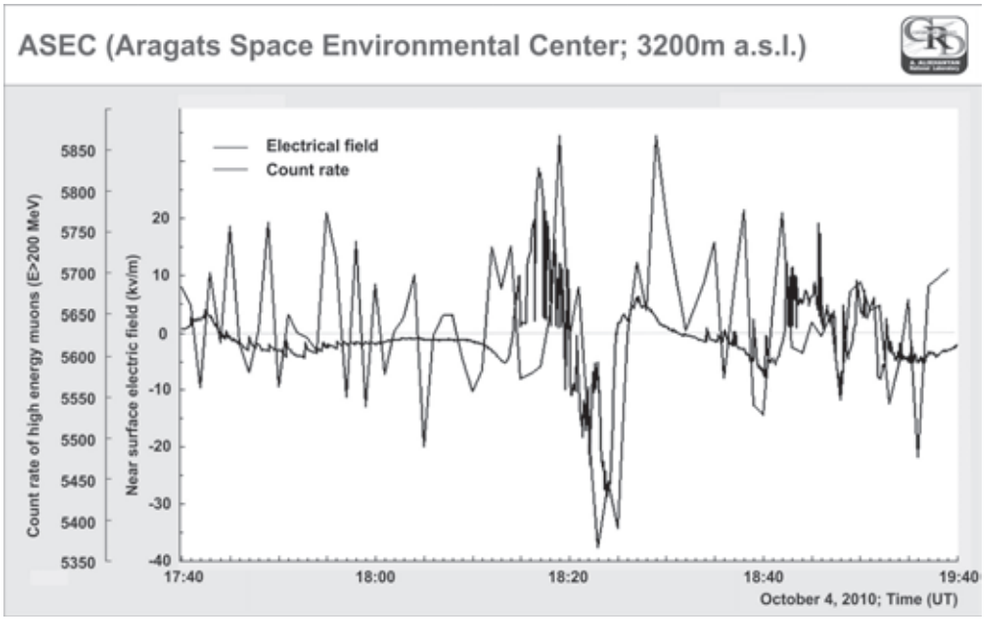


FIG. 4. Deficit of the >200 MeV muons during large negative near surface electrical field.

positive muons compared with the negative ones, we expect a dip in the time series of the high-energy muons at the same time when we detect enhancements of electrons and gamma rays. A SEVAN detector cannot distinguish between negative and positive muons—both charged particles are contributed to the time series registered by the detector—therefore, the detector count rate (the sum of negative and positive muons) after crossing the electrical field diminished because in the cosmic ray flux positive muons are 1.3 times more abundant than negative muons.

On 4 October we detected a deficit of the high-energy muons registered by SEVAN detectors' 111 combination (signals in each of the 3 layers of the assembly of 3 stacked scintillators interlayered by 10 cm of lead); see Fig. 4. As we can see in Fig. 4 the dip in the time series of high-energy muons coincides with a large negative field measured by an electrical mill located on the roof of the building where particle detectors are located.[3] At the same time, with the same detector (see Fig. 1) we detect a huge enhancement of the gamma ray flux (a combination 010 of SEVAN).

The detected dip in the high-energy muon count rate indicates that the positive field in the thundercloud stopped the positive muons. Because the number of positive muons in the secondary cosmic rays' flux is ~1.3 times more compared with negative muons, we detect overall depletion of the muon flux (see Fig. 4). From the measured dip of ~6% in muon flux we calculate an expected deficit of the positive muons and enhancement of the negative muons. GEANT4 calculations indicate that the enhancement of the negative muons can reach ~15% (consequently the reduction of positive muons is 20%). Consequently, the additional negative muons' incident on the ANM can be captured in the 5 cm thick lead producers of the ANM and form so-called mesic atoms where an electron orbiting the atom nucleus is substituted by the muon. Deexcitation of the nucleus occurs with emission of several MeV energy neutrons [22]. The details of nuclear muon capture and consequent decay with emission of several neutrons can be found in the review [26]. Therefore, several fractions of the neutron count rate enhancement can be attributed to these negative muons.

In Fig. 5 we depict the energy dependence of the efficiency of a negative muon to generate NM counts [27]. The efficiency of neutron detection is significant only in the energy range of 50–230 MeV. However, as demonstrated by our simulations the enhancement of the number of negative muons in this energy range after crossing the

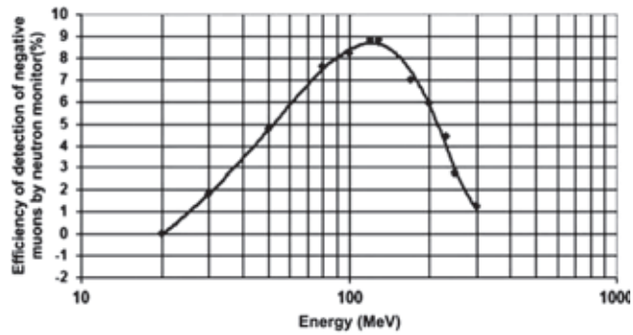


FIG. 5. Energy dependence of the NM detection efficiency of the negative muons.

[3]Almost all TGEs are detected during an abrupt decrease of the near surface electrical field down to $\sim -30$ kV/m.

electrical field is not very large. Therefore, from this calculation we cannot expect any significant (greater than 10–20) excess of NM count rate due to enhancement of the negative muons.

Another estimate of the additional count rate due to an enhanced number of negative muons [Eq. (30) from [22] ] gives ~20 additional counts of the ANM. A simpler way to calculate additional NM counts is based on the estimate that 5%–7% of the overall NM counts is due to negative muons [28]. Let us assume that 6% of the NM count rate is generated by the negative muons; taking from Table I the ANM count rate (all 18 proportional tubes, ~1 $m^2$ surface each) we will obtain $37\,700 \times 0.06 = 2262$ additional counts from ambient population of secondary negative muons. On 4 October we estimated maximally ~15% of additional negative muons; therefore we can expect an additional $2262 \times 0.15 = 340$ NM counts; normalizing the additional flux to 1 $m^2$ we get ~20 additional counts among 124 detected on 4 October 2010.

### C. Evidence of the "bare" proportional chamber

The bare (without lead producer and polyethylene moderator) proportional counter CNM-15, of the same type as is used in the ANM, was located directly above the ANM for detection of the low-energy neutrons. The bare counter registered enhancement on 4 October 2010 was well correlated with the ANM peak (see Fig. 6).

The number of neutrons detected during the 4 October 2010 TGE normalized to 1 $m^2$ was less than that of the ANM (54 and 124 correspondingly). Our simulations demonstrate that the MeV neutron flux incident on the neutron monitor thermalized in the polyethylene moderator and a significant fraction of the thermal neutrons is emitted upwards from the polyethylene moderator covering the ANM

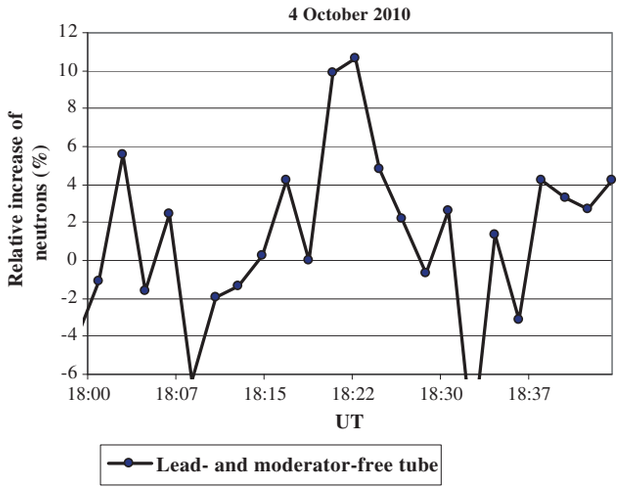


FIG. 6 (color online). Time series of the neutrons detected by bare proportional counter, located just on the ANM, 4 October 2010.

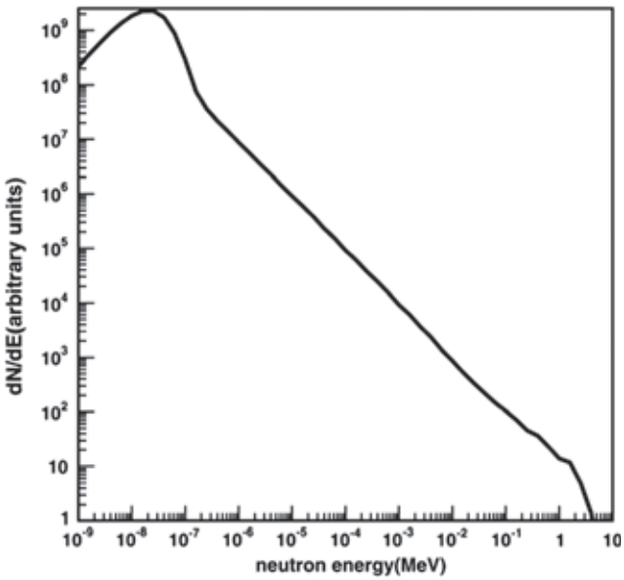


FIG. 7. Energy spectrum of the neutrons emitting upward from the polyethylene top layer of the ANM (logarithmic energy scale).

(the energy spectrum of the thermalized neutrons is depicted in Fig. 7).

The bare counter registered these neutrons having energies in the range (0.025–0.1 eV) with high efficiency [29]. Proceeding from the photonuclear neutron energy spectrum (Fig. 2) and the upward thermal neutron spectrum (Fig. 7), we simulate the expected number of hits in the bare counter on 4 October 2010 and come to an estimate of the neutron flux comparable with one we obtain by the NM counts.

## II. DISCUSSION

Simultaneous detection of the electrons, gamma rays, and neutrons by experimental facilities of the Aragats Space Environmental Center provides a convincing confirmation of the photonuclear mechanism for neutron production during thunderstorms. The "lightning" origin of the neutrons can be ruled out because not all TGEs were accompanied by lightning occurrences[4] and because the time scale of the neutron peaks in TGEs (minutes) drastically differs from the lightning time scale (milliseconds). The origin of the TGE is an extended region within a thundercloud between a negative charged layer and a positive charged layer in the bottom of the cloud (see Fig. 10 in [30]). Despite big varieties of electrical field profiles measured in the thundercloud the following basic structure of the electrical field in thunderclouds is widely accepted: from the ground up to the cloud base there is usually a low

[4]During the largest by neutron content 4 October 2010 TGE, with the neutron enhancement lasting ~5 minutes, we detected only one intracloud lightning occurrence.

magnitude field (both positive and negative); a relatively small positively charged ''pocket'' is lowermost just in the cloud base (comprising only ~20% of the negative charge higher up); a larger positive field prolongs up to a negative charge layer at 1–2 km above the cloud base; and the main positive charge is located about 1–4 km above the negative layer [31]. The lower positive charge region with the main negative layer in the middle of the cloud form, the so-called lower dipole, is responsible for the downward electron acceleration and also plays a major role in initiation of cloud-to-ground and intracloud lightning occurrences. Many researchers outline the dominant role the lower positive charge region plays in initiating/triggering intracloud and cloud-to-ground lightning discharges [32–34]. We suggest that development of the lower positive charge region also has a major role in TGE initiation.

The locality of the RREA can be explained by the small sizes of the lower positive charge region. Based on the detection of the winter thunderstorms in Japan, the authors of [35] estimate the radii of the circle of intense RREA radiation to be 600 m. Another Japanese group [36] detected movement at the speed of 7 m/ sec of an energetic radiation source at the height of 300 m along with the negatively charged region within a thundercloud at the height of around 1 km. The radiation was emitted from a downward hemispherical surface with radii of 700 m. These findings demonstrate the locality of the RREA process and imply that the number of additional gamma rays can vary significantly depending on the ''impact parameter'' of the thundercloud relative to detection site (see also [37]). Therefore, a large discrepancy of the gamma ray content can be explained by the existence of 2 types of TGE events: one with a thundercloud above the detector location, and the second outside the detector location.

Gamma rays within the RREAs are radiated in a rather narrow cone; therefore they are illuminated in a limited area below the thundercloud. Only if RREAs occurred occasionally just above the site where particle detectors are located can we expect large fluxes of the RREA electrons and gamma rays like we detected during the 19 September 2009 and 4 October 2010 TGEs. The location of the majority of TGE events is outside the detector location site and detectors measure scattered gamma ray flux; the flux enhancement usually is rather small; the amplitude of 99% of TGEs is less than 10% of the cosmic ray background. Neutrons born in the photonuclear reactions have a much wider lateral distribution and can hit a neutron monitor even if the RREA is far from the detector site. And we can expect that the ratio of neutron-to-gamma ray content of the TGE will rise proportionally to the distance of the detector from the projection of the ''center'' of the lower dipole on the Earth's surface.

To prove this statement we simulate RREA development and register gamma rays and neutrons in the circles of growing radii around the symmetry axes of the electron-gamma ray avalanche. We again put the gamma ray source at 5000 m above the detector site located at 3200 m. The number of neutrons and gamma rays was counted in concentric rings of radii enlarging on each step by 20 m. As we can see from Fig. 8 the gamma content at distances less than 100 m is prevailing and the ratio is below 2%; however, at distances above 100 m the neutron-to-gamma ray ratio starts to rise very quickly reaching 12% at 160 m. As we can see in the last column of Table II the neutron-to-gamma ray ratio reconstructed for the 2 largest events is 2.5% and 3.3%; for the rest of the events, although we cannot recover intensities of the particle flux, proceeding from the measured count rate ratio we can expect a much larger value of neutron-to-gamma ray intensities. Of course, we recognize that the TGE is due to multiple RREA processes started from numerous points in an extended region in the thundercloud; however, as we discuss above, this region is local and the edge effect will lead to dependence of the neutron-to-gamma ray ratio similar to the one we display in Fig. 8.

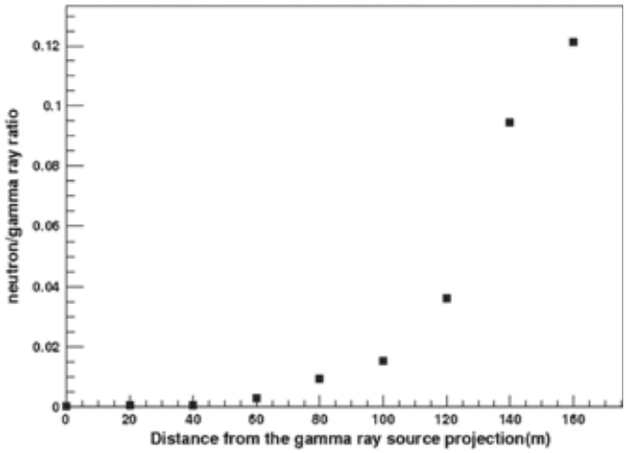


FIG. 8. Dependence of the detected-in-TGE neutron/gamma ray ratio on the distance from RREA center.

## III. CONCLUSIONS

We unambiguously prove the existence of the neutron flux linked to theTGEs and well correlated with the gamma ray flux. The mechanism of the neutron generation in the thunderclouds is the photonuclear reaction of the gamma rays born in the electron–gamma ray avalanches unleashed in the strong electrical fields of the thunderclouds (the RREA process).

Detection of the dips in the time series of the high-energy muons simultaneously with detection of very large peaks in low-energy gamma rays proves the existence of a large positive electrical field in the thunderclouds that accelerates electrons downward and demonstrates the developed positively charged layer in the bottom of the thundercloud.

## ACKNOWLEDGMENTS

This work was partly supported by Armenian government grants and by Grant No. A1554 ISTC. The authors are grateful to participants of the conference TEPA-2010 and to members of the seminar of the cosmic ray division of the Yerevan Physics Institute for useful discussion and to S. Chilingaryan for developing the ADEI multivariate visualization tool [38] for the treatment of the ASEC data flow. One of the authors (A. C.) is grateful to Brant Carlson for useful discussions on the start of work explaining the neutron content of TGE.

[1] D. Klir *et al.*, Phys. Plasmas **15**, 032 701 (2008).
[2] R. L. Fleischer, J. Geophys. Res. **80**, 5005 (1975).
[3] G. N. Shah, H. Razdan, C. L. Bhat, and Q. M. Ali, Nature (London) **313**, 773 (1985).
[4] A. Shyam and T. C. Kaushik, J. Geophys. Res. **104**, 6867 (1999).
[5] G. N. Shah, P. M. Ishtiaq, S. Mufti, and M. A. Darzi, in Burst Profile of the Lightning Generated Neutrons Detected by Gulmarg Neutron Monitor, 30th International Cosmic Ray Conference, Merida, Mexico, 2007.
[6] I. M. Martin and M. A. Alves, J. Geophys. Res. **115**, A00E11 (2010).
[7] J. Chadwick and M. Goldhaber, Nature (London) **134**, 237 (1934).
[8] L. P. Babich and R. A. Roussel-Dupré, J. Geophys. Res. **112**, D13303 (2007).
[9] A. V. Gurevich, G. M. Milikh, and Roussel-Dupre, Phys. Lett. A **165**, 463 (1992).
[10] J. R. Dwyer, B. W. Grefenstette, and D. M. Smith, Geophys. Res. Lett. **35**, L02815 (2008).
[11] H. Carmichael, "Cosmic Rays" (IQSY Instruction Manual, #7), London, 1964.
[12] C. J. Hatton, in *Progress in Elementary Particles and Cosmic Ray Physics*, edited by J. G. Wilson and S. A. Wouthuysen (North Holland, Amsterdam, 1971), Vol. 10, p. 1.
[13] A. Chilingarian *et al.*, J. Phys. G **29**, 939 (2003).
[14] A. Chilingarian *et al.*, Nucl. Instrum. Methods Phys. Res., Sect. A **543**, 483 (2005).
[15] A. Chilingarian and A. Reymers, Ann. Geophys. **26**, 249 (2008).
[16] A. Chilingarian, A. Daryan, K. Arakelyan, A. Hovhannisyan, B. Mailyan, L. Melkumyan, G. Hovsepyan, S. Chilingaryan, A. Reymers, and L. Vanyan, Phys. Rev. D **82**, 043009 (2010).
[17] A. Hovhannisyan and A. Chilingarian, Adv. Space Res. **47**, 1544 (2011).
[18] B. E. Carlson, N. G. Lehtinen, and U. S. Inan, J. Geophys. Res. **115**, a00e19 (2010).
[19] J. M. Clem and L. I. Dorman, Space Sci. Rev. **93**, 335 (2000).
[20] E. A. Maurchev, B. B. Gvozdeckij, Yu. V. Balabin, and E. V. Vashenuk, Simulation of the Response Function of Neutron Monitors, official CD of Russian Cosmic Ray Conference, Moscow State Univ., 2010.
[21] K. Watanabe *et al.*, Astrophys. J. **592**, 590 (2003).
[22] L. I. Dorman and I. V. Dorman, Adv. Space Res. **35**, 476 (2005).
[23] Y. Muraki *et al.*, Phys. Rev. D **69**, 123010 (2004).
[24] J. Wentz, I. M. Brancus, A. Bercuci, D. Heck, J. Oehlschläger, H. Rebel, and B. Vulpescu, Phys. Rev. D **67**, 073020 (2003).
[25] M. Bahmanabadi, F. Sheidaei, M. Khakian Ghomi, and J. Samimi, Phys. Rev. D **74**, 082006 (2006).
[26] N. C. Mukhopadhyay, Phys. Rep. **30**, 1 (1977).
[27] J. M. Clem, in *26th International Cosmic Ray Conference* (Salt Lake City, 1999), Vol. 7, p. 317.
[28] E. B. Hughes and P. L. Marsden, J. Geophys. Res. **71**, 1435 (1966).
[29] T. W. Crane and M. P. Baker, *Passive Nondestructive Assay of Nuclear Materials*, edited by D. Reilly *et al.* (Los Alamos National Laboratory, Los Alamos, NM, USA, 1991), Chap. 13, Technical Report No. NUREG/CR-5550, LA-UR-90-732.
[30] A. Chilingarian, G. Hovsepyan, and A. Hovhannisyan, Phys. Rev. D **83**, 062001 (2011).
[31] M. Stolzenburg, T. C. Marshall, and W. D. Rust, J. Geophys. Res. **103**, 14 079 (1998).
[32] A. Nag and V. A. Rakov, Geophys. Res. Lett. **36**, L05815 (2009).
[33] S. D. Pawar and A. K. Kamra, J. Geophys. Res. **109**, D02205 (2004).
[34] X. Qie, T. Zhang, C. Chen, G. Zhang, T. Zhang, and X. Kong, Atmos. Res. **91**, 244 (2009).
[35] H. Tsuchiya *et al.*, J. Geophys. Res. **116**, D09113 (2011).
[36] T. Torii, T. Sugita, M. Kamogawa, Y. Watanabe, and K. Kusunoki, Geophys. Res. Lett. **38**, L24801 (2011).
[37] L. Babich, E. Bochkov, I. Kutsyk, and R. Roussel-Dupre, J. Geophys. Res. **115**, A00E28 (2010).
[38] S. Chilingaryan, A. Beglarian, A. Kopmann, and S. Vöcking, J. Phys. Conf. Ser. **219**, 042 034 (2010).

PHYSICAL REVIEW D **86,** 093017 (2012)

# Remarks on recent results on neutron production during thunderstorms

A. Chilingarian,* N. Bostanjyan, T. Karapetyan, and L. Vanyan

*Yerevan Physics Institute, Alikhanyan Brothers 2, Yerevan 000036, Armenia*

(Received 24 June 2012; published 13 November 2012)

We analyze the neutron fluxes correlated with thunderstorm activity recently measured at mountain altitudes by the Tien-Shan, Tibet, and Aragats groups. We perform simulations of the photonuclear reactions of gamma rays born in the electron-gamma ray avalanches and calculate the expected count rates of the neutron detectors used by the three groups. We also present results of an independent experiment performed at the Nor Amberd high altitude research station in Armenia. Our analysis supports the Tibet and Aragats groups' conclusions on the photonuclear nature of thunderstorm-correlated neutrons (directly in the neutron monitor and in the atmosphere). The photonuclear reactions of the gamma rays born in the electron-photon avalanches in the thunderstorm atmospheres interacting with the air atoms and with lead producer of a neutron monitor can provide neutron yield compatible with additional count of neutron monitors registered during thunderstorm ground enhancements.

DOI: 10.1103/PhysRevD.86.093017 PACS numbers: 92.60.Pw, 13.40.−f, 94.05.Dd

## I. INTRODUCTION: NEUTRON PRODUCTION SIMULATIONS

Recently, three papers were published [1–3] on measuring the sizable neutron fluxes that were registered during thunderstorms. All three measurements were done at high altitudes[1] with neutron monitors [4] and thermal neutron counters. The Aragats and Tibet groups measure coinciding in time with neutrons gamma ray fluxes, although the Tibet group with a very high threshold of 40 MeV. Plastic scintillators (60 and 40 cm thick) were used to detect gamma rays. The Aragats and Tien-Shan groups, in addition to NMs, also used counters that were sensitive to neutrons (energy range of 0.025–1 eV). In all three experiments, the near surface electric field was monitored; at Tien-Shan and Mt. Aragats, the atmospheric discharges were monitored as well.

However, the three groups drastically differ in their explanations of the origin of neutron flux. The Tien-Shan group reports large fluxes of thermal neutrons correlated with atmospheric discharges; the Aragats and Tibet groups do not relate the neutron flux to lightning occurrences, but rather to photonuclear reactions of the bremsstrahlung gamma rays born in the relativistic runaway electron avalanches (RREA) [5] (also referred to as runaway breakdown [6]) in the thunderstorm atmospheres. However, the Tibet group assumes that gamma rays directly initiate NM counts by photonuclear reactions with lead producer of NM [3]; the Aragats group accepts the photonuclear reaction of the RREA gamma rays with the atmosphere as a source of neutrons [1].

The Tien-Shan group's hypothesis on the origin of neutrons is based on the large thermal neutron flux detected by an outdoor neutron detector correlated in time with atmospheric discharges. To prove their claims, the Tibet and Aragats groups, along with presenting the measured neutron fluxes, also perform the Geant4 simulations to calculate the detector response. To resolve apparent ambiguity and to clarify neutron production mechanisms, we analyze in depth the simulation schemes used for predicting the neutron yield.

In Ref. [7], the neutron production was simulated by placing the "parent" photon source at heights of 5, 7.5, 10, 15, and 20 km in the atmosphere. Gamma ray energies were drawn from the bremsstrahlung spectrum initiated by the electrons in the atmosphere regions where electrical field is above the RREA threshold. For these heights and the used gamma ray spectrum, the neutron yield relative to gamma ray flux above the photonuclear reaction threshold ($\sim$ 10 MeV) was estimated to be $\sim$0.6%.

Reference [8] simulated a homogeneous gamma ray source in the form of a disk located at the fixed altitude. The gamma ray energy was simulated according to universal spectrum of bremsstrahlung photons initiated by the RREA electrons. The neutron yield relative to 10 MeV photon flux was estimated to be $\sim$0.43%. The authors conclude that most likely the photonuclear reactions in the air account for the neutron flux increases observed at mountain altitudes.

The model used by the Aragats group for neutron yield estimation was the same as described above. The relative yield of neutrons was estimated to be 0.3–0.6%, depending on the simulation conditions [1].

The simulations performed in Ref. [3] confirmed the above-mentioned estimates of relative neutron yield. By combining neutron and photon fluxes with an efficiency of NM to register gamma rays with energies above 10 MeV and neutrons above 1 keV (Fig. 1 of Ref. [3]), the Tibet group found that bremsstrahlung gamma rays interacting with lead producer of NM explained the signal obtained by the Tibet NM, and neutrons born in photonuclear

*chili@aragats.am

[1]Aragats, 3200 m; Tien-Shan, 3340 m; Tibet, 4300 m.

 

reactions in the atmosphere give only a small fraction of the signal.

Additionally they conclude, ''Consequently, not neutrons but gamma rays may possibly dominate enhancements detected by the Aragats neutron monitor (ANM).''

To check this statement and to decide on the nature of the detected peaks in the ANM, we perform a simulation of the RREA process in the strong electric field of the thunderstorm atmosphere. Instead of putting the gamma ray source on the fixed height, we direct simulate the RREA process using the seed electrons from the ambient cosmic ray population and follow the unleashed electron-gamma-ray avalanches till their attenuation. The electron and gamma ray content of RREA as well as neutrons born in the photonuclear reactions were traced till ground level. Also, we inject electrons not from one point but from an extended area. According to estimates done in Refs. [9,10] the gamma ray emitting area has dimensions of 600–700 m. The locality of the particle-emitting region is explained by the small sizes of the lower positive charge region (LPCR) [11] located on the base of the cloud. LPCR with a negatively charged region above it in the thundercloud constitutes the so-called lower dipole, which accelerates electrons downward. Therefore, the size of the particle-emitting region cannot be greater than the size of the LPCR.

From the survived particles' rates we calculate the neutron and photon fluxes reaching the detector location on 3200 m asl. Due to much broader neutron angular distribution compared with the gamma ray one, the neutron relative yield will be a strictly increasing function of the distance from the projection of the center of radiation region in the thundercloud to the detector location (see Fig. 1). The bremsstrahlung gamma rays are producing

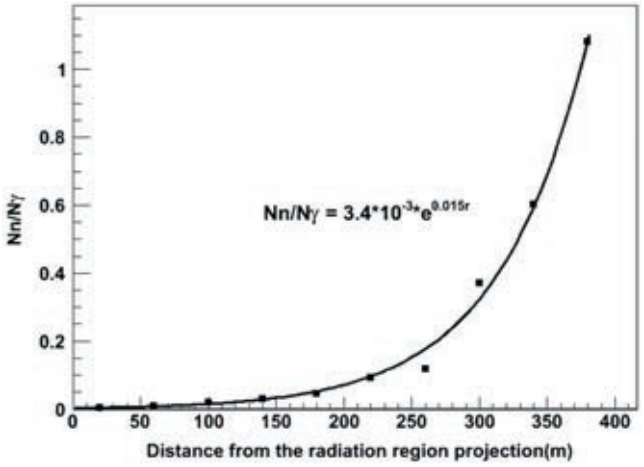


FIG. 1. Dependence of the neutron/gamma ray ratio on distance from the projection of the radiating region. Gamma rays are injected from an altitude of 4700 m according to energy spectrum measured during TGE on October 4, 2010. The detectors were located at 3200 m.

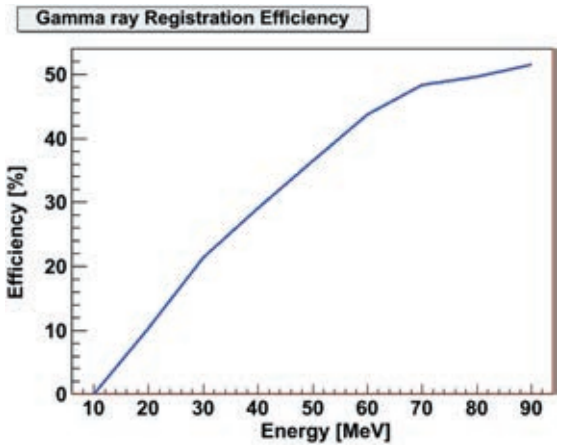


FIG. 2 (color online). The energy dependence of the photon detection efficiency by the 60-cm-thick scintillator.

in the narrow cones around vertically accelerated electrons; in contrast, neutrons emitted by the exciting nucleolus are distributed much broader.

## II. EXPLAINING NEUTRON MONITOR COUNTS: PHOTONUCLEAR REACTIONS IN THE AIR AND IN LEAD

To calculate the yield of neutrons from the photonuclear reactions of the gamma ray flux in lead, we need to recover the gamma ray flux fallen on the neutron monitor. The shape of the gamma ray flux will not differ significantly from the shape of the flux above the roof of the building, which we recovered and published in Ref. [12] for the two largest thunderstorm ground enhancements (TGEs) detected on September 19, 2009 and October 4, 2010 (see details in Refs. [13,14]). The energy dependence of the efficiency of gamma ray registration by the 60-cm-thick scintillator of the Aragats Solar Neutron Telescope is depicted in Fig. 2.

In Table I we demonstrate the bin-to-bin folding of the power law energy spectrum[2] with energy dependent efficiency acquired from Fig. 2. In the first column we depict the energy bin; in the second column we show the fraction of this particular bin relative to the energy range of 10–100 MeV; in the third column we show the efficiency of photon registration in this bin; in the last column we show the ''folded'' efficiency of the bin—the relative fraction multiplied to efficiency.

The aggregate folded efficiency of ASNT to register gamma ray flux fallen on the detector equals ~8%; we obtain this value by summing the ''partial'' efficiencies from the last column. Taking into account the registration efficiency and proceeding from the count rate enhancement of 10 280 per minute per $m^2$ at the maximal flux minute as measured by ASNT on October 4, 2010, we come to

[2]For simplicity we assume the differential energy spectrum of gamma rays in the form of $dN/dE \sim E^{-3}$.

TABLE I. The efficiency of gamma ray registration by ASNT (gamma ray spectrum is adopted from Chilingarian *et al.*, 2012b, $dN/dE \sim E^{-3}$).

| Bin size [MeV] | Bin fraction [%] | Efficiency of registration [%] | "Folded" efficiency |
|---|---|---|---|
| 10–20 | 75.00 | 4.83 | 0.0362 |
| 20–30 | 13.89 | 15.66 | 0.0217 |
| 30–40 | 4.86 | 25.58 | 0.0124 |
| 40–50 | 2.25 | 33.21 | 0.0074 |
| 50–60 | 1.22 | 40.11 | 0.0049 |
| 60–70 | 0.74 | 45.23 | 0.0033 |
| 70–80 | 0.48 | 48.76 | 0.0023 |
| 80–90 | 0.33 | 51.07 | 0.0016 |
| 90–100 | 0.23 | 51.94 | 0.0012 |

gamma ray flux incident the neutron monitor of $10\,280/0.08 \sim 130\,000$ per minute per $m^2$. To estimate how many counts in NM this flux will generate, we adopt from Fig. 1 of Ref. [3] the energy dependence of the NM efficiency to detect photons. Analogically with Table I, we obtain partial efficiencies to register gamma rays (via generated in the lead neutrons) by NM; the details are depicted in Table II.

The aggregate efficiency of the registration of gamma rays obtained by summing the partial efficiencies depicted in the last column equals ~0.095%. The expected NM count rate we obtain by multiplying the incident gamma ray flux on the aggregate detection efficiency $130\,000 * 0.00095 \sim 120$ counts per minute per $m^2$, in good agreement with the measurement by the Aragats NM on October 4 (ANM) (see Table 2 of Ref. [1]).

The estimate of expected NM counts from another "super TGE" on September 19, 2009 [13] also proves hypothesis of neutron producing by photons in lead absorber. The number of additional gamma rays detected by ASNT on September 19 was 7452 per minute per $m^2$; the recovered gamma ray flux above NM was $7\,452/0.08 \sim 93\,000$ per minute per $m^2$; the number of

TABLE II. The efficiency of gamma ray registration by neutron monitor (gamma ray spectrum is adopted from Chilingarian *et al.*, 2012b, $dN/dE \sim E^{-3}$).

| Bin size [MeV] | Bin fraction [%] | Efficiency of registration [%] | "Folded" efficiency |
|---|---|---|---|
| 10–20 | 75.00 | 0.10 | 0.000750 |
| 20–30 | 13.89 | 0.09 | 0.000130 |
| 30–40 | 4.86 | 0.04 | 1.94E-05 |
| 40–50 | 2.25 | 0.08 | 0.000018 |
| 50–60 | 1.22 | 0.09 | 0.000011 |
| 60–70 | 0.74 | 0.10 | 7.37E-06 |
| 70–80 | 0.48 | 0.10 | 4.78E-06 |
| 80–90 | 0.33 | 0.10 | 3.28E-06 |
| 90–100 | 0.23 | 0.10 | 3.28E-06 |

expected ANM was $93\,000 * 0.00095 \sim 88$ counts per minute per $m^2$, compatible with what was measured in the experiment.

However, from Table 2 of Ref. [1] we see that only for these two "super events," the large intensity of gamma rays can generate in lead enough neutrons to explain the detected NM count rate. For rest 10 smaller by gamma ray content events the neutron yield will be too small to explain the additional NM counts by the direct gamma rays' interactions with lead producer of NM. If we again look at Fig. 1, we can see that small neutron/gamma ray ratios and corresponding large gamma ray fluxes can occur infrequently when the radiating region is just above the detector. At any offset of the detector location related to the radiated region in the thundercloud, the gamma ray content will quickly diminish. In contrast, the neutron content due to a much broader angular distribution will remain more or less constant on much larger distances. Therefore, we can expect that the neutron content on large distances can reach several tens of percent of detected gamma ray flux, and if the radiation region is far from the detector location site we can detect only neutrons without gamma ray contribution. This category of neutron events (much more abundant compared with the "large gamma" events considered above) can be explained by the photonuclear reactions of gamma rays in the atmosphere. For the ten "small" events from Table 2 of Ref. [1], we can estimate that the neutron/gamma ray ratio is equal to ~5–15%, which is rather probable from pure geometrical consideration. We do not recover gamma ray intensity for the small events due to the scarcity of the energy deposit histograms measured by the 60-cm-thick scintillator. However, we can roughly estimate this intensity by considering the count rates and recovered intensities of the two largest events. The numbers of counts and recovered intensities above the roof of a building for the September 19, 2009 and October 4, 2010 events are correspondingly, 7452–104 000 and 10 280 and 153 000 per minute per $m^2$. The ratio of recovered/detected is 14 and 14.9, and the mean is 14.5. By the analogy, we can estimate the intensity of the May 21, 2009 event's registered gamma ray enhancement of 1920 as $1920 * 14.5 = 27\,840$ gamma rays per minute per $m^2$. If we assume a neutron/gamma ray ratio of 10%, we will have 2784 neutrons above the roof of the building, and proceeding from the aggregate efficiency of detecting photonuclear neutron spectra estimated to be 2.4%, we come to expect neutron monitor counts of 67 per minute per $m^2$, which is in good agreement with the 83 counts per minute per $m^2$ measured by ANM.

## III. CHECK OF HYPOTHESIS ON THERMAL NEUTRON FLUXES

Reference [2] reported the registration of intensive fluxes of low-energy neutrons generated during thunderstorms. The authors connect registered neutron fluxes with

atmospheric discharges. Unfortunately, the empirical data on neutron detector count rates were not supported by the detector response calculation and with a model of neutron generation. Only several episodes of the detected one-minute count rate enhancements that were possibly correlated in time with the lightning occurrences were presented. Reported observations were done with the Tien-Shan 18NM64 neutron monitor (TSNM) and thermal neutron counters (TSNC) located outdoors and indoors, respectively (see Fig. 2 in Ref. [15]). The counters were filled with $He^3$ gas. Because of the absence of producing and moderating material, these counters can register effectively only neutrons having energies in the range of 0.01–1 eV Gurevich *et al.*, 2012. On August 20, 2010 at 12:54, 12:56, 12:58, 13:00, and on August 10, 2010 at 8:06 and 8:08 the external counters register the following enhancements [2]: 1558, 720, 758, 2055, 1673, and 1225 per minute. The same type of TSNM counters located indoors (internal) register the following enhancements: 641, 418, 323, 716, 927, and 922 per minute, i.e., 35–75% of the outdoor (external) counters.

Neutron fluxes fell on the roof of the building where the TSNM and indoor (internal) TSNC were located. The building roof matter was comprised of 2 mm iron tilt, 20 cm carbon [2], and 2.5 cm wood. The Geant4 simulations of the neutron transport through the roof material demonstrated that only 7% (compared with 35–75% calculated above) of the thermal neutron flux can penetrate the roof.

To compare the reported TSNM counts with those expected from the detector response calculation, we have to recover the intensity of thermal neutrons that fell on the roof. A product of the registration efficiency and the total area of six helium counters is 0.45 $m^2$ [15]. Accordingly, we readily obtain the flux of thermal neutrons for six considered neutron events: 3462, 1600, 1684, 4567, 3717, and 2722 neutrons per $m^2$ per minute. Assuming 0.5% efficiency [2] of TSNM to detect thermal neutrons, we cannot expect more than 40 counts of the TSNM for all six neutron events. However, the TSNM counts reported in Ref. [2] are 804, 1136, 913, 587, 2821, and 2112 per minute.

We can assume that along with thermal neutron flux there is also a flux of neutrons born in photonuclear reaction in the thunderstorm atmosphere not detected by the outdoor TSNC. To date, the maximal estimated neutron flux at Mt. Aragats is $\sim$5000 neutrons per $m^2$ per minute. By considering the higher location of Tien-Shan we can double this number and assume that photonuclear neutron flux at Tien-Shan can reach 10000 neutrons per $m^2$ per minute. Geant4 simulations demonstrate that only $\sim$20% of photonuclear neutrons can penetrate the roof material; additionally, the 20-cm-thick carbon layer effectively termalized neutrons, and 97% of the initial neutrons incident on the indoor detectors will be termalized. Therefore, 2000 (20% of 10000) neutrons per minute per $m^2$ falling on the indoor TSNM will generate approximately the same number of counts (40 per minute per $m^2$) as the thermal neutron flux. Thus, the hypothesis of the photonuclear nature of neutron flux in Tien-Shan also cannot explain the reported count rate enhancements. Measured by the outdoor TSNC, thermal neutron flux should be five to ten times more intensive to explain the TSNC counts and 20–50 times more intensive to explain the TSNM counts.

## IV. SIMULTANEOUS DETECTION OF CHARGED AND NEUTRAL FLUXES BY NOR AMBERD DECTECTOR ASSEMBLY

New experimental evidence on neutron production correlated with thunderstorms originates from another experimental setup located on the slopes of Mt. Aragats at the Nor Amberd research station. The experimental facilities located at Nor Amberd operated as a part of the Aragats Space Environmental Center [16] and measure fluxes of gamma rays, thermal and high-energy neutrons, and high-energy muons; we consider the registration of multiple particle fluxes as an absolutely necessary condition for making physical inference on the neutron origin.

Detector assemblies measuring secondary cosmic ray fluxes that originated from protons and ions accelerated on the Sun and in the Galaxy are located on the slopes of Mt. Aragats at the Nor Amberd research station at 2000 m above sea level. The Nor Amberd detecting system consists of an 18NM64 neutron monitor (NANM) with three sections of six neutron counters in each, and a multidirectional muon monitor (NAMMM) with two layers of 5-cm-thick plastic scintillators overviewed by a photomultiplier above and below two sections of NANM. Also included are two proportional counters without a lead producer and a polyethylene moderator for detecting thermal neutrons (see Fig. 3). The energy threshold of the upper scintillators is determined by the roof matter and by data acquisition electronics and equals $\sim$10 MeV. The upper scintillator registered charged flux above the threshold with very high efficiency reaching 99%; however, the 5-cm plastic scintillator also registers neutral flux (gamma rays and neutrons) although with much smaller efficiency of $\sim$5–10%. The bottom layer of scintillators is located under a significant amount of matter including 10 cm of lead and its energy threshold is $\sim$350 MeV; therefore, the bottom layer measures mostly high-energy muons.

Data acquisition electronics calculates all possible coincidences of the upper and bottom scintillators for both sections of the NAMMM. By counting the coincidences of upper and bottom scintillators it is possible to monitor muon fluxes for 12 incident directions. The NANM operates with three dead times ranging from 0.4 to 1250 $\mu$s. The monitor counts with shortest dead time give possibility

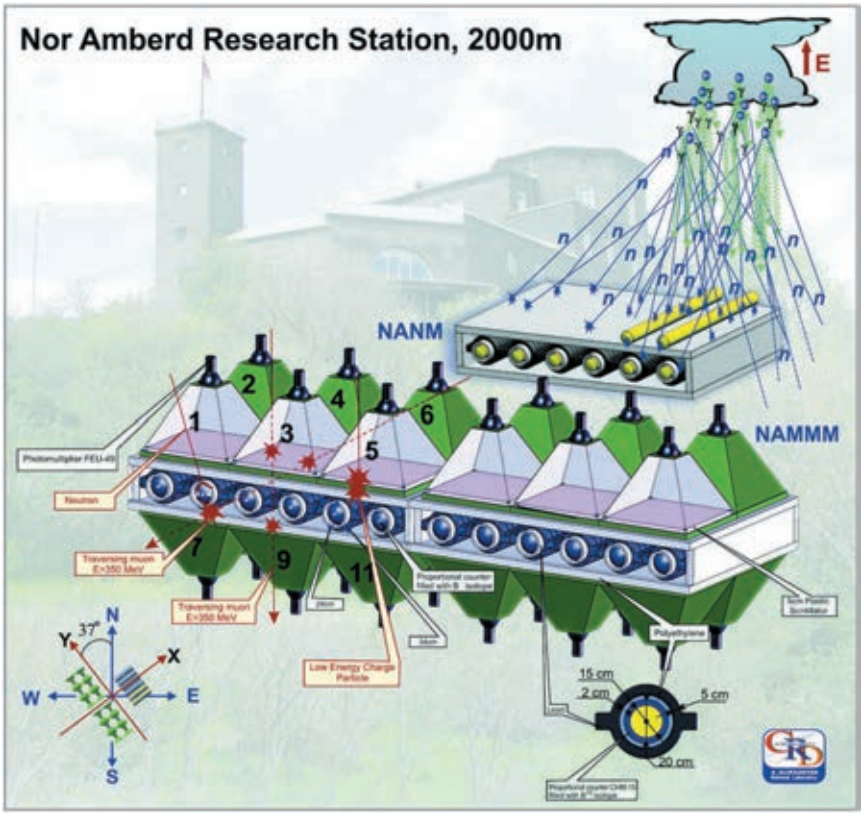


FIG. 3 (color online). Nor Amberd multidirectional muon monitor arranged above and below two sections of the Nor Amberd Neutron Monitor; ''bare'' proportional counters are located on the third section of NANM.

to count almost all thermal neutrons entering the sensitive volume of the proportional chamber; the long dead time provides a one-to-one relation between the counts and the high energy atmospheric hadrons incident on the detector. If neutron bursts are incident on detector the shortest dead time will provide a registration of almost all neutrons; the longer dead time will miss additional neutrons coming simultaneously within 1250 $\mu$s.

In Fig. 4 we post the measured enhancements of time series taken on March 28, 2009 of one-minute count rates of NAMMM top (mostly gamma rays) and bottom layers (mostly muons) as well as NANM one-minute time series corresponding to shortest dead time.

The statistical accuracy of the measurements and significances of the detected peaks are posted in Table III. In Fig. 4 we see a large enhancement of the counts in the upper layer of NAMMM conditioned in the absence of a signal in the lower layer (combination 10—a signal in the upper layer and no signals in the bottom layer of the scintillators); a significant enhancement of the count rate of the neutron monitor and a depletion of counts of high-energy muons. The deficit of muons measured simultaneously with an enhancement of gamma rays is one of the characteristics of the so-called TGEs (see details in Ref. [12]).

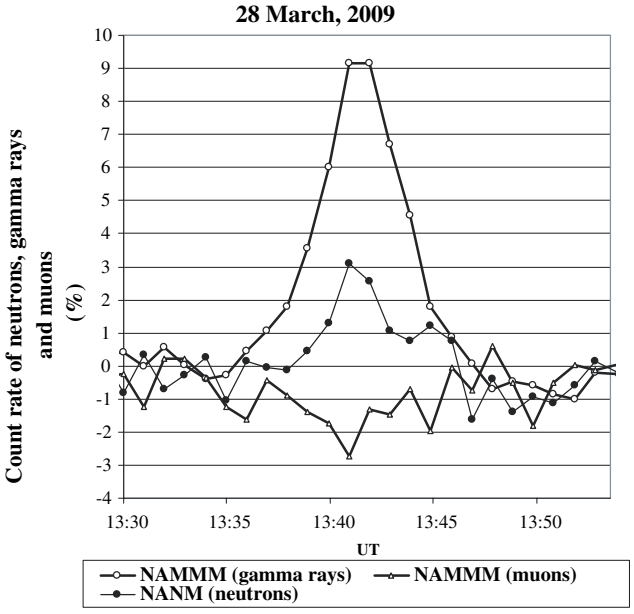


FIG. 4. The one-minute time series of count rates of upper and top layers of NANM and NANM.

TABLE III. Statistical characteristics of detectors and detected peaks and dips on March 28, 2009 at 13:43.

| Detector | Mean count rate per minute | Standard deviation-SD ($\sigma$) and relative standard deviation | Percent of enhancement | Number of SD ($\sigma$) in peak | Number of additional particles (or deficit for muons) at minute of maximal excess ($\mathrm{min}^{-1}\,\mathrm{m}^{-2}$) |
|---|---|---|---|---|---|
| NANM neutrons | 30000 | 300 (1%) | 3.2% | $3.2\sigma$ | 53 |
| NAMMM upper (10) | 121150 | 348 (0.29%) | 9.2% | $32\sigma$ | 924 |
| NAMMM (muons $>$ 350 MeV); vertical direction excluded | 24000 | 155 (0.65%) | $-2$, 2% | $3.5\sigma$ | $-$**45** |

## V. POSSIBLE SYSTEMATIC ERRORS

The assumed in the simulations charge structure of the thundercloud (strengths and elongations of the electric field, cloud height, and size of the radiating region); although they are in good agreement with rare *in situ* measurements they, can significantly deviate from the conditions of the Aragats thunderstorms, which give rise to detected TGE events. We do not measure the elongation and strength of the electrical field in the particular thundercloud. We also do not directly measure the size of the radiation region in the thundercloud. Therefore, the obtained estimates of the neutron-to-gamma-ray ratio give us overall understanding of the neutron generation process and dependence on the parameters that we cannot locate yet (distance to and geometry of the radiation region).

Estimating the neutron monitor efficiency for low-energy neutrons ( $>$ 1 keV) and photons ( $>$ 10 MeV) by simulations with Geant4 code is rather difficult due to very small values of efficiencies ( $\sim$ 0.1–2%).

In our Geant4 simulations of the Tien-Shan detectors response we used known from publications detector setup. However, it possibly changed from the published one during the experiment. Additional calculations are needed (better by the Tien-Shan group) to finally understand the measurements presented in Ref. [2].

## VI. CONCLUSIONS

We analyzed the data on recently reported neutron fluxes correlated with thunderstorms. The Tibet group explained the detected count rate enhancement in the neutron monitor by the previously neglected direct registration of gamma ray photons by NM. According to their estimates, the photonuclear reactions of gamma rays in lead producer of NM exceed the contribution of the neutrons born in the photonuclear reactions in the atmosphere. The Aragats group supported another hypothesis of the neutron production in the photonuclear reactions in the atmosphere.

A new realistic simulation of the RREA process in the thunderstorm atmosphere checked the situation. We found that the explanation of the Tibet group is supported by a new simulation if the radiation region is just above the neutron detector. At any offset of the radiation region relative to the detector location, the contribution to the NM counts of direct gamma ray interactions in a lead absorber quickly diminished and the ''atmospheric'' neutron contribution enlarged.

Therefore, both photonuclear processes in the air and in the lead absorber of NM should be considered to explain the neutron fluxes correlated with thunderstorms.

Also, we find that the simulations of neutron yield with gamma ray source located on the fixed altitude above the detector gives optimistically biased relative neutron yield. Proceeding from the thermal neutron count rates measured by the outdoor thermal neutron counter reported in Ref. [2], we calculate the expected counts of the indoor Tien-Shan neutron monitor and the indoor thermal neutron counter taking into account the detector response. The calculated fluxes of the indoor detectors are much lower than the reported ones. Thus, the reported data on indoor and outdoor detectors are not consistent.

The Aragats and Tibet measurements do not support the hypothesis of particle fluxes directly related to the atmospheric discharges, accepted by the Tien-Shan group. Accordingly, during the developed lower positive charge region in the thundercloud (necessary condition of the creation of lower dipole accelerated electrons downward), the flash rate is quite low [11,17].

[1] A. Chilingarian, N. Bostanjyan, and L. Vanyan, Phys. Rev. D **85**, 085017 (2012).

[2] A. V. Gurevich, V. P. Antonova, A. P. Chubenko, A. N. Karashtin, G. G. Mitko, M. O. Ptitsyn, V. A. Ryabov, A. L. Shepetov, Y. V. Shlyugaev, L. I. Vildanova, and K. P. Zybin, Phys. Rev. Lett. **108**, 125001 (2012).

[3] H. Tsuchiya, K. Hibino, K. Kawata *et al.*, Phys. Rev. D **85**, 092006 (2012).

[4] C. J. Hatton and H. Carmichel, Can. J. Phys. **42**, 2443 (1964).
[5] L. P. Babich, I. M. Kutsyk, E. N. Donskoy, and A. Y. Kudryavtsev, Phys. Lett. A **245**, 460 (1998).
[6] A. V. Gurevich, G. M. Milikh, and R. A. Roussel-Dupre, Phys. Lett. A **165**, 463 (1992).
[7] B. E. Carlson, N. G. Lehtinen, and U. S. Inan, J. Geophys. Res. **115**, a00e19 (2010).
[8] L. P. Babich, E. I. Bochkov, I. M. Kutsyk, and R. A. Roussel-Dupre, J. Geophys. Res. **115**, A00E28 (2010).
[9] H. Tsuchiya *et al.*, J. Geophys. Res. **116**, D09113 (2011).
[10] T. Torii, T. Sugita, M. Kamogawa, Y. Watanabe, and K. Kusunoki, Geophys. Res. Lett. **38**, L24801 (2011).
[11] A. Chilingarian and R. Mkrtchyan, Phys. Rev. D **86**, 072003 (2012).
[12] A. Chilingarian, B. Mailyan, and L. Vanyan, Atmos. Res. **114–115**, 1 (2012).
[13] A. Chilingarian, A. Daryan, K. Arakelyan, A. Hovhannisyan, B. Mailyan, L. Melkumyan, G. Hovsepyan, S. Chilingaryan, A. Reymers, and L. Vanyan, Phys. Rev. D **82**, 043009 (2010).
[14] A. Chilingarian, G. Hovsepyan, and A. Hovhannisyan, Phys. Rev. D **83**, 062001 (2011).
[15] A. P. Chubenko, A. L. Shepetov, V. P. Antonova, P. A. Chubenko, and S. V. Kryukov, J. Phys. G **35**, 085202 (2008).
[16] A. Chilingarian *et al.*, Nucl. Instrum. Methods Phys. Res., Sect. A **543**, 483 (2005).
[17] X. Qie, T. Zhang, G. Zhang, T. Zhang, and X. Kong, Atmos. Res. **91**, 244 (2009).

Astroparticle Physics 48 (2013) 1–7

Contents lists available at SciVerse ScienceDirect

Astroparticle Physics

journal homepage: www.elsevier.com/locate/astropart

# Observation of Thunderstorm Ground Enhancements with intense fluxes of high-energy electrons

Ashot Chilingarian, Levon Vanyan, Bagrat Mailyan *

*Yerevan Physics Institute, Cosmic Ray Division, Yerevan, Armenia*

ARTICLE INFO

*Article history:*
Received 1 April 2013
Received in revised form 4 June 2013
Accepted 17 June 2013
Available online 27 June 2013

*Keywords:*
Secondary cosmic rays
Atmospheric electricity
Particle detectors

ABSTRACT

The high altitude (~3200 m above sea level) of Aragats Space Environmental Center (ASEC) and low elevation of the thunderclouds provides a good opportunity to detect Thunderstorm Ground Enhancements (TGEs), particles of which rapidly attenuate in the atmosphere. In 2012, we have estimated the energy spectra of several TGEs and revealed significant electron fluxes extended till 30–40 MeV. Measured in the one and the same event gamma ray and electron fluxes allow to estimate the height of the thundercloud above the detector. Proceeding from the energy spectra and the height of the cloud we estimate the electron spectra on the exit from the electric field of the thundercloud, the number of excess electrons in the cloud and avalanche multiplication rate.



## 1. Introduction

Thunderstorm Ground Enhancements (TGEs) are direct proof of the high-energy phenomena in the terrestrial atmosphere; see review by Dwyer et al. [15] and references therein.

The origin of a TGE is a strong electrical field in a thundercloud, giving rise to rather complicated physical processes, including the following phenomena:

- Relativistic Runaway Electron Avalanches (RREA, [25,17,3,14,18];
- Modification of the Secondary cosmic ray (electrons, muons, protons and charged mesons) energy spectra (MOS, [13,20];
- Photonuclear reactions of the RREA gamma rays [10,11,24,4];
- Roentgen and gamma radiation from the lightning [16].

The direct measurement of the RREA by extended surface array of plastic scintillators was performed at Aragats in 2009 [8]. Largest TGEs consist of multiple individual electron/gamma ray avalanches. However, the electron fluxes are very difficult to study due to fast attenuation in the lower atmosphere, till now only for one TGE event it was possible to estimate the electron energy spectrum and calculate avalanche multiplication rate [7,9].

On October 7, 2012 a TGE consisting of two peaks at 14:11 and 15:08 was detected at Aragats Space Environmental Center (ASEC; [5,19]. Different types of the detector assembly operating on Aragats, quipped with sophisticated coincidences techniques, allowed performing electron/gamma ray separation and proving the existence of the large fraction of the high-energy electron flux at 15:08. At 14:11 TGE mainly consists of enhanced gamma ray flux, as the most of TGEs detected at ASEC and worldwide. Because of very fast attenuation of electrons in the atmosphere, usually TGE gamma ray flux significantly exceeds the electron flux; only for very low thunderclouds it is possible to detect electron flux. Thus, even for very low efficiencies of gamma ray registration the gamma ray contamination can be sizable in the overall TGE. To overcome this difficulty, we use in our analysis data from numerous ASEC particle detectors. Among these detectors are STAND3 layered detector and hybrid[1] ASNT (Aragats Solar Neutron Telescope, [6] and Cube detectors [2]. First we will analyze the STAND3 data, for distinguishing the high-energy electrons. Thereafter, we double check for the presence of significant electron fluxes using ASNT data. ASNT data also allows estimating the gamma ray flux. Based on these measurements and assumed spectral shape of the gamma ray flux we decide if the high-energy electrons were detected or only large fluxes of TGE gamma rays are responsible for the detector count rate enhancement. Finally, the estimated flux will be checked with Cube detector data, which allows selecting the neutral component of TGE flux. If the results from these 3 different detectors are consistent, we apply procedures of energy spectra recovery (see details in [9] and get gamma ray and electron energy spectra.

* Corresponding author. Tel./fax: +374 10 34 47 36.
*E-mail address:* mbagrat@gmail.com (B. Mailyan).

[1] Hybrid detectors consist from thick and thin plastic scintillators and due to sophisticated DAQ electronics are sensitive to both charged and neutral fluxes.

0927-6505/$ - see front matter © 2013 Elsevier B.V. All rights reserved.
http://dx.doi.org/10.1016/j.astropartphys.2013.06.006

## 2. Experimental data of the October 7, 2012 TGE

The new generation of ASEC detectors comprises from 1 and 3 cm thick molded plastic scintillators arranged in stacks (STAND1 and STAND3 detectors) and in cubical structures surrounding thick scintillators and NaI crystals for purification of detected neutral flux (Cube1 and Cube3 detectors). Light from the scintillators is reradiated by optical spectrum-shifter fibers to the long-wavelength region and passed to the FEU-115 M type photomultiplier (PM). Maximum of luminescence is on about 420 nm wavelength and luminescence time is about 2.3 ns [27]. The tuning of STAND detectors consists in selections of PM high voltage and signal discrimination threshold. The threshold is chosen to guarantee both high efficiency of signal detection and maximal suppression of the electronics noise. Tuning of STAND was made by means of the 8-channel signal analyzer developed at ASEC for online data processing [1]. Proper tuning of the detector provides 98–99% signal detection efficiency simultaneously suppressing electronic noise down to 1–2%. The data acquisition (DAQ) electronics measures and stores all coincidences of the signal appearance in the detector channels. Coincidence "1000" corresponds to signal registration only from upper scintillator, "1100" – from the first two upper scintillators, and so on. GEANT4 simulations demonstrate that STAND3 detector (see Fig. 1), can measure count rate of incident electrons with energy thresholds 5, 15, 25, 35 MeV (combinations "1000", "1100", "1110" and "1111"). The 5 MeV electrons can give signal above the discrimination level only in the upper scintillator, to be absorbed then in the scintillator body, or in the metallic tilts of scintillator housing; the 15 MeV electrons can penetrate and be registered also in the second scintillator, and so on. In this way, measuring the enhancements of count rates of above mentioned 4 combinations of detector layer operation we can recover the integral energy spectra of TGE electrons, of course, after subtracting the gamma ray contamination. The peaks of October 7, 2012 TGE measured by the layers of STAND3 detector are shown in the Fig. 2. The increases of the maximal minute count rate corresponding to various coincidences of STAND3 are shown in Table 1 in standard deviations of the measurements (number of $\sigma$).

As we can see in Table 1, at 15:08 October 7 2012, STAND3 detector registered high-energy electron TGE. Electrons with energies above 35 MeV can reach and be registered by the 1111 combination of STAND3 with efficiency dependent on energy. The efficiencies for electron detection by STAND3 detector are shown in Fig. 3. The electronics signal threshold[2] is ~3 MeV, thus, all 4 STAND3 layers can detect gamma rays with energies greater than ~3 MeV, although with much smaller registration efficiencies comparing with electron detection efficiencies. In Fig. 4, the gamma ray detection efficiencies by coincidences of STAND3 detector layers are shown. Gamma rays should have high enough energy to create high-energy charged particles, which can reach bottom layer (the gamma ray energy should be above 40 MeV to generate signal in all 4 layers with probability 1%).

Electrons with energies greater than 35 MeV will contribute to "1111" combination. In contrast, only a small fraction of high-energy gamma rays will be detected as "1111" combination. Therefore, we conclude that STAND3 data of "1111" combination proves the existence of the high-energy particles above 25 MeV at 15:08. Using GEANT 4 simulations and data from ASNT and Cube detectors we will find if there is a sizeable contamination from gamma rays.

In Fig. 5, ASNT detector consisting of upper 5 cm and lower 60 cm thick scintillator layers is depicted. Each layer consists of 4 scintillators and each scintillator has an area of 1 $m^2$. In Fig. 6, the gamma ray detection efficiencies of 5 cm and 60 cm scintillators are presented. Thicker is the scintillator more is the probability of gamma rays to interact and create charged particles, which will deposit their energy in the scintillator.

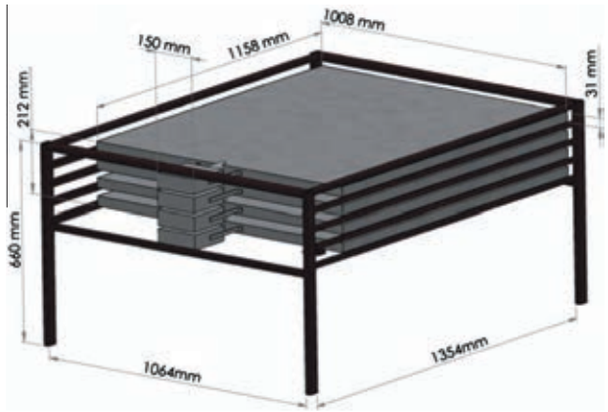


**Fig. 1.** STAND3 detector; each of 4 stacked horizontally plastic scintillators is 3 cm thick and 1 $m^2$ area.

During October 7, 2012 TGE at 15:08, the increase detected by 5 cm scintillators of the ASNT detector was twice larger than that of 60 cm scintillators (see Table 2). However, the neutral particle detection efficiency of the thick scintillator is much higher; especially for the gamma rays with energies above 30 MeV (see Fig. 6). Taking into account energy loses in the material of the roof and the electronics threshold, the minimal energy of electrons should be ~15 MeV to be measured by the 5 cm detector. Only electrons having energies above ~30 MeV can pass through the roof and the upper 5 cm scintillator layer and be detected also by 60 cm scintillator ("11" coincidence).

Detected at 15:08 small increase was measured by ASNT vertical "11" coincidence - a simultaneous signal in both scintillators (see Table 2), the probability of gamma ray detection by this coincidence is vanishingly small (the efficiency of gamma ray detection is near zero at energies <20 MeV). The increase observed by ASNT vertical coincidence confirms the "electron" nature of TGE of 15:08.

In [9], we discussed and analyzed two largest TGEs of September 19, 2009 and October 4, 2010. The September 19, 2009 TGE has the largest ever detected electron intensity. The October 4, 2010 TGE has the largest ever detected gamma ray intensity, with small electron contamination. The ratio of the enhancements in 5 cm and 60 cm thick scintillators of ASNT on September 19 was ~4 and on October 4 ~2; i.e. the largest "electron" TGE has 2 times larger ratio of thin/thick scintillator counts comparing with largest "gamma-ray" TGE. In this concern, it is worth mentioning that for the first peak detected at 14:11 October 7, 2012 the ratio of thin/thick is ~1.21, see Table 2; two times less than at 15:08. Therefore, greater is the ratio, larger is the fraction of electrons reaching the Earth's surface.

Recovered electron/gamma ray ratios above the roof of the laboratory building for the energies above 10 MeV were estimated to be 0.6 and 0.007 for September 19, 2009 and October 4, 2010 TGEs respectively (see details in [9].

The Cube assembly (Fig. 7) consists of two 20 cm thick scintillation detectors of 0.25 $m^2$ area each surrounded by 1 cm thick 1 $m^2$ area scintillators. This design ensures that no particle can hit the inside 20 cm detectors without passing through one of 1 cm scintillators. Both 20 cm thick plastic scintillators are overviewed by the PM FEU- 49 with large cathode, operating in low-noise mode.

[2] The threshold of the shaper-discriminator feed by the PM output.

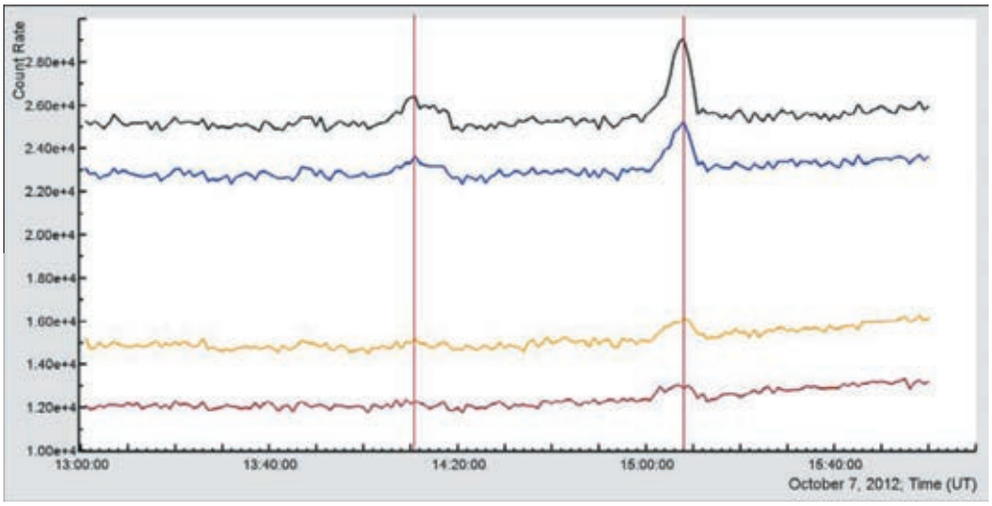


**Fig. 2.** Thunderstorm Ground Enhancements of October 7, 2012 measured by STAND3 detector; the higher count rate corresponds to the upper position of scintillator in the stack. Vertical lines show the minutes of maximal TGE flux, namely 14:11 and 15:08 UT.

**Table 1**
Count rate enhancements (or deficit) detected by STAND3 on October 7, 2012 in standard deviations.

| STAND3 Combinations | [1000] Number of σ | [1100] Number of σ | [1110] Number of σ | [1111] Number of σ |
|---|---|---|---|---|
| 14:11 | 10 | 4 | 1 | 0 |
| 15:08 | 27 | 9 | 5 | 4 |

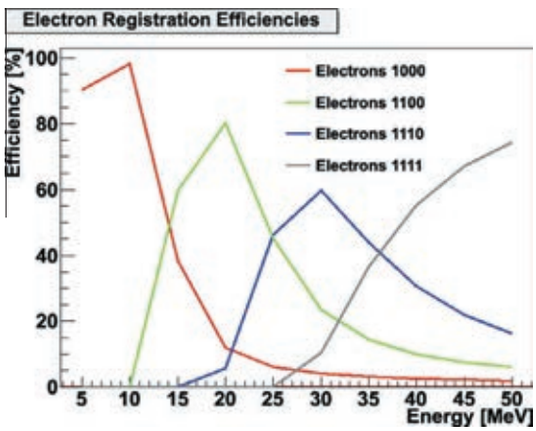


**Fig. 3.** Efficiencies of detection of the electrons by the STAND3 coincidences.

Surrounding detectors (6 units) are 1 cm thick molded plastic scintillators.

Unfortunately, the upper veto scintillator fails on October 7, 2012. Nonetheless, we have used the lower 20 cm Cube scintillator to check for the gamma ray intensity, since electrons with energies less than 50 MeV attenuate till reaching the bottom scintillator. There is no evidence of the presence of such high-energy electrons in the detected at Aragats TGEs and simulations of the RREA also demonstrate that maximal electron energy reaching ASEC detectors is 40–50 MeV [9]. On October 7 2012, Cube lower 20 cm thick scintillator detects a small increase. The increase was ∼150 and ∼250 particles at 14:11 and 15:08 respectively. We suppose that particles giving these enhancements are gamma rays with energies

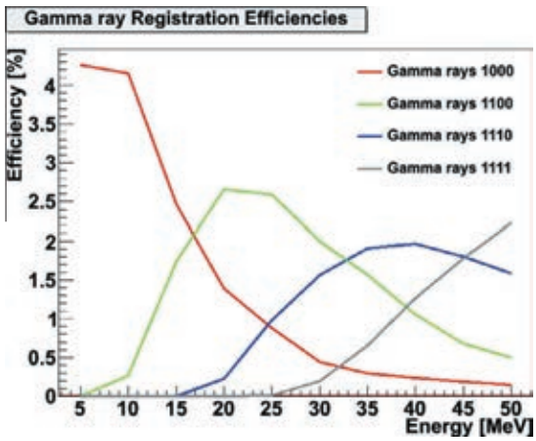


**Fig. 4.** Efficiencies of detection of the gamma rays by the STAND3 coincidences.

above 15 MeV[3], since electrons attenuate in detector substance. This data along with ASNT data helps to check for the gamma ray spectrum of the TGE and consequently to disentangle the electron and gamma ray fractions of the detected TGE.

## 3. Recovered energy spectra of electrons and gamma rays

After demonstrating that the 15:11 TGE contains high energy electrons, we shall investigate the enhancements measured by above mentioned 3 particle detectors in more details having the goal to recover the energy spectra of gamma rays and electrons.

We use the multiple spectra testing method [7] to reproduce in simulations of gamma ray fluxes the observed by STAND3 detector peaks. Dependent on the simulated gamma ray spectrum index, more or less gamma rays have to be generated to fit the measurements: hard $E^{-1}$ spectrum requires simulation of only ∼20,000 gamma rays above 10 MeV to get the measured number of STAND3 "1111" coincidence additional counts, softer $E^{-3}$ needs more

[3] On October 7, 2012, due to the high electronics threshold (all energy thresholds along with count rates are registered and stored), the particles depositing less than 15 MeV were not detected by PM.

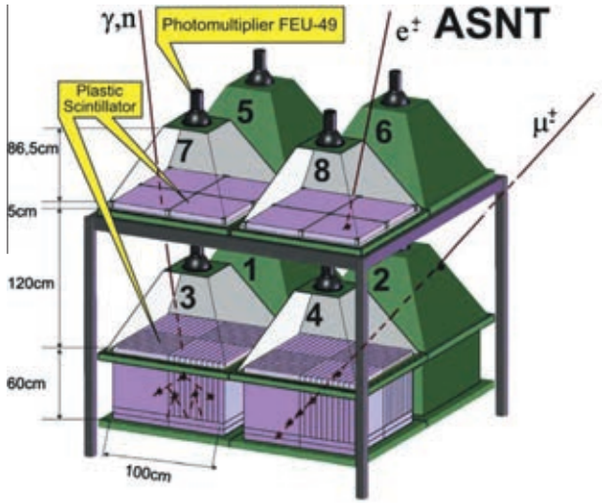


**Fig. 5.** Aragats Solar Neutron Telescope (ASNT).

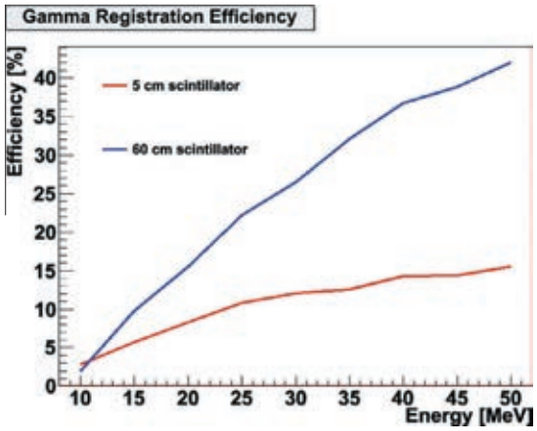


**Fig. 6.** The efficiency of gamma ray registration by ASNT 5 cm and 60 cm thick plastic scintillators.

**Table 2**
The enhancements of ASNT upper and lower layers on 7 October, 2012.

| ASNT | 60 cm | 5 cm | 5 cm/60 cm | "11" coincidence |
|---|---|---|---|---|
| The first peak 14:11 | 919 | 1110 | 1.21 | 99 |
| The second peak 15:08 | 1018 | 2357 | 2.31 | 135 |

particles, ∼150,000 to reproduce the observed peaks. Bottom 20 cm scintillator of Cube and ASNT "01" coincidence registers mostly TGE gamma rays. The anticoincidence scheme of ASNT rejects charged particles and electrons should have energy above 50 MeV to be detected by lower scintillator of Cube. In Table 3, we post required in the simulation amounts of gamma rays to reproduce the enhancement measured by the "1111" combination of STAND3 and corresponding counts of ASNT 01 and Cube bottom 20 cm scintillator along with actually measured by these detectors enhancements.

As we can see, if we assume that enhancement in "1111" coincidence of STAND3 is due to gamma rays, Cube and ASNT should measure much more particles than they do.

If we assume $E^{-2}$ spectrum, and decrease simulated intensity 4 times, we will correctly reproduce intensities measured by ASNT and Cube. Thus, only quarter of the STAND 3 "1111" combination increase can be due to gamma rays. In Table 4 we depict the intensities of measured TGE particles, along with estimated gamma ray and electron intensities, assuming $E^{-2}$ shape of the gamma ray spectrum. First supposing that the enhancements measured by STAND3 detector are due to gamma rays only, using Geant4 simulations, we estimate expected count rates of all 4 coincidences of layered detector (third row of Table 4). Then, subtracting the estimated gamma ray flux from the experimentally measured increase we obtain the residual increase, which we relay to the electron flux incident on the detector (the fourth row of Table 4). In this way we determine the fractions of electron and gamma ray fluxes in the total TGE flux from the thundercloud reaching the detector assembly. The intensities presented in Table 4 are in a good agreement with ASNT and Cube data for the high-energy electrons and gamma rays.

From the data of Table 4, we can recover electron energy spectra. The electron integral spectrum is very flat and can be fitted by the $\sim E^{-1}$ function, see Fig. 8, where the background electron spectrum at 3200 m a.s.l. and electron spectra of the largest TGEs on September 19, 2009 and October 4, 2010 are shown as well. Although at high energies the background significantly enhanced the TGE electron flux, nonetheless the relative error of the ASEC detectors is rather small (see [12]) and 2–3% enhancement of the detector count rate can be reliably identified and enumerated. The increases detected by STAND3 at 15:08, October 7, 2012 are 23%, 10%, 10% and 7% for "1000", "1100", "1110" and "1111" combinations respectively. The October 2012 TGE significantly differs from the largest TGEs on September 19, 2009 and October 4, 2010 not only by electron/gamma ray ratios, but also by spectral shapes. On September 19, 2009 TGE electron spectrum was best fitted by the exponential function $\sim\exp(-0.3*E)$ and gamma ray spectrum by the power law $\sim E^{-3}$. We have supposed that the reason of the flat spectra can be the shorter electric field lengths, since the RREA spectra will be less modified and closer to the background secondary cosmic ray electron spectra. RREA simulations show that if the length of the electric field is near 500 m, the RREA electron and gamma ray spectra's shapes are close to the seed particle (cosmic ray electron) spectra. While the field length is larger

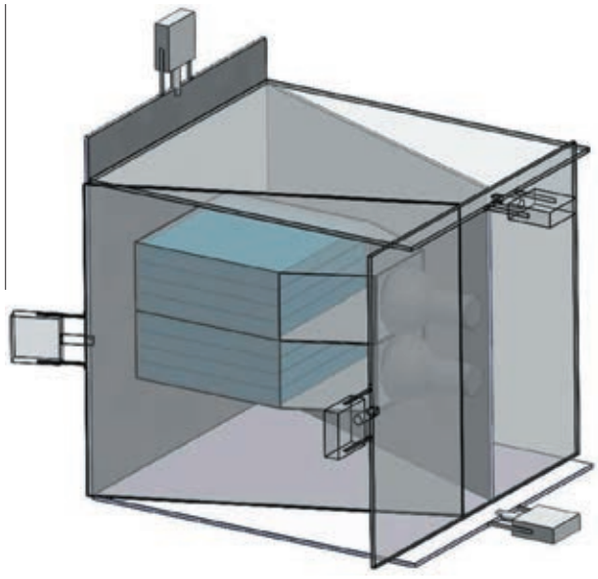

**Fig. 7.** Cube detector assembly; two 20 cm thick plastic scintillators are fully surrounded by the 1 cm thick molded plastic scintillators (veto system).

**Table 3**
Simulated gamma ray flux and corresponding ASNT 01 and Cube bottom 20 cm thick scintillator intensities along with experimentally measured values at 15:11, 7 October 2012.

| | Simulated intensity of required Gamma ray flux reproducing measured enhancement by "1111" combination of STAND3 | The same as in second column for the ASNT "01" combination | The same as in second column for the Cube bottom 20 cm thick scintillator |
|---|---|---|---|
| $E^{-1}$ | 20,000 | 3900 | 884 |
| $E^{-2}$ | 50,000 | 3500 | 1288 |
| $E^{-3}$ | 150,000 | 3400 | 2213 |
| Experimental measurements | | ~900 | ~250 |

**Table 4**
Count rates of the STAND3 and estimated numbers of electrons and gamma rays, assuming $E^{-2}$ gamma ray spectrum and electron threshold corresponding to 30% efficiency; 15:11, 7 October 2012.

| STAND3 | >5 MeV (1000) | >15 MeV (1100) | >25 MeV (1110) | >35 MeV (1111) |
|---|---|---|---|---|
| Total | 3821 ± 86 | 1531 ± 84 | 763 ± 89 | 319 ± 76 |
| Gamma ray | 2682 | 197 | 85 | 84 |
| Electron | 1139 | 1334 | 678 | 235 |

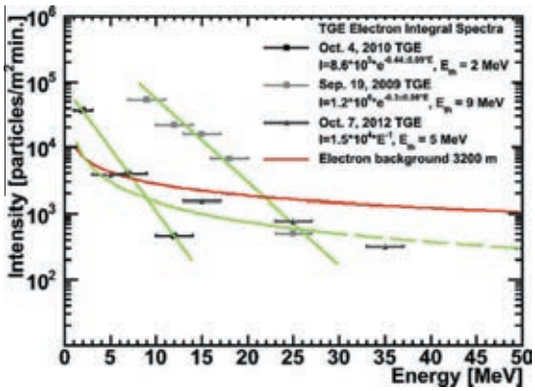


**Fig. 8.** October 7, 2012 TGE electron integral spectrum along with the largest TGE and background cosmic ray electron spectra.

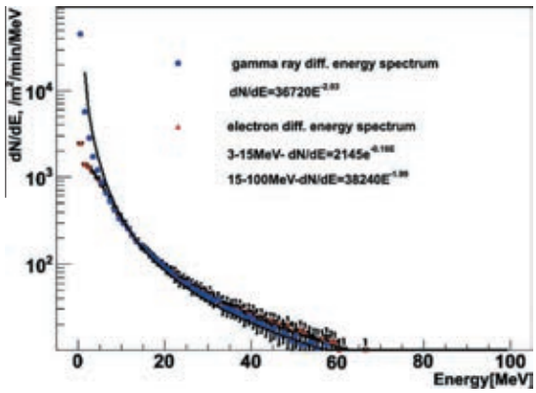


**Fig. 9.** The electron and gamma ray differential energy spectra after the electric field in thundercloud obtained from the simulations of RREA process in 500 m of 1.8 kV/cm electric field.

(1500 m), the TGE spectra differ significantly from the background spectra, due to the greater influence of unleashed runaway avalanches. Shorter electric field length could explain the spectra of 15:08, October 7, 2012 TGE, which are close to the background secondary cosmic ray electron and gamma ray spectra [21].

The results of simulations of RREA process in 500 m of 1.8 kV/cm strength uniform electric field are presented in Fig. 9. As we can see, the spectra of electrons and gamma rays are flatter in comparison to those presented in Chilingarian et al. [9] for the 1500 m of electric field length. The differential spectrum of the electrons after 500 m is well described by power function $\sim E^{-2}$ at energies >15 MeV (smaller energies do not reach the observational level, see [9]. The corresponding electron integral spectrum is fitted by function $\sim E^{-1}$, which coincidences with the recovered energy spectrum rather well. The gamma ray spectrum obtained in simulation is also in a good agreement with the estimated spectrum presented in Fig. 10.

Because of the short electric field length, gamma ray maximal energy does not reach ~100 MeV [9] as for the longer field lengths and ends near 60 MeV. Electron intensity and path length are smaller and less is the probability to emit high-energy gamma rays.

The estimated gamma ray spectrum fitted by the power function $E^{-2}$ is presented in Fig. 10 along with background gamma ray spectrum at 3200 m and spectra of the largest TGEs on September 19, 2009 and October 4, 2010. The enhancements against background are 16, 8, 5 and 4% for >10, >20, >30 and >40 MeV gamma rays respectively.

## 4. The "gamma ray" TGE at 14:11, October 7, 2012

The TGEs like occurring at 15:08 October 7, 2012 with high electron/gamma ray ratio and large maximal energy are rather rare events. The TGE occurred earlier on October 7, 2012 at 14:11 belongs to the class of more frequent events with predominant portion of gamma rays. At 14:11 the thin scintillators of ASNT have detected near the same amount of excess particles as thick scintillators; ratio of thin/thick is 1.21 see Table 2. Moreover, thick scintillators have detected near the same number of excess particles at 14:11 and 15:08. This points on the smaller electron contamination at 14:11 in comparison to the 15:08 peak (see Fig. 6). The reason of the absence of electrons can be the higher thundercloud height at 14:11. Abrupt changes in wind speed, atmospheric pressure (0.5 mbar change in half an hour) and rain rate (reaching 3 mm/h at 14:30, October 7, 2012) measured by Davis Vantage Pro weather station [26], point on the highly variable weather conditions.

Using STAND3, ASNT and Cube data, we estimate the gamma ray intensity at 14:11. From the measurements of STAND3 it is obvious that there are no electrons with energies greater than 15 MeV, since the coincidences "1111" and "1110" do not show any boost.

We have performed simulations of STAND3 detector response using the multiple spectra selection method to reproduce the ob-

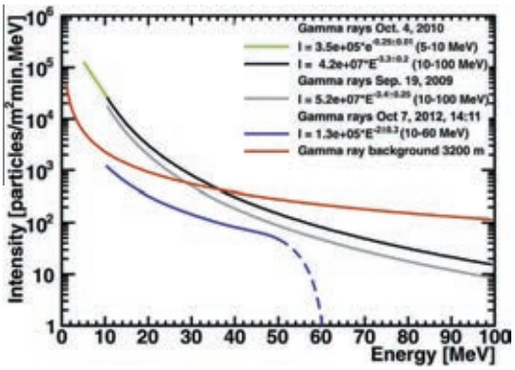


**Fig. 10.** The gamma ray spectrum of October 7, 2012 TGE along with largest TGE spectra and background gamma ray spectrum at 3200 m.

**Table 5**
STAND3 detector response simulations and measurements at 14:11, October 7, 2012.

| STAND3 | [1000] | [1100] | [1110] | [1111] |
|---|---|---|---|---|
| 14:11 | 819 | 334 | 56 | −35 |
| Simulation $\sim E^{-1}$ | 680 | 331 | 226 | 342 |
| Simulation $\sim E^{-2}$ | 906 | 136 | 44 | 63 |
| Simulation $\sim E^{-3}$ | 689 | 34 | 6 | 4 |

**Table 6**
ASNT 01 and Cube lower 20 cm scintillator data and simulation values.

| | ASNT 01 | Cube |
|---|---|---|
| $E^{-1}$ | 5529 | 872 |
| $E^{-2}$ | 1402 | 232 |
| $E^{-3}$ | 267 | 47 |
| 14:11 | ∼900 | ∼150 |

served peaks in the "1000" and "1100" combinations. Again the power law spectral shape was used with spectral indexes of −1, −2, −3 and spectral coefficient of 20,000/sq m. The gamma ray energy interval in simulation was 3–100 MeV. In Table 5, the simulation results along with the experimental measurements are presented.

As we can see from Table 5, the small enhancement detected by "1110" coincidence can be explained assuming a pure gamma ray flux using $\sim E^{-2}$ spectrum, or other spectra with diminished or increased intensities. However, the data of various coincidences do not agree with each other without involving low energy electron flux (at energies less than 15 MeV). No test spectrum supports the pure gamma ray flux and absence of electrons at all energy ranges. Again, as for the previous analyzed TGE, we use ASNT and Cube lower 20 cm detector data to estimate the number of gamma rays on October 7, 2012 at 14:11. In Table 6, the measurements and simulations are presented. As we can see, the spectrum $\sim E^{-2}$ agrees with experiment after diminishing the intensity ∼1.5 times. The spectrum $\sim E^{-3}$ also may provide a good agreement with the measurements after enlarging the incident spectrum 3.5 times; however, the STAND3 data do not support this hypothesis.

Assuming the gamma ray spectrum $\sim E^{-2}$ and diminishing the intensity in a way to fit the Cube lower 20 cm scintillator and ASNT 01 count, we obtain the electron and gamma ray fraction presented in Table 7. As we can see, the estimated >5 MeV electron number is very small in comparison to the largest TGEs and ∼4 times smaller than at 15:08.

**Table 7**
STAND3 measurements of 14:11, October 7, 2012 TGE.

| STAND3 coincidence | [1000] | [1100] | [1110] | [1111] |
|---|---|---|---|---|
| Total | 819 ± 86 | 334 ± 84 | 56 ± 89 | −35 ± 76 |
| Gamma ray simulated | 604 | 91 | 29 | 42 |
| Electron simulated | 215 | 243 | – | – |

## 5. Possible systematic errors

We do not estimate the exact length of the electric field in the thundercloud and strength of electric field; however, the obtained spectra are closer to the simulation results for 500 m rather than 1500 m field length. Additional simulation should be performed to find the relation between the field length, strength and the TGE particle spectra. Moreover, in our simulations we assume that seed electrons enter the field region at a definite height; meanwhile, secondary cosmic ray seed particles are distributed in the whole volume of the electric field in the thundercloud and are continuously accelerated from. Also different instrumentation were used to recover the TGE spectra of the largest events and the new events in 2012, which may cause uncertainties connected with the energy threshold estimation, while comparing various TGEs.

## 6. Discussion and conclusions

We have estimated the electron and gamma ray spectra of the TGE observed at 15:08 on October 7, 2013, and the gamma ray spectrum of the preceding TGE at 14:11.

The intensities and spectral indices of gamma ray fluxes are near the same for both TGEs, the difference is due to the more intense electron flux at 15:08. The gamma ray intensities at energy range >10 MeV are ∼13,000 particles/min $m^2$, ∼10 times less than for the largest gamma ray TGE on October 4, 2010.

Both gamma ray spectra have power law shape at energies above 10 MeV, with a spectral index about −2, which is harder than the spectra for the largest observed TGEs on September 19, 2009 and October 4, 2010. The electron spectrum is also harder than the previously measured spectra [7]. Since the obtained spectra shapes are closer to the background secondary cosmic ray electron spectrum, we proposed that the electric field length for October 7, 2012 TGE at 15:08 UT is shorter in comparison with the largest TGEs. We have checked the hypothesis on the short field lengths using GEANT4 simulations. The results of the simulation also support the hypothesis on short field lengths, based on the rather hard recovered spectra.

After estimating the electron and gamma ray energy spectra at the observational level (3200 m a.s.l), based on the electron/gamma ray ratio, we have estimated the thundercloud height to be ∼100 m (we assume electric field strength 1.8 kV/cm and 500 m field length). Thereafter, we have estimated the electron energy spectrum at 3300 m, i.e. ∼100 m above the observational level to be ∼130,000 per minute per $m^2$. Consequently, the multiplication rate is ∼33 and taking into account that the field length is 500 m, we can estimate the e-folding length as ∼150 m.

The maximal energy of TGE electrons and gamma rays obtained in simulations is approximately 50 MeV for the field length 500 m, i.e. gamma ray maximal energy is smaller than that obtained for longer field lengths [9]. Thundercloud height was low enough at 15:11, allowing electrons to be observed at 3200 m. We have also calculated the total number of RREA electrons assuming the electric field region having a radius 1 km, after estimating the TGE particle intensities just below the electric field in thundercloud to be $\sim 4.2 * 10^{11}$, which is $\sim 10^2$ times less than for September 19, 2009

TGE and $\sim 10^4$ less than for October 4, 2010 TGE. This is another argument supporting the hypothesis of the short electric field.

Tsuchiya et al. [23] had measured the fluence of gamma rays at sea level for energies above 1 MeV to be $\sim 2*10^4\,m^{-2}$, which is comparable to our results. However intensities obtained for Aragats are higher, because of lower thundercloud height.

Experiments carried by the Japanese group [24] are in a good agreement with our results. The estimated gamma ray spectrum index was also $\sim 2$, however the thundercloud height was 600–900 m, which did not allow to measure the electron spectrum.

Tsuchiya et al. [24] have measured TGE gamma ray spectra, whereas, till now only Chilingarian et al. [7] had reported on the TGE electron spectra. The indices of estimated gamma ray spectra are in good agreement also with the measurements of TGF spectrum reported by Tavani et al. [22].

## References


[1] K. Arakelyan et al., New electronics for the Aragats Space-Environmental Center (ASEC) Detectors, in: Proc. of FORGES 2008 international synposium, Tigran Mets, 2009, pp. 105–116.
[2] K. Avakyan, K. Arakelyan, A. Chilingarian, A. Daryan, L. Melkumyan, D. Pokhsraryan, D. Sargsyan, New low threshold detectors for measuring electron and gamma ray fluxes from thunderclouds, J. Phys. Conf. Ser. 409 (2013) 012223.
[3] L.P. Babich, I.M. Kutsyk, E.N. Donskoy, A.Yu. Kudryavtsev, New data on space and time scales of relativistic runaway electron avalanche for thunderstorm environment: Monte Carlo calculations, Phys. Lett. A 24A (1998) 460.
[4] L.P. Babich, E.I. Bochkov, I.M. Kutsyk, A.N. Zalyalov, On amplifications of photonuclear neutron flux in thunderstorm atmosphere and possibility of detecting them 2013, published in Pis'ma v Zhurnal Eksperimental'noi i Teoreticheskoi Fiziki, 97(6), 2013, pp. 333–339, JETP Lett. 97 (6) (2013) 291–296. © Pleiades Publishing, Inc..
[5] A. Chilingarian, K. Arakelyan, K. Avakyan, et al., Correlated measurements of secondary cosmic ray fluxes by the Aragats Space-Environmental Center monitors, Nucl. Instrum. Methods Phys. Res. Sect. A 543 (2–3) (2005) 483–496.
[6] A. Chilingarian, L. Melkumyan, G. Hovsepyan, A. Reymers, The response function of the Aragats Solar Neutron Telescope, Nucl. Instrum. Methods Phys. Res. Sect. A 574 (2007) 255–263.
[7] A. Chilingarian, A. Daryan, K. Arakelyan, et al., Ground-based observations of thunderstorm-correlated fluxes of high-energy electrons, gamma rays, and neutrons, Phys. Rev. D 82 (2010) 043009.
[8] A. Chilingarian et al., Particle bursts from thunderclouds: natural particle accelerators above our heads, Phys. Rev. D 83 (2011) 062001.
[9] A. Chilingarian, B. Mailyan, L. Vanyan, Recovering of the energy spectra of electrons and gamma rays coming from the thunderclouds, Atmos. Res. 114–115 (2012) 1–16.
[10] A. Chilingarian et al., Neutron bursts associated with thunderstorms, Phys. Rev. D 85 (2012) 085017.
[11] A. Chilingarian et al., Remarks on recent results on neutron production during thunderstorms, Phys. Rev. D 86 (2012) 093017.
[12] A. Chilingarian, H. Mkrtchyan, Role of the Lower Positive Charge Region (LPCR) in initiation of the Thunderstorm Ground Enhancements (TGEs), Phys. Rev. D 86 (2012) 072003.
[13] L. Dorman I, I. Dorman V, Possible influence of cosmic rays on climate through thunderstorm clouds, Adv. Space Res. 35 (2005) 476–483.
[14] J.R. Dwyer, A fundamental limit on electric fields in air, J. Geophys. Res. 30 (20) (2003) 2055, http://dx.doi.org/10.1029/2003GL017781.
[15] J.R. Dwyer, D.M. Smith, S.A. Cummer, High-energy atmospheric physics: terrestrial gamma-ray flashes and related phenomena, Space Sci Rev. (2012), http://dx.doi.org/10.1007/s11214-012-9894-0.
[16] J.R. Dwyer, M.M. Schaal, E. Cramer, S. Arabshahi, N. Liu, H.K. Rassoul, J.D. Hill, D.M. Jordan, M.A. Uman, Observation of a gamma-ray flash at ground level in association with a cloud-to-ground lightning return stroke, J. Geophys. Res. 117 (2012) A10303, http://dx.doi.org/10.1029/2012JA017810.
[17] A.V. Gurevich, G.M. Milikh, R.A. Roussel-Dupre, Runaway electron mechanism of air breakdown and preconditioning during a thunderstorm, Phys. Lett. A 165 (1992) 463.
[18] N.S. Khaerdinov, A.S. Lidvansky, V.B. Petkov, Cosmic rays and electric field of thunderclouds: evidence for acceleration of particles (runaway electrons), Atmos. Res. 76 (2005) 346–354.
[19] B. Mailyan, A. Chilingarian, Investigation of diurnal variations of cosmic ray fluxes measured with using ASEC and NMDB monitors, Adv. Space Res. 45 (2010) 1380.
[20] Y. Muraki et al., Effects of atmospheric electric fields on cosmic rays, Phys. Rev. D 69 (2004) 123010.
[21] T. Sato, A. Endo, M. Zanki, N. Petoussi-Henss, K. Niita, Fluence-to- dose conversion coefficients for neutrons and protons calculated using the PHITS code and ICRP/ICRU adult reference computational phantoms, Phys. Med. Biol. 54 (2009) 1997.
[22] M. Tavani et al., Terrestrial gamma-ray flashes as powerful particle accelerators, Phys. Rev. Lett. 106 (2011) 018501.
[23] H. Tsuchiya, T. Enoto, S. Yamada, et al., Detection of high-energy gamma rays from winter thunderclouds, Phys. Rev. Lett. 99 (2007) 165002.
[24] H. Tsuchiya, K. Hibino, K. Kawata, et al., Observation of thundercloud-related gamma rays and neutrons in Tibet, Phys. Rev. D 85 (2012) 092006.
[25] C.T.R. Wilson, The acceleration of b particles in strong electric fields such as those of thunderclouds, Proc. Cambridge Philos. Soc. 22 (1925) 534–538, http://dx.doi.org/10.1017/S0305004100003236.
[26] http://www.davisnet.com/.
[27] http://www.ihep.su/.

Journal of Atmospheric and Solar-Terrestrial Physics 107 (2014) 68–76

Contents lists available at ScienceDirect

Journal of Atmospheric and Solar-Terrestrial Physics

journal homepage: www.elsevier.com/locate/jastp

# Thunderstorm ground enhancements—Model and relation to lightning flashes

A. Chilingarian*

*Yerevan Physics Institute, Armenia*

ARTICLE INFO

*Article history:*
Received 16 March 2013
Received in revised form
6 November 2013
Accepted 7 November 2013
Available online 15 November 2013

*Keywords:*
Atmospheric electricity
Thunderstorms
Electron acceleration
Lightning initiation

ABSTRACT

In the beginning of last century C.T.R. Wilson proposed that strong electric field of the thunderclouds might accelerate electrons to very high energies. However, this and many other electromagnetic processes in our atmosphere are poorly understood till now; the key questions about the thundercloud electrification and lightning initiation remain unanswered. During recent decades several observations of gamma ray, electron and neutron fluxes correlated with thunderstorms were reported. Nonetheless, the origin of these fluxes is under debate till now. The direct registration of the particle showers initiated by the runaway electrons (the most popular theory) was missing. We present the experimental evidence of the microsecond duration electron bursts originated from runaway electrons accelerated in thunderclouds. The electron acceleration downward becomes possible after creation of the Lower Positive Charged Region below the main negative charged layer in the middle of the thundercloud. Our analysis is based on the vast thunderstorm data from the Aragats Mountain in Armenia, 3200 m above sea level. Varieties of particle detectors located at Aragats Space Environmental Center are registering neutral and charged particle fluxes correlated with thunderstorms, so-called Thunderstorm Ground Enhancements. Simultaneously the electric mills and lightning detectors are monitoring the near-surface electric field and lightning flashes. In the paper we present the model of TGE initiation. We demonstrate the necessity of the Lower positive charge region development for the lower dipole operation and TGE initiation. Our observations establish direct relationship of the negative electric field strength and rain rate with TGE.


## 1. Introduction

One of the first particle physicists and researchers of the atmospheric electricity Nobel award winner sir C.T.R. Wilson in the beginning of last century recognized that "the occurrence of exceptional electron encounters has no important effect in preventing the acquisition of large kinetic energy by particles in a strong accelerating field" (Wilson, 1925a). It was the first publication introducing an enigmatic physical phenomenon of electron acceleration by the strong electric fields in thunderclouds called "runaway" electrons by the astronomer Eddington (1926).

Of course, in 1925 the particle cascade theory was not yet established, the measurements of the electric field in thunderclouds were not done and C.T.R. Wilson overestimated the scale of electron acceleration. He thought that electrons could gain unlimited energy from the electric field: "The general effect of an accelerating field is that a beta-particle, instead of dying as it were a natural death by gradual loss of energy, is continually acquiring more and more energy and increasing its chance of surviving all accidents other than direct encounters with the nuclei of atoms" (Wilson, 1925a) and "A particle may thus acquire energy corresponding to the greater part of the whole potential difference between the poles of the thundercloud, which may be of the order of $10^9$ V" (Wilson, 1925b). However, that is not possible, due to abundant radiation losses of electrons with energies greater than 50 MeV traversing the atmosphere. The first measured runaway electron spectrum in thunderstorm ground enhancements faded around 50 MeV (Chilingarian et al., 2010). The potential difference as large as $10^9$ V also seems to be not feasible according to direct measurements of the intracloud electric fields with the balloon experiments (Stolzenburg and Marshall, 2008).

The first model of the structure of the electric field in thunderclouds anticipates a dipole between negative charged layer in the middle of the thundercloud and positive layer on the top. This, so called, main negative dipole[1] accelerated electrons upward. Wilson wrote: "In the central dipole region, where the downward-directed electric field is greatest, the electrons are accelerated upward to the positive layer but once above the positive layer, their motions are retarded by the electrostatic field

* Tel.: +37 435 2041; fax: +374 135 2041.
*E-mail address:* chili@aragats.am

1364-6826/$ - see front matter © 2013 Elsevier Ltd. All rights reserved.
http://dx.doi.org/10.1016/j.jastp.2013.11.004

[1] We adopt the "atmospheric electricity" sign convention: the positive field (E kV/m) accelerates electrons downward in the direction of the Earth; the negative field (−E kV/m) vice-versa accelerates electrons upward in the direction of space.

and their trajectories bend downward again (Wilsons notebooks, cited by Williams (2009)) and "Fast beta rays can then reach the atmosphere or be bent around by magnetic field to reach Earth at varying distances according to energy and initial directions" (letter to B.F.J. Schonland, cited by Williams (2009)).

The more realistic tripole structure of the thundercloud electric field introducing the short leaving Lower positive charged region (LPCR) below the main negative was established only recently and till now its origin is not fully understood. The LPCR on the base of cloud with middle negatively charged layer constitute lower negatively charged dipole, which accelerates electrons downwards. Electrons accelerated by the lower dipole produce, so-called, thunderstorm ground enhancements—TGEs, intense fluxes of electrons, gamma radiation and secondary neutrons (Chilingarian et al., 2011). The idea of Wilson that accelerated electrons can reach the atmosphere find proof after launching of the orbiting gamma ray observatories. Numerous terrestrial gamma flashes (TGFs) are routinely observed at ~500 km above Earth in correlation with strong equatorial thunderstorms (Fishman et al., 1994). The origin of TGFs is believed to be the electrons accelerated by the upper dipole as Wilson suggested in 1925.

The first attempts to observe the runaway electrons on the earth surface were carried out by Wilson's co-workers Schonland, Viljoen and Halliday in South Africa with the cloud chambers. However, due to low sensitivity of cloud chambers to low energy gamma rays (the majority of particles reaching the earth surface from the electron–photon avalanches unleashed by runaway electrons in the thunderclouds are gamma rays) the results of these experiments were discouraging. Looking for the electrons with energies up to 5 GeV incident to the earth surface following the force lines of geomagnetic field surely could not give a positive outcome (see Halliday, 1941). The observation of the runaway electron phenomena turns to be rather difficult. "In summary and as introduction to the present set of experiments, after 70 years of repeated theoretical and experimental investigations, it is still not clear whether or not the runaway electron acceleration mechanisms operates in a significant manner in either thunderstorms or lightning" (Suszcynsky et al., 1996). In last 2 decades there was significant progress in detection of the particles (mostly gamma rays) from thunderclouds (Parks et al., 1981; McCarthy and Parks, 1985; Aglietta et al., 1989; Eack et al., 2000; Brunetti et al., 2000; Alexeenko et al., 2002; Torii et al., 2002; Tsuchiya et al., 2007). However, till now there are numerous unsolved problems concern complicated TGE phenomena. Some of these problems, i.e., the model of TGE; the nature of emerging LPCR; TGE relation to atmospheric discharges will be presented and discussed in the paper.

## 2. Research made on Aragats Space Environmental Center (ASEC)

Cosmic Ray Division (CRD) of the A. Alikhanyan National lab (Yerevan Physics Institute) during recent 20 years commissioned and operated on the research station Aragats and Nor Amberd numerous particle detectors uninterruptedly registering fluxes of charged and neutral cosmic rays. The main topic of research was physics of the high-energy cosmic rays accelerated in our Galaxy and beyond. Surface arrays consisting of hundreds of plastic scintillator were measuring Extensive air showers (EASs), the cascades of particles born in interactions of primary high-energy proton or fully stripped nuclei with atoms of terrestrial atmosphere. Aragats physicists investigate the, so-called, knee region, where energy spectrum of protons and nuclei suddenly change the spectral index from −2.7 to −3. A new developed method of distinguishing between showers initiated by primary particles lead to possibility of measuring partial spectra and the exploration of the particle acceleration mechanism by the shock waves in vicinity of exploding super-novae stars. MAKET-ANI experiment proves very sharp knee in light nuclei energy spectrum at energies of 2–3 PeV and absence of knee in heavy nuclei energy spectrum up to 20 PeV (Chilingarian et al., 2004). This finding of charge dependent position of the knee was later confirmed by the KASCADE experiment (Antoni et al., 2005).

After finishing EAS experiments on Aragats was started a new excited topic—Solar physics and Space Weather. The neutron monitors located at 3200 and 2000 m and numerous new particle detectors measuring charged and neutral components of secondary cosmic rays making Aragats one of the largest centers for researching of solar-terrestrial connections. During 23-rd solar activity cycle were measured many important Solar energetic events, including largest series of GLEs (Ground level enhancements) and Forbush decreases in November 2003 (so-called Halloween events) and discovery of the highest energy solar protons at 20 January 2005 (Chilingarian, 2009). Culmination of the solar physics research was creation of the SEVAN (Space Environmental Viewing and Analysis Network) a network of particle detectors located at middle and low latitudes, which aims to improve fundamental research of space weather conditions and to provide short and long-term forecasts of dangerous consequences of space storms (Chilingarian and Reymers, 2008). The SEVAN network consists of hybrid detectors registering charged and neutral components of secondary cosmic rays. The network detects changing fluxes of different species of secondary cosmic rays at different altitudes, longitudes and latitudes, thus turning into a powerful integrated device used to explore solar modulation effects.

Starting from 2008 during very quiet 24-th solar activity cycle the CRD turns to investigations of the high-energy phenomena in the atmosphere. Existing and new designed particle detectors and unique geographical location of Aragats station allow to observe in 5 years more than 300 particle bursts, which were called TGEs—thunderstorm ground enhancements. TGEs observed on Aragats are not only gamma rays, but also sizable enhancements of electrons (Chilingarian et al., 2013b) and rarely also neutrons, usually lasting 10 min or more. Aragats physicists enlarge the possibilities for TGE research by coherent detection of the electrical and geomagnetic fields, rain rate, temperature, relative humidity and other meteorological parameters, as well as by detection of the lightning. Adopted multivariate approach of investigations allows connecting different fluxes, fields and lightning occurrences and finally establishing comprehensive model of the TGE.

The same approach allows unambiguously proving the existence of the neutron fluxes linked to the TGEs and well correlated with the gamma ray fluxes. The mechanism of the neutron generation by the photonuclear reaction of the gamma rays born in thunderclouds was suggested in Babich and Roussel-Dupré (2007) and observed at Aragats during the strongest TGEs (Chilingarian et al., 2012a). A new realistic simulation of the RREA process in the thunderstorm atmosphere helps to clarify contribution of the direct gamma ray production in a lead absorber to the Neutron monitor counts (NM, Tsuchiya et al., 2012). At any offset of the "emitting region" relative to the detector location the "direct neutron production" quickly diminished and the "atmospheric" neutron contribution enlarged (Chilingarian et al., 2012b). Therefore, both photonuclear processes in the air and in the lead absorber of NM should be considered to explain the neutron fluxes correlated with thunderstorms.

## 3. Extensive cloud showers—Experimental proof of the runaway process

Gurevich et al. (1992) developed a theory of the runaway process. They showed that when Møller scattering (electron–electron elastic scattering) is included, the runaway electrons described by Wilson will undergo avalanche multiplication, resulting in a large number of

relativistic runaway electrons and gamma rays for each energetic seed electron injected into the strong electrical field region. Further development of the theoretic knowledge on the runaway process continued with intensive implementation of the Monte Carlo simulation. Sophisticated codes was used to model the propagation of energetic electrons in electric field; codes include energy losses from ionization and atomic excitation, Møller scattering and angular diffusion from elastic scattering with atomic nuclei and other (Lehtinen et al., 1999; Babich et al., 2001; Dwyer, 2003, 2007).

Recently the CERN based GEANT 4 code (Agnsotelli et al., 2003) is widely used for study of the propagation of the runaway electron avalanches in the atmosphere (Carlson et al., 2010; Chilingarian et al., 2012c). It is interesting to note that the runaway process is naturally embedded from the GEANT4 simulations: when you switch on appropriate electrical field and use incident cosmic ray electron flux as seeds; the electrons gain energy from field, knock-out atomic electrons and cascade process unleashed; it is another proof that simulation is a creative tool to discover new physical phenomena. The initial name of the cascade released by the runaway electron—the Runaway breakdown (RB, given by Gurevich et al. (1992)), pointed on the relation with lightning occurrence (not proven yet), is recently often replaced by the term RREA (Relativistic Runaway electron avalanches) without any relation to discharge process.

The first observation of the avalanches initiated by the runaway electrons was made at Aragats in 2009 (Chilingarian et al., 2010, 2011). An array of 16 plastic scintillators (Fig. 1, see details of experimental facility in Chilingarian et al. (2004)) was used for detection of extended atmospheric particle showers.

If signals from the first 8 scintillators covering $\sim$400 m$^2$ area coincide within the trigger window time of 400 ns the amplitudes of all photomultiplier signals (proportional to the number of particles hitting each scintillator) are stored. At fair weather the surface array registered EASes initiated by the primary protons with energies above $\sim$50 TeV ($\sim$25 EAS per minute, 8-fold coincidences) and 100 TeV ($\sim$8 EAS per minute, 16-fold coincidences).

In Fig. 2 we demonstrate the detection of the largest TGE ever measured at Aragats. The significance of detection at energies above 7 MeV exceeds 350$\sigma$. Measuring electron flux with different thresholds allows recovering for the first time the electron integral energy spectrum (see details in Chilingarian et al. (2010)).

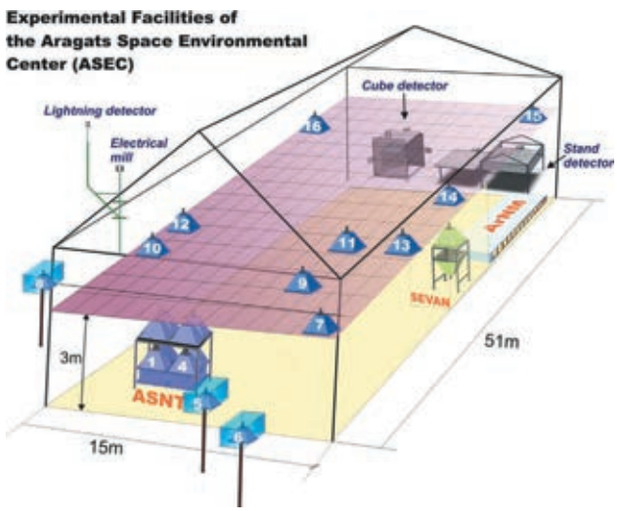


**Fig. 1.** Experimental facilities of the ASEC; 5 cm thick and 1 m$^2$ area plastic scintillators belonging to the MAKET surface array are denoted by numbers from 1 to 16. On the roof of building are located Electrical mill EFM 100 and lightning detector LD-250 of BOLTEK firm.

The time series of the surface array triggers also demonstrate huge enhancement, see Fig. 3. During 7 min of the TGE $\sim$200 additional triggers were registers; the count rate at 22:47, 19 September 2009 was enhanced $\sim$8 times for the 16-fold coincidences and 5 times for the 8-fold coincidences.

The minute of the maximal count of triggers coincides with maximal flux of particles registered by other detectors sensitive to electrons, gamma rays and neutrons. The statistical analysis of detected showers reveals their systematic difference from the EAS events (see for details Chilingarian et al. (2011)): the density of shower particles hitting the scintillators was much lower and spatial spread was much more uniform (spatial distributions of the EASes has characteristic bell-like form). Therefore, the showers of electrons and gamma rays from the thunderclouds constitute different from EAS physical phenomena —extensive cloud showers (ECSs, Chilingarian and Hovsepyan (2013)). ECS phenomenon is very rare: only 3 TGEs from 300 observed were accompanied by ECSes. ECSes originated from individual runaway electrons accelerated in the cloud just above the detector. Duration of ECS is expected to be very short: the arrival time of the shower particles from the thundercloud located not higher than few hundreds of meters above the detector could not be large. We do not measure shower particle arrival on microsecond scale; however the statistical analysis of particle second-by-second distribution within the minutes of maximal flux allows estimating the upper limit of ECS duration to be 50 ms (see for details Chilingarian et al. (2011)).

Like multiple EASs from the primary cosmic rays are sustaining stable flux of secondary cosmic rays, multiple ECSes provide transient enhancement of the TGEs lasting minutes. ECS phenomenon is very local and depends on the height of cloud above detector and on the strength of electric field in it. Both parameters are fast changing and only during several minutes cascades from runaway electrons can develope enough to cover several thousand square meters of surface. Only very suitable location and large sizes of the scintillators allow detecting ECSes on Aragats and for the first time directly proving existence of RREA phenomena.

The variety of particle detectors on Aragats allows also measuring the integral spectrum of TGE electrons and differential energy spectrum of gamma rays up to 100 MeV (before the gamma ray energy spectrum was measured only till 20 MeV). The energy spectra of the electrons have an exponential shape and extend up to 40–50 MeV. Recovered energy spectra of the gamma rays are power law and extend up to 100 MeV.

Prolonged up to 100 MeV gamma ray spectrum also was obtained by gamma ray observatory onboard of AGILE satellite (Tavani et al., 2011). Summed over 130 events fluence spectrum does not exhibit the exponential decay at 50–60 MeV as expected from the “pure” RREA mechanism.

Energy spectra of largest TGE events detected in 2009 and 2010 were recovered by the solving inverse problem of cosmic rays—fitting trial energy spectra by simulating the energy response of 60 cm thick plastic scintillator (see details in Chilingarian et al. (2012c)). After installing the network of large NaI crystals in 2011 the energy spectra of gamma rays were measured directly (Chilingarian et al., 2013).

Maximal flux of gamma rays exceeds background of secondary cosmic rays by $\sim$1000% in the energy range of 2–20 MeV and by 1–10% in the energy range up to 100 MeV. Very large enhancements can be explained only by invoking the RREA process. Ambient population of secondary cosmic ray electrons in the electric fields with strength greater than the critical value unleashes the electron-gamma ray avalanches and total number of particles on the exit from cloud can be multiplied by several orders of magnitude. A GEANT4 simulation helps to estimate characteristics of the thunderclouds

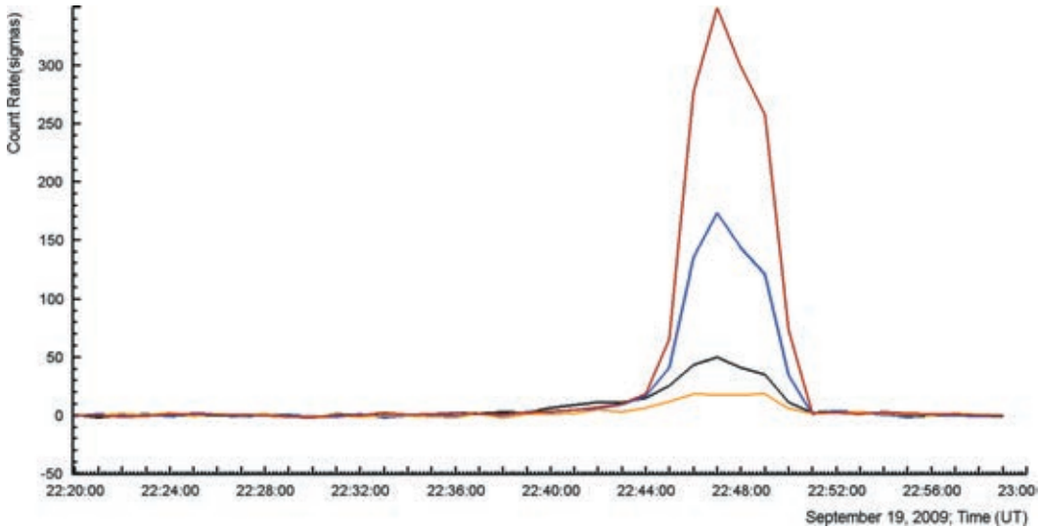


**Fig. 2.** The enhancements of ASEC detectors measured on 19 September 2009 (the maximum of flux at 22:47 UT) in numbers of standard deviations (number of $\sigma$). The 1 $m^2$ area 5 cm thick outdoor and indoor plastic scintillators measure electron flux with energies above 7 and 10 MeV (2 upper curves); the same type plastic scintillators of SEVAN – with energies larger that 15 MeV (next curve) and coincidence of 5 and 60 cm scintillators of ASNT – with energies above 30 MeV (lowest curve). Corresponding significance of peaks are 350, 170, 50 and 20 standard deviation.

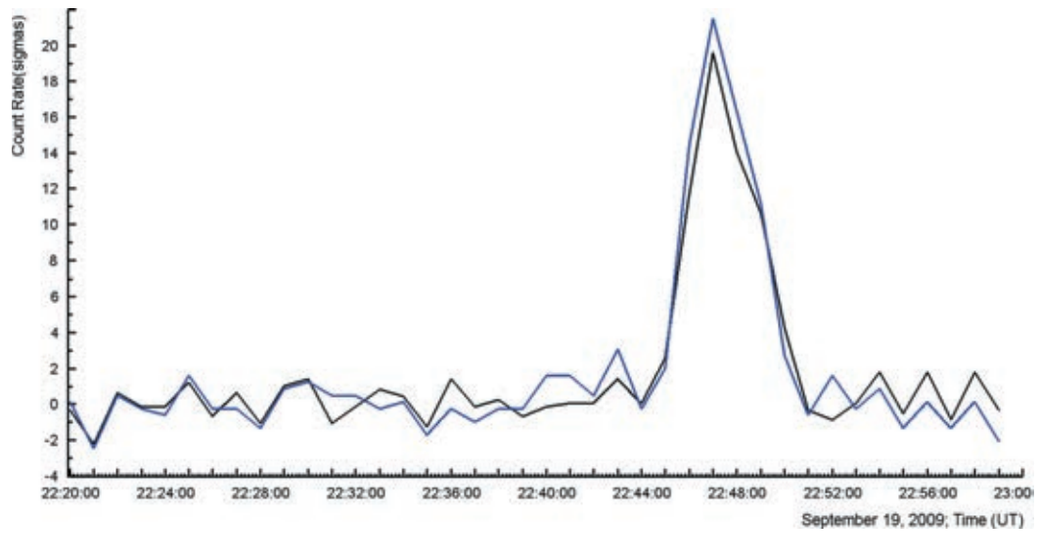


**Fig. 3.** Largest TGE event occurred on 19 September 2009; Minute time series of the triggers of MAKET surface array (16-fold – upper curve – and 8-fold – lower curve – coincidences).

responsible for TGE initiation (the strength of the electrical field and potential drop in the thundercloud, height of thundercloud above detector site). Estimated values of 1.8 kV/cm with elongation of 1–1.5 km and cloud height of 50–150 m for largest events are in good agreement with available measurements (Torii et al., 2011; Tsuchiya et al., 2011). However, the energy spectrum of gamma rays prolonged up to 100 MeV cannot be explained in the framework of the RREA process, as for assumed realistic parameters of the thundercloud maximal energy of the runaway electrons does not exceed 40–50 MeV. GEANT4 simulations demonstrate that these high-energy photons can be explained by the Modification of the energy Spectra (MOS) of charged particles in the electric field of thunderclouds (Muraki et al., 2004; Dorman and Dorman, 2005). The CR relativistic electrons entering prolonged electric field in thundercloud live longer and radiate more gamma rays thus enlarging the gamma ray flux from the thundercloud. The strength of the electric field not necessarily should exceed the RREA initiation threshold. MOS process has no threshold and amplitude of TGE events may be very small if field is weak or/and its elongation is short (see statistics of TGE events in Chilingarian et al. (2013a)).

## 4. The model of TGE; TGE amplitude and near-surface electric field

During milliards years of its evolution Earth was bombarded by the protons and fully striped ions accelerated in Galaxy in tremendous explosions of the supernovas and by other exotic stellar sources. This flux was changed during the passage of sun through the four galactic arms in its course around the center of Galaxy and, may be, was affected several times by huge explosions of nearby stars. Nonetheless, on the shorter time scales the galactic cosmic ray flux is rather stable. High-energy protons and fully stripped nuclei entering the terrestrial atmosphere and colliding

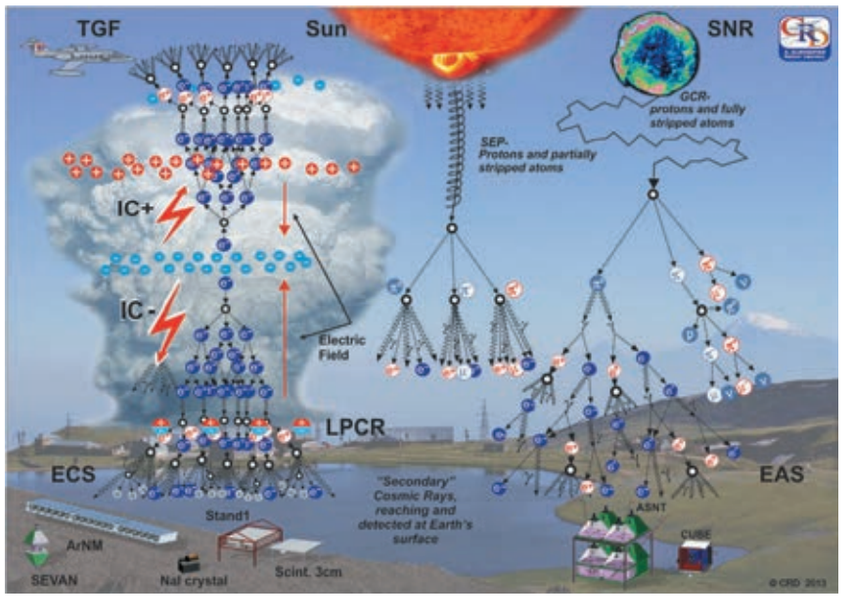


**Fig. 4.** Sources of the secondary cosmic rays detected on the Earth's surface.

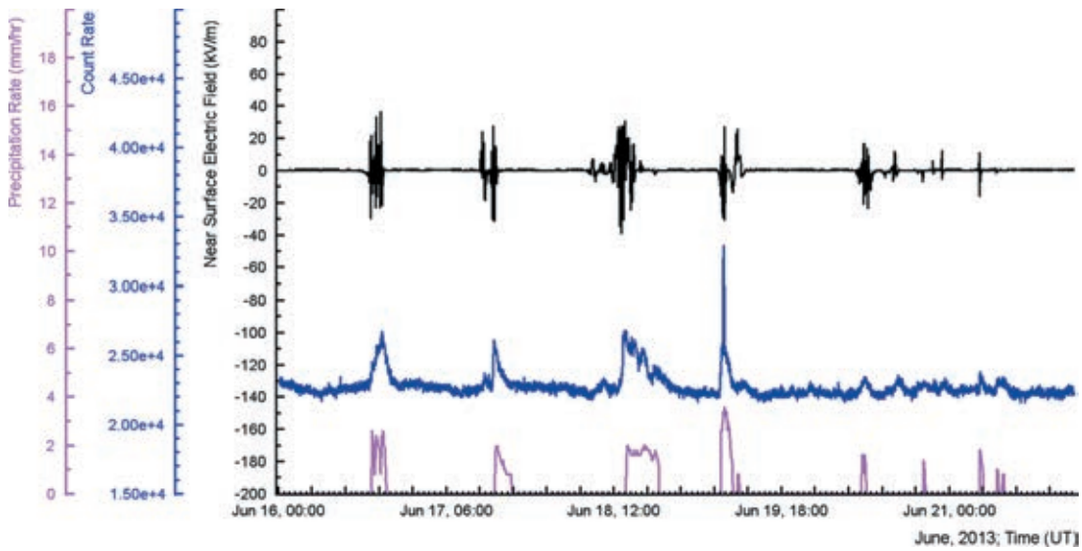


**Fig. 5.** Time series of the rain rate (bottom); time series of the count rate of outdoor plastic scintillator with energy threshold 1.5 MeV (middle); time series of the disturbances of near surface electric field. (Time series of numerous particle detectors, field meters and weather stations are available from the site of Cosmic ray division of Yerevan physics institute http://crd.yerphi.am).

with nitrogen and oxygen atoms generate extensive air showers—cascades of particles developing in atmosphere comprising secondary cosmic rays, see right side of Fig. 4.

Sun influences earth in different ways by emission of radiation, plasma clouds and high-energy particles and ions. Although the overall energy fraction of the high-energy particles is very small compared with visible light energy, nonetheless, on several occasions' solar particles if energetic enough can generate cascades contaminating stable flux of the secondary comic rays initiated by galactic primaries. Influence of sun on the secondary cosmic ray flux can be described as modulation of the stable cosmic ray "background" by the sun activity. The most energetic in the solar system flaring process releases up to $10^{33}$ erg of energy during few minutes. Along with broadband electromagnetic radiation the explosive flaring process results in ejection of huge amounts of solar plasma and in acceleration of the copious electrons and ions (so called solar energetic phenomena —SEP). Particles can be generated either directly in the coronal flare site with subsequent escape into interplanetary space, or they can be accelerated in the shocks that propagate through corona and interplanetary space (Aschwanden, 2004). These particles, along with neutrons, produced by protons and ions within the flare, constitute Solar cosmic rays (SCR). Only few of SEP events (usually not more than a dozen during solar activity cycle of ~1 years) can be detected by surface monitors, see middle sketch in Fig. 4. Such events comprise, so called Ground Level Enhancement (GLE).

Another, newly discovered phenomenon modulated flux of secondary cosmic rays is the high-energy phenomena in thunderclouds. The identified drivers of the TGE are the Relativistic runaway electron

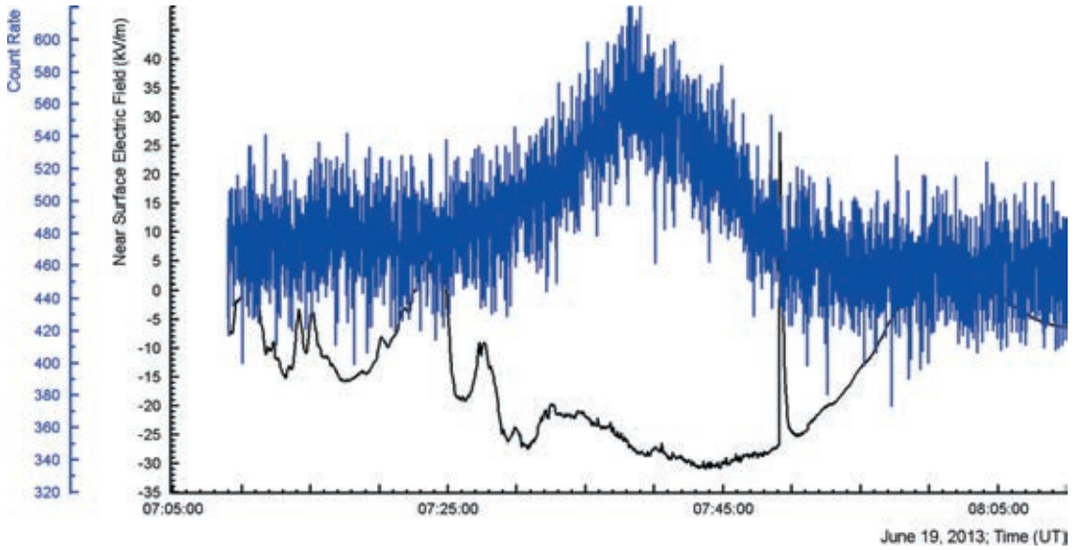


**Fig. 6.** The 2013 largest TGE of 19 June. Prolonged negative electric field initiates large TGE measured by 1-s time series of 3 cm thick outdoor scintillator.

avalanches (RREA) and Modification of energy spectra (MOS) processes (Chilingarian et al.,, 2012c).

The Lower positive charge region (LPCR, see left bottom of Fig. 4) with main negative layer in the middle of the cloud forms lower dipole, responsible for the downward electron acceleration and TGE origination. Many researchers outline the dominant role that LCPR plays in initiating/triggering an intracloud and cloud-to-ground lightning discharges (Pawar and Kamra, 2004; Nag and Rakov, 2009; Qie et al., 2005, 2009). The size of LPCR is much smaller than the size of the main negative charge layer. The transient character of LPCR can explain the duration of the TGE. LPCR's are short-lived because, being composed of precipitation, they fall out of the cloud and carry their charge to the ground (Holden et al., 1980). As one can see in Fig. 5, the all TGEs observed in June 2013 was accompanied by rain.

Rain started during TGE in progress and after it stops TGE fast declines. The TGE amplitude is approximately proportional to the rain rate.[2] Consequently, we can deduce that charge is resided on the rain droplets. The positive and negative ions can be separated in the droplet under the action of the ambient electric field, thus forming two residual stretched charged clusters (Gurevich and Karashtin, 2013, see left bottom side of Fig. 4). Therefore, the upper part of droplet forms with main negative layer of the thundercloud the lower dipole accelerated electrons downward; and the negatively charged bottom of the droplet is responsible for the large negative near surface electric field measured by the EFM-100 electrical mill.[3] The TGE amplitude should be proportional to the total positive charge in LPCR; and, therefore—to the amount of rain droplets (water) in the bottom of cloud. An estimate of amount of water in cloud is the rain rate. For the TGEs on June 20–21 (right side of Fig. 5) the charge accumulated in the droplets was not sufficient to provide strong electric field to unleash RREA process and we detect only modest enhancements of particle fluxes due to MOS process. On June 16–19 the rain rate was sufficient to stipulate large and prolonged TGEs. Zooming Fig. 5 we can investigate each TGE in more details. In Fig. 6 we post the 2013 largest TGE of 19 June.

[2] Measured by Professional Davis Instruments Vantage Pro2, http://www.davisnet.com/.

[3] Boltek firm electrical mill EFM100, measurement accuracy 5%, http://www.boltek.com/efm100.html.

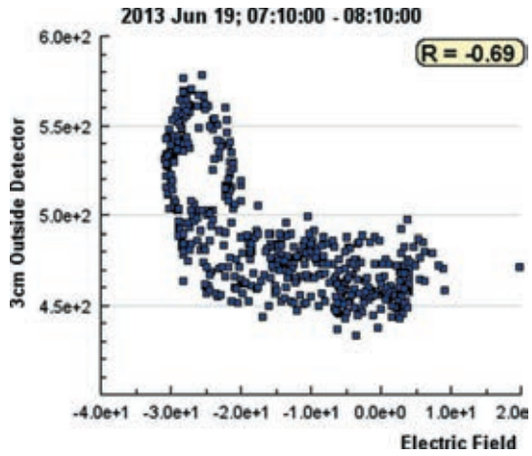


**Fig. 7.** The scatter plot of particle flux and near surface electric.

As we can see in Fig. 6 as electric field dipping to negative domain at ~7:25 the particle flux gradually enhanced, peaking at 7:36 when near surface electric field get the value of −30 kV/m. Rain consequently washed out the LPCR and particle flux started to decay, fully stopping at 7:50.

In Fig. 7 we can see the typical for the large TGEs pattern showing inverse dependence of the particle flux on near surface electric field strength. Apparent anti-correlation of 2 variables can be explained by enhancement of the positive charge of LPCR (resided on the rain droplets) and consecutive increase of negative charge (resided on the bottom of droplets and measured by the field mills located on Earth's surface). The larger is electric field of lower dipole—more electrons are accelerated and unleashing avalanches and more boost get TGE.

## 5. TGEs and lightning occurrences

TGE particle flux was often accompanied with intracloud lightning occurrences (IC−) and suppression of cloud-to-ground lightning occurrences (CG−). This structure of lightning occurrences supports creation of developed lower positive charge region as a fundamental

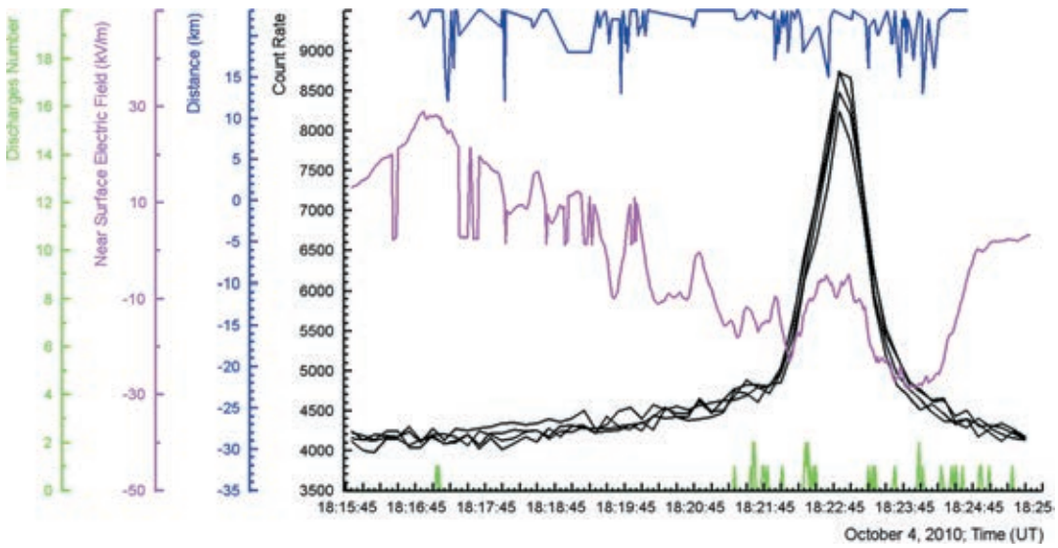


**Fig. 8.** The large TGE of October 4, 2010 measured by 41 $m^2$ area scintillators; electric field, distance to lightning and lightning occurrences registered by EFM 100 and Srorm tracker.

condition of TGE origination (Chilingarian and Mkrtchyan, 2012). Large fluxes of electrons and gamma rays detected on the Earth's surface are only possible when LPCR is well developed and, consequently, lower dipole is accelerated electrons downward. Lower dipole as well can initiate negative intraclaud lightning[4]; however TGEs and lightning are not obligatory correlated. Simultaneous measurements of the particle fluxes, electrical field disturbances and lightning occurrences at Aragats in the seasons of 2011–2013 do not give any evidence on causative relation of lightning occurrences to TGEs.

Lightning flashes are detected by 2 devices both produced by Boltek company. The electrical mill EFM-100 traced short-range (30 km) lightning flashes by the abrupt change of the near surface electrical field monitored by electric mill (only CG, cloud-to-ground lightnings are registered by EFM-100). Boltek's StormTracker[5] for each lightning stroke analyzes a signal waveform in real time. The discrimination between IC and CG is based on the shape and amplitude of the waveform, i.e., the rise and decline times. The direction is determined by looking at the magnetic field ratios for each stroke. The initial distance is determined by looking at the signal strength.

In Fig. 8 we present the large TGE event of 4 October 2010. The TGE amplitude measured by the four identic 1 $m^2$, 5 cm thick plastic scintillators belonged to ASNT detectors reached 150%. The duration of the TGE peak on the half-maximum (FDHM) was only 40 s, from 18:22:25 till 18:23:05. Lightning activity was modest during this event. In 5 km range Storm Tracker detects 12 IC− lightning flashes at 18:21:20–18:22:30; 8 IC− lightnings at 18:23:15–18:25:15; 2 IC+ lightning flashes at 18:24–18:25:20 and CG− lightning flash at 18:24:51 and CG± at 18:25:35. Only 1 lightning flash was detecting during FDHM of TGE. Distance to cloud-ground lighting flashes measured by EFM-100 was rather far —above 12 km.[6]

We do not expect that lightning flashes on the distances larger than 10 km can influence TGE. Based on the detection of the winter thunderstorms Tsuchiya et al. (2011) estimate the radii of the circle of intense RREA radiation to be 600 m. Another Japanese group (Torii et al., 2011) detects moving at the speed of 7 m/s energetic radiation source at the height of 300 m; the radiation was emitted from a downward hemispherical surface with radii of 700 m. Intracloud lightning flashes also are too rare to explain minutes long TGE.

Additionally, hundreds of nearby intracloud discharges and numerous cloud-to-ground lightning flashes was registered during the same thunderstorm at 22:00–22:10, October 4, 2010. Nonetheless, this very strong lightning activity was not accompanied by any significant enhancement of particle flux as it is demonstrated in Fig. 9.

From discussed above TGE event we may deduce that a causative relation does not connect large particle fluxes and lightning occurrences. Reported correlation of lightning signals and TGFs can be induced by the one and the same origin of TGFs and lightnings—strong electric fields in the thundercloud. Recently FERMI group infers that the detected VLF signals are from the relativistic electron avalanches that are responsible for the flash of gamma rays rather than are related to intracloud lightning (Connaughton et al., 2013). However, as we can see in Fig. 8 after the maximum of the particle flux enhancement on the stage of LPCR decaying few discharges occurred. Therefore, we cannot reject that the high-energy TGE electrons may create a conductive channel and “assist” lightning flashes to occur. The opposite hypothesis that lightning discharges themselves produce the observed particle flux seem not reasonable because the rise of TGE started far before the lightning occurrences.

## 6. Conclusion

Early in the last century Wilson made ingenious predictions, which still represent the frontiers of the new field of high-energy atmospheric physics (Dwyer et al., 2012a; Williams, 2010); some of them are still under debate. For instance: “By its accelerating action on particles the electric field of a thundercloud may produce extremely penetrating corpuscular radiation and this

[4] Large LPCR prevents negative CG− flashes from occurrence because abundant lower positive charges make an IC− discharge with negative charge region preferable, see for instance Qie et al., 2009.

[5] Boltek's stormTracker lightning detection system, powered by the software from Astrogenic systems, http://www.boltek.com/stormtracker.

[6] The EFM-100 detects near lightning flashes much more precise than Storm Tracker. Therefore, if any discrepancy on short distances EFM-100 detection is preferable.

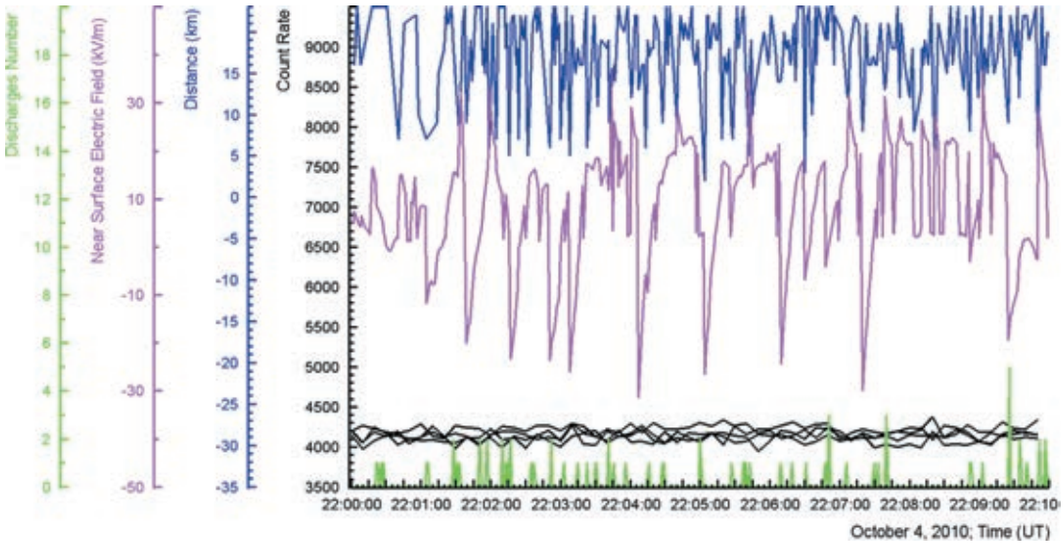


**Fig. 9.** Huge thunderstorm on October 4, 2010 along with electric field disturbances and lightning occurrences; no significant TGE is detected.

may occur even when there is no thunder" (Wilson, 1925b). This statement concerns one of the hottest topics of the modern research. Are the particles from the clouds due to electric field only (Torii et al., 2011; Chilingarian and Mkrtchyan, 2012) or lightning occurrence is mandatory for emerging particle fluxes (Gurevich et al., 2012)?

Our observations support first hypothesis. Although lightning itself can produce electrons and gamma rays (Dwyer et al., 2012b), the TGE observations prove that lightning is not necessary condition for the particle fluxes initiation. Residing on the rain droplets in the bottom of thundercloud LPCR with main negatively charged layer form a lower dipole. Electrical field of lower dipole effectively transfer field energy to electrons; electrons generate gamma rays and gamma rates by photonuclear reaction born neutrons. Runaway electrons generate secondary electron bursts of microsecond duration; overall duration of TGE is usually ~10 min and more; during tens of minutes large amount of short bursts happen. Large TGEs occur during large negative near surface electric field. Amplitude of TGE is proportional to the absolute value of the electric field strength. Atmospheric discharges and TGEs are competitive processes and at maximal TGE flux usually no discharges are detected. However, ECSes provide ionization of atmosphere continuously on the minute time-scale and intracloud negative lightning (IC−) may use the conductive path opened by multiple ECSs. Only when the LPCR is degraded the lightning leader can propagate till the earth surface and classical negative cloud-to-ground lightning flashes (CG−) can occur.

## References


Aglietta, M., EAS-TOP Collaboration, 1989. The EAS-TOP array at $E_0 = 1014–1016$ eV: stability and resolutions. Nucl. Instrum. Methods Phys. Res., Sect. A 277, 23–28.

Antoni, T., Apel, W.D., Badea, F., et al., 2005. KASCADE measurements of elemental groups of cosmic rays: results and open problems. Astropart. Phys. 24, 1–25.

Aschwanden M.J.. In: N. Gopalswamy et al. (Eds.), AGU Monograph of AGU Chapman Conference "Solar Energetic Plasmas and Particles". 2–6 August 2004, Turku, Finland.

Agnsotelli, S., Allison, J., Amako, K., et al., 2003. GEANT4—a simulation toolkit. Nucl. Instrum. Methods Phys. Res., Sect. A 506, 250–303.

Alexeenko, V.V., Khaerdinov, N.S., Lidvansky, A.S., Petkov, V.B., 2002. Transient variations of secondary cosmic rays due to atmospheric electric field and evidence for pre-lightning particle acceleration. Phys. Lett. A 301, 299–306, http://dx.doi.org/10.1016/qS0375-9601(02)00981-7.

Babich, L.P., et al., 2001. Comparison of relativistic runaway electron avalanche rates obtained from Monte Carlo simulations and kinetic equation solution. IEEE Trans. Plasma Sci. 29 (3), 430–438, http://dx.doi.org/10.1109/27.928940.

Babich, L.P., Roussel-Dupré, R.A., 2007. Origin of neutron flux increases observed in correlation with lightning. J. Geophys. Res. 112, D13303.

Brunetti, M., Cecchini, S., Galli, M., Giovannini, G., Pagliarin, A., 2000. Gamma-ray bursts of atmospheric origin in the MeV energy range. Geophys. Res. Lett. 27 (11), 1599–1602. (art. no. 2000, GL003750).

Carlson, B.E., Lehtinen, N.G., Inan, U.S., 2010. Terrestrial gamma ray flash production by active lightning leader channels. J. Geophys. Res. 115, A10324, http://dx.doi.org/10.1029/2010JA015647.

Chilingarian, A., Gharagyozyan, G., Hovsepyan, G., Ghazaryan, S., Melkumyan, L., Vardanyan, A., 2004. Light and heavy cosmic-ray mass group energy spectra as measured by the MAKET-ANI detector. Astrophys. J. 603, L29–L32.

Chilingarian, A., Reymers, A., 2008. Investigations of the response of hybrid particle detectors for the space environmental viewing and analysis network (SEVAN). Ann. Geophys. 26, 249–257.

Chilingarian, A., 2009. Statistical study of the detection of solar protons of highest energies at 20 January 2005. Adv. Space Res. 43, 702–707.

Chilingarian, A., Daryan, A., Arakelyan, K., Hovhannisyan, A., Mailyan, B., Melkumyan, L., Hovsepyan, G., Chilingaryan, S., Reymers, A., Vanyan, L., 2010. Ground-based observations of thunderstorm-correlated fluxes of high-energy electrons, gamma rays, and neutrons. Phys. Rev. D: Part. Fields 82 (4), 043009.

Chilingarian, A., Hovsepyan, G., Hovhannisyan, A, 2011. Particle bursts from thunderclouds: natural particle accelerators above our heads. Phys. Rev. D: Part. Fields 83 (6), 062001.

Chilingarian, B., Mailyan, Vanyan, L., 2012c. Recovering of the energy spectra of electrons and gamma rays coming from the thunderclouds. Atmos. Res. 114–115, 1–16.

Chilingarian, A., Mkrtchyan, H., 2012. Role of the lower positive charge region (LPCR) in initiation of the thunderstorm ground enhancements (TGEs). Phys. Rev. D: Part. Fields 86, 072003.

Chilingarian, A., Bostanjyan, N., Vanyan, L., 2012a. Neutron bursts associated with thunderstorms. Phys. Rev. D: Part. Fields 85, 085017.

Chilingarian, A., Bostanjyan, N., Karapetyan, T., Vanyan, L, 2012b. Remarks on recent results on neutron production during thunderstorms. Phys. Rev. D: Part. Fields 86, 093017.

Chilingarian, A, Hovsepyan, G, 2013. Extensive cloud showers (ECS)—new high-energy phenomena resulting from the thunderstorm atmospheres. J. Phys. Conf. Ser. 409, 012221.

Chilingarian, A., Karapetan, T, Melkumyan, L., 2013a. Statistical analysis of the thunderstorm ground enhancements (TGEs) detected on Mt. Aragats. J. Adv. Space Res. 52, 1178.

Chilingarian, A., Vanyan, L., Mailyan, B., 2013b. Observation of thunderstorm ground enhancements with intense fluxes of high-energy electrons. Astropart. Phys. 48, 1.

Chilingarian, Hovsepyan, Kozliner, 2013. Thunderstorm ground enhancements gamma ray differential energy spectra. Phys. Rev. D: Part. Fields 88, 073001.

Connaughton, V., et al., 2013. Radio signals from electron beams in terrestrial gamma ray flashes. J. Geophys. Res. Space Phys. 118, 2313–2320, http://dx.doi.org/10.1029/2012JA018288.
Dorman, L.I., Dorman, I.V., 2005. Possible influence of cosmic rays on climate through thunderstorm clouds. Adv. Space Res. 35, 476–483.
Dwyer, J.R., 2007. Relativistic breakdown in planetary atmospheres. Phys. Plasmas 14 (4), 042901, http://dx.doi.org/10.1063/1.2709652.
Dwyer, J.R., 2003. A fundamental limit on electric fields in air. Geophys. Res. Lett. 30 (20), 2055, http://dx.doi.org/10.1029/2003GL017781.
Dwyer, J.R., Smith, D.M., Cummer, S.A., 2012a. High-energy atmospheric physics: terrestrial gamma-ray flashes and related phenomena. Space Sci. Rev. http://dx.doi.org/10.1007/s11214-012-9894-0.
Dwyer, J.R., Schaal, M.M., Cramer, E., Arabshahi, S., Liu, N., Rassoul, H.K., Hill, J.D., Jordan, D.M., Uman, M.A., 2012b. Observation of a gamma-ray flash at ground level in association with a cloud-to-ground lightning return stroke. J. Geophys. Res. 117, A10303.
Eack, K.B., Suszcynsky, D.M., Beasley, W.H., Roussel-Dupre, R., Symbalisty, E.M.D., 2000. Gamma- ray emissions observed in a thunderstorm anvil. Geophys. Res. Lett. 27, 185–188, http://dx.doi.org/10.1029/1999GL010849.
Eddington, A.S., 1926. The source of stellar energy. Nature 117, 25–32, http://dx.doi.org/10.1038/117025a0.
Fishman, G.J., Bhat, P.N., Mallozzi, R., Horack, J.M., Koshut, T., Kouveliotou, C., Pendleton, G.N., Meegan, C.A., Wilson, R.B., Paciesas, W.S., Goodman, S.J., Christian, H.J., 1994. Discovery of intense gamma ray flashes of atmospheric origin. Science 264 (5163), 1313–1316.
Gurevich, A., Antonova, V.P., Chubenko, A.P., et al., 2012. Strong flux of low-energy neutrons produced by thunderstorms. Phys. Rev. Lett. 108, 125001.
Gurevich, A.V., Milikh, G.M., Roussel-Dupre, R., 1992. Runaway electron mechanism of air breakdown and preconditioning during a thunderstorm. Phys. Lett. A 165 (5-6), 463–468.
Gurevich, A.V., Karashtin, A.N., 2013. Runaway breakdown and hydrometeors in lightning initiation. Phys. Rev. Lett. 110, 185005, http://dx.doi.org/10.1103/PhysRevLett.110.185005.
Halliday, E.C., 1941. The thundercloud as a source of penetrating particles. Phys. Rev. 60, 101–106, http://dx.doi.org/10.1103/PhysRev.60.101.
Holden D.N., C.R. Holmes, C.B. Moore, W.P. Winn, J.W. Cobb, J.E. Griswold, D.M., Lytle, Local charge concentration in thunderclouds. In: Sixth International Conference on Atmospheric Electricity (University of Manchester, Manchester, England, 1980).
Lehtinen, N.G., Bell, T.F., Inan, U.S., 1999. Monte Carlo simulation of runaway MeV electron breakdown with application to red sprites and terrestrial gamma ray flashes. J. Geophys. Res. 104, 24,699–24,712, http://dx.doi.org/10.1029/1999JA900335.
McCarthy, M., Parks, G.K., 1985. Further observations of X-rays inside thunderstorms. Geophys. Res. Lett. 12, 393–396, http://dx.doi.org/10.1029/GL012i006p00393.
Muraki, Y., Axford, W.I., Matsubara, Y., et al., 2004. Effects of atmospheric electric fields on cosmic rays. Phys. Rev. D: Part. Fields 69, 123010.
Nag, A., Rakov, V.A., 2009. Some inferences on the role of lower positive charge region in facilitating different types of lightning. Geophys. Res. Lett. 36, L05815, http://dx.doi.org/10.1029/2008GL036783.
Parks, G.K., Mauk, B.H., Spiger, R., Chin, J., 1981. X-ray enhancements detected during thunderstorm and lightning activities. Geophys. Res. Lett. 8, 1176–1179, http://dx.doi.org/10.1029/GL008i011p01176.
Pawar, S.D., Kamra, A.K., 2004. J. Geophys. Res. 109, D02205.
Qie, X., Zhang, T., Chen, C., Zhang, G., Zhang, T., Wei, W., 2005. The lower positive charge center and its effect on lightning discharges on the Tibetan Plateau. Geophys. Res. Lett. 32, L05814, http://dx.doi.org/10.1029/2004GL022162.
Qie, X., Zhang, T., Chen, C., Zhang, G., Zhang, T., Kong, X., 2009. Atmos. Res. 91, 244.
Stolzenburg, M., Marshall, T.C., 2008. Series profiles of electrostatic potential in five New Mexico thunderstorms. J. Geophys. Res. 113, D13207, http://dx.doi.org/10.1029/2007JD009495.
Suszcynsky, D.M., Roussel-Dupre, R., Shaw, G., 1996. Ground-based search for X-rays generated by thunderstorms and lightning. J. Geophys. Res. 101, 23,505–23,516, http://dx.doi.org/10.1029/96JD02134.
Tavani, M, et al., 2011. Terrestrial gamma-ray flashes as powerful particle accelerators. Phys. Rev. Lett. 106, 018501.
Torii, T., Takeishi, M., Hosono, T., 2002. Observation of gamma-ray dose increase associated with winter thunderstorm and lightning activity. J. Geophys. Res. 107, 4324, http://dx.doi.org/10.1029/2001JD000938.
Torii, T., Sugita, T., Kamogawa, M., et al., 2011. Migrating source of energetic radiation generated by thunderstorm activity. Geophys. Res. Lett. 38, L24801.
Tsuchiya, H., Enoto, T., Yamada, S., et al., 2007. Detection of high-energy gamma rays from winter thunderclouds. Phys. Rev. Lett. 99, 165002.
Tsuchiya, H., Enoto, T., Yamada, S., et al., 2011. Long-duration gamma ray emissions from 2007 to 2008 winter thunderstorms. J. Geophys. Res. 116, D09113.
Tsuchiya, H., Hibino, K., Kawata, K., et al., 2012. Observation of thundercloud-related gamma rays and neutrons in Tibet. Phys. Rev. D: Part. Fields 85, 092006.
Williams, E.R., 2010. Origin and context of C. T. R. Wilson's ideas on electron runaway in thunderclouds. J. Geophys. Res. 115, A00E50, http://dx.doi.org/10.1029/2009JA014581.
Wilson, C.T.R., 1925a. The acceleration of b-particles in strong electric fields such as those of thunderclouds. Proc. Cambridge Philos. Soc. 22, 534–538, http://dx.doi.org/10.1017/S0305004100003236.
Wilson, C.T.R., 1925b. The electric field of a thundercloud and some of its effects. Proc. R. Soc. London, Ser. A 37, 32D–37D.

epl A Letters Journal Exploring the Frontiers of Physics

June 2014

EPL, **106** (2014) 59001 www.epljournal.org
doi: 10.1209/0295-5075/106/59001

# On the origin of the particle fluxes from the thunderclouds: Energy spectra analysis

A. Chilingarian, G. Hovsepyan and L. Vanyan

*Yerevan Physics Institute - Alikhanyan Brothers 2, Yerevan, Armenia*

received 4 March 2014; accepted in final form 29 April 2014
published online 29 May 2014

PACS 92.60.Pw – Atmospheric electricity, lightning
PACS 13.40.-f – Electromagnetic processes and properties
PACS 94.05.Dd – Radiation processes

**Abstract** – Simultaneous measurements of the gamma ray differential energy spectra, electric field disturbances, and meteorological conditions provided by experimental facilities located at Mt. Aragats in Armenia allows to establish the model of particle acceleration and propagation in thunderstorm atmosphere. We present comparisons of measured and modeled thunderstorm ground enhancements (TGEs). The origin of the majority of TGEs is the MOS process —the modification of energy spectra of cosmic ray electrons in the atmospheric electric fields. The gamma ray differential energy spectra are well described by the power law function with indexes in the range $-1.5 \div -2.5$ for the electric field strengths 0.8–1.5 kV/cm at altitudes of 3400–5000 m a.s.l. The good agreement of the characteristics of experimental and simulated TGEs gives hope to estimate the intracloud electric field by the observed parameters of TGE gamma ray energy spectra.



**Introduction.** – Recent reports on intense fluxes of high-energy electrons, gamma rays and neutrons associated with thunderstorms illustrate that new interesting physics is still being discovered in our atmosphere [1,2]. Measuring as much as possible parameters of particle fluxes, electric field disturbances and meteorological environments allows for the first time to simultaneously detect and describe electron, gamma ray and neutron fluxes from the thunderclouds [3], observe relativistic runaway electron avalanches (RREA) [4] and finally develop a comprehensive model of the thunderstorm ground enhancement (TGE[1]) [5].

Due to difficulties of observation of the structure of the intracloud electric field, research of high-energy phenomena in atmosphere heavily used computer simulation. Here we report experimental observations of intense gamma ray fluxes by the network of the surface particle detectors located at mountain altitudes supported by the modeling of particle propagation in the thunderstorm atmosphere. The parameters estimated both from simulations and observations allow direct comparisons and unambiguous physical inference on the nature of the TGE. TGE originated from the lower dipole between the main negatively charged layer in the middle of the thundercloud and the transient lower positive charge region (LPCR) [6] in the bottom of the thundercloud. The lower dipole accelerates electrons from the ambient population of secondary cosmic rays (CR) downward. The electric field effectively transfers energy to the electrons modifying their energy spectra (MOS process) [7,8]. As thunderclouds at mountain altitudes usually are very close to the Earth's surface, the electron and gamma ray fluxes escaping from the thundercloud do not completely attenuate in the atmosphere and reach the Earth's surface enhancing a rather stable CR "background" flux in the energy range 1–100 MeV. If the electric field strength exceeds the critical value, the relativistic runaway avalanches (RREA) [9–11] may be unleashed, enlarging the electron and gamma ray fluxes several times. RREA, called also extensive cloud showers (ECS) [4], are systematically different from the extensive air showers (EASs) originating from the galaxy or from the high-energy solar cosmic rays incident on the Earth's atmosphere.

Most of the enhancements embedded in the time series of the particle count rates are rather small —only

[1]The name was introduced in [4]. Another name has been given to "thunderstorm" particles in [2], *i.e.* "gamma-ray glows". However, we will continue to refer to this emission as TGE, since it reflects the observed physical phenomenon and is directly linked to the analogical phenomena of terrestrial gamma flashes (TGFs) and ground level enhancements (GLEs).

a few percent above the cosmic ray background (see the statistical analysis of TGE events in [12]). The simulations of secondary cosmic ray electron propagation in weak electric fields (with the strengths smaller than the threshold value $E_{\rm th}$, necessary for starting the RREA process) were performed with the GEANT4 code. Electric fields provide additional energy to CR electrons by modifying their spectra; consequently the electron lifetime increases, and additional path lengths in the atmosphere enlarge the probability of the gamma ray production. As a result, we obtain additional gamma rays at the observation level. Terrestrial gamma flashes (TGFs) [13] and thunderstorm ground enhancements (TGEs) are usually explained by invoking a runaway process, requiring very strong electric fields emerging in clouds. For instance, the authors of ref. [14] stated: "Any intense burst of gamma-rays in our atmosphere with energies exceeding 7 MeV, almost certainly is produced by runaway electrons experiencing RREA multiplication". However, in contrast to TGFs the MOS process is dominating in the TGE generation, especially in the energy range above 40 MeV. The MOS process can only provide sufficient number of gamma rays with energies larger 40 MeV; the RREA process generates gamma rays with energies below 40 MeV although with a much larger intensity.

Minute-to-minute differential energy spectra of gamma rays measured by the NaI spectrometers located at an altitude of 3200 m (see details in [15]) were used to compare the power law indexes and intensities of gamma ray differential spectra with simulations in order to relate the characteristics of the measured TGE spectra to electric field strength in thunderclouds.

**Simulation of the MOS process.** – The secondary cosmic ray electrons with energies up to 300 MeV were generated with the PARMA code [16]. Particle propagation and multiplication were simulated by the GEANT4 code in the thunderstorm atmosphere's uniform electric field prolonged from 5000 m till 3400 m and then an extra 200 m till the particle detector location at 3200 m. An additional "thunderstorm" gamma ray energy spectrum is compared with the ambient CR spectrum in figs. 1, 2; the spectrum of surplus gamma rays is prolonged up to 100 MeV. The MOS/CR ratio is ∼10% up to energies of ∼20 MeV. Then the ratio is quickly decreased, demonstrating that the MOS process provides a minor enhancement of gamma rays above energies of ∼40 MeV; nonetheless large-area particle detectors located at Aragats can reliably register these small enhancements. To consider the influence of high-energy electrons the energy spectrum of gamma rays originated from electrons with energies in the range 1–100 MeV is compared with the energy spectrum obtained from electrons with energies in the range 1–300 MeV. As we can see in fig. 2 if the electric field strength is low (0.8 kV/cm, well below the RREA threshold) the number of gamma rays originated from electrons with energies 1–100 MeV is much smaller than the

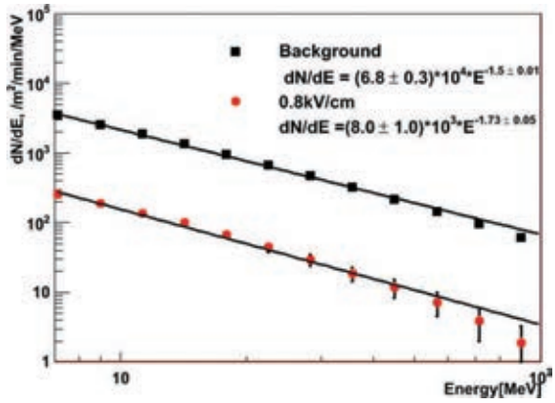


Fig. 1: (Colour on-line) Comparison of the energy spectrum of the secondary CR gamma rays (background) with the MOS gamma ray spectrum at 3200 m altitude; the electric field of 0.8 kV/cm strength is prolonged 1600 m.

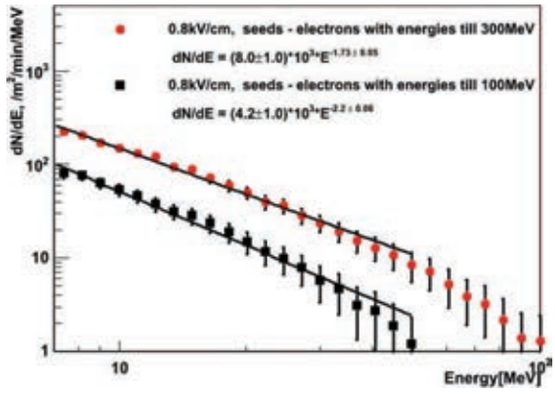


Fig. 2: (Colour on-line) Comparison of gamma ray energy spectra originated from electrons with energies from intervals 1–300 and 1–100 MeV; the electric field of 0.8 kV/cm strength is prolonged 1600 m.

number of gamma rays originated from electrons with energies 1–300 MeV, although the number of seed electrons with energies 1–100 MeV is 10 times more than the number of electrons with energies 100–300 MeV. Thus, the RREA process accelerated electrons up to ∼40 MeV [8] and enhancing the electron and gamma ray fluxes more than an order of magnitude cannot be responsible for the majority of TGEs registered at Aragats. The MOS process enhances electron and gamma ray fluxes for a few percent, however, for much larger energies than RREA, is the major player responsible for TGE process.

In fig. 3 the dependence of the MOS gamma ray spectra on the electric field strength is demonstrated. We can see that not only the number of gamma rays increased with the electric field strength, but also the absolute value of the spectral indexes increased by more than 1 unit. For the field with strength 0.8 kV/cm the energy spectra is described by the power law $\mathrm{d}N/\mathrm{d}E \sim E^{-1.73}$; for strong electric fields "touching" and exceeding the RREA threshold (1.7 and 1.8 kV/cm) the absolute value of the

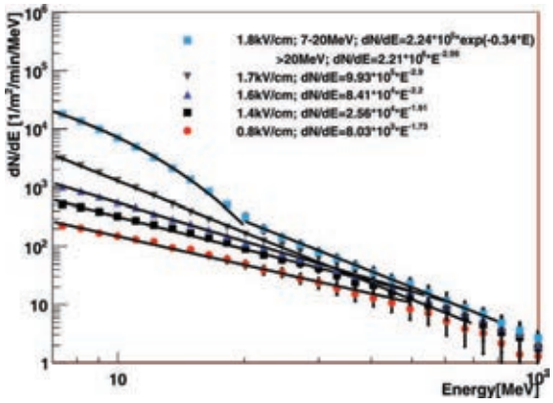


Fig. 3: (Colour on-line) Differential energy spectra of TGE gamma rays generated by secondary cosmic ray electrons in the atmosphere accelerated by electric fields of different strength. Uniform electric field prolonged from 5000 to 2400 m; observation level: 3200 m; energy range 7–100 MeV. To avoid statistical fluctuation due to the scarce population of high-energy bins the power law fit was done in the intensity range above 10 particles per min per m.

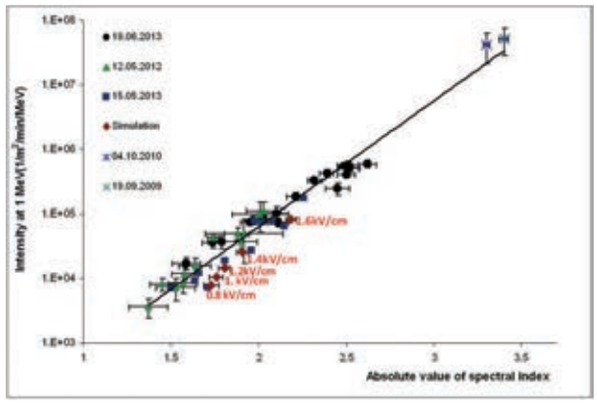


Fig. 4: (Colour on-line) Correlation between observed intensity and absolute value of the power index of the TGE gamma ray energy spectra; the electric field strength is written near the symbols representing simulations of the TGE process.

gamma ray spectral index is larger —approaching −3. The exponential shape of the gamma ray energy spectrum in the energy range 7–20 MeV for the strength of the electric field 1.8 kV/m reveals an avalanche process in the atmosphere.

**TGE flux temporal evolution and its connection with changing the intracloud electric field.** – A network of NaI spectrometers located at an altitude of 3200 m allows to measure the differential energy spectra of gamma rays on the one-minute scale in the energy range 7–100 MeV [15]. Five large NaI crystals provide enough statistics for the reliable approximation of the detected energy releases with the power law fit. For instance, the minute-to-minute surplus of the count rate registered on 19 June from 7:28 to 7:45 is rather large (3000–7000 additional particles); the total number of registered additional gamma quanta were ∼80000. In fig. 4 we show the scatter plot of the power fit parameters (absolute value of power index *vs.* coefficient of power law extrapolated to 1 MeV) of minute gamma ray energy spectra measured on May 12, May 15 and June 19, 2013 along with simulation results from fig. 3. For the comparison purposes we plot as well 2 "super-TGEs" (detected on 19 September 2009 and 4 October 2010) with measured individual RRE avalanches [3,4].

Emphasized in fig. 4 is the relation between experimentally observed and modeled gamma ray energy spectra parameters which allows to at least roughly estimate the electric field in the thundercloud responsible for the TGE. "Super-TGEs" located in the upper-right corner of fig. 4 are linked to the RREA process that exponentially increased the intensity. Correspondingly, the absolute values of the power index of the extrapolate energy spectra rise up to ∼3.5.

**Discussion and conclusions.** – We demonstrate that modest electric fields not reaching the RREA threshold initiate the majority of TGEs in the thunderstorm atmospheres. The power law shape of the gamma ray differential energy spectra tends to soften with increasing electric field strength. When the intracloud electric field reaches the RREA initiation threshold the TGE intensity exponentially grows and an exponential fit, as we see in fig. 3, is suitable for the spectra interpolation at energies 7–20 MeV; at higher energies the power law fit describes the spectrum rather well. The absolute value of the spectral index approaching 3.5 for the largest TGEs is connected with the RREA process with direct observation of individual runaway avalanches [3,4].

The comparison of the experimentally measured gamma ray energy spectra parameters with simulations of the TGE process for different strengths of the intracloud electric field provides calibration data for the approximate estimation of the electric field during TGE. We recognize that for the reliable recovering of the electric field in the thundercloud we will need a more precise direct method of remote measuring of the electric field. A lidar-based method aiming at an accurate estimation of the strength of the electric field in the thunderclouds is now developing in our institute [17].

Terrestrial gamma flashes (TGFs) [13] are believed to originate from electrons accelerated in the upper dipole between the main negative and main positive layer in the upper part of the thundercloud. Gamma rays emitted by accelerated upward electrons propagate in space (generating electron-positron pairs) and reach gamma ray spectrometers in an orbit several hundred kilometers above the Earth's surface. The space-based gamma ray observatories are intended primarily to detect gamma bursts and other energetic processes in the Universe. Modified triggers of gamma ray events allow a copious detection of the TGFs mostly from equatorial thunderstorms. However, the distant locations of the fast moving particle detectors

on the Earth's orbit lead to several difficulties in the verification of the TGF models. The millions of gamma ray photons detected from copious TGEs detected at Aragats allow a detailed analysis of the energy spectra evolution in time and can serve as well for the confirmation of the TGF models.

High-energy processes in the magnetosphere and atmosphere like TGEs, TGFs, TLEs (transient luminous events) and the recently discovered relativistic electron acceleration in the Earth's outer radiation belt [18] trigger various dynamic processes in the Earth's environments and have broad astrophysical relevance. Investigation of the "accelerated" structures in the geospace plasmas can shed light on the particle acceleration to a much higher energy by the similar structures of space plasmas in the most distant objects in the Universe. As it was mentioned in [19] the Earth's broad environment is a real laboratory for high-energy astrophysics.

* * *

Authors thank the staff of Aragats Space Environmental Center for the uninterruptable operation of Aragats research station facilities. The data for this paper are available via the multivariate visualization software (ADEI) [20] in the WEB page of the Cosmic Ray Division (CRD) of Yerevan Physics Institute, `http://adei.crd.yerphi.am/adei`.

REFERENCES

[1] Dwyer J. R., Smith D. M. and Cummer S. A., *Space Sci. Rev.*, **173** (2012) 133.
[2] Dwyer J. R. and Uman M. A., *Phys. Rep.*, **534** (2014) 147.
[3] Chilingarian A., Daryan A., Arakelyan K. *et al.*, *Phys. Rev. D*, **82** (2010) 043009.
[4] Chilingarian A., Hovsepyan G. and Hovhannisyan A., *Phys. Rev. D*, **83** (2011) 062001.
[5] Chilingarian A., *J. Atmos. Sol. Terr. Phys.*, **107** (2014) 68.
[6] Chilingarian A. and Mkrtchyan H., *Phys. Rev. D*, **86** (2012) 072003.
[7] Lidvansky A. S. and Khaerdinov N. S., *Izv. Rossiiskoi Akad. Nauk, Ser. Fiz.*, **71** (2007) 1052 (in Russian).
[8] Chilingarian A., Mailyan B. and Vanyan L., *Atmos. Res.*, **114-115** (2012) 1.
[9] Wilson C. T. R., *Proc. Cambridge Philos. Soc.*, **22** (1925) 534.
[10] Gurevich A. V., Milikh G. M. and Roussel-Dupre R., *Phys. Lett. A*, **165** (1992) 463.
[11] Babich L. P., Kutsyk I. M., Donskoy E. N. and Kudryavtsev A. Yu., *Phys. Lett. A*, **245** (1998) 460.
[12] Chilingarian A., Karapetan T. and Melkumyan L., *J. Adv. Space Res.*, **52** (2013) 1178.
[13] Fishman G. J., Bhat P. N., Mallozzi R. *et al.*, *Science*, **264** (1998) 1313.
[14] Dwyer J. R., Schaal M. M., Cramer E. *et al.*, *J. Geophys. Res.*, **117** (2012) A10303.
[15] Chilingarian A., Hovsepyan G. and Kozliner L., *Phys. Rev. D*, **88** (2013) 073001.
[16] Sato T., Yasuda H., Nitta K. *et al.*, *Radiat. Res.*, **170** (2008) 244.
[17] Ghalumyan A., Hakhumyan R. and Hakhumyan H., in *Proceedings of the International Symposium on Thunderstorms and Elementary Particle Acceleration*, edited by Chilingarian A. (TIGRAN METS, Yerevan) 2013, pp. 102–104.
[18] Mozer F. S., Bale S. D., Bonnell J. W. *et al.*, *Phys. Rev. Lett.*, **111** (2013) 235002.
[19] Zimbardo G., *Physics*, **6** (2013) 131.
[20] Chilingaryan S., Beglarian A., Kopmann A. and Vöcking S., *J. Phys.: Conf. Ser.*, **219** (2010) 042034.

Astroparticle Physics 69 (2015) 37–43

Contents lists available at ScienceDirect

Astroparticle Physics

journal homepage: www.elsevier.com/locate/astropart

# Calibration of particle detectors for secondary cosmic rays using gamma-ray beams from thunderclouds

A. Chilingarian [a,*], S. Chilingaryan [a,b], G. Hovsepyan [a]

[a] Yerevan Physics Institute, Alikhanian Brothers 2, Yerevan 36, Armenia
[b] IPE, Karlsruhe Institute of Technology, Postfach 3640, 76021 Karlsruhe, Germany

ARTICLE INFO

*Article history:*
Received 11 August 2014
Received in revised form 29 March 2015
Accepted 30 March 2015
Available online 4 April 2015

*Keywords:*
Particle detectors
Atmospheric electricity
Thunderstorm Ground Enhancements

ABSTRACT

After observation of hundreds of Thunderstorm Ground Enhancements (TGEs) we measure energy spectra of particles originated in clouds and directed towards Earth. We use these "beams" for calibration of cosmic ray detectors located beneath the clouds at an altitude of 3200 m at Mount Aragats in Armenia. The calibrations of particle detectors with fluxes of TGE gamma rays are in good agreement with simulation results and allow estimation of the energy thresholds and efficiencies of numerous particle detectors used for studying galactic and solar cosmic rays.



## 1. Introduction

Networks of particle detectors located on the Earth's surface continuously measure the incident flux of cosmic rays. These networks cover areas up to thousands of square kilometers and are investigating ultrahigh energy cosmic rays (UHECR) which have been accelerated during the most violent explosions in the Universe. Smaller surface arrays of a few square kilometers or less are detecting mostly galactic cosmic rays (GCR) to locate their sources and identify the acceleration mechanisms. Worldwide networks of particle detectors of several square meters area detect solar cosmic rays (SCR) with the aim of understanding solar accelerators and solar terrestrial connections, in particular space weather phenomena. Last but not least, small size spectrometers at atomic power stations monitor radioactive isotopes escaping to the atmosphere. Interestingly, all these four types of detectors are used for research in the emerging field of high-energy physics in the atmosphere, measuring particle fluxes from thunderclouds [9,10].

The Aragats Space Environmental Center (ASEC, [2]) consists of different particle detectors registering almost all types of the secondary cosmic rays. ASEC is operated by the Cosmic Ray Division (CRD) of the Yerevan Physics Institute and is located at altitudes of 2000 and 3200 m, respectively, on the slopes of Mt. Aragats in Armenia. Research at ASEC includes registration of Extensive Air Showers (EAS) with large particle detector arrays, investigation of solar acceleration mechanisms, monitoring of space weather and observations of high-energy particles from thunderclouds. Nearly 500 particle detectors (mostly plastic scintillators read out with photomultipliers) are sending data every minute (or second) to the CRD headquarters in Yerevan. In addition to particle detectors, ASEC includes facilities measuring electric and geomagnetic fields, lightning occurrences and locations, broadband radio emission, a variety of meteorological parameters, and optical images of clouds and lightnings.

Dealing with ultra-high energy, galactic and solar cosmic rays, one of the most important tasks is the determination of the detector response. Usually it is estimated with the help of the GEANT detector simulation package [1], a standard tool in high-energy and astroparticle physics. However, it is important to perform calibration experiments with particle beams, too, with the aim to validate the calculated energy threshold, the response to different types of particles and the efficiency of their detection. While calibration with artificial particle beams is standard practice in accelerator experiments, there are only few attempts to calibrate cosmic ray surface detectors with particle beams. These attempts are related to the calibration of fluorescence detectors with lidars or linear accelerators. For instance, the Telescope Array has used an electron linac with beam pulses of one microsecond length and $10^9$ electrons of 40 MeV, injected vertically upwards into the atmosphere to calibrate its fluorescence detectors. The calculated energy deposit of the beam in the atmosphere together with the fluorescence yield per deposited energy gives the number of photons expected at the telescope, which can be compared with the measured number of photons [12].

* Corresponding author.
*E-mail address:* chili@aragats.am (A. Chilingarian).

http://dx.doi.org/10.1016/j.astropartphys.2015.03.011
0927-6505/

At Mt. Aragats, Thunderstorm Ground Enhancements (fluxes of electrons, gamma rays and neutrons from thunderclouds, [3,4]) are usual phenomena, due to frequent storms, especially in spring and autumn. Large fluxes of the registered gamma rays allow precise recovery of the shape (usually a power law) and the slope of the gamma-ray spectrum. A network of large NaI crystals recently installed at ASEC opens new opportunities to use the measured beams of gamma rays *a posteriori* for the determination of the detector response. On a very small energy scale (the energies of electrons accelerated in thunderclouds do not exceed 50 MeV and gamma rays are below 100 MeV), this can be seen as the realization of an old vision of cosmic ray physicists: to arrange a particle accelerator in the atmosphere just above the EAS detectors. The proposed methodology allows estimation and monitoring of one of the important parameters of particle detectors, their energy threshold. We use the gamma ray "beams" to calculate the detector response of various particle detectors located beneath the thundercloud. We demonstrate, how the energy threshold of plastic scintillation counters to MeV gamma rays from the atmosphere can be calibrated with the help of neighboring NaI counters. The basic steps are the following:

(a) We perform a continuous monitoring of the secondary cosmic ray fluxes with the ASEC particle detectors and spectrometers.
(b) We select a data sample of ionizing atmospheric radiation from the thunderclouds (TGE events) where we know that gamma rays contribute a significant part.
(c) We measure the energy spectrum of the TGE events with the help of the network of large NaI spectrometers.
(d) We observe a power law spectrum between 4 and 100 MeV, which we assume to extend below the threshold for the NaI configuration.
(e) We select TGE events for which the electron/gamma ratio in the plastic scintillators should be no larger than 1–2%.
(f) We compare the count rates of plastic scintillators of various types and sizes to the integral energy spectrum recovered by the network of NaI crystal. Assuming a pure power law between 0.5 and 10 MeV and normalizing the scintillator apertures to the NaI aperture, the counting rate can be translated to an integral energy spectrum $J_E$ (with $E > E_{threshold}$).

## 2. Short description of some of the particle detectors

The NaI network consists of five NaI crystal scintillators, each in a sealed 1-mm-thick aluminum housing. The hygroscopic NaI crystal is protected against humidity by 0.5 cm thick sheets of magnesium, with a transparent window directed to the photo-cathode of the photomultiplier tube PM-49; see Fig. 1. The large photocathode of PM-49 (15-cm diameter) provides good light collection. The range of spectral sensitivity of PM-49 is 300–850 nm, which covers the emission spectrum of NaI(Tl). The sensitive area of each NaI crystal is $\sim$0.032 m$^2$; the total area of the five crystals is $\sim$0.16 m$^2$; the efficiency to detect a gamma ray is $\sim$80%.

SEVAN (Space Environmental Viewing and Analysis Network) is a network of particle detectors aimed to improve research of particle acceleration in the vicinity of the Sun as well as solar terrestrial relations. The modules of the SEVAN network (Fig. 2) simultaneously measure the flux and variations of three species of secondary cosmic rays to explore solar modulation effects. Two identical assemblies of $100 \times 100 \times 5$ cm$^3$ plastic scintillators and lead absorbers sandwich a smaller scintillator assembly of $50 \times 50 \times 20$ cm$^3$.

The new generation of ASEC detectors comprises 1 and 3 cm thick molded plastic scintillators arranged in stacks (STAND1 detector, Fig. 3) and in cubical structures (CUBE detector, Fig. 4),

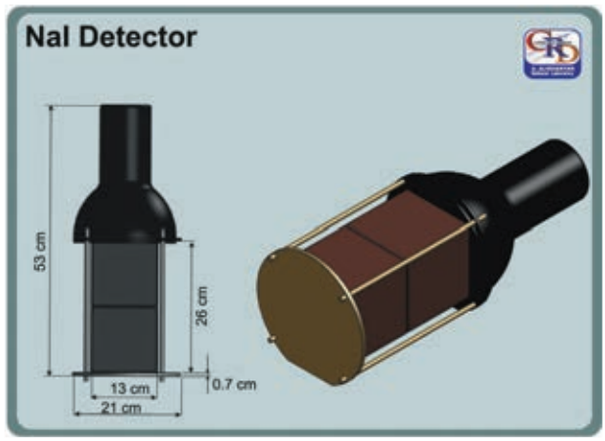


**Fig. 1.** Configuration of the NaI(Tl) spectrometer.

light from the scintillators is re-radiated by wavelength shifting optical fibers at larger wavelengths and propagates to photomultipliers of the type PM-115M. The DAQ electronics stores all configurations of the signals in the detector channels. If a signal is detected only in the upper scintillator, we register the code "100". The code "010" corresponds to a signal only in the middle scintillator, and so on.

The Cube detector (Fig. 4) consists of six 1-cm thick plastic scintillators of the same type as used in the STAND1 detector. They surround two stacked 20 cm thick scintillators and can veto charged particles crossing the thick inner scintillators. They allow enrichment of the data sample with neutral particles and in particular estimating the fraction of electrons in the mixed electron and gamma ray flux. Furthermore, there other detectors used which are not described here. The detailed detector charts with all sizes are available from the WEB site of the Cosmic Ray Division of Yerevan Physics Institute: http://crd.yerphi.am/.

## 3. Recovering gamma ray spectra: the TGE detected on 27 May 2014

The electron flux in the atmosphere is much more attenuated than the gamma ray flux. Therefore, most of the particles registered by the surface detectors are gamma rays. However, sometimes, when a thundercloud is very low above the Earth's surface, the fraction of electrons in the total flux can be sizeable (see details in [6]). For calibration purposes we select from the observed TGEs those with a fraction of electrons not exceeding 1–2% of the total flux. We demonstrate the techniques to select approximately "pure gamma ray" TGEs with the help of a double peaked TGE detected on May 27, 2014.

On May 27, 8:40 UTC, the electric mill located at the Aragats research station recorded a large disturbance in the near-surface electric field related to the arrival of a large thundercloud, see Fig. 5. Ten minutes after a positive boost of the electric field (reaching a maximal value of +15 kV/m), at 8:50 the electric field abruptly changed the polarity to a field strength of −15 kV/m. The decrease of the solar radiation from 1200 to 100 W/m$^2$ during the TGE confirms the presence of the dense cloud just above the detectors. The high humidity of 88–97% allows the development of a Lower Positively Charged Region (LPCR) formed by the polarized micro-droplets of water [11]. Two oppositely charged layers – the positively charged LPCR and the negatively charged layer above – in the thundercloud formed a lower dipole accelerating electrons downward (see for details [8]).

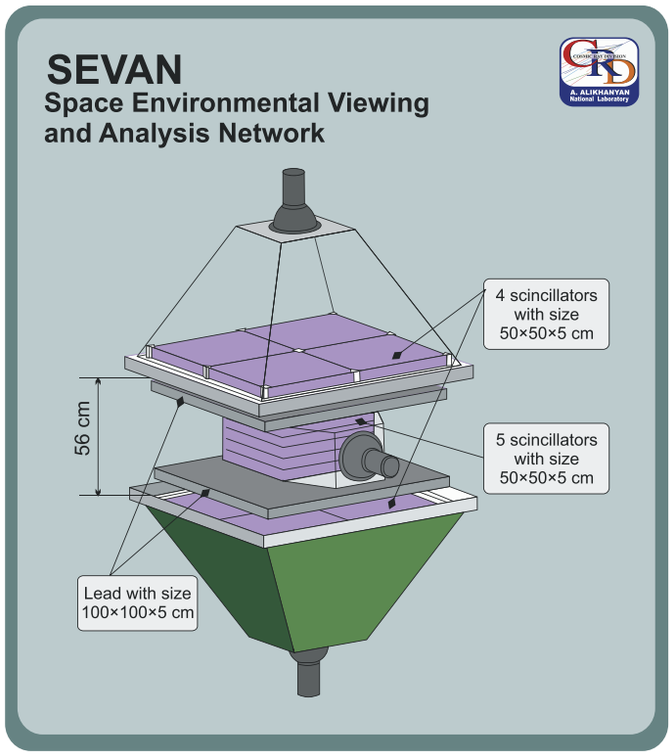


**Fig. 2.** A SEVAN particle detector.

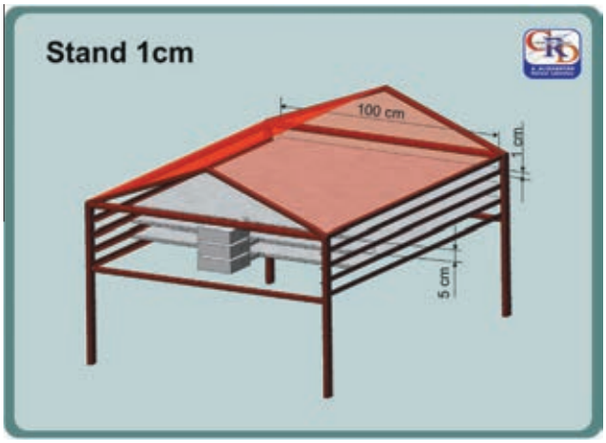


**Fig. 3.** STAND1 stacked detector.

Coincidentally, the particle fluxes observed by the network of NaI crystals and other particle detectors just beneath the cloud start to increase at 8:50, see Fig. 6. The figure does not show the time series of the count rates itself, but the time series of the $p$-values of the peak significance test. The $p$-value is the most comprehensive measure of the reliability of detecting peaks in a time series. Large $p$-value corresponds to small chance probabilities that the observed peak is a background fluctuation and not a genuine signal. Therefore, we can safely reject the null hypothesis (background fluctuation) and confirm the TGE. Very large $p$-values not only prove the unambiguous existence of a particle flux from the cloud, but also serve as a comparative measure of the TGE observations using different detectors. The largest $p$-value of 82 $\sigma$ (standard deviations) is observed at 9:02 by the Aragats Multivariate Muon Monitor (AMMM), an array of 25 plastic scintillators with dimensions $100 \times 100 \times 1$ cm$^3$ located outdoors in iron housings. The peak registered by the STAND1 detector at the same time has a $p$-value of $\sim$30 $\sigma$, that of the CUBE detector of $\sim$22 $\sigma$. The differences in $p$-values are due to various sizes and energy thresholds of detectors. Thus, the indoor CUBE detector with its higher energy threshold did not detect the small peak at

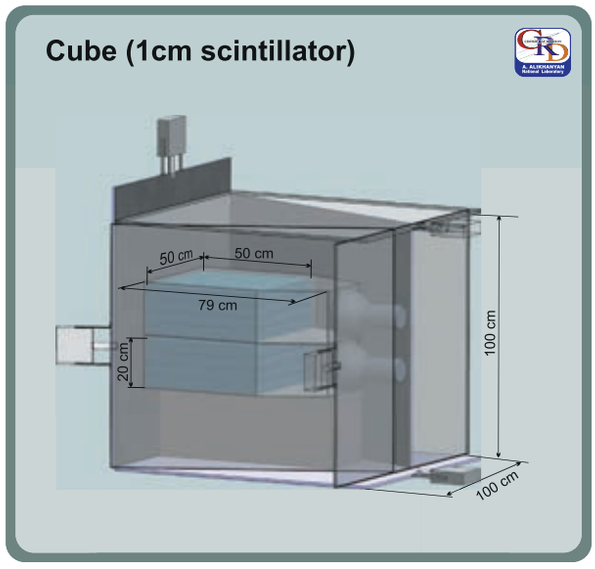


**Fig. 4.** The Cube detector with a veto against charged particles.

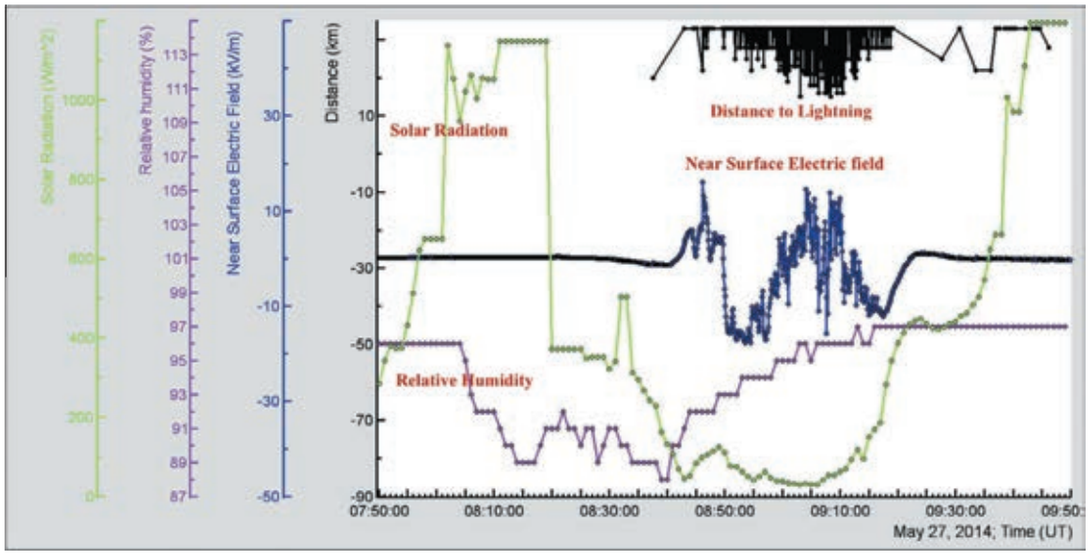


**Fig. 5.** Time series of the meteorological conditions (solar radiation, relative humidity, near-surface electric field) and the distance to the lightning during the TGE on May 27, 2014. The distance is measured using an electric mill EFM-100 (BOLTEK).

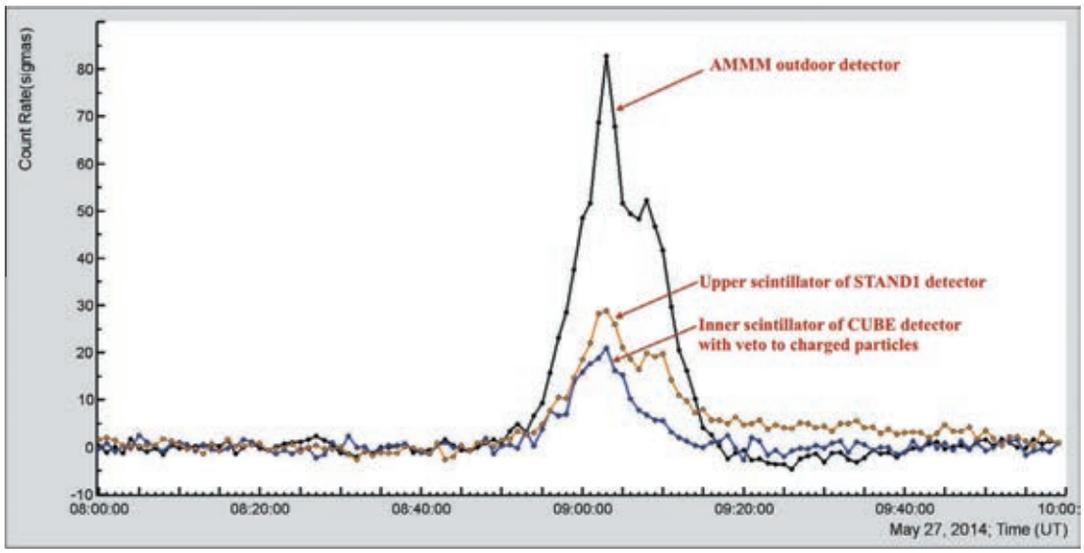


**Fig. 6.** One-minute time series of the significances of the measured peak values against the background-only hypothesis. ($p$-values of $t$-test).

9:08 seen by the outdoor detectors AMMM and STAND1. To reveal this enhancement in more details we present in Fig. 7 the one-second time series of the 3 cm thick outdoor plastic scintillator, apparently showing the second peak at 9:08.

The disturbance of the electric field finished at 9:23. According to the pattern of the electric field generated by three differently charged layers in the thundercloud, the lower two of which are responsible for the particle acceleration towards Earth. This TGE belongs to the 1st category of our classification (see [5]): after a few minutes in the positive domain the electric field changes polarity and mostly remains in the negative domain; simultaneously the particle flux abruptly increases.

The stacked detector assembly allows a rough estimate of the fraction of electrons in the particle flux of the TGE. The existence of two neighboring peaks in the TGE allows the estimation of the electron contamination of the gamma ray flux.

From simulations and from calibration experiments[1] we estimate the efficiency of the STAND1 scintillators for charged particles as 98.5%. Consequently, the probability to miss a particle is 1.5%. Using the energy spectrum recovered by the NaI spectrometers network (see details in [7]) we estimate with the GEANT code the probability of registering a gamma ray during the 27 May TGE of the upper, middle and bottom layers of STAND1 detector to be 1.6%, 1.9% and 2.0%, respectively. Using these efficiencies we can

[1] For instance, by comparing "111" and "101" coincidences in the STAND1 detector (signals in all three layers and signals only in layers 1 and 3) and dividing $N_{101}/N_{111}$, we estimate the efficiency of electron detection to be ~98.5%

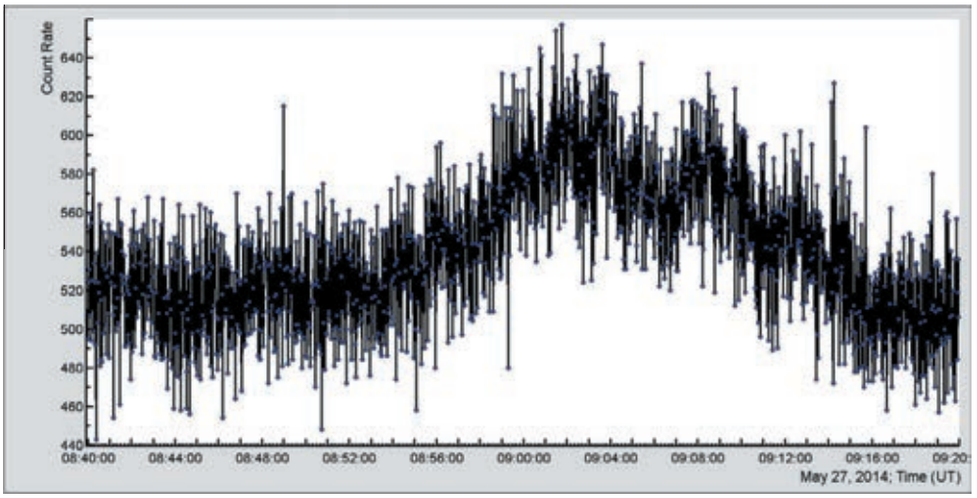


**Fig. 7.** 1-s time series of the stand-alone $100 \times 100 \times 3$ cm$^3$ outdoor plastic scintillator.

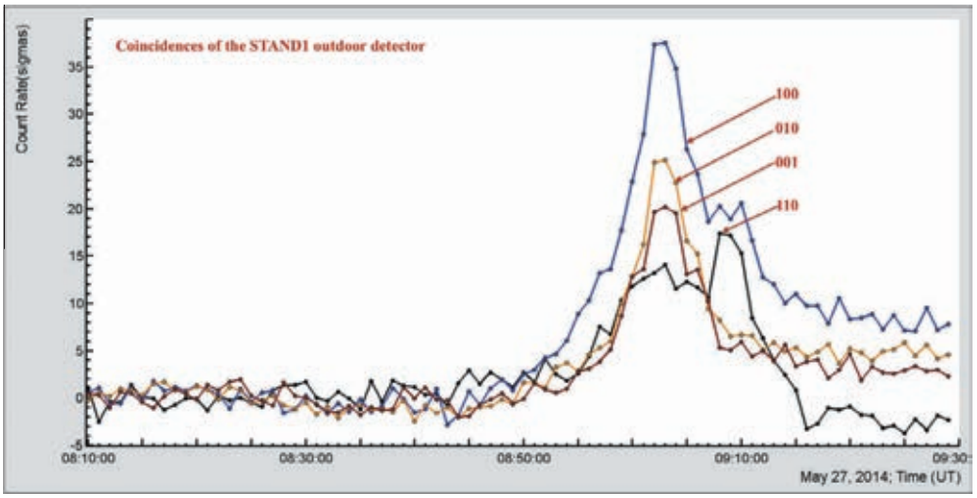


**Fig. 8.** One-minute time series of different codes of the 3-layered STAND1 detector ($p$-values).

easily calculate the conditional probabilities of each trigger condition to be originated by an electron or a gamma ray.

As we can see in Fig. 8, the "110" trigger pattern is the only one revealing a second peak at 9:08 larger than that at 9:02. In turn, the pattern "001" does not reveal any peak at 9:08. We estimate the probabilities that pattern "110" is due to gamma rays or electrons, respectively. The probability that a gamma ray is registered in two successive layers and not detected in the last one is only $\sim 3 \times 10^{-4}$. For an electron the probability of such a pattern is at least 50 times larger. Therefore, we can deduce that the trigger pattern "110" selects mostly electrons. The probability that an electron misses two successive layers and gives signal in the last one is only $\sim 2.2 \times 10^{-4}$, for gamma rays this probability is $\sim$100 times larger. Therefore, we can deduce that the pattern "001" selects mostly gamma rays. This analysis demonstrates that the peak around 9:02 originates mostly from gamma rays and the peak at 9:08, is mainly due to electrons. At 9:01–9:03 the intensity of electrons is much lower than the intensity of gamma rays. Therefore, we can use this particular TGE for the calibration of the ASEC particle detectors. The differential energy spectrum of the particle flux detected at 9:01–9:03 by all five NaI spectrometers along with the power-law fit parameters is depicted in Fig. 9.

## 4. Estimation of the "effective" energy thresholds of the ASEC detectors

According to the techniques described in the previous section we select five TGEs with a small fraction of electrons from all TGE events detected in 2013–2014. These are TGEs observed on May 12, 2013, on June 19, 2013, on July 9, 2013, on May 27, 2014 and on June 12, 2014. The joint sample of the energy releases detected during these TGEs was converted into energies of particles and an averaged integral energy spectrum was calculated. The same averaging procedure was used for the count rates of other particle detectors.

In Fig. 10 we depict the integral spectrum of gamma rays obtained with the NaI network along with counts (integral spectra) of several ASEC detectors, measured during the same time intervals.

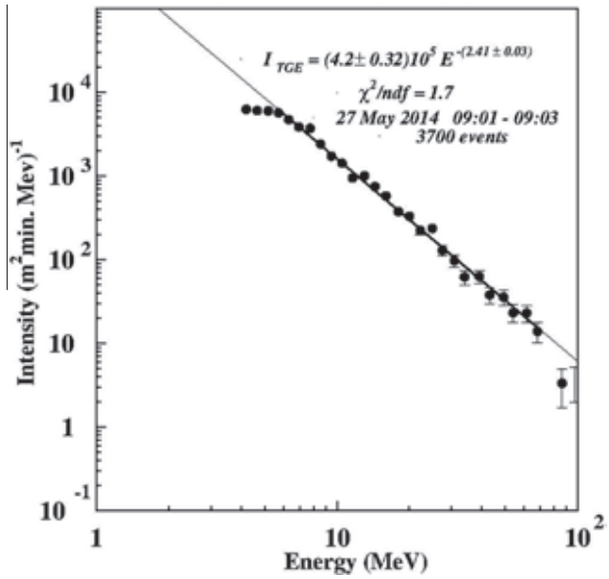


**Fig. 9.** The differential spectrum recorded with the five NaI crystal detectors between 9:01 and 9:03 at 27 May, 2014.

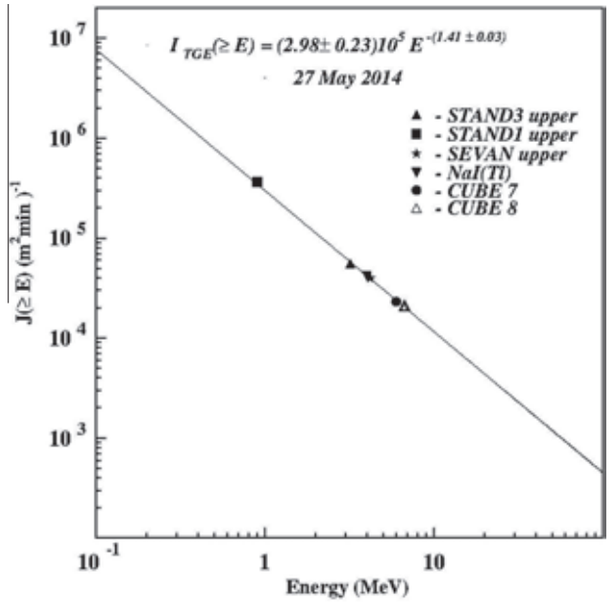


**Fig. 10.** The integral energy spectra of gamma rays with intensities measured with different ASEC particle detectors.

All of the ASEC detectors use scintillators or NaI crystals read out with photomultipliers. To avoid spurious low-amplitude pulses due to photomultiplier noise we use discriminators with predefined threshold values[2]. However, particles with energies equal or near to this "electronic" energy threshold are not registered with 100% efficiency. The notion of the "physical" energy threshold is not firmly established. We can arbitrarily define the physical energy threshold of a detector as the energy at which the particles are registered with 10%, 50%, 90% or even 99% efficiency. To avoid this arbitrariness we introduce the notion of "effective" energy threshold by simply comparing the detector count rate with the energy spectrum measured with the more precise spectrometers. As it is shown on Fig. 10 we simply place the value of the particular particle detector count rate on the *y*-axis of the integral energy spectrum. By reading the corresponding energy from the *x*-coordinate axis beneath, we obtain the "effective" threshold.

In Table 1 we compare the mean values of the "effective thresholds" obtained with five selected TGEs with a small fraction of electrons for several ASEC detectors. The fraction of electrons was estimated for all five events according to the statistical techniques described in the previous section. In the second column of Table 1 we show the "effective thresholds" obtained by reading the *x*-coordinate of Fig. 10 when the *y*-coordinate (intensity measured by particular detector) was placed on the integral gamma-ray energy spectrum. In the third column we list the previously estimated thresholds obtained from the measured CR background count rates showing the single-muon peak. The maximum intensity in the CR

**Table 1**
Effective energy threshold of ASEC detectors estimated by the mean flux of the five selected TGEs.

| Detector | Estimated "effective" energy threshold (MeV) | Estimated energy threshold based on CR background (MeV), "ADC count = 1" energy |
|---|---|---|
| CUBE inner 20-cm thick scintillator (upper) | 5.3 ± 0.6 | 5.8 ± 0.6 |
| CUBE inner 20-cm thick scintillator (bottom) | 5.4 ± 1.1 | 6.4 ± 0.6 |
| SEVAN upper 5-cm thick scintillator | 3.6 ± 0.6 | [a] |
| STAND1 upper 1-cm thick scintillator | 0.7 ± 0.1 | [a] |
| STAND 3 upper 3-cm thick scintillator | 2.9 ± 0.3 | 3.5 ± 0.4 |

[a] SEVAN and STAND1 detectors measure only count rates and not energy releases as other ASEC detectors, therefore we cannot estimate their energy threshold using the muon peak.

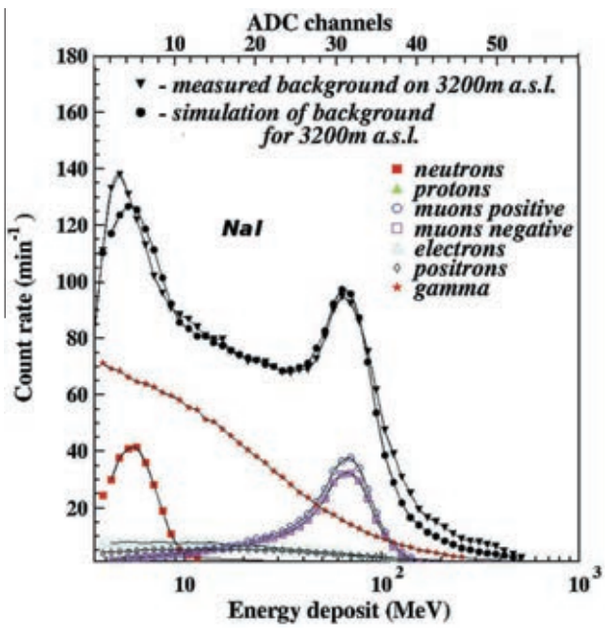


**Fig. 11.** Comparison of the simulated secondary cosmic ray flux on 3200 m height with the SCR flux measured by the NaI spectrometer.

[2] Sometimes the electronics threshold is artificially enlarged to cut the low energy particle flux.

background, the so-called muon peak, is used for the calibration of the energy deposit histogram by establishing the correspondence between ADC counts and energies in MeV.

In Fig. 11 we present the simulated background spectrum (in MeV) by calculating the response to almost all species of secondary cosmic rays. The simulated spectrum is compared with the experimentally measured spectrum of ADC counts, which gives the correspondence between the scales in energy and ADC counts. We know from simulations that the second peak in the background spectrum is due to the traversal of 60 MeV muons (corresponding to the most probable energy release in a 12 cm thick NaI crystal). The same peak in the spectrum measured with the NaI spectrometers is located near the ADC count 31. Thus the 31st ADC count corresponds to ∼60 MeV and ADC count 1 (determining the energy threshold) to ∼3.6 MeV.

## 5. Conclusions

We are continuously measuring energy spectra of gamma rays from thunderclouds, so called Thunderstorm Ground Enhancements, with the help of NaI crystals. We use these spectra to calibrate the plastic scintillation detectors of the Aragats Space Environmental Center. We introduced the notion of an ‘‘effective energy threshold’’ which permits to avoid the arbitrariness of the previously used method of the estimation of the energy corresponding to the first ADC count. Our method is also applicable to particle detectors measuring only the count rate and not the spectra of the deposited energy. It can be used for the multi-year monitoring of the characteristics of large arrays of particle detectors registering fluxes of secondary cosmic rays.

## Acknowledgments

The authors are grateful to the staff of Aragats research high-altitude station of the Yerevan Physics Institute for the uninterrupted operation of the ASEC facilities, and to participants of the seminar of the Cosmic Ray Division for useful discussions.

A.C. and S.C. are grateful to Harutun Vaporciyan for support.

Christian Spiering’s suggestions have highly improved the quality of the paper, author greatly appreciate his time and efforts.

## References

[1] S. Agostinelli, J. Allison, K. Amako, et al., GEANT4 – a simulation toolkit, Nucl. Instrum. Methods A 506 (2003) 250.
[2] A. Chilingarian, K. Arakelyan, K. Avakyan, et al., Correlated measurements of secondary cosmic ray fluxes by the Aragats space-environmental center monitors, Nucl. Instrum. Methods A 543 (2–3) (2005) 483.
[3] A. Chilingarian, A. Daryan, K. Arakelyan, et al., Ground-based observations of thunderstorm-correlated fluxes of high-energy electrons, gamma rays, and neutrons, Phys. Rev. D 82 (2010) 043009.
[4] A. Chilingarian, G. Hovsepyan, A. Hovhannisyan, Particle bursts from thunderclouds: natural particle accelerators above our heads, Phys. Rev. D 83 (2011) 062001.
[5] A. Chilingarian, H. Mkrtchyan, Role of the lower positive charge region (LPCR) in initiation of the thunderstorm ground enhancements (TGEs), Phys. Rev. D 86 (2012) 072003.
[6] A. Chilingarian, L. Vanyan, B. Mailyan, Observation of thunderstorm ground enhancements with intense fluxes of high-energy electrons, Astropart. Phys. 48 (2013) 1.
[7] A. Chilingarian, H. Hovsepyan, L. Kozliner, Thunderstorm ground enhancements – gamma ray differential energy spectra, Phys. Rev. D 88 (2013) 073001.
[8] A. Chilingarian, Thunderstorm ground enhancements – model and relation to lightning flashes, J. Atmos. Solar-Terr. Phys. 107 (2014) 68.
[9] J.R. Dwyer, D.M. Smith, S.A. Cummer, High-energy atmospheric physics: terrestrial gamma-ray flashes and related phenomena, Space Sci. Rev. 173 (2012) 133.
[10] J.R. Dwyer, M.A. Uman, The physics of lightning, Phys. Rep. 534 (2014) 147.
[11] A.V. Gurevich, A.N. Karashtin, Runaway breakdown and hydrometeors in lightning initiation, Phys. Rev. Lett. 110 (2013) 185005.
[12] T. Shibata, M. Beitollahi, M. Fukushima, For the telescope array collaboration absolute energy calibration of the telescope array fluorescence detector with an electron linear accelerator, EPJ Web Conf. 53 (2013) 10004.

A Letters Journal Exploring the Frontiers of Physics

May 2015

EPL, **110** (2015) 49001
doi: 10.1209/0295-5075/110/49001

www.epljournal.org

# Lightning origination and thunderstorm ground enhancements terminated by the lightning flash

A. Chilingarian, G. Hovsepyan, G. Khanikyanc, A. Reymers and S. Soghomonyan

*Yerevan Physics Institute - Alikhanyan Brothers 2, Yerevan, Armenia*

received 26 February 2015; accepted in final form 13 May 2015
published online 11 June 2015

PACS 92.60.Pw – Atmospheric electricity, lightning
PACS 52.80.Mg – Arcs; sparks; lightning; atmospheric electricity
PACS 13.40.-f – Electromagnetic processes and properties

**Abstract** – Proceeding from the measurements of the lightning occurrences, slow and fast electric-field disturbances, particle flux enhancements and their abrupt terminations, we formulate a lightning origination model. Registration of the extensive air shower simultaneously with lightning detection allows us to propose a solution to the long-standing problem of its role in the lightning initiation. Our analysis is based on the numerous Thunderstorm Ground Enhancements detected in 2012–2014 at Mt. Aragats in Armenia.



**Introduction.** – The problem of how lightning is initiated inside thunderclouds is not only one of the biggest unsolved problems in lightning physics, it is also probably one of the biggest mysteries in the atmospheric sciences [1]. The relationship between thundercloud electrification, lightning activity, wide-band radio emission and particle fluxes has not been yet unambiguously established. One of the most intriguing opportunities opened by the observation of the high-energy processes in the atmosphere [2] is their relation to lightning initiation. The basic charge structure of a thundercloud can be viewed as a vertical tripole consisting of three charge centers (regions), the main positive region at the top, the main negative region in the middle, and a transient lower positively charged region (LPCR) below the main negative one. Thus a positive field extends from the LPCR in the cloud base up to the main negative-charge region in the middle of the cloud, and it is transformed into a negative field that extends to the main positive-charge region on the top of the thundercloud. Consequently, the lower dipole accelerates electrons of the ambient population of secondary cosmic rays downward in the direction of the Earth and the upper dipole accelerates electrons in the direction of the open space. Wilson postulated the acceleration of the electrons in the strong electric fields inside thunderclouds in 1924 [3]. In 1992 Gurevich *et al.* [4] developed the theory of the runaway breakdown, now mostly referred to as relativistic runaway electron avalanches (RREA, [5]). The separation of positive and negative charges in the thundercloud and the existence of a stable ambient population of the MeV electrons (secondary cosmic rays) in the atmosphere enables the acceleration of the electrons in the direction of the Earth's surface (thunderstorm ground enhancements, TGEs, [6,7]) and to open space (terrestrial gamma flashes, TGFs, [8]. Recent measurements of the TGEs shed light on the size of the particle-emitting region [9,10], energy spectra of electrons [11] and gamma rays [12]. The vast amount of TGE events registered by facilities of the Aragats space environmental center (ASEC, [13]) at an altitude of 3200 m in 2009–2014 allows us to develop a comprehensive model of TGE initiation [14]. The energy of accelerated electrons can reach ∼40–50 MeV and gamma rays 100 MeV. The flux of electron and gamma rays with energies above few MeV registered on the Earth's surface can exceed the cosmic-ray background up to 20 times.

TGEs are often associated with the negative polarity of the near-surface electric field [15] and with the suppression of the cloud-to-ground lightnings [7,9,10].

When the LPCR is vertically deeper and has a large horizontal extent, a descending negative leader would likely change its direction of propagation to predominantly horizontal; consequently the negative cloud-to-ground (−CG) lightnings will be suppressed and mostly negative intracloud (−IC) lightning will occur [16]. TGFs are believed to be generated during thunderstorms by the upper dipole and are associated with the initiation of the strong positive intracloud (+IC) lightning (see discussion in [17]). Thus, both TGEs and TGFs precede the lightning activity and can be used for the research of poorly understood

lightning initiation processes, providing a new research tool —the flux of elementary particles originated in the thunderclouds. Information acquired from the time series of TGEs and TGFs along with the widely used information on the temporal patterns of the radio emission waveforms will help to develop a reliable model of lightning initiation. Copiously measured during thunderstorms bipolar pulses known as preliminary breakdown (PB) pulse trains are thought to be an intra-cloud process that initiates or leads to the initiation of the stepped leader [18]. Nag and Rakov [16] claim that it is likely that the PB pulse trains provide a manifestation of the interaction of a downward-extending negative current with the LPCR; *i.e.* the pulse train occurs when a descending negative leader encounters a LPCR. Another indication of the LPCR existence is the enhanced particle flux detected on the Earth's surface —thunderstorm ground enhancement (TGE). The temporal pattern of the TGE, lightning and PB pulse train provide a unique information on the processes of the lightning initiation.

We select several TGE events detected in 2012–2014 by the ASEC facilities, which were terminated by the cloud-to-ground (CG) lightning flash. The measurements include one-second and one-minute time series of the elementary-particle count rates, gamma-ray energy spectra, meteorological conditions, fast and slow disturbances of near-surface electric field and others. Simultaneous registration of these parameters allows us to investigate their causal relation to lightning initiation.

**Instrumentation.** – The new emerging field of high-energy physics in the atmosphere involves measuring as many parameters as possible, such as particle fluxes, electric-field disturbances, radio emissions from the thunderclouds, and meteorological environments.

TGEs analyzed in the present study were observed by 3 cm thick scintillators with a sensitive area of 1 $m^2$ operated in the particle counter mode. The light collection is implemented by 84 spectrum-shifter fibers with a diameter of 1 mm. Light from the scintillator is re-radiated by the optical spectrum-shifter fibers to the long-wavelength region and passed to the FEU-115M photomultiplier. The scintillator is manufactured by injection molding in the form of $120 \times 100 \times 5\,mm^3$ dimensions plate with grooves for the spectrum-shifter fibers. The maximum of luminescence is at ∼420 nm and the luminescence time is 2.3 ns. The registration efficiency is ∼99% for electrons and ∼5% for gamma rays, the energy threshold is ∼1 MeV.

Extensive air showers are registered by the Aragats Solar Neutron Telescope (ASNT), see details in [6]. The ASNT consists of 4 upper (5 cm thick) and 4 lower (60 cm thick) scintillators, each having an area of 1 $m^2$. The distance between the layers is 1.2 m. All scintillators are located in iron lightproof housings and are overviewed by the FEU-49 photomultipliers. The data acquisition system registers all coincidences of the detector signals from the upper and lower layers and energy releases (number of particles) in the lower 60 cm thick scintillators. The signals ranging from 0.5 mV to 5 V, from each of the 8 photomultipliers, are passed to the programmable threshold discriminators. The output signals are fed in parallel to the 8-channel logical OR gate triggering device and to a buffer. The ASNT trigger condition is defined by detecting at least one signal in the 8 data channels. The duration of the entire data readout and the signal processing procedure is less than 10 $\mu$s.

A 52 cm diameter circular flat-plate antenna followed by a passive integrator is used to record the fast electric-field waveforms. The output of the integrator is directly connected to a 8-bit digitizing oscilloscope (Picoscope 3206) with a 60 cm long RG58 coaxial cable. The sampling rate is 10 ns, and record duration 5 ms, including 1 ms pre-trigger time. The recording system has a frequency bandwidth of 16 Hz–50 MHz and is triggered by a signal from a commercial MFJ-1022 active whip antenna that covers a frequency range from 300 kHz to 200 MHz.

The static electric field between the thunderclouds and the ground and the distance to the nearby lightning are measured with the EFM-100 electric-field mills of the Boltek company installed on the roofs of the buildings where the particle detectors are located. The electrical-field measurements are taken 20 times per second. The electric-field mill detects the net charge directly above in the atmosphere; the sensitivity range extends up to ∼30 km. Comparisons of measurements made by the network of three identical EFM-100 electrical mills prove reliability and rather high accuracy (∼20%) of near-surface electric-field estimation.

**Simultaneous detection of the lightnings and enhanced particle fluxes.** – Amid numerous TGEs detected by the ASEC facilities (see statistical analysis of the TGEs observed on Aragats in [19]) we select those abruptly terminated by the lightning analogical to the selection reported in [20]. Duration of TGE usually lasts from a minute to ten minutes with rather flat beginning and slow decay. However, in some cases smooth changes of the particle flux are sharply terminated by the lightning, see figs. 1 and 2.

Lightning very rarely occurs in the beginning of TGE (left side of fig. 1(b)) and at the maximum of TGE (fig. 1(c)). Usually, lightning terminates particle flux at the declining phase of TGE, when LPCR is dissipating due to the movement of the cloud or fading of the electric field in the cloud (fig. 1(a); right side of fig. 1(b); fig. 1(d); and fig. 2).

Table 1 contains the essential parameters of the selected TGEs. In the first column, we list the date of the event, in the second the time of the TGE maximum and relative amplitude (importance) of the particle flux peak in percent of the fair weather value and in number of standard deviations ($p$-value). In the third column we list the full width at half-maximum (FWHM) of the TGE. In the fourth–sixth columns we list the times of the lightning

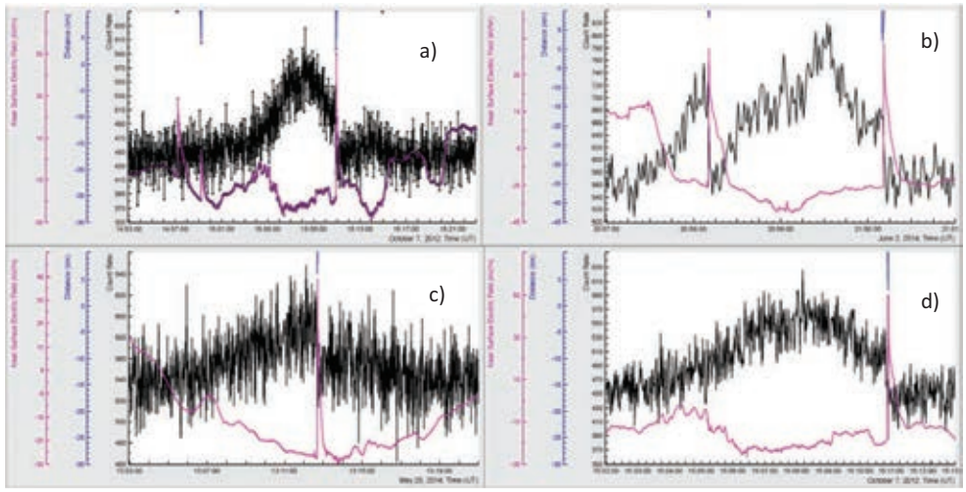


Fig. 1: (Colour on-line) Time series of the 1 second count rates of the outdoor 3 cm thick scintillator sharply terminated by the lightning and disturbances of the near-surface electric field; in the top of figures the distance to lightning from particle detectors is shown.

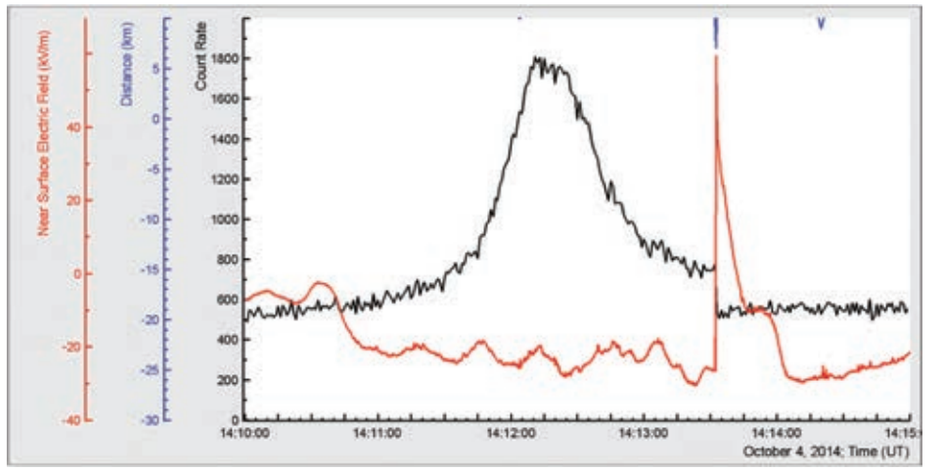


Fig. 2: (Colour on-line) Time series of the 1 second count rates of the outdoor 3 cm thick scintillator abruptly stopped by lightning and disturbance of the near-surface electric field; in the top of the figure the distance to lightning from particle detectors is shown.

start (sharp increase of the near-surface electric field), the time of the near-surface electric-field maximum and the time of FWHM along with the corresponding strengths of the near-surface electric field. In the seventh column, we list the fall of the particle detector count rate due to lightning occurrence. The eighth column shows the distance to lightning estimated by the electric-field mill EFM-100 and in the last column we list the time of the detection of the nearest extensive air shower (EAS), initiated by the high-energy primary hadron in the atmosphere above particle detectors.

As we can see from table 1 the statistical significance of the selected TGE events is rather high. TGE's maxima have mean enhancement above the background fluxes of $35 \pm 12\%$. The mean fall of the count rate caused by lightning is $21 \pm 7\%$.

From the table 1 we can outline the typical features of the negative cloud-to-ground lightning occurred on Aragats:

1) mean electric field before the start of the lightning $\sim -24.7 \pm 2.9\,\mathrm{kV/m}$;

2) the mean maximum value of the enhanced electric field $\sim 51 \pm 2.7\,\mathrm{kV/m}$ (after reaching the maximum the near-surface electric field slowly returns to pre-lightning values due to continuous charge separation processes in the cloud);

3) mean FWHM $\sim 4.8 \pm 3.1$ min;

4) mean electric field at FWHM $\sim 13.1 \pm 3\,\mathrm{kV/m}$;

Table 1: Main parameters of the TGE events terminated by lightnings.

| Date (UT) | Time and importance of TGE | FWHM TGE min. | Start of lightning (UT); El. field (kV/m) | El. field maximum time (UT) and maximum value (kV/m) | FWHM (UT) El. field (kV/m) | Time (UT) and drop of $\gamma$-ray flux (%) | Dist. (km) | EAS, ASNT (UT) |
|---|---|---|---|---|---|---|---|---|
| 07/10/2012 | 15:08<br>35%<br>($5.7\sigma$) | 6 | 15:10:53<br>−17.9 | 15:10:53.15<br>50.2 | 15:10:59.5<br>16 | 15:10:48–<br>15:10:52<br>22 | 2.9 | 15:10:52.7 |
| 26/05/2014 | 13:12<br>18%<br>($3.4\sigma$) | 8 | 13:12:41.5<br>−32 | 13:12:41.7<br>44 | 13:12:48.2<br>6 | 13:12:42–<br>13:12:44<br>13 | 6 | 13:12:41.5 |
| 02/06/2014 | 20:58<br>33%<br>($8\sigma$) | 0.5 | 20:58:10.2<br>−23.7 | 20:58:10.35<br>49.5 | 20:58:13.6<br>13 | 20:58:10–<br>20:58:11<br>24 | 8 | 20:58:09.4 |
| 02/06/2014 | 20:59:30<br>46%<br>($11\sigma$) | 1.5 | 21:00:10.7<br>−23.2 | 21:00:10.9<br>52.2 | 21:00:13.9<br>14.5 | 21:00:10–<br>21:00:11<br>22 | 2 | 21:00:10.7 |
| 04/10/2014 | 14:12:15<br>45%<br>($8.5\sigma$) | 0.5 | 14:13:32.4<br>−26.6 kV/m | 14:13:32.5<br>59.5 | 14:13:37.5<br>16 | 14:13:32–<br>14:13:33<br>31 | 6.8 | 14:13:31.3 |

5) mean time from the start of the electric-field sharp enhancement till its maximum $\sim 160 \pm 50$ ms;

6) mean distance to lightning $\sim 4.8 \pm 3$ km.

The very large amplitude of the negative lightning field changes ($\sim$75 kV/m) achieved in very short time ($\sim$160 ms) and the large recovery time of the electric field (tens of seconds) indicate strong discharge processes at nearby distances ($\sim$10 km and less) in the thunderclouds above Aragats. The time delay between the EAS registered by all the 8 scintillators of the ASNT detector (see details of the detector in [6]) and the start of lightning is $0.3 \pm 0.05$, $0.8 \pm 0.05$ and $1.1 \pm 0.05$ seconds for the events with lightning occurred at the decay phase of the TGE. Thus, we conclude that for these events the lightning occurrence is not connected with high-energy EAS. For both events occurred at the beginning and at the maximum of the TGE the time delay was $0 \pm 0.05$ seconds. We may connect the lightning initiation for these events with large EAS hitting occasionally the thundercloud and initiate step leaders to breakthrough ever "deep" LPCR.

**Waveforms of fast and slow disturbances of the electric field related to October 4, 2014 event.** – On 4 October 2014, 14:11:10 UT thunderclouds completely covered the sky at Aragats and the near-surface electric field abruptly goes down, reaching −22 kV/m. Simultaneously the particle count rate of 3 cm thick outdoor plastic scintillator starts to increase and reaches a maximum of 1808 counts per second at 14:12:14 (mean value with fine weather is 525 counts per second, MSD $\sim$23). The TGE particle flux enhancement was enormous; reaching 340% at the maximum flux second which is equivalent to the $p$-value of $53\sigma$, see fig. 2. At 14:13:31.5 the electric field starts its sharp increase, in 100 ms changing from −26.6 kV/m up to 59.5 kV/m. The large potential drop of the near-surface electric field of 86 kV/m occurred in 100 ms with consequential very long recovery of the pre-lightning electric field (the near-surface electric field returns to the negative domain after 40 seconds and reaches −27 kV/m at 14:13:53) indicates a huge negative charge deposited on the ground, *i.e.* the negative CG flash. In the same second the scintillator count rate decreases by 30% from 779 counts to the value of 541.

Fast electric-field waveform observed on October 4 at 14:13:31 is shown in fig. 3. The first of the two strong and short pulses of the same polarity with FWHM of $\sim 1\,\mu$s each, and amplitudes of 200 mV and 300 mV, separated by $10\,\mu$s triggers the data acquisition system. Prior to the strong signal, there are two weak nanosecond scale pulses observed at $\sim -8.4\,\mu$s and at $\sim -41\,\mu$s at the pre-trigger time with a single negative bipolar pulse in between at $-24\,\mu$s.

Nanosecond scale pulses that have the shape of a distorted sine wave with an average period of oscillation of $\sim$20–30 ns and typical full duration of 0.1–2 $\mu$s were frequently observed in the course of studying the wide-band

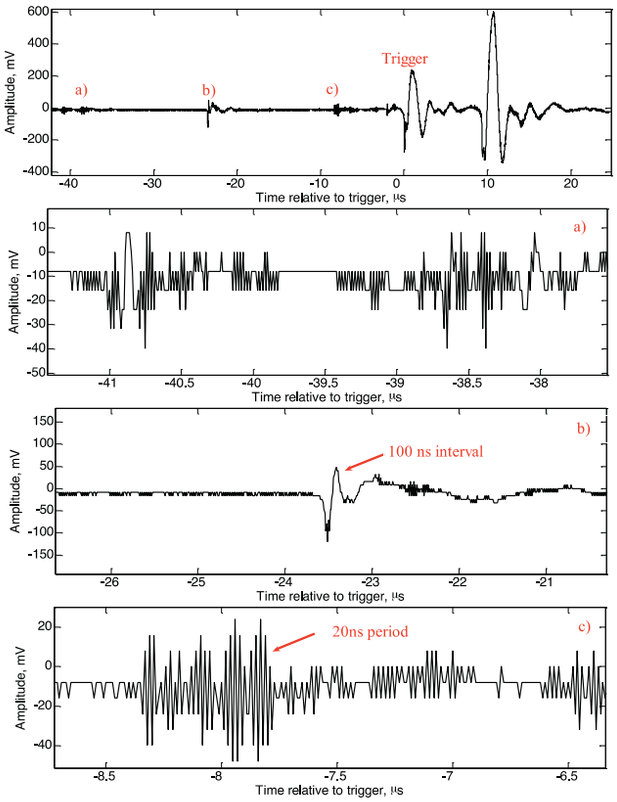


Fig. 3: (Colour on-line) Fast electric-field waveforms recorded on 4 October and associated with −CG lightning, which terminates the TGE shown in fig. 2. Panels (a), (b) and (c) are magnifications of the corresponding areas in the entire waveform.

electric fields connected with atmospheric discharges in the sky above the Aragats mountain. The preliminary stage of a −CG flash develops in a large positive electric field between the main negatively charged region in the middle of the cloud and the transient lower positively charged region (LPCR) in the bottom of the cloud. Probably, nanosecond scale pulses followed by large-amplitude electric-field disturbances can be considered as a precursor to the main lightning event (return-stroke).

**Conclusion.** – Electron and gamma-ray fluxes from the thundercloud are originated in the lower dipole formed by the main negatively charged region in the middle of the cloud and the transient lower positively charged region (LPCR). The LPCR prevents the lightning leader from reaching the ground and usually no −CG lightning occurs during mature LPCR when the particle flux is sizable. Only after decaying of the LPCR lightning the stepped leader makes its path to the ground.

TGEs and lightning are concurrent processes both discharging high potential difference in the cloud and switching off the electric field [21]. Continuous attempts to start the stepped leader produce a large number of low-energy (few eV) electrons by ionizing the air [22]. The low-energy electrons then drift in the thunderstorm electric field producing electric currents and radiofrequency emissions. The current resulting from the high-energy particles and their associate ionization could be some of the largest produced by the thunderstorm [23]. Therefore, this current will certainly increase the conductivity of the particular region of the thundercloud, facilitate its discharge and lead to the creation of a propagating hot leader channel [1,4]. Weak bipolar nanosecond scale radiofrequency pulses (fig. 3(a)) possibly originated from these discharges represent an early stage of formation of the conducting channel in the thundercloud (initial breakdown). Further development of the −CG lightning depends on the degradation of the LPCR. We adopted the hypothesis that the LPCR resides on water droplets (hydrometeors —HMs). The strong electric field polarizes and stretches water droplets and enhances the electric field in the bottom of the thundercloud. Our observations show that only at high humidity the TGEs at Aragats are possible and rains terminate the particle fluxes [14]. Local discharges on HMs stimulated by electrons [24] and propagation of the lightning step leader may generate a series of bipolar radiofrequency pulses (fig. 3(b) and (c)) reflecting a preliminary breakdown process of the lightning flash (fig. 3).

* * *

The authors thank the staff of the Aragats Space Environmental Center for the uninterruptible operation of Aragats research station facilities. The data for this paper are available via the multivariate visualization software (ADEI) [25] on the WEB page of the Cosmic Ray Division (CRD) of the Yerevan Physics Institute, `http://adei.crd.yerphi.am/adei`.

REFERENCES

[1] Dwyer J. R., Smith D. M. and Cummer S. A., *Space Sci. Rev.*, **173** (2012) 133.
[2] Dwyer J. R. and Uman M. A., *Phys. Rep.*, **534** (2014) 147.
[3] Wilson C. T. R., *Proc. Cambridge Philos. Soc.*, **22** (1925) 534.
[4] Gurevich A. V., Milikh G. M. and Roussel-Dupre R., *Phys. Lett. A*, **165** (1992) 463.
[5] Babich L. P., Kutsyk I. M., Donskoy E. N. and Kudryavtsev A. Yu., *Phys. Lett. A*, **245** (1998) 460.
[6] Chilingarian A., Daryan A., Arakelyan K. *et al.*, *Phys. Rev. D*, **82** (2010) 043009.
[7] Chilingarian A., Hovsepyan G. and Hovhannisyan A., *Phys. Rev. D*, **83** (2011) 062001.
[8] Fishman G. J., Bhat P. N., Mallozzi R. *et al.*, *Science*, **264** (1998) 1313.
[9] Torii T., Sugita T., Kamogawa M. *et al.*, *Geophys. Res. Lett.*, **38** (2011) L24801.
[10] Tsuchiya H. *et al.*, *Phys. Rev. Lett.*, **102** (2009) 255003.
[11] Chilingarian A., Vanyan L. and Mailyan B., *Astropart. Phys.*, **48** (2013) 1.
[12] Chilingarian A., Hovsepyan G. and Kozliner L., *Phys. Rev. D*, **88** (2013) 073001.

[13] Chilingarian A., Arakelyan K., Avakyan K. *et al.*, *Nucl. Instrum. Methods Phys. Res. A*, **543** (2005) 483.
[14] Chilingarian A., *J. Atmos. Sol.-Terr. Phys.*, **107** (2014) 68.
[15] Chilingarian A. and Mkrtchyan H., *Phys. Rev. D*, **86** (2012) 072003.
[16] Nag A. and Rakov V. A., *Geophys. Res. Lett.*, **36** (2009) L05815.
[17] Dwyer J. R., Liu N. Y. and Rassoul H. K., *Geophys. Res. Lett.*, **40** (2013) 4067.
[18] Rakov V. A. and Uman M. A., *Lightning: Physics and Effects* (Cambridge University Press, New York) 2003.
[19] Chilingarian A., Karapetan T. and Melkumyan L., *J. Adv. Space Res.*, **52** (2013) 1178.
[20] Tsuchiya H. *et al.*, *Phys. Rev. Lett.*, **111** (2013) 015001.
[21] Østgaard N., Gjesteland T., Carlson B. E. *et al.*, *Geophys. Res. Lett.*, **40** (2013) 2423.
[22] Gurevich A. V. and Zybin K. P., *Phys.-Usp.*, **44** (2001) 1119.
[23] Dwyer J. R., Uman M. A. and Rassoul H. K., *J. Geophys. Res.*, **114** (2009) D09208.
[24] Gurevich A. V. and Karashtin A. N., *Phys. Rev. Lett.*, **110** (2013) 185005.
[25] Chilingaryan S., Beglarian A., Kopmann A. and Vočking S., *J. Phys.: Conf. Ser.*, **219** (2010) 042034.

PHYSICAL REVIEW D **93,** 052006 (2016)

# Mount Aragats as a stable electron accelerator for atmospheric high-energy physics research

Ashot Chilingarian,[1,2] Gagik Hovsepyan,[1] and Eduard Mnatsakanyan[1]

[1]*A. Alikhanyan National Lab (Yerevan Physics Institute), Alikhanyan Brothers 2, Yerevan 0036, Armenia*

[2]*National Research Nuclear University MEPhI (Moscow Engineering Physics Institute), Moscow 115409, Russian Federation*

(Received 28 September 2015; published 7 March 2016)

Observation of the numerous thunderstorm ground enhancements (TGEs), i.e., enhanced fluxes of electrons, gamma rays, and neutrons detected by particle detectors located on the Earth's surface and related to the strong thunderstorms above it, helped to establish a new scientific topic—high-energy physics in the atmosphere. Relativistic runaway electron avalanches (RREAs) are believed to be a central engine initiating high-energy processes in thunderstorm atmospheres. RREAs observed on Mount Aragats in Armenia during the strongest thunderstorms and simultaneous measurements of TGE electron and gamma-ray energy spectra proved that RREAs are a robust and realistic mechanism for electron acceleration. TGE research facilitates investigations of the long-standing lightning initiation problem. For the last 5 years we were experimenting with the "beams" of "electron accelerators" operating in the thunderclouds above the Aragats research station. Thunderstorms are very frequent above Aragats, peaking in May–June, and almost all of them are accompanied with enhanced particle fluxes. The station is located on a plateau at an altitude 3200 asl near a large lake. Numerous particle detectors and field meters are located in three experimental halls as well as outdoors; the facilities are operated all year round. All relevant information is being gathered, including data on particle fluxes, fields, lightning occurrences, and meteorological conditions. By the example of the huge thunderstorm that took place at Mount Aragats on August 28, 2015, we show that simultaneous detection of all the relevant data allowed us to reveal the temporal pattern of the storm development and to investigate the atmospheric discharges and particle fluxes.

DOI: 10.1103/PhysRevD.93.052006

## I. INTRODUCTION

The theoretical investigation of the high-energy processes in the atmosphere was started 90 years ago by the Nobel Prize winner and creator of one of the first particle detectors C. T. R. [1]. Numerous papers published in recent decades by Gurevich, Dwyer, Babich, Lidvansky and coauthors (see citations to original publications in [2]) introduced the runway breakdown (RB), otherwise cited as relative runaway electron avalanches (RREAs) as a central engine of the high-energy processes in thunderstorm atmospheres. Measurements of particle fluxes on high mountains and in regions of Japan with low charge centers in thunderclouds prove the existence of particle fluxes that last up to a few tens of minutes correlated with thunderstorm activity (see details and references to original publications in the review of [3]). The first detection of huge fluxes of electrons, gamma rays, and neutrons on Mount Aragats in 2009 ([4]) has unambiguously established a new physical phenomenon—thunderstorm ground enhancement (TGE), increased fluxes of electrons, gamma rays, and neutrons detected by particle detectors located on the Earth's surface. The *in situ* observation of RREAs during the strongest thunderstorms on Aragats ([5]) and simultaneous measurements of TGE electrons and gamma-ray energy spectra ([6]) proved that RREA is a realistic and robust mechanism for electron acceleration in the atmosphere. These publications emphasized that lightning and TGEs are alternative mechanisms for the discharging of the atmospheric "electric engine"; they also introduced the origin of the highest energy gamma photons—modification of the cosmic-ray (CR) electron energy spectrum (MOS) in the strong electric field of the thundercloud. In [7], emphasized the role of the transient lower positive charge region (LPCR) in electron–gamma ray avalanche unleashing. Detailed measurements of the gamma-ray energy spectra by large NaI spectrometers on Aragats ([8]) allow us to reliably extend the energy range of the "thunderstorm" gamma rays up to 100 MeV. All these results were obtained at the Aragats research station in Armenia during the last 5 years with the "beams of the electron accelerator" operating in thunderclouds above the research station. The Aragats Space Environmental Center (ASEC, [9]) is located at an altitude of 3200 m on the plateau near a large lake and clouds usually form just above it (see Fig. 1).

Numerous particle detectors and field meters are located in three experimental halls as well as outdoors; the facilities are operated all year round. After understanding the TGE physics, we plan to apply this new evidence, i.e., fluxes of particles from the thundercloud, to approach the long-standing problems of lightning initiation and lightning leader propagation.

 

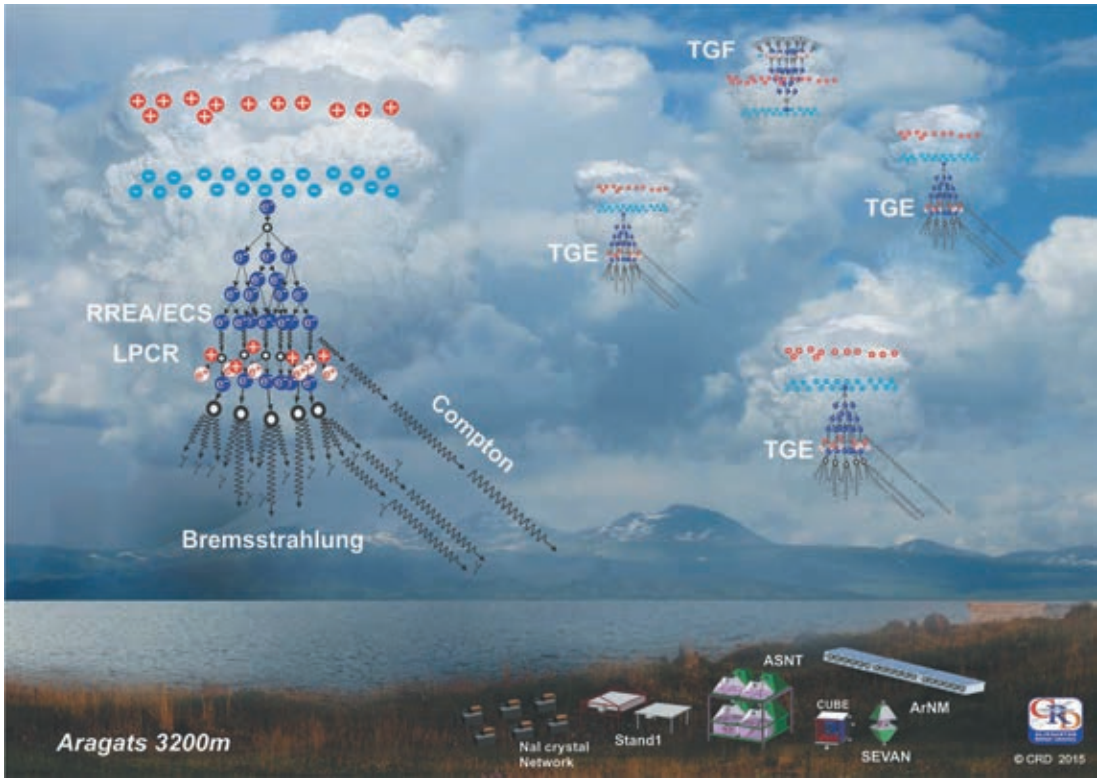


FIG. 1. Artistic view of the multiple RREA cascades in the thunderstorm atmosphere directed to Earth's surface (TGEs) and to space (TGF).

All the relevant information is being gathered, including data on particle fluxes, fields, lightning occurrences, and meteorological conditions. By the example of the huge thunderstorm that took place at Mount Aragats on August 28, 2015, we show that simultaneous detection of all the relevant data allowed us to reveal the temporal pattern of the storm development and to investigate the atmospheric discharges and particle fluxes. The paper is comprised of the following sections: instrumentation; chain of positive lightning strikes; chain of negative lightning strikes; small size TGE; and large size TGE. Thunderstorms are very frequent above Aragats, with peak activity in May–June and September–October. Almost all of them are accompanied with enhanced particle fluxes. In Fig. 1 we see an artistic view of multiple electron–gamma ray avalanches directed to the Earth's surface and to open space. The first ones originated TGEs registered by the ground-based particle detectors; the second ones originate from terrestrial gamma flashes (TGFs) ([10]) observed by the orbiting gamma-ray observatories.

By analyzing a particular stormy day at Aragats, namely, August 28, 2015, we will demonstrate the operation of the electron "accelerator" in the vicinity of the station and present the stages of our physical inference on the discovery of the new phenomenon of "long TGEs"—enhancements of low-energy gamma-ray fluxes (0.4–2 MeV) that last for several hours.

## II. INSTRUMENTATION

The particle detectors of the Aragats Space Environmental Center (ASEC) ([9]) can measure the fluxes of the species of secondary cosmic rays (electrons, gamma rays, muons, and neutrons), which have different energy thresholds. Numerous thunderstorm-correlated events, detected by the ASEC facilities, constitute a rich experimental set for the investigation of the high-energy phenomena in the thunderstorm atmosphere. The new generation of ASEC detectors consist of 1- and 3-cm-thick molded plastic scintillators arranged in stacks and cubic structures. The "STAND1" detector is comprised of three layers of 1-cm-thick, 1-$m^2$ sensitive area molded plastic scintillators fabricated by the High Energy Physics Institute, Serpukhov, Russian Federation; see Fig. 2. The light from the scintillator through optical spectrum-shifter fibers is reradiated to the long-wavelength region and passed to the photomultiplier FEU-115M. The maximum of luminescence is emitted at the 420-nm wavelength, with a luminescence time of about 2.3 ns. The STAND1 detector is tuned by changing the high voltage applied to photomultiplier (PM) and setting the thresholds for the discriminator shaper.

The threshold should be chosen to guarantee both high efficiency of signal detection and maximal suppression of photomultiplier noise. Proper tuning of the detector provides ~99% efficiency of charged particle detection. The data

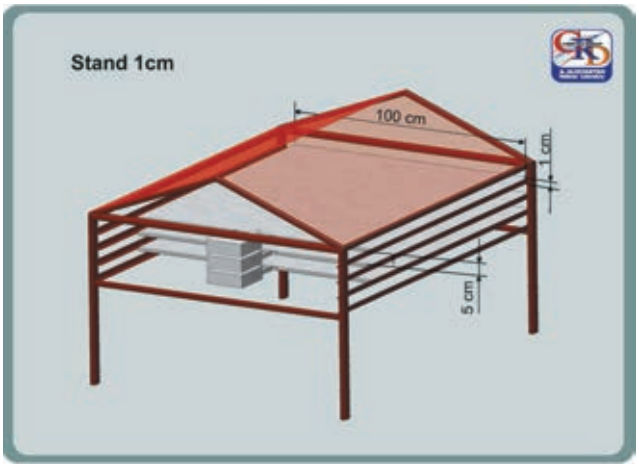


FIG. 2. STAND detector consisting of three layers of 1-cm-thick scintillators.

acquisition (DAQ) system counts and stores all coincidences of the detector channels. Coincidence "100" means that a signal has been registered in the upper detector only. This combination registered low-energy electrons with an efficiency of ∼99%; the threshold energy of ∼1 MeV is one of the lowest among all ASEC detectors. The gamma-ray detecting efficiency of this combination is about 2%. For the coincidence 010, the gamma ray detection efficiency is increased to ∼3% due to creation of the additional electron-positron pairs in the substance of the upper scintillator. Coincidence "111" means that all three layers register particles; the minimal energy of charged particles giving a signal in all three layers is ∼10 MeV. With the same DAQ electronics are registered the time series of a similar (but 3-cm-thick) particle detector stand near the stacked structure.

Special experimental facilities were designed and installed at Aragats in order to separate electron and gamma-ray fluxes. Two 20-cm-thick plastic scintillators are surrounded by 1-cm-thick molded plastic scintillators (see Fig. 3). Thick scintillators detect charged flux with a very high efficiency (∼99%); they can also detect neutral flux with an efficiency of ∼20%. Thin scintillators also detect charged flux with very high efficiency (∼99%), though the efficiency of detecting neutral flux is highly suppressed and equals 1%–2%. Thus, using the coincidences technique, it is possible to purify the neutral flux detected by inside scintillators, rejecting the charged flux by the veto signals from surrounding thin scintillators. The calibration of the cube detector proves that the veto system (preventing the counting signal in the thick scintillator if there is a signal in at least one of the six surrounding thin scintillators) can reject 98% of the charged flux (see details in [6]).

The histograms of the energy deposits in the two inner thick scintillators are stored every minute. The one-minute count rates of the surrounding 6 scintillators are measured and stored as well.

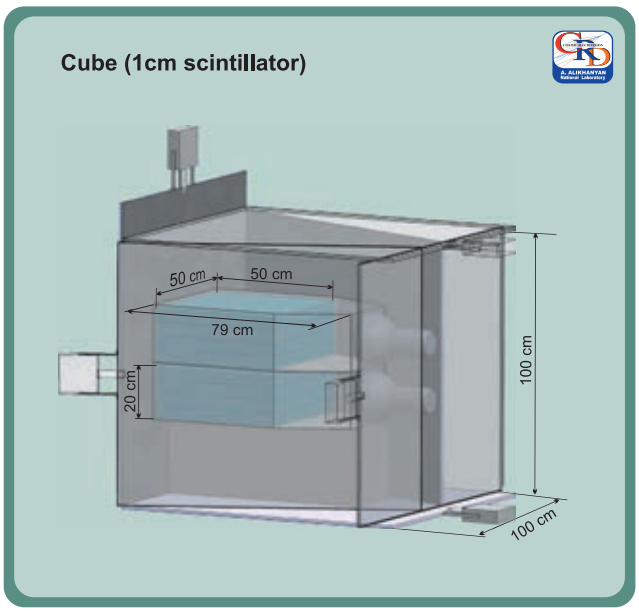


FIG. 3. CUBE detector. The thick scintillators located inside are measuring neutral flux with purity ∼98%.

The detector network measuring particle energy consists of four NaI crystal scintillators packed in a sealed 3-mm-thick aluminum housing. The NaI crystal is coated by 0.5 cm of magnesium (MgO) by all sides (because the crystal is hygroscopic) with a transparent window directed to the photo-cathode of a FEU-49 PM; see Fig. 4.

The large cathode of FEU-49 (15-cm diameter) provides a good light collection. The spectral sensitivity range of FEU-49 is 300–850 nm, which covers the spectrum of the light emitted by NaI(Tl). The sensitive area of each NaI crystal is ∼0.0348 $m^2$, the total area of the four crystals is ∼0.14 $m^2$, and the gamma-ray detection efficiency is ∼80%. A logarithmic analog-digit converter (LADC) is used for the coding of PM signals. Calibration of LADC

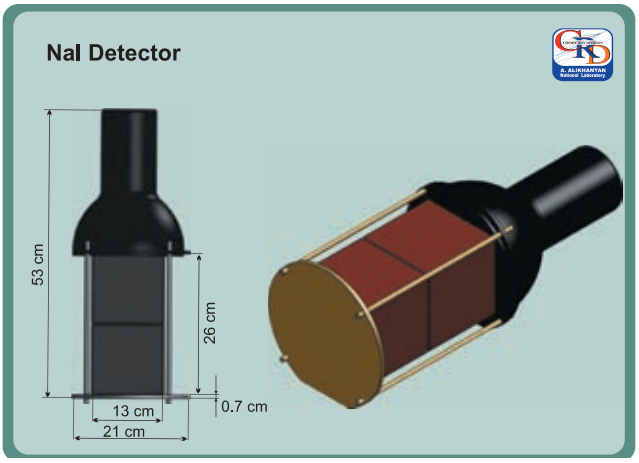


FIG. 4. NaI(Tl) crystal assembly.

and code-energy conversion was made by detecting the peak from exposed $^{137}$Cs isotope emitting 662 keV gamma rays and by the high-energy muon peak (55 MeV) in the histogram of energy releases in the NaI crystal. The PM high voltage was tuned to contain both structures (peaks) in the histogram of LADC output signals (codes) and to ensure linearity of LADC in the energy region of 0.4–60 MeV. A detailed description of other ASEC detectors, including charts with all sizes, is available from the WEB site of the Cosmic Ray Division of Yerevan Physics Institute http://crd.yerphi.am/ADEI in the WIKI section of the multivariate visualization platform and from ([4,11]).

The count rate of a particle detector depends on the chosen energy threshold of the shaper discriminator, the size of the detector, and the amount of matter above it. The inherent discrepancy of the parameters of PMs also can add ∼15% difference to the particle detector count rates. A significant amount of substance above the sensitive volume of NaI crystals (0.7 mm of roof tilt, 3 mm of aluminum, and 5 mm of MgO) prevents electrons with energy lower than ∼3 MeV from entering the sensitive volume of the detector. Thus, the network of NaI spectrometers below 4 MeV can detect gamma rays only.

The small sizes of the NaI crystals and short duration of TGE pose a limitation on the lowest gamma-ray flux that can be reliably observed. The usual requirement on the minimal amount of particles in a histogram bin is >5; therefore, the minimal flux that can be reliably detected by the NaI network should be above 200 per minute per m$^2$ (the area of four crystals is 0.14 m$^2$ and the required number of particles in four crystals is greater than 20). For smaller fluxes, fluctuations overwhelm the signal.

The significance of detecting peaks in the time series of the particle count rates is determined by the p-values of the peak significance test, i.e., by the value of the peak divided by the standard deviation of the count rate (number of standard deviations contained in the peak, N$\sigma$). The p-value is the most comprehensive measure of the reliability of detecting peaks in a time series. A large p-value corresponds to small-chance probabilities that the observed peak is a background fluctuation and not a genuine signal. Therefore, we can safely reject the null hypothesis (background fluctuation) and confirm the TGE. Very large p-values not only prove the unambiguous existence of a particle flux from the cloud, but also serve as a comparative measure of the TGE observations using different detectors.

The deep negative near-surface electric field is a necessary condition for the TGE origination. Moreover, the observed changes of the electric field, along with detected particle fluxes, encompass information on the dynamics of the cloud electrification, which is very difficult to acquire by *in situ* measurements. A network of three electric mills continuously monitors the disturbances of the electric field on Mount Aragats. The electrical mill EFM 100 produced by the Boltek Company operates with a 20-Hz frequency, performing 20 measurements of the near-surface electric field per second. Comparisons of electric field strengths obtained by the three identical EFM-100 electrical mills prove the reliability and high accuracy (discrepancy of device readings do not exceed 10%) of electric field measurements.

## III. SERIES OF POSITIVE LIGHTNINGS AT ∼12:00–13:00

On August 28, almost all day long, the thunderstorms at Aragats were accompanied with numerous nearby lightning strikes and several episodes of the enhanced particle fluxes registered by the detectors located at ASEC.

The network of NaI spectrometers had detected an enhanced flux of low-energy gamma rays with several

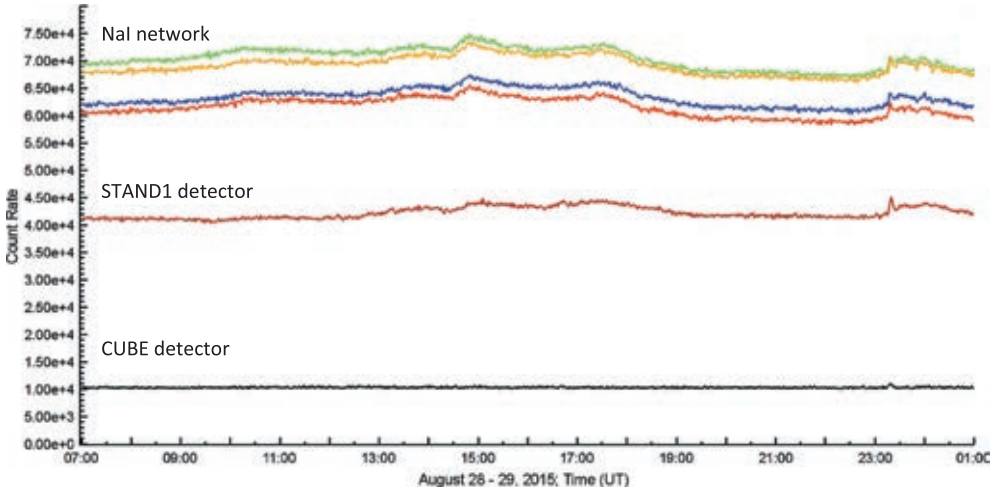


FIG. 5. One-minute count rates of the network of four NaI spectrometers. TGE at 23:18–23:21 contains high-energy gamma rays detected by all ASEC particle detectors.

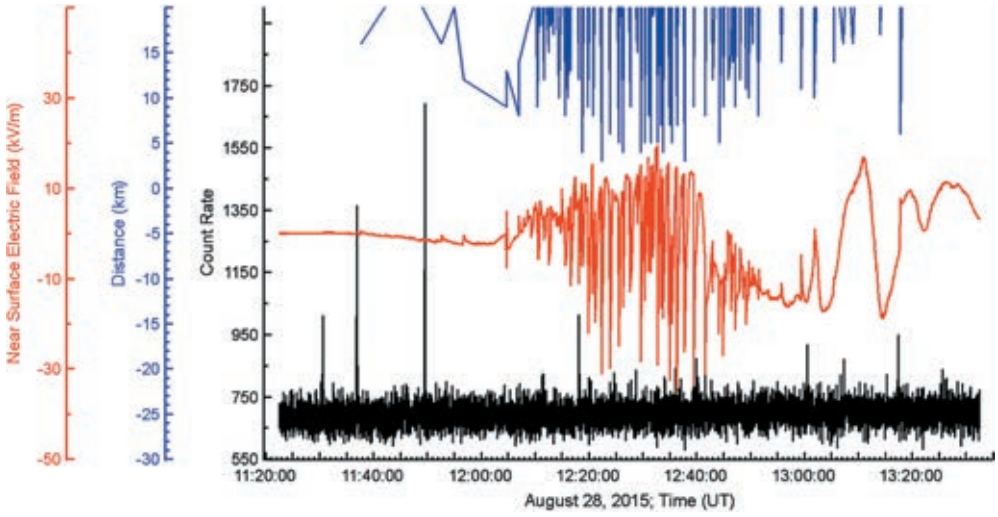


FIG. 6. Positive lightning series observed on August 28, 2015, 12:00–13:00. The top lines show distance to lightning, the middle curve shows disturbances of the near-surface electric field, and the bottom shows the 1-second time series of count rates of the 3-cm-thick, 1-$m^2$ area plastic scintillator.

episodes of abrupt bursts, as shown in Fig. 5. In spite of the fact that the NaI crystals are much smaller than the plastic scintillators, due to the low-energy threshold (0.4 MeV) and higher efficiency to register gamma rays the count rates of each of the four spectrometers are higher than the counts of larger plastic scintillators. The ∼15% discrepancy of the count rates of the four spectrometers is explained by the differences in PM parameters. This discrepancy does not influence the amplitude of TGE (peak value of the count subtracted by background value), which is the same for all four spectrometers. The matter above the sensitive volume of NaI spectrometer absorbs electrons with energies below 3 MeV; the detection of electrons and gamma rays of higher energy is possible. In Fig. 5 we can see that the time series of the CUBE detector (a 20-cm-thick detector located inside the veto housing with energy threshold ∼4 MeV) demonstrates enhancement only around 23:20 when, as we will see later, the gamma-ray flux exceeded 4 MeV due to presence of the bremsstrahlung gamma rays from the runaway electrons. The STAND1 detector (energy threshold ∼1 MeV) showing a flux enhancement coherent to NaI at a smaller scale had also demonstrated a pronounced peak around 23:20.

For recovering electron and gamma-ray intensity in the TGE flux at energies above 4 MeV we use data from the CUBE detector, vetoing the charge flux.

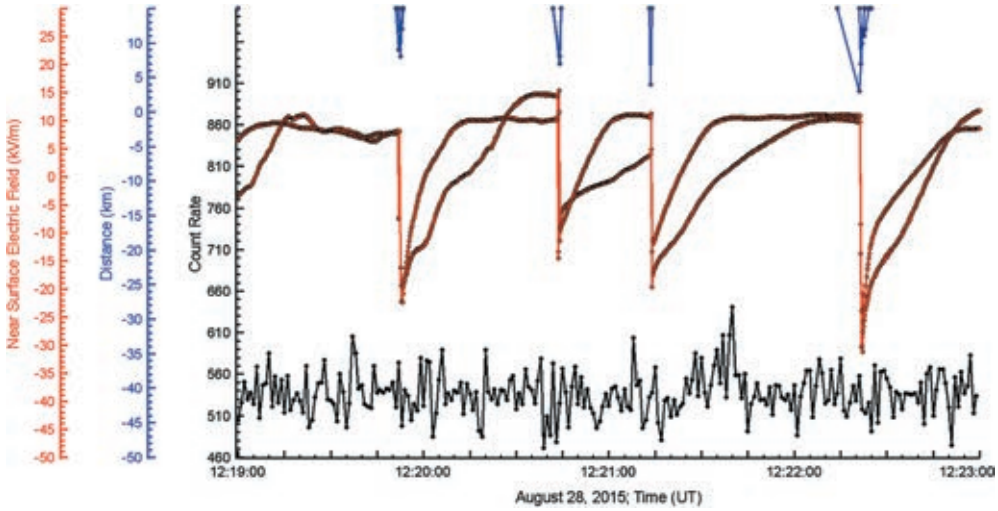


FIG. 7. One episode of positive lightning series observed on August 28, 2015, at 12:00–13:00. The top lines show distance to lightning, the middle two curves show disturbances of the near-surface electric field measured by electric mills located at a distance of 300 m from each other, and the bottom shows the 1-second time series of count rates of the 3-cm-thick, 1-$m^2$ area plastic scintillator.

TABLE I. Main characteristics of a sample of lightning occurrences at 12:19–12:23 on August 28, 2015.

| Start of lightning (UT) and el. field value (kV/m) | Time of el. field minimum (UT) and field minimal value (kV/m) | Duration (sec) | Recovering (sec) | Drop of el. field | Dist. (km) | WWLLN time | WWLLN dist. |
|---|---|---|---|---|---|---|---|
| 12:19:52.1 8 | 12:19:52.75 -23 | 0.65 | 21 | −31 | 8 | | |
| 12:20:43.7 15 | 12:20:43.8 -18 | 0.1 | 29 | −33 | 7 | | |
| 12:21:13.8 10 | 12:21:14.0 -20 | 0.2 | 23 | −30 | 4 | | |
| 12:22:21.3 10 | 12:22:21.8 -30 | 0.5 | 31 | −40 | 3 | | |
| 12:51:31.15 -14 | 12:51:31.55 -8 | 0.4 | 29 | 6 | 8 | 12:51:31.23–12:51:31.47 | 5–9 |

Due to the small sensitive area of NaI spectrometers, we can recover differential energy spectra at energies above $\sim 10^3/\mathrm{m}^2$ min, equivalent to 5–10 registered particles in an energy bin. Histograms of the energy releases in NaI crystals are collected and stored each minute; therefore we can recover 1440 energy spectra daily. To achieve better statistical accuracy, we use the data from all four spectrometers and combine several minutes around the peak values of the count rate. The energy spectra were recovered, according to the methodology described in ([12]), for four TGE episodes at 14:49–14:52, 16:37–16:44, 23:18–23:21, and 23:29–23:31. The relative enhancement was calculated by subtracting from the peak value of the count rates the background measured just before the enhancement started. Only the relative enhancement in measurements with NaI crystals has physical meaning in the described series of measurements. The NaI spectrometers were located just below the iron tilts of the roof. In August at Aragats, the sun is extremely strong and the temperature under the iron roof reached 50–60 C°. The high temperature influenced DAQ electronics and, respectively, the detector count rate increased at peak temperatures up to 10% as compared with nighttime count rate when the temperature drops down to 5–10 C°. Therefore, though the maximal absolute count rate was achieved at ∼15:00, the TGE at 23:20 has larger amplitude and was much more significant; it could be explained by the bremsstrahlung gamma rays emitted by the runaway electrons in the thundercloud just above the detectors.

The electric field disturbances on August 28, 2015, were prolonged and deep, reaching −35 kV/m; lightning activity was strong and some of the lightning strikes were within 5 km of the station. Numerous positive lightning strikes that started at ∼8:00 stipulate small disturbances of the near-surface electric field. The network of three EFM-100 electric mills measured the near-surface electric field. The devices operated according to the "atmospheric electricity" sign convention (a positive electric field at ground is produced by positive charge overhead and negative electric field on the ground is produced by negative charge overhead). Thus, the recorded positive field change corresponds to negative lightning, which decreases the negative charge overhead and negative field change corresponds to positive lightning, which decreases the positive charge overhead. The heavy-duty storm that started at ∼12:00 was followed by copious positive lightning strikes lasting until ∼13:00 (Fig. 6). In Fig. 6 we show the electric field disturbances measured by the electric mill located on the roof of the MAKET building, the corresponding distance to the lightning and one-second time series of 1-$\mathrm{m}^2$ plastic scintillator. The spikes in the particle count rates are due to the showers hitting the scintillator. In one-minute time series they are smoothed by integration over 60 seconds, but in 1-second time series spikes are visible.

In Fig. 7 we show four minutes of stormy weather matched with four positive lightning strikes (zoomed from Fig. 6).

The pattern of rapid decrease of the electric field was approximately the same for both electric mills located at a distance ∼300 m from each other. The abrupt decrease of the near-surface electric field followed by relatively slow recovery indicates the neutralization of a positive charge in the thundercloud. However, the operation of the charging engine permanently recovers the positive charge region in the thundercloud. In Table I we post the characteristic of

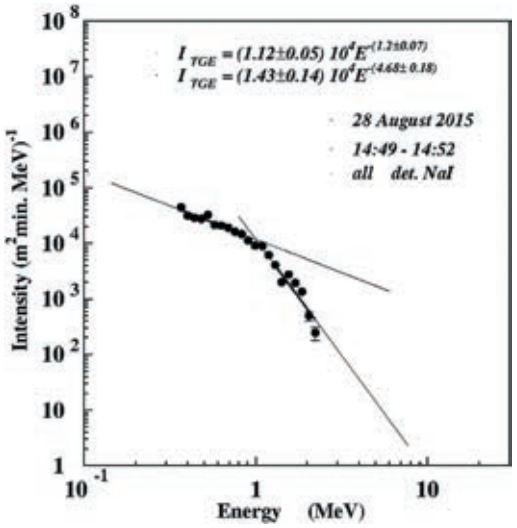


FIG. 8. The differential energy spectrum of the sum of 4 NaI spectrometers. The background was measured just before the TGE started. Flux intensity is $0.18 \times 105/\mathrm{m}^2$ min, knee position is 0.9 MeV, and intensity after knee is $0.50 \times 10^4/\mathrm{m}^2$ min.

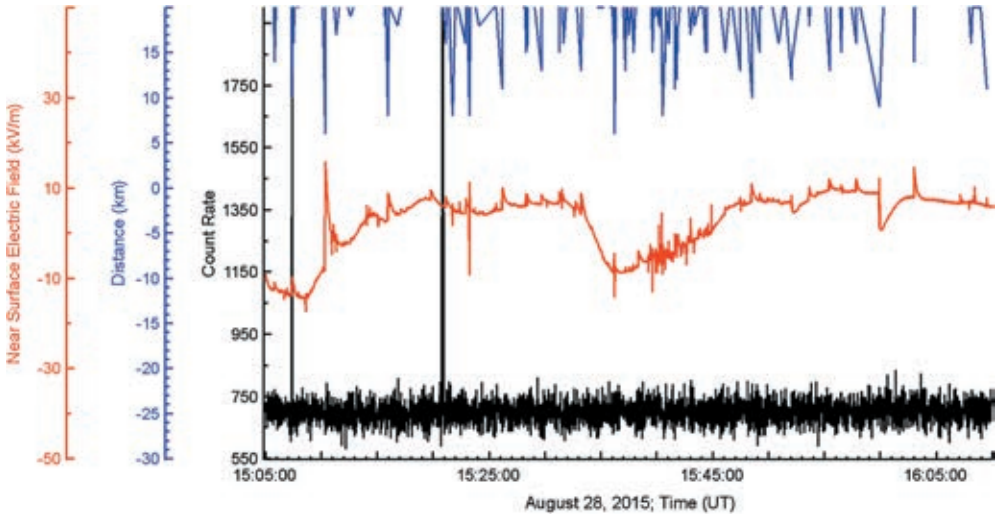


FIG. 9. Multiple negative lightning strikes detected at 14:45–16:30. The top lines show distance to lightning, the middle curve shows disturbances of the near-surface electric field, and the bottom shows 1-second time series of the count rates of the 3-cm-thick, 1-$m^2$ area plastic scintillator.

four positive (+CG) lightning strikes from ∼100 that occurred on August 28, 2015; at the end of an hour-long series of positive lightning strikes, they changed to the negative ones.

Although the amplitudes of negative lightning strikes were small, four strikes (at 12:51:31.23–12:51:31.47) were registered by the Worldwide Lightning Location Network (WWLLN), one of the nodes of which is installed at the Cosmic Ray Division (CRD) headquarters in Yerevan, ∼50 km from Aragats station.

From Table I, where we present the main characteristics of the lightning strikes shown in the previous figure we can outline typical features of the positive cloud-to-ground lightning that occurred on Aragats on August 28, 2015:

1. Mean electric field before the start of the lightning ∼8–15 kV/m;
2. Typical values of the drop of electric field ∼ − 30– − 40 kV/m;
3. After reaching its minimum, the near-surface electric field slowly returned to the prelightning values due to continuous charge separation processes in the cloud in 21–31 seconds;
4. Time from the start of electric field sharp decrease till its minimum was ∼0.1–0.65 sec;
5. Distance to lightning was ∼3–8 km.

The rather large amplitude of the positive lightning field changes (−30– − 40 kV/m) achieved in less than 1 sec and the large recovery time of electric field (tens of seconds) indicate strong discharge processes at nearby distances (10 km). Several high masts are located near the station; from their tops the electron streamers can propagate to the positive charge regions in the thunderclouds above. As usual during a series of positive lightning strikes no enhancements of particle flux were registered.

The strong rain that started at 13:22 stopped at 14:00. The temperature started to rise from 4 C° at 13:00 to 6 C° at 14:30 and then abruptly dropped to 3.4 C° at 14:50 UT. The relative humidity decreased from 95% at 13:00 to 75% at 14:30. The electric field was in the negative domain −8 to −24 kV/m; few lightning strikes were detected. At

TABLE II. Main characteristics of a sample of lightning occurrences at 15:38–16:03 on August 28, 2015.

| Start of lightning (UT) and el. field value (kV/m) | Time of el. field maximum (UT) and field maximal value (kV/m) | Duration (sec) | Recovering (sec) | Drop of el. field | Dist. (km) | WWLLN time | WWLLN dist. |
|---|---|---|---|---|---|---|---|
| 15:38:21.8 -7 | 15:38:22.7 -4 | 0.9 | 32 | 3 | 14 | 15:38:22.41 | 21 |
| 15:53:39.4 7 | 15:53:40.3 (15:53:39.9) 10 | 0.9 | 41 | 3 | 18 | 15:53:39.5 | 14 |
| 15:59:54.4 9 | 15:59:54.6 12 | 0.2 | 0.1 | 3 | 9 | 15:59:54.32 | 14 |
| 15:59:54.85 9 | 15:59:55.0 2 | 0.15 | 180 | −7 | 20 | 15:59:54.34 | 8 |
| 16:03:01.05 8 | 16:03:01.55 15 | 0.5 | 27 | 7 | 13,15 | 16:03:01.0 – 16:03:01.86 | 11–21 |

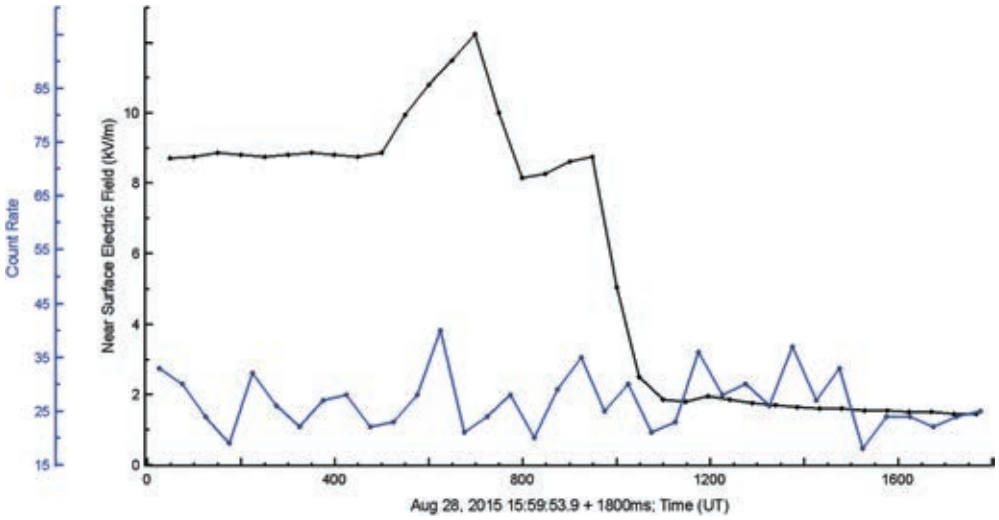


FIG. 10. Disturbance of the near-surface electric field when the negative discharge suddenly turned to a positive one. The bottom line shows the 50-m sec time series of the 3-cm-thick, 1-$m^2$ area, outdoor plastic scintillators.

14:30 the gamma-ray flux started to rise, reaching maximum at 14:50. The differential energy spectrum of the gamma-ray flux is shown in Fig. 8. We fit the energy spectrum with two power law dependences; the point where interpolating dependence changes is usually named the "knee." The knee position is located at ∼1 MeV and is rather smooth. The energy spectrum extends to ∼2 MeV and then quickly decays.

In the next hour the lightning activity became stronger; see Fig. 9. However, the atmospheric discharges were far from the Aragats station and, therefore, the amplitudes of the near-surface electric field disturbances were small, as shown in Table II. The relative humidity (RE) successively increased from 75% at 14:30 to 92% at 15:45 when the rain resumed. At the same time, the wind speed decreased from 2 m/ sec to 0.2–0.6 m/ sec and the temperature decreased from 3.4 C° to 2.9 C°.

## IV. SERIES OF NEGATIVE LIGHTNING STRIKES AT ∼15:00–16:00

After 15:00, as we can see from Fig. 9 and the Table II that the pattern of disturbances of electric field drastically changed as compared with the ones registered 2 hours before (Figs. 6 and 7). The lightning locations were 10–20 km from the station (confirmed by WWLLN; see the last column of Table II). Therefore, the amplitude of disturbances of the near-surface field was small, −3–7 KV/m. Lightning strikes were mostly negative; i.e., the large amount of negative charge overhead was decreased. No TGEs were detected. The spike in 1-sec time series of the plastic scintillator was due to the particle shower that hit the detector at 15:07:23.

The illustration of the 3 seconds of time series of the near-surface electric field, revealing the pattern of an unusual lightning strike that occurred at 15:59:54.4–15:59:55, is given in Fig. 10. In 0.6 seconds the negative discharge (abrupt enhancement of the electric field) with amplitude 3 kV/m suddenly turned to a positive one (abrupt decrease of the electric field) with amplitude −7 kV/m (see also Table II).

## V. SMALL SIZE TGE WITH MAXIMUM AT ∼16:40

At 16:20 the electric field moved to a negative domain and at 16:43 it dropped to −23 kV/m. Between 16:36 and 16:43 at the large negative electric field several small "bumps" appeared with an amplitude less than 5 kV/m. During that "bumpy" time (16:37–16:44) several ASEC

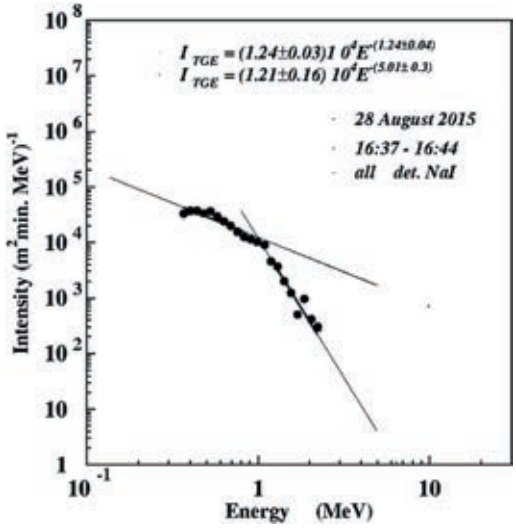


FIG. 11. Differential energy spectrum of the "small size" TGE. Flux intensity is $0.95 \times 10^4/m^2$ min, knee position is 0.9 MeV, and intensity after knee is $0.25 \times 10^4/m^2$ min.

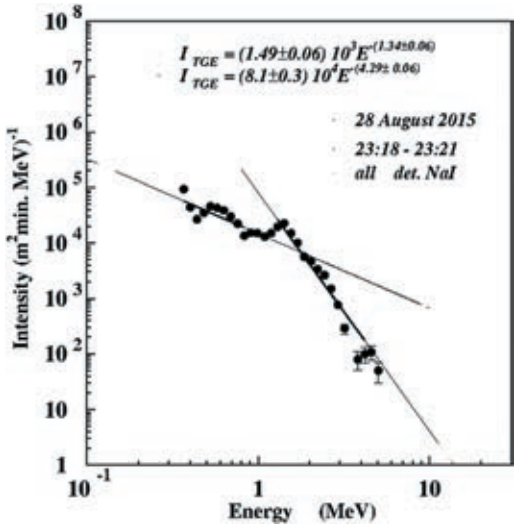


FIG. 12. Differential energy spectrum of TGE obtained by the 4 NaI spectrometers: flux intensity is $0.34 \times 10^5/\mathrm{m}^2$ min, knee position is 1.2 MeV, and intensity after knee is $0.17 \times 10^5/\mathrm{m}^2$ min.

particle detectors registered TGE. The intensity of the event was two times less than previous TGE; see Fig. 11. The knee position is analogous to the previous spectrum and the change of the interpolating power law function is smooth too. The energy spectrum continues to ∼2 MeV.

The relative humidity (RE) was 92–95% during TGE (high RE is another necessary condition to unleash large TGE) and wind speed was ∼1 m/ sec. The temperature started to fall at 16:26 from 3.5 C° down to 2.9 C° during TGE. Wind direction was 180°N. It stopped raining at 16:27 and resumed at 17:00. Consequently, there was no rain during TGE.

## VI. LARGE TGE OCCURRED AT ∼23:18–23:21

Disturbances of the electric field and lightning strikes took place until 17:30 and the rain did not stop until 22:00. After the rain stopped, the electric field started to decrease at 23:00 reaching −28 kV/m at 23:21. The relative humidity (RE) went up from 89% at 23:14 to 92% at 23:17 and remained there until 23:23. Wind speed abruptly increased from 0 m/ sec at 23:13 to 7.5 m/ sec at 23:19, and then decreased down to 1 m/ sec at 23:23. The temperature started to decrease at 23:13 from 3.9 C°, reaching 0.8 C° at 23:23. Wind direction was 200N. The TGE flux reached maximum at 23:19; energy spectra of TGE extended to 6 MeV (see Fig. 12). The TGE event duration was ∼10 minutes; intensity and maximal energy were greatest on August 28. Knee position shifted to 1.2 MeV and the knee was sharper than in previous TGEs. The intensity of TGE is the highest among those observed on August 28, 2015.

The veto system of the CUBE detector rejected most of the charged particles by six 1-cm-thick plastic scintillators with 1-$m^2$ area shaped in a cubic structure. The two 20-cm thick scintillators located inside an area of 0.25 $m^2$ registered neutral particles with the veto system switched on. The CUBE detector with two inner 20-cm-thick plastic scintillators with energy threshold ∼4 MeV also demonstrated pronounced peaks (Fig. 13). Figure 13 does not show the time series of the count rates itself, but the time series of the p-values of the peak significance test. The large p-values of peaks observed by the two inner 20-cm-thick scintillators of the CUBE detector allows us to estimate charged and neutral fluxes of TGE above ∼4 MeV (NaI spectrometers allow us to measure pure gamma-ray flux below 3–4 MeV and mixed flux above 3–4 MeV).

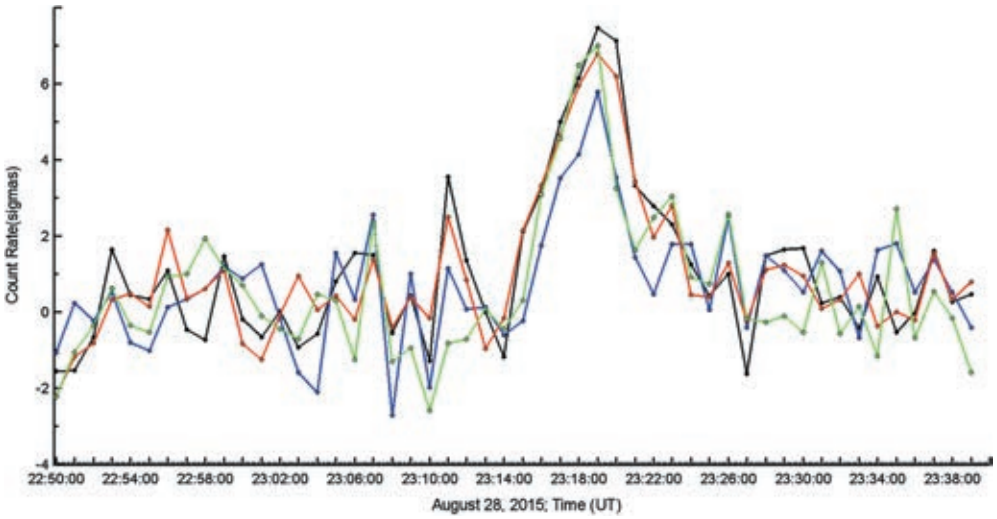


FIG. 13. TGE observed by the CUBE detector's two stacked 20-cm-thick plastic scintillators with and without the veto system switched on.

TABLE III. Count rate of 20 cm thick plastic scintillator with and without veto (minutes after 23:00 UT).

| August 28 (UT) | | | | |
|---|---|---|---|---|
| 23:16 | 10548 | 8614 | 4526 | 3577 |
| 23:17 | 10736 | 8749 | 4633 | 3647 |
| 23:18 | 10853 | 8797 | 4735 | 3739 |
| **23:19** | **10990** | **8923** | **4802** | **3764** |
| 23:20 | 10954 | 8750 | 4755 | 3585 |
| 23:21 | 10564 | 8589 | 4534 | 3507 |
| 23:22 | 10508 | 8516 | 4418 | 3548 |
| 23:23 | 10459 | 8617 | 4484 | 3575 |

From Table III we can see that at 23:19 the CUBE scintillators registered maximal count rate; for that minute we calculate the electron and gamma-ray intensities incident on the CUBE detractor.

Due to a nonzero probability of electrons to miss registration in the 1-cm-thick plastic scintillator of the veto system, and due to a nonzero probability for the detection of the gamma ray by the same scintillator, we have made corrections to recover intensities (see details in [6]). However, these corrections are below ∼2% as compared with calculation of the gamma-ray intensity directly from the amplitude of the peak observed by the thick scintillator with the veto switched on (538 counts). The intensity of gamma rays above ∼4 MeV is $\sim 10^4/\mathrm{m}^2$ min, and the intensity of electron flux is $-8 \times 10^2/\mathrm{m}^2$ min. Thus, the fraction of electrons at energies above 4 MeV does not exceed ∼7%.

In Table IV we show the mean values of count rate, the peak value, amplitudes of the peaks (also in the number of standard deviations), and calculated intensities (integral spectra) of gamma-ray and electron flux above ∼4 MeV. We assume the efficiency of gamma-ray detection by the 20-cm-thick scintillator to be equal to 20% and detection of electrons 99%.

The efficiency of detecting gamma rays by the "veto" 1-cm-thick scintillators is 2% and electrons 99%. Particles to be registered in the bottom thick scintillator (see Fig. 3) should traverse through the upper one; therefore due to attenuation of the particle flux, intensities measured by the bottom scintillator are significantly lower.

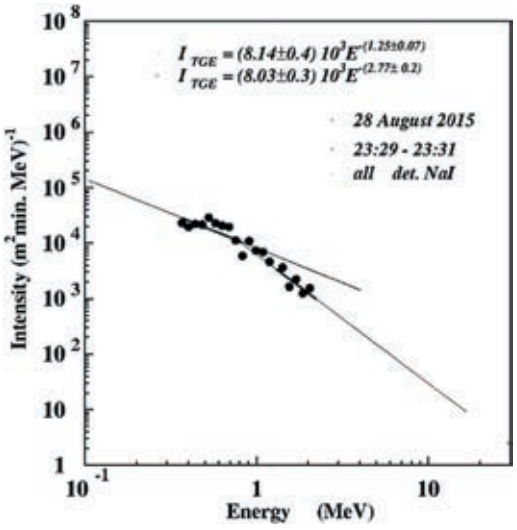


FIG. 14. The differential energy spectrum of the sum of the 4 NaI spectrometers measured after large TGE. Entire intensity is $0.21 \times 10^5/\mathrm{m}^2$ min, knee position is 1.2 MeV, and intensity after knee $0.4 \times 10^4/\mathrm{m}^2$ min.

After the decline of TGE at 23:23 the low-energy particle flux measured by NaI spectrometers remained high. However, the conditions required for unleashing large TGE did not last and the energy spectrum measured at 23:39–23:41 contained only low-energy particles (see Fig. 14).

## VII. DISCUSSION AND CONCLUSIONS

The model of TGEs can be formulated briefly as follows ([13]): electrons from the ambient population of cosmic rays (CR) are accelerated downward (towards the Earth) by the positive dipole formed by the main negatively charged layer in the middle of the cloud and a transient lower positive charge region in the bottom of the cloud. In very strong electric fields, the energy gained from the field surpasses the electron energy losses in the atmosphere and the intensive process of the electron multiplication and acceleration initiate large particle avalanches reaching and being registered on the Earth's surface (TGE). If the strength of the electric field is not enough to start RREA, nonetheless the energy of an electric field is transferred to

TABLE IV. Calculated intensities of TGE electron and gamma-ray fraction; threshold 4 MeV.

| Name | Mean | $\sigma$ | 23:19 peak | TGE–ΔN (N$\sigma$) | e intensity ($1/\mathrm{m}^2$ min) | $\gamma$ intensity ($1/\mathrm{m}^2$ min) | e/$\gamma$ |
|---|---|---|---|---|---|---|---|
| Cube 7 | 10258 | 108 | 10990 | 742 (6.9) | 800 | 10920 | 7.3% |
| Cube 8 | 8494 | 81 | 8923 | 429 (5.3) | 368 | 6768 | 5.4% |
| 7 with veto | 4294 | 79 | 4802 | 538 (6.8) | not applicable | not applicable | not applicable |
| 8 with veto | 3431 | 47 | 3764 | 333 (7.1) | not applicable | not applicable | not applicable |

the electrons, changing their energy spectrum and enhancing the probability of bremsstrahlung (MOS process). Both MOS and RREA processes have been experimentally observed at Aragats high-mountain research station in good agreement with simulations ([6]). Recently as well intense fluxes of gamma rays were measured by the airborne detector near the end of a downward RREA, consistent with another positive dipole occurring between the main positive charge layer and the negative screening layer above it (the authors named them "gamma glows" [14]).

However, in our previous publications we consider TGE events, mostly large ones, when the RREA was unleashed just above the detector site during several minutes. In this paper, we consider data collected on a whole day of August 28, 2015. The day was stormy, electric field disturbances continuous, lightning strikes enormous, and the electron accelerator above provided evidence on several long, low-energy TGEs and intensive and energetic enhancements. For the first time we describe and analyze not only isolated TGE events, but also the whole temporal history of the long duration thunderstorm, including high- and low-energy TGEs, periods of positive and negative lightning strikes, meteorological conditions, and disturbances of the near-surface electric field. By scrutinizing a particular stormy day at Aragats we demonstrate operation of the "moving electron accelerator" generated high-energy (up to 6 MeV) bremsstrahlung gamma photons when RREA is above the station and low-energy (0.4–2 MeV) Compton-scattered gamma rays when a strong electric field moved several kilometers away from the station.

NaI spectrometers registered an additional (compared to the fair weather day) ∼1.8 million gamma rays in total. TGE differential energy spectra were estimated by the network of the NaI spectrometers for 4 TGE episodes. Three of them contained only low-energy gamma rays with energies below 2 MeV; large TGE with maximal flux at 23:19 also contain gamma rays with energies up to 6 MeV. The spectrometer data are confirmed by the count rate measurements of other ASEC detectors. The 1-minute time series of the CUBE detector with an energy threshold above ∼4 MeV does not demonstrate any enhancements for the low-energy TGEs. The same time series demonstrates pronounced peaks with very high statistical significance for the high-energy TGE. The energy spectra are of a broken power law type. Due to the very large number of registered gamma rays we estimate spectra for each of the TGE events. We fit our spectra with two power law dependences that allow physical inference on the possible origin of two gamma-ray populations. According to the model of TGE initiation ([13]) the intense RREA process in the cloud originates bremsstrahlung photons that follow the passage of electrons. The electrons from the ambient population of secondary cosmic rays were accelerated up to energies 30–40 MeV. The size of LPCR does not extend more than 1 km; therefore high-energy bremsstrahlung photons illuminate the Earth's surface only locally under the thundercloud. The Compton-scattered photons of lower energy due to much broader angular distribution can illuminate a much larger surface under a cloud. Only on a few occasions when LPCR is above the detector site do we register large TGE with maximal energies above 3–4 MeV. These episodes are usually short because the wind moves the cloud relative to the particle detector location. The Compton scatter photons can reach the detector site from several RRE avalanches periodically emerging in the large thundercloud for the much longer time; see Fig. 1. The position of the knee at 1.2 MeV supported our assumption. The intensity of the gamma rays with energies above the pair production threshold (1.022 MeV) should be abruptly decreased due to catastrophic energy losses of the electrons and positrons in the atmosphere.

## ACKNOWLEDGMENTS

The authors thank the staff of the Aragats Space Environmental Center for the uninterruptible operation of Aragats research station facilities. The data for this paper are available via the multivariate visualization software ADEI on the Web page of the Cosmic Ray Division (CRD) of the Yerevan Physics Institute [15]. The authors wish to thank the World Wide Lightning Location Network [16], a collaboration among more than 50 universities and institutions, for providing the lightning location data used in this paper. The research was supported by the Armenian Government Grant 15T-1C011.

[1] C. T. R. Wilson, The acceleration of β-particles in strong electric fields such as those of thunderclouds, Proc. Cambridge Philos. Soc. **22**, 534 (1925).

[2] J. R. Dwyer, D. M. Smith, and S. A. Cummer, High-energy atmospheric physics: Terrestrial gamma-ray flashes and related phenomena, Space Sci. Rev. **173**, 133 (2012).

[3] J. R. Dwyer and M. A. Uman, The physics of lightning, Phys. Rep. **534**, 147 (2014); J. R. Dwyer, D. M. Smith, and S. A. Cummer, High-energy atmospheric physics: Terrestrial

gamma-ray flashes and related phenomena, Space Sci. Rev. **173**, 133 (2012).
[4] A. Chilingarian, A. Daryan, K. Arakelyan, A. Hovhannisyan, B. Mailyan, L. Melkumyan, G. Hovsepyan, S. Chilingaryan, A. Reymers, and L. Vanyan, Ground-based observations of thunderstorm-correlated fluxes of high-energy electrons, gamma rays, and neutrons, Phys. Rev. D **82**, 043009 (2010).
[5] A. Chilingarian, G. Hovsepyan, and A. Hovhannisyan, Particle bursts from thunderclouds: Natural particle accelerators above our heads, Phys. Rev. D **83**, 062001 (2011).
[6] A. Chilingarian, B. Mailyan, and L. Vanyan, Recovering of the energy spectra of electrons and gamma rays coming from the thunderclouds, Atmos. Res. **114–115**, 1 (2012).
[7] A. Chilingarian and H. Mkrtchyan, Role of the lower positive charge region (LPCR) in initiation of the thunderstorm ground enhancements (TGEs), Phys. Rev. D **86**, 072003 (2012).
[8] A. Chilingarianb, G. Hovsepyan, and L. Kozliner, Thunderstorm ground enhancements gamma ray differential energy spectra, Phys. Rev. D **88**, 073001 (2013).
[9] A. Chilingarian, K. Arakelyan, and K. Avakyan *et al.*, Correlated measurements of secondary cosmic ray fluxes by the Aragats space-environmental center monitors, Nucl. Instrum. Methods Phys. Res., Sect. A **543**, 483 (2005).
[10] G. J. Fishman, P. N. Bhat, R. Mallozzi, J. M. Horack, T. Koshut, C. Kouveliotou, G. N. Pendleton, C. A. Meegan, R. B. Wilson, W. S. Paciesas, S. J. Goodman, and H. J. Christian, Discovery of intense gamma ray flashes of atmospheric origin, Science **264**, 1313 (1994).
[11] A. Chilingarian, S. Chilingaryan, and A. Reymers, Atmospheric discharges and particle fluxes, J. Geophys. Res. **120**, 5845 (2015).
[12] A. Chilingarian, L. Melkumyan, G. Hovsepyan, and A. Reymers, The response function of the Aragats Solar Neutron Telescope, Nucl. Instrum. Methods Phys. Res., Sect. A **574**, 255 (2007).
[13] A. Chilingarian, Thunderstorm ground enhancements: Model and relation to lightning flashes, J. Atmos. Terr. Phys. **107**, 68 (2014).
[14] N. A. Kelley, D. M. Smith, and J. R. Dwyer *et al.*, Relativistic electron avalanches as a thunderstorm discharge competing with lightning, Nat. Commun **6**, 7845 (2015).
[15] http://adei.crd.yerphi.am/adei.
[16] http://wwlln.net.

Nuclear Inst. and Methods in Physics Research, A 874 (2017) 19–27

Contents lists available at ScienceDirect

Nuclear Inst. and Methods in Physics Research, A

journal homepage: www.elsevier.com/locate/nima

# In situ measurements of the Runaway Breakdown (RB) on Aragats mountain

A. Chilingarian [a,b,c,*], G. Hovsepyan [a], B. Mailyan [d]

[a] A. Alikhanyan National Lab (Yerevan Physics Institute), Yerevan, Armenia
[b] National Research Nuclear University MEPhI, Moscow, Russia
[c] Space Research Institute of RAS, Moscow, Russia
[d] Florida Institute of Technology, Melbourne, FL, United States

ARTICLE INFO

*Keywords:*
Atmospheric high-energy physics
Electron acceleration
Electron energy estimation
Scintillators

ABSTRACT

Acceleration and multiplication of the cosmic ray electrons by strong electric fields in the thundercloud are well-established phenomena comprising the core of the atmospheric high-energy physics. The majority of experimental data on particle acceleration in the thunderclouds comes from space-born experiments detecting Terrestrial Gamma flashes (TGFs) and from networks of particle detectors located on the earth's surface observing Thunderstorm Ground Enhancements (TGEs). Models for explaining both TGF and TGE are based on the concept of a Runaway Breakdown (RB) introduced by A. Gurevich. Prove of these models requires registration of the electromagnetic avalanches developing in the thundercloud and reaching the earth's surface. Unfortunately due to high location of cloud and fast attenuation of electrons in the atmosphere the registration of such an avalanches are very rare. On Aragats mountain in Armenia, where the cloud location is very low we observe several TGE events with sizable electron contribution. We present direct measurements of such an avalanches lasting less than a microsecond; hundreds of such avalanches comprise a TGE lasting few minutes. We recovered as well the differential energy spectra of electron and gamma ray content of avalanches. The abrupt termination of the particle flux by nearby lightning indicates that RB process precedes (initiates) the lightning flash.



## 1. Introduction

The high-energy physics in the atmosphere is a new emerging scientific field dealing with electromagnetic cascades originated in the thunderstorm atmospheres. The initial name of the cascade released by a runaway electron—the Runaway breakdown (RB, given by Gurevich et al., [1]), is recently often replaced by the term RREA (Relativistic Runaway Electron Avalanches, [2,3]). However, recent measurements on Aragats of the enhanced particle fluxes abruptly terminated by the lightning flashes show that the initial hypothesis of A. Gurevich that intense electron fluxes in atmosphere can initiate lightning flashes finally finds its prove.

Gurevich et al. (1992) [1] showed that when Møller scattering (electron–electron elastic scattering) is considered the runaway electrons would undergo avalanche multiplication, resulting in a large number of relativistic runaway electrons and gamma rays for each energetic seed electron injected into the strong electrical field region. Seed electrons belong to steady population (specific to the height in the atmosphere, latitude, and longitude of detection site) of the secondary cosmic rays, a product of numerous small and large cascades initiated in the atmosphere (Extensive Air Showers—EASs) by copious protons and fully stripped nuclei accelerated in the Galaxy and bombarded terrestrial atmosphere with a rather stable intensity.

Further development of the theoretic knowledge on the runaway process continued with intensive implementations of the Monte Carlo simulation. Sophisticated codes were used to model the propagation of energetic electrons in electric fields [2,4–7]. The runaway process is naturally embedded in simulations: when you switch on the appropriate electrical field and use incident cosmic ray electron flux as seeds; the electrons gain energy from the field, knock-off atomic electrons and cascade process develops in the atmosphere. Very popular, relativistic feedback discharge model (RFDM, [2]) was used for explaining Terrestrial Gamma flashes (TGFs, [8,9]). When the large-scale electric field in the cloud become relatively high the backward propagating positrons and backscattered X-rays generate new avalanches. Therefore, according to

* Corresponding author at: A. Alikhanyan National Lab (Yerevan Physics Institute), Yerevan, Armenia.
*E-mail address:* chili@aragats.am (A. Chilingarian).

http://dx.doi.org/10.1016/j.nima.2017.08.022
Received 29 June 2017; Accepted 13 August 2017
Available online 24 August 2017
0168-9002/

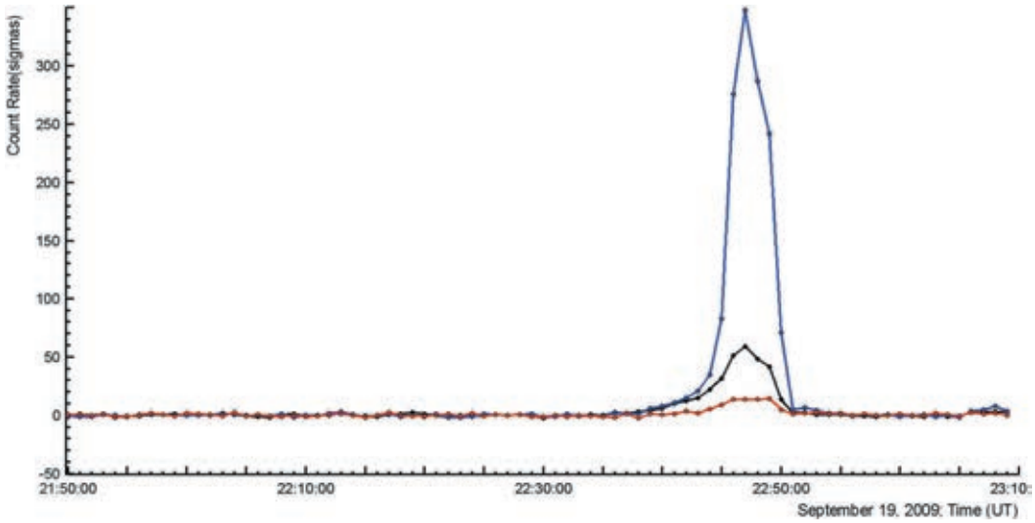


**Fig. 1.** "Significance" of TGE in the number of standard deviations from the mean value of 1-minute time series of count rate. Top curve corresponds to upper scintillators of the ASNT detector, middle—to lower and the bottom—to vertical particle transition through both scintillators.

this model, the avalanche becoming self-sufficient and can prolong until the conditions for the feedback are still effective.

The most difficult and most important part of the model validation is the comparison of competitive hypotheses with the measurements. The high-energy atmospheric physics (HEAP) includes 2 main sources of the experiential data: Terrestrial Gamma Flashes (TGFs)—brief burst of gamma radiation (sometimes also electrons and positrons) registered by the orbiting gamma ray observatories in the space and Thunderstorm ground enhancements (TGEs)—the prolonged particle fluxes registered on the ground level. The central engine initiated TGF and TGE is believed to be RB/RREA mechanism accelerated seed electrons in the terrestrial atmosphere up to 40–50 MeV. The *in situ* observation of numerous TGEs during strong thunderstorms on Aragats resulting in the first simultaneously measured energy spectra of TGE electrons and gamma rays [10]. Further measurements of the gamma ray energy spectra by the network of NaI spectrometers allow to reliably extending energy range of the "thunderstorm" gamma rays up to 100 MeV [11] due to another "thunderstorm" gamma ray production mechanism—MOdification of the electron energy Spectrum (MOS, [12]). The measurements performed on Aragats allow formulating a comprehensive model of TGE [13].

TGFs and TGEs share many common features, as they are results of RB. The drastic time difference (minutes for TGE and hundred of microseconds for TGF) is not essential because prolonged TGEs are nothing more than a superposition of the short microsecond scale avalanches, which Aragats group has named Extensive cloud shower (ECS), and Alex Gurevich et al., Micro runaway breakdown (MRB).

There exist numerous papers on simulations of particle cascades in the atmosphere, but very few of them contain comparisons with experimentally measured parameters. The goal of our paper is to present experimental data in the form that allows validation of the models. We analyze in details the largest TGE event from 19 September 2009 and 4 October 2014 and compare the time distribution of the ECSs with expected results from RDFM and TGE models.

## 2. *In situ* measurements of the RB process on Aragats

The first observation of the avalanches initiated by the runaway electrons was made at Aragats in 2009 [10]. MAKET and ASNT detectors (see supplement information for detector description) were used for the *in situ* detection of RB process (electron–photon avalanches originated in the thundercloud above detector site). In Fig. 1, we present the abrupt surge in the 1-minute particle count rate observed in the 1-minute time series of ASNT detector on 19 September. The flux started slow surge, then rockets for 4 min to the maximal value and then fast decays. This TGE is the largest ever-observed on Aragats. On 22:47 the upper scintillators of the ASNT detector registered 108% enhancement corresponding to 270 standard deviations from the mean value (270$\sigma$); the bottom scintillators registered 16% enhancement (60.7$\sigma$); the near-vertical flux (coincidences 3–7, 5–1, 6–2, 8–4) enhanced by 11.2% (16.8 $\sigma$).

In Fig. 2 we show particle flux enhancement registered by the 4 identical 5 cm thick plastic scintillators located above four 60 cm scintillators. Small differences in the count rates are explained by the individual variation of the photomultipliers (PMT). Registered TGE particles flux was rather large $\sim 30,000$ per min per m$^2$.

Thus, we observe particle flux continuing several minutes. This flux cannot be associated with an active solar event (there was no such an event registered by the gamma ray and X-ray sensors on board of Space Weather monitoring satellites) and with Extensive Air Showers (only one additional count will be registered on traversal of thousands of EAS particles in a few tens of nanosecond).

Consequently, we decide that it was a particle flux of the atmospheric origin. First of all, we check the direction of incoming particles. As one can see in Fig. 3 particles come from near-vertical direction (solid black curve with pronounced 4-minute duration peak) coinciding with the direction of the vertical electric field in the thundercloud. Other directions (selected by coincidences 5–4, 8–3, etc.) do not demonstrate any peak relative to the cosmic ray background. The background is due to EASs from galactic protons and nuclei that are not connected with thunderstorm. Another evidence of "thunderstorm" origin of particle flux comes from MAKET array's (see supplement information for detector description) 16 and 8-fold coincidences within trigger window of 1 μs (Fig. 4a and b). The electronics of the MAKET surface array counts number of events per minute, in which particles hit 8 scintillators within a window of 1 μs. Then, by off-line analysis we select events, in which all 16 scintillators were "fired". The abrupt enhancement of the coincidences occurred the same minutes when the flux of particles surges (128 and 67 counts for 8- and 16-fold coincidences, see Fig. 4b and a).

At fair weather (background counts), the surface array registered ~26.8 +/- 4.9 counts per minute (8-fold coincidences) and ~8.4 +/- 2.8 counts per minute (16 fold coincidences). Thus at 22:47 MAKET array observed ~730% enhancement of the 16-fold coincidences, corresponding to ~22$\sigma$ and 380% enhancement of the 8-fold coincidences,

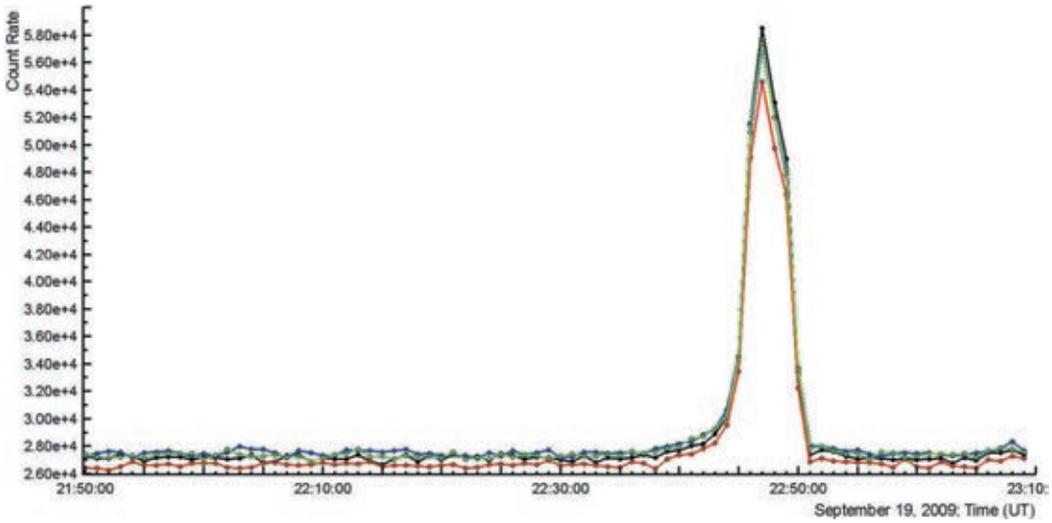


**Fig. 2.** Particle flux enhancement as measured on 19 September 2009 by four 5 cm thick 1 $m^2$ area plastic scintillators on top of ASNT detector; energy threshold ~ 7 MeV.

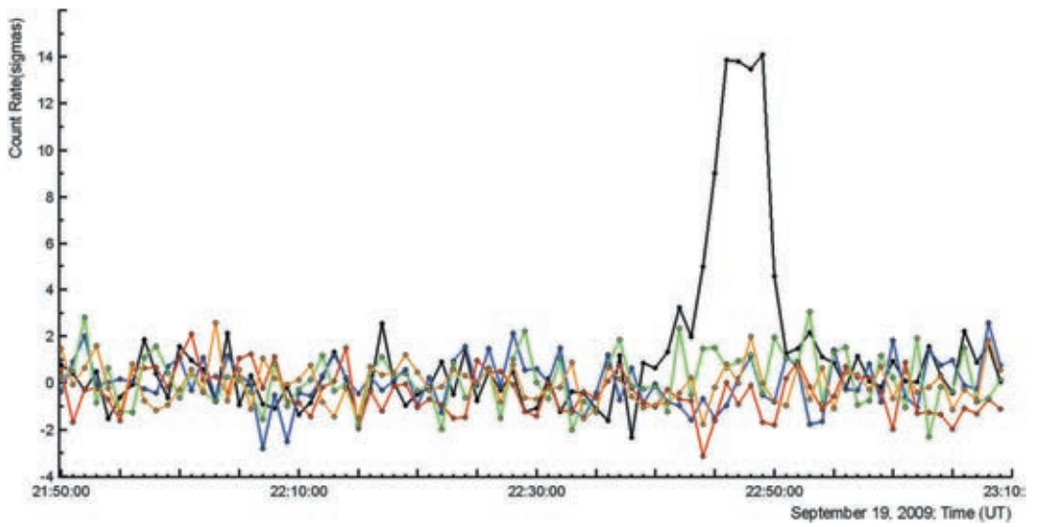


**Fig. 3.** The count rate of particles coming from different directions. The peak lasting 4 min is formed by particles coming from a near-vertical direction only (0–20°, black curve, coincidences of scintillators stacked vertically); the particles coming from the inclined directions (coincidences of scintillators that are shifted from each other, see Fig. 1 of supplement) do not show any enhancement. We present the count rates in numbers of deviations from the mean value to present data in the comparable scale. The count rates from inclined directions are less comparing with near-vertical one.

corresponding to ~20$\sigma$. Numerous "Extensive cloud showers" (ECSs, or Micro Runway Breakdowns—MRB, [14]) enhance the stable count rate of EASs generated by galactic cosmic rays. Both processes EAS and ECS independently contribute to the MAKET array count rate. The minutes long enhanced particle flux comprises from multiple ECSs initiated by a runaway electrons randomly injected into the strong electrical field region. In Fig. 5a and b we demonstrate the distribution of the registered by MAKET array showers during fair weather and during the minute when maximal flux was detected correspondingly.

The significant excess in shower number observed this minute (~100, Fig. 7b) comparing with showers observed during fair weather (Fig. 7a) is due to randomly distributed within this minute ECSs, several times occurred in triplets and quadruplets per second, but never more. If the RB process will be self-consistent i.e. the RREA will not stop and continuously generate showers via feed back positrons and scattered gamma rays (RDFM model, [2]) we should observe much more counts of ECSs. The maximal dead time of the MAKET array is 100 μs; thus after each 100 μs another shower can be registered by the surface particle array. Therefore, we can expect up to 10,000 showers per second (if the RDFM process prolongs 1 s), however, we register not more than 4.

## 3. Energy release spectra

ASNT data acquisition system registers energy release histograms both for events with and without veto i.e., if we have a signal in 5 cm thick scintillator the measured energy release is "vetoed" and do not participate in the histogram. In this way, we obtained the energy spectra of the neutral particles i.e. TGE gamma rays, originated from bremsstrahlung of accelerated in the RB process electrons (Fig. 6). In addition, extracting histogram obtained with veto from the histogram obtained without veto we readily come to the histogram of electron energy releases (Fig. 6).

The intensity of electron flux is ~ 20 times less comparing with gamma ray intensity. Because of very fast attenuation of electrons in

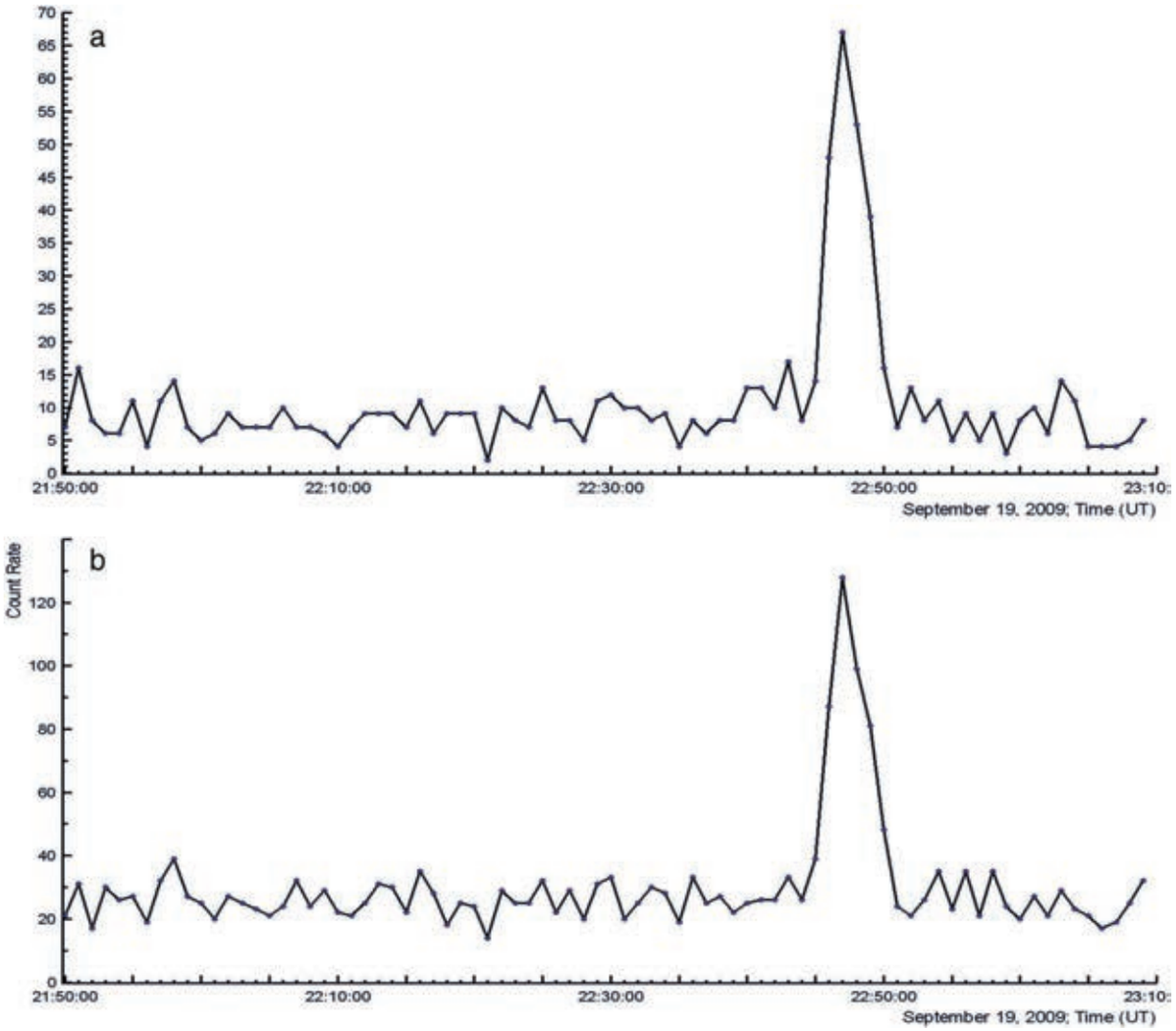


**Fig. 4.** 8 and 16-fold coincidences in the channels of MAKET surface array.

the atmosphere, TGE gamma ray flux significantly exceeds the electron flux; only for very low thunderclouds it is possible to detect electron flux (see Fig. 2, from [15]). The measured maximal energy release of TGE electrons in the 60 cm thick scintillator was ~25 MeV, for gamma rays maximal energy release ~35 MeV. Not the whole energy of particles is released in the scintillator; highest energy particles can escape from the scintillator sides. Thus, energy release is less or (in the best case) equal to the energy of particle. TGE particles in order to be registered in the 60 cm thick scintillator have to traverse significant amount of matter above the detector, see Fig. 8. The electron energy losses in the matter above the scintillator (~10 g/cm$^2$) are ~20 MeV. Thus, we come to maximal electron energy above the roof ~45 MeV in a good agreement with the model of the TGE initiation [12,13].

The gamma rays produce neutrons in the photonuclear interactions with atoms of the air. As well, the gamma rays and atmospheric hadrons produce secondary neutrons in nuclear reactions in the lead [16–18]. Aragats Neutron Monitor (ArNM, see supplement information for detector description) registered significant enhancement (>6$\sigma$ ) at 22:47 on 19 September 2009; the same time as the gamma ray and electron enhancement. The count rates corresponding to dead times of 0.4, 250, and 1250 μs are approximately identical. In contrast, EAS can enhance count rates observed with the minimal dead time of 0.4 μs only. Neutrons born in the photonuclear reactions of the TGE gamma rays with air atoms (or—in the lead absorber of ArNM) are randomly distributed within 4 min of the high-energy gamma ray flux alike the TGE particles, shown in Fig. 5b. In both cases, the origins of neutrons are the photonuclear reactions of TGE gamma rays (see Fig. 9).

## 4. The super TGE event occurred on October 4

After observing the first large TGE in 2009 on Aragats were established new facilities for particle detection, for monitoring of near surface electric field, for location of lightning flashes and for measuring of meteorological parameters [19]. The multi-parameter, multi-detector approach for TGE research allows establishing causal relations between meteorological parameters, particle fluxes and atmospheric discharges and formulation of the model of lightning initiation [20]. Particularly, we estimate the height of electric field in the thundercloud above earth's surface by measuring outside temperature and dew point. In Fig. 10 we show large TGE occurred on 4 October 2014, first described in [21]. The particle count rate of 3 cm thick outdoors plastic scintillator of the STAND1 detector (see supplement information for detector description) reaches a maximum of 1808 counts per second at 14:12:14 (mean value with fine weather is 525 counts per second, MSD ~23). The

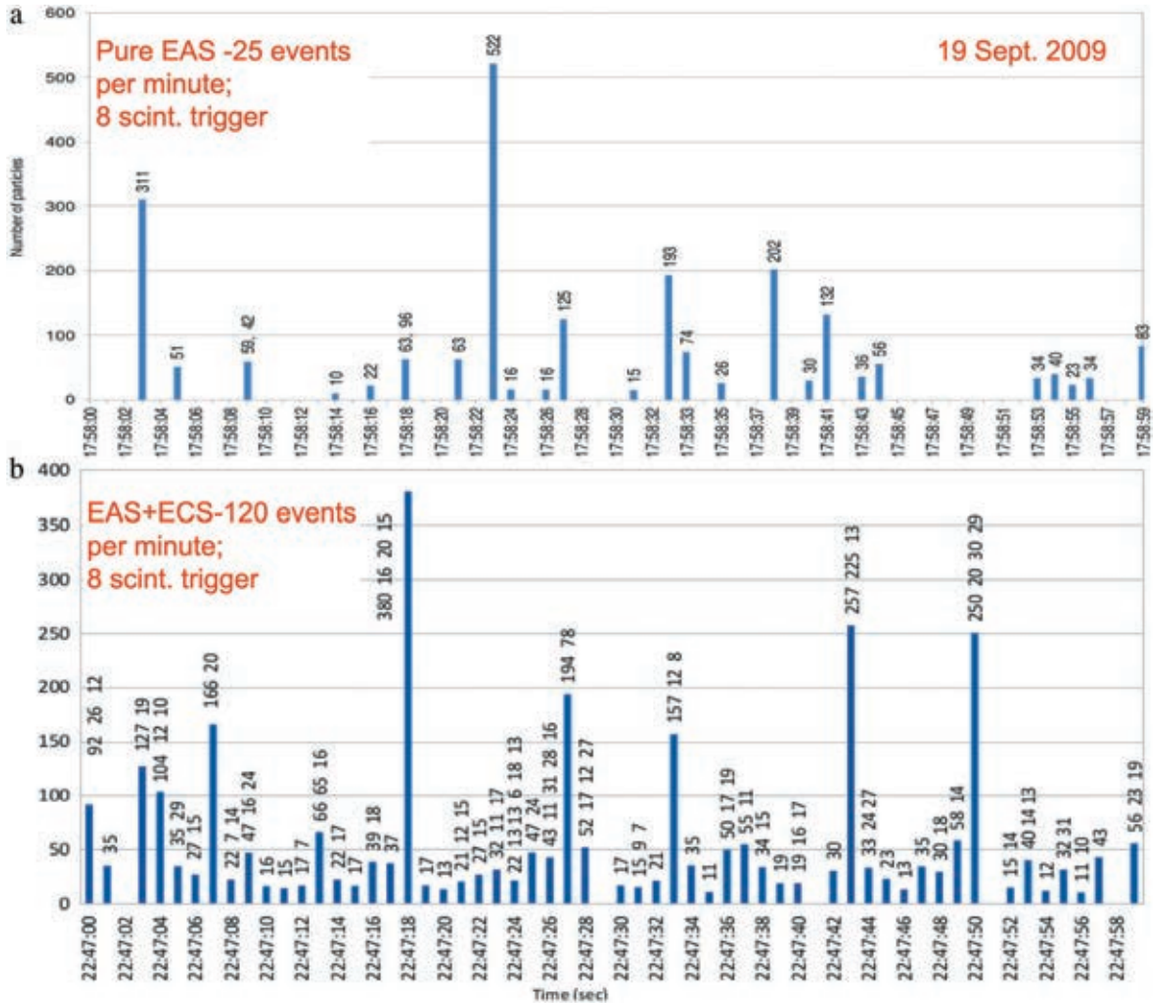


**Fig. 5.** Particle showers (EASs) detected during 60 s of the fair weather (a) and during a thunderstorm at maximal particle flux (EASs +ECSs) (b). Vertical bars show the number of particles in showers. If there were more than one shower in a second the height of a bar is equal to the size (number of particles) of the largest shower, next number after an interval is the number of particles in the next ECS, and so on. Note that maximal number of ECSs in a second is 4.

TGE particle flux enhancement was enormous; reaching 340% at the maximum flux second which is equivalent to the $p$-value of $53\sigma$. The height of the cloud is calculated by the measured "spread" parameter—the difference between the surface temperature and the dew point. The calculation of the height of cloud base is based on the assumption that the air temperature drops 9.84 degrees C per 1000 m of altitude and the dew point drops 1.82 degrees C per 1000 m altitude. In WEB there are several calculators designed to approximate the altitude of a cloud (see, for instance http://www.csgnetwork.com/cloudaltcalc.html). The simplified estimate consists in simple multiplication of spread measured in C degrees by 122 m. With this approach we readily obtain ~25 m for the cloud base (see Fig. 10). The approximate energy losses of high energy electron in the 50 m of air on altitude 3250 m are ~5 MeV.

The maximal energy release of the electrons in the 60 cm thick scintillator was 20 MeV (Fig. 11), in the construction above detector electron losses estimated to be ~20 MeV. Thus we come to the maximal energy of electrons leaving the cloud 25 m above detector to be 45 MeV in good agreement with estimates obtained in [12] and with the larger TGE occurred on 19 September 2009 (the meteorological parameter measurement were not available at that time). The maximal energy of gamma rays equal to 35 MeV also agreed with "parent" electrons energy. Thus, this event is another evidence of the runaway avalanche process in the thunderclouds.

## 5. Discussion and conclusions

By measuring the electrons from electromagnetic avalanches unleashed by the runaway electrons in the thunderstorm atmosphere we prove the existence of the Runaway Breakdown process. The energy release histograms of TGE electrons reaching and registering in the 60 cm thick scintillators of the ASNT detector prolonged up to 25 MeV. The energy losses in the matter below the roof of the building are ~20 MeV. Taking into account the amount of matter above the 60 cm thick scintillator we estimate the maximal energy of the electrons above the roof to be 40–50 MeV. Thus, the energy spectra of the super-events occurred on 19 September 2009 and 4 October 2014 are in good agreement with the model of TGE initiation [12,13].

Measured TGE temporal distribution (Fig. 7b) proves that the large fluxes of electrons and gamma rays detected during thunderstorms comprise from the numerous very short RB cascades registered by the particle detectors located on the mountain altitudes. During TGE, a large number of very short bursts (individual runaway avalanches, Extensive cloud showers, or Micro runaway breakdowns, [14]) were developed in the thundercloud. An only very low location of the thunderclouds on Aragats allows measuring electrons. Estimates of the height of cloud made with meteorological information as well as estimates performed

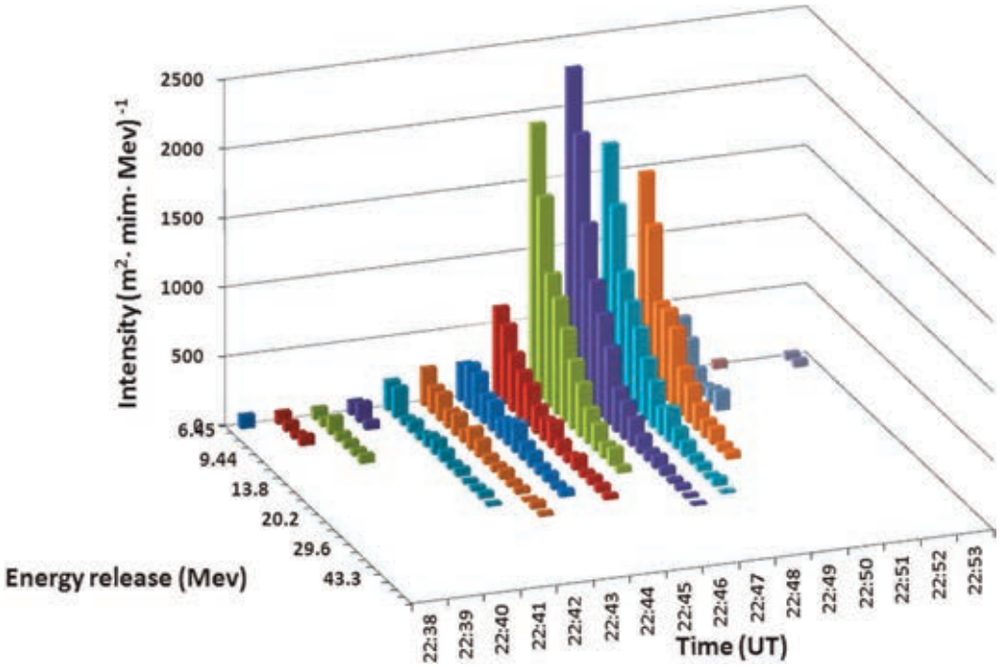


**Fig. 6.** Differential energy release histogram of the TGE gamma rays obtained in 60 cm. Thick scintillators of the ASNT array.

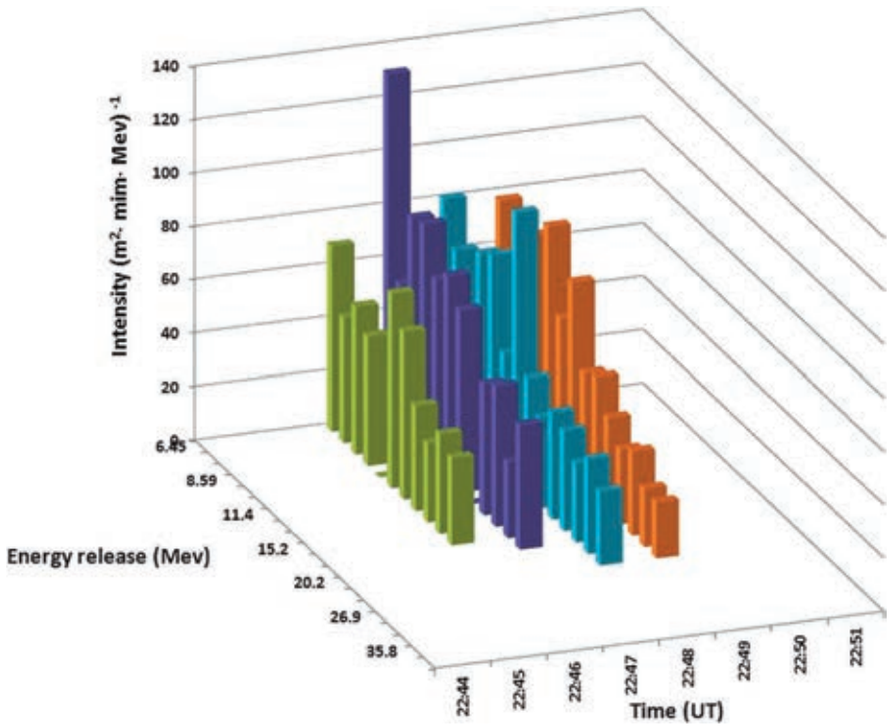


**Fig. 7.** Differential energy release histogram of the TGE electrons obtained in 60 cm. Thick scintillators of the ASNT detector.

with measured maximal energy of the TGE electrons well coincide with TGE model predictions.

The validity of the RDFM model is very difficult to prove with TGF data only; TGF measurements are performed with orbiting gamma ray observatories at the distances hundreds of km from thunderclouds, from which the particle is assumed to reach fast moving satellite. With such an experiment arrangement self-sustained acceleration of electrons is very difficult to prove. The detected TGFs are very short, maybe parented by very few seed electrons injected into the strong electrical field region. The TGEs, in contrast, can prolong minutes, 6 orders of magnitude longer than TGFs. The RB continued down to several tens of meters above firmly fixed particle detectors. Thus, various RB models

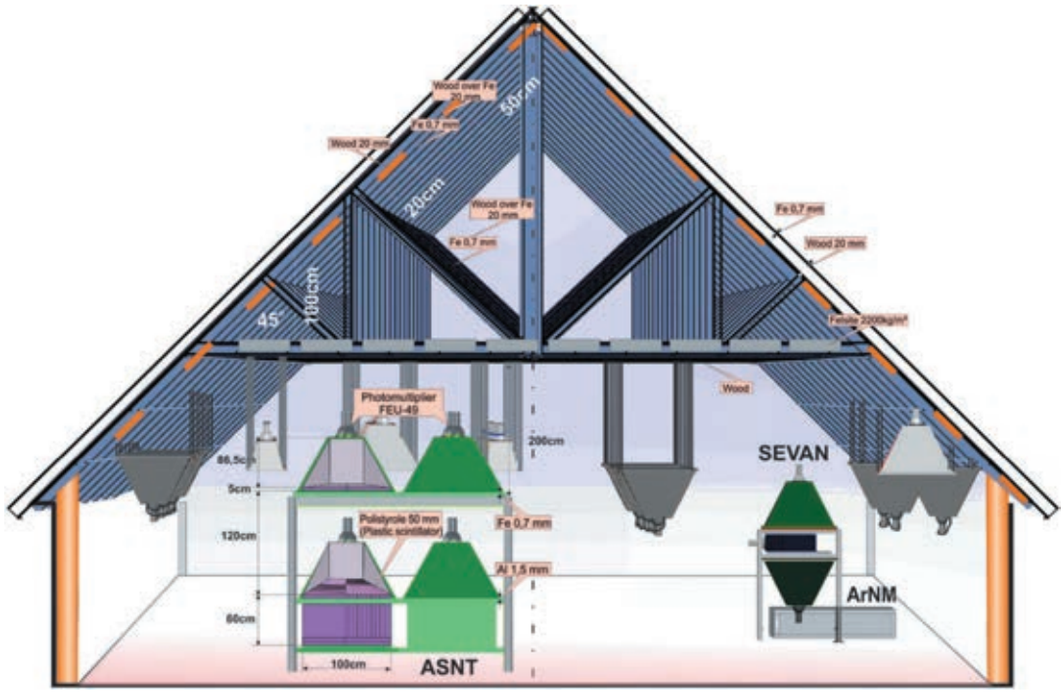


**Fig. 8.** Setup of ASNT detector in the MAKET experimental hall.

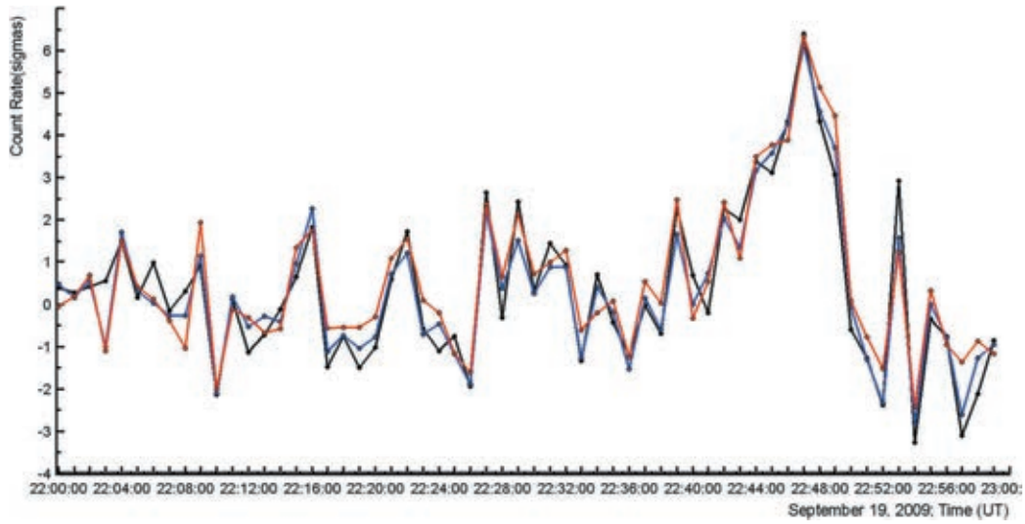


**Fig. 9.** Time series of ArNM 1-minute count rate displayed in the number of standard deviations. Time series corresponding to 3 dead times are approximately identical.

can be validated by *in situ* measurements on Aragats, the natural electron accelerator provided many tens of TGEs each year [19,22].

If the RB process due to feedback prolonged continuously we can expect much more detections per second (up to $10^4$, as a maximal dead time of MAKET array of ~100 μs); however the experimentally measured number of ECSs per second is 4, see Fig. 5b). Thus, the temporal distribution of ECSs rejects the hypothesis of continuous acceleration of electrons in the cloud, i.e. the RFDM hypothesis, at least on the timescale of a millisecond. Sure TGFs and TGEs are not fully symmetrical processes the first one is propagated in the thin atmosphere becoming thinner as avalanches propagate upward; TGEs are propagating in the dense atmosphere becoming denser as TGE approach Earth's surface. However, the runaway process is in the heart of both and experimental evidence acquired from TGE observations can be used to validate TGF models.

## Acknowledgments

The authors thank the staff of the Aragats Space Environmental Center for the uninterruptible operation of Aragats research station facilities. The data for this paper are available via the multivariate visualization software ADEI on the WEB page of the Cosmic Ray Division (CRD) of the Yerevan Physics Institute, http://adei.crd.yerphi.am/adei. A.C. appreciates the support by Russian Science Foundation grant (project No. 17-12-01439).

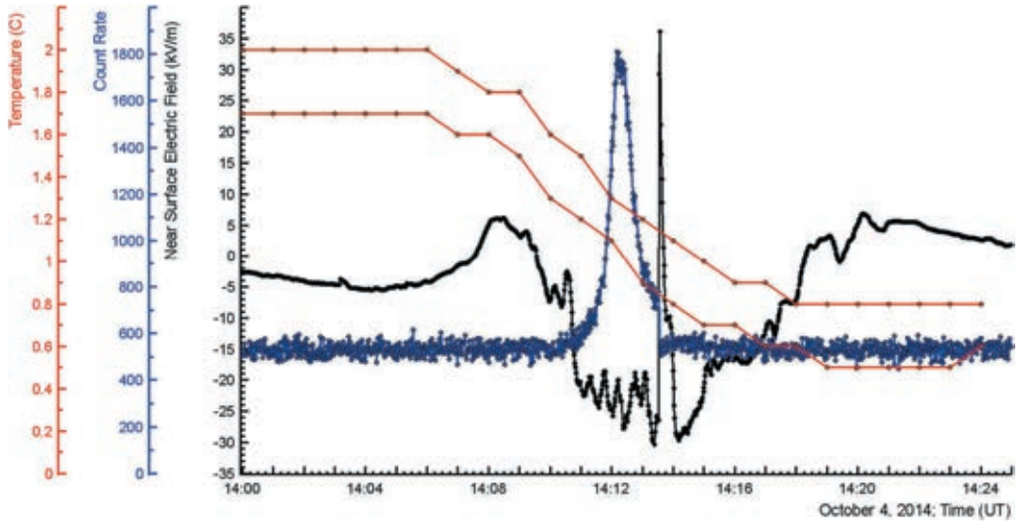


**Fig. 10.** 1 sec time series of count rate of 3 cm thick plastic scintillator (blue), near surface electric field (black); temperature (~1.3 °C) and dew point (~1.1 °C) used for the spread calculation (red). Strong lightning flash abruptly terminates TGE on 14:13:38. (For interpretation of the references to colour in this figure legend, the reader is referred to the web version of this article.)

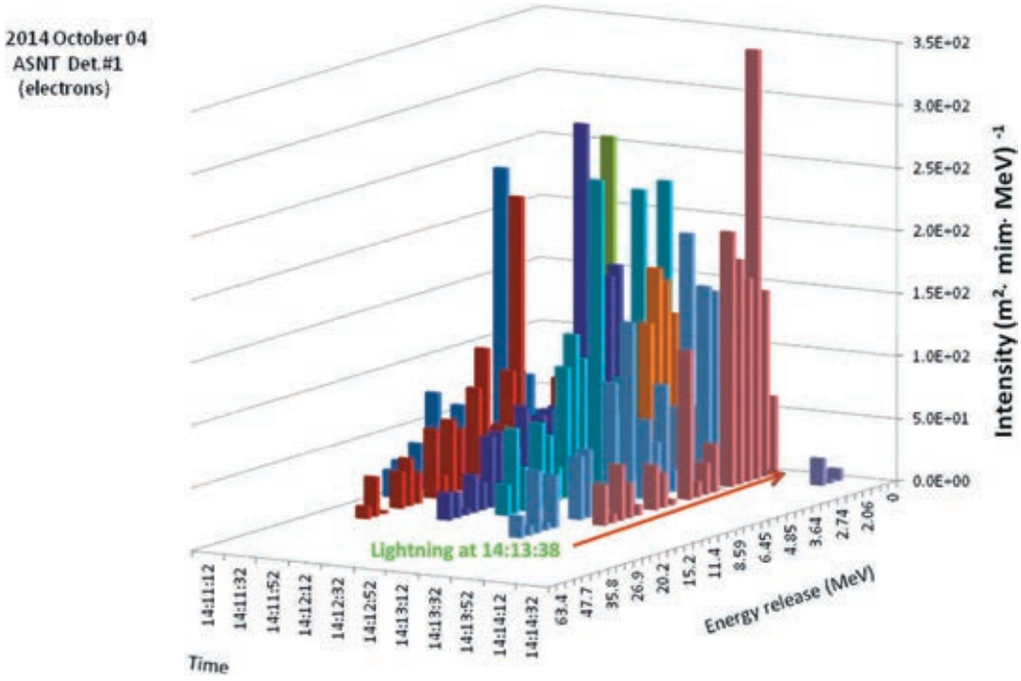


**Fig. 11.** Differential Energy spectra of RB electrons; maximal energy equals 20 MeV. After lightning flash flux of electrons abruptly terminates.

## Appendix A. Supplementary data

Supplementary material related to this article can be found online at http://dx.doi.org/10.1016/j.nima.2017.08.022.

## References

[1] A.V. Gurevich, G.M. Milikh, R. Roussel-Dupre, Runaway electron mechanism of air breakdown and preconditioning during a thunderstorm, Phys. Lett. A 165 (5–6) (1992) 463–468.
[2] J.R. Dwyer, The relativistic feedback discharge model of terrestrial gamma ray flashes, J. Geophys. Res. 117 (2012) A02308.
[3] J.R. Dwyer, M.A. Uman, The physics of lightning, Phys. Rep. 534 (4) (2013) 147–241.
[4] N.G. Lehtinen, T.F. Bell, U.S. Inan, Monte Carlo simulation of runaway MeV electron breakdown with application to red sprites and terrestrial gamma ray flashes, J. Geophys. Res. 104 (1999) 24,699–24,712. http://dx.doi.org/10.1029/1999JA900335.
[5] L.P. Babich, et al., Comparison of relativistic runaway electron avalanche rates obtained from Monte Carlo simulations and kinetic equation solution, IEEE Trans. Plasma Sci. 29 (3) (2001) 430–438.
[6] J.R. Dwyer, A fundamental limit on electric fields in air, Geophys. Res. Lett. 30 (20) (2003) 2055. http://dx.doi.org/10.1029/2003GL017781.
[7] J.R. Dwyer, Relativistic breakdown in planetary atmospheres, Phys. Plasmas 14 (4) (2007) 042901. http://dx.doi.org/10.1063/1.2709652.

[8] G.J. Fishman, P.N. Bhat, R. Mallozzi, et al., Discovery of intense gamma ray flashes of atmospheric origin, Science 264 (5163) (1994) 1313.
[9] M.S. Briggs, et al., Electron-positron beams from terrestrial lightning observed with fermi GBM, Geophys. Res. Lett. 38 (2011) L02808.
[10] A. Chilingarian, A. Daryan, K. Arakelyan, A. Hovhannisyan, B. Mailyan, L. Melkumyan, G. Hovsepyan, S. Chilingaryan, A. Reymers, L. Vanyan, Ground- based observations of thunderstorm-correlated fluxes of high-energy electrons, gamma rays, and neutrons, Phys. Rev. D 82 (4) (2010) 043009.
[11] A. Chilingarian, G. Hovsepyan, L. Kozliner, Thunderstorm ground enhancements: Gamma ray differential energy spectra, Phys. Rev. D 88 (2013) 073001.
[12] A. Chilingarian, B. Mailyan, L. Vanyan, Recovering of the energy spectra of electrons and gamma rays coming from the thunderclouds, Atmos. Res. 114–115 (2012) 1.
[13] A. Chilingarian, Thunderstorm ground enhancements –model and relation to lightning flashes, J. Atmos. Sol.-Terr. Phys. 107 (2014) 68–76.
[14] A.V. Gurevich, K.P. Zybin, R.A. Roussel-Dupre, Lightning initiation by simultaneous of runaway breakdown and cosmic ray showers, Phys. Lett. A 254 (1999) 79.
[15] J.R. Dwyer, et al., Implications of x-ray emission from lightning, Geophys. Res. Lett. 31 (2004) L12102.
[16] A. Chilingarian, N. Bostanjyan, T. Karapetyan, L. Vanyan, Remarks on recent results on neutron production during thunderstorms, Phys. Rev. D 86 (2012) 093017.
[17] A. Chilingarian, N. Bostanjyan, L. Vanyan, Neutron bursts associated with thunderstorms, Phys. Rev. D 85 (2012) 085017.
[18] Tsuchiya H., Hibino K., Kawata K., et al., Observation of thundercloud-related gamma rays and neutrons in Tibet, Phys. Rev. D 85 (2012) 092006. Nominated.
[19] A. Chilingarian, G. Hovsepyan, L. Kozliner, Extensive air showers, lightning, and thunderstorm ground enhancements, Astropart. Phys. 82 (2016) 21–35.
[20] A. Chilingarian, S. Chilingaryan, T. Karapetyan, et al., On the initiation of lightning in thunderclouds, Sci. Rep. 7 (2017) 1371. http://dx.doi.org/10.1038/s41598-017-01288-0.
[21] A. Chilingarian, G. Hovsepyan, G. Khanikyanc, A. Reymers, S. Soghomonyan, Lightning origination and thunderstorm ground enhancements terminated by the lightning flash, Europhys. Lett. 110 (2015) 49001.
[22] A. Chilingarian, G. Hovsepyan, E. Mantasakanyan, Mount aragats as a stable electron accelerator for atmospheric high-energy physics research, Phys. Rev. D 93 (2016) 052006.

Available online at www.sciencedirect.com

ScienceDirect

Advances in Space Research 61 (2018) 2680–2696

ADVANCES IN SPACE RESEARCH (a COSPAR publication)

www.elsevier.com/locate/asr

# The SEVAN Worldwide network of particle detectors: 10 years of operation

A. Chilingarian [a,b,c,*], V. Babayan [a], T. Karapetyan [a], B. Mailyan [d], B. Sargsyan [a], M. Zazyan [a]

[a] A. Alikhanyan National Lab (Yerevan Physics Institute), 2 Alikhanyan Brothers, Yerevan 0036, Armenia
[b] National Research Nuclear University MEPhI (Moscow Engineering Physics Institute), Moscow 115409, Russian Federation
[c] Space Research Institute of RAS, Moscow, Russian Federation
[d] Department of Physics and Space Sciences, Florida Institute of Technology, Fl, USA

Received 9 June 2017; received in revised form 23 February 2018; accepted 24 February 2018
Available online 2 March 2018

**Abstract**

The Space Environment Viewing and Analysis Network (SEVAN) aims to improve the fundamental research on particle acceleration in the vicinity of the sun, on space weather effects and on high-energy physics in the atmosphere and lightning initiation. This new type of a particle detector setup simultaneously measures fluxes of most species of secondary cosmic rays, thus being a powerful integrated device for exploration of solar modulation effects and electron acceleration in the thunderstorm atmosphere. The SEVAN modules are operating at the Aragats Space Environmental Center (ASEC) in Armenia, in Croatia, Bulgaria, Slovakia, the Czech Republic (from 2017) and in India. In this paper, we present the most interesting results of the SEVAN network operation during the last decade. We present this review on the occasion of the 10th anniversary of the International Heliophysical Year in 2007.


*Keywords:* Cosmic rays; Networks of particle detectors

## 1. Introduction

The sun influences earth in different ways by emission of electromagnetic radiation, solar plasmas, and high-energy particles. Although the total energy of the emitted particles comprises a very small fraction of the energy of the visible light, the study of these particles provides valuable information on the huge solar explosions which affect the near-earth space, space-borne and surface technologies, i.e. on the so-called space weather. In 1957, in an unprecedented international cooperation, more than 66.000 scientists and engineers from 67 nations perform measurements of the major geophysical parameters in the framework of the International Geophysical Year (IGY1957, Chapman, 1959).

Fifty years on, the International Heliophysical Year (IHY 2007, Thompson et al., 2009) again drew scientists and engineers from around the globe in a coordinated observation campaign of the heliosphere and its effects on planet earth. The United Nations Office for Outer Space Affairs, through the United Nations Basic Space Science Initiative (UNBSSI), assisted scientists and engineers from all over the world in participating in the IHY. The most successful IHY 2007 program was to deploy arrays of small, inexpensive instruments around the world to get global measurements of ionospheric and heliospheric phenomena. The small instrument program was (and still is) a partnership between instrument developers and instrument hosts in developing countries. The lead scientist prepared and installed the instruments and helped to run it; the host

* Corresponding author at: A. Alikhanyan National Lab (Yerevan Physics Institute), 2 Alikhanyan Brothers, Yerevan 0036, Armenia.
*E-mail address:* chili@aragats.am (A. Chilingarian).

https://doi.org/10.1016/j.asr.2018.02.030
0273-1177/

countries provided manpower for instrument operation and maintenance. The lead scientist's institution developed joint databases, prepared tools for user-friendly access to the data, assisted in staff training and paper writing to promote space science activities in developing countries.

The sun is a tremendously variable object, capable of changing the fluxes of the Solar Cosmic Rays (SCR) by 3–4 orders of magnitude in a span of a few minutes. These transient events are called "Solar Proton Events (SPEs)" and "Solar Energetic Particle (SEP) events". Because of the sun's closeness, the effects of the changing fluxes can have a major influence on the earth, including climate, safety, and other areas. The sun "modulates" the low energy Galactic Cosmic Rays (GCR) in several ways. Along with broadband electromagnetic radiation, the explosive flaring processes on the sun usually result in Coronal Mass Ejections (CME) and in acceleration of copious electrons and ions. Particles can be generated either directly in the coronal flare site with a subsequent escape into interplanetary space, or they can be accelerated in CME-associated shocks that propagate through the corona and interplanetary space. These particles are effectively registered by spectrometers located at the Lagrangian point L1 (SOHO, ACE) and on satellites (GOES, SDO). In recent years, the increasing precision and extended energy range of direct cosmic ray measurements supplied by AMS-02 and PAMELA allow shedding light on the details of the solar modulation during solar cycles 23 and 24 (Corti et al., 2016). However, the small size of satellite-based detectors and the small number of satellites does not provide sufficient statistics in the high-energy region for real-time monitoring of the space weather. Therefore, space and ground observations should be conducted simultaneously in a way to provide complementary information.

Networks of particle detectors on earth, located at different latitudes and altitudes are monitoring the solar activity for many decades without interruptions. The highest energy SCRs generate particle showers in interactions with atmospheric nuclei that can reach the earth surface and generate signals in surface particle detectors (similar to ones initiated by GCRs). Such events are called Ground Level Enhancement (GLE). The latitude dependence of the geomagnetic field provides the possibility to use worldwide networks of Neutron Monitors (NM; Hatton (1971a, b), Simpson, 2000) as a spectrometer, registering GCR in the energy range from 0.5 to 10 GeV.

The spectra of GCR can be approximated by a power law $dJ/dE \sim E^{-\gamma}$ with $\gamma \sim 2.7$. The intensity of the SEP events at energies above hundreds of MeV usually decay very fast (with exponential cut-off of the power-law spectrum; Miroshnichenko and Nymmik, 2014). Only for some events, such as the one on 20 January 2005, the spectra of SCR are considerably "harder", reaching energies up to 1 GeV (see Fig. 1 from Labrador et al., 2005 and Table 1 in Asvestari et al., 2017). Thus, for the GeV energies the intensity of the GCR becomes increasingly higher than the intensity of the largest observed SEP events and we are confronted with the very complicated problem of detecting a small signal from the sun against the huge "background" of the GCR. Most existing networks of particle detectors are unable to reliably detect very low particle fluxes of SEP events in the GeV region. Therefore, the maximal energy of solar accelerators is still not determined (Miroshnichenko and Nymmik, 2014). However, measurements at the Aragats Space-Environmental Center (ASEC, Chilingarian et al., 2005) of the huge SEP of January 2005 with a large underground muon detector allowed an estimate of the maximal energy of solar proton accelerators to be up to 20 GeV and more (Bostanjyan et al., 2007, Chilingarian and Bostanjyan, 2009). Through measurements of enhanced secondary fluxes of the various charged and neutral particles at the surface of the earth, it is possible to estimate the power law index of the SEP energy spectra. Considerably large values of the recovered spectral index ($\gamma = 4$–5) at GeV energies is a very good indicator for the upcoming severe radiation storm (abundant SCR protons and ions with energies 50–100 MeV, see Chilingarian and Reymers, 2008), dangerous for astronauts, high polar airplane flights and satellite electronics. Each of the measured secondary particle fluxes has a different, most-probable energy of the primary "parent" (i.e. proton or nucleus). As we demonstrated in (Zazyan and Chilingarian, 2009), for the Aragats facilities these energies vary from 7 GeV (most probable energy of primary protons creating neutrons) to 20–40 GeV (most probable energy of primary protons generating muons with energies above 5 GeV). Thus, for predicting upcoming radiation storms it is necessary to monitor changing fluxes of the different species of secondary cosmic rays with various energy thresholds. To cover a wide range of secondary cosmic rays energies we need networks of particle detectors at different latitudes longitudes and altitudes.

Other solar modulation effects also influence the intensity of the cosmic rays in the vicinity of the earth. Huge magnetized plasma structures usually headed by shock waves travel into the interplanetary space with velocities up to 3000 km/s (so-called interplanetary coronal mass ejection – ICME) and disturb the interplanetary magnetic field (IMF) and magnetosphere. These disturbances can lead to major geomagnetic storms harming multibillion assets in the space and at ground. At the same time, these disturbances introduce anisotropy in the GCR flux. Thus, time series of intensities of high-energy particles can provide highly cost-effective information also for the forecasting of the geomagnetic storm (Leerungnavarat et al., 2003). With data from networks of particle detectors, we can estimate the GCR energy range affected by ICME and reveal the energy-dependent pattern of the ICME modulation effects. For instance, surface particle detectors can precisely measure the attenuation of the GCR flux in the course of a few hours with following recovering during several days (Forbush decreases, FD, see Bostanjyan, Chilingarian, 2009). Measurements of the FD magnitude in the fluxes of different secondary CR species reveal important correla-


Fig. 1. SEVAN network: red asterisks – operating, blue triangles – planned locations. (For interpretation of the references to colour in this figure legend, the reader is referred to the web version of this article.)

tions with the speed, size of the ICME and the "frozen" in ICME magnetic field strength (Chilingarian and Bostanjyan, 2010). Measurements of all the secondary cosmic-ray fluxes at one and the same location are preferable due to effects of the longitudinal dependence of the FD magnitudes (Haurwitz et al., 1965). The research of the diurnal variations of GCR by the observed fluxes of charged and neutral secondary CR also opens possibilities to correlate the changes of parameters of the daily wave (amplitude, phase, maximal limiting rigidity) with the energy of GCRs (Mailyan and Chilingarian, 2010).

Thus, for the basic research of solar physics, solar-terrestrial connections and space weather, as well as for establishing services of alerting and forecasting of dangerous consequences of space storm the networks of particle detectors located at different geographical coordinates and measuring various species of secondary cosmic rays are of vital importance.

A network of particle detectors located at middle to low latitudes known as SEVAN (Space Environment Viewing and Analysis Network, Fig. 1, Chilingarian and Reymers, 2008, Chilingarian et al., 2009) was developed in the framework of the International Heliophysical Year (IHY-2007) and now operates and continues to expand within International Space Weather Initiative (ISWI). SEVAN detectors measure time series of charged and neutral secondary particles born in cascades originating in the atmosphere by nuclear interactions of protons and nuclei accelerated in the Galaxy and nearby the sun. The SEVAN network is compatible with the currently operating high-latitude neutron monitor networks "Spaceship earth" (Kuwabara et al., 2006), coordinated by the Bartol Research Center, the Solar Neutron Telescopes (SNT) network coordinated by Nagoya University (Tsuchiya et al., 2013), the Global Muon Detector Network (GMDN) (Munakata et al., 2000, Rockenbach et al., 2011), the Neutron Monitor Data Base (NMDB, Mavromichalaki et al., 2011, http://www.nmdb.eu/), International GLE database http://gle.oulu.fi/ and a new muon–neutron telescope constructed at Yangbajing, Tibet, China (Zhang et al., 2010).

Three SEVAN modules are operating in Armenia (on the slopes of Aragats Mt.: 40.25N, 44.15E, altitude 2000, 3200 m and in Yerevan, altitude 1000 m), in Croatia (Zagreb observatory: 45.82N, 15.97E, altitude 120 m), Bulgaria (Mt. Musala: 42.1N, 23.35E, altitude 2930 m), India (New-Delhi JNU Univ.: 28.61N, 77.23E, altitude 239 m) and in Slovakia (Mt. Lomnicky Stit: 49.2N, 20.22E, altitude 2634 m). In fall 2017 SEVAN module was installed on Milesovka hill (50.6N, 13.9E, altitude 837 m) in Czech republic. The potential recipients of SEVAN modules are Italy, Israel, Germany and France. The analogical detector is in operation in China (Tibet: 30.11N, 90.53E, altitude 4300 m, Zhang et al., 2010).

The particle fluxes measured by the new network at medium to low latitudes, combined with information from satellites and particle detector networks at high latitudes will provide experimental evidence on the most energetic processes in the solar system and will constitute an important element of the global space weather monitoring and forecasting service. In this paper, we present the description of SEVAN modules, its capacity to measure charged and neutral fluxes; expected purities and efficiencies of sec-

ondary cosmic ray registration, as well as the first physical results of the SEVAN network coordinated operation. Also, we demonstrate the ability to measure the energy spectra of the solar protons, possibilities to distinguish between neutron- and proton-initiated GLEs, and some other important properties of hybrid particle detectors. A separate chapter is dedicated to registration of the Thunderstorm ground enhancements (TGEs), new high-energy phenomena in the atmosphere. SEVAN modules, operating at the slopes of Mt. Aragats in Armenia during recent years have detected many TGE events in the fluxes of electrons and gamma rays, proving the existence of the strong electric fields in the thunderclouds in which the relativistic run-away electrons create avalanches in the thunderstorm atmospheres (Chilingarian et al., 2010; Chilingarian and Hovhannisyan, 2011). SEVAN detectors were calibrated by the gamma ray flux of the most powerful TGEs and furthermore, the time series of the high energy muons detected by SEVAN open possibility to estimate the electrical structure of the thunderclouds, the key parameter for creating models of both TGE and lightning occurrences.

In the appendix, we add the calculations of the barometric coefficients and diurnal variations for the SEVAN network.

## 2. The basic module (unit) of the SEVAN network

Basic module of the SEVAN network (Fig. 2) is assembled from plastic scintillator slabs of $50 \times 50 \times 5\ cm^3$ size. Between two identical assemblies of $100 \times 100 \times 5\ cm^3$ scintillators (four standard slabs) two $100 \times 100 \times 4.5\ cm^3$ lead absorbers and thick $50 \times 50 \times 20\ cm^3$ scintillator stack (5 standard slabs) are located. Scintillator lights capture cones and Photomultipliers (PMTs) are located on the top, bottom and in the intermediate layers of the detector.

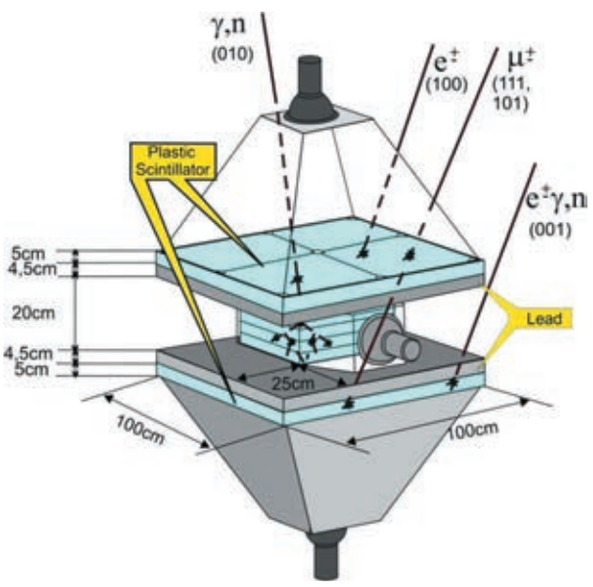


Fig. 2. SEVAN module measuring charged and neutral secondary cosmic rays.

Incoming neutral particles undergo nuclear reactions in the thick 20 cm plastic scintillator and produce charged particles. In the upper 5 cm thick scintillator charged particles are registered very effectively; however, for the nuclear interactions of neutral particles there is not enough matter. When a neutral particle traverses the top thin (5cm) scintillator, usually no signal is produced. The absence of the signal in the upper scintillators, coinciding with the signal in the middle scintillator, indicates neutral particle traversal (gamma-ray or neutron). The coincidence of signals from the top and bottom scintillators indicates the traversal of high-energy muons. Microcontroller-based Data Acquisition (DAQ) electronics provides registration and storage of all logical combinations of the detector signals for further off-line analysis and for online alerts issuing. If we denote by "1" the signal from a scintillator and by "0" the absence of a signal, then the following combinations of the detector output are possible:

111 and 101—traversal of high energy muon; 010—traversal of a neutral particle; 100—traversal of a low energy charged particle stopped in the scintillator or in the first lead absorber. 110—traversal of a high energy charged particle stopped in the second lead absorber. 001—registration of inclined charged particles. The DAQ allows also the remote control of the PMT high voltage and of other important parameters of the detector. 10 years of operation prove high reliability of DAQ electronics. There no failures were noticed in the Eastern European SEVAN modules during operation period.

## 3. Characteristics of secondary cosmic ray fluxes detected by SEVAN modules

The modules of the SEVAN network located on different latitudes, longitudes and altitudes are probing different populations of primary cosmic rays. The SEVAN modules measure fluxes of neutrons and gamma rays, of low energy charged particles and high-energy muons. To quantify statements on the detection of different types of particles by the SEVAN modules (efficiencies, purities of fluxes), we need to perform a detailed simulation of the detector response. We use simulated cascades of the charged and neutral secondary particles obtained with the CORSIKA (version 6.204) Monte Carlo code (Heck and Knapp, 1998). All secondary particles were tracked until their energy dropped below the predetermined value (50 MeV for hadrons, 10 MeV for muons and 6 MeV for electrons and gamma rays) or reached all the way to the ground level. The spectra of primary protons and helium nuclei (99% of the flux at energies up to 100 GeV) are selected to follow the proton and helium spectra reported by the CAPRICE98 balloon-borne experiment (Boezio et al., 2003). Among the different species of secondary particles, generated in nuclear-electromagnetic cascades in the atmosphere, muons, electrons, γ-rays, neutrons, protons, pions

Table 1
The range of the most probable energies (in GeV) of primary protons producing secondary fluxes at different SEVAN sites.

| Station | GCR ($\gamma = 2.7$) | | | | SCR ($\gamma = 4, 5, 6$) | | | |
|---|---|---|---|---|---|---|---|---|
| | Charged particles | Muons ($E > 250$ MeV) | Muons ($E > 5$ GeV) | Neutron | Charge particles | Muons ($E > 250$ MeV) | Muons ($E > 5$ GeV) | Neutron |
| Yerevan (Armenia) | 14.6 | 18.4 | 38.4 | 7.1 | 8.2–10.2 | 10–11.6 | 21.2–31.9 | 7.1 |
| Nor-Amberd (Armenia) | 13.1 | 14.9 | 41.2 | 7.1 | 7.6–10.6 | 9.7–11.3 | 20.5–31.3 | 7.1 |
| Aragats (Armenia) | 10.9 | 14.3 | 37 | 7.1 | 7.4–10 | 7.6–10.6 | 21.2–27 | 7.1 |
| Musala (Bulgaria) | 10.6 | 13.3 | – | 7.4 | 6.6–7.4 | 7.1–9.5 | – | 7.6–9.4 |
| Zagreb (Croatia) | 17.4 | 17.3 | – | 7.6 | 9.4–12.9 | 9.1–13.4 | – | 5.1–5.7 |
| LomniskyStit (Slovakia) | 11.5 | 14.5 | – | 4.1 | 4.1–6.5 | 5.2–8.3 | – | 4 |
| Delhi JNU (India) | 18.1 | 18.1 | – | 16.5 | 14.2–15.1 | 14.3–15.3 | – | 14.3–14.4 |

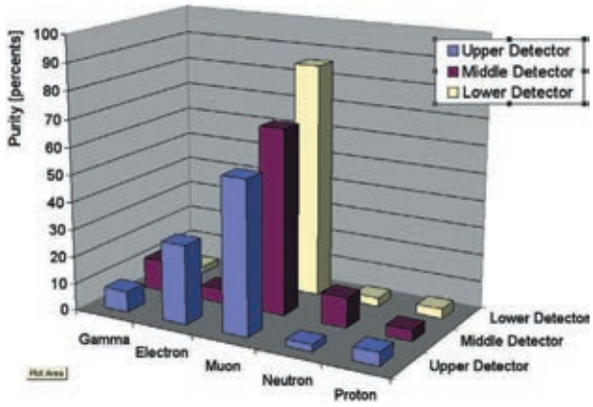


Fig. 3. The purity of the SEVAN detector layers.

and kaons were followed by CORSIKA and stored. These particles were used as input for the GEANT3 package (GEANT, 1993), implemented for detector response simulation. Also, we take into account the light absorption in the scintillator (Chilingarian and Reymers, 2008).

We show in Table 1 the most probable energies of primary protons to which the SEVAN modules are sensitive (Zazyan and Chilingarian, 2009). The calculations were made for different values of the spectral index of the power law: for the GCRs ($\gamma = -2.7$), columns 2–5; and for the SEP events ($\gamma = -4$, $-5$, and $-6$), columns 6–9. Because in the simulations we use 3 values of SCR spectral indices we give an interval of energies of primary protons. From the Table, we can see that SEVAN network provides registration of the SEP events in a broad energy range including very poorly researched energies above 10 GeV. For instance, the neutron flux measured at Lomnisky Stit, Slovakia is sensitive to 4 GeV solar protons; and the high-energy muon flux measured at Delhi is sensitive to 18 GeV solar protons. Taking into account intermediate energies measured at Aragats, Armenia, Zagreb, Croatia and Musala, Bulgaria we can reliably recover SEP energy spectrum with satisfactory accuracy.

The efficiency of the charged particle detection by all 3 layers of the SEVAN detector is above 95%; the neutron detection efficiency in the middle "thick" scintillator reaches 30% at 200 MeV, the efficiency of the gamma ray detection reaches 60% at the same energies. The purity (relative fraction of different species registered) of three SEVAN detecting layers is presented in Fig. 3.

In Fig. 3, we see that majority of registered particles in all three layers are muons; the first layer also registers electrons. The fraction of neutral particles is uppermost in the middle layer, although it is less than 10% there. It is apparent that using only layer counts we will not be able to research the modulation effects the sun poses on different species of secondary cosmic rays; we should "enrich" the detected fluxes by the particles of definite types. The coincidence techniques described in the previous section allow us to perform this task by registering different combina-

tions of signals in the 3-layered detector. In Fig. 4, we post the fraction of different particles registered by various combinations of the SEVAN module operation. The pattern is significantly improved: fraction of electrons selected by combination 100 is above 40%; the fraction of neutral particles selected by combination 010 – is larger than 85% and the fraction of high energy muons selected by combinations 111 and 101 reaches 95%. Therefore, by analyzing combinations, instead of layer counts, we can get clues how 3 types of secondary cosmic rays are influenced by meteorological and/or solar modulation effects. The data from Figs. 3 and 4 are tabulated in Table 2. The figures in the table show that coincidences of the detector layer can be used for selecting different particles of the secondary cosmic rays incident on the detector. For instance, ~81% of particles registered by combination 100 (signal only in the upper scintillator) are electrons and muons; ~86% of particles registered by combination 010 (signal only in the middle scintillator) are neutrons and gamma rays.

Of course, the purity is not the only parameter we are interested in; the efficiency of particle registration is also of the topmost interest in detector design and operation. In Fig. 5, we post the purity-efficiency diagram explaining which fraction of primary flux will contribute to different SEVAN combinations.

In Fig. 5, we see that the high-energy muons are registered with both high efficiency and purity. Neutrons are registered with rather a satisfactory efficiency and purity (both ~30%). It is worth to mention that the efficiency of neutron monitor is reaching 30% only for highest energy neutrons. On the other hand, NM can distinguish neutrons from the gamma rays. Gamma rays are selected with lower efficiency by all possible combinations of SEVAN layers; nonetheless, efficiency of electron registration is above 90%; therefore, the low energy electromagnetic component is registered efficiently by SEVAN. Moreover, combining SEVAN and NM measurements we can highly improve neutron-gamma ray discrimination.

In Table 3, we post the most probable energies (medians of the energy distribution of the parent protons) producing different elementary particles in the terrestrial atmosphere. Higher energy protons are responsible for the muon flux registered by SEVAN, lower energy primary protons can produce neutrons, registered by SEVAN.

As we can see, in Table 2 and in Fig. 5, SEVAN can register the low energy charged component, neutral component, and high-energy muons. In Table 4, we compare the simulated and measured one-minute count rates of these particles. Low energy charged particles, as well as neutrons and gamma rays, are attenuated very fast as they penetrate deep in the atmosphere. High-energy muons did

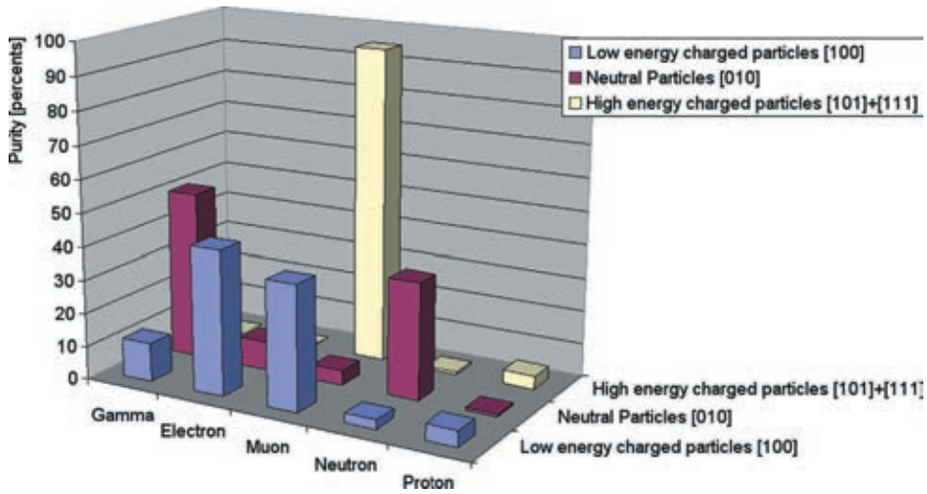


Fig. 4. Purity of SEVAN combinations.

Table 2
Summary of purity of selected particles by SEVAN layers and combinations.

| | Gamma % | Electron % | Muon % | Neutron% | Proton % |
|---|---|---|---|---|---|
| Low energy charged part. [1 0 0] | 11.6 | 43.3 | 37.4 | 2.8 | 4.8 |
| Neutral particles [0 1 0] | 50.6 | 8.8 | 4.4 | 35. 1 | 1.0 |
| High energy charged part. [1 0 1] + [1 1 1] | 0.0 | 0.11 | 94.9 | 0.81 | 4.1 |
| Upper detector | 7.6 | 28.9 | 56.1 | 2.4 | 4.8 |
| Middle detector | 11.6 | 5.2 | 67.9 | 11.0 | 4.2 |
| Lower detector | 2.7 | 4.4 | 85.9 | 3.3 | 3.6 |

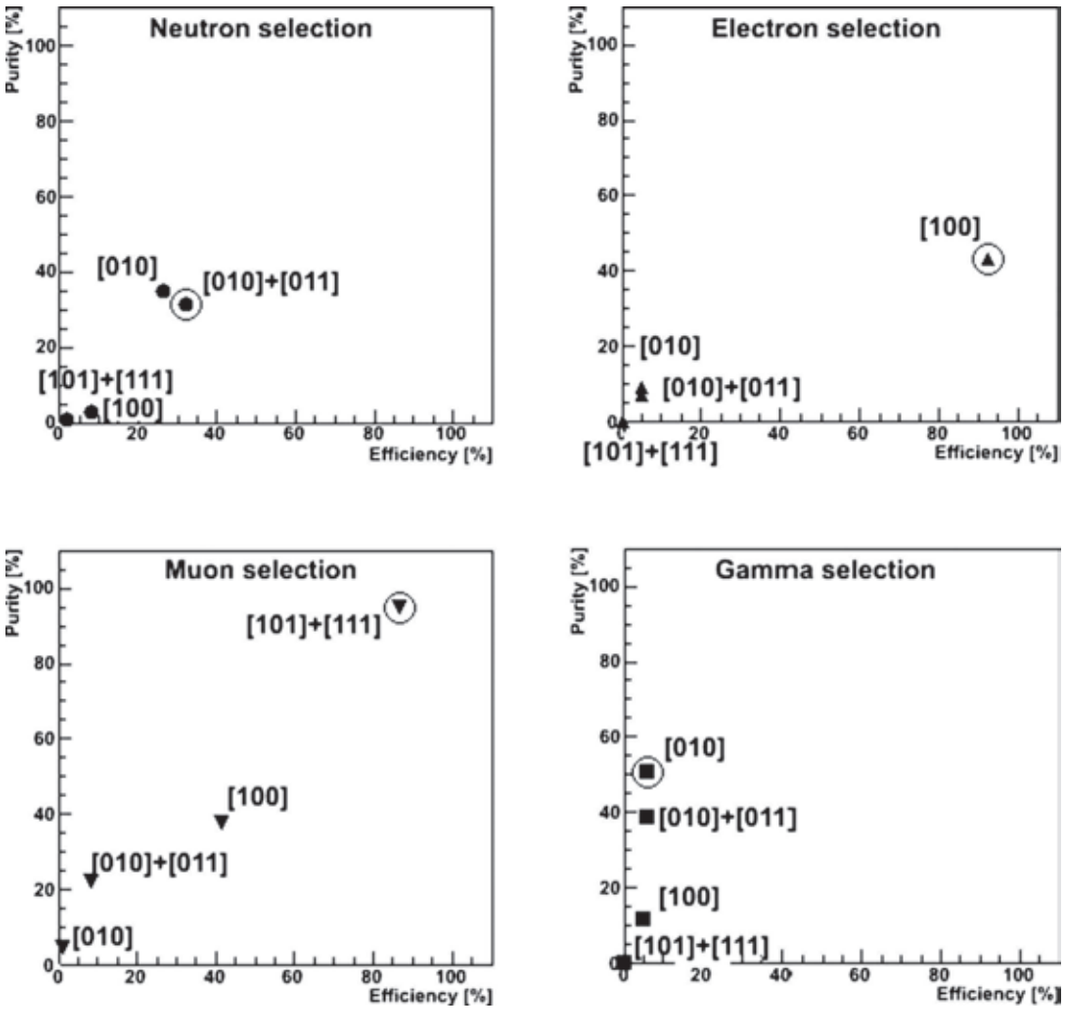


ig. 5. The purity-efficiency diagram of the SEVAN combinations registering ambient population of the secondary cosmic rays generated by interactions f GCR with atmosphere.

ıot attenuate so fast as one can see in the last row of Table 4.

### . Response of SEVAN particle detectors to GLEs initiated y the solar protons and neutrons

By observing solar neutrons, we can estimate the proluction time of the solar ions and also probe their energy pectrum. Thus, measurements of the time series of the olar neutrons will shed light on the operation of the solar ccelerators. However, neutron events are very rare and it s not easy to distinguish them from more frequent proton vents. The comparison of the count rate enhancements in he layers of the SEVAN module (measured in the number of standard deviations – "Nσ") allows one to distinguish he GLE's originated from solar neutrons incident on the errestrial atmosphere. Table 5 shows that for neutron prinaries there is a significant enhancement in the SEVAN hick layer and much less enhancement in a thin layer.

Table 3
Most probable energies of the GCRs registered by the SEVAN detector at 3200 m above sea level.

| Layers of detector located at 3200 m | Most probable energy of GCR (GeV) |
|---|---|
| Upper layer | 11.5 |
| Middle 25 cm layer | 8.5 |
| Bottom layer | 14.5 |

For proton primaries the situation is vice versa: the significant enhancement is in the thin layer, and much less in the thick layer.

The one-minute count rate of the SEVAN upper layer (~25,500) is comparable to count rate of the Aragats standard 18NM64 type neutron monitor (~25,000), in spite the surface of SEVAN (1 $m^2$) is 18 times smaller than one of neutron monitor (18 $m^2$). The one-minute count rate of the SEVAN middle layer (~7700, surface 0.25 $m^2$) is

Table 4
Experimental and simulated one-minute count rates measured by three scintillators of the SEVAN.

| Type of secondary particle | Yerevan (1000 m) | | NorAmberd (2000 m) | | Aragats (3200 m) | |
|---|---|---|---|---|---|---|
| | Measured count rate | Simulated count rate | Measured count rate | Simulated count rate | Measured count rate | Simulated count rate |
| Low energy charged particles | 8862 ± 108 | 7202 | 11,593 ± 161 | 10,220 | 16,010 ± 130 | 17,330 |
| Neutral particles | 363 ± 19 | 359 | 690 ± 27 | 795 | 2007 ± 46 | 1680 |
| High energy muon | 4337 ± 67 | 5477 | 4473 ± 99 | 5548 | 4056 ± 64 | 8051 |

Table 5
Simulated enhancements (in standard deviations) of the "5-min" count rates corresponding to the GLEs initiated by primary neutrons, energy spectrum adopted from Watanabe et al., 2006) and primary protons (Energy spectrum adopted from Zazyan and Chilingarian, 2009).

| Detector layer | Solar protons | Solar neutrons |
|---|---|---|
| Upper 5 cm scintillator | 4.8 σ | 2.6 σ |
| Middle 20 cm scintillator | 1.7 σ | 6.4 σ |

~3.2 times less than count rate of the Aragats standard 18NM64 type neutron monitor (25,000). However, most of neutron monitors of the worldwide network consists usually from only one section (6NM64). Thus, SEVAN provides approximately the same statistical significance in detecting neutral particles as 6NM64. Both low-energy charged particles registered by the upper layer and mostly neutral particles registered by the middle layer are sensitive to the modulation effects that solar activity pose on the intensity and directivity of the GCRs and these effects can be observed and researched by the SEVAN network. However, for the reliable registration of the differential energy spectra of very strong SEPs in the GeV region, we need particle detectors with the larger area and higher energy threshold. For instance, the most energetic particles from the GLE occurred on 20 January 2005 (energy of primary SEP $\geq$ 20 GeV) were registered only by the 100 $m^2$ - array of underground muon detector of the GAMMA experiment (see details in Chilingarian, 2009). Of course, large magnetic spectrometer located on mountain altitudes will be a best solution for registration of highest energy solar cosmic rays. Unfortunately, the 40 $m^2$ area and 3 TeV maximal detectable momentum magnetic spectrometer of ANI experiment (Danilova et al., 1982) planned in 80-ths by Yerevan Physics Institute and Lebedev Physical Institute was not finished due to collapse of Soviet Union.

## 5. Forbush decrease events detected by the SEVAN network in the 24-th solar activity cycle

The Solar Cycle 24, the weakest solar cycle in more than a century, the solar maximum of this cycle having peaked at 82 (smoothed Monthly value of the sunspot number) in **April 2014**; the lowest of any cycle since 1928 when Solar Cycle 16 peaked at 78 (http://www.swpc.noaa.gov/prod-

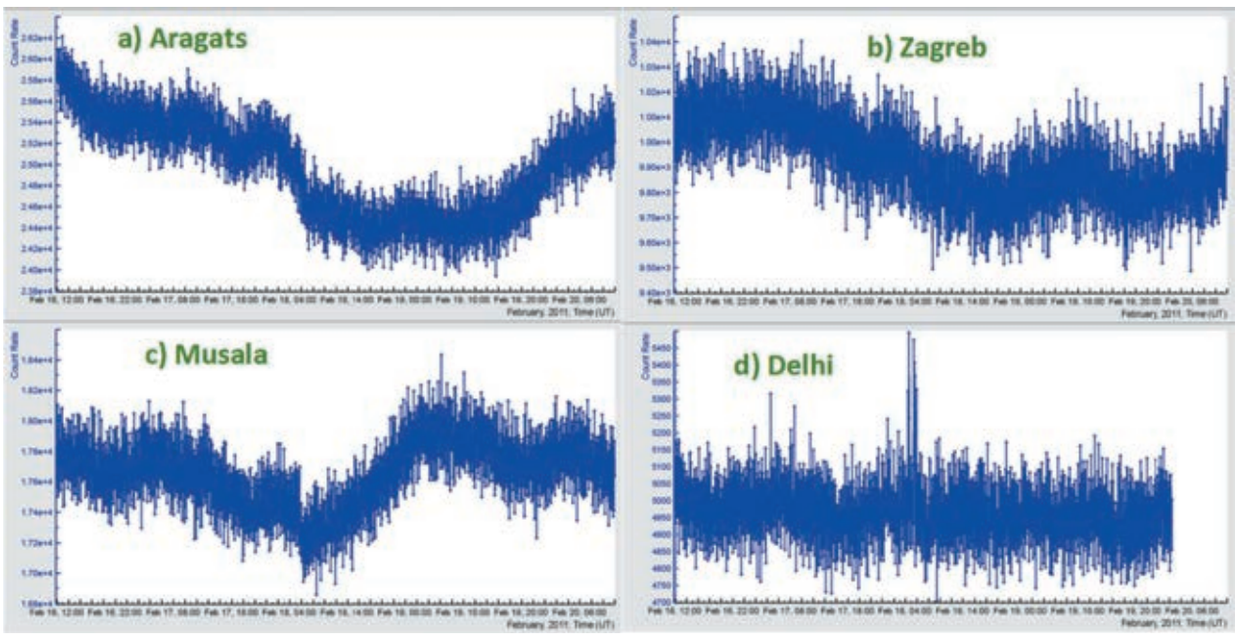


Fig. 6. The time profiles of the FD on 18 February 2011 measured by Aragats, Zagreb, Musala, and Delhi SEVAN monitors. The low energy charged particles (combination 100) time series.

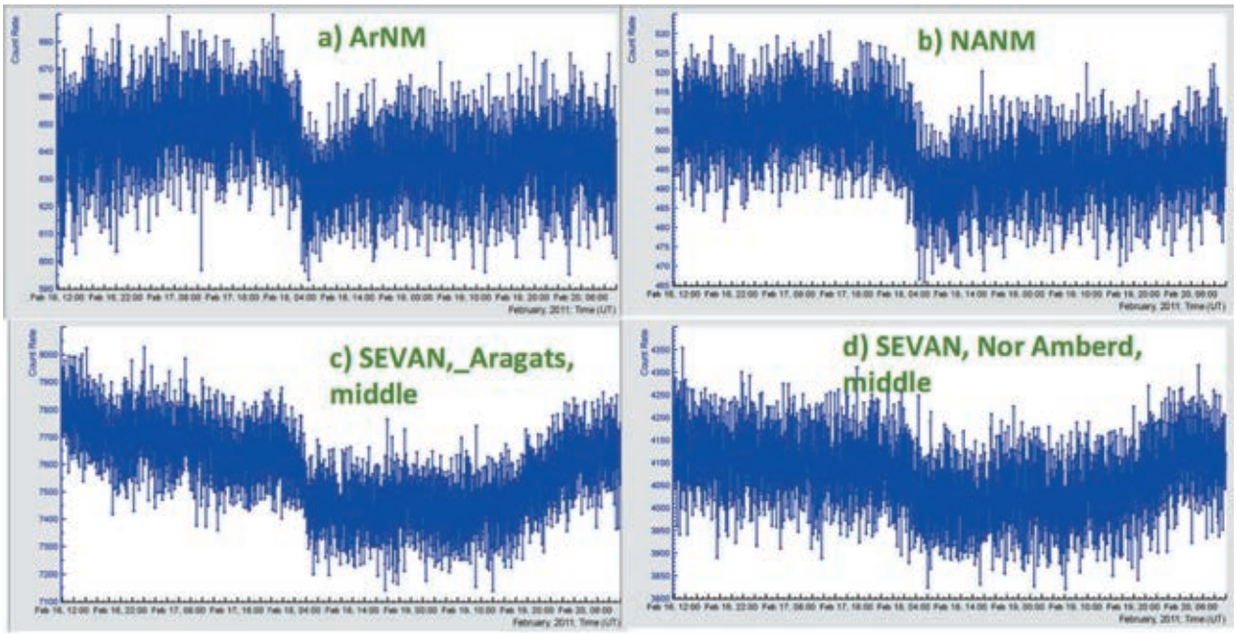


Fig. 7. Comparison of the FD detection by neutron monitors (from NMDB, normalized to 1 s count rate) and middle layer of SEVAN detector on Aragats and in Nor Amberd (1-min count rate).

ucts/solar-cycle-progression) in agreement with the Gleissberg cycle with the period 90–100 years (Brajša et al., 2015). The number of SEP events was very low and only two of them has GLE components: 2012 May 17 Gopalswamy et al., 2013) and 2014 January 6 (sub-GLE, Thakur et al., 2014). GLE and sub-GLE events were primarily observed by the South Pole neutron monitors (the increase of ~2.5%) while a few other neutron monitors recorded smaller increases; the proton acceleration during GLE 71 and sub-GLE occurred up to rigidities $R \sim 2.3$–2.5 GV (Kravtsova and Sdobnov, 2017). Aragats Neutron Monitors and SEVAN network detectors located on Aragats did not register these events due to large cutoff rigidity ($R \geq 7.5$ GV). The latest GLE 72 occurred on 10 September 2017 also were not detected by Aragats Neutron Monitors and SEVAN modules. Only high-latitude neutron monitors detected count rate enhancements, follow for details: http://www.nmdb.eu/?q=node/501.

However, we detect several Forbush decreases by both SEVAN detectors and Neutron Monitors. In the middle of February 2011 the active region, AR 11,158 produced 3 solar flares of class M6.6 (13 February, solar coordinates S19, W03), M2.2 (14 February, solar coordinates S20, W14) and strongest X2.2 (15 February, solar coordinates S19, W03S21, W18). All 3 flares were accompanied with CMEs headed to the earth's direction. The worldwide network of neutron monitors detects at 18 February sizeable Forbush decrease. The SEVAN network as well detects Forbush decrease by 3 monitors located in Armenia and by monitors located in Zagreb observatory (Croatia) and Mt. Musala (Bulgaria). The SEVAN module located in India did not register Forbush decrease due to large geomagnetic cutoff. In Fig. 6 we see that Forbush decrease is much more pronounced on the mountain altitudes (6a and 6b) comparing with seal level (6c). Also, the recovery time of Aragats SEVAN is much longer compering with Musala SEVAN. In Fig. 7 we compare Forbush decrease registration by the neutron monitors and SEVAN detectors located on Aragats and in Nor Amberd research station on altitudes 3200 and 2000 m correspondingly. There is a good coherence of Forbush decrease detection by different type detectors; Nor Amberd SEVAN is less sensitive to disturbances of the geomagnetic storm due to its location under

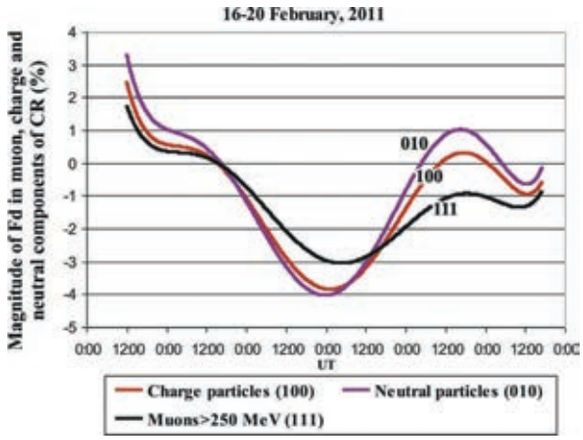


Fig. 8. FD as detected by different species of secondary cosmic rays (Aragats SEVAN detector combinations).

Table 6
The magnitudes of Forbush decrease (FD) measured by SEVAN network and Aragats neutron monitor on 18 February.

| | Magnitude of FD Aragats, 3200 m (%) | Magnitude of FD by Nor Amberd, 2000 m (%) | Magnitude of FD by Zagreb 130 m (%) | Magnitude of FD Musala 2900 m (%) | India, New Delhi JNU |
|---|---|---|---|---|---|
| SEVAN(1 0 0) | −3.8 | −2.1 | −3 | −3 | 0 |
| SEVAN(0 1 0) | −4 | −4.2 | −3 | – | 0 |
| SEVAN(1 1 1) | −3 | 2.3 | −3 | – | 0 |
| Aragats NM | −4.2 | −4.0 | | | |

a large amount of matter; i.e. low energy neutrons, most sensible to Forbush decrease are attenuated in the concrete slabs above the detector.

The Forbush decrease phenomena is a global phenomena influenced whole globe (excepting the equatorial regions only where the cutoff rigidity is the largest); nevertheless, the detection of the local differences in time profiles of Forbush decreases produced by primary particles of different energies is very important and allows to recover the event anisotropy and sometimes also the shape of the ICME. The SEVAN network located at different longitudes (from Zagreb to Delhi) gives a possibility to explore the shape and the magnitude of the FD longitudinal dependence and its source (Belov et al., 1995; Ruffolo et al., 1999). In this respect, the registration of FDs also in low and high-energy charged particle fluxes can bring additional information for the developing of the ICME. The amplitude of FD is dependent on the disturbance of the interplanetary magnetic field caused by the ICME propagation and ICME interaction with the geomagnetic field. Both effects are dependent on the strength of the magnetic field "frozen" in the ICME (Chilingarian and Bostanjyan, 2010). GCRs are traversing the regions of the disturbed IMF and dependent on their energy are deflected from their path and miss encounter with earth atmosphere. As we demonstrate above different components of secondary cosmic rays detected on the earth surface are generated in the terrestrial atmosphere by interactions of CRs of various energies; neutrons are generated by protons of lower energies than ones generating electrons; electrons, in turn, are generated by protons with energies lower than ones generated high energy muons. Therefore, the amplitudes of Forbush decrease in neutron, electron, and muon fluxes are expected to reflect these energy relations.

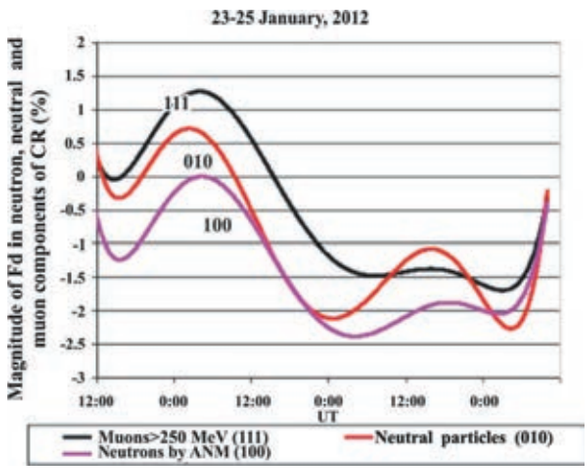


Fig. 9. FD of 24 January detected by the Aragats Neutron monitor and SEVAN (0 1 0) and 111 combinations.

In the Fig. 8 and Table 6 we see that neutral component measured by Aragats SEVAN 010 combination demonstrate 4% decrease practically coinciding with FD measured by the Aragats neutron monitor (4.2%), the low energy charged component (100 combination) demonstrates ~3.8% decrease and the 111 combination (high energy muons) ~3% decrease. Nor Amberd SEVAN also demonstrated the biggest magnitude of FD for the neutral particles; however, the magnitude of the low energy charged particles (1 0 0) is a bit lower compared with the magnitude of FD measured in the high-energy muon flux. In Zagreb, magnitudes of Forbush decrease for all combinations were −3%.

Another solar eruption from active region AR1402 on 23 Jan 2012 at 03:38 UT, produced an M8.7 flare is associated with full halo CME of 2000 km/s speed reached earth at 24 January; in Fig. 9 and Table 7, we show FD detection by SEVAN network.

SEVAN network detects the Forbush decreases of 18 February 2011 and 24 January 2012 in the fluxes of neutrons, low energy charged particles and high-energy muons. The patterns of Forbush decrease in different secondary particle species are very similar to ones measured by the NMs only in atmospheric neutron fluxes. However, in addition to neutron monitors, SEVAN simultaneously measures FD patterns of other species of secondary cosmic rays giving additional clues for the recovering of the shape and frozen magnetic field of the ICME interacted with the magnetosphere.

Table 7
The magnitudes of FD measured by SEVAN network and Aragats neutron monitor on 24 January 2012.

| | Magnitude of FD Aragats, 3200 m (%) | Magnitude of FD by Nor Amberd, 2000 m (%) |
|---|---|---|
| SEVAN(1 0 0) | −1.8 | −2.1 |
| SEVAN(0 1 0) | −2.1 | −3 |
| SEVAN(1 1 1) | −1.5 | −2 |
| Aragats NM | −2.4 | −2.2 |

## 6. Thunderstorm ground enhancements (TGE) detected by SEVAN and muon deficit

Copious observations of the Thunderstorm ground Enhancements (TGEs, Chilingarian et al., 2010; Chilingarian and Hovhannisyan, 2011), i.e. enhanced fluxes of electrons, gamma rays and neutrons detected by particle detectors located on the earth's surface and related to the strong thunderstorms overhead, posed the question of their origin. According to the TGE initiation model (Chilingarian, 2014), the electric field of the lower dipole in the thundercloud effectively transfers the field energy to secondary cosmic ray electrons. Electrons by a Runaway Breakdown (RB, Gurevich et al., 1992) now referred as a Relativistic runaway electron avalanches (RREA, Babich et al., 1998, Dwyer, 2007, Khaerdinov et al., 2005) generate electron-gamma ray avalanches and gamma rays by photonuclear reaction create neutrons (Chilingarian et al., 2012a,b). TGEs occur during the extended periods of large negative electric fields measured at earth's surface (Chilingarian and Mkrtchyan, 2012). To produce large TGEs, clouds should be very close to the earth's surface (25–100 m) to allow electrons and gamma rays reach the particle detectors. Facilities of the Aragats Space Environment Center (ASEC, Chilingarian et al., 2005) observe charged and neutral fluxes of secondary cosmic rays by the variety of particle detectors located in Yerevan and on slopes of Mt. Aragats at altitudes 2000 and 3200 m. Observational data of the Aragats station's monitors obtained during 2008–2017 brings >500 TGE events allowing the detailed analyses and taxonomy of new high-energy phenomena in the atmosphere (HEPA). In Fig. 10 we show one of the largest TGE events observed by SEVAN detector. On October 4, 2010 a huge excess of low energy gamma rays and electrons was detected by the upper scintillator of SEVAN detector (combination 100) reaching $60\sigma$ at 18:23! The energy threshold of the upper detector due the matter of the roof above is ~7 MeV. The peak in the time series of middle SEVAN scintillator located under 4.5 cm of lead is due to penetrated high-energy gamma rays of electron-gamma ray avalanche originated in the thundercloud. For the same minutes, the channels 111 (muons) shows pronounced decrease $\sim -6\%$. The energy of particles (mostly muons) necessary to penetrate lead filters and be detected in all three layers (combination 111) is ~250 MeV.

The huge flux of the gamma rays measure at 18:23 on 4 October 2010 was used to check the Aragats SEVAN ability to detect gamma ray flux by 010 the combination (signal only in the middle scintillator). The differential energy spectrum of the TGE event was recovered using energy-release histograms measured by the 60 cm thick plastic scintillators of the Aragats Solar Neutron Telescope (ASNT, see details in Chilingarian et al., 2012a,b). Using known energy spectrum and simulating the passage of the gamma-rays through the matter of roof and detector, and taking into account the detector response to gamma rays and electrons, we have estimated the expected number of gamma rays detected by the "010" combination to be 1459 respectively. This value is in a good agreement with the experimentally measured value of $1452 \pm 42$ (statistical errors only).

Observation of numerous TGEs by the Japanese, Chines, Slovakian groups (Kuroda et al., 2016, Zeng et al., 2013, Wang et al., 2015, Torii et al., 2011, Tsuchiya et al., 2013, Kollárik et al., 2016) prove that RB/RREA is a robust and realistic mechanism for electron acceleration and multiplication leaving no doubts about correctness of the model of TGE initiation. Slovakian group detects TGEs with the SEVAN detector installed on Lomnický štít in 2014–207 (Kudela et al., 2017). Bulgarian group detected first TGEs as well on Musala Mt., the

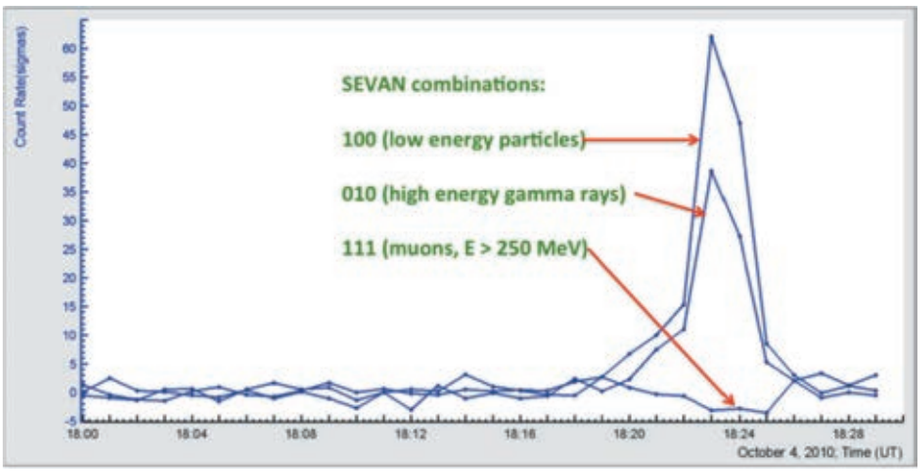


Fig. 10. The count rates of SEVAN 100, 010, and 111 combinations in a number of standard deviations from the mean value measured at the fair weather before a thunderstorm. Huge TGE is detected in high-energy gamma ray flux (0 1 0) and low energy particle flux (1 0 0). Simultaneously deficit is detected in high-energy muon flux (>250 MeV).

highest peak of Eastern Europe. Thus, SEVAN network becomes an important facility for the high-energy physics research in the atmosphere, as well as for the solar physics and space weather.

## 7. Conclusion

Reliable forecasts of major geomagnetic and radiation storms are of great importance because of associated Space Weather conditions leading to failures of space and ground-based technologies as well as posing radiation hazards on crew and passengers of satellites and aircraft. Measurements of Solar Wind parameters performed at spacecraft located at L1 provide too short time span for mitigation actions to be taken. Networks of particle detectors on earth's surface provide timely information and constitute an important element of planetary Space Weather warning services. The big advantage of ground-based particle detectors is their consistency, 24 h coverage, multi-year operation and large area. In contrast, the planned life of the satellites and spacecraft is only a few years, they are affected by the same solar blast that they should alert, and space-born facilities instead of sending warnings are usually set in the standby mode during violent space storms.

The multi-layered detectors proposed in the present paper will probe different populations of primary cosmic rays. The basic detector of the SEVAN network is designed to measure fluxes of neutrons and gamma rays, of low energy charged particles and high-energy muons. The rich information obtained from the SEVAN network will allow estimating the solar modulation effects posed on different species of GCRs and fluxes of charged and neutral particles from the highest energy SEP. To understand the sensitivity of the new type of particle detectors to high-energy solar ions we investigate the response of SEVAN modules to galactic and solar protons of highest energies. SEVAN network will be able to detect the hard spectra of solar ions (like 20 January 2005 GLE, Bostanjyan et al., 2007) preceded the upcoming very intense solar ion flux with rigidities >50 MV dangerous for satellite electronics and astronauts. The SEVAN network detectors will also allow distinguishing very interesting GLEs initiated by the primary neutrons.

The network of hybrid particle detectors, measuring neutral and charged fluxes provide the following advantages over existing detector networks measuring single species of secondary cosmic rays (Neutron Monitors and Muon detectors):

- Measure count rates of the 3 species of the Secondary cosmic rays: charged particles with energy threshold 7 MeV, neutral particles (gamma rays and neutrons) and high-energy muons (above 250 MeV);
- Probe different populations of primary cosmic rays with rigidities up to GV;
- Reconstruct SEP spectra and determine position of the spectral "knees";
- Classify GLEs initiated by solar protons and neutrons;
- Give possibilities to investigate energy dependences of the barometric coefficients and diurnal wave;
- Significantly enlarge the reliability of Space Weather alerts due to detection of three particle fluxes;
- Detect TGEs in high-energy gamma ray and low energy charged particle fluxes;
- Address one of the most important problems of the atmospheric physics – cloud electrification by measuring surge and deficit of detected particle fluxes;
- Research the runaway electron acceleration during thunderstorms and the enigma of lightning initiation;
- 10 years of operation prove high reliability of the SEVAN modules: there were no failures in the Eastern European SEVAN modules during whole operation period;
- Data Acquisition (DAQ) is Microcontroller-based provides registration and storage of all logical combinations of the detector signals and the remote control of the PMT high voltage and of other important parameters of the detector m asl.
- SEVAN modules comprised from plastic scintillators are relatively cheap compared with ones using more expensive sensors, for instance $^{3}$He counters.

The phenomenon of decreasing of the high-energy muon flux measured by SEVAN detector during TGEs can be explained by the shifting of energetic spectra of muons in the electric fields inside cloud. During positive electric field in the lower dipole that accelerates electrons and negative muons downwards spectrum of negative muons shifts right, whereas spectrum of positive muons shifts left proportional to the net potential difference of the electric field. As a result of such a transformation, the fluxes of muons are changed: the flux of negative muons increases, while the flux of positive muons decreases. Thus, the total particle's flux decreases because the number of positive muons is greater (~30% at energies below 100 MeV) than the number of negative muons. By the measured deeps in high energy muon time series it is possible to remotely estimate the total potential drop in a thundercloud; the problem that escapes the solution till now because of the absence of adequate techniques for the measuring of the electric field inside thunderclouds. SEVAN modules installed on mountains Aragats, Lomnický štít, Musala and in Zagreb observatory are actively participating in the research in the new emerging field of high-energy physics in the atmosphere (HEPA). Thus, with one and the same detector, we can measure both the solar-terrestrial relations due to violent bursts on the sun and atmospheric high-energy physics activity due to strong atmospheric storms. Cheap and reliable SEVAN detectors can be installed in other countries on different latitudes and longitudes to participate in the global network of monitoring Solar-terrestrial relations. Eastern European SEVAN network was expanded in 2017 by establishing SEVAN node at Milesovka hill in Czech republic (50°33′18″N, 13°55′53″E, 837).

**Acknowledgements**

SEVAN network was developed in the framework of IHY-2007 initiative, and we thank H. Haubold, J. Davila, N. Gopalswamy for being so instrumental in helping us in this scientific endeavor. Authors thank K. Arakelyan and D. Pokhsraryan for commissioning the SEVAN units in India, Bulgaria, Croatia and Slovakia and A. Reymers for calculating SEVAN units' response function. Authors thanks SEVAN instrument hosts D. Rosa, N. Nikolova, K. Kudela, S. Mukherjee and O. Ploc for their interest to be a part of SEVAN network and for operating SEVAN modules. A.C. appreciates the support by Russian Science Foundation grant (project No. 17-12-01439). Time series from all nodes of SEVAN network are available from the WEB analysis platform ADEI: http://www.crd.yerphi.am/adei.

## Appendix A. Calculation of the barometric coefficients for the SEVAN network

To recover and analyze the solar modulation of the Galactic Cosmic Rays (GCR) the influence of the meteorological effects on the flux of the secondary particles reaching the Earth surface should be carefully disentangled. Theory of meteorological effects (Dorman and Dorman, 2005) gives the detailed classification of the metrological effects; it mentioned the barometric one as major influencing particle fluxes. Therefore, it is the greatest importance to accurately measure the barometric coefficients to "unfold" the solar modulation effects. Besides this main goal, there exist several independent research problems connected with rigidity, height and solar cycle phase dependence of the barometric coefficient. All these dependences can be investigated by SEVAN network due to different altitudes, various cutoff rigidities and planned long-term operation. At the minimum of solar activity, the GCR flux is enriched by abundant low energy (below 10 GeV) particles, blown out from the solar system by the intense solar wind at years of the maximum of solar activity. Particle detectors located at high latitudes are sensitive to lower primary energies as compared with detectors located at middle-low latitudes, because of lower cutoff rigidity. Detectors located at high altitudes are sensitive to lower primary energies and register more secondary particles than sea level detectors. Detectors registering muons are sensitive to higher energies of primary particles compared with detectors measuring neutrons. Thus, the following relations between barometric coefficients of various particle detectors located in different places and measuring diverse species of secondary CR can be expected:

- Barometric coefficient absolute value for the same secondary particle flux is greater for detectors located at high latitudes as compared with low latitudes;
- Barometric coefficient absolute value for the same secondary particle flux should be greater at minimum of solar activity as compared with maximum;
- Barometric coefficient absolute value for the same secondary particle flux should be greater for high mountain altitudes as compared with lower locations;
- Barometric coefficient absolute value should be larger for neutrons as compared with muons;
- Barometric coefficient absolute value should be larger for low energy muons as compared with high energy muons;
- Barometric coefficient absolute value should be inversely proportional to zenith angle of incident particle flux;
- Barometric coefficient absolute values should be lower for the greater dead times of neutron monitor.

All the mentioned dependences were investigated and discovered during the last 50 years by the networks of neutron monitors and muon detectors (Shea and Smart, 2000). However, due to the peculiarities of detection techniques, scarce statistics, highly different local meteorological conditions, cycle-to-cycle variations of solar activity, the obtained results on the mentioned dependencies are yet more qualitative and additional investigations of the interrelations of barometric coefficients are needed. SEVAN provides an ideal platform for such researches. Data for calculation of barometric coefficients of SEVAN modules were selected in 2008, when there were higher than 15 mb continuous changes of atmospheric pressure during the day, and also there were no disturbances of the Interplanetary Magnetic Field (day variations do not exceed 1.5–2 nT). The values of the IMF were obtained from instrument SWEPAM, Advanced Composition Explorer (ACE) spacecraft (http://www.srl.caltech.edu/ACE/ASC/level2/lvl2DATA_MAG.html). The least square method was used to obtain the regression coefficients. Large values of the correlation coefficient prove the correct selection of the reference data. In Table A1 we summarize the calculated barometric coefficients of SEVAN modules. In the columns accordingly are posted the altitude; cutoff rigidity; barometric coefficient; goodness of fit in the form of the correlation coefficient; count rate; relative error; "Poisson" estimate of relative error (standard deviation divides by average count rate).

The values posted in the last two columns should be very close to each other if the Poisson process can describe the particle arrival. Any small deviation manifested the correlation between detector channels; any large correlation – failures in electronics or data acquisition software (see for details Hovhannisyan and Chilingarian, 2011). In Tables A1 and A2 we present barometric coefficients for SEVAN detectors combinations, selecting different species of secondary cosmic rays. Of course, we cannot measure "pure" flux of neutrons, due to the contamination of gamma-quanta, and muons. However, as we see from Table A2, events selected as "neutrons" (coincidences 010 and 011) demonstrate barometric coefficients approximately twice as events selected as muons.

Table A1
Barometric coefficients, count rates and relative errors of SEVAN units.

| Monitor | Altitude (m) | RC (GV) | Barometric coefficient (%/mb) | Correlation coefficient | Count rate (min) | Relative error | $\frac{1}{\sqrt{N}}$ |
|---|---|---|---|---|---|---|---|
| Aragats SEVAN upper detector | 3200 | 7.1 | $-0.466 \pm 0.018$ | 0.994 | 20,768 | 0.005 | 0.0069 |
| Aragats SEVAN middle detector | 3200 | 7.1 | $-0.406 \pm 0.012$ | 0.996 | 6573 | 0.011 | 0.0123 |
| Aragats SEVAN lower detector | 3200 | 7.1 | $-0.361 \pm 0.016$ | 0.992 | 12,481 | 0.008 | 0.0089 |
| Nor Amberd SEVAN upper detector | 2000 | 7.1 | $-0.274 \pm 0.016$ | 0.975 | 9100 | 0.011 | 0.0105 |
| Nor Amberd SEVAN middle detector | 2000 | 7.1 | $-0.342 \pm 0.023$ | 0.969 | 3988 | 0.015 | 0.0158 |
| Nor Amberd SEVAN lower detector | 2000 | 7.1 | $-0.262 \pm 0.017$ | 0.973 | 5103 | 0.014 | 0.0141 |
| Yerevan SEVAN upper detector | 1000 | 7.1 | $-0.251 \pm 7.85E-05$ | 0.994 | 14,815 | 0.008 | 0.0082 |
| Yerevan SEVAN middle detector | 1000 | 7.1 | $-0.238 \pm 0.014$ | 0.981 | 3414 | 0.016 | 0.0171 |
| Yerevan SEVAN lower detector | 1000 | 7.1 | $-0.190 \pm 0.025$ | 0.903 | 9505 | 0.011 | 0.0102 |

Table A2
Barometric coefficients, count rates and relative errors of SEVAN monitors for different coincidences.

| Monitor | Altitude (m) | Rc (GV) | Barometric Coeff. %/mb | Correlation coefficient | Count rate [min] | Relative error | $\frac{1}{\sqrt{N}}$ |
|---|---|---|---|---|---|---|---|
| Aragats SEVAN Low energy charged particles (Coincidence 100) | 3200 | 7.1 | $-0.5 \pm 0.018$ | 0.995 | 15,389 | 0.007 | 0.0080 |
| Aragats SEVAN High energy muons (Coincidence 111 + Coincidence 101) | 3200 | 7.1 | $-0.351 \pm 0.038$ | 0.96 | 3868 | 0.014 | 0.0161 |
| Aragats SEVAN neutrons (Coincidence 010) | 3200 | 7.1 | $-0.511 \pm 0.018$ | 0.995 | 1959 | 0.019 | 0.0225 |
| Nor Amberd SEVAN Low energy charged particles (Coincidence 100) | 2000 | 7.1 | $-0.281 \pm 0.022$ | 0.957 | 5941 | 0.013 | 0.0129 |
| Nor Amberd SEVAN High energy muons (Coincidence 111 + Coincidence 101) | 2000 | 7.1 | $-0.242 \pm 0.022$ | 0.952 | 1988 | 0.026 | 0.0224 |
| Nor Amberd SEVAN neutrons (Coincidence 010) | 2000 | 7.1 | $-0.54 \pm 0.070$ | 0.899 | 674 | 0.037 | 0.0385 |
| Yerevan SEVAN Low energy charged particles (Coincidence 100) | 1000 | 7.1 | $-0.3 \pm 0.014$ | 0.987 | 9446 | 0.010 | 0.0102 |
| Yerevan SEVAN High energy muons (Coincidence 111 + Coincidence 101) | 1000 | 7.1 | $-0.149 \pm 0.035$ | 0.765 | 4714 | 0.015 | 0.0145 |
| Yerevan SEVAN neutrons (Coincidence 010) | 1000 | 7.1 | $-0.4 \pm 0.039$ | 0.943 | 425 | 0.048 | 0.0485 |

## Appendix B. Investigation of diurnal variations of cosmic rays using SEVAN network

The diurnal variations are the result of complex phenomena involving IMF, magnetosphere and, in addition, dependent on the latitude, longitude and altitude of detector location on the Earth. The diurnal CR variations comprise an important tool for understanding basic physics of the heliosphere and the Earth's magnetosphere. Diurnal variations can be characterized by the amplitude (maximal value) measured in daily time series and by phase (time of the maximal amplitude). Different species of the secondary CR undergo different diurnal variations. It is obvious that more the most probable primary energy of the monitored CR species – less should be the amplitude of diurnal variation. Therefore, the third parameter, characterizing the diurnal variations at definite location and time, is so called upper limiting rigidity, i.e., the threshold rigidity not influenced by the solar, interplanetary and geomagnetic disturbances. The detailed investigation of the diurnal variations can comprise a basis of scientific data to be used in a wide context of solar-terrestrial connections (Mailyan and Chilingarian, 2010). In this section we present measurements of the phase, amplitude for the SEVAN monitors at the minimum of the solar activity year. This data will be used for physical analysis of SEVAN particle detectors data as 24-th solar activity cycle proceeds.

In Fig. 11 we can see that detectors located at close geographic coordinates demonstrate similar patterns of the daily variations. When comparing Aragats, Croatian and Bulgarian monitors we can deduce that both latitude and longitude of site location influence the diurnal variations' pattern. However, the very large amplitude of Musala monitor's middle scintillator point on possible defects in light proofing of the middle detector. Filtered and pressure corrected (Chilingarian and Karapetyan, 2011) daily data from Fig. 11 were fitted by the harmonic approximation function for each day of the selected period. In this way, distributions of amplitudes and phases of daily variation were got. The following approximation was used to be consistent with previous research (Kudela et al., 2008):

$$f(t_i) = A + B * \cos(\omega t_i + \psi) \quad (1)$$

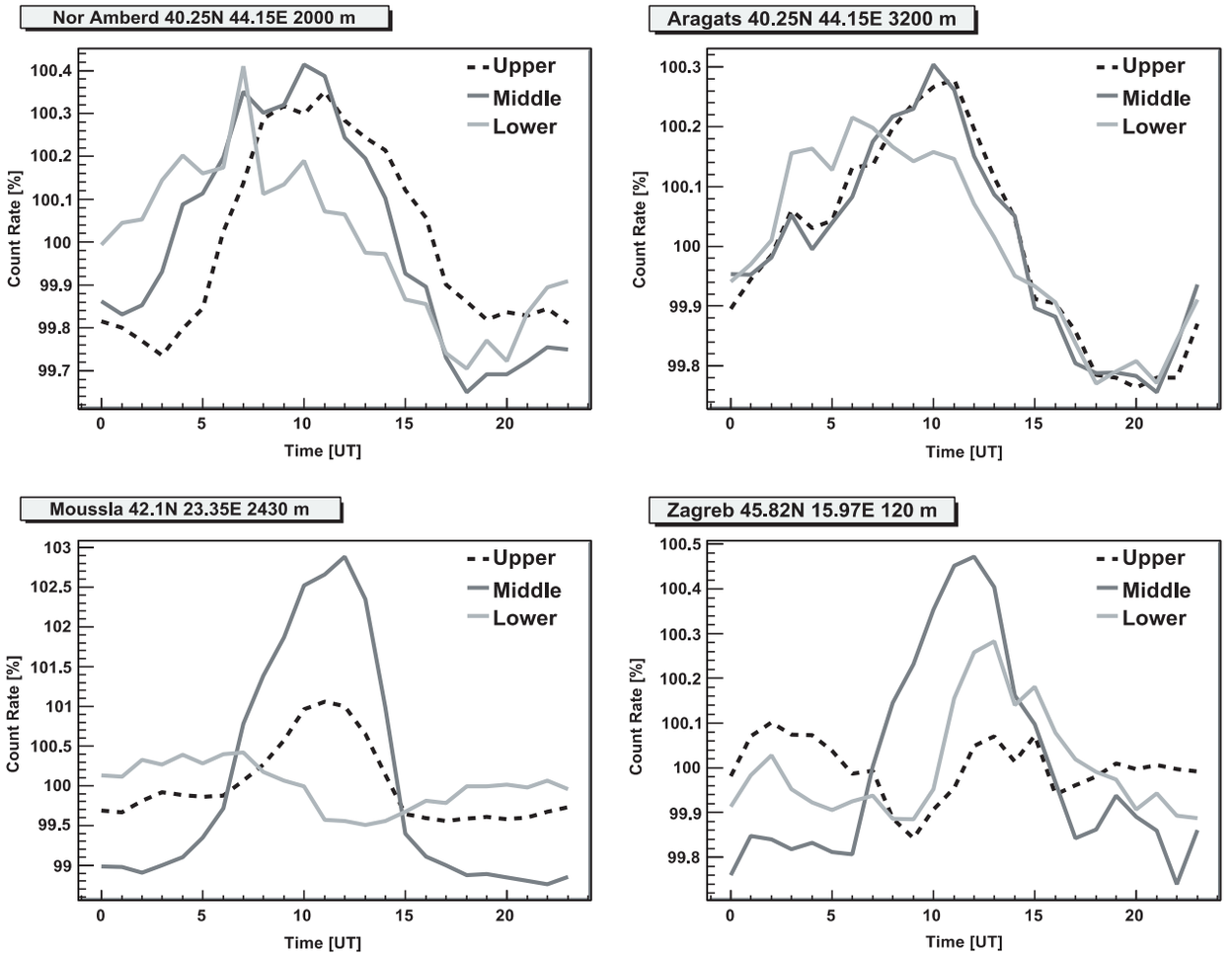


Fig. 11. Daily variations of high (lower layer) and low energy (upper layer) charged fluxes and neutral fluxes (middle layer) according to the SEVAN detectors located in Nor Amberd, Aragats, Musala and Zagreb. Month-averaged daily count rates of Nor Amberd May 2008 data, Aragats–October 2008, Musala and Zagreb December 2008–January 2009.

Here $A$ is the daily average value of cosmic ray intensity, B is the amplitude of daily variations, $\omega$ is the angular frequency and $\psi$ is the phase of daily variations. The quality of fit $d$, the difference between experimental data and the fit is calculated according to Kudela et al. (2008):

$$d^2 = \sum_{i=1}^{n} d_i^2 = \sum_{i=1}^{n} [Y_i - f(t_i)]^2 \quad (2)$$

Amplitudes and phases obtained from Eq. (1), and fit quality calculated by Eq. (2) are presented in Table A3.

Table A3
Daily variations of the SEVAN data; Nor Amberd data of May 2008, Aragats data of October 2008, Musala and Zagreb data of December 2008–January 2009.

| | Median amplitude (%) | Median phase (local time) | Quality of he fit (d) | Most probable primary energies (GV) |
|---|---|---|---|---|
| Nor Amberd SEVAN upper detector | 0.28 | 15:13 | 1.33 | 14.6 |
| Nor Amberd SEVAN middle detector | 0.34 | 12:55 | 1.15 | 7.1 |
| Nor Amberd SEVAN lower detector | 0.24 | 10:36 | 0.18 | 18.4 |
| Aragats SEVAN upper detector | 0.23 | 12:42 | 0.71 | 14.6 |
| Aragats SEVAN middle detector | 0.21 | 12:27 | 0.62 | 7.1 |
| Aragats SEVAN lower detector | 0.20 | 11:17 | 0.33 | 18.4 |
| SEVAN Musala upper detector | 0.55 | 11:58 | 2.31 | |
| SEVAN Musala middle detector | 1.80 | 12:33 | 8.16 | |
| SEVAN Musala lower detector | No peaks | | | |
| SEVAN Zagreb upper detector | Two peaks | | | |
| SEVAN Zagreb middle detector | 0.28 | 12:39 | 1.35 | |
| SEVAN Zagreb lower detector | 0.12 | 14:43 | 0.51 | |

We do not fit curves with two peaks and without an apparent peak. For Nor Amberd SEVAN daily changes are bigger for the middle layer (enriched by neutrons and gamma rays). For Aragats all layers show similar behavior. In local times the maximums are at 12:00–15:00 for the upper detectors, and a few hours earlier for the lower detector. Aragats' scintillators also show maximum with magnitude about 0.2% at ~12:00 LT.

The primary data available from SEVAN network demonstrate that charged component variations are comparable with neutron variation and that diurnal variations are sensitive to longitude of site location.

## References


ACE News #87 – Feb 23, 2005. Space Weather Aspects of the January 20, 2005 Solar Energetic Particle Event. <http://www.srl.caltech.edu/ACE/ACENews/ACENews87.html>.

Asvestari, E., Willamo, T., Gil, A., et al., 2017. Analysis of Ground Level Enhancements (GLE): extreme solar energetic particle events have hard spectra. Adv. Space Res. 60, 781–787.

Babich, L.P., Donskoi, E.N., Kutsyk, I.M., et al., 1998. Terrestrial gamma-ray flashes and neutron pulses from direct simulations of gigantic upward atmospheric discharge. Phys. Lett. A 245, 460.

Belov, A.V., Dorman, L.I., Eroshenko, E.A., et al., 1995. Search for predictors of forbush decreases. Proc. 24th Inter. Cosmic Ray Conf, 4, 888–891.

Boezio, M., Bonvicini, V., Schiavon, P., et al., 2003. The cosmic-ray proton and helium spectra measured with the CAPRICE98 balloon experiment. Astropart. Phys. 19, 583–604.

Bostanjyan, N., Chilingaryan, A., Eganov, V., et al., 2007. On the production of highest energy solar protons on 20 January 2005. Adv. Space Res. 39, 1454–1457.

Brajša, G., Verbanac, D., Sudar, L., et al., 2015. A comparison between the observed and predicted amplitude of the 24th solar cycle r. Cent. Eur. Astrophys. Bull. 39 (1), 135–144.

Chapman, S. (Ed.), Annals of the International Geophysical Year, Pergamon Press, New York, vol. 1, 1959.

Chilingarian, A., 2009. Statistical study of the detection of solar protons of highest energies at 20 January 2005. Adv. Space Res. 43, 702–707.

Chilingarian, A., 2014. Thunderstorm Ground Enhancements – model and relation to lightning flashes. J. Atmos. Solar – Terr. Phys. 107, 68–76.

Chilingarian, A., Bostanjyan, N., 2009. Cosmic ray intensity increases detected by Aragats Space Environmental Center monitors during the 23rd solar activity cycle in correlation with geomagnetic storms. J. Geophys. Res. 114 (A9), A09107.

Chilingarian, A., Bostanjyan, N., 2010. On the relation of the Forbush decreases detected by ASEC monitors during the 23rd solar activity cycle with ICME parameters. Adv. Space Res. 45, 614–621.

Chilingarian, A., Bostanjyan, N., Karapetyan, T., Vanyan, L., 2012a. Remarks on recent results on neutron production during thunderstorms. Phys. Rev. D 86, 093017.

Chilingarian, Hovsepyan, G., Hovhannisyan, A., 2011. Particle bursts from thunderclouds: natural particle accelerators above our heads. Phys. Revi. D 83, 062001.

Chilingarian, A., Karapetyan, T., 2011. Calculation of the barometric coefficients at the start of the 24th solar activity cycle for particle detectors of Aragats Space Environmental Center. Adv. Space Res. 47, 1140–1146.

Chilingarian, A., Arakelyan, K., Avakyan, K., et al., 2005. Correlated measurements of secondary cosmic ray fluxes by the Aragats Space-Environmental Center monitors. Nucl. Instrum. Methods Phys. Res. Sect. A 543 (2–3), 483–496.

Chilingarian, A., Reymers, A., 2008. Investigations of the response of hybrid particle detectors for the Space Environmental Viewing and Analysis Network (SEVAN). Ann. Geophys. 26, 249–257.

Chilingarian, A., Hovsepyan, G., Arakelyan, K., et al., 2009. Space environmental viewing and analysis network (SEVAN), earth. Moon Planets 104 (1), 195.

Chilingarian, A., Daryan, A., Arakelyan, K., et al., 2010. Ground-based observations of thunderstorm- correlated fluxes of high-energy electrons, gamma rays, and neutrons. Phys. Rev. D 82, 043009.

Chilingarian, A., Mkrtchyan, H., 2012. Role of the Lower Positive Charge Region (LPCR) in initiation of the Thunderstorm Ground Enhancements (TGEs). Phys. Rev. D 86, 072003.

Chilingarian, B., Mailyan, Vanyan, L., 2012b. Recovering of the energy spectra of electrons and gamma rays coming from the thunderclouds. Atmos. Res. 114–115, 1–16.

Corti, C., Bindi, V., Consolandi, C., et al., 2016. Solar modulation of the proton local interstellar spectrum with AMS-02, Voyager 1 and Pamela. Astrophys. J. 829, 8.

Danilova, T., Dunaevsky, A., Erlykin, A., et al., 1982. Project of hadron interaction in the energy ranges103-105 TeV experiment (ANI Experiment). Proceedings of Academy of Science of Armenian Soviet Republic, Physics Series, vol. 17, issue 3–4.

Dorman, L.I., Dorman, I.V., 2005. Possible influence of cosmic rays on climate through thunderstorm clouds. Adv. Space Res. 35, 476–483.

Dwyer, J.R., 2007. Relativistic breakdown in planetary atmospheres. Phys. Plasmas 14, 042901.

Gopalswamy, N., Xie, H., Akiyama, S., et al., 2013. The first ground level enhancement event of solar cycle 24: direct observation of shock formation and particle release heights. Astrophys. J. 765, L30.

Gurevich, A.V., Milikh, G.M., Roussel-Dupre, R.A., 1992. Runaway electron mechanism of air breakdown and preconditioning during a thunderstorm. Phys. Lett. A 165, 463.

Hatton, C.J., 1971b. The Neutron Monitor. In: Wilson, J.G., Wouthuysen, S.A. (Eds.), Progress in Elementary Particle and Cosmic Ray Physics X. North Holland Publishing Co., Amsterdam.

Hatton, C.J., 1971a. Progress in Elementary Particles and Cosmic Ray Physics, 10, 1–100. North Holland.

Haurwitz, M.W., Yoshida, S., Akasofu, S.I., 1965. Interplanetary magnetic field asymmetries and their effects on polar cap absorption effects and Forbush decreases. J. Geophys. Res. 70, 2977–2988.

Heck, D., Knapp, J., 1998. A Monte Carlo Code to Simulate Extensive Air Showers, Forschungszentrum, Karlsruhe, FZKA Report 6019.

Hovhannisyan, A., Chilingarian, A., 2011. Median filtering algorithms for multichannel detectors. Adv. Space Res. 47 (9), 1554–1557.

Khaerdinov, N.S., Lidvansky, A.S., Petkov, V.B., 2005. Cosmic rays and the electric field of thunderclouds: evidence for acceleration of particles (runaway electrons). Atmos. Res. 76, 346.

Kollárik, M., Kudela, K., Langer, R., et al., 2016. First results from the measuring equipment SEVAN on Lomnický štít: possible connections with atmospheric phenomena, Proceedings TEPA-2015, TIGRAN METS, 31-34, INSPIRE C15-10-02.

Kravtsova, M.V., Sdobnov, V.E., 2017. Ground level enhancements of cosmic rays in solar cycle 24. Astron. Lett. 43, 501.

Kudela, K., Chum, J., Kollárik, M., et al., 2017. Correlations between secondary cosmic ray rates and strong electric fields at Lomnický Štít. J. Geophys. Res.: Atmos. 122, 10700–10710.

Kudela, K., Firoz, K.A., Langer, R., et al., On diurnal variation of cosmic rays: statistical study of neutron monitor data including LominskýŠtit. In: Proc. 21st ECRS, Kosice, Slovakia, 2008, s 4.15, pp. 371–375. Available from link: <http://ecrs2008.saske.sk/dvd/s4.15.pdf>.

Kuroda, Y., Oguri, S., Kato, Y., et al., 2016. Observation of gamma ray bursts at ground level under the thunderclouds. Phys. Lett. B 758, 286–291.

Kuwabara, T., Bieber, J.W., Clem, J., et al., 2006. Realtime cosmic ray monitoring system for space weather. Space Weather 4, S08001.

Labrador, A.W., Cohen, C.M.S., Cummings, et al., 2005. Solar-particle energy spectra during the large events of October-November 2003 and January 2005. In: Proceedings of the 29th International Cosmic Ray

Conference, vol.1. Tata Institute of Fundamental Research, Pune, India, pp. 111–114.
Leerungnavarat, K., Ruffolo, D., Bieber, J.W., 2003. Loss cone precursors to forbush decreases and advance warning of space weather effects. Astrophys. J. 593, 587–596.
Mailyan, B., Chilingarian, A., 2010. Investigation of diurnal variations of cosmic ray fluxes measured with using ASEC and NMDB monitors. Adv. Space Res. 45, 1380–1387.
Mavromichalaki, H., Papaioannou, A., Plainaki, C., et al., 2011. Applications and usage of the real-time neutron monitor database for solar particle events monitoring. Adv. Space Res. 47, 2210–2222.
Miroshnichenko, L.I., Nymmik, R.A., 2014. Extreme fluxes in solar energetic particle events: methodological and physical limitations. Radiat. Meas. 61, 6–15.
Munakata, K., Bieber, J.W., Yasue, S., et al., 2000. Precursors of geomagnetic storms observed by the muon detector network. J. Geophys. Res. 105 (A12), 27457–27468.
Rockenbach, M., Dal Lago, A., Gonzalez, W.D., et al., 2011. Geomagnetic storm's precursors observed from 2001 to 2007 with the Global Muon Detector Network (GMDN). J. Geophys. Res. 38, L16108.
Ruffolo, D., Bieber, J.W., Evenson, P., et al. Precursors to forbush decreases and space weather prediction. Proceedings of the 26th International Cosmic Ray Conference. August 17–25, 1999, Salt Lake City, Utah, USA.
Shea & Smart, 2000. Fifty years of cosmic radiation data. SSR 93, 229–262.
Simpson, J.A., 2000. The cosmic ray nucleonic component: the invention and science uses of the neutron monitor. Space Sci. Rev. 93, 11–32.
Thakur, N., Gopalswamy, N., Xie, H., et al., 2014. Ground level enhancement in the 2014 January 6 solar energetic particle event. Astrophys. J. 790, L13.
Thompson, B.J., Gopalswamy, N., Davila, J.M., Haubold, H.J. (Eds.), . Putting the "I" in IHY: The United Nations Report for the International Heliophysical Year 2007. Springer, Wien-New York.
Torii, T., Sugita, T., Kamogawa, M., et al., 2011. Migrating source of energetic radiation generated by thunderstorm activity. Geophys. Res. Lett. 38, L24801.
Tsuchiya, H., Enoto, T., Iwata, K., et al., 2013. Hardening and termination of long-duration gamma rays detected prior to lightning. Phys. Rev. Lett. 111, 015001.
Wang, X., Zhou, X., Huang, D., et al., 2015. Effects of the near-earth thunderstorms electric field on intensity of the ground cosmic ray electron at YBJ, PoS. ICRC, 233.
Watanabe, K., Gros, M., Stoker, P.H., et al., 2006. Solar neutron events of 2003 October–November. Astrophys. J. 636, 1135–1144.
Zazyan, M., Chilingarian, A., 2009. Calculations of the sensitivity of the particle detectors of ASEC and SEVAN networks to galactic and solar cosmic rays. Astropart. Phys. 32, 185–192.
Zeng, Y., Zhu, F.R., Jia, H.Y., 2013. For the ARGO-YBJ collaboration. Correlation between cosmic ray flux and electric atmospheric field variations with the ARGO-YBJ experiment, 33ICRC, Rio de Janeiro, Brazil.
Zhang, J.L., Tan, Y.H., Wang, H., et al., 2010. The Yangbajing Muon-Neutron Telescope. NIMA 623, 1030–1034.

# Long lasting low energy thunderstorm ground enhancements and possible Rn-222 daughter isotopes contamination

A. Chilingarian[1,2,3]

[1]*A. Alikhanyan National Lab (Yerevan Physics Institute), Yerevan 0036, Armenia*
[2]*National Research Nuclear University MEPhI, Moscow 115409, Russia*
[3]*Space Research Institute of RAS, Moscow 117997, Russia*

(Received 6 May 2018; published 11 July 2018)

Thunderstorm ground enhancements (TGEs) comprise large particle fluxes coming from the clouds that usually coincide with thunderstorms. Most of TGEs observed at the Aragats research station in Armenia during the last ten years originated from "beams of the electron accelerator" operating in the thunderclouds above the research station. Observed TGEs contain high-energy electrons and gamma rays (as well as neutrons) and usually last a few minutes. Starting from 2014, we use particle detectors tuned for the registration of lower energies particles coming from thunderclouds (starting from 0.3 MeV). In 2016, we already noticed that TGEs measured by particle detectors with a low energy threshold demonstrated a drastically larger duration. The flux of the high-energy particles (with energies up to 40 MeV) lasts 1–10 min; the lowest ones (less than 3 MeV)—more than two hours. All intense TGEs contain a high-energy peak and a prolonged low-energy extension lasting 2–3 h. In the presented paper, we describe examples of long-lasting TGEs and discuss correlations of enhanced particle fluxes with disturbances of the electric field and with precipitation.

DOI: 10.1103/PhysRevD.98.022007

## I. INTRODUCTION

The bulk of information on particle fluxes correlated with thunderstorms (thunderstorm ground enhancements, TGEs, [1–3]) can be used to better understand the electrical structure of thunderclouds and high-energy processes in the atmosphere. In the strong intracloud electric fields, seed electrons from the ambient population of secondary cosmic rays gain such an amount of energy that they surpass the electron energy losses and "run away", giving rise to electron-photon avalanches. Thus, the bulk of runaway electrons and gamma rays results in a runaway breakdown (RB, [4]), recently referred to as a relativistic runaway electron avalanche (RREA, [5–7]).

In the last decade, TGEs were investigated at the Aragats research station of the Yerevan Physics Institute. The Aragats research station is located at an altitude of 3200 m on the plateau near a large lake, and the height of the cloud base above the ground is typically 25–50 m in spring, increasing to 100–200 m in the summer. In the 2017–2018 campaigns on Aragats, we paid special attention to the long lasting low energy TGEs (LLL TGE). NaI spectrometers and large area plastic scintillators were used to detect enhanced fluxes of low energy fluxes (less than 3 MeV) of gamma rays. A concern is that it is very important to distinguish particle avalanches initiated by runaway electrons, from the radiation of environmental isotopes; those fluxes are also possibly increased during a thunderstorm [8,9].

Analysis of TGE data allows us to associate the particle flux enhancement with the acceleration of electrons in the strong electric fields emerging in a thundercloud [10]. However, even without noticeable disturbances of the near surface electric field, the flux of the low energy gamma rays is observed. We relate this phenomenon to the detection of Compton scattered gamma rays from remote electron-gamma ray cascades and/or randomly emerging small size stochastic electric fields above the detector site [11].

Neutral and charged particle fluxes are measured on Aragats with various elementary particle detectors. Count rates are measured with plastic scintillators, proportional chambers, and NaI and CsI crystals on the time scale from tens of nanoseconds to minutes. Energy release histograms are measured each minute with NaI crystals and each 20 s with 60-cm thick plastic scintillators. Energy release histograms are transformed to differential energy spectra using a detector response function calculated by GEANT simulations. Details of the particle detector operation and spectra deconvolution can be found in [12]. We also measure the near-surface electrostatic field with four electric field mills EFM-100 produced by the Boltek company. The stormy weather is usually accompanied by precipitation that possibly brings the radioactive isotopes, lightning flashes, strong wind, and fast changes of the atmospheric pressure. Abrupt decrease of atmospheric pressure can also increase the flux of most species of cosmic rays (although not exceeding $\sim -0.5\%/\mathrm{mb}$).

 

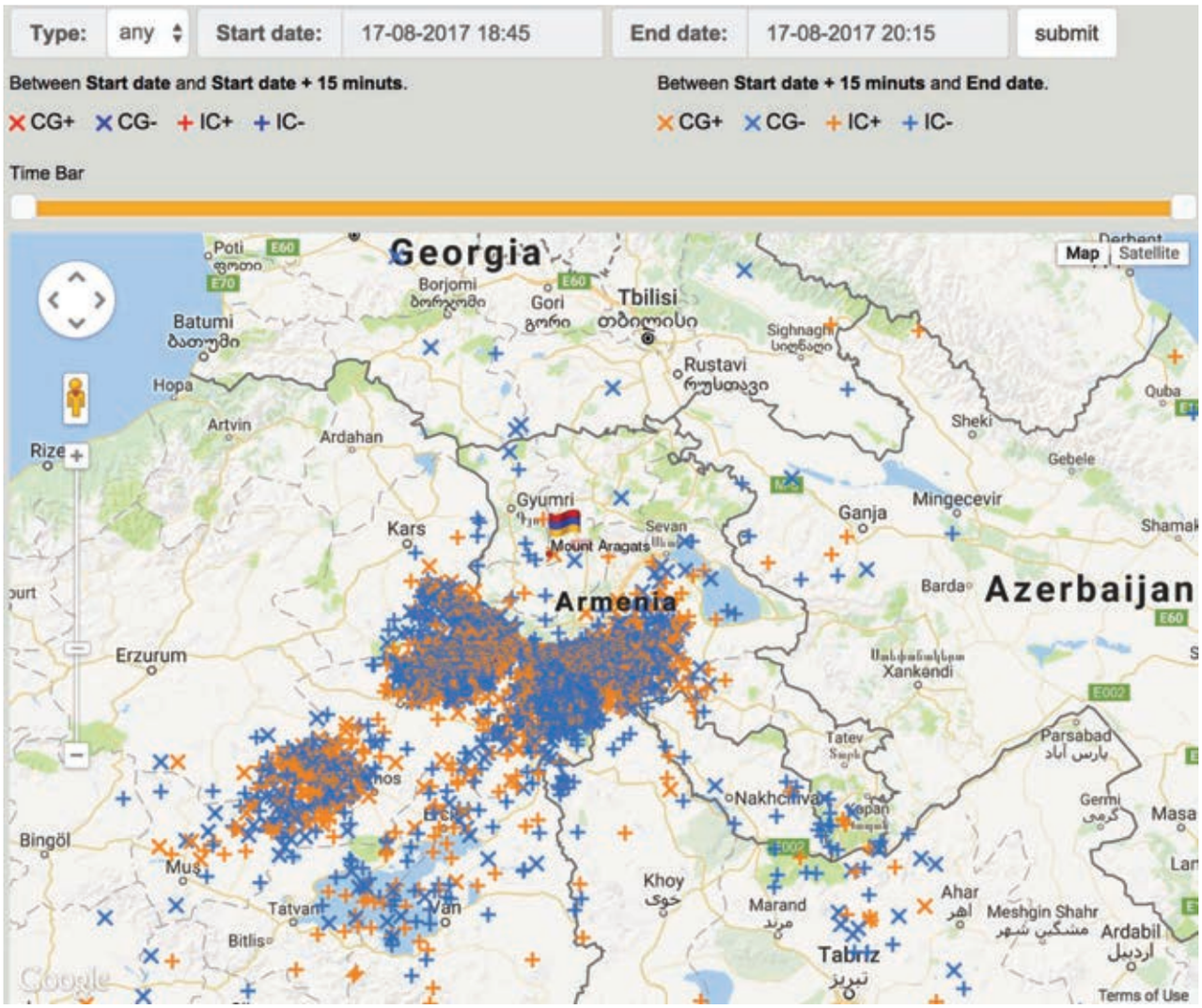


FIG. 1. Pattern of the storm in Armenia mapped by lightning flashes showing the approaching storm front; the Aragats station position on the map is flagged.

Thus, several meteorological factors can be responsible for the measured enhancements of the particle flux. One of the goals of this paper is to find out which of these factors is responsible for the long-lasting TGEs. That is why, in addition to the particle flux measurements, we are continuously monitoring a set of meteorological parameters with the Professional Davis Instruments Vantage Pro2 weather station (http://www.davisnet.com/). Also, we trace the evolution of the stormy weather on Aragats by mapping the approaching storm front with a sequence of atmospheric flashes registered by the lightning detector of the Boltek company (Boltek's StormTracker Lightning Detection System, powered by the software from Astrogenic systems, http://www.boltek.com/stormtracker).

The wideband fast electric field is measured by three circular flat plate antennas attached to fast digital oscilloscopes, which are triggered by the signal from active whip antennas [13]. The oscilloscopes are also used to monitor signals from particle detectors. In our first papers on TGE measurements [1,2,14,15], we used particle detectors from the MAKET surface array [16], registering the electron content of extensive air showers (EAS). The energy threshold of these detectors was ~7 MeV, suitable for the EAS research. In the presented paper, we analyze measurements obtained with particle detectors having a significantly smaller energy threshold of ~0.3 MeV and ~0.7 MeV that allows us to discover new important features of TGE.

## II. DETAILED ANALYSIS OF THE SUMMER TGE EVENT OCCURRED ON AUGUST 17, 2017

August 2017 was very stormy on Aragats with numerous lightning flashes, and the first snow appeared on mountain

peaks. On August 17, 2017, a storm started as usual in the Armenian highlands in Turkey, southwest from Aragats, and rapidly moved to Armenia's border, see Fig. 1. The meteorological environments on August 17, 2017 changed abruptly as the storm reached Aragats, see Fig. 2, where we show in the top of the picture the outside temperature and dew point, the rain rate in the bottom, and atmospheric pressure and disturbances of the near surface electric field in the middle. The height of the cloud is estimated by the measured "spread" parameter—the difference between the air temperature and the dew point. The calculation of the height of cloud base is based on the assumption that the air temperature drops 9.84 °C per 1000 m of altitude and the dew point drops 1.82 °C per 1000 meters' altitude. There are several WEB calculators for the estimation of the altitude of a cloud (see, for instance, http://www.csgnetwork.com/cloudaltcalc.html). The simplified estimate consists in multiplying the spread measured in °C by 122 m. With this approach, we estimate the height of cloud before the start of the storm to be $(9.1–6.0) * 122 \sim 400$ m; sharply decreased to ∼130 m on the start of the storm $(7.0 - 5.9) * 122$. Relative humidity also increased from 81% up to 92%, which signaled the decreasing of the height of the cloud base. During the spring storms when clouds were "sitting" on the station, the height of cloud base was 25–50 m and RH 96%–98%.

Atmospheric pressure increased from 694.8 at 18:40 up to 695.9 at 18:58 and back to 684.9 at 20:10,

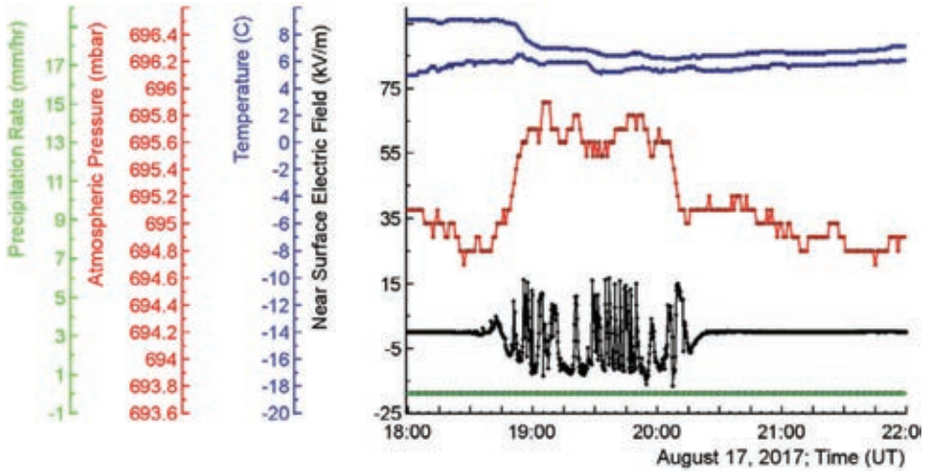


FIG. 2. Meteorogical parameters measured on August 17, 2017. On the top of the picture, one-minute time series of the outside temperature and dew point are shown; in the middle—the atmospheric pressure and the disturbances of electric field; in the bottom—the rain rate.

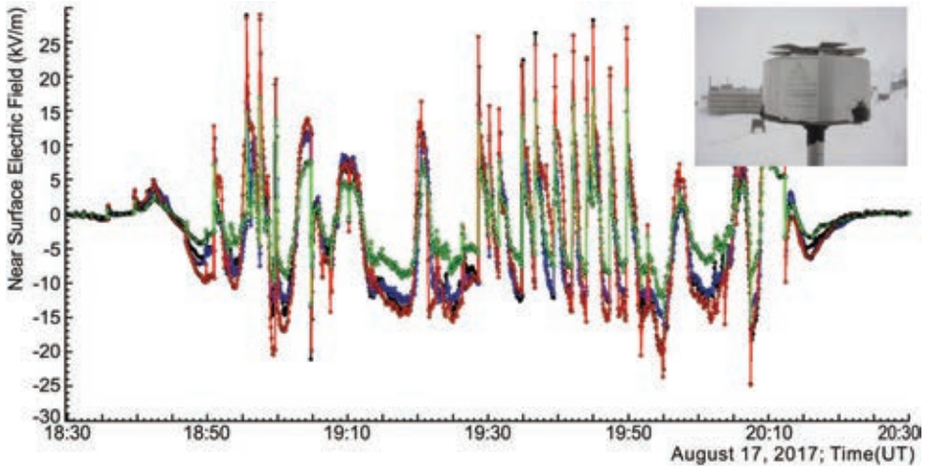


FIG. 3. The lightning activity during a large summer storm on Aragats was coherently detected by the network of the four electric mills EFM-100 of the Boltek company (see inset in the top right corner of the picture).

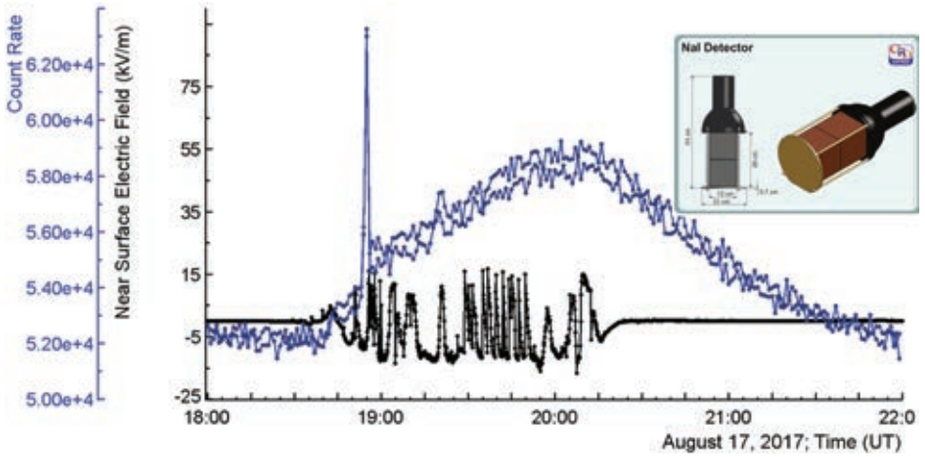


FIG. 4. Thunderstorm ground enhancement (TGE) as measured by the first and second crystals of the NaI network (see inset, energy threshold 0.3 MeV).

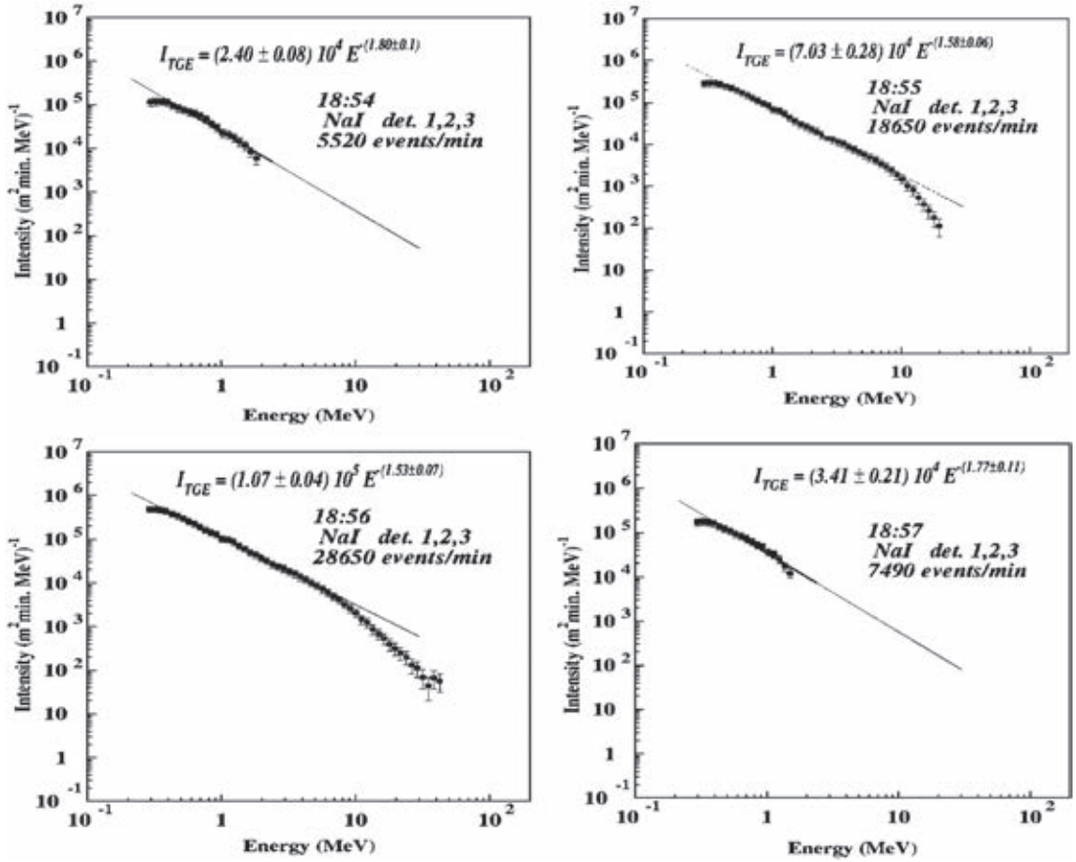


FIG. 5. The differential energy spectra of four subsequent minutes of TGE, recovered from the energy release histograms measured by the N1 and N2 crystals of the NaI network.

precisely coinciding in time with the disturbances of the near-surface electric field (from −25 to 30 kV/m) measured by the electric mill located on the roof of the MAKET experimental hall. No rainfall was detected by the Davis weather station located in the same place.

The storm started on Aragats at 18:36; the near-surface electric field remained disturbed for 1 h 42 min until 20:20,

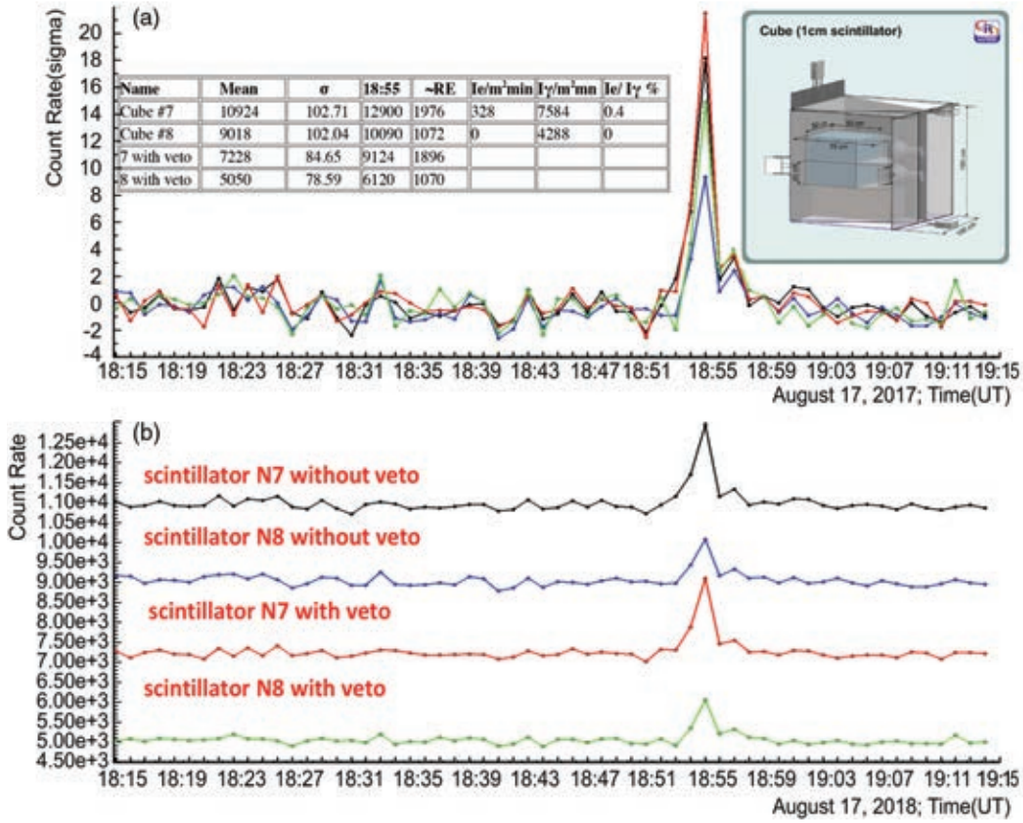


FIG. 6. Recovery of gamma rays and electron fluxes with the CUBE detector. Scintillators N7 and N8 are 20 cm thick 0.25 $m^2$ stacked plastics. In the Table inset, the recovered fluxes measured by both thick scintillators are shown.

see Fig. 2. The storm was accompanied with numerous lightning flashes (which produced abrupt changes of the electrostatic field of positive and negative polarity) detected by all four electric mills located on the Aragats station, see Fig. 3.

The rise of the particle flux measured by large NaI crystals (12.5 × 25 cm, energy threshold 0.3 MeV, see inset in Fig. 4) started at 18:40; after 13 min there occurred a 2-min long huge burst of particles coming from the cloud. At 18:55–18:56, the flux enhancement was 120%, corresponding to 43 standard deviations from the flux mean value measured before TGE. At 19:00–21:00, the particle flux enhancement was 3%–10%. In Fig. 4, we see that after the short burst, the particle flux continued to rise until the disturbances finished at ∼20:20. After the storm calmed down at ∼20:20, the flux started to decay and finally declined at ∼22:00. Thus, the enhanced flux continued for ∼2.5 h and during the last hour—without any detectable disturbance of the electric field.

From Fig. 2, it is obvious that precipitation plays no role in this TGE origination. As there was no rain through the ∼4-h duration of the TGE, we cannot connect the enhanced flux with the Radon daughter's decays. The observed enhancement of the atmospheric pressure also cannot explain the TGE: the change of 1 mb can lead only to an ∼0.5% enhancement of the gamma ray flux, and only if the atmospheric pressure is decreasing and not increasing as we see in Fig. 2.

Also, we can notice that the flux enhancement coincides with disturbances of the electric field (a proxy of the intracloud electric field) and with a low location of the cloud base. According to the standard TGE model [17,18], the main negatively charged region with the emerged lower positively charged region (LPCR) formed a dipole which accelerates cosmic ray electrons downwards to the particle detectors located on the Earth's surface. If the electric field is strong enough, a RREA process is unleashed resulting in the large TGE. The explanation of the TGE decay phase that started at 20:20 in the absence of disturbances of the electric field needs additional simulation and experimental efforts and will be discussed in the Conclusions section.

In Fig. 5, we show the energy spectra of the TGE measured during the particle burst and just before and after it. The energy release histograms were measured with the same NaI crystals (N1 and N2); those count rates are posted in the Fig. 4. The differential energy spectra were recovered taking into account the spectrometer's response function for each of NaI crystal (see, for details, the supplement to [12]).

As we can see in Fig. 5, for 2 min only, the particle flux contains particles with energies up to 40 MeV. We identify

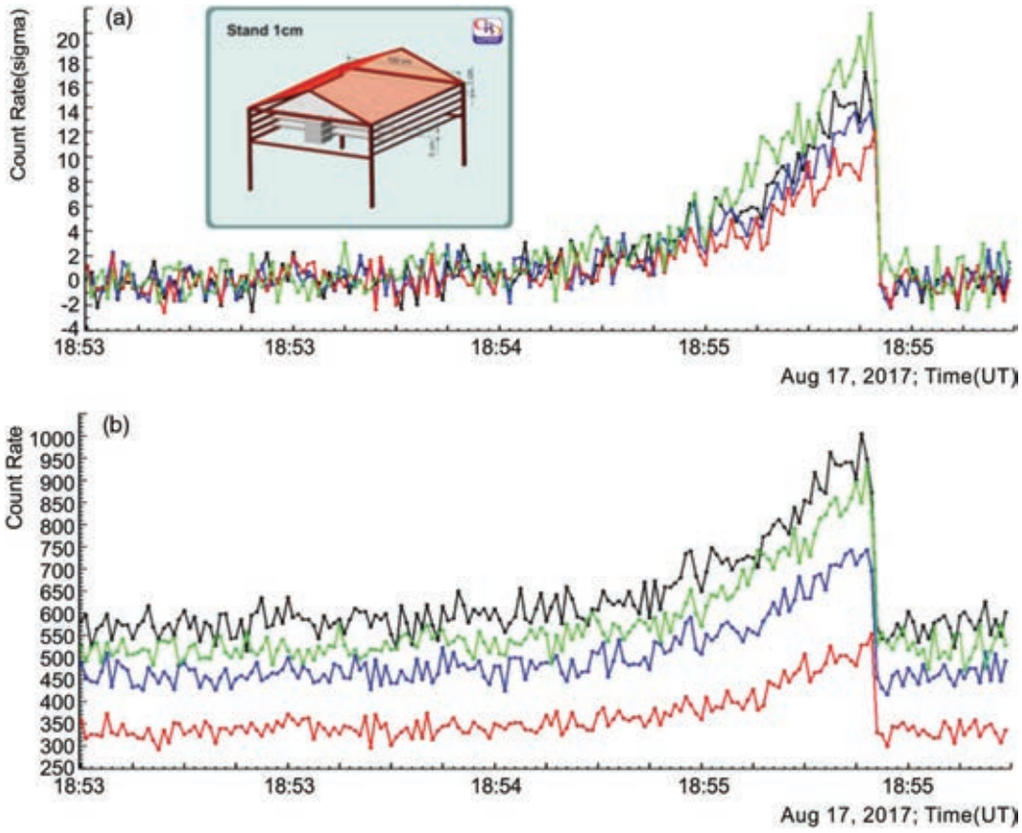


FIG. 7. One-second count rates of the STAND1 detector located nearby the MAKET experimental hall.

the high-energy particle flux with the RB/RRE avalanches released just above the particle detectors site. After the avalanche process stopped (or moved away), the energy spectra resumed to the lower energies, not exceeding few MeV. The cover of the NaI crystals stopped the electrons with energies below ~3 MeV; thus, the particle registered by the NaI spectrometers before and after the 2-min burst were gamma rays only.

The RB/RREA cascade after leaving the lower dipole propagates in the air and, depending on the cloud height, the fraction of the electrons reaching the Earth's surface will dramatically change due to a much larger attenuation of electrons (see Fig. 19 of [14]). Usually, the RB/RREA flux as measured on the Earth's surface consists mostly of gamma rays contaminated by a small fraction of electrons. To estimate the electron fraction, we use a CUBE detector (inset in Fig. 6; see, for details, the supplement of [12]).

The CUBE detector consists of two stacked 20 cm thick plastic scintillators of a 0.25 $m^2$ area surrounded by the "veto" that consists of six 1 cm thick and 1 $m^2$ area plastic scintillators. A CUBE detector registered 1-min count rates of all eight scintillators and counts of the inner thick scintillators under the condition of the absence of an electronic signal from anticoincidence shielding. Because the 1 cm thick scintillators have a nonzero probability to miss the registration of a charged particle as well as to register a neutral particle, we develop a special method to estimate "true" intensities (integral energy spectra) of gamma ray and electron fluxes (see Appendix A of [14]). In Fig. 6(b), we show the count rates of thick scintillators with and without the veto option. In Fig. 6(a), we show the same count rates but in the units of standard deviation (the number of). In the inserted table, we show the mean values of the count rates and variances before a particle burst and

TABLE I. The characteristics of short burst of high-energy particles occurred on August 17, 2017.

| Name | Mean | $\sigma$ | 18:55:33 | Sign. peak N$\sigma$ | % of drop |
|---|---|---|---|---|---|
| STAND1 MAKET Ch. 1 | 571.4 | 25.4 | 1002 | 17 | 76 |
| STAND1 MAKET Ch. 2 | 456.3 | 22.7 | 741 | 14 | 62 |
| STAND1 MAKET Ch. 3 | 329.7 | 18.1 | 553 | 12 | 67 |
| STAND1 MAKET Ch. 4 | 510.9 | 22.3 | 932 | 21 | 75 |

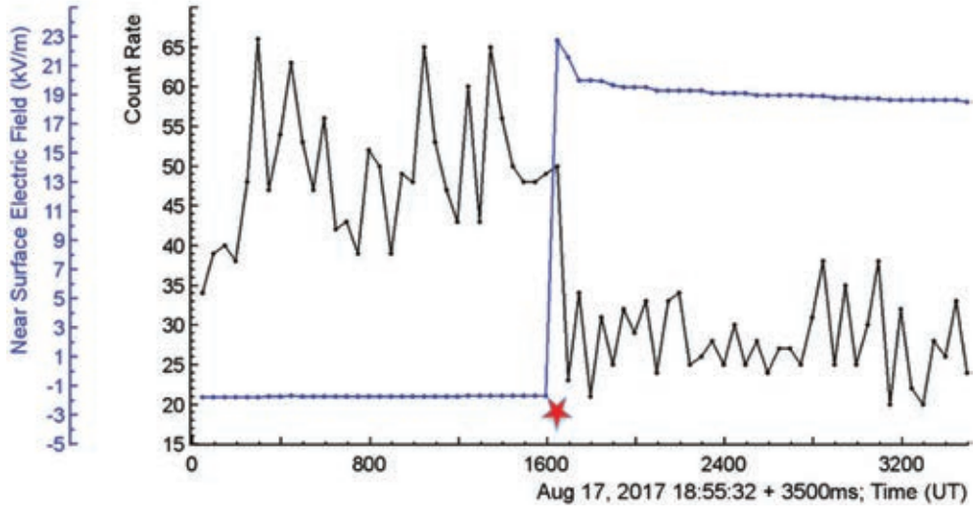


FIG. 8. The 50-ms time series of the STAND1 upper scintillator count rate (located outdoors nearby the MAKET experimental hall) and of the near surface electric field measurements. The asterisk indicates the time of lightning flash registered by the World-Wide Lightning Location Network (WWLLN, detection at 18:55:33.630). The horizontal axes started from 18:55:32; each tick on the axes corresponds to 100 ms.

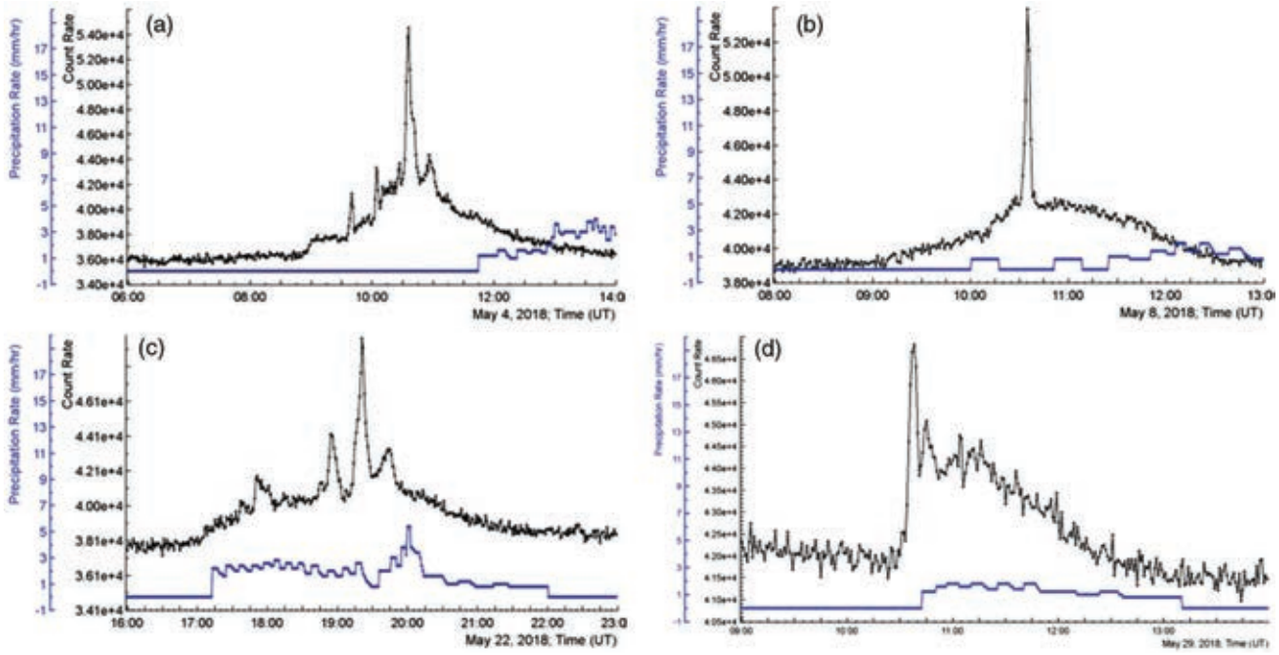


FIG. 9. One-minute time series of the count rates of the 1 cm thick 1 $m^2$ area plastic scintillator. In the bottom of the frames, we show rain rate in mm per hour.

during the minute of maximal flux, recovered intensities, and electron fractions for both inner 20 cm thick scintillators. The energy thresholds of thick scintillators are estimated to be 5.8 and 6.4 MeV (scintillator N7 is above N8, see Table 1 in [19]). For a lower energy threshold (scintillator N7), the electron contamination is ∼4% and vanishing at higher energies (scintillator N8).

To understand the dynamics of TGE and to investigate the relation of the particle fluxes and lightning flashes, we need to register the time series of the TGEs and electric field disturbances in much more detail. Fast electronics provide the registration of TGEs on time scales of 1 sec and 50 ms, compatible with the fast processes in thunderstorm atmospheres. In Figs. 7 and 8, we demonstrate the

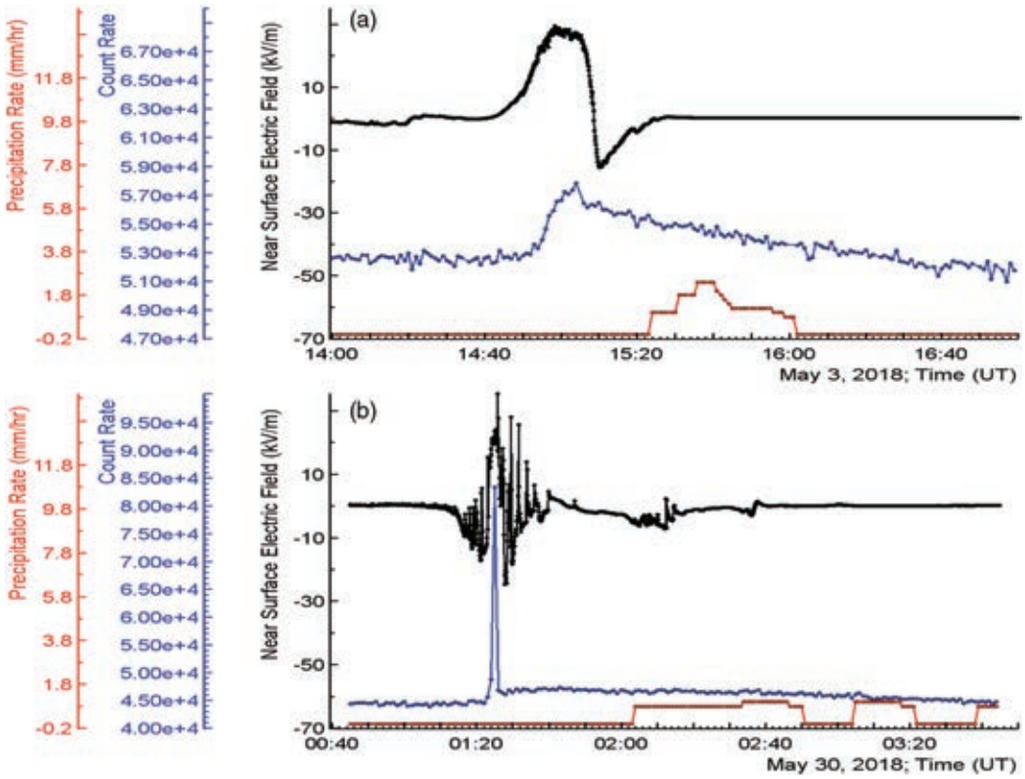


FIG. 10. TGE events registered by the NaI detector. In the top of figures, we show disturbances of the near surface electric field; in the bottom—the rain rate. In the middle—the one-minute count rate of the NaI detector.

possibilities of TGE and lightning analysis at these time scales. The abrupt decay of the TGE is better shown in the one-second time series of the STAND1 detector shown in Fig. 7. The network of the STAND1 detectors comprises three identical units located on Aragats station, each of which consists of three stacked 1 cm thick and 1 $m^2$ area plastic scintillators and one stand-alone 3 cm thick plastic scintillator of the same type (inset in Fig. 7; see, for details, the supplement of [12]).

In Fig. 7(b), we show the one-second count rates of the stacked and stand-alone scintillators. In Fig. 7(a), we show the same count rates, but plotted in units of the standard deviations from the mean value measured just before the TGE. In Table 1, we demonstrate the numerical values, significances of peaks (in), and count rate drops for each scintillator. The sharp decay of particle flux that occurred at 18:55:33 is enforced by a lightning flash which stopped the RB/RREA process in the cloud [20,13]. In [21], we demonstrate that strong particle fluxes usually precede lightning flashes.

For the in-depth research of the lightning-particle flux relations, we use a fast data acquisition system based on the National Instruments myRIO board, which produced the GPS time stamp of the record and provided registration of the 50 ms time series of detector count rates (see details in [22]).

In Fig. 8, we can see that the rearrangement of the electric field started at 18:55:33.600 The near surface electric field of −1.6 kV/m after 50 ms reached a value of 22 kV/m, i.e., the amplitude was. ∼23.6 kV/m The abrupt decay of the particle flux started at the same time; the flux decreased from 50 to 23 particles, i.e., by 54% in 50 ms. This flash was registered by the World-Wide Lightning Location Network (WWLLN, detection at 18:55:33.630).

## III. LONG LASTING TGES AND RAINFALLS

In Fig. 9, we summarize typical shapes of TGEs observed in May 2018, when an GEespecially rich harvest of TGEs was collected. We consider only TGEs accompanied with rainfall to examine its possible influence on the particle flux. The one-minute time series of count rates were measured by a 1 cm thick 1 $m^2$ area plastic scintillator (energy threshold ∼0.7 MeV, [19], Fig. 10, Table 1) located outdoor nearby the MAKET experimental hall; the rain rate was measured by the Davis weather station located on the roof of the same building.

Displayed TGEs contain a high-energy part (sharp peaks—gamma rays and electrons with energies up to ∼40 MeV) lasting a few minutes and a low-energy part (gamma rays below 3 MeV) lasting several hours; see an example of the energy spectra in Fig. 5. In Fig. 9, we can see that TGEs are not connected with rainfall. In Fig. 9(a),

the rain started only at the end of the TGE; in Figs. 9(b), 9(c), and 9(d) strengthening of the rainfall coincides with the decay phase of the TGE. Many other TGEs were not accompanied with rain at all. The TGEs of May 2018 occurred at a highly disturbed near-surface electric field. For the clarity of the displayed information, we do not post the time series of the near surface electric field in Fig. 9 (it is similar to one shown in Fig. 4).

In Fig. 10, we show the count rate enhancement, disturbances of the near-surface electric field, and the rain rate of two TGE events that occurred in the May 2018. The May 3, 2018 event [Fig. 10(a)] is rather small: ∼10% enhancement of the count rate of the NaI detector. Rainfall that started after the TGE reached the maximum did not influence the count rate; the decay of the TGE continued. A large event (∼100% count rate enhancement) occurred on May 30, 2018 [Fig. 10(b)], again accompanied by a rainfall at the decay phase of TGE. For both TGEs, rain apparently does not influence the count rate. The atmospheric pressure was not strongly disturbed during both events; the fluctuation does not exceed 1 mb. Thus, we can connect the initiation of a TGE only with disturbances of the electric field and not with precipitation or atmospheric pressure variations.

## IV. CONCLUSIONS

Each year, Aragats facilities register more than 100 TGEs, proving that Mount Aragats is a stable electron accelerator for atmospheric high-energy physics research [23]. TGEs varied significantly in intensity and continuation; nonetheless, we can outline some important features confirming Aragats 10-year observations [1,14,18]:

(i) TGEs occurred during strong storms approaching Armenia mostly from the Armenian highlands in Turkey, southwest from Aragats, which disturbed the near surface electric field at a particle detector location.

(ii) A strong TGE started with a low energy flux (less than 3 MeV), turning to a short (1–10 min) and intense peak containing high-energy particles (up to 40 MeV).

(iii) After an abrupt decline of the high-energy part of the TGE, usually forced by a lightning flash, the low-energy flux continued with a prolonged decay. Thus, we detected a sizable flux of gamma rays during the hours of the "fair weather" when the near surface electric field was not disturbed.

(iv) The radioactive decay from radon isotopes contained in the rain, as well as the variations of atmospheric pressure (barometric effect) are not the cause of TGEs.

There are two main hypotheses about the origin of the prolonged gamma ray flux in the absence of sizable disturbances of the near-surface electric field:

(i) TGEs originated in the thunderstorm atmospheres due to an emerging strong electric field between differently charged layers in the clouds [14,18,24]. Seed electrons from the ambient population of secondary cosmic rays "run away" [4], accelerated, and form electron-gamma ray avalanches reaching and detected at the Earth's surface. If the cloud with a strong electric dipole inside migrates from the detector site, Compton scattered gamma rays can reach the detector under large zenith angles and be registered for an extended time span.

(ii) Small-scale stochastic electric fields randomly emerging in a thundercloud accelerate electrons and enhance the probability of bremsstrahlung radiation and boosts the low energy gamma ray flux.

## ACKNOWLEDGEMENTS

The detailed analysis of these scenarios will be presented in our next publication. The data for this paper are available via the multivariate visualization software ADEI on the WEB page of the Cosmic Ray Division (CRD) of the Yerevan Physics Institute in Ref. [25]. Author thanks the staff of the Aragats Space Environmental Center for the uninterruptible operation of Aragats research station facilities. Author thanks Hovsepyan Gagik for recovering the energy spectra posted in Fig. 5 and M. Panasuk and V. Bogomolov for useful discussions. Author received support from the Russian Science Foundation grant (Project No. 17-12-01439).

[1] A. Chilingarian, A. Daryan, K. Arakelyan, A. Hovhannisyan, B. Mailyan, L. Melkumyan, G. Hovsepyan, S. Chilingaryan, A. Reymers, and L. Vanyan, Ground-based observations of thunderstorm-correlated fluxes of high- energy electrons, gamma rays, and neutrons, Phys. Rev. D **82**, 043009 (2010).

[2] A. Chilingarian, G. Hovsepyan, and A. Hovhannisyan, Particle bursts from thunderclouds: Natural particle accelerators above our heads, Phys. Rev. D **83**, 062001 (2011).

[3] A. Chilingarian, G. Hovsepyan, and E. Mantasakanyan, Mount Aragats as a stable electron accelerator for atmospheric high-energy physics research, Phys. Rev. D **93**, 052006 (2016).

[4] A. V. Gurevich, G. M. Milikh, and R. A. Roussel-Dupre, Runaway electron mechanism of air breakdown and preconditioning during a thunderstorm. Phys. Lett. **165A**, 463 (1992).

[5] J. R. Dwyer, A fundamental limit on electric fields in air, Geophys. Res. Lett. **30**, 2055 (2003).
[6] L. P. Babich, E. N. Donskoy, R. I. Il'kaev, I. M. Kutsyk, and R. A. Roussel-Dupre, Fundamental parameters of a relativistic runaway electron avalanche in air, Plasma Phys. Rep. **30**, 616 (2004).
[7] V. V. Alexeenko, N. S. Khaerdinov, A. S. Lidvansky, and V. B. Petkov, Transient variations of secondary cosmic rays due to atmospheric electric field and evidence for pre-lightning particle acceleration, Phys. Lett. A **301**, 299 (2002).
[8] F. Fabró, J. Montanyà, N. Pineda, J. Montanyà, N. Pineda, O. Argemí, O. A. van der Velde, D. Romero, and S. Soula, Analysis of energetic radiation associated with thunderstorms in the Ebro delta region in Spain, J. Geophys. Res. Atmos. **121**, 9879 (2016).
[9] V. Bogomolov, A. Chilingarian, G. Garipov *et al.*, Study of TGEs and gamma-flashes from thunderstorms in 20–3000 keV energy range with SINP MSU gamma-ray spectrometers, *Proceedings of 6-th TEPA Symposium*, p. 50, Nor Amberd, 2015 (Tigran Mets, Yerevan, 2015); http://www.iaea.org/inis/collection/NCLCollectionStore/_Public/48/037/48037534.pdf.
[10] A. Chilingarian, G. Hovsepyan, and L. Vanyan, On the origin of the particle fluxes from the thunderclouds: Energy spectra analysis, Europhys. Lett. **106**, 59001 (2014).
[11] D. I. Iudin Lightning initiation as a noise induced kinetic transition, Radiophys. Quantum Electron. **60**, 374 (2017).
[12] A. Chilingarian, G. Hovsepyan, and B. Mailyan, In situ measurements of the runaway breakdown (RB) on Aragats mountain, Nucl. Instrum. Methods Phys. Res., Sect. A **874**, 19 (2017).
[13] A. Chilingarian, Y. Khanikyants, E. Mareev, D. Pokhsraryan, V. A. Rakov, and S. Soghomonyan, Types of lightning discharges that abruptly terminate enhanced fluxes of energetic radiation and particles observed at ground level, J. Geophys. Res. Atmos. **122**, 7582 (2017).
[14] A. Chilingarian, B. Mailyan, and L. Vanyan, Recovering of the energy spectra of electrons and gamma rays coming from the thunderclouds, Atmos. Res. **114–115**, 1 (2012).
[15] A. Chilingarian, G. Hovsepyan, and L. Kozliner, Thunderstorm ground enhancements: Gamma ray differential energy spectra. Phys. Rev. D **88**, 073001 (2013).
[16] A. Chilingarian, G. Gharagyozyan, S. Ghazaryan, G. Hovsepyan, E. Mamidjanyan, L. Melkumyan, V. Romakhin, A. Vardanyan, and S. Sokhoyan, Study of extensive air showers and primary energy spectra by MAKET-ANI detector on mountain Aragats, Astropart. Phys. **28**, 58 (2007).
[17] A. Chilingarian and H. Mkrtchyan, Role of the lower positive charge region (LPCR) in initiation of the thunderstorm ground enhancements (TGEs), Phys. Rev. D **86**, 072003 (2012).
[18] A. Chilingarian, Thunderstorm ground enhancements—Model and relation to lightning flashes, J. Atmos. Terr. Phys. **107**, 68 (2014).
[19] A. Chilingarian, S. Chilingaryan, and G. Hovsepyan, Calibration of particle detectors for secondary cosmic rays using gamma-ray beams from thunderclouds, Astropart. Phys. **69**, 37 (2015).
[20] A. Chilingarian, S. Chilingaryan, and A. Reymers, Atmospheric discharges and particle fluxes, J. Geophys. Res. **120**, 5845 (2015).
[21] A. Chilingarian, S. Chilingaryan, T. Karapetyan, L. Kozliner, Y. Khanikyants, G. Hovsepyan, D. Pokhsraryan, and S. Soghomonyan, On the initiation of lightning in thunderclouds, Sci. Rep. **7**, 1371 (2017).
[22] D. Pokhsraryan, Fast data acquisition system based on NI-myRIO board with GPS time stamping capabilities for atmospheric electricity research, *Proceedings of TEPA 2015* (Nor Amberd, Tigran Mets, 2015), p. 23.
[23] A. Chilingarian, G. Hovsepyan, and L. Kozliner, Extensive air showers, lightning, and thunderstorm ground enhancements, Astropart. Phys. **82**, 21 (2016).
[24] K. Kudela, J. Chum, M. Kollárik *et al.*, Correlations between secondary cosmic ray rates and strong electric fields at Lomnický štít, J. Geophys. Res. **122**, 70010 (2017).
[25] http://adei.crd.yerphi.am/adei.

Astroparticle Physics 105 (2019) 54–62

Contents lists available at ScienceDirect

Astroparticle Physics

journal homepage: www.elsevier.com/locate/astropartphys

# On the origin of particle fluxes from thunderclouds

A. Chilingarian[a,b,c,*], S. Soghomonyan[a], Y. Khanikyanc[a], D. Pokhsraryan[a]

[a] Alikhanyan National Lab (Yerevan Physics Institute), Alikhanyan Brothers 2, Yerevan 0036, Armenia
[b] National Research Nuclear University MEPhI (Moscow Engineering Physics Institute), Moscow 115409, Russia
[c] Space Research Institute of RAS, Moscow, Russia

ARTICLE INFO

*Article history:*
Received 26 June 2018
Revised 14 October 2018
Accepted 15 October 2018
Available online 17 October 2018

*Keywords:*
Atmospheric electricity
lightning physics
thunderstorm ground enhancements

ABSTRACT

We present the observational data on registration of atmospheric discharges simultaneously with the detection of elementary particles obtained during thunderstorms at an altitude of 3200 m above sea level on Mt. Aragats in Armenia. Throughout the 2016 summer and 2018 spring campaigns on Aragats, we monitored lightning occurrences and signals from NaI spectrometers, plastic scintillators and Neutron Monitor proportional counters, and analyzed the shape of registered pulses. Particle detector signals were synchronized with lightning occurrences at a few nanoseconds level.

Analysis of shapes of the simultaneously detected pulses of the fast wideband electric field produced by a lightning flash and pulses from particle detectors discloses that all additional detector pulses registered during lightning flash were the electromagnetic interference signals and not particles originated directly from the lightning bolt. Thus, we observe no evidence of the direct production of electrons, neutrons or gamma rays during a lightning flash. We conclude that the entire particle fluxes detected on Aragats research station (more than 250 TGEs) can be explained by the generation of MeV electromagnetic cascades in the strong atmospheric electric fields.



## 1. Introduction

Copious observations of the thunderstorm ground enhancements (TGEs) [7,8], i.e. enhanced fluxes of electrons, gamma rays and neutrons detected by particle detectors located on the Earth's surface and related to the strong thunderstorms overhead, posed the question of their origin. According to the TGE initiation model [11,16], the electrical field of the lower dipole effectively transfers field energy to secondary cosmic ray electrons. Electrons generate copious gamma rays by a runaway breakdown (RB) [21], now referred mostly as relativistic runaway electron avalanches (RREA) [4,5,18]. High-energy gamma rays (with energies above 10 MeV) in interaction with atmosphere atoms generate neutrons by photonuclear reaction [10]. Large TGEs usually occurred during large negative electric fields observed near the earth's surface [9]. Multiyear observations of particle fluxes and lightning occurrences on Aragats prove that during large TGEs the lightning activity is suppressed; lightning reduces particle fluxes and does not accelerate them [12,15].

Observation of numerous TGEs by the Japanese, Chinese, and Slovakian groups [6,26,27,30,31] proves that RB/RREA process reliably accelerates and multiplies electrons producing numerous TGEs.

In contrast, there are observations of an alternative source of thundercloud particles.

Physicists performing experiments at the Tien-Shan Mountain Cosmic Ray Station, Kazakhstan (altitude of 3340 m) in several papers reported the existence of high-energy emissions, i.e. electron, gamma and neutron fluxes that are directly connected with yet unknown processes in the lightning bolt. Gurevich et al. [23] "report for the first time about the registration of an extraordinary high flux of low-energy neutrons generated during thunderstorms. The measured neutron count rate enhancements are directly connected with thunderstorm discharges". Gurevich et al. [25] confirm that "the intensity both of electrons and gamma rays in lightning discharge prevail the background emission by 1.5 to 2 orders of magnitude"

Another group from the Lebedev Institute in Moscow, Russian Federation, reported the emission of neutrons in the energy range up to tens of MeV in a one-meter long high-voltage discharge produced in laboratory [2]; and that "neutrons were registered within the range from thermal energies up to the energies above 10 MeV. It was found that the neutron generation takes place at the initial phase of electric discharge and is correlated with the generation of x-ray radiation" [3].

* Corresponding author.
*E-mail address:* chili@aragats.am (A. Chilingarian).

https://doi.org/10.1016/j.astropartphys.2018.10.004
0927-6505/

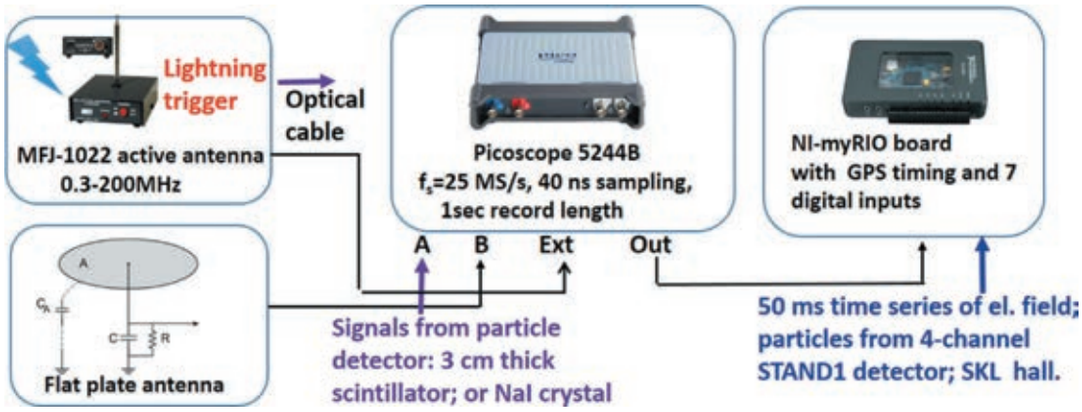


**Fig. 1.** The fast synchronized data acquisition (FSDAQ) system for the research of particle flux–lightning relations.

Another observation of the lightning-induced gamma ray flux was reported by the group from the International Center for Lightning Research and Testing (ICLRT) [20] in north central Florida. The gamma ray flux intensity was able to saturate the electronics throughout 50 μs following the system trigger. The authors claim that the primary factor that triggered the very intensive gamma ray flux was the upward positive leader approaching a negative charge region.

Despite these pieces of evidence, the physical model of the particle origination in the thunderbolt is not yet well explained. Usually, the physical model is not formulated at all; the only detection of particles is described:

Ref. [24]: it is established that "the neutrons are generated during thunderstorm atmospheric discharges. Often the neutrons are emitted in short bursts; the burst width is 200–400 μs."

Ref. [2]: "Currently, there is no reasonable model or mechanism to explain the generation of neutron bursts during atmospheric discharge in air. A special mystery is the origin of the neutrons with energies above 10 MeV."

The systematic research of the lightning-related X-ray radiation was made at the lightning observatory in Gainesville (LOG), Florida [29]. The 7.6 cm long cylindrical NaI (Tl) scintillator, circular flat-plate antennas were used for correlated measurements of the X-ray photons, electric field, and electric field derivative. Measured X-ray radiation, lightning leader and return-stroke onset times, helped to establish a correspondence between leader steps and X-ray pulses. For 23 (8 first and 15 subsequent) strokes within 2 km of the lightning observatory in Gainesville; X-rays were detected 88% of the time. The authors present the time series of gamma ray count rates before the lightning (Fig. 5 of [29]) on a microsecond time scale.

During a thunderstorm on 6 February 2017 in Japan, a $\gamma$-ray flash with duration of less than 1 ms was detected at monitoring sites 0.5–1.7 km away from the lightning. The subsequent $\gamma$-ray afterglow subsided quickly, with an exponential decay constant of 40–60 ms, and was followed by prolonged line emission at about 0.511 MeV, which lasted for a minute [19]. Authors claim a conclusive evidence of positrons and neutrons being produced after the lightning.

Few bursts of gamma ray showers have been observed in coincidence with downward propagating negative leaders in lightning flashes by the telescope array surface detector (TASD) [1]. The authors claim that observed energy deposit is consistent with forward-beamed showers of $10^{12}$–$10^{14}$ or more primary photons above 100 keV, distributed according to a RB/RREA spectrum. However, no model was presented to justify such a huge amount of high-energy particles associated with a lightning flash.

In summary, two models are suggested in the literature:

(a) The RB/TGE model—electrons from the ambient population of CR accelerated in the strong electric field in the lower part of the cloud, runaway, generate bremsstrahlung gamma rays and the gamma rays produce neutrons via photonuclear reactions;
(b) The lightning model—the electron, gamma, and neutron fluxes originate in the lightning flashes. The model of particle generation in the lightning bolt, or around the lightning bolt is yet not well specified.

To solve this controversy, we need to unambiguously answer the question: do lightning flashes emit high-energy electrons, positrons, gamma rays and neutrons with single energies of several tens of MeV? [28]. Therefore, we perform experiments with simultaneous recording of the pulse shape from particle detectors and from atmospheric discharges. During the summer 2016 to spring 2018 campaigns on Aragats completed by the staff of cosmic ray division (CRD) of Yerevan Physics Institute (YerPhI) hundreds strong storms with numerous lightning flashes were observed, and some of the most violent ones produced electromagnetic interferences (EMI) in some of the particle detectors and data acquisition electronics (DAQ). Taking as examples the huge storms occurred on Aragats we demonstrate that with new fast electronics we can reliably distinguish EMI from genuine particle registration in a variety of particle detectors that are in operation on Aragats. No particle fluxes correlated with lightning flashes were detected at Aragats during the whole time of observations.

## 2. Instrumentation

The correlation analysis of the TGEs and lightning discharges poses stringent requirements on the time resolution and synchronization of the data flow from particle detectors, near surface electric field sensors and sensors of the fast electric field. The recently developed fast synchronized data acquisition (FSDAQ) system (see Fig. 1) is triggered by a commercial MFJ-1022 active whip antenna that covers a frequency range from 300 kHz to 200 MHz. A flat-plate antenna followed by passive integrator is used to record fast electric field waveforms. The output of the integrator is directly connected to the digital oscilloscope (2-channel Picoscope 5244B) with 60 cm long RG58 coaxial cable. The data capture length is 1 s, including 200 ms pre-trigger time and 800 ms post-trigger time. The sampling rate is 25 MS/s, corresponding to 40 ns sampling interval, and the amplitude resolution is 8 bit.

The trigger output of the oscilloscope is connected to the input of GPS timing system of the national instrument's (NI) MyRiO board. Any event recorded by the oscilloscope generates an output trigger, causing the GPS card to trigger at the same instant and produce a timestamp.

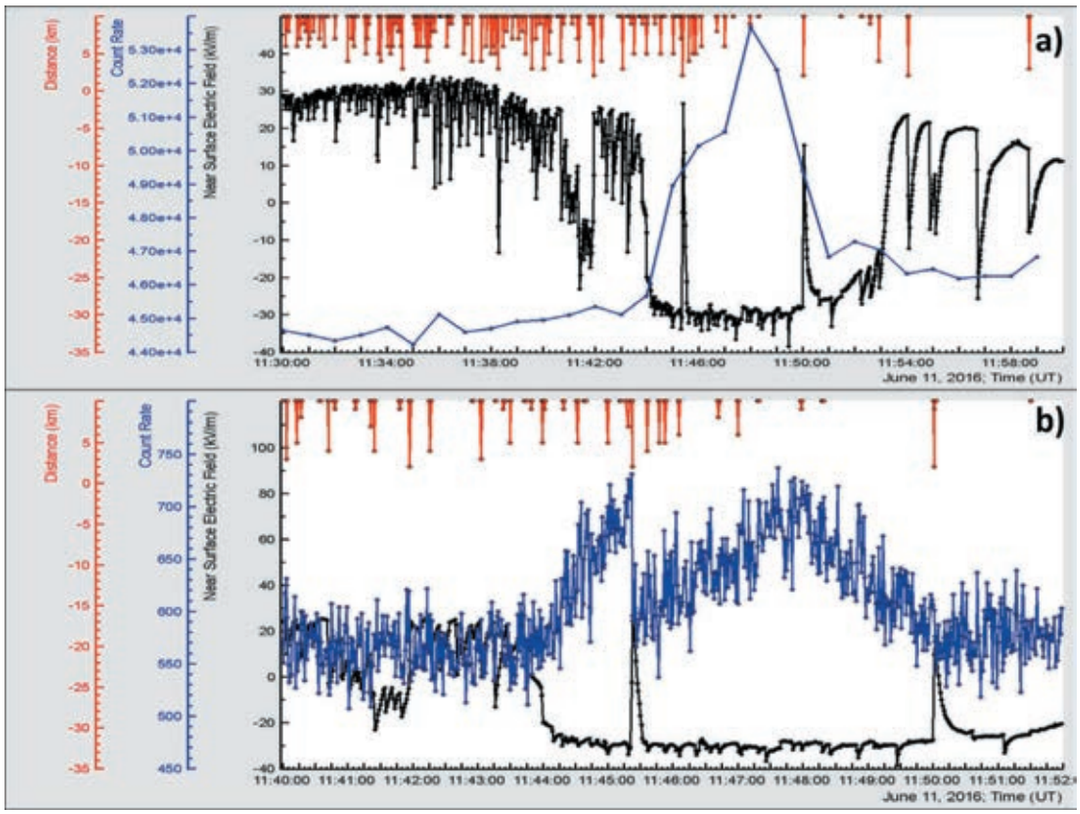


**Fig. 2.** (a) Disturbances of the near surface electrostatic field, distance to lightning and 1 min count rate of STAND1 (MAKET) upper scintillator; energy threshold ~1 MeV; (b) 1 s time series of the 3 cm thick plastic scintillator of the same detector. A strong lightning discharge is seen as a vertical line interrupted TGE.

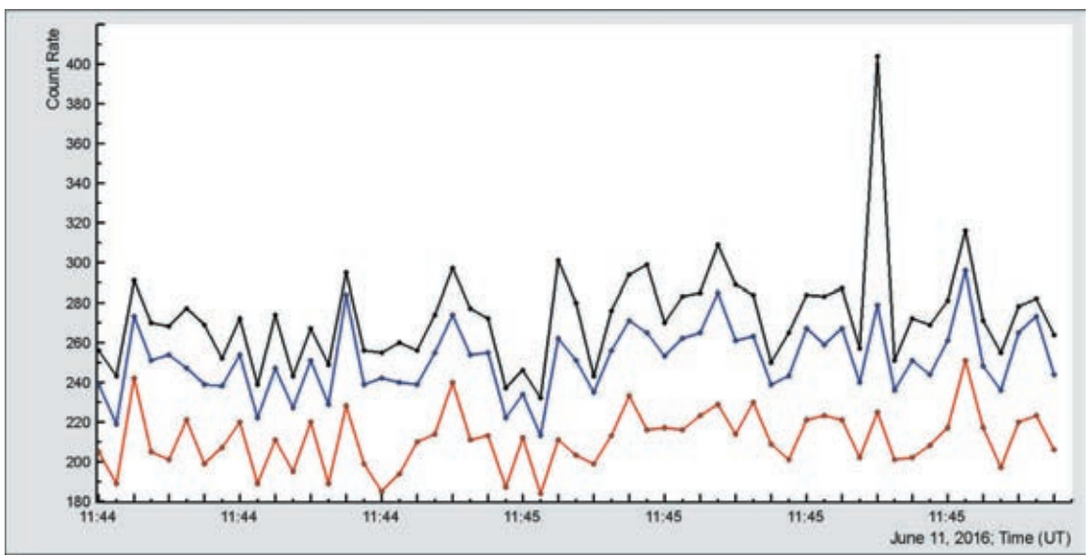


**Fig. 3.** Event on 11/6/2016, 11:44 UT. The 1 s time series of ArNM. Only time series corresponding to 0.4 μs dead time (upper curve) demonstrates large peak due to counting multiple secondary neutrons coming within time span ~1 ms; the time series corresponding to 750 and 1200 μs dead time demonstrate no peak.

The heart of the DAQ system is the NI-myRIO board. It includes eight analog inputs, four analog outputs, 32 digital I/O lines, programmable FPGA, and a dual-core ARM Cortex-A9 processor (a high-performance processor implementing the full richness of the widely supported ARMv7-A architecture). With reconfigurable FPGA technology, we perform high-speed signal processing, high-speed control, inline signal processing, and custom timing and triggering. For the control systems, one can also run advanced control algorithms directly in the FPGA fabric to minimize latency and maximize loop rates. “LabVIEW FPGA Module”, which extends the LabVIEW graphical development platform, provides an alternative to HDL (Hardware description language) graphical programming

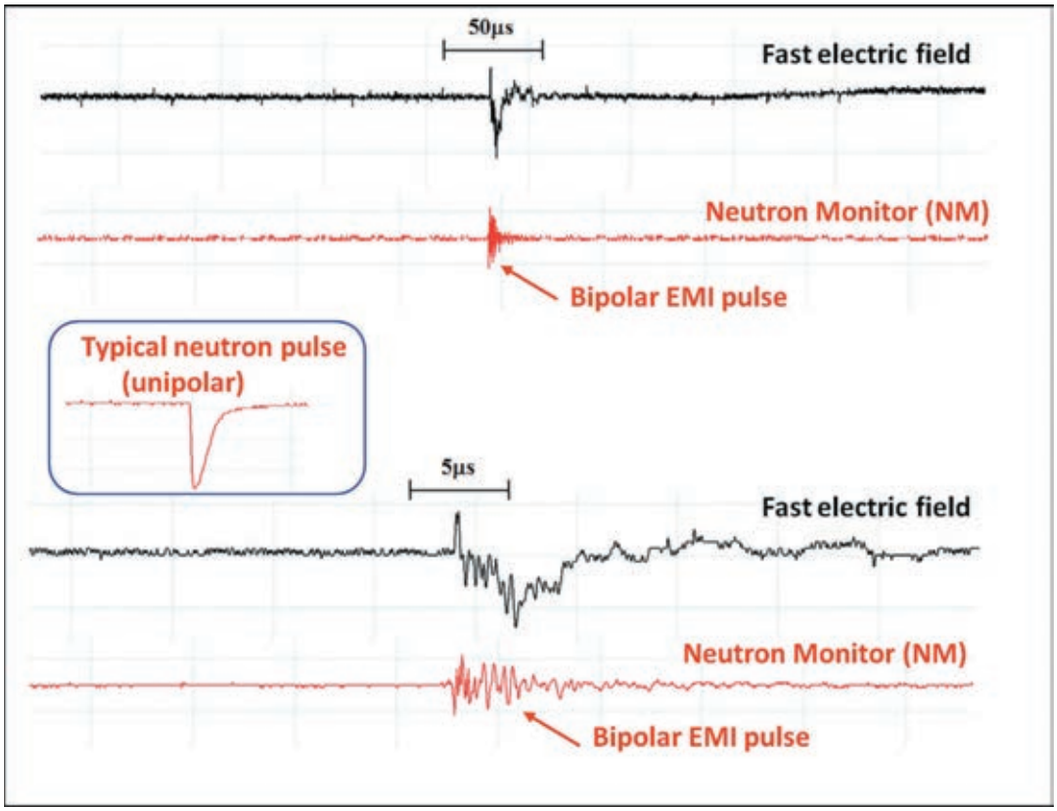


**Fig. 4.** Synchronized waveforms of fast electric field and neutron monitor shown in different time scales along with a typical waveform of neutron signal from the proportional counter of NM. Lightning flash occurred on 11 June 2016 at 11:44 UT.

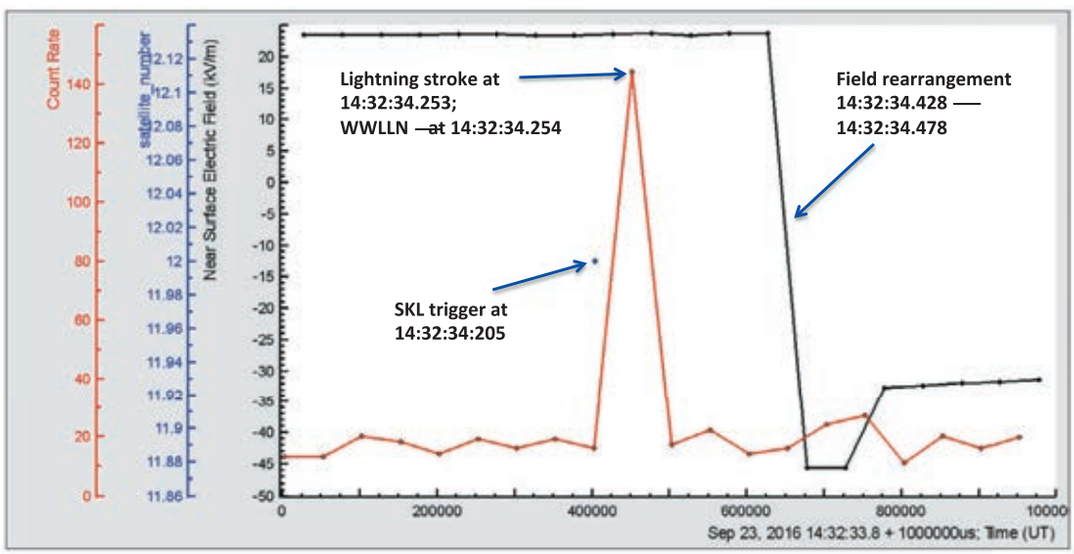


**Fig. 5.** 50 ms time series of the bottom scintillator of STAND1 detector and electrostatic field disturbances. The negative change of electrostatic field of 69.3 kV/m is produced by an inverted-polarity lightning flash.

approach that simplifies the task of interfacing to I/O and communicating data.

The commercial GPS receiver sends two types of data-stream to the board. The first is RS-232 ASCII data telling what time it is, at what latitude, longitude, and altitude the receiver is, and information about the satellites the receiver is using. An embedded 25 MHz counter on FPGA gives the exact time of the trigger. The 1PPS (one pulse per second) stream of the 5 V, 100 ms pulses resets this counter at each second. The leading edges of 1PPS signals from GPS receivers are synchronized within the accuracy of the non-military GPS system (about 100 ns). This feature allows time synchronization with 100 ns resolution.

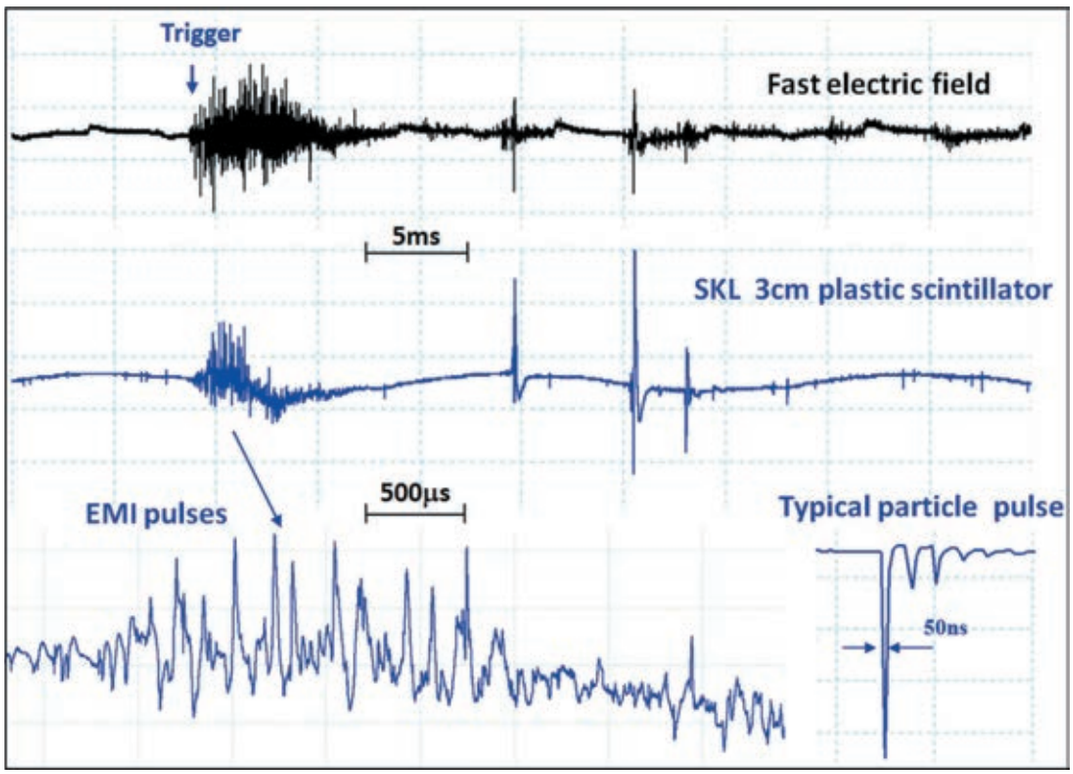


**Fig. 6.** Typical EMI signature from atmospheric discharges in the particle detector waveform. Synchronised time-series of the pulses of fast electric field and signals from the plastic scintillator. SKL trigger occurred on 23 September 2016 at 14:32:34.205 UT.

Eight digital inputs of myRIO board are used for feeding signals from the variety of particle detectors operated on Aragats. Since the 2016 summer season, we connected to myRIO the STAND1 detector comprised of three vertically stacked plastic scintillators (thickness = 1 cm, area = 1 $m^2$, energy threshold ~0.8 MeV) and one stand-alone plastic scintillator (thickness = 3 cm, area = 1 $m^2$, energy threshold ~2 MeV), proportional counters of Aragats neutron monitor (ArNM) and NaI crystal based spectrometers (energy threshold ~0.3 MeV). Details on the performance of these particle detectors can be found in [13,14].

The myRIO pulse counting system can provide registration of very short time series (down to 1 ms) that enables the investigation the dynamic of TGE development and its relation to the lightning initiation (50 ms time series are stored currently).

Signals from the electric field sensor (electric mill EFM-100) were fed to the myRIO board via the TCP-IP connection (WiFi). The electrostatic field changes were recorded at a sampling interval of 50 ms; the amplitude resolution of electric field measurement was 0.01 kV/m, and the lightning location accuracy was ≈1.5 km. The firmware application provided by Boltek has a feature to share the electric field data via a network (it acts as a server for a client running under myRIO). The 8th channel is reserved for the synchronization pulse (the trigger) from a fast waveform recording device or from any of particle detectors.

At any triggering signal, the MyRio board generates a special output containing current value of particle detector counts, near-surface electric field value and precise time of arriving of the trigger signal. Thus, the fast waveform patterns are synchronized with particle fluxes and with slow (20 Hz) near surface electric field measurements.

The time series of particle detector count rates, electrostatic field measurements and service information (status of myRIO, time delays, a number of satellites used for GPS timing), as well as the files containing digital oscilloscope data, are transferred via online PC to the mySQL database on CRD headquarters in Yerevan. All information is available via ADEI multivariate visualization code at the website http://adei.crd.yerphi.am; explanations are located in the WiKi section [17].

Two DAQ systems are operated independently in MAKET and SKL experimental halls on Aragats; triggers issued by both fast DAQ systems usually coincide within few ms. However, an optical link can transfer the trigger signal from SKL to MAKET experimental hall located at a distance of 100 m for the joint triggering of 2 networks of particle detectors and field meters.

## 3. *In situ* measurements of the thunderstorm particles on Aragats

Throughout this paper, we use the atmospheric electricity sign convention, according to which the downward-directed electric field or field change vector is considered to be positive. On 11 June 2016, large disturbances of the near-surface electrostatic field started at 10:45 UT (see Fig. 2(a)). The atmospheric pressure was 690.8 mbar; relative humidity—75%; wind speed 3—4 m/s; temperature ~5 °C; no rain was registered. In Fig. 2(a) and (b) we show disturbances of the near-surface electric field; 1 min and 1 s time series of plastic scintillators of STAND1 array and distance to lightning in the top of both Fig. 2(a) and (b). Note the difference in the horizontal axes of Fig. 2(a) and (b): for 1 min time series, it is half of the hour, for 1 s time series it is 12 min. The typical shape of the electrostatic field disturbances (the electrostatic field in the deep negative domain for several minutes possibly accompanied by several short “bursts” touching positive domain and 1–2 negative lightning flashes with large amplitude) shown in Fig. 2(a)

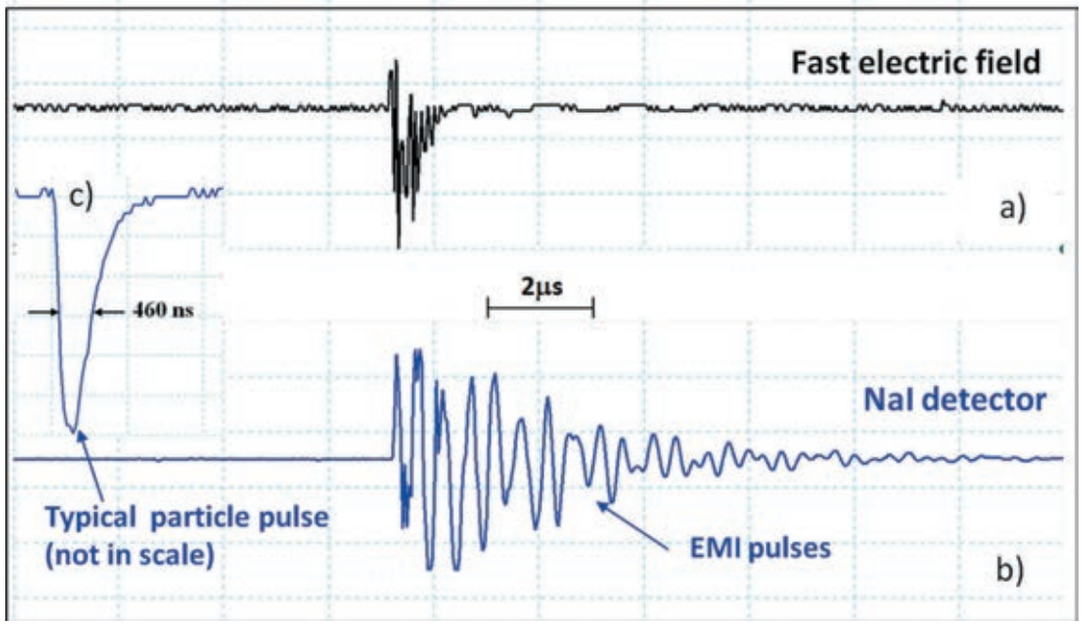


**Fig. 7.** Registration of the lightning flash occurred on May 15, 2016, 12:48:25. Waveforms of the fast electric field (a); NaI detector output (b); in the inset (c) is shown a typical shape of NaI detector response to an incident particle.

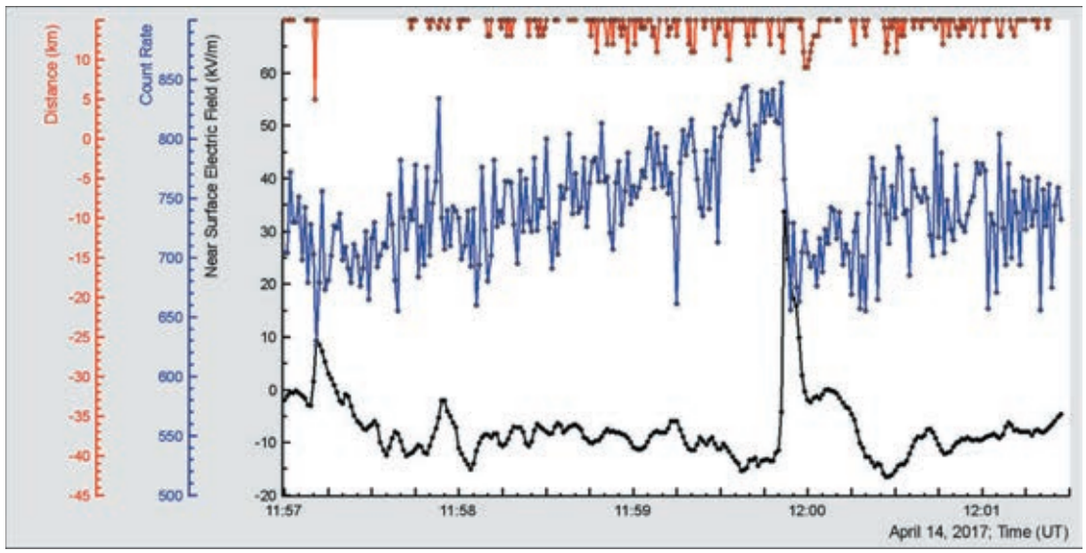


**Fig. 8.** TGE abruptly terminated by the lightning flash at 11:59:51.82; trigger was registered in MAKET and SKL hall at 11: 59:51.75; a surge of the electrostatic field started at 11:59:51.94; a decline of particle flux started at 11:59:51.83.

indicates the establishment of the lower dipole, which accelerates the CR electrons downwards. Accelerated electrons unleash multiple relativistic runaway avalanches measured on the earth's surface [7,8]. The enhanced particle flux (TGE) is shown in Fig. 2(a) by the 1 min time series of count rate of 1 cm thick plastic scintillator of STAND1 detector located nearby MAKET experimental hall (upper detector of 3 stacked above each other). The count rate enhancement was ≈25% corresponding to more than 35 standard deviations. From the recovery of the differential energy spectrum of TGE (see for instance Fig. 5 in [16]) it is apparent that after lightning flashes high-energy particle flux is totally terminated, whereas the flux of low energy particles (below 3 MeV) continues.

A strong lightning discharge that occurred at 11:45:22 abruptly terminated the TGE. However, the TGE restarted and was continuing ~4.5 min until 11:50, when second strong lightning discharge finally terminated particle flux. The electrostatic field change caused by the lightning has a rise time of few hundreds milliseconds and recovery time of several seconds. Abrupt termination of particle flux caused by first lightning is shown in Fig. 2(b) with 1 s time series of the 3 cm thick scintillator of the same STAND1 detector. Count rate decreases from 731 at 11:45:22 down to 592 (19%) at 11:45:23. The electrostatic field starts to rise from an initial value of −30.6 kV/m at 11:45:22.48, and shows a maximum of 39.7 kV/m at 11:45:22.58; the amplitude of field change was

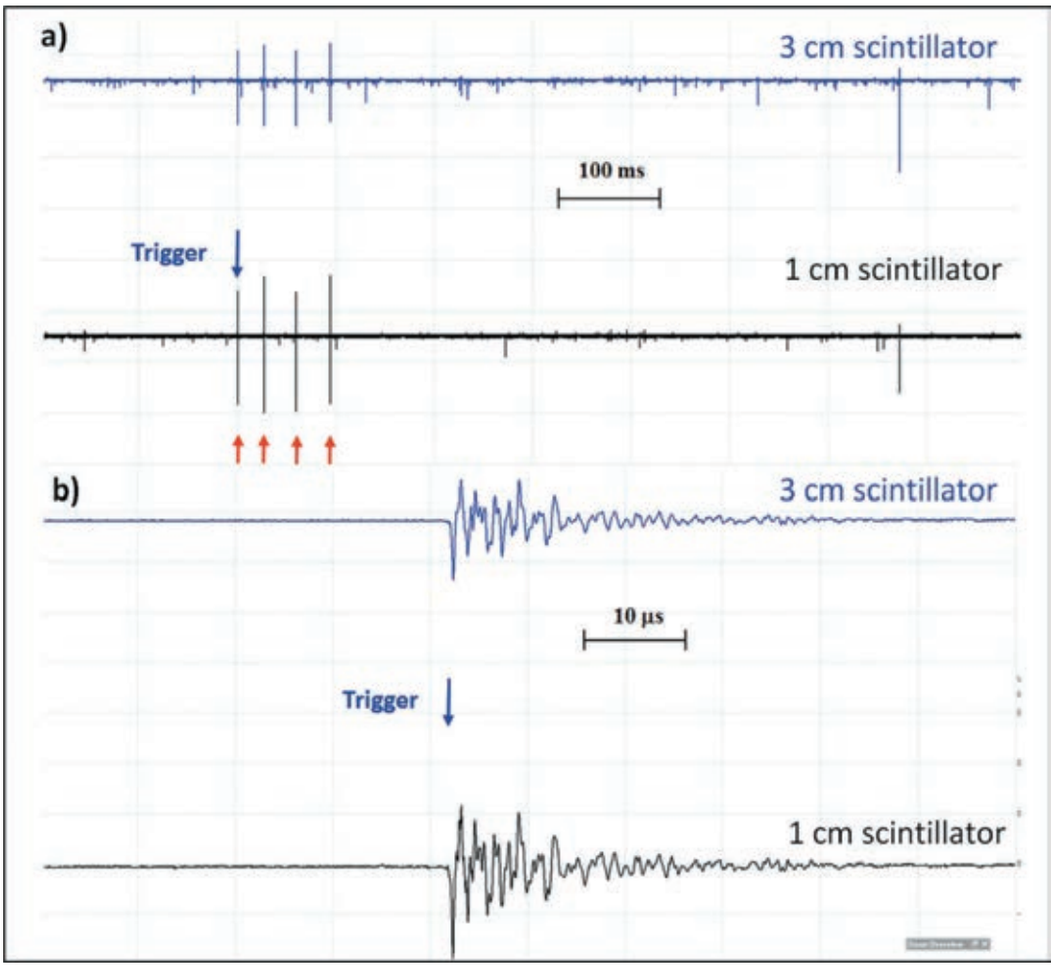


**Fig. 9.** The "Shower Burst" event detected on 14 April 2017 by 1 cm thick and 3 cm thick 1 m area plastic scintillators located in the experimental hall MAKET. The signal shapes were synchronized with lightning flash (atmospheric discharge trigger was detected at 11: 59:51.75). The "bursts" are denoted by 4 small arrows in (a). The zoomed version of the first burst is shown in (b).

70.3 kV/m reached in 100 ms. Field recovery took much longer time ~10 s.

The lightning discharge is a powerful wideband radio-wave emitter, which produces electric pulses in the cables, DAQ electronics, and power lines. To check if the registered pulses are electromagnetic interferences (EMI) or signals from relativistic particles born in the lightning bolt we performed synchronized measurements of the waveforms of fast electric field caused by atmospheric discharges and signals from particle detectors. The Aragats neutron monitor (ArNM, see details in [14]) measures the 1 s time series of count rates from 16 proportional counters filled with Boron gas. Neutrons and protons incident the detector's 5 cm thick lead absorber generate in nuclear reactions numerous secondary neutrons, which are detected by the proportional counter.

In Fig. 3 we show three time series of detector count rates recorded with 3 different dead times. For the shortest dead time of 0.4 μs, all secondary neutrons that enter the proportional counter are detected. For larger dead times of 750 μs and 1250 μs the particle count is suppressed after detecting the first neutron. Thus, a hypothetic particle burst from the lightning will be registered by ArNM as a large peak in the 1 s time series of ArNM count rate corresponding to 0.4 μs dead time, and will not be registered with 750 μs and 1250 μs dead times, as it is shown in Fig. 3.

To prove that detected peak is due to burst of neutrons we need to examine the pulse shapes recorded by the oscilloscope. In Fig. 4, we demonstrate fast electric field waveforms from flat plate antenna and pulses from one of the proportional counters of ArNM and their zoomed versions. As a reference, a typical shape of the genuine neutron pulse is also shown.

By detecting the large peak at 11:45:23 in time-series of ArNM shown in Fig. 3 only, we can erroneously conclude that simultaneously with atmospheric discharge a large number of neutrons is generated in the lightning bolt. However, comparing the detailed pattern of the detected lightning bipolar pulses with the typical unipolar pulse that neutron generates on the output of the proportional counter (Fig. 4) we should reject the hypothesis of neutron production in the lightning bolt. All additional counts detected by the proportional counter at 11:45:23 are due to EMI.

On 23 September 2016 on Aragats station, a severe storm was observed with strong lightning activity and heavy rain at 13:50–14:50 UT. The temperature dropped from 3.6 °C to 1.3 °C; relative humidity was very high—98%, rain rate for 20 min touched a level of 1 mm/h. In Fig. 5 we show the trigger time, the estimated lightning flash time (by the large EMI pulse registered by one of the particle detectors) confirmed by the World-Wide Lightning Location Network (WWLLN) observation and the time series of the electric field rearrangement.

During the time span of several tens of ms after the trigger and before the lightning stroke, numerous atmospheric discharges induce plenty of pulses in a 52 cm diameter circular flat-plate antenna and simultaneously we observe bipolar pulses from particle detector (Fig. 6). A large number of bipolar "fake" signals ("trains" of pulses) from the 3 cm thick plastic scintillator of STAND1 detector mimicked a particle burst correlated with lightning. If one counts the number of particles in a burst only, it is possible to come to an erroneous inference that a registered peak is due to particles from the lightning bolt. However, the pulse from the charged particle registered by the scintillator has a typical unipolar shape (right bottom corner of Fig. 6). Using a fast digital oscilloscope, we can reliably distinguish bipolar pulses from atmospheric discharges and unipolar pulses from the particle detectors.

In Fig. 7(b) we show bipolar pulses registered by another detector, NaI crystal based spectrometer [13] produced by the strong atmospheric discharge (Fig. 7(a)). Signals from charged or neutral particles detected by NaI spectrometer are always unipolar.

Thus, we observe that all examined particle detectors (plastic scintillators, NaI crystals and proportional counters) can be triggered by a strong nearby lightning. However, by examining the shape of registered pulses we can easily discriminate EMI from the genuine particle pulse.

To confirm our results on the nature of "bursts" in the particle detectors we perform the pulse shape analysis from 3 particle detectors operated on Aragats Mountain. Two FSDAQ systems located in MAKET and SKL experimental halls separated by a distance of ~100 m were triggered by two independent whip antennas. Several particle detectors were connected to both FSDAQ systems; data files with 1 s capture length and 40 ns sampling intervals were stored after each trigger (200 ms before and 800 ms after trigger). In April–June 2017 we detected numerous lightning flashes, which triggered the both FSDAQ systems; ~250 joint triggers of MAKET and SKL DAQ system were registered. Careful examining of the shapes of output signals from flat plate antenna and from particle detectors proves that there was no genuine signal from any of the 3 particle detectors. All output "bursts" were bipolar and can be easily distinguished from the unipolar signals from particles traversing the detector. As an example of 2017 observations, we present the April 14 TGE, the first TGE of 2017 abruptly terminated by a lightning flash (Fig. 8). The outputs of the 2 plastic scintillators synchronized with trigger worked out by the whip antenna are shown in Fig. 9. We can detect 4 "Shower Bursts" in the Fig. 9(a); however, examining of the zoomed version shown in Fig. 9(b) proves that bi-directional signals from the DAQ electronics are EMIs and not genuine unipolar particle signals.

## 4. Discussion and conclusion

New emerging field of atmospheric high-energy physics is still lacking firmly established theoretical model. Our paper is an attempt to clarify one of the often-discussed problems: the origin of extremely rare particle "bursts" coinciding with a lightning flash.

During numerous storms observed from 2016 summer to 2018 spring we did not observe any lightning producing relativistic particles in any of continuously monitored detectors. There were no intense particle bursts in monitored particle detectors within 200 ms before atmospheric discharge trigger and 800 ms after. However, as we mentioned, in our previous papers, we do not exclude that propagation of lightning leaders and emerging of strong electric fields around leader tips can produce X-rays and additional seed electrons involved in the runaway process.

For many years of observations, there are not more than a half-of-dozen reported events of possible lightning origin. In contrast, only on Aragats we detect hundreds of TGE events comprising of millions and millions of "ECSs"—extensive cloud showers [11]; or Micro Runaway Breakdowns ("MRBs") [22]. All these alternative terms (Shower Burst [1], Inverse TGF [20], ECS [8], and MRB [22]) are related to one and the same entity—a runaway cascade developed in the strong electric field in the thunderstorm atmosphere. Continuum of gamma rays detected in Japan, China, Armenia, Slovakia and other countries can prolong till the return stroke and obviously include as well few gamma ray showers that coincide with the stepped leader propagation. Routinely observed copious gamma ray bursts integrated into a prolonged TGE can be explained by a standard RB/RREA theory with cosmic ray electron seeds [11,16,21].

If thunderclouds are high above particle detectors (1–2 km), like in Utah and Florida most gamma rays and all electrons are absorbed in the atmosphere. This is why the detection of TGEs at such sites is so rare. In contrast, thunderclouds at Aragats can be as low above particle detectors as 25–50 m. Only when the electric field in the cloud is extremely large the runaway electrons can collect from the electric field energy enough to unleash cascades so large, that gamma rays from RB/RREA cascades can be observed 1–2 km below the cloud on the earth's surface. It is why the reported "lightning origin" events are so rare and so short.

To finally resolve the enigma of the lightning correlated high-energy particles we need more observation at many sites with various particle detectors and improved time resolution.

## Acknowledgments

Authors would like to thank the staff of the Aragats Space Environmental Center for the uninterruptible operation of Aragats research station facilities. Authors are grateful to Yuri Stenkin for useful discussions and valuable comments. Work was supported by the Russian Science Foundation grant (project No. 17-12-01439).

The data for this paper are available on the WEB page of the Cosmic Ray Division (CRD) of the Yerevan Physics Institute, http://adei.crd.yerphi.am/adei. Figures from the paper can be easily reproduced with embedded multivariate visualization on-line program ADEI [17].

## References

[1] R.U. Abassi, T. Aby-Zayyad, M. Allen, et al., Gamma-ray showers observed at ground level in coincidence with downward lightning leaders, JGR Atmos. 123 (2018) 6864.
[2] A.V. Agafonov, A.V. Bagulya, O.D. Dalkarov, et al., Observation of neutron bursts produced by laboratory high-voltage atmospheric discharge, Phys. Rev. Lett. 111 (2013) 115003.
[3] A.V. Agafonov, V.A. Bogachenkov, A.P. Chubenko, et al., Observation of hard radiations in a laboratory atmospheric high-voltage discharge, J. Phys. D 50 (2017) 165202.
[4] L.P. Babich, E.N. Donskoy, I.M. Kutsyk, et al., Comparison of relativistic runaway electron avalanche rates obtained from monte carlo simulations and from kinetic equation solution, IEEE Trans. Plasma Sci. 29 (2001) 430.
[5] L.P. Babich, E.N. Donskoy, R.I. Il'kaev, I.M. Kutsyk, R.A. Roussel-Dupre, Fundamental parameters of a relativistic runaway electron avalanche in air, Plasma Phys. Rep. 30 (2004) 616.
[6] B. Bartoli, P. Bernardini, X.J. Bi, et al., Observation of the thunderstorm-related ground cosmic ray flux variations by ARGO-YBJ, Phys. Rev. D 97 (2018) 042001.
[7] A. Chilingarian, A. Daryan, K. Arakelyan, et al., Ground-based observations of thunderstorm-correlated fluxes of high-energy electrons, gamma rays, and neutrons, Phys. Rev. D 82 (4) (2010) 043009.
[8] A. Chilingarian, G. Hovsepyan, A. Hovhannisyan, Particle bursts from thunderclouds: natural particle accelerators above our heads, Phys. Rev. D 83 (6) (2011) 062001.
[9] A. Chilingarian, H. Mkrtchyan, Role of the lower positive charge region (LPCR) in initiation of the thunderstorm ground enhancements (TGEs), Phys. Rev. D 86 (2012) 072003.
[10] A. Chilingarian, N. Bostanjyan, T. Karapetyan, L. Vanyan, Remarks on recent results on neutron production during thunderstorms, Phys. Rev. D 86 (2012) 093017.
[11] A. Chilingarian, Thunderstorm ground enhancements—model and relation to lightning flashes, J. Atmos. Solar-Terr. Phys. 107 (2014) 68–76.
[12] A. Chilingarian, G. Hovsepyan, G. Khanikyanc, et al., Lightning origination and thunderstorm ground enhancements terminated by the lightning flash, EPL 110 (2015) 49001.

[13] A. Chilingarian, G. Hovsepyan, E. Mantasakanyan, Mount Aragats as a stable electron accelerator for atmospheric high-energy physics research, Phys. Rev. D 93 (2016) 052006.
[14] A. Chilingarian, G. Hovsepyan, L. Kozliner, Extensive air showers, lightning, and thunderstorm ground enhancements, Astropart. Phys. 82 (2016) 21–35.
[15] A. Chilingarian, Long lasting low energy thunderstorm ground enhancements and possible Rn-222 daughter isotopes contamination, Phys. Rev. D 98 (2018) 022007.
[16] A. Chilingarian, G. Hovsepyan, S. Soghomonyan, M. Zazyan, M. Zelenyy, Structures of the intracloud electric field supporting origin of long-lasting thunderstorm ground enhancements, Phys. Rev. D 98 (2018) 082001.
[17] S. Chilingaryan, A. Beglarian, A. Kopmann, S. Vöcking, Advanced data extraction infrastructure: web based system for management of time series data, J. Phys. Conf. Ser. 219 (2010) 042034.
[18] J.R. Dwyer, A fundamental limit on electric fields in air, Geophys. Res. Lett. 30 (2003) 2055.
[19] T. Enoto, Y. Wada, Y. Furuta, et al., Photonuclear reactions triggered by lightning discharge, Nature 551 (7681) (2017) 481.
[20] B.M. Hare, M.A. Uman, J.R. Dwyer, et al., Ground-level observation of a terrestrial gamma ray flash initiated by a triggered lightning, J. Geophys. Res. Atmos. 121 (2016) 6511.
[21] A.V. Gurevich, G.M. Milikh, R. Rouseel-Dupre, Runaway electron mechanism of air breakdown and preconditioning during a thunderstorm, Phys. Lett. A 165 (1992) 463 1992.
[22] A.V. Gurevich, K.P. Zybin, R.A. Roussel-Dupre, Lightning initiation by simultaneous of runaway breakdown and cosmic ray showers, Phys. Lett. A 254 (1999) 79.
[23] A.V. Gurevich, V.P. Antonova, A.P. Chubenko, et al., Strong flux of low-energy neutrons produced by thunderstorms, Phys. Rev. Lett. 108 (2012) 125001.
[24] A.V. Gurevich, V.P. Antonova, Chubenko, et al., The time structure of neutron emission during atmospheric discharge, Atmos. Res. 164 (2015) 339.
[25] A.V. Gurevich, A.M. Almenova, V.P. Antonova, Observations of high-energy radiation during thunderstorms at Tien-Shan, Phys. Rev. D 94 (2016) 023003.
[26] K. Kudela1, J. Chum, M. Kollárik, R. Langer, I. Strh.rsky´, J. Baše, Correlations between secondary cosmic ray rates and strong electric fields at Lomnicky´štít, J. Geophys. Res. 122 (2017) 10700.
[27] Y. Kuroda, S. Oguri, Y. Kato, R. Nakata, Y. Inoue, C. Ito, M. Minowa, Observation of gamma ray bursts at ground level under the thunderclouds, Phys. Lett. B 758 (2016) 286–291.
[28] C. Köhn, G. Diniz, M.N. Harakeh, Leptons, hadrons and photons and their feedback close to lightning leaders, J. Geophys. Res. Atmos. 122 (2017) 1365.
[29] S. Mallick, V.A. Rakov, J.R. Dwyer, A study of X-ray emissions from thunderstorms with emphasis on subsequent strokes in natural lightning, J. Geophys. Res. 117 (2012) D16107, doi:10.1029/2012JD017555.
[30] T. Torii, T. Sugita, M. Kamogawa, et al., Migrating source of energetic radiation generated by thunderstorm activity, Geophys. Res. Lett. 38 (2011) L24801.
[31] H. Tsuchiya, T. Enoto, K. Iwata, et al., Hardening and termination of long-duration gamma rays detected prior to lightning, Phys. Rev. Lett. 111 (2013) 015001.

# Structures of the intracloud electric field supporting origin of long-lasting thunderstorm ground enhancements

A. Chilingarian,[1,2,3] G. Hovsepyan,[1] S. Soghomonyan,[1] M. Zazyan,[1] and M. Zelenyy[3,4]
[1]*A. Alikhanyan National Lab (Yerevan Physics Institute), Yerevan 0036, Armenia*
[2]*National Research Nuclear University MEPhI, Moscow 115409, Russia*
[3]*Space Research Institute of RAS, Moscow 117997, Russia*
[4]*Institute of Nuclear Research of RAS, Moscow 117312, Russia*

(Received 15 August 2018; published 3 October 2018)

The problem of thundercloud electrification is one of the most difficult ones in atmospheric physics. The structure of electric fields in clouds escapes from the detailed *in situ* measurements; few balloon flights reveal these rather complicated structures. To gain insight into the problem of the charge structure of a thundercloud, we use new key evidence—the fluxes of particles from a thundercloud, the so-called thunderstorm ground enhancements—TGEs. TGEs originate from electron acceleration and multiplication processes in the strong electric fields in the thundercloud, and the intensity and energy spectra of electrons and gamma rays as observed on the Earth's surface are directly connected with the atmospheric electric field. Discovery of long-lasing TGEs poses new challenges for revealing structures in the thundercloud responsible for hours-extending gamma ray fluxes. In the presented paper, we demonstrate that experimentally measured intensities and energy spectra of the "thundercloud particles" give clues for understanding charge structures embedded in the atmosphere. A rather short "runaway" process above the detector site, which is consistent with the tripole structure of the cloud electrification, is changing to a much less energetic emission that lasts for hours. Measurements of enhanced particle fluxes are accompanied by the simulation experiments with CORSIKA and GEANT4 codes.

DOI: 10.1103/PhysRevD.98.082001

## I. INTRODUCTION

One of the main problems of the atmospheric electricity is the study of the spatial-temporal structure of the electric field in the thunderclouds. Precise measurement of the electric potential within thunderclouds is extremely difficult because of the time variability and the need to make spatially separated simultaneous measurements within the highest field regions of the storm [1]. The charge structure of a thundercloud can be viewed as a vertical tripole consisting of three charge regions. The main positive charge region is located at the top, the main negative in the middle, and an additional positive below the main negative [2]. Reference [3] observed a tripole charge structure, with a large lower positively charged region (LPCR) in the thunderclouds over the Tibetan plateau of China, and noticed that the large LPCR prevents negative cloud-to-ground (CG) flashes from occurring and, instead, facilitates inverted-polarity intracloud (IC) flashes. Different lightning scenarios that may arise depending upon the magnitude of the LPCR have been examined in [4]. Reference [5] examined different patterns of the near-surface electric field occurring during the thunderstorm ground enhancements (TGEs, [6,7]). A hypothesis that electrons of the ambient population of cosmic rays are accelerated and multiplied in the bottom dipole formed by the main negative charge layer and the LPCR was proposed. Reference [8] also considered the electric field of the same direction formed by the main negative charge in the cloud and its mirror image on the ground.

The possibility that the intracloud electric field could be evaluated by ground-based measurements of the gamma ray and electron spectra was considered in [9]. However, there were only a few cases when electron energy spectra were measured at the ground level [10] due to fast attenuation of the electron flux in the air. Nonetheless, measured gamma ray spectra are in good agreement with the RREA model [11,12].

The relation of particle fluxes and lightning flashes also provides valuable information on the cloud electrification. During the TGE, lightning flashes are suppressed, and, when this happens, they usually abruptly terminate the high-energy particle flux [13,14]. Simultaneous detection of the particle fluxes and atmospheric discharges with microsecond time resolution on Aragats enables us to associate the lightning types abruptly terminated particle fluxes with the electric structure within thundercloud [8].

However, the TGE-electric field relation is still far from fully understood, and the study of various charge structures that can initiate the TGEs should be accompanied by Monte Carlo simulation of the passage of particles through the region of the assumed intracloud electric fields.

 

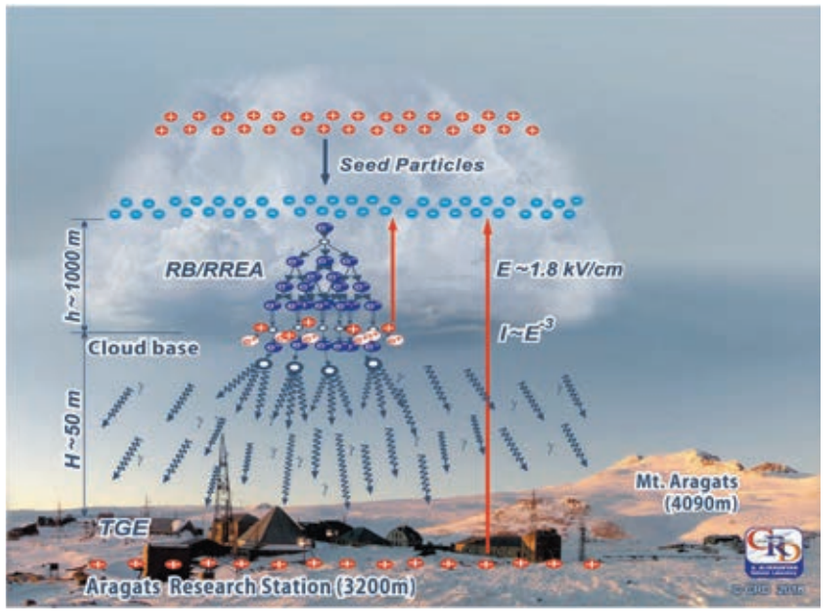


FIG. 1. Cartoon demonstrating electron acceleration and multiplication in the electric field of the lower dipole of the thundercloud and in the electric field beneath the cloud.

Thus, we use a new type of key evidence in the atmospheric electricity research, namely, the particle fluxes from the thunderclouds, to scrutinize the atmospheric electricity problem. The origin of the fluxes of electrons, gamma rays, and neutrons detected on the Earth's surface are the runaway breakdown (RB) processes [15] now mostly referred to as relativistic runaway electron avalanches (RREA, [16,17]). The electron acceleration in the Earth's direction is due to the electric field between the main negative charge region in the middle of the cloud and the positive charge that is induced on the ground. This field can be significantly increased by the electric field between the main negative region and the emerged lower positively charged region (LPCR) in the bottom of the cloud. The maximal intensity (and maximal energy of particles) of the TGE is observed when the strength of the total electric field in the cloud exceeds the "runaway" threshold in the atmosphere and the RB/RREA avalanches start to develop in the direction of Earth. Such a condition corresponds to the maximum dimension and charge of the LPCR; thus, the lightning leader cannot make its path through the LPCR, and cloud-to-ground flashes are suppressed [4]. The decay of the gamma ray flux and its termination by the lightning flash indicates the degradation of the bottom dipole.

In the presence of weak electric fields in the atmosphere (lower than RB/RREA threshold) when cosmic ray seed electrons cannot "runaway" and originate avalanches, the electric field effectively transfers energy to the electrons modifying their energy spectra (MOS process, [18]) and making the probability of emitting bremsstrahlung gamma rays larger. In contrast to RB/RREA, the MOS process is dominating in the energy range above ≈50 MeV; the RREA process generates gamma rays with energies below ≈50 MeV although with a much larger count rate.

In the cartoon (Fig. 1), we show the electron–gamma ray avalanche developed in the bottom of the thundercloud above the Aragats high altitude research station of the Yerevan Physics Institute [19]. The avalanche comes out of the base of the cloud and illuminates various particle detectors, measuring count rates of charged and neutral particles and their energy. The distance to the cloud base at Aragats in the spring and autumn seasons is usually rather small $H = 25$–$100$ m; in summer, it is larger, $H = 50$–$500$ m. In our simulation studies of TGEs, we will assume the strength of the electric field in the cloud up to 1.8 kV/m and elongation up to 1 km. Both values are ordinary and have been measured in balloon flights [20].

The recently discovered phenomenon of long-lasting TGEs [21] gives additional clues to understanding embedded charged structures in thunderclouds. With numerous observations of TGEs in the 2017–2018 seasons and incorporated appropriate Monte Carlo simulations, we will demonstrate how intracloud electric fields originate the particle fluxes that continue for hours.

## II. DISTURBANCES OF THE NEAR-SURFACE ELECTRIC FIELD DURING TGES

The spring season on Aragats usually continues from April to middle of May. It is characterized by low-lying clouds (25–100 m); high relative humidity (RH) of 95%–98%; large disturbances of the near-surface electric field

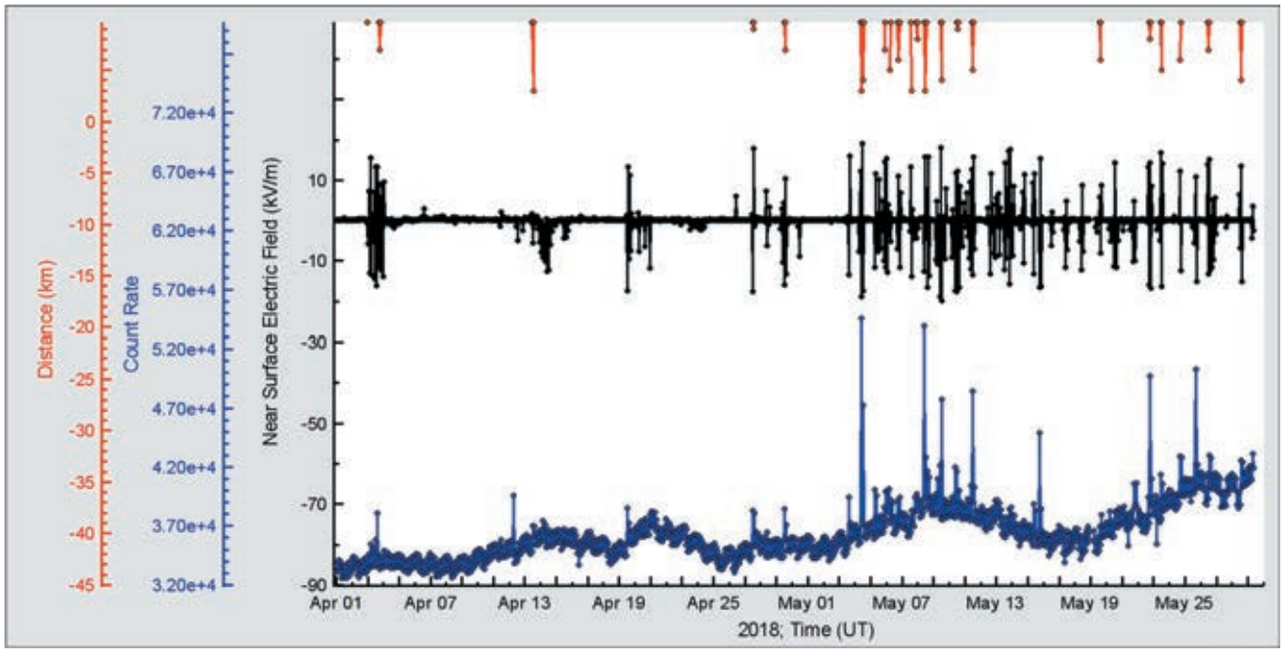


FIG. 2. At the top, vertical lines show the distance to lightning flash; in the middle, we show near-surface electric field disturbances measured by EFM-100 electric mill; at the bottom, one-minute time series of 1-cm-thick 1 $m^2$-area outdoor plastic scintillator located outdoor nearby MAKET experimental hall.

(sometimes dropping into the negative region down to $-30$ kV/m for several minutes); intense lightning activity (approaching the station for a few kilometers), and numerous TGEs—see Fig. 2. Large TGEs occurred usually when the outside temperature was in the range from $-2$ to $+2$ C° degrees.

In Fig. 2, we see that TGE activity peaked in the first days of May, providing multiple episodes of large fluxes of electrons and gamma rays. The mean count rate of the outdoor scintillator is increasing in May due to melting of the snow covering it in winter months (mean count rate is also dependent on the atmospheric pressure).

On May 22, 2018, thunderclouds approached the borders of Armenia, moving as usual from the Armenian highlands into Turkey. In Fig. 3, we show the approaching front of the storm as mapped by atmospheric discharges registered by the Boltek StormTracker lightning detector. At 16:00, the electrified clouds reached the Aragats mountain environment, inducing large disturbances of the near-surface electric field accompanied with lightning flashes; see Fig. 4.

In Fig. 4, we show the typical spring TGE with several maxima of high-energy particle (HEP) emissions, coinciding, as a rule, with the episodes when the near-surface electric field dropped into the deep negative region for at least several minutes. The emerging structures in the measured time series of the near-surface electrostatic field posted in the middle of Fig. 4 are reflecting the complicated structure of charged layers in the thundercloud. We speculate that when the mature LPCR arrives (or emerges) above the detector location, the strength of the electric field in the lower dipole reaches the "runaway" threshold, and an unleashed electron-photon avalanche provides the maximum flux of TGEs. The intensity of the particle flux reaches the maximum if the LPCR is above the detector; when the cloud moves away from the detector site, the TGE declines.

In Fig. 4, along with the disturbances of the electric field, we also show the time-series of count rates of large NaI crystals. After the peak, the prolonged tail of the TGE is comprised of the low-energy gamma rays (with max energy 3 MeV or less). The NaI spectrometers have energy threshold of $\approx$0.3 MeV, besides the fifth one, whose threshold is $\approx$3 MeV. Thus, spectrometers with a higher-energy threshold register only peaks of TGE; they do not detect the long-lasting "pedestal" which comprises the low-energy particles.

At 20:15–22:15, without noticeable disturbances of the near-surface electric field, the NaI crystals continue to register decaying gamma ray flux. To gain insight into these two modes of the cloud radiation, we look at the electric field disturbances in more detail.

In Fig. 5, we show a zoomed version of the near surface electric field along with the count rate of the 1-cm-thick outdoor plastic scintillator (rather good coinciding with count rate of the NaI network), outside temperature, dew point, and relative humidity. From the picture, it is apparent that the most important feature, which is responsible for the particle burst, is the sufficiently long time period during which the near surface electric field remains

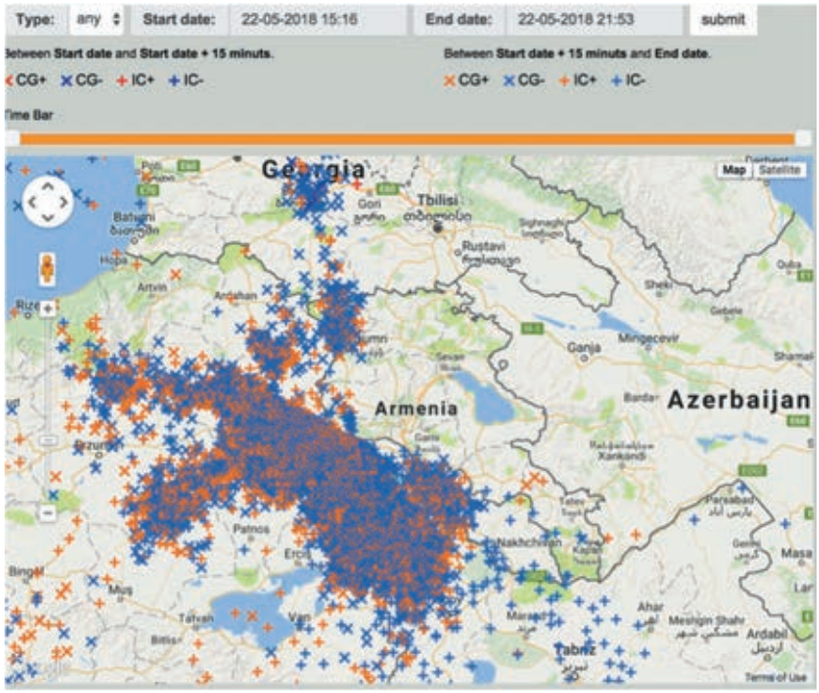


FIG. 3. The Google Map with lightning flashes shows the thunderstorm of May 22, 2018, approaching Armenia.

in the deep negative domain ($\approx -15$ kV/m). We measure the peak significance in the units of relative enhancement (percent) and in numbers of standard deviations from the mean value measured before the TGE started (critical value of the peak significance test, N$\sigma$). The critical value (and corresponding p-value—integral of probability density distribution from the critical value to infinity) is the most comprehensive estimate of the reliability of detecting

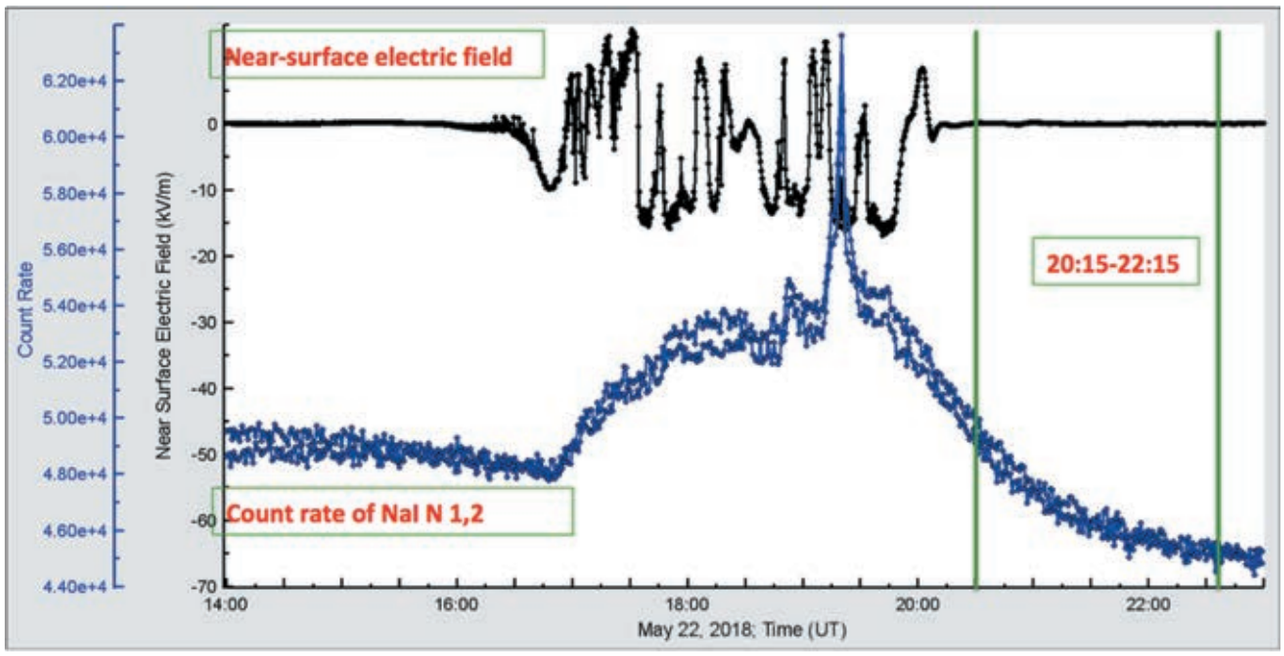


FIG. 4. LL TGE lasting approximately from 17:00 to 22:15; at the top, disturbances of the near-surface electric field measured by the EFM-100 electric mill located on the roof of MAKET experimental hall; at the bottom, one-minute time series of the NaI network's spectrometers N 1 and 2 (energy threshold 0.3 MeV). The inset shows time series of NaI N5 spectrometer (energy threshold 3 MeV).

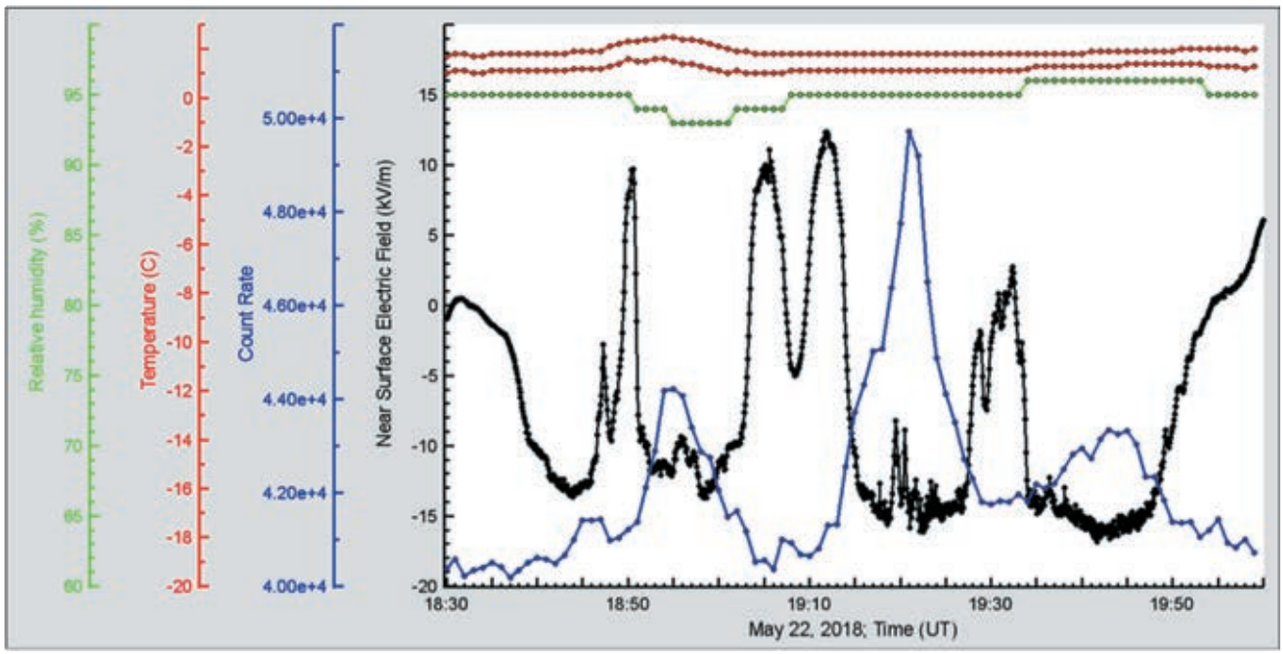


FIG. 5. Triple peak structure of HEP TGE: in the top outside temperature, dew point, and relative humidity.

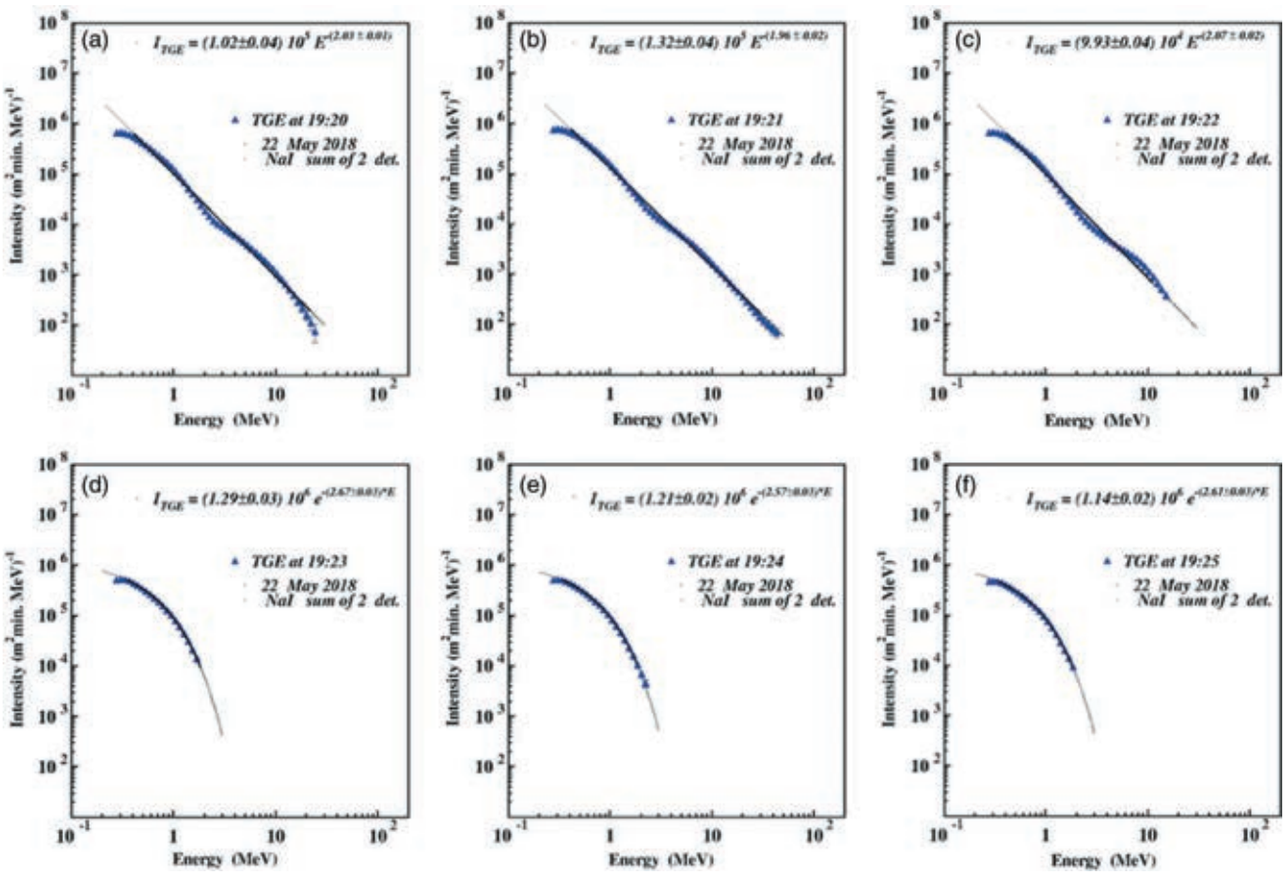


FIG. 6. The differential energy spectra of TGE particles registered by NaI network (N 1 and N 2 spectrometers); minutes 19:20–19:26.

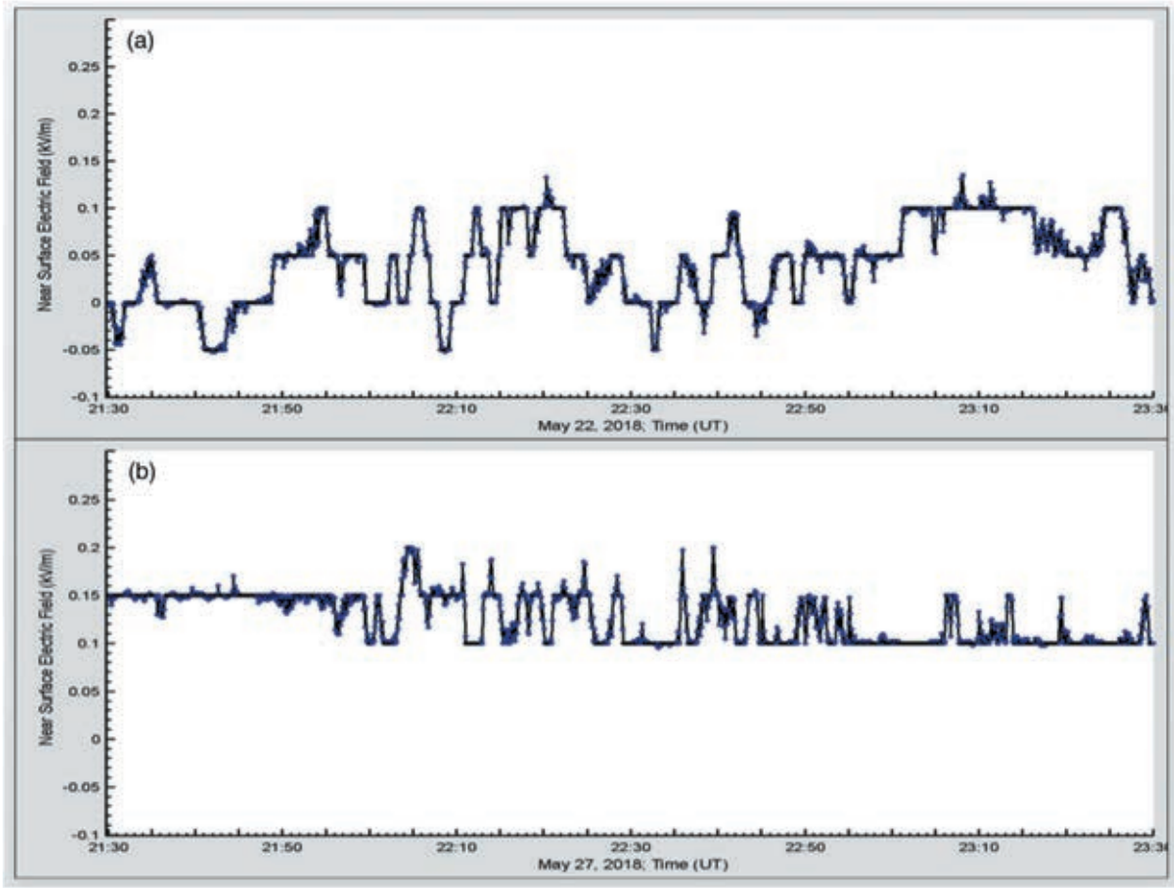


FIG. 7. The disturbances of near-surface electric field measured by EFM-100 electric mills with a sampling rate of 1 Hz on Aragats during LL TGE (6a), and during fair weather (6b).

peaks in the time-series. Large critical values correspond to small probabilities that the observed peak is a background fluctuation and not a genuine peak (TGE). Therefore, we can safely reject the null hypothesis (background fluctuation) and confirm the TGE. Very large critical values not only prove the unambiguous existence of a particle flux from the cloud but also serve as a comparative measure of the TGE observations using different detectors. During first peak (significance $\approx 13\%/13\sigma$), near-surface field values were below $-10$ kV/m at 18:52–19:01, 9 min; during middle largest peak (significance $\approx 30\%/30\sigma$) at 19:15–19:28, 13 min; for the third peak (significance $\approx 12\%/12\sigma$) at 19:34–19:49, 15 min. These extended periods of negative field were accompanied by small outbursts with field strength of several kV/m. We speculate that these outbursts are possibly connected with the LPCR emergence. However, outbursts are small and, therefore, the LPCR is not mature. The location of the cloud base estimated by the, so-called, "spread" parameter [22] is ≈100 m.; the relative humidity is ≈95%; the maximal count rate measured by the 1-cm-thick and 1 $m^2$ area outdoor plastic scintillator reaches 50,000 per minute.

For understanding the relation between HEP bursts and long-lasting, low-energy emissions, we measure differential energy spectra during full duration of the TGE. In Fig. 6, we show the energy spectra of the LL TGE. To obtain a pure TGE signal, the cosmic ray background (containing muons, neutrons, and other energetic particles) measured at fair weather just before TGE should be bin-by-bin extracted from the histogram containing both background and additional counts from the avalanches initiated in the thundercloud. After background extraction, the histogram is fitted by an analytical distribution function (usually power law or exponential). For the recovery of the differential energy spectra measured by the NaI network, the spectrometer response function was calculated with the CERN GEANT package.

The sizeable intensity TGE was observed during 3 minutes (19:20–19-22). At the beginning [Fig. 6(a)] and in the end [Fig. 6(c)] of the high-energy TGE, the maximal energy of the flux reached 20 MeV and, at the minute of maximal flux [Fig. 6(b)], −40 MeV. The particle flux was well approximated by the power law dependence with spectral index $\approx -2$. After fading of the high-energy particle, the shape of the flux spectrum abruptly changed to

exponential dependence with maximal energy not exceeding 3 MeV. Such an abrupt change of the flux shape spectrum and maximal energy can be connected with transient structure in the intracloud electric field. We associate it with the lower positively charged region, which significantly enhanced the total flux in the cloud for a few minutes. The charge and size of the main negatively charged region in the middle of the cloud is at least an order of magnitude larger than the charge and size of the LPCR. Thus, for a few minutes when the LCPR develops, the field in the cloud exceeds the runaway threshold, and the electrons which enter this enhanced field region are accelerated and multiplied, producing the TGE on Earth's surface. As the cloud is rather high (≈100 m), due to the attenuation of particle flux in the air, the significance of the TGE does not exceed ≈**30**% corresponding to ≈30 standard deviations.

As we can see in Figs. 4 and 6, the gamma ray flux is lasting for hours after the disturbance of the near-surface electric field calms down. To check the exact pattern of electric field fluctuations, we compare the electric field measured by electric mill EFM-100 just after TGE and at the same time during a fair weather period. In Fig. 7(a), we can see that the disturbances measured by the electric mill during TGE are not very large, but not negligible, and have excursions to the negative domain. For the fair weather, the field value never goes below 0.1 kV/m, and variance is much smaller [Fig. 7(b)]. For the post-TGE electric field, the near-surface electric field values differ from the expected value of ∼140 V/m typical for the fair weather [Fig. 7(b)]. The electric field strength difference of the fair weather and post-TGE electric field is 0.9 kV/m. In the next section, we will analyze small disturbances of the near-surface electric field, which accompany the small TGE events.

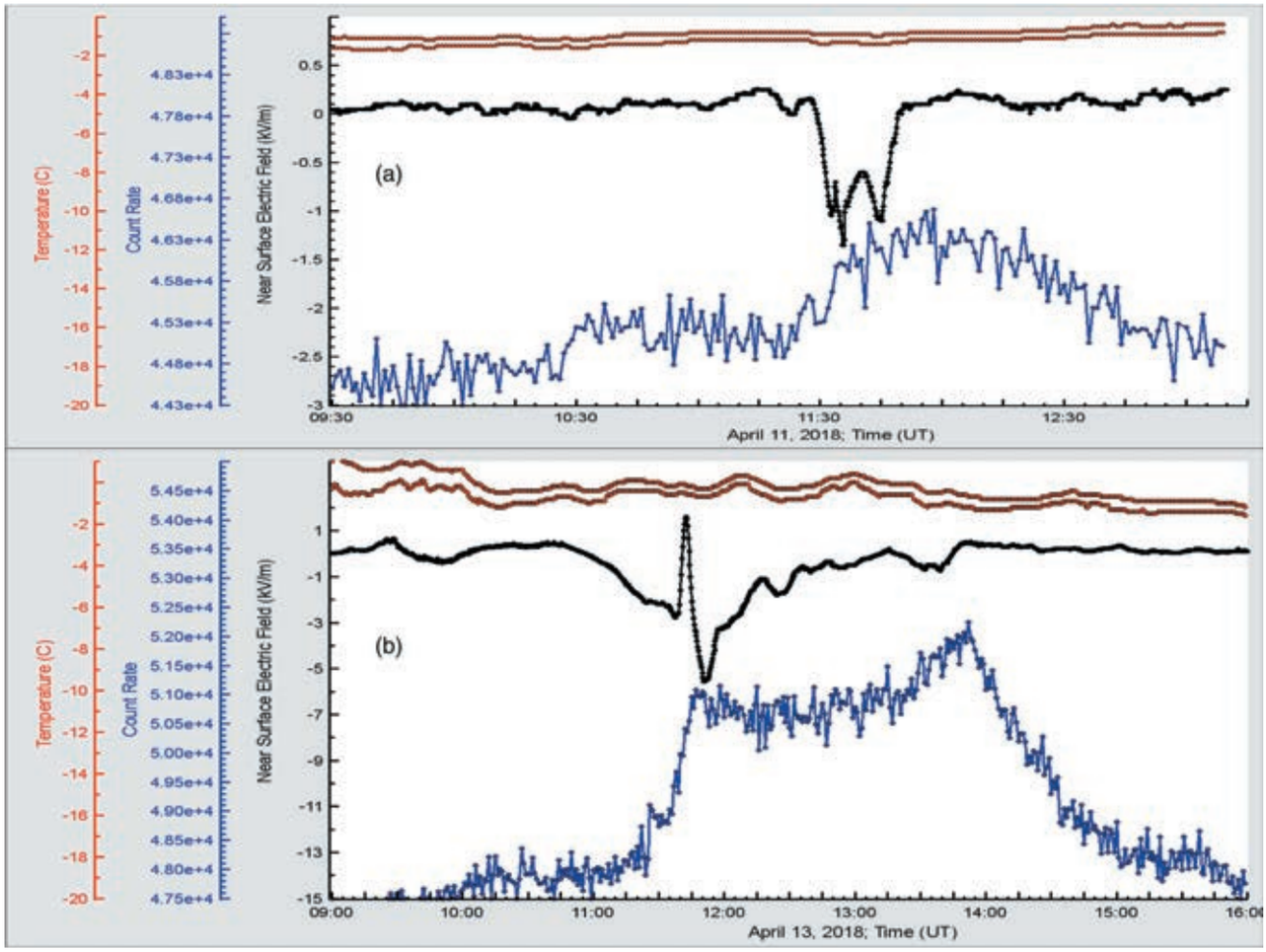


FIG. 8. Small TGEs observed in April 2018. At the top of each frame, we show outside temperature and dew point; in the middle, disturbances of the near-surface electric field; at the bottom, one-min count rate measured by the NaI crystal (energy threshold—0.3 MeV).

## III. LOW-ENERGY LONG-LASTING GAMMA RAY FLUXES FROM THUNDERCLOUDS

In the previous section, we outlined some specific characteristics of the field disturbance pattern that are supporting TGEs. The TGE observed in the low-energy particle flux is very different from the one observed in the high-energy flux. The high-energy particles (HEP) come from RB/RRE avalanches unleashed above the detector site; particles are accelerated in the lower dipole of the cloud formed by the main negative layer and emerged LPCR. As we have seen in the previous section, the necessary conditions for the high-energy particle bursts are the deeply negative near-surface electric field and the closeness of the cloud base to the Earth's surface. During the high-energy phase of TGEs, the amplitude of disturbances of the near-surface electric field can reach 60–70 kV/m. However, we observe also the TGE events not connected with large disturbances of the electric field and lightning activity. Both the amplitude of disturbances and the significance of peaks are much smaller compared with TGEs containing HEP. In Fig. 8, we show two such events that occurred in April 2018.

Estimated parameters for the April 11 event [Fig. 8(a)] are the following:

(i) Duration of TGE: 11:25–12:45, 80 min;
(ii) Duration of field disturbances 11:32–11:46, 13 min;
(iii) Estimate of the height of cloud base: $(-0.8\text{–}1.2)\,\mathrm{C}^\circ * 122\ \mathrm{m} \approx 50\ \mathrm{m}$
(iv) Relative humidity (RH) ~97%;
(v) TGE significance (NaI crystal)–4.8% (10.4$\sigma$).

TGE observed two days later was more prolonged and larger:

(i) Estimated parameters for April 13 event [Fig. 8(a)] are as following:
(ii) Duration of TGE: 11:25–12:45, 80 min;
(iii) Duration of field disturbances 11:32–11:46, 13 min;
(iv) Estimate of the height of cloud base: $(-0.8\text{–}1.2)\,\mathrm{C}^\circ * 122\ \mathrm{m} \approx 50\ \mathrm{m}$
(v) Relative humidity (RH) ~97%;
(vi) TGE significance (NaI crystal) −4.8% (10.4$\sigma$).

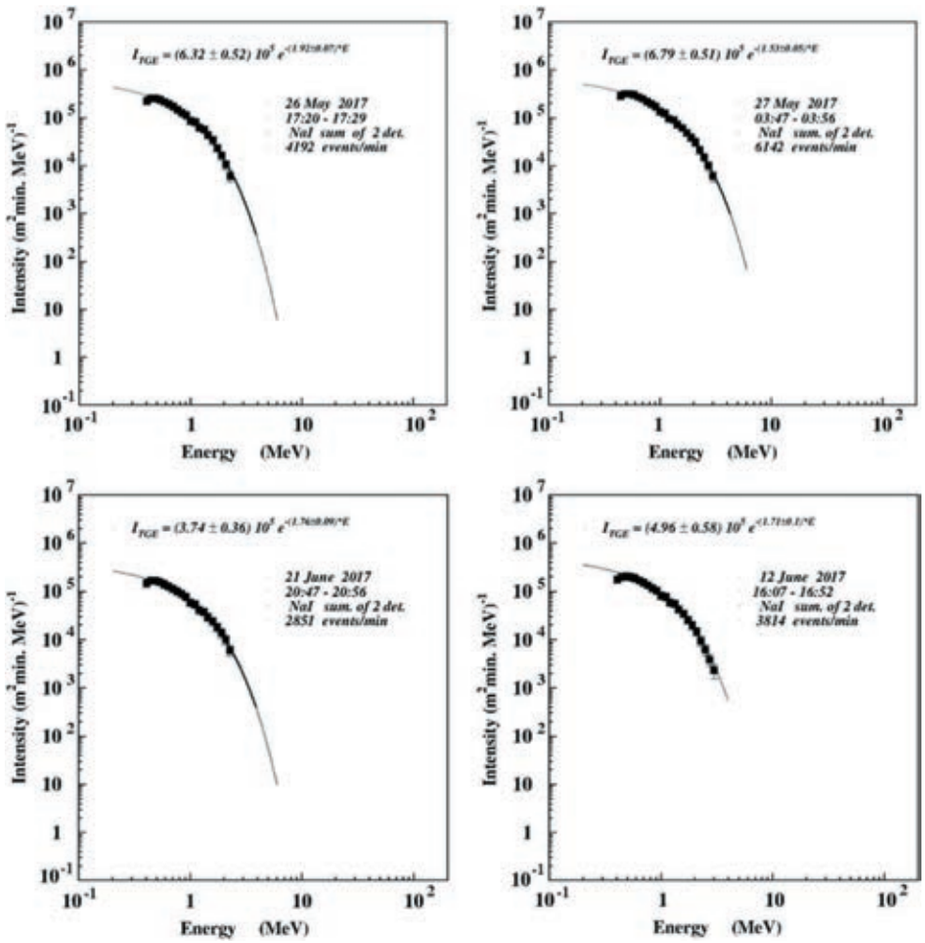


FIG. 9. Energy spectra of the TGE events coinciding with small disturbances of the near-surface electric field (possibly pure MOS process).

Neither TGE observed in April 2018 contained HEP or was accompanied by lightning activity.

Thus, there are two independent processes related to the particle fluxes from the thundercloud: the intense burst of particles from RB/RRE avalanches connected with LPCR development and prolonged low-energy gamma ray flux due to a MOS process [11]. The first one operates between the main negative charged layer and the LPCR; the second operates between the same main negative charged layer and the positive charge in the ground induced by the main negative charge. Thus, radiation processes in the clouds are not only connected with avalanches unleashing in the presence of the electric field above a threshold. Weak electric fields well below the RB/RREA initiation threshold also enhance gamma ray fluxes, although much less intensely than those with RB/RREA. Such small events can be fitted by a simple exponential dependence, with index varying from 1.5 to 1.9; see Fig. 9.

## IV. TGES AND LIGHTNING FLASHES

In Fig. 10, we show the TGE observed by the one-cm-thick, one-$m^2$ area outdoor plastic scintillator on May 6, 2017. At 12:35, the electric field fell into the deep negative domain and remained there for ~12 minutes. Thus, a lower dipole was formed and started to accelerate electrons downwards in the direction of the Earth. On the Earth's surface, all particle detectors register sizable TGE (the peak p-value for 1-minute count rate detected by 1 $m^2$ area plastic scintillator was $\sim 50\sigma$). Two lightning flashes terminated the particle flux at 12:42:22 count rate drops from 665 to 547 in two s and at 12:47:38 from 664 to 490 in 4 s. Both flashes were identified as a negative cloud-to-ground (CG) (see Fig. 12 and explanation in the text below). Thus, negative CG lightning partially destroyed the lower dipole; however, it was recovered in a few seconds, and the TGE was reestablished two times in five minutes.

In Fig. 11, we show the differential energy spectra as one-minute histograms slices. The arrows denote lightning flashes. Each time after lightning, the high-energy portion of the TGE is declined. Thus, the lightning flash decreases the strength of the electric field in the lower dipole and electrons cannot "run away" anymore and accelerate to tens of MeV. However, the electric field in the cloud is still sizable to enhance gamma ray radiation by the MOS process.

Electromagnetic emission produced by two mentioned lightning flashes was detected by a fast wideband (50 Hz to 12 MHz) electric field measurement system. We used a 52-cm-diameter circular flat-plate antenna followed by a passive integrator (decay time constant = 3 ms), the output of which was connected via a 60-cm double-shielded coaxial cable to a Picoscope 5244B digitizing oscilloscope. The sample interval of the oscilloscope was 40 ns, and the recorded length was 1 s. The oscilloscope was triggered by the signal from a commercial MFJ-1022 active whip antenna that covers a frequency range of 300 kHz to 200 MHz.

The fast electric field record of the first flash that occurred at 12:42:23.501 shows characteristic return stroke (RS) signatures, which are indicative of–CGs (Fig. 12).

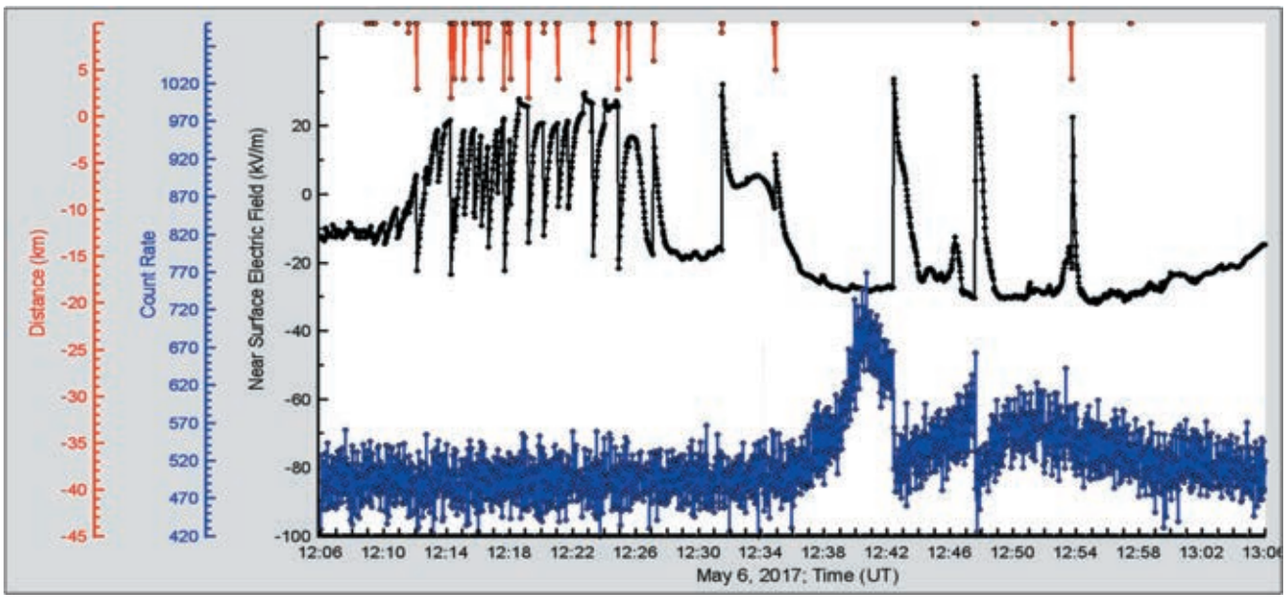


FIG. 10. From top to bottom: distance to lightning flash; disturbances of near surface electric field; one-second time series measured by 1-cm-thick outdoor plastic scintillator (energy threshold 0.7 MeV).

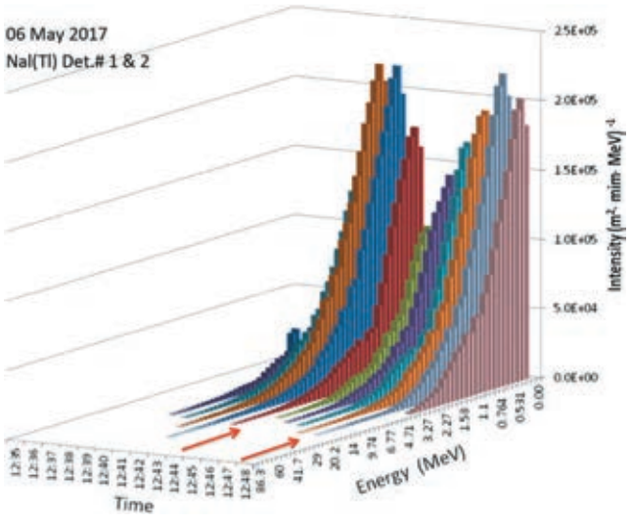


FIG. 11. The differential energy spectra measured by the NaI crystals minute-by-minute during TGE. By red arrows are denoted lightning flashes terminated high-energy particle flux.

Two RS pulses are observed at 177.6 ms and 210.8 ms after the trigger. The fast electric field record of the second flash that occurred at 12:47:36.302 also shows characteristic return stroke (RS) signatures, which are indicative of CGs. Four RS pulses are observed at 462.7 ms, 474.2 ms, 587.1 ms, and 787.6 ms after trigger; see Fig. 12.

## V. MONTE CARLO SIMULATION OF PARTICLE PROPAGATION IN THE INTRACLOUD ELECTRIC FIELD

In previous sections, we show that TGEs can last for many hours and comprise short high-energy bursts and extended lower-energy gamma ray flux. To check these findings, we performed simulations with CORSIKA and GEANT4 codes [23,24]. The theoretical bases of our simulation experiments are well-known processes of charged and neutral particle interactions with the terrestrial atmosphere and very simple models of cloud electrification. We assume the presence of the positive electric field of

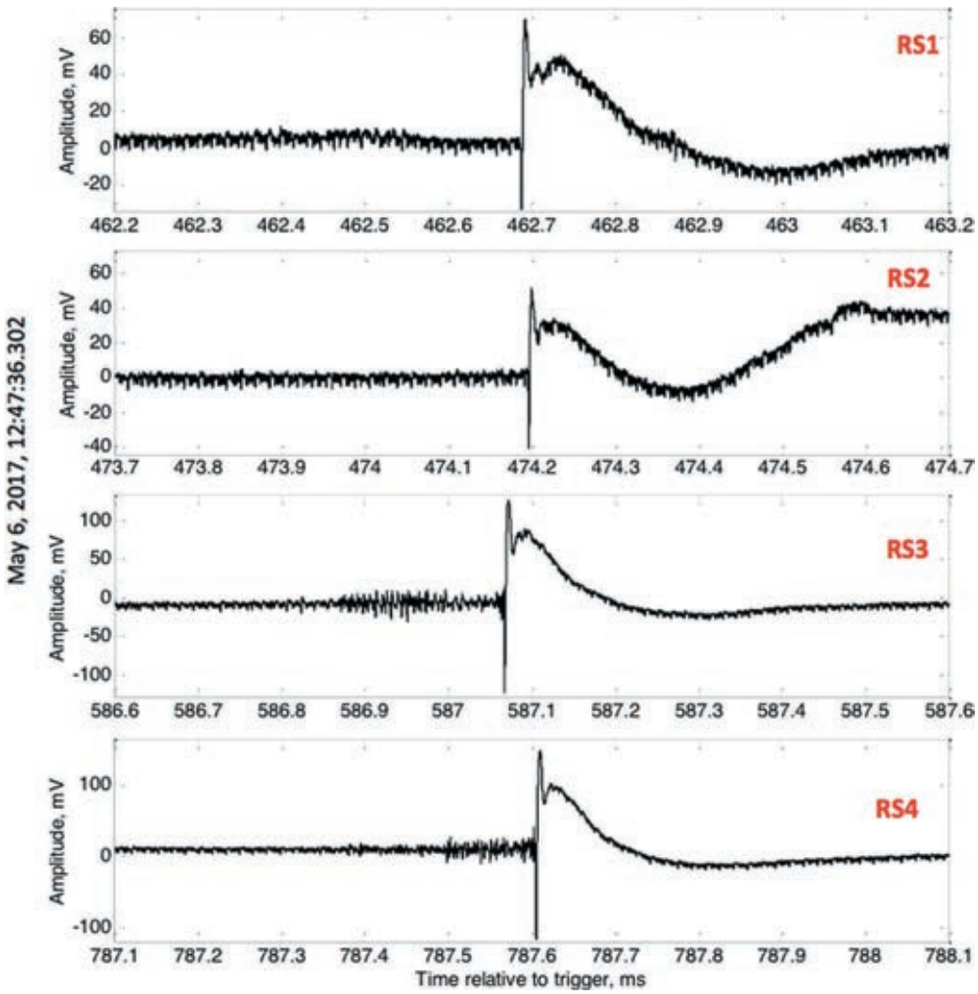


FIG. 12. Four RS pulses are observed at 462.7 ms, 474.2 ms, 587.1 ms, and 787.6 ms after trigger at 12:47:36/302.

different strength and spatial extent in the lower part of the cloud; the cloud base height was selected according to measurements on Aragats. Each simulation trial consists of $10^8$ vertical gamma ray and electron showers with energies in the interval 1–100 MeV. The differential energy spectrum of gamma rays from the ambient population of cosmic rays follows the power law with spectral index $\gamma = -1.42$ (on the heights 4–5 km). We follow the cascade particles till their energy is above the energy cutoff of E = 0.05 MeV. The observation level $H_{obs} = 3200$ m above sea level is the Aragats research station elevation. In Fig. 13, we show the dependence of enhanced particle flux on the strength of the electric field in the cloud changing from 0.1 to 1, 8 kV/cm. The spatial extent of the electric field was 1 km, and the height of the cloud base above the detectors was 50 m; see Fig. 1 for the arrangement of simulations.

In Fig. 13, we can see that although particle flux is dramatically enhanced by reaching the RB/RREA threshold (≈1.8 kV/m on 4000 m height above sea level), the enhanced particle fluxes are nonetheless also evident for smaller electric fields. We assume that these electric fields originate in the cloud below the main negatively charged layer and extend to Earth's surface. Starting from the lowest tested field of 0.1 kV/m, we can see small enhancements of particle flux in good agreement with observations. Thus, the low electric fields in the atmosphere above the detector site can explain prolonged gamma radiation after the high-energy phase of TGE.

Another possible explanation of the long-lasting gamma ray flux is the detection of Compton-scattered gamma rays from the remote RB/RRE avalanches. According to our views, the RB/RRE avalanches are continuously emerging in the different parts of the thundercloud filling it with radiation [25]. To test the possibility of detecting remote RRE avalanches, we investigate the radial distribution of the gamma ray flux originated from large TGE. Each simulation set consists of $10^8$ vertical gamma ray showers initiated by particles with energies in the interval 1–100 MeV (the differential energy spectrum was a power law, spectral index $\gamma = -3$), leaving the cloud on different heights above Earth's surface. The particles were followed until $H_{obs} = 3200$ m above sea level. The secondary particle energy cut was E = 0.05 MeV; the lowest energy threshold of particle detectors operated on Aragats was 0.3 MeV. The cloud was located at four different heights: H = 50 m, 200 m, 400 m, and 1000 m above the observation level. In Fig. 14, we show the lateral distribution of gamma rays with energies above 0.3 MeV born in the cascade initiated by gamma rays leaving the thundercloud at different heights above the particle detectors.

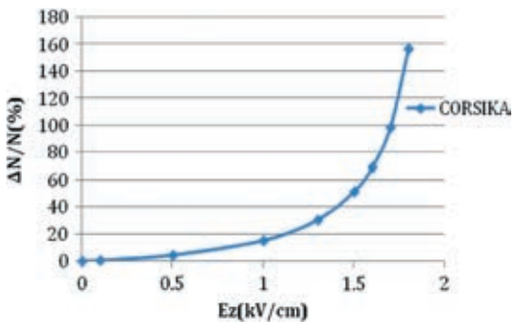


FIG. 13. Dependence of particle flux on the strength of the 1 km extended intracloud electric field.

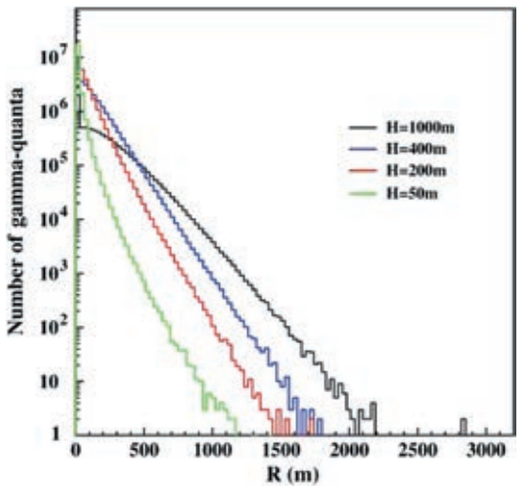


FIG. 14. Lateral distributions of gamma rays leaving thundercloud on different heights above the surface (located at 3200 m above sea level).

In Fig. 14, we can see that scattered gamma rays from RRE avalanches can barely contribute to particle flux on distances larger than 1 km. Furthermore, as we see in Fig. 15, the zenith angle distribution for such gamma rays peaked on very large angles, making registration of gamma

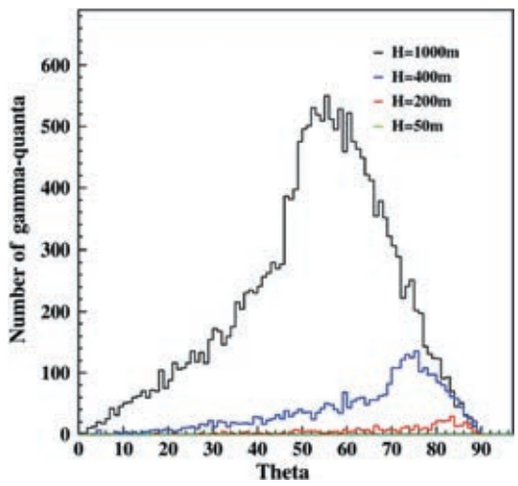


FIG. 15. Angular distributions of secondary gamma-quanta at distances R > 1000 m from the shower core.

rays with stacked horizontal particle detectors very problematic.

## VI. VALIDATION OF MC SIMULATIONS

After verification of the simulation results performed by using different MC programs with the same parameters (we use CORSIKA and GEANT4 codes), the most important issue is the model validation, i.e., checking if the models used do more or less precisely describe the nature. The MC simulations described in the previous section were validated with a TGE that occurred on May 30, 2018, one of the four largest TGEs observed on Aragats in the last decade; see Fig. 16.

On May 30, the outside temperature was 1.61 C°, dew point–0.86 C°; thus, the estimated height of the cloud base was ≈25 m. Very high humidity of 98% also confirms very low location of the cloud base. The huge single peak (peak value of particle flux 76,000 per m, per $m^2$, significance $\approx 78\%/126\sigma$) shown in Fig. 16 occurred during the time span when the field was mostly in the negative domain (≈25 m, from 1:15 to 1:40). However, during the 4 minutes coinciding with the particle outburst, the near-surface electric field abruptly increased and remained in the positive domain. In analogy with Fig. 5, where we show the May 22 TGE, we can assume that, during this 4 minutes, a very strong LPCR was just above the detector site, producing a large electric field in the lower dipole of the cloud. Thus, the strength of the electric field in the lower dipole for a few minutes exceeded the runaway threshold and, due to the low location of the cloud, a huge particle flux was registered.

The differential energy spectra of the May 30 TGE is posted in Fig. 17. Here, again, similar to the May 22 event (Fig. 6), we observe 3 minutes of HEP flux extrapolated with "broken" power law dependence. The power index for the low-energy (below 7–8 MeV) particle is very hard −1.2, changing after turnover to a very steep one of ≈ − 3. And, again, before [Fig. 17(a)] and after [Fig. 17(c)] the minute of maximal flux [Fig. 17(b)], we observe the maximal energy of 20 MeV, at maximal flux −40 MeV. The difference between the May 22 and May 30 TGEs is the size of the LPCR deduced from the amplitude of the positive field excursion during the deep negative near-surface electric field. We can assume that because the distance of the cloud base is very small (≈25 m) on May 30, compared with May 22 (≈100 m), the influence of the LCPR on the total near-surface electric field is much larger. Thus, we have on May 30 one of the largest TGEs ever detected, with much larger intensity and significance than the May 22 TGE. We can explain the broken power law dependence as being due to a larger-than-usual LPCR that produced multiple avalanches that reached the ground and were registered. Thus, very large intensity of the TGE at energies below 8 MeV changed to an abrupt decline at higher energies (we already observed such a behavior; see Fig. 4 of [18]); the cumulative differential energy spectra measured by the MCAL calorimeter onboard the AGILE satellite also demonstrated very steep turnover at high energies [26]. After the decline of the TGE caused by the

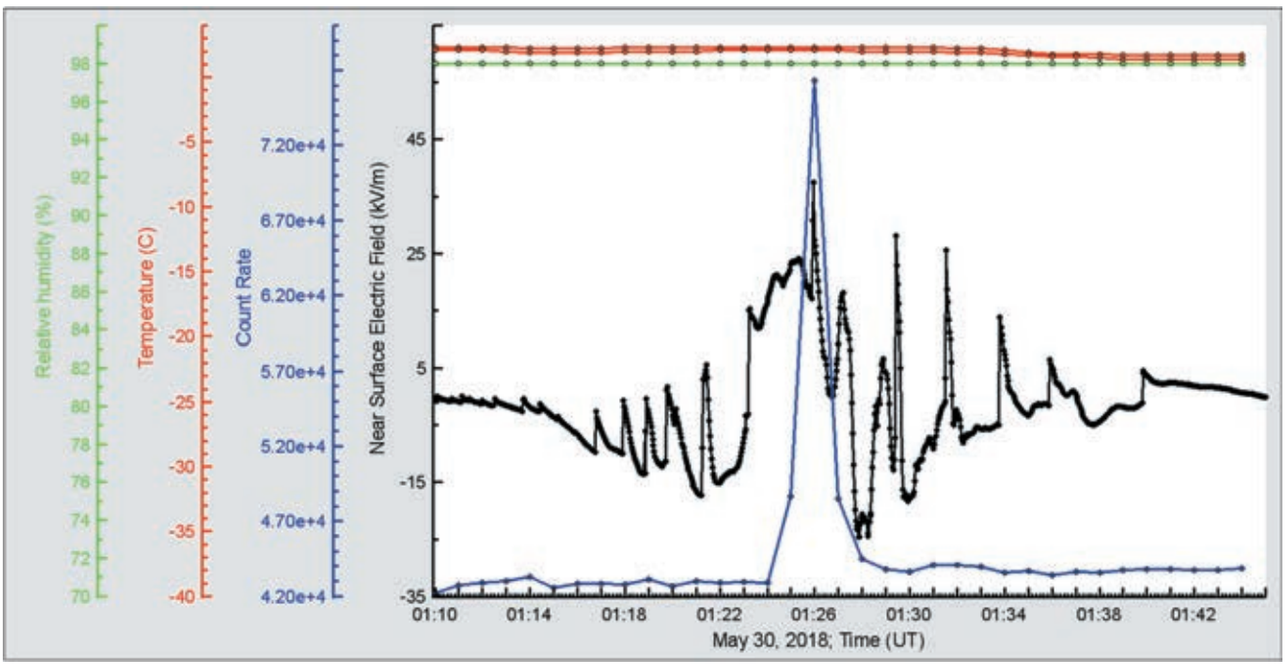


FIG. 16. Super-TGE occurred on May 30, 2018. At the top, outside temperature, dew point, and relative humidity and the middle disturbances of the near-surface electric field; at the bottom, 1-minute count rate of the 1-cmthick 1 $m^2$ -area outdoor plastic scintillator.

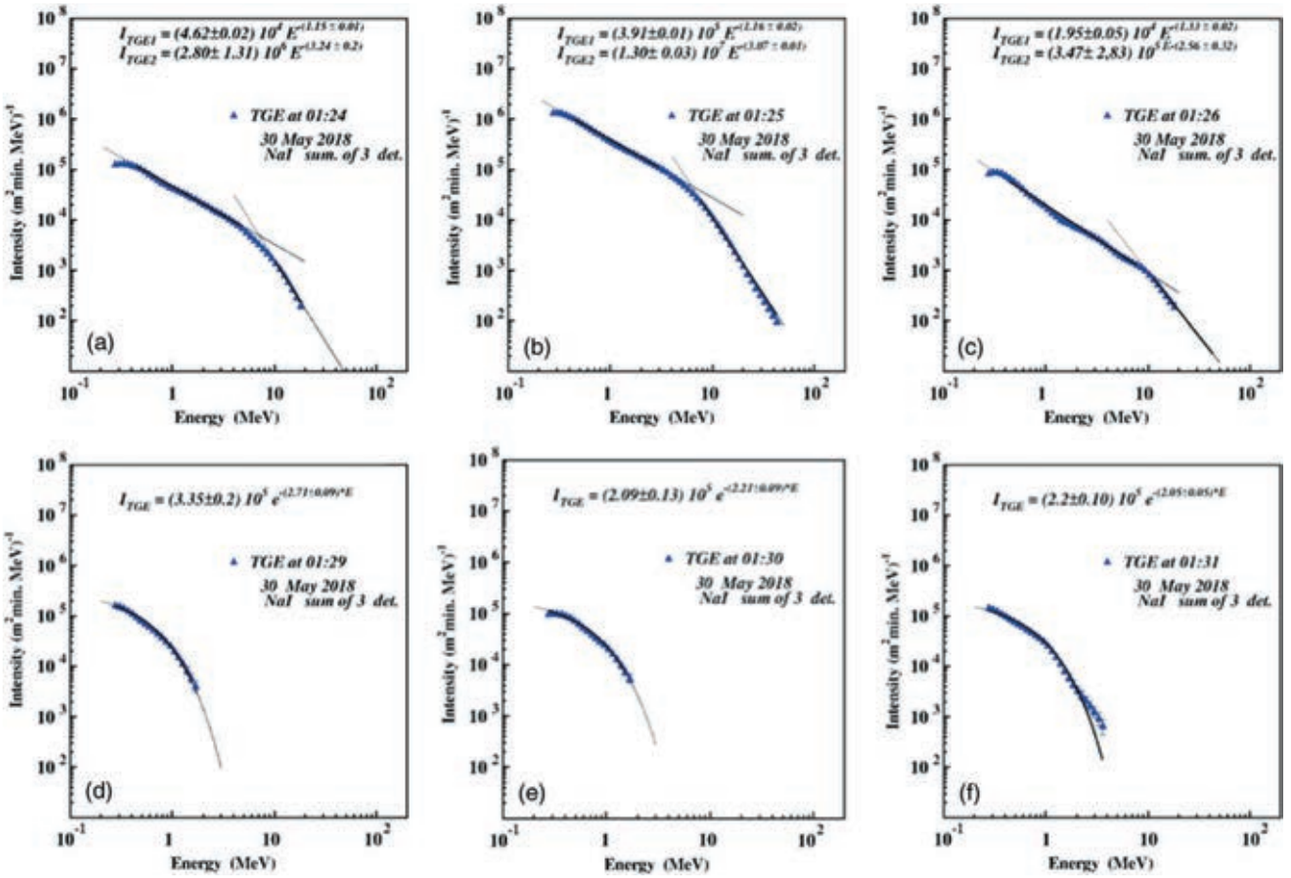


FIG. 17. The differential energy spectra of TGE particles registered by NaI network (N 1 and N 2 spectrometers); minutes 1:24–1:30.

near lightning flash, the particle flux continued for 1 hour with sizable count rate; however, the HEP particles disappeared [Figs. 6(d)–6(f)], the same as on May 22.

In Fig. 18, we show the differential energy spectra of the background gamma rays (obtained with WEB calculator PARMA/EXPACS, [27]), mostly originated from the interactions of the Galactic cosmic rays with the terrestrial atmosphere, and the spectrum measured by three large NaI crystals at 01:25 on May 30, 2018.

From the plots and from integral spectra shown in the left bottom corner, we see that overall TGE flux (mostly gamma rays with very small contamination of electrons) more than 2 times exceeds natural gamma radiation. Even after turnover (knee) at ≈8 MeV, TGE flux continues to exceed background until 20 MeV. Obtained integral spectra for 5 and 6 MeV thresholds well coincide with the fluxes observed by another particle detector—CUBE, supplied with veto effectively rejecting charged particles [28].

To gain insight into the size of the radiation-emitting region in the bottom of the cloud, we use measurements from the STAND1 particle detector network located on the

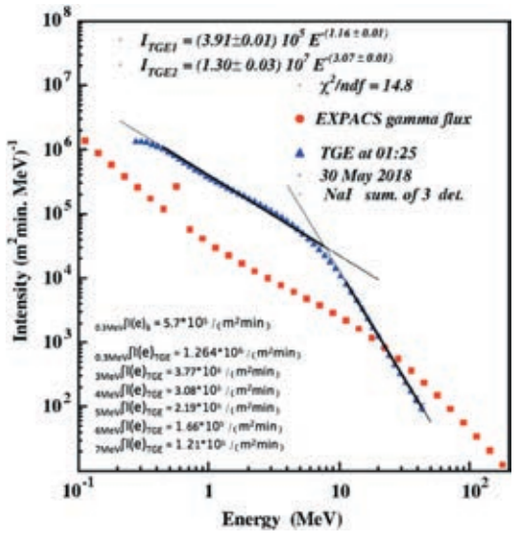


FIG. 18. Background spectrum and TGE spectrum observed on May 30, 2018. In the left bottom corner, values of integral spectrum calculated for different energy thresholds.

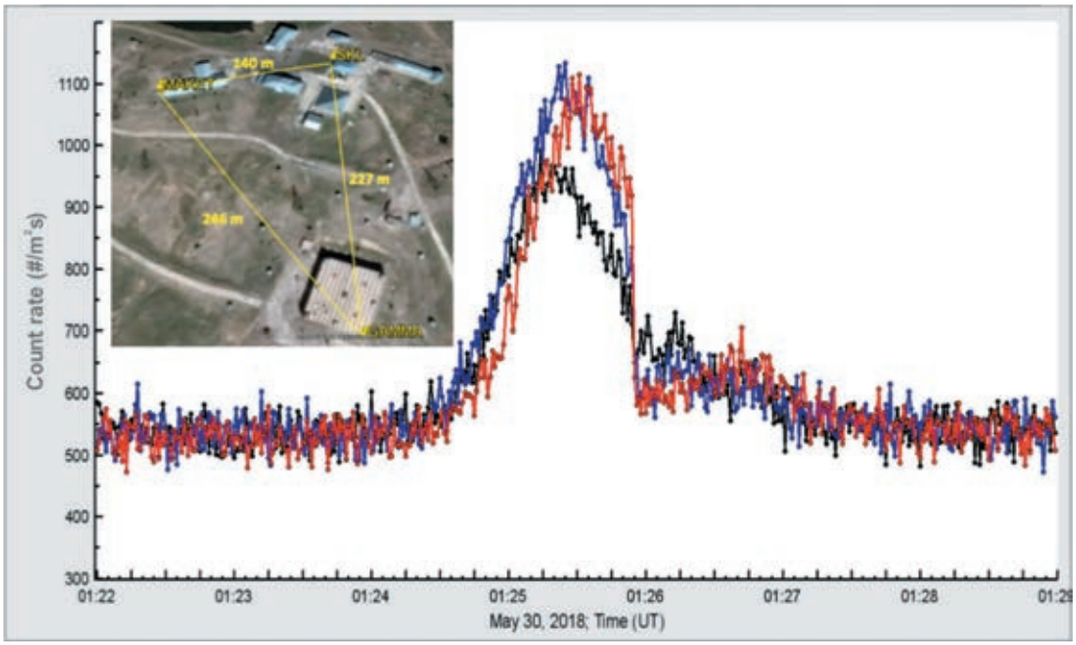


FIG. 19. One second time series of the STAND1 particle detector network count rates; in the inset, the map of detector units location.

Aragats station. In Fig. 19, we show the one-second time series of the May 30 TGE as measured by the three-cm-thick and one-$m^2$-area outdoor plastic scintillators. The detectors are arranged in a triangle with unequal sides as shown in the inset in Fig. 19. Usually, the TGE measured by all three detectors coincides very well, as shown in the patterns of the one-second count rates displayed in Fig. 19; thus, the size of the emitting region in the cloud is rather large, exceeding at least 100 m.

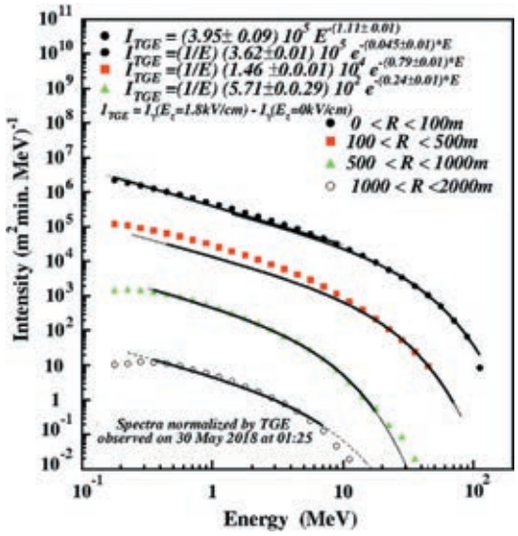


FIG. 20. Energy spectra of simulated TGE estimated by the particles fallen in the "rings" at different distances from the shower axes coincided with detector location site.

We use the recovered energy spectra at 1:25 on May 30 [Fig. 17(b)] for comparison and calibration of the simulated events containing high-energy particles. In Fig. 20, we present spectra of simulated events selected in different rings around the shower axes. We can see that, departing from the shower axes, the shape of the energy spectra become exponential and the maximal energy reduces in good agreement with observed energy spectra posted in Figs. 6, 9, and 17. We assume that when disturbances of the near-surface electric field calm down, but sizable flux of the TGE continues [see TGE intensities at 20:15–22:15, Fig 4. and Figs. 6(d)–(f) and 17(d)–(f)], the electric field originated by the transient LPCR fades, and we can detect only low-energy gamma rays according to the MOS process and large-angle Compton scattered gamma rays.

The comparisons with simulation for such a complicated scientific domain as atmospheric electricity can provide only quantitative results. We are not aware of the localization and strength of intracloud electric fields. In simulations, we use the simplest tripole model with a uniform electric field between layers. The nature is much more complicated; nonetheless, TGEs give us new types of information (intensities and shapes of the "thundercloud" particle spectra) that overall agree with simulations.

## VII. CONCLUSIONS

Observation of numerous TGEs by the Japanese, Chinese, and Slovakian groups [28–32] proves that RB/RREA and

MOS are robust and realistic mechanisms for electron acceleration and multiplication, confirming the correctness of the model of TGE initiation [5,13,33].

However, there are observations of the alternative source of thundercloud particles.

Physicists performing experiments at the Tien-Shan Mountain Cosmic Ray Station, Kazakhstan (altitude of 3340 m), reported the existence of high-energy emissions, i.e. the electron, gamma, and neutron fluxes that are directly from the lightning bolt [34]. Another observation of the lightning-induced gamma ray flux was reported by the group from the International Center for Lightning Research and Testing [35] in North Central Florida. The authors claimed the observation of very intensive gamma ray flux was associated with upward positive leaders approaching a negative charge region. The systematic research of the lightning-related x-ray radiation was made at the Lightning Observatory in Gainesville (LOG), Florida [36]. During a thunderstorm on February 6, 2017, in Japan, a $\gamma$-ray flash with duration of less than one millisecond was detected at monitoring sites 0.5–1.7 km away from the lightning. The subsequent $\gamma$-ray afterglow subsided quickly, with an exponential decay constant of 40–60 milliseconds, and was followed by prolonged line emission at about 0.511 MeV, which lasted for a minute [37]. Authors claimed conclusive evidence of positrons and neutrons being produced after the lightning. Few bursts of gamma ray showers have been observed coincident with downward-propagating negative leaders in lightning flashes by the Telescope Array Surface Detector [38]. The authors claimed that the observed energy deposit is consistent with forward-beamed showers of $10^{12}$–$10^{14}$ or more primary photons above 100 keV, distributed according to a RREA spectrum. However, no model was presented to justify such a huge number of high-energy particles associated with a lightning flash.

During numerous storms observed from 2016 to 2018, we did not observe on Aragats any lightning producing relativistic particles in any of the continuously monitoring detectors. However, we do not exclude that propagation of lightning leaders and emerging of strong electric fields around leader tips can produce x rays and additional seed electrons involved in a runaway process. More registered events associated with lightning flash are needed to make a realistic model of such an exotic phenomenon.

In the present paper, we scrutinize the TGE model and propose the structure of the electric field in the thunderstorm atmosphere that accelerates and multiplies electrons, resulting in the huge particle fluxes reaching the Earth's surface.

The new key evidence, namely, intensities and energy spectra of the TGEs, along with associated disturbances of the near-surface electric field and lightning flashes, allows us to develop the comprehensive model of electric fields in the thundercloud. Discovered in 2017, long-lasting TGEs prove that two independent mechanisms are responsible for bursts of high-energy particles and prolonged emissions of low-energy gamma rays.

HEP TGEs mostly occur when the near-surface electric field is in the deep negative domain and when the cloud base is 25–50 m above Earth's surface. The maximal energy of electrons in the RB/RREA avalanches can reach and exceed 40 MeV. Proof of the runaway process is the abrupt decline of the HEP bursts after the lightning flash, reestablished several seconds later when the electric field within the lower dipole again enhances the "runaway" threshold. Hours-long, low-energy gamma ray fluxes can be explained by the MOS process (modification of the cosmic ray electron energy spectra) in rather weak electric fields not triggering the RB/RREA process (low strength field originated between the main negative layer and its mirror on the Earth's surface).

LL TGEs start with small-intensity, low-energy gamma ray fluxes originated in weak electric fields between a mature main negative charge region in the middle of the cloud and its mirror on the Earth's surface. After several tens of minutes, or faster, with emerging of the LPCR above the detector site, the cumulative field surpasses the runaway threshold in the atmosphere, and the RB/REEA avalanches start in the cloud. If the cloud base is close to the Earth's surface (the case of Aragats storms in spring and autumn), TGE intensity can reach very high levels, exceeding the background radiation many times, and the maximal energy of the electrons and gamma rays reaches 40 MeV and more. Because the size of the LPCR is much smaller than the main negative region, the high-energy phase of the TGE is prolonged for only a few minutes, changing again to the low-energy gamma ray flux that can last for several hours.

The electron acceleration model based on the "classical" tripole charge structure of the thundercloud, which is used in our analysis [5,9,25], is the simplest one; however, we do not exclude more sophisticated scenarios of the electric field emergence in the thundercloud. Nearly (50%) of TGEs abruptly terminated by lightning flashes are associated not with cloud-to-ground but with normal-polarity intracloud flashes, signaling that charge of the main negative region is rather large and the lightning leader can make its path to the upper positively charged region. Another ≈20% of TGEs abruptly terminated by lightning flashes are associated with inverted-polarity intracloud flashes. Observation of the TGE-terminating inverted-polarity IC flash which occurs in the lower dipole proves that the downward electron-accelerating electric field is significantly enhanced by the field formed by the main negative charge in the cloud and the LPCR and, thus, enables the TGE development. The inverted-polarity IC flash reduces the main negative charge and, thus, leads to the reduction or elimination of this field inside the cloud. As a result, the TGE is abruptly terminated.

Numerous TGEs observed on Aragats and appropriate Monte Carlo simulations confirm our model; however, many questions remain unanswered, including

(i) The way of LPCR development;
(ii) The size and shape of the particle-emitting region;
(iii) The possible changes of radio emission patterns due to TGE propagation in the atmosphere [39];
(iv) The influence of remote lightning flashes on disturbances of the near-surface electric field;
(v) How the intracloud electric fields can be deduced from the ground-based measurements of the near-surface electric field.

*In situ* measurements of charge and field distribution in clouds by a Lightning Mapping Array (LMA) or interferometer facilities (operation on Aragats begins in 2018) will improve our understanding of cloud electrification.

## ACKNOWLEDGMENTS

The data for this paper are available via the multivariate visualization software ADEI on the web page of the Cosmic Ray Division (CRD) of the Yerevan Physics Institute, http://adei.crd.yerphi.am/adei. We thank the staff of the Aragats Space Environmental Center for the consistent operation of the Aragats research station facilities. We also thank E.Mareev and V.Rakov for useful discussions and appreciate the support of the Russian Science Foundation Grant (Project No. 17-12-01439).

[1] J. R. Dwyer, The initiation of lightning by runaway air breakdown, Geophys. Res. Lett. **32**, L20808 (2005).
[2] E. R. Williams, The tripole structure of thunderstorms, J. Geophys. Res. **94**, 13151 (1989).
[3] X. Qie, T. Zhang, C. Chen, G. Zhang, T. Zhang, and X. Kong, Electrical characteristics of thunderstorms in plateau regions of China, Atmos. Res. **91**, 244 (2009).
[4] A. Nag and V. Rakov, Some inferences on the role of lower positive charge region in facilitating different types of lightning, GRL **36**, L05815 (2009).
[5] A. Chilingarian and H. Mkrtchyan, Role of the lower positive charge region (LPCR) in initiation of the thunderstorm ground enhancements (TGEs), Phys. Rev. D **86**, 072003 (2012).
[6] A. Chilingarian, A. Daryan, K. Arakelyan, A. Hovhannisyan, B. Mailyan, L. Melkumyan, G. Hovsepyan, S. Chilingaryan, A. Reymers, and L. Vanyan, Ground-based observations of thunderstorm-correlated fluxes of high- energy electrons, gamma rays, and neutrons, Phys. Rev. D **82**, 043009 (2010).
[7] A. Chilingarian, G. Hovsepyan, and A. Hovhannisyan, Particle bursts from thunderclouds: Natural particle accelerators above our heads, Phys. Rev. D **83**, 062001 (2011).
[8] A. Chilingarian, Y. Khanikyants, E. Mareev, D. Pokhsraryan, V. A. Rakov, and S. Soghomonyan, Types of lightning discharges that abruptly terminate enhanced fluxes of energetic radiation and particles observed at ground level, J. Geophys. Res. Atmos. **122**, 7582 (2017).
[9] A. Chilingarian, G. Hovsepyan, and L. Vanyan, On the origin of the particle fluxes from the thunderclouds: Energy spectra analysis, Europhys. Lett. **106**, 59001 (2014).
[10] A. Chilingarian, B. Mailyan, and L. Vanyan, Observation of Thunderstorm Ground Enhancements with intense fluxes of high-energy electrons, Astropart. Phys. **48**, 1 (2013).
[11] A. Chilingarian, B. Mailyan, and L. Vanyan, Recovering of the energy spectra of electrons and gamma rays coming from the thunderclouds, Atmos. Res. **114–115**, 1 (2012).
[12] E. S. Cramer, B. G. Mailyan, S. Celestin,and J. R. Dwyer, A simulation study on the electric field spectral dependence of thunderstorm ground enhancements and gamma ray glows, J. Geophys. Res. Atmos. **122**, 4763 (2017).
[13] A. Chilingarian, Thunderstorm ground enhancements—Model and relation to lightning flashes, J. Atmos. Terr. Phys. **107**, 68 (2014).
[14] A. Chilingarian, G. Hovsepyan, Y. Khanikyanc, A. Reymers, and S. Soghomonyan, Lightning origination and thunderstorm ground enhancements terminated by the lightning flash, Europhys. Lett. **110**, 49001 (2015).
[15] A. V. Gurevich, G. M. Milikh, and R. A. Roussel-Dupre, Runaway electron mechanism of air breakdown and preconditioning during a thunderstorm., Phys. Lett. **165A**, 463 (1992).
[16] L. P. Babich, E. N. Donskoy, R. I. Il'kaev, I. M. Kutsyk, and R. A. Roussel-Dupre, Fundamental parameters of a relativistic runaway electron avalanche in air, Plasma Phys. Rep. **30**, 616 (2004).
[17] J. R. Dwyer, A fundamental limit on electric fields in air, Geophys. Res. Lett. **30**, 2055 (2003).
[18] A. Chilingarian, G. Hovsepyan, and L. Vanyan, On the origin of the particle fluxes from the thunderclouds: energy spectra analysis, Europhys. Lett. **106**, 59001 (2014).
[19] A. Chilingarian, G. Hovsepyan, and E. Mantasakanyan, Mount Aragats as a stable electron accelerator for atmospheric High-energy physics research, Phys. Rev. D **93**, 052006 (2016).
[20] T. C. Marshall, M. Stolzenburg, Paul R. Krehbiel *et al.*, Electrical evolution during the decay stage of New Mexico thunderstorms, J. Geophys. Res. **114**, D02209 (2009).
[21] A. Chilingarian, Long lasting low energy thunderstorm ground enhancements and possible Rn-222 daughter isotopes contamination, Phys. Rev. D **98**, 022007 (2018).
[22] A. Chilingarian, G. Hovsepyan, and B. Mailyan, In situ measurements of the runaway breakdown (RB) on Aragats mountain, Nucl. Instrum. Methods Phys. Res., Sect. A **874**, 19 (2017).

[23] D. Heck, J. Knapp, J. N. Capdevielle, G. Schatz, and T. Thouw, Report No. FZKA 6019, 1998, Forschungszentrum, Karlsruhe, https://www.ikp.kit.edu/corsika/70.php.
[24] S. Agostinelly, J. Allison, A. Amako *et al.* Geant4—a simulation toolkit, NIM **506**, 250 (2003).
[25] A. Chilingarian, S. Chilingaryan, T. Karapetyan, L. Kozliner, Y. Khanikyants, G. Hovsepyan, D. Pokhsraryan, and S. Soghomonyan, On the initiation of lightning in thunderclouds, Sci. Rep. **7**, 1371 (2017).
[26] M. Marisaldi, F. Fushino, M. Tavani *et al.*, Properties of terrestrial gamma ray flashes detected by AGILE MCAL below 30 MeV, J. Geophys. Res. Space Phys. **119**, 1337 (2014).
[27] T. Sato, Analytical Model for Estimating the Zenith Angle Dependence of Terrestrial Cosmic Ray Fluxes, PLoS One **11**: e0160390 (2016).
[28] T. Torii, T. Sugita, M. Kamogawa, Y. Watanabe, and K. Kusunoki, Migrating source of energetic radiation generated by thunderstorm activity. Geophys. Res. Lett. **38**, L24801 (2011).
[29] H. Tsuchiya, T. Enoto, K. Iwata *et al.*, Hardening and Termination of Long-Duration Gamma Rays Detected Prior to Lightning, Phys. Rev. Lett. **111**, 015001 (2013).
[30] Y. Kuroda, S. Oguri, Y. Kato, R. Nakata, Y. Inoue, C. Ito, and M. Minowa, Observation of gamma ray bursts at ground level under the thunderclouds, Phys. Lett. B **758**, 286 (2016).
[31] B. Bartoli, P. Bernardini, X. J. Bi *et al.*, Observation of the thunderstorm-related ground cosmic ray flux variations by ARGO-YBJ, Phys. Rev. D **97**, 042001 (2018).
[32] K. Kudela, J. Chum, M. Kollárik, R. Langer, I. Strhárský, and J. Baše, Correlations between secondary cosmic ray rates and strong electric fields at Lomnický štít, J. Geophys. Res. **122**, 10700 (2017).
[33] A. Chilingarian, Long lasting low energy thunderstorm ground enhancements and possible Rn-222 daughter isotopes contamination, Phys. Rev. D **98**, 022007 (2018).
[34] A. V. Gurevich, V. P. Antonova, A. P. Chubenko *et al.*, Strong Flux of Low-Energy Neutrons Produced by Thunderstorms, Phys. Rev. Lett. **108**, 125001 (2012).
[35] B. M. Hare, M. A. Uman, J. R. Dwyer *et al.*, Ground-level observation of a terrestrial gamma ray flash initiated by a triggered lightning, J. Geophys. Res. Atmos. **121**, 6511 (2016).
[36] S. Mallick, V. A. Rakov, and J. R. Dwyer, A study of X-ray emissions from thunderstorms with emphasis on subsequent strokes in natural lightning, J. Geophys. Res. **117**, D16107 (2012).
[37] T. Enoto, Y. Wada, Y. Furuta *et al.*, Photonuclear reactions triggered by lightning discharge, Nature (London) **551**, 481 (2017).
[38] R. U. Abassi, T. Aby-Zayyad, M. Allen *et al.*, Gamma-ray Showers Observed at Ground Level in Coincidence With Downward Lightning Leaders, JGR Atmosphere **123**, 6864 (2018).
[39] P. Schellart, T. N. G. Trinh, S. Buitink *et al.*, Probing Atmospheric Electric Fields in Thunderstorms through Radio Emission from Cosmic-Ray-Induced Air Showers., Phys. Rev. Lett. **114**, 165001 (2015).

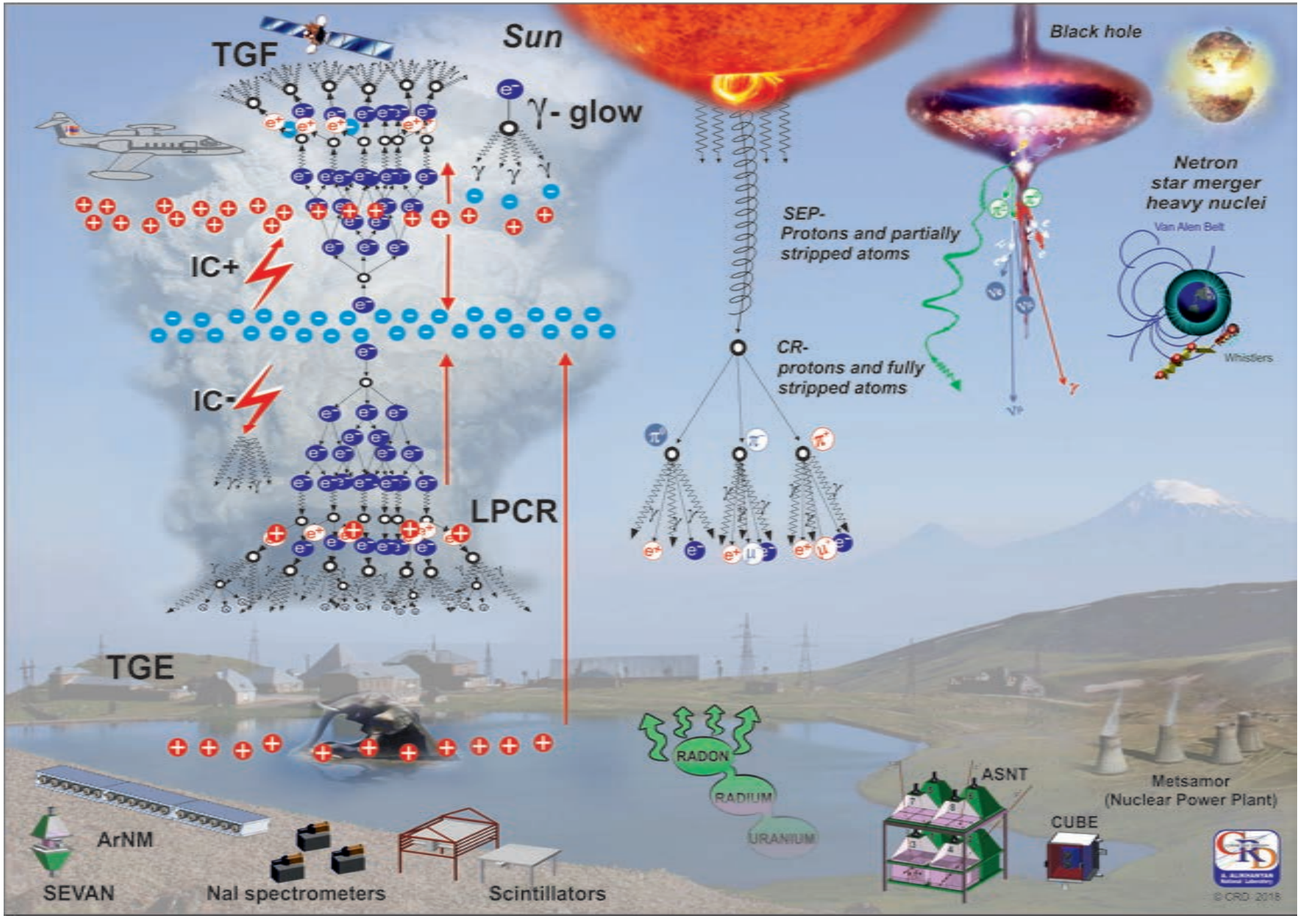
TGF
Sun
γ- glow
Black hole
Netron
star merger
heavy nuclei
Van Allen Belt
Whistlers
SEP-
Protons and partially
stripped atoms
CR-
protons and fully
stripped atoms
IC+
IC-
LPCR
TGE
RADON
RADIUM
URANIUM
ASNT
CUBE
Metsamor
(Nuclear Power Plant)
ArNM
SEVAN
NaI spectrometers
Scintillators
© CRD 2018

*First year on Aragats: horizontal Muon Spectrometer on Aragats, wire spark chambers, maximal detectable momentum, alignment. A. Chilingarian in 1971.*

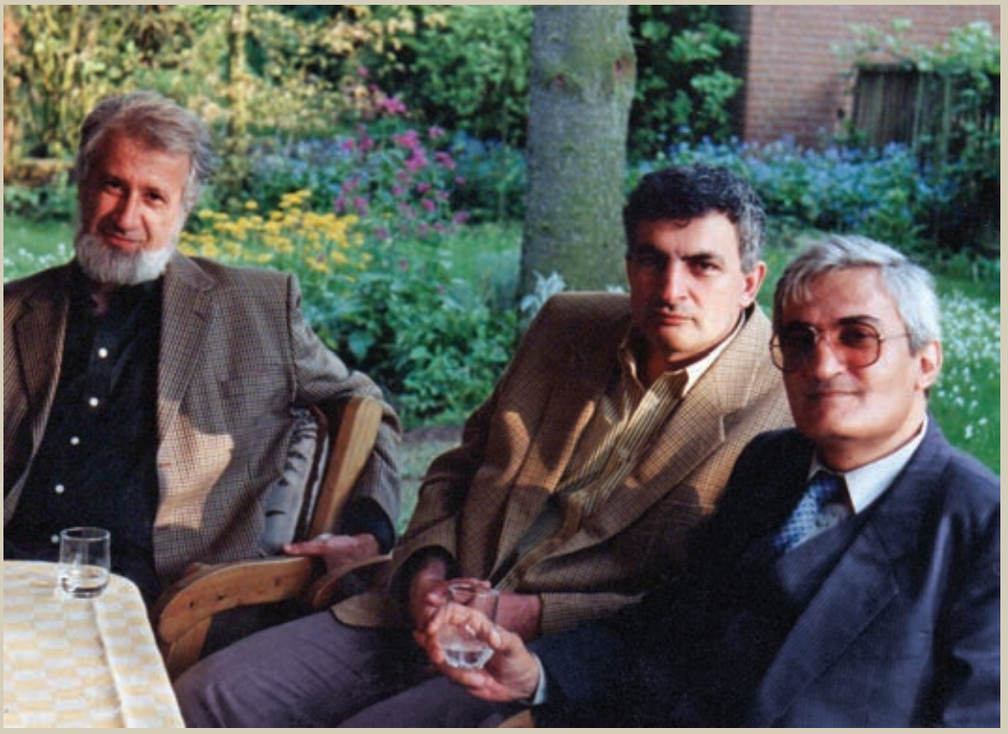

*Norik Akopov, Ashot Chilingaryan, Albert Avetisyan. Collaboration with DESY, 1997*

*Caro Lucas, professor of Tehran University and Ashot Chilingaryan. Armenian- Iranian meeting series on Neural Networks and Machine Learning, 1998.*


*Hrachik Torosyan, Yuri Oganessian, Ashot Chilingaryan and Nina Demechina visiting Aragats Research Station . Summer 1998.*


*2000, International Science Technology Center (ISTC) Headquarters, signing project agreement "Development of a Prototype Detector System for Space Weather Monitoring and Forecasting World-Wide Network" with Japanese partners (one of 5 ISTC projects wined by CRD)*

*Ashot Chilingaryan, Suren Chilingaryan, Ararat Vardanyan, Hartmut Gemmeke (Director of Institute of electronics and data analysis, HPE, Forschungszentrum Karlsruhe institute), collaborative visgarnit on development of the software for the neurochip SAND and machine learning algoritgaryahms, 2001.*

*Heinigerd Rebel (Director of Institute of Nuclear physics of IK3, Forschungszentrum Karlsruhe institute), Iliana Brancus (head of Romanian group) with Ashot Chilingaryan. workshop on KASCADE and ANI experiments. Nor Amberd, 2001.*

*A. Chilingaryan. Lecture for CRD students. January 1, 2001.*

*Attempts to bring Bessy-2 light source to Armenia from Berlin, visit to Aragats. May 15, 2001.*

*MAGIC collaboration meeting in Nor Amberd. May 15, 2001.*

*Looking with Nerses Gevorgyan on on famous Halloween events (October, 2003, violent bursts on the Sun precisely observed by the Aragats facilities)*


*Ashot Chilingaryan, Aram Yegikyan, Melanya Grigoryan, Nerses Gevorgyan, and Gayane Kostanyan, the team received the first award on World Summit on Information Society, Geneva, December 2003, as the world's best project in the category of e-science ("Data Visualization Interactive Network for the Aragats Space-environmental Center" – DVIN for ASEC).*

*Ashot Chilingaryan, Razmik Mirzoyan, Eckart Lorenz, Johannes Knapp, Heidelberg International Symposium on Gamma-Ray Astronomy, 2004*

*Delegation of US Armenians visiting CRD. Januay 2004.*

*Conference Solar Extreme Events; Ashot Chilingaryan, Nataniel Gopalswamy, Bagrat Mailyan and Armen Hohannisyan, Nor Amberd 2005.*

*Northern peak of Aragats, 2004*

*29th International Cosmic Ray Conference (ICRC 2005), Markus Roth, Ashot Chilingaryan, Gagik Hovsepyan, Andreas Haungs. 03-10 August, Puna, India.*

*Ashot Chilingaryan and Director of Nuclear Physics Institute of Bulgarian Academy of Science Jordan Stamenov, MAGIC collaboration meeting. April 6, 2005 .*

*8th Hvar Astrophysical Colloquium, Dynamical Processes in the Solar Atmosphere; Daria Marichich, Ashot Chilingaryan and Dragan Rosa. September 24-29, 2006.*

*Visit of US children to CRD. June 2006.*

*Ashot Chilingaryan and COSPAR President Rene Bonnet, Committee on Space Research 36th Scientific Assembly Paris, France. 18 - 25 July 2004*

*Ashot Chilingaryan, Haroutun Vapourchyan, Anahid Yeremyan and Joe Dagdigyan, celebration of The Armenian Engineering and Scientists of America-Michigan Section (AESA-Mth anniversary, DetI) 10roit, US. Oct 28, 2007.*

*European Cosmic Ray conference in Athens, Ashot Chilingaryan, Karen Arakelyan and Aram Yeghikyan. September 15, 2007.*

*The chair of the European Cosmic Ray symposium board Sir Arnold Wolfendale and Ashot Chilingaryan, Thunderstorms and Elementary Particle Acceleration (TEPA) meeting in Nor Amberd. September 11, 2008.*

*SNRS delegation in Nor Amberd with officials of State Committee of Science. June 27, 2008*

*Hrachik Torosyan, Ashot Barsegyan, Erik Mamidjanyan, Aelita Danagulyan, Joint Institute of Nuclear Research (JINR) Director Aleksej Sisakyan, Ashot Chilingaryan and Lebedev Physical Institute Director Yuri Moroz. September 7, 2008.*

*Ashot Chilingaryan and Manfred Fleischer, Deputy research Director, DESY. September 2008*

*Ashot Chilingaryan and world-renowned sculptor Arto Chakmakjian, visiting Montreal for COSPAR meeting. July 22, 2008.*

*International Heliophysical Year 2007 Workshop (UN/ESA/NASA/JAXA Workshop), Sozopol, Bulgaria, Karen Arakelyan, Aram Yeghikyan, Armen Hoivhannisyan, Gagik Hovsepyan, Ashot Chilingaryan , Tigran Karapetyan with senior scientist of the UN office of outer space Hans Huboldt and Jadranka Rosa from Zagreb observatory. 2-6 June, 2008.*

*Visit of the International expert commission to Aragats, Ashot Chilingaryan , Johannes Knapp, Albrecht Wagner, John Ellis. Armen Hovhannisyan, Bagrat Mailyan, Levon Vanyan . July 25, 2009.*

*Felix Aharonyan and Ashot Chilingaryan. April, 2009.*

*Yuri Oganessian, Ashot Chilingaryan and Aleksej Sisakyan in Nor Amberd. April 22, 2009.*


*International Cosmic Ray conference in Lodz, Poland, Ashot Chilingaryan and Anatoly Petrukhin, Russian Nuclear University MEFI. May 24, 2009.*

*UK-RF Closed Nuclear Cities Partnership (CNCP) delegation in YerPhI. May 5, 2009.*

*Armenian technicians working in DESY (preparing OLYMPUS experiment foundation), Hamburg, Samvel Kazaryan, Ashot Chilingaryan, Gegam Rostomyan, Tatul Karapetyan, Ashot Bagdasaryan, Mafred Fleischer. April 2009.*

*Neutron Monitor Data Base (NMDB) meeting in Kiel, Germany, Rainer Hippler, the INTAS project coordinator ("Solar and galactic cosmic ray particle acceleration and modulation"), Greifswald University, Lev Dorman, Tel-Aviv University, Erwin Flückiger, Bern University, Ashot Chilingaryan. 3-5 December, 2008.*

*Lecture. Yerevan, August 2009.*


*Lecture. Yerevan, August 2009.*

*Seminar in Tel-Aviv University. January 5, 2010.*

*Prof. Michail Panasyuk, director of the Skobeltsyn Institute of Nuclear physics, Moscow State Univ.; Prof. Gerald Fishman, NASA-Marshall Space Flight Center, Huntsville, Alabama; Prof. Ashot Chilingarian, director of Artem Alikhanyan National Laboratory; Sir Arnold Wolfendale, Royal astronomer, Great Britain at the Aragats cosmic ray research stations standing near the new measurement set up to detect elementary particles from thunderstorm clouds (TEPA-2010 conference).*


*Visit to Thomas Jefferson National Accelerator Facility in 2010. Bogdan Wojtsekhowski and Ashot Chilingarian.*


*Geneva, 2012.*

*Bagrat Mailyan, Gagik Hovsepyan, Levon Vanyan, Ashot Chilingaryan and Nikolaj Bostanjyan, the team received the Armenia president award in Physics: High Energy Phenomena in the Thunderstorm Atmosphere (2013)*


*2017 Cambridge Science Festival (MIT), Panel discussion: new perspectives: Lightning, Ckoud electrification, Climate change, and Natural accelerators, moderator Dr. Mike Wankum and Ashot Chilingarian;*

*Ashot Chilingaryan. Yerevan 2016.*

*After lecture in Worcester Polytechnic Institute, MA, US*

*N. Akopov, A.Chilingarian, meetings in MAGATE, 2016*

*Armenian delegation at AGU 2018 fall meeting: B. Mailyan, H. Mkrtchyan, A. Saroian, A. Chilingarian; 12.12.2018*